Methods in Molecular Biology 1665

Springer Protocols

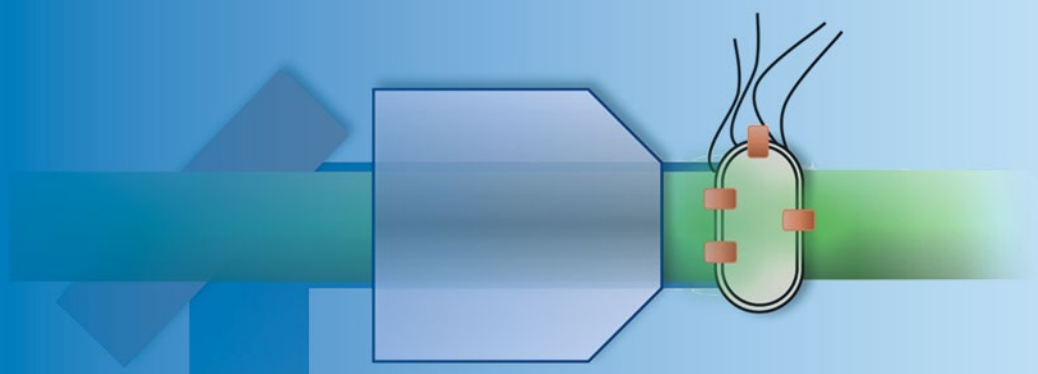

Erwin J. G. Peterman *Editor*

Single Molecule Analysis

Methods and Protocols

Second Edition

Humana Press

METHODS IN MOLECULAR BIOLOGY

Series Editor
John M. Walker
School of Life and Medical Sciences
University of Hertfordshire
Hatfield, Hertfordshire, AL10 9AB, UK

For further volumes:
http://www.springer.com/series/7651

Single Molecule Analysis

Methods and Protocols

Second Edition

Edited by

Erwin J. G. Peterman

Department of Physics & Astronomy, Vrije Universiteit
Amsterdam, The Netherlands

Humana Press

Editor
Erwin J. G. Peterman
Department of Physics & Astronomy
Vrije Universiteit
Amsterdam, The Netherlands

ISSN 1064-3745 ISSN 1940-6029 (electronic)
Methods in Molecular Biology
ISBN 978-1-4939-7270-8 ISBN 978-1-4939-7271-5 (eBook)
DOI 10.1007/978-1-4939-7271-5

Library of Congress Control Number: 2017950872

Printed on acid-free paper

This Humana Press imprint is published by Springer Nature
The registered company is Springer Science+Business Media LLC
The registered company address is: 233 Spring Street, New York, NY 10013, U.S.A.

Preface

Life scientists have been brought up for ages with the idea that life is driven, directed, and shaped by biomolecules, working on their own or in concert. Only over the past three decades it has become possible to study the properties of molecules in ultimate isolation: individual molecules. Technical breakthroughs in the field of sensitive fluorescence microscopy have made it possible to observe single fluorescent molecules and measure their properties. Other researchers have developed optical tweezers into a method to measure the mechanic properties of single molecules. Around the same time atomic force microscopy has been developed, with a spatial resolution good enough to resolve single biomolecules. Together, these techniques (and several other ones) have been applied more and more to the study of biologically relevant molecules, such as DNA, DNA-binding proteins, and motor proteins. These single-molecule approaches have led to new views into how biomolecules bring about biology, but also to novel insights in the way physical and statistical principles underlie the behavior and mechanism of biomolecules. By now, single-molecule tools are slowly becoming commonplace in molecular biophysics, biochemistry, and molecular and cell biology. This is not only thanks to their success, but also thanks to their accessibility: in the beginning these tools were solely developed and custom-built by (bio)physicists, and now commercial tools are becoming available. We foresee that this trend will prevail and single-molecule tools will play an even more prominent role in molecular biology.

The aim of *Single Molecule Analysis* is to provide a broad overview of single-molecule approaches applied to biomolecules on the basis of clear and concise protocols. In addition, we provide a solid introduction to the most widely used single-molecule techniques. The idea is that these introductions, together with the protocols, provide enough basis for nonspecialists to make the step to single-molecule experiments. The protocols contain a "Notes" section, in which the authors provide tips and tricks, rooted in experience, that are often decisive between failure and success.

In this second edition of *Single Molecule Analysis* several of the chapters (Chapters 1, 2, 5, 10, and 14) are updated from the first edition, while most chapters are completely new, highlighting the fast and exciting developments in the field. The volume opens with four chapters that mostly deal with optical tweezers. In Chapter 1, a general overview of the method is provided. In the next chapters, protocols of applications of optical tweezers to studies of DNA/RNA (Chapter 2), protein folding (Chapter 3), and motor proteins (Chapter 4) are presented. The second part of the volume (Chapters 5–12) deals with single-molecule fluorescence tools. First a general overview of these techniques is provided (Chapter 5), followed by protocols for fluorescent labeling of proteins (Chapter 6). In the following chapters, applications to motor proteins and membrane proteins in vivo (Chapters 7 and 8), super-resolution methods (Chapter 9), combinations with microfluidics (-Chapter 10), and the deployment of advanced fluorescence modalities like polarization (Chapter 11) and Förster resonance transfer (Chapter 12) are presented. The next part of the volume deals with atomic force microscopy (Chapters 13–15). Also this part opens with a general overview of the approach (Chapter 13), followed by protocol chapters describing applications to DNA and DNA-binding proteins, including combinations with fluorescence microscopy (Chapter 14), and applications to viruses (Chapter 15). In the following chapters of the book magnetic tweezers (Chapter 16) and tethered particle motion

(Chapter 17) are described, followed by two very new techniques acoustic force spectroscopy (Chapter 18) and centrifugal force microscopy (Chapter 19).

I have taken care to provide another broad and thorough overview of the exciting and still emerging field of single-molecule biology in this second edition of *Single Molecule Analysis*. It is unavoidable that there is some overlap between the chapters. Furthermore, it will be very likely that within a few years new techniques will emerge that are not discussed here. Nevertheless, I hope that the presented protocols will be useful to many researchers, inspire them, and help them to go single molecule!

Amsterdam, The Netherlands ***Erwin J.G. Peterman***

Contents

Part III Atomic Force Microscopy and Other Force Methods

Contributors

Jason P. Beech • *NanoLund and Department of Physics, Lund University, Lund, Sweden*

Matthieu P.M.H. Benoit • *Department of Physiology and Biophysics, Albert Einstein College of Medicine, Bronx, NY, USA*

Thierry Bizebard • *Expression Génétique Microbienne, UMR8261 CNRS/Université Paris 7, IBPC, Paris, France*

Ulrich Bockelmann • *Nanobiophysics, ESPCI Paris, Paris, France*

Yves J.M. Bollen • *LaserLaB and Department of Molecular Cell Biology, Vrije Universiteit, Amsterdam, The Netherlands*

Trusanne G.A.A. Bos • *Cell Biology, Faculty of Science, Utrecht University, Utrecht, The Netherlands*

Kathy R. Chaurasiya • *Leiden Institute of Chemistry, Leiden University, Leiden, The Netherlands*

Remus T. Dame • *Leiden Institute of Chemistry, Leiden University, Leiden, The Netherlands*

David Dunlap • *Department of Physics, Emory University, Atlanta, GA, USA*

Laura Finzi • *Department of Physics, Emory University, Atlanta, GA, USA*

Joachim Fritzsche • *Chalmers University of Technology, Gothenburg, Sweden*

Laurent Geffroy • *Nanobiophysics, ESPCI Paris, Paris, France*

Arne Gennerich • *Department of Anatomy and Structural Biology and Gruss-Lipper Biophotonics Center, Albert Einstein College of Medicine, Bronx, NY, USA*

Małgorzata Grosbart • *Department of Molecular Genetics, Erasmus MC, Rotterdam, The Netherlands*

Maren Hülsemann • *Department of Anatomy and Structural Biology and Gruss-Lipper Biophotonics Center, Albert Einstein College of Medicine, Bronx, NY, USA*

Iddo Heller • *LaserLaB and Department of Physics and Astronomy, Vrije Universiteit, Amsterdam, The Netherlands*

Mercedes Hernando-Pérez • *Department of Structure of Macromolecules, Centro Nacional de Biotecnología (CNB–CSIC), Madrid, Spain*

Douwe Kamsma • *Department of Physics and Astronomy, Vrije Universiteit Amsterdam, Amsterdam, The Netherlands; LaserLaB Amsterdam, Vrije Universiteit Amsterdam, Amsterdam, The Netherlands*

Lukas C. Kapitein • *Cell Biology, Faculty of Science, Utrecht University, Utrecht, The Netherlands*

Daniel T. Kovari • *Department of Physics, Emory University, Atlanta, GA, USA*

Aida Llauró • *Department of Physiology & Biophysics, University of Washington, Seattle, WA, USA*

Joost van Mameren • *Institute of Physics, University of Amsterdam, Amsterdam, The Netherlands*

Pierre Mangeol • *Nanobiophysics, ESPCI Paris, Paris, France; UMR7288 CNRS/ Université Aix-Marseille, Developmental Biology Institute of Marseille (IBDM), Marseille, France*

Natalia Martín-González • *Departamento de Física de la Materia Condensada, C-3, Universidad Autónoma de Madrid, Madrid, Spain*
David P. Minde • *AMOLF Institute, Amsterdam, The Netherlands*
Fatemeh Moayed • *AMOLF Institute, Amsterdam, The Netherlands*
Mauro Modesti • *Cancer Research Center of Marseille, CNRS UMR7258, Inserm U1068, Institut Paoli-Calmettes, Aix-Marseille Université UM105, Marseille, France*
F. Moreno-Madrid • *Departamento de Física de la Materia Condensada, C-3, Universidad Autónoma de Madrid, Madrid, Spain*
Keir C. Neuman • *Laboratory of Single Molecule Biophysics, National Heart, Lung, and Blood Institute, National Institutes of Health, Bethesda, MD, USA*
Alvaro Ortega-Esteban • *Departamento de Física de la Materia Condensada, C-3, Universidad Autónoma de Madrid, Madrid, Spain*
Felix Oswald • *LaserLaB and Department of Physics and Astronomy, Vrije Universiteit, Amsterdam, The Netherlands*
Pedro J. de Pablo • *Departamento de Física de la Materia Condensada, C-3, Universidad Autónoma de Madrid, Madrid, Spain; Solid Condensed Matter Institute IFIMAC, Universidad Autónoma de Madrid, Madrid, Spain*
Fredrik Persson • *Vanadis Diagnostics, Sollentuna, Sweden*
Erwin J.G. Peterman • *LaserLaB and Department of Physics and Astronomy, Vrije Universiteit, Amsterdam, The Netherlands*
Melissa C. Piontek • *Moleculaire Biofysica, Zernike Instituut, Rijksuniversiteit Groningen, Groningen, The Netherlands*
Bram Prevo • *LaserLaB and Department of Physics and Astronomy, Vrije Universiteit, Amsterdam, The Netherlands*
Lu Rao • *Department of Anatomy and Structural Biology and Gruss-Lipper Biophotonics Center, Albert Einstein College of Medicine, Bronx, NY, USA*
Dejan Ristić • *Department of Molecular Genetics, Erasmus MC, Rotterdam, The Netherlands*
Wouter H. Roos • *Moleculaire Biofysica, Zernike Instituut, Rijksuniversiteit Groningen, Groningen, The Netherlands*
Humberto Sánchez • *Faculty of Applied Sciences, Department of Bionanoscience, Kavli Institute of Nanoscience, Delft University of Technology, Delft, The Netherlands*
Yeonee Seol • *Laboratory of Single Molecule Biophysics, National Heart, Lung, and Blood Institute, National Institutes of Health, Bethesda, MD, USA*
Hernando Sosa • *Department of Physiology and Biophysics, Albert Einstein College of Medicine, Bronx, NY, USA*
Sander J. Tans • *AMOLF Institute, Amsterdam, The Netherlands*
Roderick P. Tas • *Cell Biology, Faculty of Science, Utrecht University, Utrecht, The Netherlands*
Jonas O. Tegenfeldt • *NanoLund and Department of Physics, Lund University, Lund, Sweden*
Jaap van Krugten • *LaserLaB and Department of Physics and Astronomy, Vrije Universiteit, Amsterdam, The Netherlands*
Aravindan Varadarajan • *LaserLaB and Department of Physics and Astronomy, Vrije Universiteit, Amsterdam, The Netherlands*
Fredrik Westerlund • *Chalmers University of Technology, Gothenburg, Sweden*
Roeland J. van Wijk • *AMOLF Institute, Amsterdam, The Netherlands*

Siet M.J.L. van den Wildenberg • *LaserLaB and Department of Physics and Astronomy, Vrije Universiteit, Amsterdam, The Netherlands; Équipe de Volcanologie, Observatoire de Physique de Globe, Clermant-Ferrand, France*

Wesley P. Wong • *Program in Cellular and Molecular Medicine, Boston Children's Hospital, Boston, MA, USA; Department of Biological Chemistry and Molecular Pharmacology, Harvard Medical School, Boston, MA, USA; Wyss Institute for Biologically Inspired Engineering, Harvard University, Boston, MA, USA*

Gijs J.L. Wuite • *LaserLaB and Department of Physics and Astronomy, Vrije Universiteit, Amsterdam, The Netherlands*

Claire Wyman • *Department of Molecular Genetics, Erasmus MC, Rotterdam, The Netherlands; Department of Radiation Oncology, Erasmus MC, Rotterdam, The Netherlands*

Yan Yan • *Department of Physics, Emory University, Atlanta, GA, USA*

Darren Yang • *Program in Cellular and Molecular Medicine, Boston Children's Hospital, Boston, MA, USA; Department of Biological Chemistry and Molecular Pharmacology, Harvard Medical School, Boston, MA, USA; Wyss Institute for Biologically Inspired Engineering, Harvard University, Boston, MA, USA*

Part I

Optical Tweezers

Chapter 1

Introduction to Optical Tweezers: Background, System Designs, and Commercial Solutions

Joost van Mameren, Gijs J.L. Wuite, and Iddo Heller

Abstract

Optical tweezers are a means to manipulate objects with light. With the technique, microscopically small objects can be held and steered, while forces on the trapped objects can be accurately measured and exerted. Optical tweezers can typically obtain a nanometer spatial resolution, a picoNewton force resolution, and a millisecond time resolution, which makes them excellently suited to study biological processes from the single-cell down to the single-molecule level. In this chapter, we will provide an introduction on the use of optical tweezers in single-molecule approaches. We will introduce the basic principles and methodology involved in optical trapping, force calibration, and force measurements. Next we describe the components of an optical tweezers setup and their experimental relevance in single-molecule approaches. Finally, we provide a concise overview of commercial optical tweezers systems. Commercial systems are becoming increasingly available and provide access to single-molecule optical tweezers experiments without the need for a thorough background in physics.

Key words Optical tweezers, Optical trap, Radiation pressure, Single molecule, Trap stiffness calibration, Force spectroscopy, Instrument design, Commercial optical tweezers, Molecular motors, DNA–protein interactions

1 Introduction

1.1 History of Optical Tweezers

At the heart of optical tweezers techniques is the interaction between light and matter. The minute forces that are generated in this interaction can be used to displace and trap microscopic objects. In 1970, Ashkin laid the foundations for present-day optical tweezers techniques. At Bell labs, Ashkin observed that micron-sized latex spheres (beads) were attracted toward the center of an argon laser beam of a few mW power [1]. It is this attractive force that makes optical trapping possible. Ashkin also observed, however, that the laser light scattered and propelled the beads forward. By using two counter propagating beams he managed to avoid forward propulsion, and thus created the first stable optical trap for beads suspended in water. It was not until 1986 that Ashkin

Erwin J.G. Peterman (ed.), *Single Molecule Analysis: Methods and Protocols*, Methods in Molecular Biology, vol. 1665, DOI 10.1007/978-1-4939-7271-5_1,

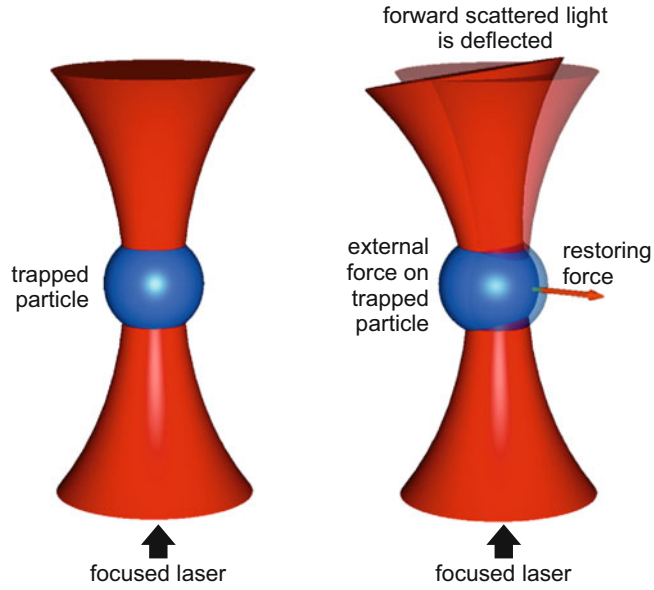

Fig. 1 Schematic of optical trapping. *Left*: a tightly focused laser beam (*cone*) attracts refractive objects (*dark sphere*) such as glass beads, nanoparticles, or even whole cells to its focus. *Right*: external forces pushing or pulling on the particle slightly displace it from the center of the focus, leading to a slight deflection of the forward scattered laser light. This deflection forms the basis for quantitatively detecting the forces and displacements experienced by the trapped object

together with Chu and others demonstrated the present form of *optical tweezers* that uses a single, *tightly focused* laser beam to stably trap particles—of diameters between 25 nm and 10 μm—in three dimensions (*see* Fig. 1, left) [2]. Later on, Chu and others used techniques inspired by optical tweezers to trap and cool atoms, which brought him the 1997 Nobel Prize in physics [3, 4].

1.2 Optical Tweezers in Biology

Currently, optical tweezers have found widespread applications in biology [5–8]. One of the important reasons for the success of optical tweezers in biology is that it provides biological scientists with "microscopic hands" to manipulate biological objects and feel or exert forces, yet with the same low level of invasiveness as light microscopy techniques. Furthermore, the length scales, time scales, and force scales accessible to optical tweezers are biologically relevant from the single-cell down to the single-molecule level. In 1987, Ashkin presented the first applications of optical tweezers in biology by manipulating individual viruses and living bacteria [9]. By a correct choice of laser power and wavelength, photodamage to biological samples could be minimized, which allowed trapping and manipulation of single living cells [10]. Since the late eighties, optical tweezers approaches have been extended down to

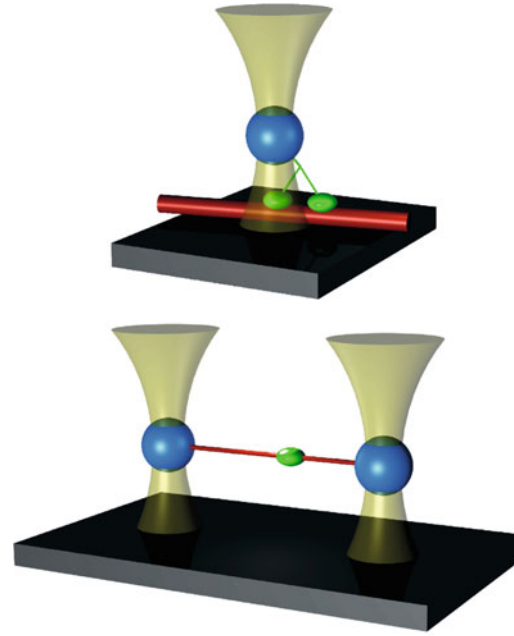

Fig. 2 Prototypical single-molecule optical tweezers assays. *Top*: a single kinesin motor protein bound with its two heads to an optically trapped bead moves along a surface-immobilized microtubule track. Its 8-nm steps, the forces exerted and the mechanics of the stepping has been elucidated in such assays. *Bottom*: DNA suspended between two optically trapped beads

the single-biomolecule level [11–22]. In these single-molecule studies, the biomolecules of interest are not themselves trapped directly, but are manipulated through optically trapped microbeads that act as handles and force transducers. A large fraction of this single-molecule work includes the study of the activity of individual motor proteins [11, 15, 22]. With optical tweezers, the motion and forces generated by these motor proteins have been studied and controlled to reveal their dynamics and energetics (Fig. 2, top). Another important area of research includes the study of biopolymers such as DNA [7, 14, 18, 23, 24]. In these experiments, the DNA molecule is attached to one or more optically trapped beads, which allows stretching the molecule and studying its mechanical properties through force spectroscopy (Fig. 2, bottom). In addition, this layout has been used to study proteins and DNA–protein interactions [13, 17, 21, 25–27]. A wide range of DNA–protein interactions affects the structure of DNA, and thus the (force-dependent) length of the DNA molecules. In optical tweezers these length changes can be observed by measuring the displacements of the microbeads. Examples include the study of DNA-binding proteins and the activity of DNA and RNA polymerases.

Over the last decade, the impact of optical tweezers in biology has further expanded due to their integration with other experimental techniques. This includes their combination with multichannel microfluidics, which not only enhances experimental throughput but also provides in-situ control of more complex multistep biological processes [28, 29]. Most notably, the combination of optical tweezers with the rich arsenal of fluorescence techniques has enabled optical tweezers analyses to venture far beyond strictly mechanical measurements [8, 28, 30].

With the advent of commercial optical tweezers systems in recent years, this powerful single-molecule technique is approaching maturation and is becoming more and more accessible to a wide range of biological scientists. As with the development of commercial fluorescence and AFM techniques, it is to be expected that commercial optical tweezers will greatly contribute to our knowledge of biology on the single-molecule level. As a final motivation to read more about optical tweezers: in an interview with Physics Today, Nobel Prize winner Steven Chu said that he would not be surprised if in the coming decennium another Nobel Prize would be attributed to groundbreaking discoveries in molecular biology facilitated by optical tweezers or other single molecule techniques [31].

2 Principles of Optical Tweezers Techniques

The basic physical principle underlying optical tweezers is the radiation pressure, exerted by light when colliding with matter. For macroscopic objects, the radiation pressure exerted by common light sources is orders of magnitude too small to have any measurable effect: we do not feel the light power of the sun pushing us away. However, for objects of microscopic dimensions (<100 μm) the radiation pressure of high-intensity light sources is sufficient to facilitate optical trapping.

2.1 Forces in an Optical Trap

When photons enter an object that has a different refractive index than its surrounding medium, part of the momentum of the photons can be transferred to this object. This transfer of momentum is the physical principle that underlies optical trapping (*see* Fig. 1, right). The forces exerted by photons on an optically trapped object can be divided into two components: the scattering force that pushes the object away from the light source, and the gradient force that pulls the object toward the region of highest light intensity. The correct physical description of optical trapping depends on the size d of the trapped object in comparison to the wavelength λ of the trapping light. In the regime $d \gg \lambda$ one speaks of the "ray-optics" regime, while the regime where $d \ll \lambda$ is called the Rayleigh regime. In biological experiments where micrometer-sized objects are trapped, the correct description is often in between

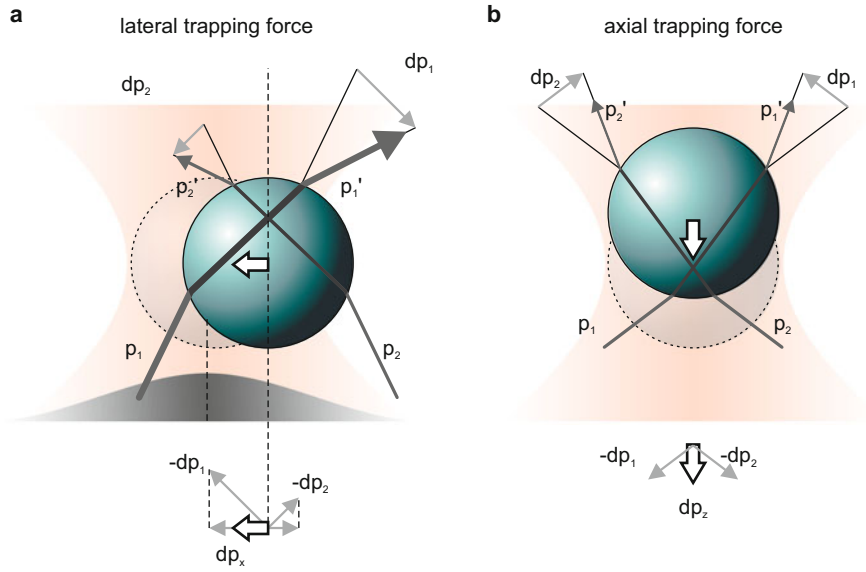

Fig. 3 Forces on an optically trapped particle in the ray-optics regime. (**a**) Lateral gradient force of a Gaussian laser beam profile. (**b**) Axial gradient force towards the focus of the trapping light. The *white arrows* indicate the net restoring force. Note that the scattering component due to reflection by the particle is not indicated

these two regimes, such that neither description is quantitatively accurate. To provide a qualitative understanding of optical trapping, we will here describe the forces in the more intuitively interpretable ray-optics regime. In the ray-optics regime, the trapping force can be understood in terms of refraction of light rays between media with different indices of refraction [32]. Figure 3 qualitatively depicts the origin of the trapping forces in this regime. The lateral gradient restoring force (Fig. 3a) can be understood as follows. If rays p_1 and p_2 have different intensity, the momentum changes of these rays (Δp_1 and Δp_2, respectively) differ in magnitude, causing a net reaction force on the refracting medium in the direction of highest intensity. The x-projection of this force, Δp_x, tends to counteract a displacement from the laser beam axis, pulling the particle toward the center of the beam. The axial gradient force is similarly caused by momentum transfer upon refraction, resulting in a restoring force towards the focus, as in Fig. 3b. The scattering force (not depicted) would cause the object to be propelled out of the focus, along the positive z-direction. The object is stably trapped only if the scattering force along the positive z-direction is compensated by the gradient force along the negative z-direction. To achieve this, a significant fraction of the incident light should come in at large angles, calling for a tightly focused trapping light source, typically obtained by using a microscope objective.

2.2 Trap Stiffness

An optical trap forms a three-dimensional potential well for the trapped particle. The particle experiences an attractive force toward the potential minimum, which is located at a stable position where the trapped particle experiences no net force. Close to the potential minimum the trap can be approximated to be harmonic, e.g. the attractive force F is directly proportional to the displacement x of the particle according to Hooke's law: $F = -kx$. Here, the spring constant κ has units [N/m] like a mechanical spring, and represents the stiffness of the optical trap. Knowledge of the trap stiffness allows accurate quantification of the external forces acting on a trapped particle from a measurement of the particle's displacement. The trap stiffness, however, is a complex function of the intensity profile and wavelength of the laser, the shape and size of the particle, the indices of refraction, and other parameters, and is difficult to calculate from first principles. Therefore, the trap stiffness is commonly determined by performing calibration experiments. Using a laser of 1 W, the typical trap stiffness that can be obtained in a single-beam optical trap is in the order of 100 pN/μm.

2.3 Principles of Trap Calibration

To allow quantitative measurement of the forces on optically trapped particles, several calibration methods to measure the trap stiffness have been developed.

Drag force calibration: The simplest way to calibrate an optical trap is to apply an external force of known magnitude and measure the displacement of the trapped particle. The external force is typically generated by inducing a fluid flow. The drag force by a fluid (viscosity η, flow velocity v) on a spherical bead of diameter d is given by Stokes' law: $F = \gamma v$, where γ is the drag coefficient $\gamma = 3\pi\eta d$. The fluid drag displaces the bead from the center of the trap until the drag force is opposite and equal to the restoring force from the optical trap, which yields $k = \gamma v/x$. The trap stiffness can thus be obtained by measuring the displacement, x, of a bead of known size due to the fluid flow of a liquid with known viscosity and velocity.

Brownian motion calibration: Another, more accurate calibration procedure is based on the Brownian motion of a bead in an optical trap, caused by the continuous and random collisions with solvent molecules. The stiffness of an optical trap can be calibrated by recording the power spectrum of the displacement fluctuations of a trapped bead of known size, as shown in Fig. 4. The power spectrum $S_x(f)$ describes how the power of these displacement fluctuations is distributed in frequency f, and is found to have a Lorentzian shape [33]:

$$S_{\mathrm{x}}(f) = \frac{k_{\mathrm{B}}T}{\gamma\pi^2\left(f_{\mathrm{c}}{}^2 + f^2\right)},$$

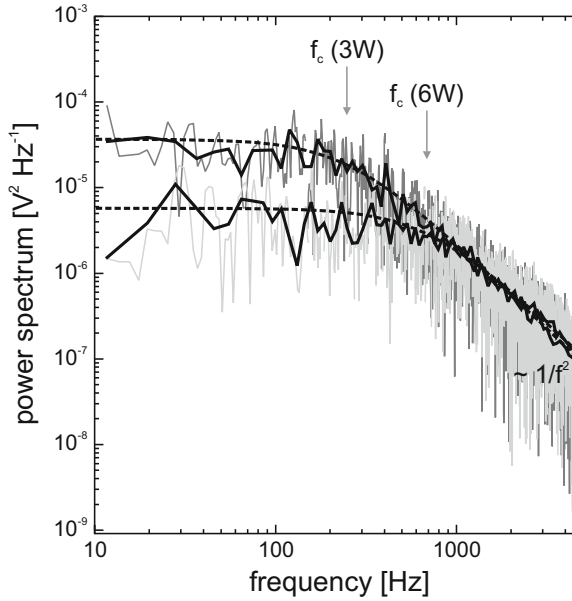

Fig. 4 Power spectra representative of the positional fluctuations of a particle trapped at different laser powers. A 1 μm diameter polystyrene bead is held in an optical trap, while the displacement signal in volts is sampled at 195 kHz. The graph shows power spectra of the displacement signal at 3 W (*dark gray*) and at 6 W (*light gray*) laser power. Both the downward shift of the low-frequency plateau S_0 and the upward shift of the corner frequency f_c (see *arrows* at 250 and 650 Hz, obtained from Lorentzian fits) for the stiffer 6 W trap can clearly be observed

where $k_B T$ is the available thermal energy. The power spectrum exhibits a characteristic corner frequency $f_c \equiv \kappa/2\pi\gamma$, which is proportional to the trap stiffness. Figure 4 shows that at low frequencies $f \ll f_c$, the power spectrum is roughly constant, $S_x(f) = S_{x,0} = 4\gamma k_B T/\kappa^2$. At high frequencies $f \gg f_c$, however, the power spectrum falls off like $1/f^2$, which is characteristic of free diffusion. The inverse of the corner frequency represents the time response of the optical trap, which is typically in the order of 1–0.1 ms. For shorter time scales, the particle does not 'feel' the confinement of the trap, which means that behavior of biological systems at time scales more rapid than this response time cannot be detected by the optical tweezers. The two power spectra of Fig. 4, acquired at two different trap stiffness values, illustrate that when a higher trap stiffness is used (i.e. by increasing the laser power), the bead fluctuations at low frequencies are reduced, and the time response of the optical trap increases. On the other hand, a higher trap stiffness implies smaller bead displacement at a given force, which implies that there is not necessarily an improvement in signal-to-noise ratio at elevated trap stiffness [34]. Typical parameters to consider for improving the signal-to-noise ratio in force

or distance measurements include: using a stiff tether (e.g. short DNA molecule or elevated tension) and/or time averaging the measurement signal. Using small beads can be of additional benefit: the faster fluctuations of small beads are more effectively filtered out by time averaging than those of large beads. Large beads, on the other hand, have the advantage that the trapping laser is focused inside the bead, where it is far away from biomolecules of interest such that potential photo-damage can be minimized.

It is important to note that, in practice, the detector used to determine the bead position reads *uncalibrated* displacement fluctuations $u(t)$ (i.e., as some voltage rather than as a displacement in nanometers). The response of the detector R, which has units m/V, relates the displacement to $u(t)$ as $x(t) = Ru(t)$. To fully calibrate an optical trap, the power spectrum of the uncalibrated displacement fluctuations $S_u(f)$ is fitted with a Lorentzian:

$$S_u(f) = \frac{S_{u,0} {f_c}^2}{\left({f_c}^2 + f^2\right)}.$$

Once the parameters $S_{u\,,\,0}$ and f_c are obtained, the trap stiffness can be calculated using.

$$\kappa = \frac{2k_B T}{\pi S_{u,0} f_c} \text{ or } \kappa = 2\pi\gamma f_c,$$

and, providing the bead diameter and solvent viscosity are known, the detector response can be calculated using.

$$R = \left[\frac{k_B T}{\pi^2 \gamma S_{u,0} {f_c}^2}\right]^{1/2} \overset{25^\circ C}{=} \left[\frac{5.0 \times 10^{-20} \mathrm{m^3 s^{-1}}}{S_{u,0} {f_c}^2 d}\right]^{1/2}.$$

Finally, to convert uncalibrated displacement data to forces, the displacement signal should be multiplied by R and the trap stiffness, such that, $F = \kappa x = \kappa R u$.

3 Optical Tweezers Systems

An optical tweezers setup consists of various dedicated components. In this section, we discuss the role of these components in optical tweezers function and performance. Below, we divide and discuss the components in five groups: the trap, the environment of the trap, trap steering, position and force detection, and the environment of the setup. In addition, we also discuss the ability to combine optical tweezers with other techniques, and the different optical trapping assays that are typically used in biological experimentation. For illustration, Fig. 5 shows the schematic layout of an optical tweezers setup that combines two steerable optical traps with fluorescence microscopy.

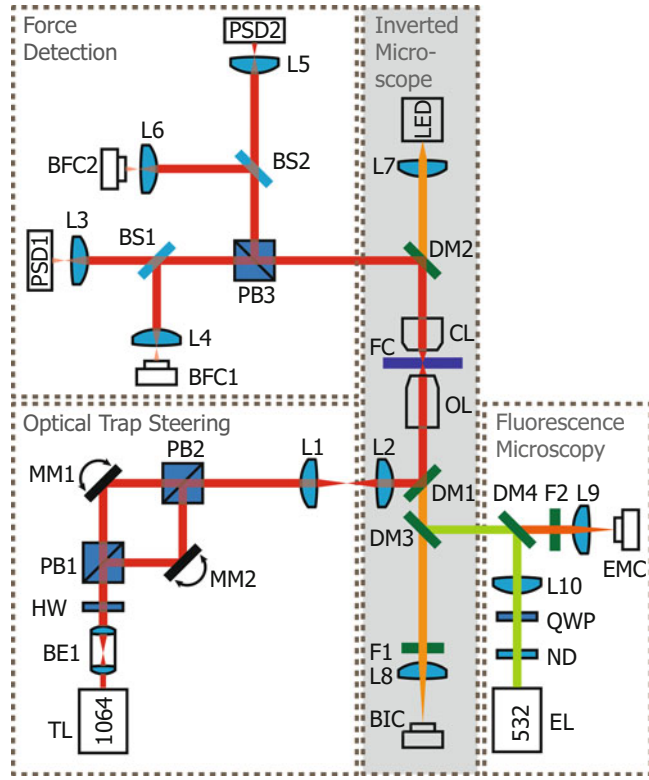

Fig. 5 Optics layout of a typical optical tweezers—fluorescence instrument. The various parts of the system as described in the text are bounded by *dashed boxes*. The optics are divided into four functional units: in the Optical Trap Steering Unit, two continuously illuminated optical traps are created from a high-power 1064 nm trapping laser (TL) using polarizing beamsplitter cubes (PB1–2) and a half-wave plate (HW). Each trap is steered using a dedicated motorized mirror (MM1–2) located in planes conjugate to the back-focal plane of the objective lens (OL). Beam expander BE1 allows changing the collimation of the traps and change their axial position. In the Force Detection Unit, two position sensitive detectors (PSD1–2) monitor the force and displacement of two orthogonally polarized traps. The Inverted Microscope Unit is based on a commercial microscope body and uses a point-source LED to illuminate the sample plane that is imaged on a bead imaging camera (BIC). The Fluorescence Microscopy Unit consists of a simple wide-field layout where an excitation laser (EL) illuminates the sample while the fluorescence signal is imaged onto an EMCCD (EMC). Diagnostic tools added include the two cameras that image the condenser's back-focal plane (BFC1,2). *BS* beam splitter, *CL* condenser lens, *FC* flow cell, *L* lens, *ND* neutral density filter, *QWP* quarter-wave plate

3.1 The Optical Trap

At the heart of every single-beam optical tweezers instrument is the *microscope objective*, which creates a tight focus to form a stable optical trap. Tight focusing implies that a significant fraction of the incident light comes in at large angles, such that the scattering force is overcome by the gradient force. The maximum incidence angle of

the light Θ_{max} is determined by the numerical aperture (NA) of the objective used to focus the laser beam. This is a measure for the solid angle over which the objective lens can gather light and is defined as: NA = n sin Θ_{max}, where n is the refractive index of the immersion medium (i.e., the medium between the objective lens and the sample) and Θ_{max} is one-half the angular aperture. The value of n varies between 1.0 for air and ~1.5 for most immersion oils. For typical oil-immersion objectives, an NA of 1.4 corresponds to a total acceptance angle of the objective of about 130°. To obtain a stable three-dimensional optical trap, the laser beam entering the objective has to be wide enough to fill or overfill the back aperture of the objective. This way, one provides sufficient convergent, high-angle rays that contribute to counteracting the scattering force.

The maximum forces that can be exerted by an optical trap can be enhanced by either increasing the laser power, or by optimizing the quality of the focal spot of the laser and the refraction of the laser by the trapped particle (i.e., choosing the proper optics and materials with proper optical densities; see below). The laser power can only be increased up to a certain limit, above which more laser light would lead to heating or photodamage of the examined system (often delicate biomaterials), or even of the optics in the instrument [35]. Therefore, care must be taken to optimize the quality of the focal spot of the trapping laser. The difference in refractive index of the trapped object n_2 compared to that of the surrounding medium n_1 determines how strongly the incident rays are refracted and, consequently, how strong the trapping force is. The required balance between gradient and scattering forces yields an optimal refractive index of $n_2 = 1.69$ [5]. One often uses silica (glass) particles ($n_2 = 1.37$–1.47) or polystyrene particles ($n_2 = 1.57$). The trapping forces that can be obtained for polystyrene particles are thus higher. When using an oil-immersion objective, the refractive index of the immersion oil matches both that of the objective lens and that of the glass of the sample. Therefore, the maximum NA can be achieved with oil-immersion objectives. However, due to the refractive index mismatch between the sample glass and the buffer, spherical aberrations deteriorate the quality of the laser focus when the distance of the focus to the sample surface increases (optical trapping in water with oil immersion objectives is typically performed within several tens of micrometers of the glass surface) [36]. To allow equally stable trapping at any distance to the surface, water-immersion objectives are often used. Despite the fact that the NA is somewhat compromised (typically NA = 1.2 for water immersion objectives), the ability to move away from the sample surface without lowering the trap quality can be a good reason to use water-immersion objectives [37].

For optical trapping, single-mode continuous wave lasers with a Gaussian beam profile (i.e. operated in the lowest, TEM_{00}, mode) are commonly used. The laser power typically ranges from a few

hundred milliwatts up to several watts. Important properties of the laser for stable trapping are low-intensity fluctuations and high pointing stability (little angular and transverse wandering of the beam). Of particular interest for biological experiments is the wavelength. Since the light intensity at the focus is very high, heating and damage through light absorption by the often delicate biological material needs to be considered. Near-infrared lasers (800–1200 nm, most often the 1064-nm line from diode-pumped solid state lasers) are typically used, because of the low absorption of biological material as well as water in this spectral range [5].

Although in current biological applications optical traps are most commonly formed by tightly focusing a single laser beam [2], the first stable optical trap was accomplished in 1970 by using two counter propagating focused laser beams [1]. The counter propagating layout does not require tight focusing, such that low NA (<1) objectives, or no objective at all may be used. Advantageously, this allows for a larger working distance and lower local light intensity at the trap, making it useful to handle living cells. The "optical stretcher," designed to probe the deformability of individual cells, is a key example of this approach [38].

3.2 Environment of the Trap

Microfluidics: To ascertain well-controlled experimental conditions in single-molecule experiments, it is often useful—if not required—to implement a way to bring the biochemical "ingredients" together under the microscope. The use of microfluidics allows for a fine control over this process by fluid flow of minute volumes of the solutions used. In addition, microfluidic control allows for drag force calibration of the trap, as well as flow stretching of biopolymers such as DNA [30]. An alternative way to induce viscous drag is by moving the fluid reservoir with respect to the trap using a motorized microscope stage. Particularly useful is the combination of either a motorized or a piezoelectric stage with a multichannel laminar flow cell. The laminar flow ensures that different buffer flows can be in contact with each other with minimal buffer mixing. By moving the stage to change the position of the trapped beads in the microfluidic device, the buffer conditions can be rapidly and completely exchanged between the regions of different buffer flow. This facilitates in-situ control of more complex multistep biological processes and it enhances experimental throughput Brewer et al. extensively reviewed the use of microfluidics devices in single-molecule experiments [29].

Temperature control: In biological experiments, temperature often plays an important role. As in conventional microscopy, temperature controlled fluidics, stages, and objectives can be used to control the temperature at which biological processes take place. In optical tweezers experiments, temperature control of the objective is, in particular, considered. Objectives with short focal lengths, required to obtain a tight focus, are necessarily in close contact with

the trapping region through the immersion medium, and act as an effective heat sink. Moreover, apart from the relevance for the temperature of the biological system, temperature control of the objective can be beneficial for the performance of the optical tweezers as well. The high laser intensities in optical trapping may produce heating of the optical components, thus causing optical drift, increased stabilization time, and/or decreased spatial resolution. A milliKelvin temperature-stabilized objective has been employed to obtain base pair resolution in optical tweezers experiments on DNA [39]. Finally, judicious design and analysis of the experiment is required when large temperature fluctuations are anticipated. Among other issues, the reliability of (real-time) calibration of optical tweezers using Brownian fluctuations is impacted by significant temperature fluctuations.

3.3 Position and Force Detection

The key to quantitative optical trapping is the accurate detection of the position of the particle in an optical trap. Within the volume of the laser focus, the displacement of the particle from its equilibrium position is directly proportional to the forces acting on this particle. Several techniques have been developed for sensitive position detection, which are discussed below.

Lateral position and force detection: The simplest position-detection scheme relies on video-based imaging of a bead in the optical trap. Using centroid-tracking or template-matching algorithms, the position of one or multiple beads can be obtained with sub-pixel resolution (down to several nanometers) either by offline or online digital video analysis [40, 41]. Although video-based position detection is simple and direct, it is limited in time resolution by the video acquisition rate (from typically 25 up to 100 Hz with faster camera's). More dedicated imaging techniques where one bead is directly imaged on a position sensitive detector (PSD) or quadrant photodiode (QPD) provide a higher time resolution, but require high magnifications and are thus limited in range and signal-to-noise ratio [42, 43]. Besides allowing the calculation of the active forces in a biological system when the trap stiffness is known, imaging also provides spatial information on the studied system; observation of the absolute position of beads in the camera's field of view can provide information on the length scale of a biological system, such as a stretched biopolymer between two beads, or the motion of a molecular motor through the field of view, independent of the optical trapping (cf. Fig. 2).

The highest time resolution (~μs) and spatial resolution (~pm) is currently obtained with laser-based interferometry techniques for position detection. Currently, the most common position detection scheme is back-focal-plane interferometry [44, 45]. Here, the interference between unscattered and forward-scattered light of a laser beam focused on a bead is used to provide positional information in the two lateral dimensions. By imaging the intensity

distribution in the back focal plane of a condenser lens on a QPD or PSD, the recorded signals are rendered insensitive to the location of the trap in the field of view. A major advantage of these interference techniques is that the trapping laser can be used to perform trapping and position detection simultaneously. In this situation, the detection and trap are intrinsically aligned and only relative displacements of the bead with respect to the trap are measured. Displacements of typically up to a few hundred nanometers away from the center of the optical trap are directly proportional to the measured shift on the photodiodes in this configuration. On top of this, simultaneous video analysis of optical images can still be used to measure absolute positions and distances in the studied system.

Axial position detection: True three-dimensional position detection allows tracking the (suppressed) Brownian motion of the trapped particle and thereby fully quantifying the forces felt by the object in the optical trap. This can be accomplished by combining axial position detection with the abovementioned lateral position detection techniques. The axial position of trapped particles has been detected by using fluorescence methods, by performing template-based analysis of bead images (as is often done in magnetic tweezers [46] experiments or acoustic force spectroscopy [47], *see* Chapters 16 and 18, respectively), by measuring the forward scattered light intensity, or by using non-imaging interference methods [6]. The non-imaging axial interference method, in which modulations in the total laser intensity are detected in the back focal plane of the condenser, is most practical since it is accurate as well as easily combined with lateral interference-based detection. Contrary to lateral detection, the best axial sensitivity is obtained when only the low-NA fraction of the light is detected [48].

3.4 Trap Steering

If microscope stage movements do not provide enough flexibility to manipulate trapped objects, the trapping beam itself can be steered through the sample. This is particularly useful for steering multiple traps. Lateral trap movement can be achieved by changing the incoming angle of the trapping beam into the objective, while axial movement is effected by changing the level of collimation of the beam.

In practice, such three-dimensional trap steering can be accomplished by moving the lenses in a telescope in front of the objective. Alternatively, the use of tip-tilt or galvanometric mirrors, for which accurate and reproducible positioning can be obtained through closed-loop feedback systems, allows rapid lateral trap movement up to several kHz. Finally, trap steering can also be accomplished using acousto-optical deflectors (AODs) and electro-optical deflectors (EODs). These provide higher scanning speeds up to the MHz range, but typically have more limited ranges. Additional drawbacks

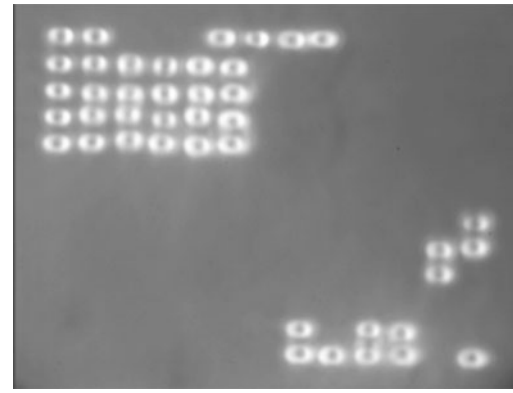

Fig. 6 Microscopy image of the time-shared optical trapping of 42 beads using AODs. This image demonstrates the smallest game of *Tetris* ever played. The corresponding video can be found online at https:/www.youtube.com/watch?v=jCdnBmQZ6_s

are the lower throughput efficiency and inhomogeneous diffraction of AODs and the high costs of EODs.

To avoid nonlinearities in the lateral trap steering, it is important to place the steering elements in the setup such that the angular deflection from the optical axis originates in planes conjugate to the back-focal plane of the objective. Otherwise, the transmitted laser power and therefore the trap stiffness will be dependent on the position in the sample. Finally, it is important to realize that trapped objects are limited in manipulation speed. Viscous drag will cause the trapped particle to escape from the trap at high steering speeds.

If scanned across multiple positions, galvanometric-mirrors and the even faster AODs, AOMs or EODs can be used to generate multiple traps from a single laser source (*see* Fig. 6). If the laser is scanned rapidly enough, a trapped particle may not sense the transient absence of the optical trap when at the other scanned positions. This way of generating multiple traps is called trap multiplexing or "time-sharing." In contrast to time-shared trapping, continuous trapping generates optical traps that are stable over all time scales. Time-shared optical traps, on the other hand, provide more flexibility in the number of traps, but typically require additional feedback-electronics to compensate for deflection-dependent variations in trap stiffness. An alternative approach to generate multiple traps from a single laser line is provided by diffractive optical elements such as spatial light modulators (SLMs). Multiple trap generation and steering in this case rely on the holographic pattern that causes the incident laser to diffract into separate foci in the sample. Holographic schemes based on SLMs are constrained in straightforward use of interferometric position and force sensing schemes.

3.5 Environment of the Setup

To ensure stability and high spatial resolution, the environment of the optical tweezers setup needs to be well controlled. Common precautions include the use of passively damping optical tables, and temperature stabilization within 0.5–0.1 K. Convection of the air in the optical pathway can induce beam deviations through local density fluctuations. These effects can be minimized either by enclosing the optical path, reducing the optical path length, and reducing the number of foci along the optical path, since the beam is more sensitive to local density fluctuations in these focal points. For the most demanding applications, optical tweezers instruments have been placed in acoustically isolated rooms with air conditioning equipment that filters out dust particles in the air. Although the ultimate resolution of a single base pair of DNA was first demonstrated using an instrument in which the ambient air was replaced by helium, the even lower refractive index of which renders the instrument less susceptible to density fluctuations of the gas, such resolution was later matched using a setup that did not replace ambient air [34, 49].

3.6 Combining Optical Tweezers with Other Techniques

Optical tweezers instruments are composed of common microscopy components and are often incorporated into commercial microscopes. This makes it attractive to combine optical tweezers, and their high level of control, with the capabilities of other optical techniques in order to study biological systems in greater detail. The design of an optical tweezers instrument, however, will directly influence its capabilities and to what extent other microscopy or related techniques can be integrated with it.

The counter propagating beams layout, for instance, which requires critical coaxial alignment, is difficult to implement in conventional microscopes, and puts strong restrictions on the optics and additional functionalities of the experimental setup. A single beam optical trap, on the other hand, requires a tightly focused laser beam for stable trapping, which in turn requires a high-NA objective lens and a suitably expanded laser beam at the input aperture. Other than that, no strong requirements are imposed on the microscope, which renders the single-beam trap the more widely used configuration.

An enabling development is the integration of sensitive fluorescence microscopy with optical tweezers [8, 30, 50–52]. The direct visualization of single molecules in controlled optical tweezers manipulation experiments has proven a powerful method for the detailed investigation of biomolecular systems, in particular for unraveling DNA-protein interactions [30, 53, 54]. In these experiments, DNA is manipulated with optical tweezers, while local and specific information on the binding and activity of proteins interacting with the DNA is directly obtained through fluorescence microscopy. Changes in DNA structure due to DNA–protein interactions or movement of proteins along DNA can thus be

simultaneously studied with force spectroscopy and fluorescence microscopy, providing a high level of versatility and unambiguity in these experiments [55]. Here, wide-field fluorescence microscopy provides robust and straightforward imaging capabilities, while confocal fluorescence microscopy allows real-time analysis of molecular activity in presence of up to two orders of magnitude higher background concentration of labeled proteins than in wide-field configuration. Furthermore, other advanced optical microscopy techniques such as polarization spectroscopy and Förster resonance energy transfer (FRET) have been successfully combined with optical tweezers [50, 56–58] New possibilities of these combinations include study of, for example, the spatial and temporal dynamics of DNA repair processes [54, 59, 60] and structure-function relationships of DNA-binding enzymes [50]. A further development involves the integration of super-resolution microscopy with optical trapping, which allows single-molecule analysis even at elevated protein densities. Such measurement allows linking idealized in vitro conditions with the dense and crowded situation in vivo [61]. Finally, fluorescence microscopy also aids analysis of mechanically less well-defined systems such as intermediate filaments [62] and membrane-based systems [63].

3.7 Optical Trapping Assays Employed in Biology

Several experimental layouts have been developed to employ optical tweezers in biology. The simplest layout consists of a single optical trap, in which particles can be manipulated and, optionally, forces between the trapped particle and its surroundings can be measured. A single optical trap has for instance been used to perform force spectroscopy on biomolecular systems that are tethered between the trap and a fixed substrate (*see* Fig. 2, top). Examples of experiments using this geometry include measurements of the mechanical and structural properties of biopolymers tethered between a trapped bead and a fixed substrate (i.e., a glass slide, or a bead held by a micropipette [17]), and measurements of the forces involved in biomolecular activity [11, 22]. This activity can be observed either directly, such as in the motion of motor proteins tethered to a trapped bead, or indirectly, by measuring structural changes in biomolecules such as DNA due to enzymatic activity.

The fixed substrate can also be replaced by a particle trapped in a second optical trap (*see* Fig. 2, bottom). In this dual trap assay, a biomolecular system tethered between two trapped beads can thus be fully suspended in solution, which prevents unwanted surface interactions. In addition, this layout suppresses noise associated with fluctuations or drift in the relative positions of the optical trap and a fixed substrate. This geometry has been employed to obtain single base pair resolution of RNA polymerase activity [49].

Finally, advanced optical trapping geometries include the use of multiple optical traps (*see* Fig. 6), which allows manipulating large biological structures, and multiple colloidal particles [64–67]. On

the single-molecule level, multiple optical traps have been used to measure interactions of multiple DNA molecules and bound proteins [25, 68] In particular in combination with fluorescence microscopy, such dual molecule experiments allow dissecting more complex molecular architectures that were previously not accessible [59].

4 Commercial Optical Tweezers Systems

The design and construction of an optical tweezers instrument can be a tedious task, requiring practical and theoretical experience in fields ranging from laser physics, optics, thermodynamics, hydrodynamics, analog, and digital electronics to computer science in order to allow some level of computer control of the instrument as well as data acquisition. In addition, the maintenance of a home-built instrument can be time-consuming as well. In view of that, it needs little explanation that many life science researchers hesitate to switch to this type of experimentation.

During the past decade, several companies have started offering commercial solutions for optical trapping experiments [31]. These solutions range from do-it-yourself kits like that of Thorlabs, Elliot Scientific, or the miniTweezers (see http://tweezerslab.unipr.it) to fully automated turn-key platforms. Most manufacturers provide instruments that can be flexibly attached or integrated into a standard research-grade inverted optical microscope. Depending on the details of the instrument, this may leave open the possibility to configure the optical microscope in order to combine optical tweezers with other microscope techniques, such as fluorescence microscopy.

A number of commercial suppliers offer optical tweezers instrumentation primarily as a micromanipulation add-on or standalone. This includes suppliers like Aresis, Elliot Scientific, Meadowlark, Molecular Machines and Industries, Thorlabs, and Zeiss. In these systems, the hardware for trap position control ranges from piezo-stages or galvanometric mirrors to AODs and holographic optical trapping. Some of these systems are integrated with microdissection equipment for controllably cutting cells or tissue such as the Zeiss PALM product series and those from Molecular Machines and Industries (MMI), which originate from the microdissection field.

Most relevant for quantitative single-molecule analyses as described in this book are accurate force-sensing optical tweezers microscopes such as the NanoTracker series from JPK Instruments and the C-Trap from LUMICKS (*see* Fig. 7). Both these systems are compatible with multichannel microfluidics and fluorescence microscopy. While the C-Trap is a complete system solution integrated with microfluidics, confocal microscopy and/or STED nanoscopy, the NanoTracker is based on a third-party inverted microscope and fluorescence microscopy hardware.

Fig. 7 *Left*: Dr. Remus T. Dame (Leiden University, The Netherlands) using his NanoTracker from JPK Instruments. *Right*: Dr. Mattijs de Groot using the C-Trap from Lumicks

When considering the purchase of a commercial optical tweezers instrument, several aspects should be kept in mind. Obviously, the first thing to define is the main application or application range for the instrument. Is the system going to be used only for manipulation, or is quantification of the forces exerted going to be useful? Do the applications demand ultra-high resolution force spectroscopy? Is fluorescence imaging required, and what level of hardware and/or software integration with optical trapping serves the biological application best? Throughput and workflow are particularly important features in single-molecule analyses that face the task of gathering large statistics on a molecule-by-molecule basis. Finally, characteristics such as workflow, throughput, and user-friendliness are best assessed in a live demonstration of the instrument.

5 Concluding Remarks

Optical tweezers techniques form an invaluable addition to the single-molecule toolkit. These minimally invasive techniques provide scientists with the ability to actively manipulate biomolecules with nanometer precision, and to measure or apply forces with (sub)picoNewton resolution. Examples of the application of these powerful tools in molecular biology include the study of active molecular motors, the mechanical properties of DNA, and the mechanochemistry of DNA–protein interactions. Commercial optical tweezers systems are becoming increasingly available, which makes this powerful and versatile technique accessible to a broad range of researchers from different backgrounds and will undoubtedly drive new biological discoveries on the single-molecule level. The following chapters will describe detailed methods and protocols of several applications of optical tweezers in molecular biology.

Competing Interest Statement: *I.H. and G.J.L.W. declare a financial interest in LUMICKS B.V. J.M. declares no competing financial interest.*

References

1. Ashkin A (1970) Acceleration and trapping of particles by radiation pressure. Phys Rev Lett 24:156–159
2. Ashkin A, Dziedzic JM, Bjorkholm JE, Chu S (1986) Observation of a single-beam gradient force optical trap for dielectric particles. Opt Lett 11:288. doi:10.1364/OL.11.000288
3. Chu S (1991) Laser manipulation of atoms and particles. Science 253:861–866. doi:10.1126/science.253.5022.861
4. Chu S (1992) Laser trapping of neutral particles. Sci Am 266:70–76
5. Svoboda K, Block SM (1994) Biological applications of optical forces. Annu Rev Biophys Biomol Struct 23:247–285. doi:10.1146/annurev.bb.23.060194.001335
6. Neuman KC, Block SM (2004) Optical trapping. Rev Sci Instrum 75:2787. doi:10.1063/1.1785844
7. Moffitt JR, Chemla YR, Smith SB, Bustamante C (2008) Recent advances in optical tweezers. Annu Rev Biochem 77:205–228. doi:10.1146/annurev.biochem.77.043007.090225
8. Heller I, Hoekstra TP, King GA, Peterman EJG, Wuite GJL (2014) Optical tweezers analysis of DNA-protein complexes. Chem Rev 114:3087–3119. doi:10.1021/cr4003006
9. Ashkin A, Dziedzic J (1987) Optical trapping and manipulation of viruses and bacteria. Science 235:1517–1520. doi:10.1126/science.3547653
10. Ashkin A, Dziedzic JM, Yamane T (1987) Optical trapping and manipulation of single cells using infrared laser beams. Nature 330:769–771. doi:10.1038/330769a0
11. Block SM, Goldstein LSB, Schnapp BJ (1990) Bead movement by single kinesin molecules studied with optical tweezers. Nature 348:348–352
12. Bustamante C, Macosko JC, Wuite GJL (2000) Grabbing the cat by the tail: manipulating molecules one by one. Nat Rev Mol Cell Biol 1:130–136. doi:10.1038/35040072
13. Davenport RJ, Wuite GJ, Landick R, Bustamante C (2000) Single-molecule study of transcriptional pausing and arrest by E. coli RNA polymerase. Science 287:2497–2500. doi:10.1126/science.287.5462.2497
14. Smith SB, Cui Y, Bustamante C (1996) Overstretching B-DNA: the elastic response of individual double-stranded and single-stranded DNA molecules. Science 271:795–799
15. Svoboda K, Schmidt CF, Schnapp BJ, Block SM (1993) Direct observation of kinesin stepping by optical trapping interferometry. Nature 365:721–727. doi:10.1038/365721a0
16. Zamft B, Bintu L, Ishibashi T, Bustamante C (2012) Nascent RNA structure modulates the transcriptional dynamics of RNA polymerases. Proc Natl Acad Sci U S A 109:8948–8953. doi:10.1073/pnas.1205063109
17. Wuite GJL, Smith SB, Young M, Keller D, Bustamante C (2000) Single-molecule studies of the effect of template tension on T7 DNA polymerase activity. Nature 404:103–106. doi:10.1038/35003614
18. Essevaz-Roulet B, Bockelmann U, Heslot F (1997) Mechanical separation of the complementary strands of DNA. Proc Natl Acad Sci 94:11935–11940. doi:10.1073/pnas.94.22.11935
19. Kellermayer MS (1997) Folding-unfolding transitions in single titin molecules characterized with laser tweezers. Science 276:1112–1116. doi:10.1126/science.276.5315.1112
20. Tskhovrebova L, Trinick J, Sleep JA, Simmons RM (1997) Elasticity and unfolding of single molecules of the giant muscle protein titin. Nature 387:308–312. doi:10.1038/387308a0
21. Wang MD, Schnitzer MJ, Yin H, Landick R, Gelles J, Block SM (1998) Force and velocity measured for single molecules of RNA polymerase. Science 282:902–907
22. Yin H, Wang MD, Svoboda K, Landick R, Block SM, Gelles J (1995) Transcription against an applied force. Science 270:1653–1657. doi:10.1126/science.270.5242.1653
23. Bustamante C, Bryant Z, Smith SB (2003) Ten years of tension: single-molecule DNA mechanics. Nature 421:423–427. doi:10.1038/nature01405
24. Gross P, Laurens N, Oddershede LB, Bockelmann U, Peterman EJG, Wuite GJL (2011) Quantifying how DNA stretches, melts and

changes twist under tension. Nat Phys 7:731–736. doi:10.1038/nphys2002

25. Dame RT, Noom MC, Wuite GJL (2006) Bacterial chromatin organization by H-NS protein unravelled using dual DNA manipulation. Nature 444:387–390. doi:10.1038/nature05283
26. Neupane K, Foster DAN, Dee DR, Yu H, Wang F, Woodside MT (2016) Direct observation of transition paths during the folding of proteins and nucleic acids. Science 352:239–242. doi:10.1126/science.aad0637
27. Woodside MT, Block SM (2014) Reconstructing folding energy landscapes by single-molecule force spectroscopy. Annu Rev Biophys 43:19–39. doi:10.1146/annurev-biophys-051013-022754
28. Gross P, Farge G, Peterman EJG, Wuite GJL (2010) Combining optical tweezers, single-molecule fluorescence microscopy, and microfluidics for studies of DNA-protein interactions. Methods Enzymol 475:427–453. doi:10.1016/S0076-6879(10)75017-5
29. Brewer LR, Bianco PR (2008) Laminar flow cells for single-molecule studies of DNA-protein interactions. Nat Methods 5:517–525. doi:10.1038/nmeth.1217
30. van Mameren J, Peterman EJG, Wuite GJL (2008) See me, feel me: methods to concurrently visualize and manipulate single DNA molecules and associated proteins. Nucleic Acids Res 36:4381–4389. doi:10.1093/nar/gkn412
31. Matthews JNA (2009) Commercial optical traps emerge from biophysics labs. Phys Today 62:26–28. doi:10.1063/1.3086092
32. Ashkin A (1992) Forces of a single-beam gradient laser trap on a dielectric sphere in the ray optics regime. Biophys J 61:569–582. doi:10.1016/S0006-3495(92)81860-X
33. Gittes F, Schmidt CF (1998) Signals and noise in micromechanical measurements. Methods Cell Biol 55:129–156
34. Moffitt JR, Chemla YR, Izhaky D, Bustamante C (2006) Differential detection of dual traps improves the spatial resolution of optical tweezers. Proc Natl Acad Sci U S A 103:9006–9011. doi:10.1073/pnas.0603342103
35. Peterman EJG, Gittes F, Schmidt CF (2003) Laser-induced heating in optical traps. Biophys J 84:1308–1316. doi:10.1016/S0006-3495(03)74946-7
36. Vermeulen KC, Wuite GJL, Stienen GJM, Schmidt CF (2006) Optical trap stiffness in the presence and absence of spherical aberrations. Appl Opt 45:1812. doi:10.1364/AO.45.001812
37. Reihani SNS, Mir SA, Richardson AC, Oddershede LB (2011) Significant improvement of optical traps by tuning standard water immersion objectives. J Opt 13:105301. doi:10.1088/2040-8978/13/10/105301
38. Guck J, Ananthakrishnan R, Mahmood H, Moon TJ, Cunningham CC, Käs J (2001) The optical stretcher: a novel laser tool to micromanipulate cells. Biophys J 81:767–784. doi:10.1016/S0006-3495(01)75740-2
39. Mahamdeh M, Schäffer E (2009) Optical tweezers with millikelvin precision of temperature-controlled objectives and base-pair resolution. Opt Express 17:17190. doi:10.1364/OE.17.017190
40. Cheezum MK, Walker WF, Guilford WH (2001) Quantitative comparison of algorithms for tracking single fluorescent particles. Biophys J 81:2378–2388. doi:10.1016/S0006-3495(01)75884-5
41. Crocker JC, Grier DG (1996) Methods of digital video microscopy for colloidal studies. J Colloid Interface Sci 179:298–310. doi:10.1006/jcis.1996.0217
42. Finer JT, Simmons RM, Spudich J (1994) Single myosin molecule mechanics: piconewton forces and nanometre steps. Nature 368:113–119. doi:10.1038/368113a0
43. Visscher K, Gross SP, Block SM (1996) Construction of multiple-beam optical traps with nanometer-resolution position sensing. IEEE J Sel Top Quant Electron 2:1066–1076
44. Denk W, Webb WW (1990) Optical measurement of picometer displacements of transparent microscopic objects. Appl Opt 29:2382. doi:10.1364/AO.29.002382
45. Gittes F, Schmidt CF (1998) Interference model for back-focal-plane displacement detection in optical tweezers. Opt Lett 23:7–9
46. De Vlaminck I, Dekker C (2012) Recent advances in magnetic tweezers. Annu Rev Biophys 41:453–472. doi:10.1146/annurev-biophys-122311-100544
47. Sitters G, Kamsma D, Thalhammer G, Ritsch-Marte M, Peterman EJG, Wuite GJL (2014) Acoustic force spectroscopy. Nat Methods 12:47–50. doi:10.1038/nmeth.3183
48. Dreyer JK, Berg-Sørensen K, Oddershede L (2004) Improved axial position detection in optical tweezers measurements. Appl Opt 43:1991. doi:10.1364/AO.43.001991
49. Abbondanzieri E, Greenleaf WJ, Shaevitz JW, Landick R, Block SM (2005) Direct observation of base-pair stepping by RNA polymerase.

Nature 438:460–465. doi:10.1038/nature04268

50. Comstock MJ, Whitley KD, Jia H, Sokoloski J, Lohman TM, Ha T, Chemla YR (2015) Direct observation of structure-function relationship in a nucleic acid-processing enzyme. Science 348:352–354. doi:10.1126/science.aaa0130
51. Comstock MJ, Ha T, Chemla YR (2011) Ultrahigh-resolution optical trap with single-fluorophore sensitivity. Nat Methods 8:335–340. doi:10.1038/nmeth.1574
52. Heller I, Sitters G, Broekmans OD, Biebricher AS, Wuite GJL, Peterman EJG (2014) Mobility analysis of super-resolved proteins on optically stretched DNA: comparing imaging techniques and parameters. ChemPhysChem 15:727–733. doi:10.1002/cphc.201300813
53. van Mameren J, Gross P, Farge G, Hooijman P, Modesti M, Falkenberg M, Wuite GJL, Peterman EJG (2009) Unraveling the structure of DNA during overstretching by using multicolor, single-molecule fluorescence imaging. Proc Natl Acad Sci 106:18231–18236. doi:10.1073/pnas.0904322106
54. van Mameren J, Modesti M, Kanaar R, Wyman C, Peterman EJG, Wuite GJL (2009) Counting RAD51 proteins disassembling from nucleoprotein filaments under tension. Nature 457:745–748. doi:10.1038/nature07581
55. King GA, Gross P, Bockelmann U, Modesti M, Wuite GJL, Peterman EJG (2013) Revealing the competition between peeled ssDNA, melting bubbles, and S-DNA during DNA overstretching using fluorescence microscopy. Proc Natl Acad Sci U S A 110:3859–3864. doi:10.1073/pnas.1213676110
56. Murade CU, Subramaniam V, Otto C, Bennink ML (2010) Force spectroscopy and fluorescence microscopy of dsDNA-YOYO-1 complexes: implications for the structure of dsDNA in the overstretching region. Nucleic Acids Res 38:3423–3431. doi:10.1093/nar/gkq034
57. Bennink ML, Scharer OD, Kanaar R, Sakata-Sogawa K, Schins JM, Kanger JS, de Grooth BG, Greve J (1999) Single-molecule manipulation of double-stranded DNA using optical tweezers: interaction studies of DNA with RecA and YOYO-1. Cytometry 36:200–208. doi:10.1002/(Sici)1097-0320(19990701)36:3<200::Aid-Cyto9>3.0.Co;2-T
58. Hohng S, Zhou R, Nahas MK, Yu J, Schulten K, Lilley DMJ, Ha T (2007) Fluorescence-force spectroscopy maps two-dimensional reaction landscape of the holliday junction. Science 318:279–283. doi:10.1126/science.1146113
59. Brouwer I, Sitters G, Candelli A, Heerema SJ, Heller I, Melo de AJ, Zhang H, Normanno D, Modesti M, Peterman EJG, Wuite GJL (2016) Sliding sleeves of XRCC4–XLF bridge DNA and connect fragments of broken DNA. Nature 535:566–569. doi:10.1038/nature18643
60. Forget AL, Kowalczykowski SC (2012) Single-molecule imaging of DNA pairing by RecA reveals a three-dimensional homology search. Nature 482:423–427. doi:10.1038/nature10782
61. Heller I, Sitters G, Broekmans OD, Farge G, Menges C, Wende W, Hell SW, Peterman EJG, Wuite GJL (2013) STED nanoscopy combined with optical tweezers reveals protein dynamics on densely covered DNA. Nat Methods 10:910–916. doi:10.1038/nmeth.2599
62. Block J, Witt H, Candelli A, Peterman EJG, Wuite GJL, Janshoff A, Köster S (2017) Nonlinear loading-rate-dependent force response of individual vimentin intermediate filaments to applied strain. Phys Rev Lett 118:48101. doi:10.1103/PhysRevLett.118.048101
63. Brouwer I, Giniatullina A, Laurens N, van Weering JRT, Bald D, Wuite GJL, Groffen AJ (2015) Direct quantitative detection of Doc2b-induced hemifusion in optically trapped membranes. Nat Commun 6:8387. doi:10.1038/ncomms9387
64. Grier DG (2003) A revolution in optical manipulation. Nature 424:810–816. doi:10.1038/nature01935
65. Liesener J, Reicherter M, Haist T, Tiziani HJ (2000) Multi-functional optical tweezers using computer-generated holograms. Opt Commun 185:77–82. doi:10.1016/S0030-4018(00)00990-1
66. Mio C, Gong T, Terray A, Marr DWM (2000) Design of a scanning laser optical trap for multiparticle manipulation. Rev Sci Instrum 71:2196. doi:10.1063/1.1150605
67. Visscher K, Brakenhoff GJ, Krol JJ (1993) Micromanipulation by "multiple" optical traps created by a single fast scanning trap integrated with the bilateral confocal scanning laser microscope. Cytometry 14:105–114. doi:10.1002/cyto.990140202
68. Noom MC, van den Broek B, van Mameren J, Wuite GJL (2007) Visualizing single DNA-bound proteins using DNA as a scanning probe. Nat Methods 4:1031–1036. doi:10.1038/nmeth1126

Chapter 2

RNA Unzipping and Force Measurements with a Dual Optical Trap

Laurent Geffroy, Pierre Mangeol, Thierry Bizebard, and Ulrich Bockelmann

Abstract

In order to mechanically unfold a single RNA molecule, an RNA/DNA hybrid construction is prepared which allows specific attachment to two micrometer-sized beads. A dual-beam optical trap thus holding the construct in solution captures the beads separately. Unfolding of a molecule is obtained by increasing the distance between the traps, one trap being slowly moved while the other is held fixed. Force is measured to sub-piconewton precision by back focal plane interferometry of the bead in the fixed trap. The experiment allows us to measure structure and base-sequence-dependent force signals. In this chapter, important technical aspects of this type of single-molecule force measurements are considered.

Key words RNA, DNA, Single-molecule, Optical trap, Force, Unzipping, Molecular construction

1 Introduction

The field of single-molecule force measurements on nucleic acids started more than 15 years ago. It has thrived ever since and has been covered by a number of reviews [1–4]. The most noteworthy feature common to all single-molecule techniques is the absence of ensemble averaging. This aspect is particularly highlighted in nucleic acid unzipping measurements. Base-sequence-dependent force signals are observed in DNA unzipping [5–9], while the signals observed upon unzipping RNA structures depend on structure and base sequence [10–21]. The double optical tweezers configuration, which can achieve very accurate and low drift measurements, enables the reproducible observation of these features on a single molecule.

Unzipping experiments require many different elements to be carefully tuned for optimal results. These preparations are the very essential condition to record high-quality force signals. There are many possible reasons for failure; some of them are listed in

Erwin J.G. Peterman (ed.), *Single Molecule Analysis: Methods and Protocols*, Methods in Molecular Biology, vol. 1665, DOI 10.1007/978-1-4939-7271-5_2,

Subheading 4. The chapter provides protocols and notes on the setup of a dual optical trap, the preparation of the molecular constructions and an example of a single-molecule RNA unzipping measurement. Other important technical points, not addressed in detail here, include the preparation and surface functionalization of the beads, the force calibration of the setup and the details of data acquisition and analysis. Methods and protocols of DNA unzipping measurements were described in the first edition of this book [22].

2 Materials

2.1 Dual Optical Trap

1. Trapping laser: CW, linearly polarized, diode pumped, Nd: YVO_4 laser, emitting at 1.064 μm with a maximum power of 10 W. Millenia IR, Spectra-Physics, Mountain View, CA, USA.
2. Trapping objective: 100× N.A. = 1.4 oil immersion objective, Plan Apo IR, Nikon, Tokyo, Japan.
3. Condenser objective: 60× N.A. = 1.2 water immersion objective, UPlanSApo, Olympus, Tokyo, Japan.
4. Beam steering: piezoelectric mirror mount with an integrated position sensor operating in a feedback loop (Mad City Labs Inc., Madison, WI, USA).
5. Acousto-optic frequency shifter (AA Optoelectronic, Orsay, France).
6. Position-sensitive detector (Pacific Silicon Sensor,Westlake Village, CA, USA).

2.2 Molecular Constructs

1. DNA oligonucleotides (*see* **Note 1**):
   - Oligo "F": 5′-TAA TAC GAC TCA CTA TAG GGA GAC CAC AAC GG-3′.
   - Oligo "R": 5′-TGA GCA TTA TGA TCA ATG CCA AAT GTG-3′.
   - Oligo "1a": 5′-TAC GAC TCA CTC GAG GGA GAC CAC-3′.
   - Oligo "1b": 5′-TGG GTT GTT TCC CTC TTC ACG ACGG-3′.
   - Oligo "2a": 5′ biotin-GCT GAG CAT TAT GAT CAA TGC CAA ATG-3′.
   - Oligo "2b": 5′-GCG ACG CTT ATG CGT TGT TGG GTA GG-3′.
2. Modified nucleotide: Biotin-14-dATP (ThermoFisher Scientific).

3. "RiboMax™ Large Scale RNA production System (T7 version)" kit (Promega), including T7 RNA polymerase and accompanying enzymes and products.
4. "Phusion® High-Fidelity PCR" kit (New England Biolabs), including Phusion DNA polymerase and accompanying products.
5. Restriction enzyme XhoI (+ buffer 'CutSmart', New England Biolabs).
6. Klenow Fragment (3′ → 5′ exo-) of *E. coli* DNA Polymerase I (New England Biolabs).
7. "NucleoSpin® Gel and PCR Clean-up" and "NucleoSpin® RNA Clean-up" nucleic acid purification kits (Macherey-Nagel).
8. Agarose and agarose gel apparatus, gel staining chemicals and gel analysis devices.
9. Hybridization buffer: 80% (V/V) formamide, 0.4 M NaCl, 40 mM Pipes pH 6.5, 1 mM EDTA).
10. Spin columns: Illustra™ MicroSpin G50 (GE Healthcare).
11. Working buffer: 100–400 mM KCl, 5 mM $MgCl_2$, 20 mM Hepes Na pH 7.6.

2.3 Sample Cell and Beads

1. Coverslips: 21 × 26 mm #1 (Menzel-Gläser).
2. Streptavidin-coated, 0.96 μm diameter Silica beads 1% (w/v) (ProActive® Microspheres, Polysciences). The beads are stored at 0.1% (w/v) concentration in Polylink wash and storage buffer (PolyLink Protein Coupling Kit for COOH Microparticles, Polysciences) supplemented with 1% (w/v) Polyvinylpyrrolidone, 0.1% (v/v) Tween 20.

3 Methods

3.1 The Dual Optical Trap Setup

Our setup is presented schematically in Fig. 1. It is based on a custom-designed inverted microscope. The optical components are mounted on an optical table for vibration isolation. For trapping and force detection, we use a diode pumped near-infrared laser. To create two independent traps, a polarizing cube C1 splits the laser beam by polarization. A half-wave plate allows us to adjust the distribution of the laser intensity on the two polarizations. The direction of one of the two beams is varied by a piezoelectric mirror mount. Moreover, the frequency of one beam is shifted compared to the frequency of the other one, with an acousto-optic modulator ("frequency shifter"). This procedure eliminates the interference taking place between the two beams on the detection plane [23] (*see* **Notes 2** and **3**). After recombination with a second polarizing

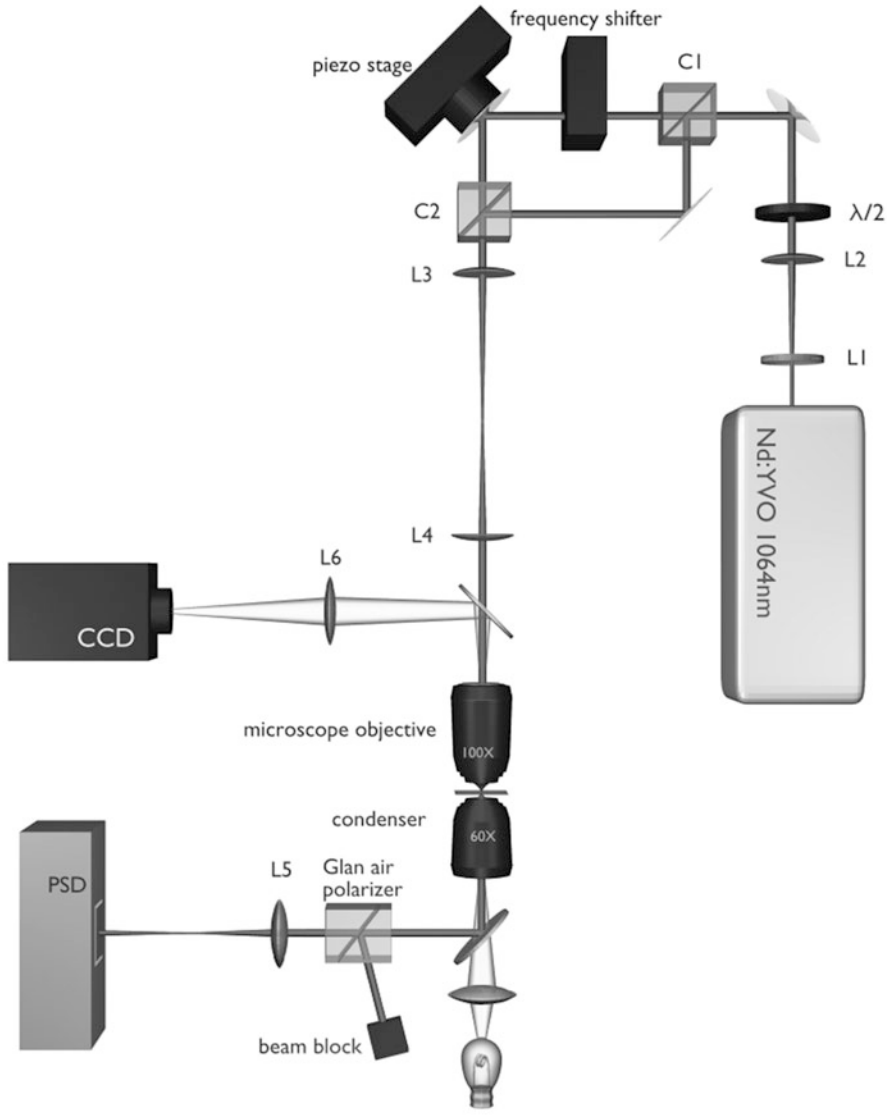

Fig. 1 Schematic layout of the dual optical trap setup. The trapping beams are indicated in *dark grey* and the illumination path in *light grey*. The optical components are described in the text

cube C2, the two beams exhibit perpendicular polarization, and their directions of propagation are slightly different, in order to create two laterally separated traps in the sample. To this end, lenses L3 and L4 image the center of the mirror mounted on the piezoelectric stage on the back focal plane of the trapping objective.

The beams are focused by the trapping objective, pass through the sample and are then collimated by the condenser objective. One of the two beams is removed with a Glan-laser polarizer. Finally, lens L5 images the back focal plane of the condenser objective on a position-sensitive detector. Part of the optical path is also used to

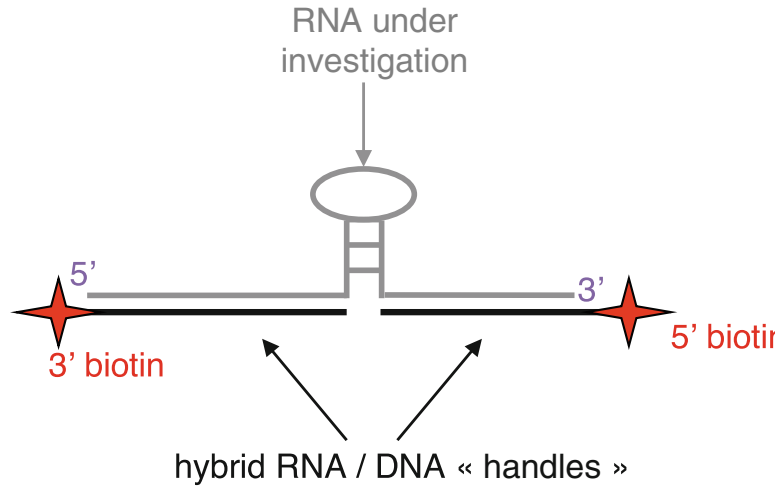

Fig. 2 The RNA/DNA hybrid molecular construction used in the force measurements: a single-stranded RNA molecule (in *grey*), containing the RNA part to be investigated (illustrated in this figure as a schematic hairpin), is hybridized to two complementary single-stranded DNAs (in *black*); each one of the ssDNA is ~2000–3000 nt long and is chemically modified at one of its extremities by a biotin moiety—so as to form two hybrid RNA/DNA "handles," which allow the single molecule to be easily manipulated

image the beads on a CCD camera. To avoid fluctuations from air currents, the optical path is fully enclosed. Most mechanical parts are custom designed to reduce drifts and vibrations.

3.2 Preparation of the Molecular Constructions

A typical RNA/DNA hybrid molecular construction is shown schematically in Fig. 2.

3.2.1 Overview

(Of note: in the following paragraphs, all volumes and concentrations refer to *final* concentrations, after all components have been added).

To synthetize all the nucleic acids (RNA and DNAs) necessary for the molecular construct shown in Fig. 2, we started from a homemade plasmid (named pT7rrnB), which contains a modified rrnB operon from *Escherichia coli*: this modification consists of the replacement of the natural promoter sequence by a standard promoter of T7 phage RNA polymerase.

The RNA sequence of interest to us in this article and in previous papers [10, 16] consists of nucleotides 991–1163 of the *E. coli* 23S rRNA-sequence, located approximately in the middle of the rrnB operon.

A flowchart of the whole procedure to synthetize the desired RNA/DNA hybrid molecular construct is shown in Fig. 3.

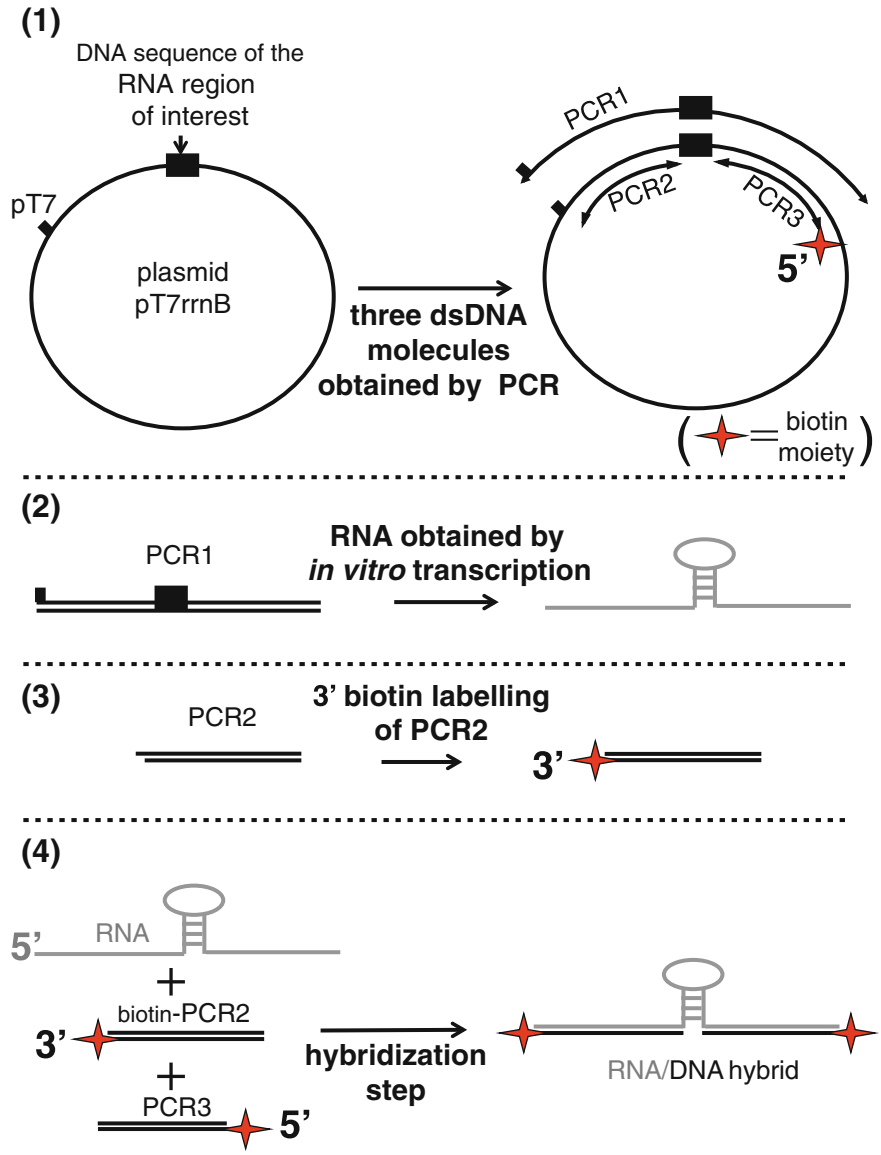

Fig. 3 Flowchart of the procedure to synthetize the desired RNA/DNA hybrid molecular construction

3.2.2 RNA Preparation

The RNA part of the construct is prepared by standard in vitro transcription: the DNA molecule necessary for transcription can be obtained either by runoff transcription from the linearization of pT7rrnB plasmid, or by an adequate PCR from the same plasmid (described below).

1. Preparation of DNA template for transcription by PCR; the reaction mix consists of: pT7rrnB (0.1 ng/μL), oligo "F" and oligo "R" at 500 nM each, dNTPs at 0.2 mM each, Phusion

DNA polymerase (0.02 U/μL), all these components in Phusion HF buffer, in a final volume of 100 μL. The PCR reaction is immediately started: 30 s at 98 °C, then 30 cycles (10 s at 98 °C, 2 min at 72 °C for each cycle), and finally 5 min at 72 °C.

2. The PCR product is desalted and purified using the 'NucleoSpin® Gel and PCR Clean-up' kit, and finally resuspended in 30 μL of elution buffer. DNA concentration is estimated from its OD at 260 nm (using an extinction coefficient of 20 $(mg/mL)^{-1}\ cm^{-1}$). PCR product purity is checked on a 0.7% agarose gel.
3. The in vitro transcription reaction mix consists of: 2.5 μg of purified PCR product, 7.5 mM of each NTP, 5 μL of 'Enzyme Mix', with buffer conditions adjusted to be in 1× 'T7 Transcription Buffer', for a final volume of 50 μL. The transcription reaction is incubated during 3 h at 37 °C. Afterwards, RQ1 DNaseI (0.05 U/μL) is added to the reaction mix and the reaction further incubated 15 min at 37 °C—in order to digest the DNA present in the mixture.
4. The RNA is purified and desalted using the 'NucleoSpin® RNA Clean-up' kit, according to the instructions of the manufacturer.
5. RNA concentration is estimated from its OD at 260 nm (using an extinction coefficient of 25 $(mg/mL)^{-1}\ cm^{-1}$). RNA transcript purity is checked on a native 0.7% agarose gel. Finally, the purified RNA is stored by aliquots either at −20 °C (short-term storage), or at −80 °C (long-term storage).

3.2.3 DNA ("Handles") Preparation

1. DNA handles are obtained by PCR. We list in Subheading 2 the primers we have used in our case: primers "1a" and "1b" for the 1st handle; primers "2a" and "2b" for the 2nd handle—please note that primer "2a" is chemically modified with a biotin at its 5′ extremity, hence allowing direct incorporation of the label in the PCR product.
2. The two PCR reaction mixtures consist of: pT7rrnB (0.2 ng/μL), the two primers (see above) at 500 nM each, dNTPs at 0.2 mM each, Phusion DNA polymerase (0.02 U/μL), all these components in Phusion HF buffer, in a final volume of 100 μL (for each PCR). The two PCR reactions are immediately started: 30 s at 98 °C, then 30 cycles (10 s at 98 °C, 30 s at 60 °C, 1 min at 72 °C for each cycle), and finally 5 min at 72 °C.
3. PCR products are desalted and purified using the 'NucleoSpin® Gel and PCR Clean-up' kit, and finally resuspended in 30 μL of elution buffer. DNA concentrations are estimated from their ODs at 260 nm (using an extinction coefficient of

20 $(mg/mL)^{-1}$ cm^{-1}). PCR products purity is checked on a 0.7% agarose gel. Finally, the purified DNAs are stored at −20 °C.

4. Biotinylation of the "1a"–"1b" DNA handle:

   Contrary to the "2a"–"2b" handle which has a label (biotin) necessary for mechanical manipulations directly incorporated to one of its 5′ extremities, the "1a"–"1b" DNA handle must be labeled at one of its 3′ extremities: one of the possible strategies to perform this 3′ extremity labeling is to digest the DNA with an appropriate restriction enzyme and to fill the ensuing 5′-overhang with a polymerase able to incorporate chemically modified nucleotides (*see* **Note 4**). The protocol we use to do this is detailed below.
5. The purified "1a"–"1b" PCR fragment (adjusted at 150 ng/μL) is incubated with restriction enzyme XhoI (2 U/μL) in 'CutSmart' buffer, during 4 h at 37 °C. Then, this mixture is directly supplemented with 35 μM dGTP, 35 μM dCTP, 35 μM dTTP, 35 μM biotin-14-dATP and Klenow Fragment (0.1 U/μL), and incubated 15 min at 25 °C. The reaction is stopped by adding EDTA (10 mM) and incubating at 75 °C during 20 min. Finally, the biotinylated DNA handle is desalted and purified using the 'NucleoSpin® Gel and PCR Clean-up' kit, and resuspended in 30 μL of elution buffer.

3.2.4 RNA/DNA Hybrid Preparation

The final RNA/DNA hybrid molecular construct shown in Fig. 2 is obtained from the single-stranded RNA (prepared as described in Subheading 3.2.2) and the two double-stranded DNA "handles" (prepared as described in Subheading 3.2.3) using the following strategy.

RNA/DNA double-stranded hybrid molecules are thermodynamically more stable than double-stranded DNA of the same sequence and consequently one can find experimental conditions where the dsDNA is (predominantly) denatured and the ds RNA/DNA hybrid is (predominantly) in native conformation. Once equilibrium in these conditions is achieved, the preparation is brought back to biochemically standard conditions, and can be used as such in single-molecule force experiments.

Practically: RNA and DNAs are first mixed in "hybridization buffer," brought to high temperature to enforce all nucleic acids to be single-stranded, then the temperature is adjusted to favor annealing of RNA/DNA hybrids.

1. The three nucleic acids are mixed together: 0.1 pmol of RNA and 0.3 pmol of each one of the two chemically modified DNA "handles" in hybridization buffer in a final volume of 25 μL.

   Using a PCR machine, the mixture is incubated 10 min at 85 °C, then during 1 hour at 56 °C (*see* **Note 5**).

2. Following the hybridization step, the mixture is twice desalted (to remove all traces of formamide) using spin columns. Finally, a RNA renaturation step is performed—to ensure that the RNA sequence of interest is properly folded: to do this, the preparation is adjusted to "working buffer" conditions and subjected to a "slow-cooling" protocol (using a standard PCR machine): first, incubation during 10 min at 60 °C, then gradual cooling to room temperature over 1 h.
3. To control the formation of the RNA/DNA hybrid and to estimate its effective concentration, 50 ng of the hybrid can be loaded on a 0.7% agarose gel, run and stained in standard conditions as routinely used for dsDNA quality control.
4. Finally, the preparation is stored by aliquots at −20 °C. It can be used as such—with no additional purification (*see* **Note 6**)—in single-molecule force experiments: simply thaw an aliquot at room temperature and dilute it in working buffer as necessary (*see* Subheading 3.3.1 **steps 1** and **2**).

3.3 Example of an Unzipping Force Measurement

3.3.1 Preparing an Unzipping Experiment

1. Prepare the complex composed of RNA/DNA hybrid and two beads. We use 0.96 μm diameter streptavidin coated silica beads and a 10–50 times dilution in "working buffer" of the molecular construct stock (*see* **Note 7**). A mixture containing 0.5 μL of the molecular construct dilution and 0.5 μL of beads (five times diluted in beads storage buffer) is centrifuged at 30 × *g* for 6 min and then incubated 1 h at room temperature.
2. Add "working buffer" up to 10 μL final and very carefully resuspend the beads (by slowly pipetting up and down: if the injection is too rough, the RNA/DNA hybrid-beads complex might break).
3. Prepare the sample cell made of two PEG-passivated coverslips glued with Parafilm (*see* Fig. 4). PEG passivation is performed according to published protocols (for example, *see* ref. 24).
4. Gently inject the RNA/DNA hybrid-beads solution through the channel by capillarity.
5. Seal the cell with wax to avoid any evaporation.
6. Switch on the laser and acousto-optic modulator 1 h before the measurements to reach thermal equilibrium (*see* **Note 8**). The laser should go through the objectives during this period.
7. Place the sample in the microscope.
8. Check that the beam is proper for detection use.

3.3.2 Sequence of a Typical Unzipping Experiment

1. Search for the appropriate bead duplexes, i.e. two 0.96 μm-sized beads separated typically by 500 nm. Such duplexes are likely to be linked by a RNA/DNA hybrid molecule and so to be opened (*see* **Note 9**).

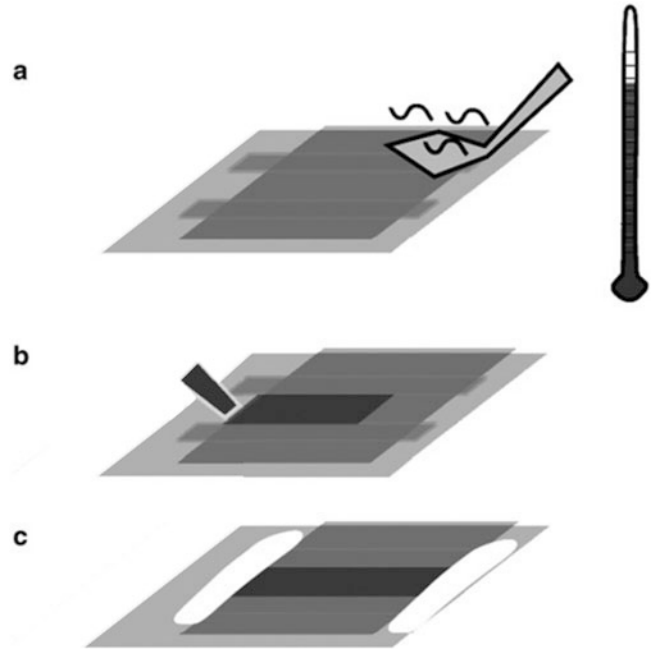

Fig. 4 Preparation of a sample cell. (**a**) Two coverslips are glued together using Parafilm. (**b**) The solution containing the RNA/DNA–bead complex is gently injected into the cell by capillarity. (**c**) The cell is sealed to avoid evaporation of the solution

2. Initially separate the two traps (about 1.2 μm for the 0.96 μm beads) so that you can trap each bead in a different trap.
3. Trap one bead in each trap.
4. Move the objective to focus the laser in the sample at about 5 μm above the glass–water interface.
5. Using the piezoelectric stage pull apart the two traps at a displacement velocity between 5 and 500 nm/s.
6. Monitor the force extension curves in real time and assure that during the cycle no free beads enter one of the traps otherwise the force measurement will be erroneous.
7. Finally stretch the molecule until it breaks and calibrate the force measurement. For instance, a power spectrum can be recorded and analyzed in order to determine the trap stiffness and the conversion factor between the force and the output voltage of the position-sensitive detector electronics.

3.3.3 Example of a Force Versus Displacement Curve

A typical force versus displacement curve is shown in Fig. 5. First, the curve exhibits an initial flat region at low displacement corresponding to a relaxed RNA/DNA hybrid molecule. Then the force increases nonlinearly with respect to displacement,

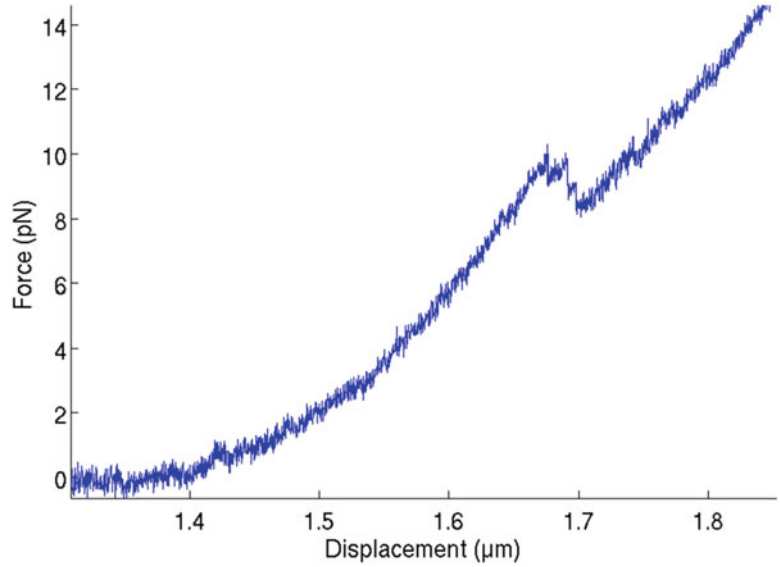

Fig. 5 Typical force versus displacement curve of an RNA/DNA hybrid molecule for 50 nm/s displacement velocity. The radii of the trapped beads have been subtracted

which corresponds to the elastic response of the double-stranded RNA/DNA hybrid under stretching.

Next, one can see saw-tooth-shaped features in the force signal which occur around 10 pN. These features correspond to the unzipping of the single-stranded RNA part of the molecular construction and involve three intermediate states. Afterwards, force rises again: one observes the elastic response of both linkers RNA/DNA hybrids in series with the fully opened single-stranded RNA.

4 Notes

1. As the correctness of all oligonucleotide sequences is of utmost importance for the success of the whole molecular construction procedure, one should ensure that all oligonucleotides are of high purity (if possible, HPLC-purified), and that they are all subjected to adequate quality-control (for example, by mass spectrometry).
2. Interference and crosstalk. The two beams used in the dual optical trap are of perpendicular polarization before entering the trapping objective. The purpose of the perpendicular polarization is to avoid interference of the two beams to allow detection and force measurement on only one trap (typically the fixed one).

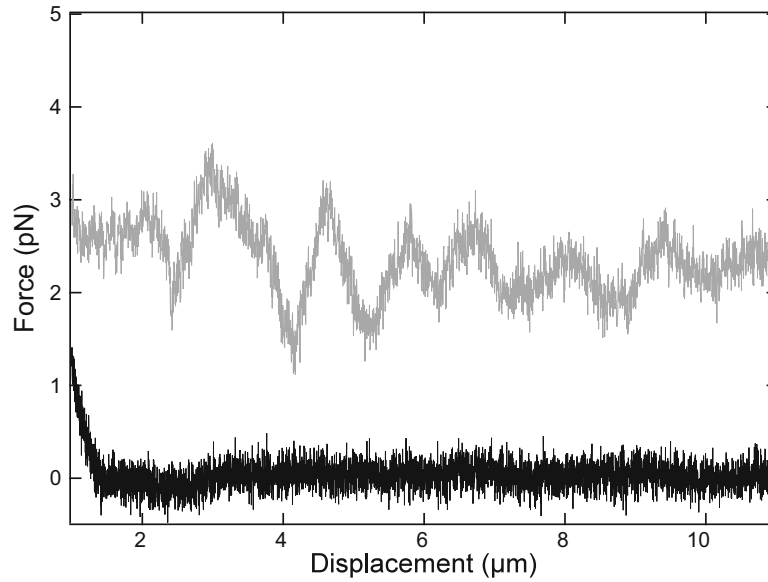

Fig. 6 Force measurements with two 0.97 μm silica beads without DNA trapped with the frequency shifter on (*bottom*: $k_f = 213$ pN/μm and $P = 910$ mW) and off (*top*: $k_f = 192$ pN/μm and $P = 800$ mW). The displacement velocity between the two beads is 1 μm/s, and sampling is done at 800 Hz with an anti-aliasing filter of 352 Hz. The signal measured without the frequency shifter on is shifted vertically for better visualization

Unfortunately, as known from polarization microscopy, the polarization of light is not fully conserved when going through conventional microscope objectives [25, 26]. The separation of the two beams before detection is therefore never complete and an important problem appears: the beams interfere and create a parasitic signal when measuring force, especially at high laser power and small distance between the traps (Fig. 6).
However, a solution for this problem is accessible. One can shift the frequency of one of the two beams with an acousto-optic modulator at a few tens of MHz [23]. The beams still interfere, but the interference pattern moves so fast that the electronics does not detect it, due to low pass filtering. The effect of interference can thus be totally eliminated (Fig. 6). A fraction of light coming from the non-desired beam is still present but it is usually small enough to be neglected (below 2% of the total force signal in our case).

3. Regulation of the relative height of the two beads. The use of an acousto-optic modulator on the path of one of the beam or trapping two different types of beads in the two traps may lead to an undesirable consequence: the two beads may not be trapped in the same plane.

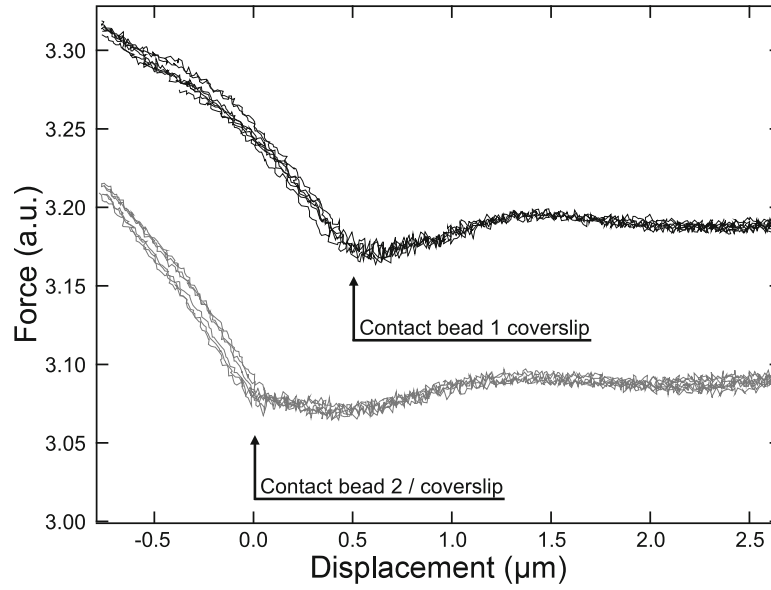

Fig. 7 Force measurement on two different trapped beads on the *z* direction while oscillating the coverslip height. When a bead touches the coverslip, the force increases quickly. *Top curve*, measurement for a 1.87 μm polystyrene bead, *bottom curve*, measurement for a 0.97 μm silica bead

A good estimation of the distance between the two beads along the axis of beam propagation (z) can be achieved if the setup has a piezoelectric translator in this direction and two photodiodes to measure the force acting on the beads in the z direction (as the total light received on the detector using the back focal plane method is proportional to this force). By oscillating the position of the translator, one can reach positions where the beads touch the coverslip and determine these positions by measuring the force acting on the bead in the z direction, as when a bead touches the coverslip the force in z direction increases quickly. An example of this measurement is shown in Fig. 7.

If the distance between the two beads is not the desired one, a telescope can be added in the path of one of the beam to adjust its diameter and change the relative height of the bead trapped by this beam. One should remind that these measurements are done close to the surface. If the experiment is carried out far away from the surface, specific calibrations have to be performed. In our case, this adjustment is still correct up to 5 μm.

4. For this, a XhoI restriction site was purposedly designed in oligo "1a" (with, of course, the mandatory verification that this restriction site was unique in the DNA sequence) to create a 5′-overhang. It is then possible to fill the overhang with a polymerase able to incorporate an adequate biotinylated

nucleotide (we have used biotin-14-dATP): the Klenow Fragment (3′→ 5′ exo-) of *E. coli* DNA Polymerase I is able to fulfill this role.

5. In our case, 56 °C corresponds to the optimal hybridization temperature for the GC content of our handles. In a more general case, one can refer to the article of Dean [27] to find the optimal hybridization temperature of any RNA/DNA hybrid construct.
6. In our hands, we have found that further purification of the desired molecular construct (i.e. hybrid RNA/DNA with two DNA handles, as in Fig. 2) was not necessary. The probable reason for this observation is the following: this molecular construct is the sole nucleic acid in the preparation possessing one attached biotin moiety at each one of its extremities. Thus, the selection of adequate couple of beads during the single-molecule force experiment (*see* Subheading 3.3.2, **step 1**) is itself a very efficient purification step!
7. Beads and molecular construct concentrations. One has to test several molecular construction concentrations to work under optimal conditions for stretching experiments. Moreover, the molecular construction concentration to be used depends on the concentration used for the beads. One can typically tune the bead concentration which allows convenient work for force measurement and find the right molecular construction dilution to be used, i.e. between 10 and 50 times in our hands.
8. Thermal drift. The trapping laser is usually chosen so that it does not significantly damage and warm up too much samples and biological molecules; near infrared lasers can solve this issue properly. However, the light power is usually high enough to induce an unavoidable rise in temperature. Local heating of the solution close to a trapped particle has been reported previously and modeled with success [28].

   We focus here on heating of the trapping objective. Even if this heating is the most obvious one, it has not been reported in the literature. It is important to know to which extent an objective is heated, first because it will expand and produce mechanical drift and second because since the immersion objective is in thermal contact to the sample it can heat the latter. Knowing the real temperature of a sample is crucial for trap calibration as well as for temperature-dependent biological processes which are studied with optical tweezers.

   We measured the temperature of the tip of the trapping objective with a thermocouple (Fig. 8). Initially the objective was at room temperature and we started the measurement when the

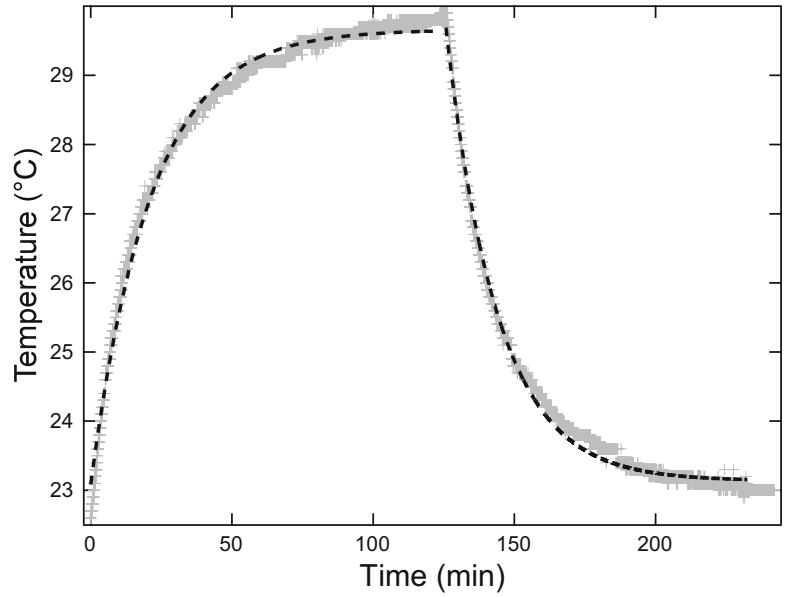

Fig. 8 Temperature measurement on the trapping objective tip (*grey crosses*) and exponential fits for temperature increasing and decreasing (*dashed curves*). The trapping laser is switched on at time $t = 0$ min and switched off at $t = 125$ min

laser started to go through the objective. After 125 min we switched off the laser and let the objective cool down. We found that both heating and cooling can be properly fitted by simple exponential laws ($\Delta T\, \mathrm{e}^{-t/\tau}$) with a typical time τ of about 20 min and a change in temperature ΔT of about 6.5 °C. The important consequences of this measurement are the following:

- Temperature variations induce mechanical drifts that can expand objectives and translate the position of the focal point by about ten micrometers.
- Before starting an experiment the laser has to go through the trapping objective for an hour at least. It should be avoided to switch off the laser for more than 5 min.
- In steady state the sample temperature can be several degrees above the ambient temperature.

9. It can be tricky for a new experimentalist to make the distinction between two stuck beads and those linked by a RNA/DNA hybrid molecule. The rule of thumb is that the beads linked by a RNA/DNA hybrid molecule would exhibit an uncorrelated Brownian motion.

References

1. Bustamante C, Bryant Z, Smith S (2003) Ten years of tension: single molecule DNA mechanics. Nature 421:423–427
2. Allemand JF, Bensimon D, Croquette V (2003) Stretching DNA and RNA to probe their interactions with proteins. Curr Opin Struct Biol 13:266–274
3. Bockelmann U (2004) Single-molecule manipulation of nucleic acids. Curr Opin Struct Biol 14:368–373
4. Neuman KC, Block SM (2004) Optical trapping. Rev Sci Instrum 75:2787–2809
5. Essevaz-Roulet B, Bockelmann U, Heslot F (1997) Mechanical separation of the complementary strands of DNA. Proc Natl Acad Sci U S A 94:11935–11940
6. Bockelmann U, Essevaz-Roulet B, Heslot F (1997) Molecular stick-slip motion revealed by opening DNA with piconewton forces. Phys Rev Lett 79:4489–4492
7. Rief M, Clausen-Schaumann H, Gaub HE (1999) Sequence dependent mechanics of single DNA molecules. Nat Struct Biol 6:346–349
8. Bockelmann U, Thomen P, Essevaz-Roulet B, Viasnoff V, Heslot F (2002) Unzipping DNA with optical tweezers: high sequence sensitivity and force flips. Biophys J 82:1537–1553
9. Danilowicz C, Coljee VW, Bouzigues C, Lubensky DK, Nelson DR, Prentiss M (2003) DNA unzipped under a constant force exhibits multiple metastable intermediates. Proc Natl Acad Sci U S A 100:1694–1699
10. Mangeol P, Bizebard T, Chiaruttini C, Dreyfus M, Springer M, Bockelmann U (2011) Probing ribosomal protein-RNA interactions with an external force. Proc Natl Acad Sci U S A 108:18272–18276
11. Bercy M, Mangeol P, Bizebard T, Tanner NK, Banroques J, Bockelmann U (2013) Investigating RNA structure and folding with optical tweezers. In: Klostermeier D, Hammann C (eds) RNA structure and folding. Walter de Gruyter GmbH, Berlin
12. Bercy M, Bockelmann U (2013) Hairpins under tension: RNA versus DNA. Nucleic Acids Res 43:9928–9936
13. Liphardt J, Onoa B, Smith SB, Tinoco I Jr, Bustamante C (2001) Reversible unfolding of single RNA molecules by mechanical force. Science 292:733–737
14. Onoa B, Dumont S, Liphardt J, Smith SB, Tinoco I Jr, Bustamante C (2003) Identifying kinetic barriers to mechanical unfolding of the T. thermophila ribozyme. Science 299:1892–1895
15. Harlepp S, Marchal T, Robert J, Léger JF, Xayaphoummine A, Isambert H, Chatenay D (2003) Probing complex RNA structures by mechanical force. Eur Phys J E 12:605–615
16. Mangeol P, Côte D, Bizebard T, Legrand O, Bockelmann U (2006) Probing DNA and RNA single molecules with a double optical tweezer. Eur Phys J E 19:311–317
17. Dumont S, Cheng W, Serebrov V, Beran R, Tinoco I Jr, Pyle AM, Bustamante C (2006) RNA translocation and unwinding mechanism of HCV NS3 helicase and its coordination by ATP. Nature 439:105–108
18. Dumont S, Cheng W, Tinoco I Jr, Bustamante C (2006) NS3 helicase actively separates RNA strands and senses sequence barriers ahead of the opening fork. Proc Natl Acad Sci U S A 104:13954–13959
19. William J, Greenleaf WJ, Frieda KL, Foster DAN, Woodside MT, Block SM (2008) Direct observation of hierarchical folding in single riboswitch aptamers. Science 319:630–633
20. Fazal FM, Meng CA, Murakami K, Kornberg RD, Block SM (2015) Real-time observation of the initiation of RNA polymerase II transcription. Nature 525:274–277
21. Garcia-Garcia C, Frieda KL, Feoktistova K, Fraser CS, Block SM (2015) Factor-dependent processivity in human eIF4A DEAD-box helicase. Science 348:1486–1488
22. Cissé I, Mangeol P, Bockelmann U (2011) DNA unzipping and force measurements with a dual optical trap. Methods Mol Biol 783:45–61
23. Mangeol P, Bockelmann U (2008) Interference and crosstalk in double optical tweezers using a single laser source. Rev Sci Instrum 79 (083103):1–8
24. Fordyce PM, Valentine MT, Block SM (2007) Advances in surface-based assays for single-molecules. In: Selvin PR, Ha T (eds) Single molecule techniques, a laboratory manual. Cold Spring Harbor Laboratory Press, Cold Spring Harbor, NY
25. Inoué S (1952) Studies on depolarization of light at microscope lens surfaces. I. The origin

of stray light by rotation at the lens surfaces. Exp Cell Res 3:199–208

26. Inoué S, Hyde WL (1957) Studies on depolarization of light at microscope lens surfaces II. The simultaneous realization of high resolution and high sensitivity with the polarizing microscope. J Biophys Biochem Cytol 3:831–838
27. Dean M (1987) Determining the hybridization temperature for S1 nuclease mapping. Nucleic Acids Res 15:6754
28. Peterman EJG, Gittes F, Schmidt CF (2003) Laser-induced heating in optical traps. Biophys J 84:1308–1316

Chapter 3

Protein Tethering for Folding Studies

Fatemeh Moayed, Roeland J. van Wijk, David P. Minde, and Sander J. Tans

Abstract

Optical tweezers allow the detection of unfolding and refolding transitions in individual proteins, and how interacting molecules such as chaperones affect these transitions. Typical methods that tether individual proteins are based on cysteine chemistry, which is less suitable for proteins with essential cysteines. Here we describe a cysteine-independent tethering protocol that can be performed in situ.

Key words Protein folding, Single-molecule detection, Protein–DNA chimera, Cysteine-independent linkages, In-situ tethering

1 Introduction

Optical tweezers allow one to study the folding and unfolding dynamics of individual proteins and subdomains. This approach has for instance provided insight into the step-wise nature of this process [1], the statistics of these transitions and the elucidation of the underlying folding landscape [2–5], the detection of the folding transition state [6], aggregation intermediate formation [7, 8] as well as the effect of chaperones on the folding process [9–11]. A common challenge in these experiments is the ability to specifically tether a single copy of the protein of interest between two trapped beads, which can be achieved using DNA strands as linkers [12]. DNA linkers of several 100 nm in length are typically used in order to limit nonspecific interactions between beads and interference between the laser bead that trap the bead particles and to minimize the risk of chemical modifications by reactive oxygen species under laser illumination.

Published methods typically make use of cysteine chemistry to couple the DNA linkers to the protein [13]. This covalent coupling method can achieve high resilience to applied forces. However, it requires the protein of interest to be otherwise free of endogenous cysteines, while many contain at least one—quite often conserved and essential. Here we describe a method to tether individual

Erwin J.G. Peterman (ed.), *Single Molecule Analysis: Methods and Protocols*, Methods in Molecular Biology, vol. 1665, DOI 10.1007/978-1-4939-7271-5_3,

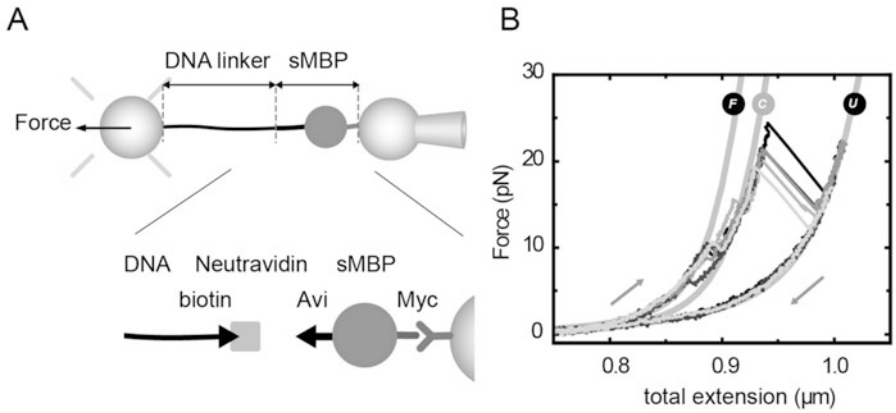

Fig. 1 Protein tethering approach (**a**) Schematic diagram. A single protein of interest (Maltose Binding Protein, sMBP) is tethered by means of a DNA linker between two beads. One is held on a position-controlled micropipette, another by an optical trap allowing force detection. At the C-terminus sMBP is attached to an Anti-c-myc-coated bead. At the N-terminus, it is connected to the DNA linker via a Neutravidin–Biotin/AviTag linkage. The DNA linker is coupled to an Anti–digoxigenin-coated bead. (**b**) Stretching–relaxation cycles show unfolding and refolding. The protein structure unfolds via two transitions (F → C and C → U). *Gray lines* show the theoretical worm like chain curves, *see* **Note 12** (reproduced with permission from ref. 10)

proteins with DNA linkers for optical tweezers applications that does not rely on cysteine chemistry (Fig. 1a). Another advantage of this method is its simplicity, as the protein can be coupled in-situ without additional chemical modification steps, directly after purification.

2 Materials

2.1 Synthesis of dsDNA Handles

1. Thermal cycler (BIO-RAD).
2. Taq DNA polymerase (New England BioLabs).
3. pUC19 plasmid DNA (New England BioLabs).
4. DNA primers (eurofins).
5. PCR buffer (New England BioLabs).
6. dNTPs (Fermentas).
7. Agarose (Roche).
8. Ethidium bromide (Sigma).
9. 0.5×TBE buffer (Sigma).
10. Gel extraction kit (QIAquick) (Qiagen).
11. Gel imaging instrument (G:Box).

2.2 Expression and Purification of Protein Constructs

1. Low to medium copy plasmid under a T7 promoter, such as pET-28a(+) (Novagen).
2. Protease-deficient expression strain of *Escherichia coli* BL21 (DE3) (Novagen).

2.2.1 In Vivo Biotinylation

1. Low copy plasmid encoding the biotin ligase BirA, such as pBirAcm (Avidity).
2. Kanamycin (50 g/L w/v solution in distilled water).
3. Chloramphenicol (25 g/L w/v solution in ethanol).
4. IPTG (Isopropyl β-D-thiogalactoside).
5. Biotin.

2.2.2 In Vitro Biotinylation

1. Coupling buffer: 20 mM Tris–HCl pH 7.5, 0.2 M NaCl, 1 mM EDTA.
2. Slide-A-Lyzer™ G2 Dialysis Cassettes (Thermo Fisher Scientific).
3. Maleimide-PEG11-Biotin (Thermo Scientific).
4. TCEP (tris(2-carboxyethyl)phosphine) (Sigma).
5. DMSO (Dimethyl sulfoxide).
6. PD-10 desalting column.

2.3 Preparation of Antibody-Coated Beads

1. Polystyrene beads (Spherotech).
2. PolyLink Protein Coupling Kit (Polysciences Inc.).

2.4 Immobilization of Protein and DNA Constructs on Antibody-Coated Beads

1. Refolding buffer (50 mM Hepes, pH 7.6, 100 mM KCl, 5 mM $MgCl_2$).
2. Neutravidin (Thermo fisher scientific).
3. Rotary mixer (Labinco B.V.).

3 Methods

The protein construct is attached to one bead using anti-myc antibodies, and tethered to a second bead by means of a single dsDNA handle. This dsDNA handle is attached on one end to the second bead using anti-digoxigenin antibodies (Fig. 1a).

3.1 Synthesis of dsDNA Handles

1. The 2553 bps DNA handles are synthesized by PCR using the Taq DNA polymerase and a pUC19 plasmid DNA as a template. Five hundred nanogram of handle is generated at a time using 50 μl of PCR reaction. The handle is generated by means of the primer 5′-DIG-GTCTCGCGCGTTTCGGTGATGACGG-DIG-G-3′ as a forward primer together with the

primer 5′-TA6GTA6CCGCTCATGAGAC 3′ as a reverse (6 is biotin-dT). Polymerase chain reaction reagents for each 50 μl reaction volume include: 1 unit of Taq polymerase, 5 μl of 10× PCR buffer, 10 pmol of the forward primer and 10 pmol of reverse primer, 5 μl of 2 mM dNTPs, and 50 ng of the plasmid DNA. The PCR profile is as follows: 1 min at 94 °C, 30 cycles of 30 s at 94 °C, 60 s at 52 °C and 3 min at 72 °C, finally followed by 10 min at 72 °C and a 4 °C soak.

2. The PCR mixture is applied on 1% agarose gels in 0.5×TBE buffer at 80 V/cm. Agarose gels are stained with ethidium bromide (EtBr). DNA handles with proper length (2553 bps) are then cut from the gel and purified using the gel extraction kit. The purified handles can be stored at −20 °C for months.

3.2 Expression and Purification of Protein Constructs

1. Four repeats of the sequence encoding the c-myc-tag (EQKLISEEDL) are introduced by PCR at the C-terminus of the protein of interest. The N-terminus is used for biotinylation (*see* **Note 1–3**).
2. Biotinylation can be done in vivo or in vitro. For in vivo biotinylation, the sequence encoding Avi-tag (GLNDIFEAQKIEWHE) is introduced at the N-terminus, whereas for in vitro biotinylation an extra cysteine residue is introduced there. The correctness of the newly made vector is confirmed by Sanger DNA sequencing.
3. The c-myc-tagged variant of protein is purified according to the same protocol as used for the unmodified protein. The only difference being that for in vivo biotinylation, the biotin ligase (BirA) is co-expressed together with the protein, while 20 mg/l Biotin is added to the expression medium in addition to 20 mg/l Chloramphenicol to maintain the BirA encoding plasmid. Note that this additional antibiotic slows down growth kinetics.
4. For in vitro biotinylation, the purified protein first is dialyzed in coupling buffer, and then incubated on ice for 15 min in 5 mM TCEP containing buffer to reduce disulfide bonds. Biotinylation is done by adding tenfold molar excess of Maleimide-PEG11-Biotin (dissolved in DMSO) to the reduced protein and incubating for 2 h at 25 °C. To remove unreacted Maleimide-PEG11-Biotin molecules, the sample can be subjected to a desalting column.
5. The purified protein sample is checked on a 8% SDS-PAGE gel, and based on the stability of protein is stored at 4 °C (for same day experiments) or after flash freezing using liquid nitrogen at −80 °C (for long-term storage).

3.3 Bead Preparation

1. Carboxylated polystyrene beads are covalently linked to Antibodies (i.e. Anti-digoxigenin and Anti-c-myc) via a Carbodiimide-mediated zero-length crosslinking reaction, as detailed in the following points.
2. 25 μl of 1% (w/v) carboxylated polystyrene microspheres are washed twice by pelleting at 17,000 × *g* (for 10 min) in a micro centrifuge tube and resuspended in coupling buffer (400 μl in the first wash and 170 μl in the second washing step).
3. 20 μl of freshly prepared EDAC (also called "EDC") solution (20 mg/ml; prepare by dissolving 1 mg EDAC in 50 μl coupling buffer) is added to the microparticle suspension and mixed gently end-over-end (*see* **Note 4**).
4. 20 μg of desired Antibody (Anti-digoxigenin or Anti-c-myc) is added and mixture is incubated for 1 h at room temperature with gentle mixing.
5. The mixture then is washed two times in 400 μl storage buffer.
6. Protein-coated beads are stored in 400 μl storage buffer at 4 °C until use (*see* **Notes 5** and **6**).

3.4 Immobilization of Protein and DNA Constructs on Beads

1. Protein-coated microspheres are made by mixing ~5 μg of c-myc-tagged-protein molecules and 1 μl Anti-c-myc-coated beads in 10 μl refolding buffer. After 30 min incubation on a rotary mixer (4 °C), the beads are diluted in 400 μl refolding buffer for use in optical tweezers experiments (*see* **Notes 7** and **8**).
2. DNA-coated microspheres are made by mixing ~70 ng of dsDNA molecules and 1 μl Anti-digoxigenin-coated beads in 10 μl refolding buffer. The beads are incubated for 30 min on a rotary mixer (4 °C) to get immobilized on the surface (*see* **Note 8**).
3. To couple Neutravidin to the DNA handles, ~1 μg Neutravidin is added and mixture is incubated for extra 15 min on the rotary mixer (4 °C).
4. Beads are washed by pelleting at 17,000 × *g* (for 10 min) in a micro-centrifuge tube at 4 °C and resuspended in 400 μl refolding buffer for use in optical tweezers experiments (*see* **Note 6**).

3.5 Tether Formation

1. The protein-coated microspheres are flown into a flow-cell that is mounted onto the optical tweezers instrument [9]. One microsphere is captured by an optical trap and held there, or subsequently positioned onto a micropipette tip.
2. DNA-coated microspheres are flown in, while the previous sample is flown out. One microsphere is held in an optical trap (*see* **Note 9**). To prevent future interference in trapping, the rest of the microspheres are flown away using the measurement buffer of choice (*see* **Note 7**).

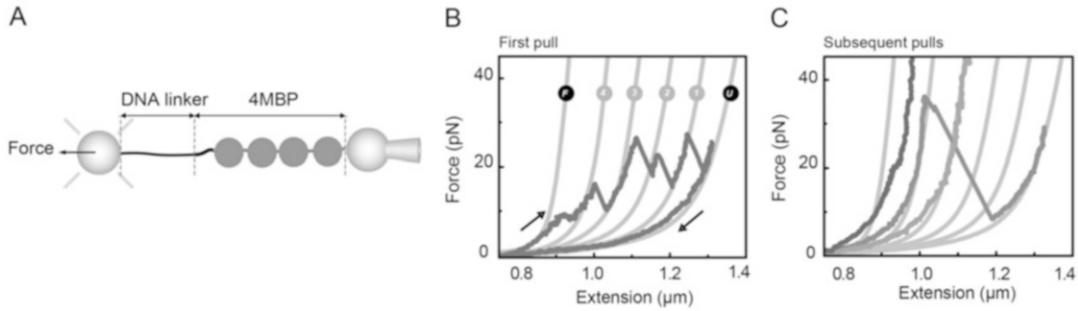

Fig. 2 Tethering of a repeat protein construct to study aggregation. (**a**) The construct is tethered as sMBP in Fig. 1a. (**b**) First stretching–relaxation curves show unfolding of natively folded 4MBP. *Grey lines* represent the theoretical WLC characterizing the DNA–protein chimera from the folded (F) to the unfolded (U) state. After C-terminal unfolding (F → 4) all four MBP repeats unfold one by one (4 → 3 → 2 → 1 → U). (**c**) Second or subsequent stretching curves after relaxation. The stretching traces allow one to probe the aggregated structure, and identify different types of sub-structures, ranging from tight aggregates that are not unfolded to weakly aggregated sub-structures that unfold at moderate forces but give rise to step-sizes larger than one MBP monomer (reproduced with permission from ref. 16)

3. To allow tether formation, the two microspheres are moved in close proximity of each other, such that a tether can be formed through interaction of the biotin on the protein end with the Neutravidin that is bound to the biotin on the DNA end (*see* **Note 10**).
4. Measurements can be performed in a number of ways (*see* **Note 11**). Briefly, cycles of stretching and relaxation allow quantification of unfolding and refolding parameters (Fig. 1; *see* **Note 12**). Interactions with buffer components including chaperones can change the stability of the protein in different stages of folding, as well as its kinetics and adopted structures (*see* **Note 13**). For instance, chaperones can affect not only the folding but also the aggregation between proteins, which can be studied using repeat-protein constructs (Fig. 2).

4 Notes

1. The experiment is sensitive to the quality of protein. It is important to realize that even low percentage of partly aggregated and/or misfolded protein molecules can lead to poor and variable results. Using different purification methods and functional tests is recommended to optimize quality.
2. Proteins are immobilized on the surface via their c-myc-tagged terminus and are connected to DNA linkers through their biotinylated terminus (using biotin-Neutravidin linkage). Hence it is important that both ends are accessible. For

proteins with non-accessible termini, extra peptide linkers can be inserted.

3. We recommend using short linkers (highlighted in **bold** below) before the c-myc-tags and between them (**LE**EQKL ISEEDL**VE**EQKLI SEEDL**VE**EQKLI SEEDL**VE**EQKLI SEEDLVD).
4. EDAC is a moisture sensitive compound and will become inactive upon hydrolysis. It is recommended to store the EDAC powder tightly sealed in the freezer in presence of desiccant.
5. To suppress the formation of bead clusters, 10% (v/v) of 1% Tween can be added to the coupling and storage buffers during the bead preparation.
6. During the coating process, beads may be lost within the sequential washing steps. To obtain appropriate samples with the correct concentration, one can change the volume of storage buffer that is used to store the coated-beads.
7. To have an efficient measurement, one needs to inject proper number of protein- and DNA-coated-beads into the flow cell. Bead trapping efficiency decreases when samples are too diluted, whereas too concentrated samples lead to the trapping of multiple particles. The concentration of bead samples can be adjusted by diluting the protein- and DNA-coated beads in refolding buffer.
8. Multiple tethers or no tethers may form when moving the microspheres together. To optimize tether formation, one can titrate the amount of dsDNA on the anti-digoxigenin microspheres up or down, until single tethers are typically observed, while no tethers or double tethers are rarely observed. Other factors are bead interaction distance and time. One may also titrate the amount of protein attached to the Anti-c-myc coated microspheres.
9. Issues with the (Antibody-)coating reaction or the presence of aggregates in the protein sample are two factors that lead to formation of bead clusters. The clustering of beads simply can be checked under a light microscope, after every preparation step. To dissolve small clusters, one can sonicate the coated beads on ice for 10–15 min.
10. Neutravidin can be substituted with other members of Avidin family, such as Streptavidin and Avidin [14]. They have similar affinity to biotin-streptavidin but different selectivity to possible contaminant proteins. Affinity does not directly predict behavior under mechanical tension as the lower affinity (i.e. nanomolar versus femtomolar) StreptagII-Streptactin was mechanically more resilient [15]. Other short affinity tags

could be explored as possible alternatives if c-myc-tag would compromise protein construct solubility or folding in specific case [14].

11. One way to study protein unfolding and refolding transitions is by moving the beads apart and back again in alternating cycles. Most of the time the trap position is moved at constant speeds, which results in an approximately constant change in force. Smaller proteins tend to refold during relaxation, while larger ones typically refold when fully relaxed. In the latter case, varying the waiting time in the relaxed state allows quantification of the refolding rate.
12. Force-extension curves measured from Protein–DNA chimera's can be fitted using the extensible worm-like chain model (EWLC) for the DNA tether and the worm-like chain model (WLC) for unfolded parts of the protein. This allows one to identify different folded states of the protein by the measured length, which is dominated by the unfolded segments of the protein chain.
13. One may study the effect of buffer conditions or molecular chaperones on the folding and unfolding process. Components can be flushed in during the experiment while the substrate protein is in different stages of folding. The interaction times can be varied to assess binding kinetics.

Acknowledgement

Work in the laboratory of S.J.T. is funded by the Netherlands Organization for Scientific Research (NWO).

References

1. Kellermayer MS, Smith SB, Granzier HL, Bustamante C (1997) Folding-unfolding transitions in single titin molecules characterized with laser tweezers. Science 276(5315):1112–1116
2. Cecconi C, Shank EA, Bustamante C, Marqusee S (2005) Direct observation of the three-state folding of a single protein molecule. Science 309(5743):2057–2060. doi:10.1126/science.1116702
3. Heidarsson PO, Naqvi MM, Otazo MR, Mossa A, Kragelund BB, Cecconi C (2014) Direct single-molecule observation of calcium-dependent misfolding in human neuronal calcium sensor-1. Proc Natl Acad Sci U S A 111 (36):13069–13074. doi:10.1073/pnas.1401065111
4. Stigler J, Ziegler F, Gieseke A, Gebhardt JC, Rief M (2011) The complex folding network of single calmodulin molecules. Science 334 (6055):512–516. doi:10.1126/science.1207598
5. Gebhardt JC, Bornschlogl T, Rief M (2010) Full distance-resolved folding energy landscape of one single protein molecule. Proc Natl Acad Sci U S A 107(5):2013–2018. doi:10.1073/pnas.0909854107
6. Neupane K, Foster DA, Dee DR, Yu H, Wang F, Woodside MT (2016) Direct observation of transition paths during the folding of proteins and nucleic acids. Science 352(6282):239–242. doi:10.1126/science.aad0637
7. Yu H, Liu X, Neupane K, Gupta AN, Brigley AM, Solanki A, Sosova I, Woodside MT (2012) Direct observation of multiple misfolding pathways in a single prion protein molecule. Proc

Natl Acad Sci U S A 109(14):5283–5288. doi:10.1073/pnas.1107736109

8. Yu H, Dee DR, Liu X, Brigley AM, Sosova I, Woodside MT (2015) Protein misfolding occurs by slow diffusion across multiple barriers in a rough energy landscape. Proc Natl Acad Sci U S A 112(27):8308–8313. doi:10.1073/pnas.1419197112
9. Bechtluft P, van Leeuwen RG, Tyreman M, Tomkiewicz D, Nouwen N, Tepper HL, Driessen AJ, Tans SJ (2007) Direct observation of chaperone-induced changes in a protein folding pathway. Science 318(5855):1458–1461. doi:10.1126/science.1144972
10. Mashaghi A, Kramer G, Bechtluft P, Zachmann-Brand B, Driessen AJ, Bukau B, Tans SJ (2013) Reshaping of the conformational search of a protein by the chaperone trigger factor. Nature 500(7460):98–101. doi:10.1038/nature12293
11. Mashaghi A, Bezrukavnikov S, Minde DP, Wentink AS, Kityk R, Zachmann-Brand B, Mayer MP, Kramer G, Bukau B, Tans SJ (2016) Alternative modes of client binding enable functional plasticity of Hsp70. Nature 539(7629):448–451. doi:10.1038/nature20137
12. Cecconi C, Shank EA, Dahlquist FW, Marqusee S, Bustamante C (2008) Protein-DNA chimeras for single molecule mechanical folding studies with the optical tweezers. Eur Biophys J 37(6):729–738. doi:10.1007/s00249-007-0247-y
13. Cecconi C, Shank EA, Marqusee S, Bustamante C (2011) DNA molecular handles for single-molecule protein-folding studies by optical tweezers. DNA Nanotechnol 749:255–271
14. Minde DP, Halff EF, Tans S (2013) Designing disorder: tales of the unexpected tails. Intrinsically Disord Proteins 1(1):e26790
15. Moayed F, Mashaghi A, Tans SJ (2013) A polypeptide-DNA hybrid with selective linking capability applied to single molecule nanomechanical measurements using optical tweezers. PLoS One 8(1):e54440. doi:10.1371/journal.pone.0054440
16. Ungelenk S, Moayed F, Ho CT, Grousl T, Scharf A, Mashaghi A, Tans S, Mayer MP, Mogk A, Bukau B (2016) Small heat shock proteins sequester misfolding proteins in near-native conformation for cellular protection and efficient refolding. Nat Commun 7:13673. doi:10.1038/ncomms13673

Chapter 4

Combining Structure–Function and Single-Molecule Studies on Cytoplasmic Dynein

Lu Rao, Maren Hülsemann, and Arne Gennerich

Abstract

Cytoplasmic dynein is the largest and most intricate cytoskeletal motor protein. It is responsible for a vast array of biological functions, ranging from the transport of organelles and mRNAs to the movement of nuclei during neuronal migration and the formation and positioning of the mitotic spindle during cell division. Despite its megadalton size and its complex design, recent success with the recombinant expression of the dynein heavy chain has advanced our understanding of dynein's molecular mechanism through the combination of structure–function and single-molecule studies. Single-molecule fluorescence assays have provided detailed insights into how dynein advances along its microtubule track in the absence of load, while optical tweezers have yielded insights into the force generation and stalling behavior of dynein. Here, using the *S. cerevisiae* expression system, we provide improved protocols for the generation of dynein mutants and for the expression and purification of the mutated and/or tagged proteins. To facilitate single-molecule fluorescence and optical trapping assays, we further describe updated, easy-to-use protocols for attaching microtubules to coverslip surfaces. The presented protocols together with the recently solved crystal structures of the dynein motor domain will further simplify and accelerate hypothesis-driven mutagenesis and structure–function studies on dynein.

Key words Microtubules, Microtubule motor proteins, Cytoplasmic dynein, Recombinant proteins, Microtubule immobilization, Fluorescence labeling, Single-molecule assays, Optical tweezers, Optical trapping, Yeast gene manipulation

1 Introduction

Cytoplasmic dynein (referred to here as dynein) is the primary motor for microtubule (MT) minus-end-directed motility in eukaryotes [1–6]. Its function is essential for numerous cellular activities, such as cell division, cell migration, and the transport of subcellular cargoes. Not surprisingly, dysfunction of dynein and its cofactors contribute to a growing number of human diseases, collectively termed "dyneinopathies" [7–9], including spinal muscular atrophy (SMA) [10, 11], SMA with lower extremity predominance (SMALED) [12–14], Charcot-Marie-Tooth disease (type 2) (CMT) [15], congenital cataracts, and gut dysmotility [9],

Erwin J.G. Peterman (ed.), *Single Molecule Analysis: Methods and Protocols*, Methods in Molecular Biology, vol. 1665, DOI 10.1007/978-1-4939-7271-5_4, © Springer Science+Business Media LLC 2018

malformations of cortical development [16–20], and other debilitating neurodevelopmental and neurodegenerative diseases [15, 18, 19, 21–24]. The molecular mechanisms of dynein and its cofactors, however, remain largely unknown [3, 25–28], posing a major barrier to treatment of dyneinopathies.

Dynein is a member of the functionally diverse family of AAA+ ATPases (AAA+: *A*TPase *a*ssociated with various cellular *a*ctivities [29]). AAA+ proteins typically assemble into hexameric, ring-shaped structures [30, 31]. In contrast, while dynein and its closest relative, midasin [32, 33], also contain six AAA+ domains arranged in a ring, their AAA+ domains are concatenated in a single heavy chain (HC) polypeptide [27, 34]. Dynein forms a dimer of two identical HCs, and binds via its tail domain to several other associated subunits and accessory proteins that are involved in the regulation of the motor and in the attachment to a diverse set of cargos [3]. Dynein's C-terminal motor domain contains the six AAA+ modules (AAA1–6), the first four of which (AAA1–4) hydrolyze and/or bind ATP [28], and three elongated structures that protrude from the AAA+ ring. The ~15-nm coiled-coil "stalk" emerges from AAA4 [35] and separates the MT-binding domain from the AAA+ ring [36], and the coiled-coil "buttress" [36] (or "strut" [37]) extends from AAA5 and contacts the stalk. The third element, the ~10-nm "linker" [38, 39], emerges from AAA1 and connects the tail to the AAA+ ring. While ensemble-based and single-molecule microscopy techniques combined with mutagenesis and structure–function studies have begun to decipher the function of these elements [40–51], how dynein's subdomains work together to generate the coordinated movements of dynein's motor domains remains unclear.

Single-molecule motility studies using total internal reflection fluorescence (TIRF) microscopy permit the measurement of key biophysical parameters of cytoskeletal motors, such as the on rate of filament binding, velocity, and processivity (the ability to take multiple steps before dissociating). To permit high-precision tracking, the recombinant dynein HC can be tagged at the C-terminal motor domain or the N-terminal tail using genetic labeling techniques, such as HaloTags® or SNAP-tags®, to covalently bind bright organic fluorophores or quantum dots. With these tools, a TIRF microscope equipped with an electron multiplying CCD (EMCCD), can resolve the nanometer-scale steps that the highly processive *S. cerevisiae* dynein takes along MTs [43, 44]. N-terminal tags can also be used to couple the motor to polystyrene trapping beads (which are coated with antibodies against the N-terminal tag) for use in optical trapping experiments [45, 46, 48]. In an optical trapping experiment, a tightly focused near-infrared laser beam (the optical tweezers [52]) is used to trap a motor-coated polystyrene bead. The experimenter can than reposition the laser beam to place the trapped bead over an MT bound to

the coverslip. Once a bead-anchored motor binds the MT and starts to move, it displaces the trapped bead from the trap center. A restoring force then acts to pull the bead back toward the trap center, causing the motor to detach or to advance until its movement ceases when its maximum force generation (stall force) is reached. Critical to both TIRF-based single-molecule fluorescence and optical trapping experiments is the rigid attachment of polymerized MTs to coverslip surfaces [53]. In case of optical tweezers, it is preferable for the long MT axes to be aligned with the long axis of the slide chamber.

Below, we provide improved protocols for the efficient generation of *S. cerevisiae* mutant strains, for the growth of *S. cerevisiae* cells expressing full-length dynein, and for the purification of the tagged dynein motors. In addition, we present three updated protocols for attaching MTs to coverslip surfaces: (1) attachment through biotin-streptavidin linkages, (2) attachment using poly-L-lysine (PLL)-coated glass surfaces (which yields MTs well aligned with the long axis of the coverslip), and (3) a new protocol we have developed which combines elements of the first two protocols in order to yield well aligned MTs that remain rigidly attached for a significantly longer period of time—an excellent option for optical trapping experiments.

2 Materials

2.1 Generation of Yeast Constructs

2.1.1 Primer design for PCR

1. Saccharomyces Genome Database (SGD): http://www.yeastgenome.org/
2. Serial Cloner software for DNA and protein sequence analysis (Serial Basics: http://serialbasics.free.fr/Home/Home.html).
3. Primer-BLAST (NCBI: https://www.ncbi.nlm.nih.gov/tools/primer-blast/) or PrimerQuest tool (Integrated DNA Technologies: https://www.idtdna.com/Primerquest/Home/Index).
4. DNA primers (Integrated DNA Technologies).
5. *Kluyveromyces lactics* URA3 gene with its promoter and terminator.

2.1.2 Generation of Linear Double-Stranded DNA

1. DNA polymerase: KOD hot start DNA polymerase (EMD Millipore, #71086), store at −20 °C.
2. PCR tubes: Thermowell Gold 0.2 mL polypropylene PCR tubes with flat cap (Corning, #3745).
3. 10 mM Tris buffer, pH 7.6.
4. TE buffer: 10 mM Tris, 1 mM EDTA, pH 7.6.
5. Amplyus miniPCR™ (*see* **Note 1**).

6. NucleoSpin Gel and PCR clean-up (Macherey-Nagel, #740609).
7. NanoPhotometer® (Implen P360).
8. Agarose: Ultrapure agarose (ThermoFisher Scientific, #16500–100).
9. 5× Tris-Borate-EDTA (TBE) buffer: For 1 L, add 54 g of Tris-base, 27.5 g of boric acid, and 20 mL of 0.5 M EDTA (pH 8.0), and fill to 1 L with ddH_2O. The working strength is 0.5×.
10. DNA gel stain: SYBR Safe DNA gel stain, 10,000× (ThermoFisher Scientific, #S33102).
11. blueGel™ electrophoresis system (Amplyus).
12. DNA ladder: 1 Kb plus DNA ladder (ThermoFisher Scientific, #10787018), store at −20 °C.
13. 5× Orange G loading dye: 0.125% (w/v) Orange G, 2.5× TBE, 50% glycerol, store at 4 °C.
14. Owl™ EasyCast™ B1A Mini Gel Electrophoresis System (ThermoFisher Scientific)

2.1.3 Transformation of Yeast Cells with PCR Products

1. Yeast stock, stored at −80 °C.
2. Wooden applicators: Fisherbrand plain-tipped applicators, wood, 15 cm (Fisher Scientific, #23–400-112).
3. Peptone: BD Bacto™ peptone, an enzymatic digest of animal protein (BD, #211677).
4. Yeast extract: BD Bacto™ yeast extract, water-soluble extract of autolyzed yeast cells suitable for use in culture media (BD, #212750).
5. Agar: BD Difco™ agar, granulated, used as a solidifying agent for culture media (BD, #214530).
6. Dextrose (D-glucose), anhydrous (Fisher Scientific, #D16).
7. Dextrose solution: 40% stock. Add 400 g of dextrose to a 1 L bottle, fill with ddH_2O to 1 L, sterilize by either autoclaving or filtering via a filter unit (Nalgene rapid-flow sterile disposable filter units with SFCA membrane, pore size 0.2 μm, diameter 90 mm, ThermoFisher Scientific, #161-0020).
8. Fisherbrand petri dishes with clear lid, 100 × 15 mm (Fisher Scientific, #FB0875713).
9. YPD plate: For 400 mL, add 8 g peptone, 4 g yeast extract, 8 g agar, and 380 mL ddH_2O to a 500 mL bottle, autoclave. Once slightly cooled down, add 20 mL of sterilized dextrose solution, mix well but do not invert. Pour 10–20 mL for each plate. Stack the plates and leave them on the bench at room temperature overnight, then store them upside down at 4 °C.

10. 2× YPD solution: In a 1 L bottle, add 40 g peptone, 20 g yeast extract, and 900 mL ddH_2O, autoclave. Once slightly cooled down, add 100 mL of sterilized dextrose solution. Mix well, but do not invert.
11. Frozen-EZ Yeast Transformation II Kit™ (Zymo Research, #T2001), store at 4 °C.
12. Yeast nitrogen base (YNB) without amino acids: Difco yeast nitrogen base without amino acids, Wickerham formula (BD, #291940).
13. Ura dropout (Ura-): Yeast media, Ura dropout mix (Clontech, #630416).
14. Adenine, semisulfate salt (Sigma-Aldrich, #A9126).
15. Syringe filter unit: Millex-GP syringe filter unit, 0.22 μm, polyethersulfone, 33 mm, gamma sterilized (EMD Millipore, #SLGP033RS).
16. 60 mL syringe without needle: 60 mL BD Luer-Lok syringe, nonsterile, polypropolene (BD, #301035).
17. SC/URA- plates: For 400 mL, add 8 g agar and 350 mL ddH_2O to a 500 mL bottle, autoclave. In a sterile 50 mL conical tube, add 2.9 g YNB without amino acids, 400 mg Ura-, 8 g dextrose, fill with 50 mL ddH_2O, nutate to dissolve, heat slightly if needed to help dissolve. Sterilize by a syringe filter unit. Add the mixture to the agar solution and mix well. Pour and store as for YPD plate.
18. Uracil (Sigma-Aldrich, #U0750).
19. 5-Fluoroorotic acid (5-FOA), monohydrate (Gold Biotechnology, #F-230), store at −20 °C.
20. SC/5-FOA plates: For 400 mL, add 8 g agar and 350 mL ddH_2O to a 500 mL bottle, autoclave. In a sterile 50 mL conical tube, add 2.9 g YNB without amino acids, 400 mg Ura-, 20 mg uracil, 400 mg 5-FOA, 8 g dextrose, fill with 50 mL ddH_2O, heat to help dissolve. Sterilize by a syringe filter unit. Add the mixture to the agar solution and mix well. Pour and store as for YPD plate.
21. 20 mM NaOH.
22. 50% glycerol, sterilized.
23. Cryogenic tubes: Nalgene general long-term storage cryogenic tubes, 2 mL (ThermoFisher Scientific, #5000–0020).

2.2 Yeast Growth and Harvest

2.2.1 Dynein Expressed Behind Native Promoter

1. 2× YP solution: In a 6 L flask, add 80 g peptone, 40 g yeast extract, and 1.75 L ddH_2O, autoclave.
2. 1 L centrifuge bottle: Nalgene 1 L super-speed centrifuge bottles with sealing closure (ThermoFisher Scientific, #3141–1006).

3. An empty pipette tip box or a plastic container.
4. A styrofoam box.
5. 50 mL serological pipet: Falcon 50 mL serological pipet, polystyrene, 1.0 increments (Corning, #357550).
6. Pipette controller: Accu-Jet® pro pipette controller with adjustable speed control (BrandTech Scientific, #26330).
7. A metal spoon.

2.2.2 Dynein Expressed Behind Galactose Promoter

1. D-(+)-raffinose, pentahydrate (Sigma-Aldrich, #R0250).
2. Raffinose solution: 20% stock. In a 150 mL bottle, add 20 g raffinose and fill with ddH_2O to 100 mL, slightly heat to dissolve. Sterilize either via filtering or autoclaving.
3. 1× YPR solution: In a 1 L bottle, add 20 g peptone, 10 g yeast extract, and 900 mL ddH_2O, autoclave. Once slightly cooled down, add 100 mL of sterilized raffinose solution. Mix well, but do not invert.
4. D-(+)-Galactose, anhydrous (Fisher Scientific, #G1).
5. Galactose solution: 40% stock. In a 1 L bottle, add 400 g galactose and fill with ddH_2O to 1 L, heat to dissolve. Sterilize either via filtering or autoclaving.

2.3 Purification of Yeast Dynein

1. DL-dithiothreitol (DTT) (Sigma-Aldrich, #D9779): dissolve in ddH_2O to 1 M stock, store at −20 °C.
2. Adenosine 5′-triphosphate·Mg (ATP.Mg) (Sigma-Aldrich, #A2383): Dissolve ATP in 100 mM $MgCl_2$ to 100 mM stock, store at −20 °C.
3. Pepstatin A (Sigma-Aldrich, #P5318): dissolve in ddH_2O to 10 μg/mL stock, store at −20 °C.
4. Leupeptin (Sigma-Aldrich, #L2884): dissolve in ddH_2O to 10 μg/mL stock, store at −20 °C.
5. Pefabloc SC (Sigma-Aldrich, #11429868001): dissolve in ddH_2O to 100 mM stock, store at −20 °C.
6. Benzamidine hydrochloride, hydrate (Sigma-Aldrich, #B6506): dissolve in ddH_2O to 200 mM stock, store at −20 °C.
7. Triton X-100: dilute to 25% (v/v) stock (Sigma-Aldrich, #X100).
8. 5× Lysis buffer (5×LB): 150 mM HEPES, 250 mM KAc, 10 mM $Mg(Ac)_2$, 5 mM EGTA, 50% glycerol
9. 1× Tev buffer (1×Tev): 50 mM HEPES, 150 mM KAc, 2 mM $Mg(Ac)_2$, 1 mM EGTA, 10% glycerol.
10. Type 70.1 Ti rotor, fixed angle, titanium, 12 × 13.5 mL, 70,000 rpm, 450,000 × *g* (Beckman Coulter, #342184).

11. TLA-110 rotor, fixed angle, titanium, 8 × 5.1 mL, 110,000 rpm, 657,000 × *g* (Beckman Coulter, #366735).
12. Beckman L7-65 ultracentrifuge.
13. Beckman Optima TLX ultracentrifuge.
14. Eppendorf Refrigerated Microcentrifuge.
15. Ti 70.1 tube: polycarbonate bottle, with cap assembly, 10.4 mL, 16 × 76 mm (Beckman, #355603).
16. TLA-110 tube: Polycarbonate tube, thickwall, 3.2 mL, 13 × 56 mm (Beckman, #362305).
17. Columns: Poly-Prep chromatography columns, 9 cm high, 2 mL bed volume (0.8 × 4 cm) (Bio-Rad, #7311550).
18. Grinder (KitchenAid model BCG1110B).
19. A metal spatula.
20. Transfer pipets: BD Falcon disposable transfer pipets, 3 mL (BD, #357524).
21. Glass Pasteur pipets: Fisherbrand disposable borosilicate glass Pasteur pipets, 9 in. (Fisher Scientific, #13–678-20C).
22. IgG beads: IgG Sepharose 6 fast flow, 10 mL (GE Healthcare, #17-0969-01).
23. A nutating mixer.
24. HaloTag fluorescent ligands (Promega) or SNAP-tag fluorescent ligands (New England BioLabs).
25. Tev protease: AcTev protease, 10 units/μL (ThermoFisher Scientific, #12575015).
26. Low retention microcentrifuge tubes: Fisherbrand siliconized low-retention microcentrifuge tubes, 0.5 mL (Fisher Scientific, #02–681-311).
27. 5× SDS loading buffer: 0.25% (w/v) bromophenol blue, 10% (w/v) sodium dodecyl sulfate (SDS), 0.5 M DTT, 0.25 M Tris, 50% (v/v) glycerol, pH 6.8.
28. Gradient gel: NuPAGE® 4–12% bis-tris protein gels, 1.5 mm, 15-well, store at 4 °C (ThermoFisher Scientific, #NP0336BOX).
29. Novex XCell SureLock™ mini-cell electrophoresis system (ThermoFisher Scientific, #EI0001).
30. Running buffer: NuPAGE® MOPS SDS running buffer, 20× (ThermoFisher Scientific, #NP0001), dilute to 1× prior to usage.
31. Gel stain: InstantBlue™ protein stain (Expedeon, #ISB1L).
32. An Odyssey® imaging system (LI-COR Biotechnology).

2.4 MT Binding and Release Purification of Yeast Dynein

2.4.1 Polymerization of MTs

1. Paclitaxel (Sigma-Aldrich, #T7191): dissolve in DMSO to 10 mM stock, store at −20 °C.
2. BRB80 with 10% glycerol: 80 mM PIPES, 2 mM $MgCl_2$, 1 mM EGTA, 10% glycerol, pH 6.8, store at room temperature for short term and at 4 °C for long term.
3. BRB80 with 60% glycerol (glycerol cushion): 80 mM PIPES, 2 mM $MgCl_2$, 1 mM EGTA, 60% glycerol, pH 6.8.
4. Guanosine 5′-triphosphate·Mg (GTP.Mg) (Sigma-Aldrich, #G8877): Dissolve GTP in 100 mM $MgCl_2$ to 100 mM stock, store at −20 °C.
5. Tubulin (purified from porcine brain; Cytoskeleton Inc., #T240): 5 mg/mL stock. Dissolve one vial of tubulin (1 mg) in 200 μL BRB80 with 10% glycerol, aliquot into 5 μL volumes, flash-freeze and store at −80 °C.
6. TLA-100 rotor tube: Polycarbonate tube, thickwall, 230 μL, 7 × 21 mm (Beckman Coulter, #343775).
7. TLA-100 rotor, fixed angle, titanium, 20 × 0.2 mL, 100,000 rpm, 436,000 × *g* (Beckman Coulter, #343837).

2.4.2 MT Binding and Release Purification

1. Sucrose cushion: 30 mM HEPES, 2 mM $MgCl_2$, 1 mM EGTA, 150 mM KCl, 25% (w/v) sucrose, 10% glycerol, pH 7.4.
2. Wash buffer: 30 mM HEPES, 2 mM $MgCl_2$, 1 mM EGTA, 150 mM KCl, 10% glycerol, pH 7.4.

2.5 Polymerization of MTs for Single-Molecule Assays

2.5.1 Polymerization of Functionalized MTs

1. Cy3- or Cy5-labeled tubulin (labeling of tubulin with mono-NHS dyes has been previously described in detail [53]): prepare aliquots with 1 μg labeled tubulin per aliquot.
2. Biotinylated tubulin (Cytoskeleton Inc., #T333P): 20 μg/vial. Dissolve one vial in 20 μL BRB80 with 10% glycerol, aliquot to 1 μL per aliquot, flash-freeze and store at −80 °C.

2.5.2 Polymerization of Polarity-Marked MTs

1. Rhodamine-labeled tubulin: 20 μg/vial (Cytoskeleton Inc., #TL590M).

2.6 Coverslip Preparation for MT Attachment

2.6.1 Immobilization via Biotin–Streptavidin Interaction

1. Coverslips: No. 1.5H, 170 ± 5 μm thickness, 18 mm × 18 mm, high performance, ISO 8255 compliant (Zeiss, #474030–9000-000).
2. Glass slides: Fisherbrand Superfrost disposable microscope slides, 1 mm thickness (Fisher Scientific, #12-550-123).
3. Coverslip rack: Wash-N-Dry™ coverslip rack (Sigma-Aldrich, #Z688568).
4. Jars: Nalgene™ straight-sided wide-mouth polycarbonate jars with closure, 125 mL (ThermoFisher Scientific, #2116–0125).
5. 1 M HCl, 100 mL.

6. Ethanol, 100 mL.
7. 30% ethanol, 100 mL.
8. 50% ethanol, 100 mL.
9. BSA-biotin (Pierce bovine serum albumin, biotinylated; ThermoFisher Scientific, #29103): Dissolve in BRB80 with 10% glycerol to create a 5 mg/mL stock solution. Aliquot into 15 μL volumes and store at −80 °C.
10. Streptavidin (Pierce streptavidin; ThermoFisher Scientific, #21122): Dissolve in BRB80 with 10% glycerol to 5 mg/mL stock, aliquot into 4 μL volumes and store at −80 °C.
11. BSA: 50 mg/mL in BRB80 with 10% glycerol, store at −20 °C.
12. BRB80 with supplements (BRB80-s): 80 mM PIPES, 2 mM $MgCl_2$, 1 mM EGTA, 20 μM paclitaxel, 1 mM DTT, aliquot into 200 μL volumes and flash-freeze, store at −20 °C.

2.6.2 Immobilization via Poly-L-Lysine

1. 25% (v/v) HNO_3 solution, 250 mL.
2. 2 M NaOH solution, 250 mL.
3. Poly-L-lysine solution (PLL) (Sigma-Aldrich, #P8920): 0.1% (w/v) stock, 100 mL, keep in a jar. Dilute 10 mL in 90 mL ddH_2O to 0.01% (w/v), keep in a jar.
4. Tween-20 solution (Tween 20 Surfact-Amps detergent solution; ThermoFisher Scientific, #28320): 10% (v/v) stock, dilute 1 mL in 99 mL ddH_2O to 0.1% (v/v), keep in a jar.

2.6.3 Immobilization via PLL and Biotin-Streptavidin Interactions

1. NHS-biotin (EZ-link NHS-biotin; ThermoFisher Scientific, #20217): Dissolve in DMSO to 100 mM stock, aliquot into 2 μL volumes, flash-freeze and store at −20 °C.
2. Coupling buffer: 100 mM Na_3PO_4, adjust to pH 7.4 with HCl.
3. HME30: 30 mM HEPES, 2 mM $MgCl_2$, 1 mM EGTA, pH 7.4.

2.7 Single-Molecule Assays

2.7.1 Single-Molecule Fluorescence Assay

1. HME30 with supplements (HME30-s): 30 mM HEPES, 2 mM $MgCl_2$, 1 mM EGTA, pH 7.4, 20 μM paclitaxel, 20 mM glucose, 1 mM DTT, 2 mM Trolox, aliquot into 200 μL volumes and flash-freeze, store at −20 °C (*see* **Note 2**).
2. β-Casein: 25 mg/mL, prepared as described in detail previously [53], store at −20 °C.
3. POC oxygen scavenging system: prepared as described in detail previously [54], store at −80 °C.
4. Vacuum grease.

2.7.2 Optical Trapping Assay

1. AntiGFP antibody-coated polystyrene beads: prepared as described in detail previously [54], store at 4 °C.

2. α-casein (Sigma-Aldrich, #C6780): 25 mg/mL stock. Prepare in the same way as β-casein, aliquot into 5 μL volumes, flash-freeze and store at −20 °C.
3. Phospho(enol)pyruvic acid, monopotassium salt (PEP) (Sigma-Aldrich, #P7127): 100 mM stock. Dissolve PEP in 100 mM $MgCl_2$ to 100 mM, store at −20 °C.
4. Pyruvate kinase (PK) (Pyruvate kinase from rabbit muscle, type III; Sigma-Aldrich, #P9136), 1 unit/μL stock. Dissolve in BRB80 with 10% glycerol to 1 unit/μL stock, aliquot into 1.5 μL volumes, flash-freeze and store at −80 °C.

3 Methods

3.1 Generation of Yeast Constructs

Yeast cell transformation with specifically designed PCR products or plasmids is indispensable for manipulating yeast genes [55]. The following protocols provide detailed steps to generate constructs for single-molecule structure–function studies. Here, we use the yeast dynein heavy chain gene as an example, but in principle it can be applied to most yeast genes (*see* **Note 3**). To generate a yeast dynein heavy chain construct that contains only the desired modification such as insertions, deletions, or mutations/replacements, we use a standard two-step PCR-mediated yeast transformation method [56] (Fig. 1a). First, the yeast selection marker URA3 is used to disrupt the target gene. A medium without uracil is then used for selection, since yeast without the URA3 insertion cannot grow in such conditions. In the second transformation step, the desired DNA sequence replaces the URA3 marker using 5-FOA as a selection reagent (*see* **Note 4**).

3.1.1 Primer Design for PCR

Because of the high efficiency homologous recombination mechanism in yeast, foreign DNA can readily be incorporated into the yeast genome. For homologous recombination to occur, the flanking sequences of the insertion gene must overlap with the 5′ and 3′ ends of the endogenous gene. To achieve good transformation efficiency, primers must be designed to ensure an adequate length of overlap between the flanking sequences of the insertion and the 5′ and 3′ ends of the endogenous gene (*see* **Note 5**).

1. Locate the dynein heavy chain gene (DYN1) in the Saccharomyces Genome Database (SGD), and obtain the genomic DNA sequence with ±1 kb (*see* **Note 6**).
2. Locate the site in the gene for the insertion, deletion, or mutation, and then select the sites for the flanking sequences (~500 bp upstream from the beginning and ~500 bp downstream from the end of the site) (*see* **Note 7**).

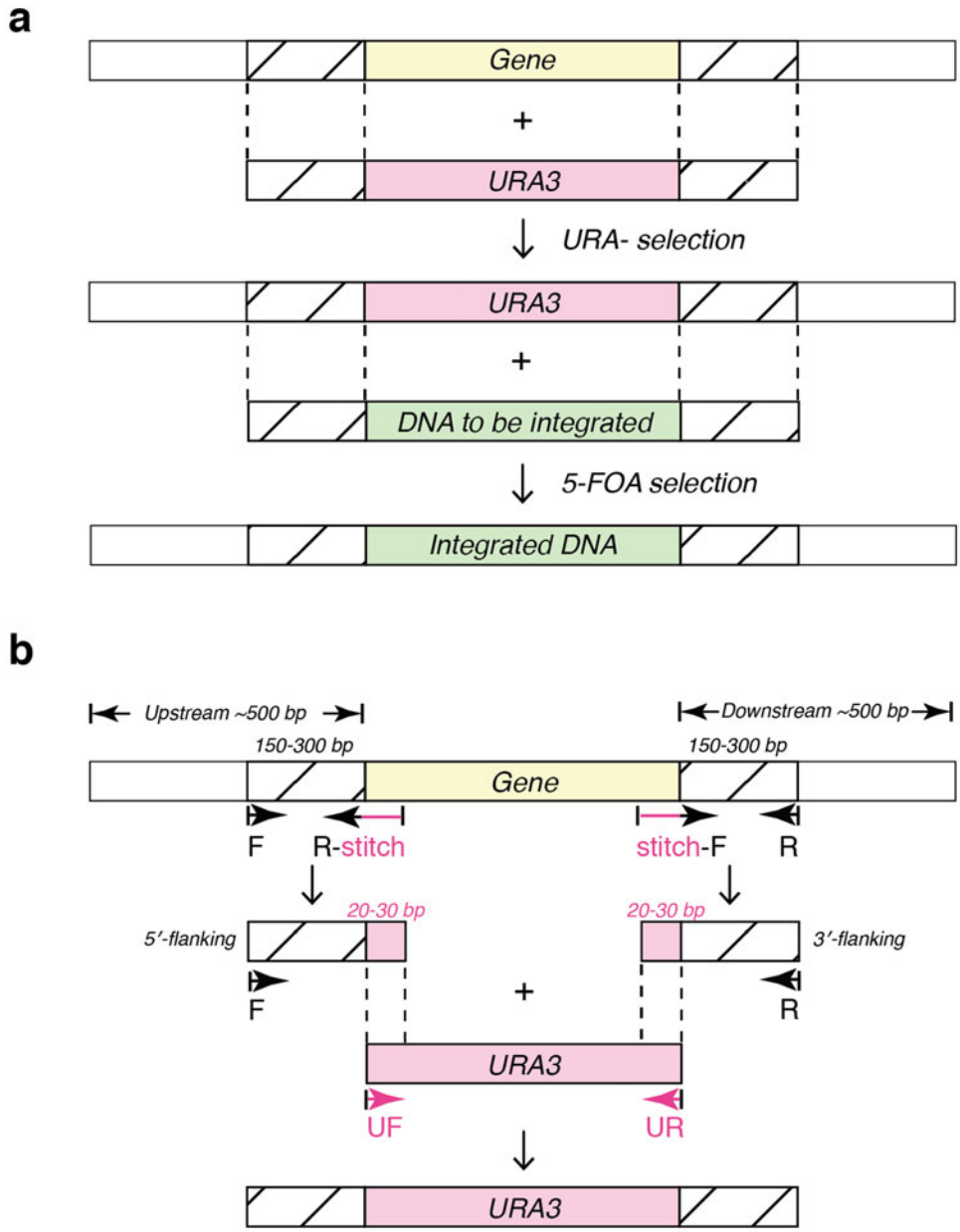

Fig. 1 (**a**) Scheme of PCR-mediated two-step yeast transformation. During the first transformation, the targeted gene (*yellow*) is replaced by linear URA3 gene (*pink*) with flanking DNA (*striped*). The flanking DNA overlaps with yeast's endogenous sequences so it can be integrated into yeast genome through homologous recombination. In the second step, the PCR product containing the target gene with intended modifications (*green*) replaces the URA3 in the genome via 5-FOA selection. (**b**) Scheme of primer design for generating URA3-containing PCR product. To generate a sequence with flanking DNA that overlaps with yeast genome, primer pairs that are upstream and downstream of the targeted sequence are obtained. The target sequence (*yellow*) together with ~500 bp both up- and downstream is selected, and the sequence is run through a primer design tool to obtain forward and reverse primers that are within ~150–300 bp from the targeted sequence ("F" and "R"). Next, pairs of primers are designed to stitch the flanking yeast sequence with URA3.

3. Design a pair of primers, 20–30 bp in length, that are ~150–300 bp upstream and downstream of the targeting site (designated "F" and "R" in Fig. 1b) (*see* **Note 8**). Make sure the reverse primer has the reverse complementary sequence of the targeted sequence.
4. Next, stitching primers need to be designed. To generate the stitching primer for the upstream flanking region, combine 20–30 bp upstream of the 5′ end of the targeted site with 20–30 bp of the 5′ end of the URA3 gene, and then convert it to its complimentary sequence (the "R-stitch" primer in Fig. 1b). For the downstream flanking region, combine 20–30 bp of the 3′ end of URA3 with 20–30 bp downstream of the targeted site as the "stitch-F" primer (Fig. 1b). The 5′-flanking sequence (with the URA3 overhang) can then be amplified with "F" and "R-stitch" primers, and the 3′-flanking sequence with "stitch-F" and "R" primers, using the yeast genome as a template (*see* Subheading 3.1.2 for gene amplification protocol).
5. The URA3 gene with its promoter and terminator can be amplified using the following primers: 5′-GTGATTCTGGGTAGAAGATCGG ("UF" in Fig. 1b) and 5′-CGATGATGTAGTTTCTGGTTTTTAA ("UR" in Fig. 1b). Note that URA3 of *Kluyveromyces lactis* is used instead of URA3 of *S. cerevisiae* to prevent undesirable recombination with its endogenous site.
6. The final gene insertion product can now be generated using "F" and "R" as primers and the mixture of 5′-flanking DNA, 3′-flanking DNA, and URA3 as template, as described in Subheading 3.1.2.

3.1.2 Generation of Linear Double-Stranded DNA

PCR is used to generate linear double-stranded DNA for yeast transformation. Protocols for PCR have been well established, and the optimization and troubleshooting of PCR have been extensively reviewed [57, 58]. Here we only intend to provide a standard

Fig. 1 (continued) To generate the stitching primer for upstream, 20–30 bp upstream of the 5′ end of the targeted site is combined with the first 20–30 bp of the 5′ end of the URA3 (*pink*), and then converted into its complementary sequence ("R-stitch" primer). To make the downstream stitching primer, the last 20–30 bp of the 3′ end of URA3 is combined with 20–30 bp downstream of the targeted site ("stitch-F" primer). Using yeast genome as template, the 5′-flanking sequence (along with the first 20–30 bp of the URA3 gene) can now be amplified with the "F" and "R-stitch" primers by PCR, while the 3′-flanking region can be amplified with the "stitch-F" and "R" primers. "UF" (5′-GTGATTCTGGGTAGAAGATCGG) and "UR" (5′-CGATGATGTAGTTTCTGGTTTTTAA) primers are used to amplify URA3 with its promoter and terminator. The final PCR product can then be generated using "F" and "R" as primers and the mixture of 5′-flanking DNA, 3′-flanking DNA, and URA3 as template. The same scheme applies for the second step of the yeast transformation, wherein the modified gene of interest (*green* in *a*) replaces the URA3 gene via homologous recombination

PCR protocol using KOD hot start DNA polymerase, which is sufficient to handle reactions described in this chapter (*see* **Note 9**).

1. Create master-mix aliquots for 50 μL PCR reactions: Pre-mix 500 μL 10× reaction buffer, 500 μL dNTPs (2 mM each), 300 μL 25 mM $MgSO_4$, and 3.2 mL ddH_2O, aliquot into PCR tubes in 46 μL volumes, flash-freeze and store at −20 °C. For each reaction, only the primers, template, and DNA polymerase need to be added.
2. Prepare primers: Dissolve the primers in 10 mM Tris buffer to 10 μM final concentration. Flick the tubes several times to help dissolving, do not sonicate. Store at 4 °C short term (up to 1 week), and −20 °C long term (*see* **Note 10**).
3. PCR: Take out one master-mix PCR aliquot from the freezer, add 1.5 μL of each primer, 1 μL 10 ng/μL template (if the template is genomic yeast DNA, *see* **steps 8** and **9** in Subheading 3.1.3), and 0.5 μL DNA polymerase, mix well. Apply standard cycling conditions to set up and start PCR. Purify the PCR products using the DNA cleanup kit. Measure the DNA concentration using the NanoPhotometer and verify the PCR products by DNA electrophoresis.
4. Prepare agarose gel: Based on the size of PCR products, choose a suitable percentage (w/v) of the agarose gel for DNA electrophoresis and calculate the weight of agarose for a 20 mL gel. Measure the agarose in a 50 mL conical tube, add 20 mL of 0.5× TBE buffer, and microwave the solution to dissolve the agarose. Do not completely tighten the cap, and make sure it does not boil. Once the gel cools down slightly, add 2 μL of DNA gel stain, mix well, and pour into the blueGel gel box with appropriate comb(s) in place. Allow the gel to cool down to solidify. Put the gel tray into the blueGel chamber, fill with 0.5× TBE buffer until it covers the gel, and gently pull out the comb.
5. Prepare and load the samples: For each sample, mix 1 μL of DNA ladder or PCR product, 1 μL of 5× Orange G loading dye, and 3 μL of ddH_2O in a 0.5 mL tube. Carefully load the samples into the wells, and run for 30–45 min.
6. Visualize DNA: Visualize the bands using blue light. If a PCR product is clean and its size is as expected, store the PCR product from **step 3** at 4 °C for short term or at −20 °C for long term.
7. Purify DNA via agarose gel: If there are side products, use gel purification to extract the correct product. Prepare 50 mL agarose gel with 5 μL of DNA gel stain, pour into the B1A gel tray, and insert the B1A-6 comb with 1.5 mm thickness. Allow the gel to solidify. Put the gel into the gel box, fill both

chambers with 0.5× TBE until it covers the gel, and gently pull the comb out. Mix 30 μL of the PCR product from **step 3** and 7.5 μL of 5× Orange G loading dye in a 0.5 mL tube. Carefully load the sample into a well. Run at 100 V for 30–45 min (*see* **Note 11**). Weigh a 2 mL tube on a fine balance and zero the balance. Carefully cut the correct DNA product out using a clean razor and put it into the 2 mL tube, measure the weight, and purify it with the DNA cleanup unit.

3.1.3 Transformation of Yeast Cells with PCR Products

Various methods have been developed for yeast transformation [59], with the LiAc/carrier DNA/PEG method being one of the standard methods [60, 61]. Here, we apply the Frozen-EZ Yeast Transformation II Kit™ instead, which is easier and faster to use, since it does not require carrier DNA and heat shock (*see* **Note 12**). Below, we describe how to transform yeast cells with DNA products and for how to verify a successful transformation. The protocol (**steps 1–12**) is executed twice, first with the URA3-containing PCR product, then with the target DNA (to displace the URA sequence inserted in the first transformation). All steps that involve yeast cells must be performed using sterile techniques.

1. Take out a glycerol stock of the mother strain (first transformation) or the yeast strain with the inserted and verified URA sequence (second transformation) from the −80 °C freezer, and place it on dry ice to prevent melting. Use a sterile wooden applicator to scrap yeast cells from the tube, and streak onto a YPD plate. Parafilm the edges of the plate and incubate at 30 °C for 2–3 days until colonies are large enough (~1–2 mm in diameter).
2. Flame the tip of a metal tweezer and use the tweezer to pick a sterile 200 μL pipette tip. Scoop a single colony from the plate and drop the pipette tip into 3–5 mL of 2× YPD media to start the inoculation. Allow the cells to grow overnight at 30 °C with shaking.
3. Measure the OD_{600} of the overnight culture (saturated at OD_{600} ~ 40) and dilute an appropriate volume of the culture into 10 mL 2× YPD to begin the growth at a starting OD_{600} of 0.2. Grow for ~4–6 h with agitation at 30 °C to reach log phase.
4. Centrifuge the culture at 1000 rcf for 3 min to pellet the cells. Discard the supernatant and use residual liquid to resuspend the cells, and then transfer to a sterile 2 mL tube.
5. Proceed to transform the yeast cells with the URA3-containing PCR products (first transformation) or with the DNA target sequence to displace URA3 (second transformation) using the Frozen-EZ Yeast Transformation II Kit™ as specified by the vendor.

6. Resuspend yeast cells in 2 mL of 2× YPD and shake at 30 °C for 2 h to recover (*see* **Note 13**).
7. Pellet the cells at 1000 rcf for 30 s and remove the supernatant, then wash once with 1 mL sterile ddH_2O. Resuspend the cell pellet in 100–200 μL of sterile ddH_2O, and then spread onto a SC/URA- selection plate (first transformation) or on a SC/5-FOA selection plate (second transformation). Parafilm the edge of the plate, and incubate at 30 °C for 2–3 days.
8. Verify that the yeast cells have correctly incorporated the PCR products by using PCR to amplify the sequence of interest using the transformed yeast genome as the template, and then sequence the PCR products. To do so, mark 4–8 colonies on the plate. For each colony, use a 200 μL pipette tip to pick half a colony and resuspend in 40 μL of 20 mM NaOH. Boil for 10 min, then vortex for 20 s, and centrifuge at max speed for 3 min to remove cell debris (for the URA insertion step, 1–2 colonies are usually sufficient).
9. Set up PCR reactions as in **step 3** in Subheading 3.1.2. Use 2 μL of the supernatant of the lysed cells of the previous step as template for a 50 μL PCR reaction. Extend the annealing time to 30 s, and use 35 cycles instead of 25 cycles.
10. Verify the PCR products by DNA electrophoresis as described in **steps 4–6** in Subheading 3.1.2.
11. Choose and purify the PCR products that have the correct size, and send for sequencing.
12. Once the sequence is confirmed, pick the correct colony and inoculate in 5 mL 2× YPD as in **step 2**. After overnight growth, add 1 mL of the overnight culture and 0.5 mL of sterile 50% glycerol to a cryogenic tube. Store at −80 °C (*see* **Note 14**).

3.2 Yeast Growth and Harvest

Yeast dynein's only known function is nuclear positioning during cell division [62, 63]. It is therefore customary to harvest yeast cells during the log phase when the cells are actively dividing, with the assumption that dynein expression is highest during cell division.

3.2.1 Dynein Expressed Behind Native Promoter

1. Inoculate the pre-culture: Streak the yeast cells and start the pre-culture as in **steps 1** and **2** in Subheading 3.1.3.
2. Grow into log phase: Inoculate 45 mL of 2× YPAD media with 5 mL of the overnight culture in a 250 mL sterile flask and shake at 30 °C overnight, then add the culture into a 6 L flask containing 1.75 L 2× YP solution and 200 mL sterile dextrose solution. Shake at 30 °C for 6–8 h.
3. Harvest the cells: Distribute the 2 L cell culture evenly between two 1 L centrifuge bottles and weigh out and balance both

bottles, then harvest the cells by centrifugation at 4000 rcf for 3 min at 4 °C.

4. Wash the cells: Discard the supernatants of both bottles, and resuspend the pellet of one bottle with 200–300 mL ddH_2O. Transfer the resuspended cells into the other bottle with the remaining pellet and add an additional 200–300 mL of ddH_2O. Resuspend the pellet, and fill up the bottle to approximately 1 L. Weigh out and balance the bottle with a centrifuge bottle containing 1 L ddH_2O and harvest the cells again by centrifugation at 4000 rcf for 3 min at 4 °C, then discard the supernatant.
5. Resuspend the cells with a 50 mL serological pipette using the residual water. If necessary, add stepwise 0.5 mL ddH_2O until the pellet can be resuspended.
6. Drop-freeze the cell slurry into liquid nitrogen: Put a used pipette tip box or a plastic container in a styrofoam box and pour liquid nitrogen into the plastic container. Use the 50 mL serological pipette to drip the cell slurry dropwise into the liquid nitrogen (*see* **Note 15**). The frozen yeast bears some resemblance to popcorn at this state (*see* **Note 16**). Chill a metal spoon in liquid nitrogen and use it to transfer droplets into a 50 mL conical tube, then store the tube at −80 °C.

3.2.2 Dynein Expressed Behind Galactose Promoter

Yeast protein expression can be induced by galactose via GAL promoters. Here, the divergent GAL1-GAL10 promoter [64] is inserted before the dynein heavy chain gene [65]. However, this method can only be used for the tail-truncated dynein, which does not bind to and whose function does not dependent on the presence of the intermediate chain, light intermediate chain, and light chain of dynein [44, 45, 65]. Full-length dynein should not be expressed behind the galactose promoter, as this would result in motility defects and aggregation due to the substoichiometric concentrations of the dynein subunits [47, 66]. For expression behind the galactose promoter, it is important to minimize the dextrose concentration during galactose induction, as the galactose promoter is strongly repressed by dextrose [67, 68]. To circumvent this problem, just before the final induction step, the pre-culture is transferred to a media containing raffinose, which is a poor carbon source that relieves the dextrose-induced repression of the galactose promoter [68].

1. Streak the yeast cells on to a YPD plate and start the pre-culture as in **steps 1** and **2** in Subheading 3.1.3.
2. Inoculate the overnight culture into 45 mL of 1× YPR and shake for 8 h at 30 °C.

3. Inoculate the 1× YPR cell culture into a flask containing 1.75 L of 2× YP solution and 200 mL sterilized galactose solution and shake for 18–24 h at 30 °C.
4. Follow **steps 3–6** in Subheading 3.2.1 to harvest cells.

3.3 Purification of Yeast Dynein

The full dynein complex ($Dyn1_{471kDa}$) is purified via its heavy chain, which contains a ZZ-tag at the N-terminus followed by a TEV cleavage site [65]. After cell lysis and an ultracentrifugation step, dynein is bound to IgG beads via the ZZ-tag. After washing the beads, dynein is cleaved from the IgG beads with TEV protease. The same method is used to purify tail-truncated dynein expressed behind the galactose promoter. The procedures, which are to be performed in the cold room if not specified otherwise, describe in detail how to purify and label dynein with a fluorescent dye.

3.3.1 Prepare the Buffers

1. Lysis buffer (LB): Add 60 µL of 1 M DTT, 100 mM ATP.Mg, 10 µg/mL pepstatin A, 10 µg/mL leupeptin, 300 µL of 100 mM pefabloc SC, 600 µL of 200 mM benzamidine, and 1.92 mL ddH_2O to 12 mL of 5× LB to yield 15 mL of 4× LB. Then, add 6 mL 4× LB to 18 mL ddH_2O to yield 24 mL 1× LB. Finally, add 288 µL of 25% (v/v) Triton X-100 to the remaining 9 mL of 4× LB. Keep on ice.
2. Tev release buffer (Tev): Add 10 µL of 1 M DTT, 100 mM ATP, 50 µL of 100 mM pefabloc SC, 80 µL 25% (v/v) Triton X-100 to 10 mL 1× Tev. Keep on ice.

3.3.2 Lyse the Cells

1. Prechill a Type 70.1 Ti rotor and a TLA-110 rotor overnight in the refrigerator. Set the Beckman L7–65 ultracentrifuge and Beckman Optima TLX ultracentrifuge to 4 °C. Prechill four Type 70.1 Ti rotor tubes with caps, four TLA-110 rotor tubes, a 250 mL glass beaker, a 50 mL serological pipette, a glass Pasteur pipette, two chromatography columns, and a 50 mL conical tube in the refrigerator.
2. Chill the coffee grinder and its plastic lid with liquid nitrogen for a few minutes. Test the functionality of grinder to make sure the blade is not stuck.
3. Take one conical tube with the frozen cell droplets from the −80 °C freezer. Transfer the droplets into the grinder and start grinding. Stop grinding as soon as a sign of melting appears on lid (~2 min).
4. Chill a metal spatula in liquid nitrogen. Use it to transfer the ground yeast powder into the prechilled 250 mL glass beaker, then add 3–4 mL 4× LB to the powder (~1 mL per 10 mL yeast powder).
5. Place the beaker immediately into a 37 °C bath to thaw the powder. Stir the powder gently with a plastic transfer pipette to

thaw the powder evenly. When the mixture is close to completely thawed, place the glass beaker quickly back on ice (make sure that the beaker is surrounded by sufficient ice so that the upper level of the powder slurry is also close to the ice).

3.3.3 Clear the cell lysate

1. Use the prechilled 50 mL serological pipet to estimate the volume of the lysate and add an additional 4× LB to the solution to achieve a 1× LB final concentration.
2. Use the pipet to fill 2–4 Type 70.1 rotor tubes with roughly equal amounts of lysate. Fill the tubes to at least 2/3 of their volumes to prevent a potential collapsing of the tubes during centrifugation. Keep them on ice.
3. Wipe off the outside of the tubes with a Kimwipe to remove ice and water, and weigh each tube together with the cap. Transfer sample between tubes using a transfer pipette to balance each pair of tubes with a precision of ±0.1 g, and then tighten the caps.
4. Dry the outside of the tubes again and place the pairs of equal weight in opposite positions in the Type 70.1 rotor. Tighten the rotor's lid and place the rotor in a Beckman L7–65 ultracentrifuge. Once the vacuum is pulled below 250 micron, centrifuge at 65,000 rpm for 30 min at 4 °C. When the centrifugation finishes, take out the rotor. Set centrifuge to 18 °C and pull vacuum again to prevent condensation.
5. Put the tubes quickly on ice, and place the prechilled 50 mL conical tube also on ice. Transfer the supernatants of all tubes into the 50 mL conical tube using the prechilled glass Pasteur pipet. Leave ~0.5 mL in each tube to avoid transferring debris near the pellets.
6. After the supernatants have been transferred, pipette the solutions left in the tubes (without disturbing the pellets) into the TLA-110 rotor tubes, and balance the tubes. Place the tubes into the TLA-110 rotor, tighten the rotor lid, and place the rotor into the Beckman Optima TLX ultracentrifuge, then centrifuge at 100,000 rpm for 10 min at 4 °C.
7. Pipette the supernatants to the 50 mL conical tube from **step 12**. Reserve 2 μL of the lysate for SDS-PAGE gel analysis (LY in Fig. 2a).
8. Estimate the volume of the lysate and add ATP.Mg and pefabloc SC to final concentrations of 0.1 mM and 0.5 mM, respectively.

3.3.4 Purify dynein via its ZZ-tag

1. During centrifugation, take the IgG beads from the refrigerator and invert the tube several times until beads are completely resuspended. Pipette 250 μL of the bead slurry into the prechilled chromatography column using a 1000 μL pipette tip cut

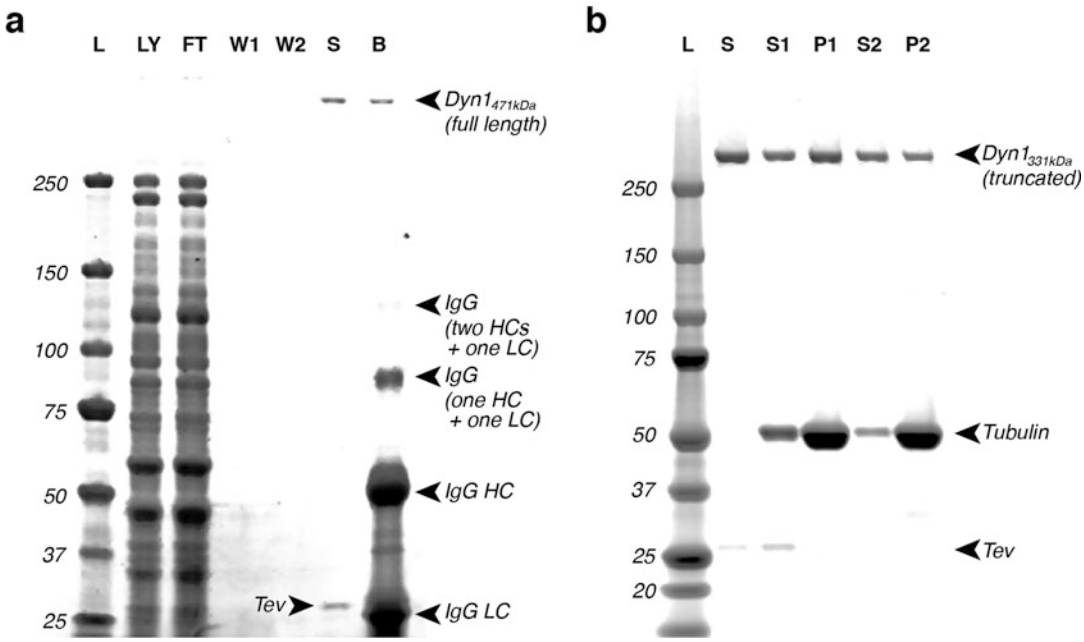

Fig. 2 (**a**) A representative SDS-PAGE 4–12% gradient gel for dynein purification. The dynein is a full-length dynein expressed behind its native promoter ($Dyn1_{471kDa}$) [65]. Due to the low concentration of native dynein, its associated subunits generally are not visible by InstantBlue staining. The lower bands in lane "B" are due to the IgG antibodies. *L* molecular ladder, *LY* lysate, *FT* flow-through, *W1* wash 1, *W2* wash 2, *S* sample, *B* beads. (**b**) A representative SDS-PAGE 4–12% gradient gel for dynein microtubule binding release purification. In this example, the dynein is a truncated construct with an N-terminal GST tag ($Dyn1_{331kDa}$) [65]. *L* ladder, *S* sample, *S1* supernatant 1, *P1* pellet 1, *S2* supernatant 2, *P2* pellet 2

at its tip. Wash twice with 2.5 mL 1× LB using a serological pipette. Cap the bottom of the column when the total volume of the bead slurry and solution in the column decreases to ~500 μL. Resuspend the beads in the column using a cut 1000 μL pipette tip and then transfer the washed beads to the lysate in the 50 mL conical tube.

2. Tighten the cap of the conical tube and seal with parafilm. Nutate the tube at 4 °C for 1 hr.
3. Take the other prechilled column from refrigerator, and transfer the lysate into the column. Allow the solution to run through the column by gravity flow. Collect 2 μL of flow-through for gel analysis (FT in Fig. 2a).
4. Wait until the solution level is close to the bead surface. Use a fresh plastic transfer pipet to wash the beads with 3 × 5 mL of 1× LB. When ~100 μL solution remains on top of the beads (~350 μL total volume), cap the end of the column. Save 8 μL of the flow-through from the final wash step for gel analysis (W1 in Fig. 2a).

3.3.5 Label dynein with fluorescence dyes

1. Add HaloTag® ligand or SNAP-tag® ligand to a final concentration of ~10 μM to the column with the beads.
2. Incubate the beads at room temperature for 10 min. Stir gently using a metal spatula but avoid stirring beads onto the column walls.
3. Bring the column back to the cold room. Remove the cap and let the solution drain completely, then wash the beads first with the remaining 1× LB, then with 3 × 3 mL of 1× Tev. Following the final wash step, cap the column again once a volume of ~200 μL is left in the column. Take an 8 μL sample of the final flow-through for gel (W2 in Fig. 2a).

3.3.6 Cleave dynein from beads

1. Place a 2 mL microcentrifuge tube on ice and cut the tip of a 200 μL pipette tip. Resuspend beads by gently pipetting up and down, and transfer the beads to the 2 mL tube. Add 200 μL 1× Tev to the column and resuspend remaining beads, then transfer to the 2 mL tube. Repeat until all beads are transferred. Let the beads settle for 5 min, then remove supernatant until 150 μL of 1× Tev is left. Add 4 μL AcTev protease.
2. Parafilm the tube and incubate for 2 h at 4 °C while slowly rotating.
3. Centrifuge the tube for 30 s at 1000 rcf at 4 °C using the refrigerated microcentrifuge. Save 8 μL of the supernatant for a gel sample "S" of native dynein or 5 μL for a sample of dynein expressed behind the galactose promoter (Fig. 2a).
4. Carefully pipette the supernatant into a 0.5 mL low retention microcentrifuge tube. Do not disturb the bead pellet. Pipette the solution that is close to the bead pellet to another tube, and then move the pipet tip into the bead pellet to get the last bit of solution. Centrifuge the second tube and carefully transfer the supernatant to the first tube (*see* **Note 17**). Aliquot into 50 μL volumes (Tev release aliquots). Drop tubes immediately into liquid nitrogen. Store at −80 °C. Use 200 μL of 1× Tev to resuspend the beads. Save 5 μL for gel (B in Fig. 2a).
5. Add 2 μL 5× SDS loading dye to each gel sample and add ddH_2O to a final volume of 10 μL, then boil the samples for 10 min. Set up a bis-tris 4–12% gel in the minigel box, fill the chambers with 1× running buffer, load the samples and run for 50 min at 200 V. Stain the gel with InstantBlue, and scan with an Odyssey® imaging system (*see* **Note 18**).

3.4 MT binding and release purification of yeast dynein

In a second affinity purification step, an MT binding and release assay is performed to remove nonfunctional and/or aggregated dynein motors and other impurities (*see* **Note 19**). Dynein is mixed with MTs in the absence of ATP (strong MT-binding state) and then released from MTs in the presence of ATP (weak MT-binding state).

3.4.1 Polymerization of MTs

1. Add 1 μL 0.1 M DTT and 0.2 μL 10 mM paclitaxel to both 100 μL BRB80 with 10% glycerol and to 100 μL glycerol cushion.
2. Dilute 1 μL 10 mM paclitaxel in 49 μL DMSO for a concentration of 0.2 mM.
3. Add 0.2 μL 25 mM GTP.Mg to 5 μL 5 mg/mL tubulin for a final concentration of 1 mM GTP and incubate at 37 °C for 15 min. Then add 0.7 μL 0.2 mM paclitaxel to the solution to stabilize the MTs. Mix well by gentle pipetting (do not vortex).
4. Add 60 μL glycerol cushion to a TLA-100 rotor tube, carefully pipette the MT solution on top of the cushion, and mark the outside edge of the tube with a permanent marker to help find the pellet position after the centrifugation. Place the tube inside the TLA-100 rotor with the mark facing outward and place a balance tube in the opposite rotor position. Centrifuge at 80,000 rpm for 10 min at room temperature.
5. Remove the supernatant, gently wash the pellet with 4 × 20 μL BRB80 with 10% glycerol, and resuspend the pellet in 5 μL BRB80 with 10% glycerol. Store at room temperature (*see* **Note 20**).

3.4.2 MT binding and release purification

1. Add 1 μL 0.1 M DTT and 0.2 μL 10 mM paclitaxel to 100 μL sucrose cushion and 2 μL 0.1 M DTT and 0.4 μL 10 mM paclitaxel to 200 μL wash buffer, mix well.
2. Add 2 μL 5× SDS loading buffer and 3 μL of ddH_2O to each of five 0.5 mL "gel-loading tubes" for SDS-PAGE gel analysis.
3. Thaw an aliquot of 50 μL Tev release dynein. Add a 5 μL sample to one gel-loading tube and label with "S" for "sample" (Fig. 2b), then flash-freeze the tube.
4. Add 0.1 μL 10 mM paclitaxel to the dynein solution, mix well by gentle pipetting (do not vortex).
5. Add 5 μL of the polymerized 5 mg/mL MT solution (prepared in Subheading 3.4.1) to the dynein solution and incubate at room temperature for 5 min to allow dynein to bind to the MTs.
6. Add 100 μL sucrose cushion into a clean TLA-100 tube, carefully layer the MT/dynein solution onto the cushion, and mark the outside edge of the tube with a permanent marker. Place the tube inside the TLA-100 rotor with the mark facing outward and place a balance tube in the opposite rotor position. Centrifuge at 40,000 rpm for 10 min at 25 °C.
7. Add 5 μL of the supernatant to a gel-loading tube and label with "S1" (supernatant 1, Fig. 2b), then flash-freeze the tube.

8. Remove the supernatant and cushion carefully. Wash the pellet gently with 20 μL wash buffer, then remove wash buffer.
9. Resuspend the pellet with 52 μL wash buffer and add a 5 μL sample to one of the three remaining gel-loading tubes and label with "P1" (pellet 1, Fig. 2b), then flash-freeze the tube.
10. Add 3 μL 100 mM ATP.Mg to the resuspended pellet and mix well. Incubate at room temperature for 2 min, then centrifuge at 40,000 rpm for 5 min at 25 °C.
11. Chill a 0.5 mL low-retention microcentrifuge tube on ice and transfer the supernatant from the TLA-100 tube to the low-retention microcentrifuge tube. Take a 5 μL sample and add it to one of the two remaining gel-loading tubes and label with "S2" (supernatant 2, Fig. 2b), then flash-freeze the tube. Aliquot the remaining dynein-containing supernatant into 1.5 μL volumes using PCR tubes. Flash-freeze the aliquots and store at −80 °C.
12. Wash the pellet with 20 μL wash buffer, remove the wash buffer, and resuspend pellet in 50 μL wash buffer. Add a 5 μL sample of the resuspended pellet to the last remaining gel-loading tubes and label with "P2" (pellet 2, Fig. 2b), then flash-freeze the tube.
13. Analyze the saved gel samples using SDS-PAGE gel electrophoresis as described in **step 27** in Subheading 3.3.

3.5 Polymerization of MTs for Single-Molecule Assays

Functionalized tubulins, such as fluorophore-tagged tubulin and biotinylated tubulin, are frequently employed to visualize and/or immobilize MTs [45, 46, 69, 70]. Functionalized tubulins are either commercially available, or can be prepared as previously described in detail [53]. Usually, functionalized tubulins are mixed with unlabeled tubulin at a low ratio, and incorporated into MTs during polymerization.

3.5.1 Polymerization of Functionalized MTs

1. Add one aliquot of fluorescently labeled-tubulin (1 μg) and one aliquot of biotinylated-tubulin (1 μg) to one aliquot of unlabeled tubulin (5 μL of 5 mg/mL; 25 μg). Mix thoroughly and incubate for 10 min on ice.
2. Follow the protocol described in Subheading 3.4.1 to polymerize a mixture of functionalized and nonfunctionalized tubulin.

3.5.2 Polymerization of Polarity-Marked MTs

Polarity-marked MTs are used to distinguish between the plus and minus ends of MTs. Tubulin with a high ratio of fluorophore-labeled-to-unlabeled tubulin is first polymerized to create bright MT seeds, then a tubulin mixture with a lower ratio of labeled-to-unlabeled tubulin is added to continue polymerization off the ends of the seeds. This procedure yields fluorophore-labeled MTs with

bright minus ends [71]. However, MTs can join end-to-end or anneal over time at room temperature [72] so that the bright seeds no longer mark the end of the MT. It is therefore recommended to prepare the polarity-marked microtubules fresh on the day of the experiment.

1. Add 0.2 μL of 1 M DTT and 2 μL of 100 mM GTP to 200 μL BRB80 with 10% glycerol, and keep on ice.
2. Dilute 1 μL 10 mM paclitaxel in 49 μL DMSO to 0.2 mM.
3. To prepare the tubulin stock for the seeds (S), take one vial of the rhodamine-labeled tubulin (20 μg) from the freezer, add 12 μL of the buffer prepared in **step 1** to solvate the tubulin, and incubate on ice. If biotinylated tubulin is needed, add the 12 μL solution with the rhodamine-labeled tubulin to a vial of biotinylated tubulin (20 μg) to solvate the biotin-tubulin. Aliquot ten 0.5 μL volumes and flash-freeze in liquid nitrogen. Store at −80 °C.
4. To prepare the tubulin stock for MT polymerization (T), add the remaining labeled tubulin solution (7 μL) to an aliquot of unlabeled tubulin (5 μL of 5 mg/mL), mix well by gentle pipetting, then incubate on ice for 10 min. Add 40 μL BRB80 with 10% glycerol, and mix well, then aliquot into ten 5 μL volumes and flash-freeze in liquid nitrogen. Store at −80 °C.
5. Polymerization of polarity-marked MTs: Take one aliquot each of the "seeds" stock (S) and the "polymerization" stock (T) from the freezer. Incubate S at 37 °C for 5 min, add T to S, and incubate at 37 °C for 15 min, then add 0.7 μL of 0.2 mM paclitaxel.
6. Follow **steps 4** and **5** of Subheading 3.4.1 to remove free tubulin.

3.6 Coverslip Preparation for MT Attachment

There are a number of different approaches for attaching MTs to glass surfaces, the choice of which depends on the assay to be performed. Here, we begin by describing two easy-to-use protocols for the surface attachment of MTs for single-molecule fluorescence and optical trapping assays. While both techniques are based on the noncovalent attachment of MTs to glass surfaces, one technique relies on the surface attachment via functionalized (biotinylated) MTs and the other uses nonfunctionalized MTs by taking advantage of the electrostatic interactions between the negatively charged tubulins and the positive charge of surface-attached PLL. Both techniques result in rigidly attached MTs for up to ~30 min in the presence of blocking reagents. Surface-attachment of biotinylated MTs through streptavidin-biotin linkages is a commonly used method. Note, however, it results in the random orientation of MTs on the coverslip surface. This is less ideal for optical trapping

experiments, where it is preferable to perform force measurements along a fixed axis. In contrast, the PLL-based method results in MTs that are aligned with the long axis of the slide chamber, because surface-attachment occurs immediately as a result of the laminar flow and the favorable initial electrostatic interactions when MTs come in contact with the surface-bound PLL while the solution is flown into the chamber. Lastly, we describe a new protocol that combines both techniques and results in aligned MTs and in rigid surface attachment for more than an hour.

3.6.1 Immobilization via Biotin-Streptavidin Interactions

The binding of biotinylated MTs to BSA-biotin via streptavidin is routinely used to attach MTs to coverslip surfaces [69, 73, 74]. First, BSA-biotin is attached to the glass surface via nonspecific interactions, and then streptavidin is applied to bind the surface-bound BSA-biotin specifically (Fig. 3a). Biotinylated MTs are then flown into the chamber and given sufficient time to rigidly bind to the streptavidin-coated surface. While this approach results in a random orientation of the attached MTs (Fig. 4a), it provides a straightforward and easy to use method for single-molecule fluorescence assays.

1. Coverslip cleaning: Place coverslips in a coverslip rack and submerge in 1 M HCl overnight. Rinse extensively with ddH_2O, then sonicate sequentially in 30% ethanol, 50% ethanol, and absolute ethanol for 30 min/solution. Store the coverslips in ethanol until usage (*see* **Note 21**).
2. Coating with biotin-BSA: Assemble a flow chamber as described before in detail [53] using the coverslips cleaned in **step 1**. Flow 15 μL biotin-BSA into the chamber and incubate for at least 30 min (*see* **Note 22**). Dilute 4 μL of 50 mg/mL BSA into 196 μL of BRB80-s and wash the chamber with 2× 20 μL BRB80-s with BSA.
3. Binding of streptavidin: Add 16 μL of BRB80-s with BSA to an aliquot of 4 μL 5 mg/mL streptavidin, mix well, and flow into the flow chamber. Incubate at room temperature for 8–10 min, and then wash with 2× 20 μL of BRB80-s with BSA.
4. Binding of MTs: Dilute the MT solution prepared in Subheading 3.5.1 (fluorescently labeled and biotinylated MTs) or Subheading 3.5.2 (fluorescently labeled, polarity-marked and biotinylated MTs) 1:10 in BRB80-s, and then add 1 μL of the diluted MT solution to 19 μL BRB80-s with BSA (to create a 1:200 final dilution of the MT solution). Flow 20 μL of the diluted MT solution into the chamber and incubate at room temperature for at least 15 min. Wash twice with 20 μL BRB80-s with BSA. Proceed with **step 1** of Subheading 3.7.1 to perform single-molecule dynein motility experiments.

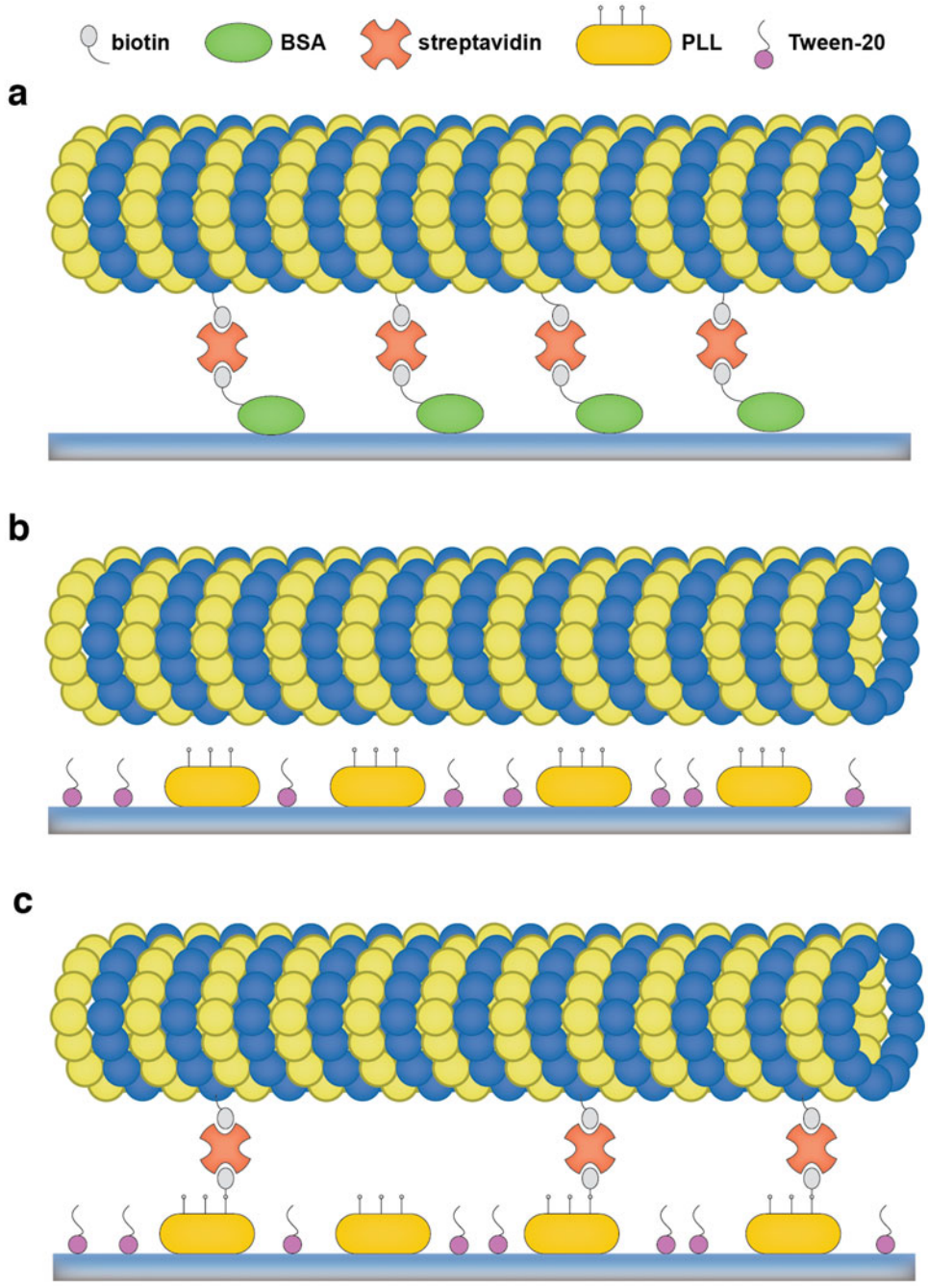

Fig. 3 (**a**) Scheme of microtubule immobilization via BSA-biotin-streptavidin attachment. BSA-biotin (*green*) adsorbs to a coverslip surface, followed by streptavidin (*orange*) that is bound to biotin. MTs with biotinlyated tubulin are then immobilized via streptavidin. (**b**) Scheme of microtubule immobilization via PLL. PLL (*yellow*) adsorbs to a coverslip surface, followed by Tween-20 (*purple*), which blocks the surface. MTs are immobilized via electrostatic interactions with the amine groups of PLL. (**c**) For optical trapping assays, the amine groups of PLL can be sparsely labeled with NHS-biotin, and biotinylated MTs can be further tightly attached via streptavidin

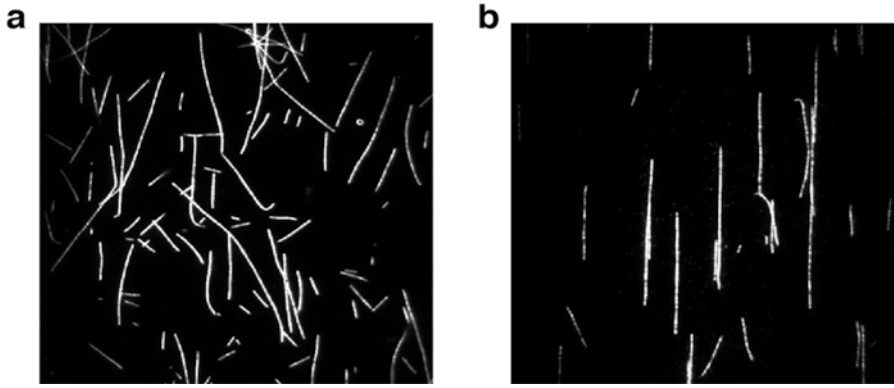

Fig. 4 (**a**) Micrograph of MTs attached to a coverslip surface via BSA-biotin-streptavidin attachment. (**b**) Micrograph of MTs attached to a coverslip using PLL

3.6.2 Immobilization via Poly-L-Lysine

While MT surface-attachment based on biotin–streptavidin interactions is a commonly used method, it is rather time-consuming due to the laborious preparation of coverslips and the long incubation times. In addition, biotin-BSA and streptavidin are costly, and the method results in the random orientation of MTs on the coverslip surface, which makes this approach less useful for many optical trapping assays.

In order to align MTs with the long axis of the flow chamber, AEAPTES (*N*-(2-aminoethyl)-3-aminopropyl triethoxysilane)-coated coverslips can be used to immobilize MTs via covalent binding [53], and we have commonly used this method in our laboratory [45, 46]. However, the coating of coverslips with AEAPTES is also time-consuming, and generates hazardous waste. Most critically, AEAPTES is labile, resulting in inconsistencies in the coverslip surface coating if it is not fresh or stored in a vacuum or inert gas [53]. Therefore, we have adopted the use of PLL-coated surfaces, a technique that is commonly used to facilitate the attachment of cell cultures to surfaces [75] (Fig. 3b). Like AEAPTES, PLL binds MTs via its positively charged amine groups, but its handling is significantly easier and more time- and cost-effective than using AEAPTES. And most importantly, as is the case for AEAPTES-based immobilization, MTs immobilized with PLL are well aligned with the long axis of the flow chamber due to the combination of the favorable initial electrostatic interactions with the positively charged surface and the laminar flow induced by the filling of the chamber (Fig. 4b).

1. Coverslip cleaning: Place coverslips in a coverslip rack and submerge the coverslips in 25% (v/v) HNO_3 for 10 min. Rinse with ddH_2O, then submerge in 2 M NaOH for 2 min (*see* **Notes 23** and **24**). Extensively rinse with ddH_2O, and then dry the coverslips on a heating block for 10–20 min.

2. Coating with PLL: Once the coverslips have cooled down, submerge them in 0.01% (w/v) PLL solution for 2 min (*see* **Note 25**), and subsequently in Tween-20 (0.1%) overnight to block the surface (*see* **Note 26**). The coverslips can be stored in Tween-20 solution for 1 week. Before usage, wash a coverslip with ddH_2O and dry it with filtered, compressed air or vacuum, then assemble a flow chamber.
3. Binding of MTs for single-molecule fluorescence and/or optical trapping experiments: Dilute the MT solution prepared in Subheading 3.5.1 or 3.5.2 1:10 in BRB80-s, and then add 1 μL of the 1:10 diluted MT solution to 19 μL BRB80-s to create a 1:200 final dilution. Flow 20 μL of the diluted MT solution into the chamber and immediately wash with 2× 20 μL BRB80-s. Proceed with Subheading 3.7.1 to perform single-molecule dynein motility experiments or Subheading 3.7.2 to perform optical trapping experiments.

3.6.3 Immobilization via PLL and Biotin–Streptavidin Interactions

The MT immobilization method solely based on surface-bound PLL (Subheading 3.6.2) will suffice for single-molecule in vitro experiments if the experiments can be carried out within ~30 min. However, the frequently used blocking reagent casein, which is very effective in passivating positively-charged surfaces due to its highly negatively charged N-terminal region [76], competes with MTs for attachment to surface-bound PLL (and likely also shields the positive charges of PLL). This results in increasingly floppy MTs and the eventual dissociation, making finding well-aligned and rigidly bound MTs increasingly difficult. To improve the time of rigid MT attachment for optical trapping assays that often last for more than an hour, we have established a new protocol that combines electrostatic and biotin–streptavidin interactions for the immobilization of MTs to coverslip surfaces (Fig. 3c). While the use of the PLL-coated surfaces facilitates the rapid attachment of MTs to the coverslip surface with their long axes aligned with the long axis of the flow chamber, the additional streptavidin/biotin-based surface binding of MTs ensures that the rigid attachment is maintained for extended times. To do so, we bind NHS-biotin covalently to a fraction of the amine groups of the surface-bound PLL and use biotinylated MTs.

1. Submerge a coverslip coated with PLL and Tween-20 (prepared in **steps 1** and **2** of Subheading 3.6.2) for 3–5 min in 0.1% PLL solution (*see* **Note 27**), and then wash it with ddH_2O. Dry the cover slip with filtered, compressed air or vacuum and assemble it into a flow chamber.
2. Add 8 μL of coupling buffer to 2 μL of 10 mM EZ-link NHS-biotin, and flow the solution into the chamber. Incubate at room temperature for 5 min, and then wash the chamber with

200 μL ddH_2O. Dry the flow chamber with filtered, compressed air or vacuum, and dilute 4 μL 5 mg/mL streptavidin in 16 μL HME30 to yield 1 mg/mL streptavidin, then flow into the chamber. Incubate at room temperature for 5 min, then wash four times with 20 μL HME30. Dry the chamber with filtered, compressed air or vacuum.

3. Dilute 0.2 μL of polarity-marked, rhodamine-biotin-MTs (prepared in Subheading 3.5.2) in 20 μL of HME30-s, flow the diluted MT solution through the chamber, and then immediately wash with 2× 20 μL of HME30-s (the more time passes before the wash step, the more MTs will attach to the coverslip surface with random orientations). Proceed with **step 1** of Subheading 3.7.2 to perform optical trapping experiments on dynein.

3.7 Single-Molecule Assays

Over the past three decades, single-molecule techniques have provided significant insights into the functions and mechanisms of motion- and force-generating mechanoenzymes, with applications across multiple disciplines [77]. In the cytoskeletal motor field, the most commonly used single-molecule techniques are based on single-molecule fluorescence measurements [65, 78, 79] and force measurements using optical tweezers [45, 46, 80–84] (or a combination of both [85]). As the technical details of both methods have been described and discussed in detail elsewhere, here we only describe the remaining steps needed to successfully set up single-molecule fluorescence and optical trapping experiments on dynein using the MT-filled slide chambers prepared in Subheadings 3.6.1–3.6.3. For more details on these assays, please refer to refs. 54, 86–88.

3.7.1 Single-Molecule Fluorescence Assay

In single-molecule fluorescence motility assays, the velocity and run length of a processive motor along MTs can be tracked and measured via a fluorescent tag using TIRF microscopy [89, 90]. Below, we describe the remaining steps that have to be executed to visualize the motility of recombinant yeast dynein.

1. Prepare a slide chamber with surface-attached MTs as described in Subheading 3.6.1 (MT immobilization via biotin–streptavidin interactions only), Subheading 3.6.2 (MT immobilization via PLL only) or Subheading 3.6.3 (MT immobilization via both PLL and biotin–streptavidin interactions). Take out one aliquot (200 μL) of HME30-s from the −20 °C freezer.
2. Add 2.5 μL of 25 mg/mL β-casein to 47.5 μL of HME30-s (for a final concentration of 1.25 mg/mL), and wash the slide chamber with 2× 20 μL of HME30-s with casein.

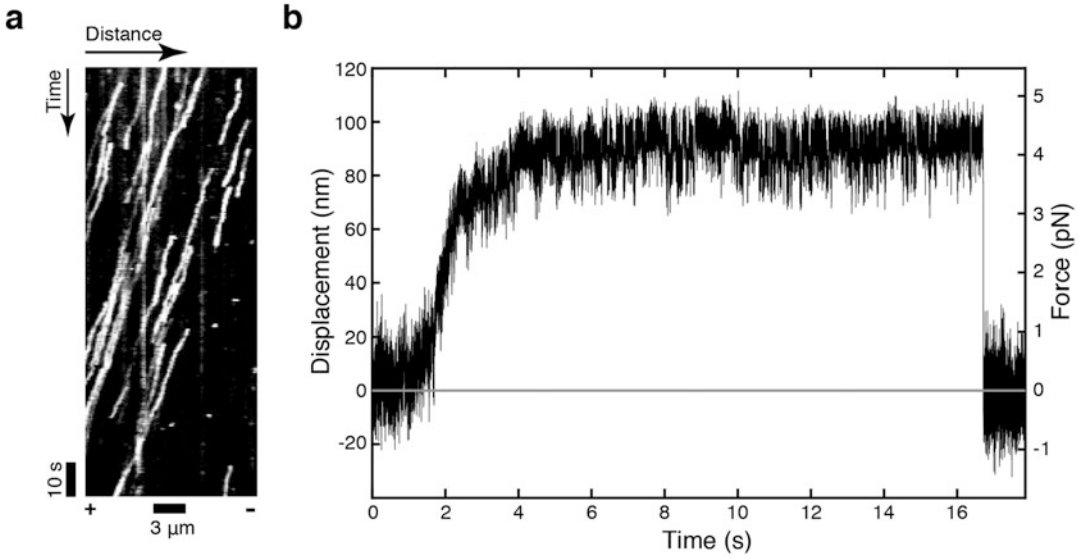

Fig. 5 (**a**) A representative kymograph of full-length dynein. The acquisition rate was 500 ms/frame. (**b**) A representative stall trace of full-length dynein. The spring constant *k* was 0.045 pN/nm

3. To a fresh 0.5 mL tube, add 43 µL of HME30-s, 5 µL β-casein, 0.5 µL ATP, 0.5 µL POC, and 1 µL of the dynein MT binding release fraction (prepared in Subheading 3.4.2). Mix well and flow 2× 20 µL of the mixture into the flow chamber, then seal the chamber with vacuum grease.
4. Mount the slide chamber to the microscope stage using a sufficient amount of immersion oil, and perform TIRF motility experiments as detailed elsewhere [89, 90].
5. Analyze the data by creating Kymographs via ImageJ (Fig. 5a) or by applying a single-particle tracking software such as FIESTA [91].

3.7.2 Optical Trapping Assay

Optical tweezers [52] is an invaluable tool to probe the nanometer-scale displacements and piconewton force generation of individual dynein molecules. In the assay described here, full-length yeast dynein is coupled to anti-GFP antibody-coated 1-µm polystyrene beads through the N-terminal GFP-tag on the motor's tail. Dynein-coated beads are captured with a fixed position optical trap and placed above a surface-bound MT using the nanopositioning stage of the microscope. Upon MT binding, a dynein-coated bead moves along the MT away from the trap center until the motor stalls and eventually releases (Fig. 5b). As we have described the technical aspects of these experiments in detail before [48, 54, 92], here we simply outline the final steps necessary to set up a trapping experiment using recombinant dynein.

1. In a 0.5 mL tube, dilute 1 μL of anti-GFP beads in 49 μL of HME30, and parafilm the tube and store the diluted beads at 4 °C.
2. Take out one aliquot (200 μL) of HME30-s from the −20 °C freezer, and thaw in a 37 °C bath or in your hand.
3. Prepare a slide chamber with surface-attached MTs as described in Subheading 3.6.3 (MT immobilization via PLL and biotin–streptavidin interactions).
4. Add 2.8 μL of 25 mg/mL α-casein to the remaining 140 μL HME30-s to a final concentration of 0.5 mg/mL, and use the solution to dilute dynein to a concentration that results in MT binding by <50% of beads in the final assay, implying binding by single motors [93] (start with a dilution of 1:1000 achieved by serially diluting the motor in tenfold steps).
5. Briefly sonicate 4 μL of diluted beads in a 0.5 mL low-retention tube.
6. Add 4 μL of the diluted dynein to the beads, mix well by gentle pipetting, then incubate on ice for 10 min.
7. Add 0.4 μL of POC, 0.4 μL of ATP, 0.4 μL of PEP, and 0.4 μL of PK (ATP regeneration system) to 31 μL of HME30-s with α-casein, and mix well, then add the mixture to the aliquot with the dynein-beads solution. Flow 2× 20 μL of the dynein-bead mixture into the chamber, and seal the chamber with vacuum grease.
8. Perform data collection and data analysis as previously described [48, 54, 92].

4 Notes

1. Normally, standard PCR machines are used. However, if a laboratory only needs to do routine PCR in a small scale, the miniPCR™ machine could be an inexpensive option. We have tested it for amplifying DNA between 150 bp and 9 kbp using different DNA polymerases such as KOD hot start DNA polymerase, Q5® (NEB), and Phusion® (NEB), and the yield and purity are comparable to those resulting from standard PCR machines.
2. Trolox is not very soluble. It is best to add HEPES, $MgCl_2$, EGTA, and Trolox to a 50 mL conical tube and nutate overnight covered with aluminum foil, and then add DTT and paclitaxel before aliquoting.
3. Most yeast genes lack introns, and deletions of these introns generally do not affect cell growth, but extra care should still be taken when working with intron-containing genes [94].

4. While 5-FOA (5-fluoroorotic acid) is nontoxic, it can be converted into the toxic compound 5-flurouracil if URA3-encoded orotidine 5′-phosphate decarboxylase is present. For more details on PCR-based yeast gene engineering, please refer to refs. 56, 95, 96.
5. Although studies have shown that having only 30 bp overlap can lead to successful homologous recombination, 60 bp overlap is recommended for high efficiency transformation [97].
6. SGD is a specialized database for *Saccharomyces cerevisiae*, but other databases such as UniProt and NCBI can be used as well.
7. We use SerialCloner (v. 2-6-1) to do DNA and protein sequence analysis for molecular cloning but other software tools can be used as well.
8. Online primer design tools, such as Primer-BLAST (NCBI) and PrimerQuest (IDT DNA), can be used to obtain the primers.
9. Other high fidelity DNA polymerases can be used as well. In particular, when more difficult reactions need to be performed, it may be necessary to optimize PCR parameters or to choose a different DNA polymerase.
10. The primers can be dissolved in TE buffer to 100 μM as stock, which can be further diluted to 10 μM in 10 mM Tris buffer. The second dilution should not contain EDTA, which would interfere with the DNA polymerase.
11. Running the gel at a lower voltage may improve the resolution, but will result in a longer running time.
12. The mechanism underlying this transformation is not fully understood.
13. While this step could be skipped for URA selection, it is critical for 5-FOA selection: Without the recovery step, the colonies that appear on the SC/5-FOA plate will mostly be false positives, with mutations in the URA3 gene that disrupt its function, rather than having incorporated the desired DNA sequence.
14. It is always a good practice to store two tubes of each yeast strain, and put one strain in a separate box as a backup, in case the other tube is contaminated.
15. Do not let the pipette get too close to the liquid nitrogen as the cell slurry might freeze inside the pipette tip.
16. Depending on the yeast strain, the volume of the pellet varies between 25 and 40 mL (dysfunctional dynein causes cells to grow slower, resulting in a smaller yield).
17. We do not recommend using a membrane filter unit to separate the solution from the beads, since dynein tends to bind to membrane surfaces.

18. If quantification of the bands is needed, BSA or actin standards should be included on the gel as well.
19. MT binding and release purification may not be applicable for some dynein mutants. In this case, although more labor intensive, size exclusion chromatography [98] or sucrose density gradient centrifugation [99] can be applied, which are better techniques for removing aggregated dynein and impurities.
20. MTs are temperature sensitive and tend to disassemble in the cold in the absence of taxol. When maintained in the presence of taxol, MTs can be used for up to 1 week when stored at room temperature.
21. It is important to submerge the coverslips in ethanol for a few hours before usage, otherwise the surface is less hydrophilic, resulting in the reduced binding of BSA-biotin.
22. The longer the BSA-biotin incubates in the chamber, the higher its surface density, and therefore the MTs will bind more strongly later. We recommend preparing the flow chambers with BSA-biotin in the morning, storing them in a humidity box at room temperature, and using them in the afternoon. Alternatively, BSA-biotin can be incubated in the flow chamber in a humidity box overnight at 4 °C.
23. The HNO_3 and NaOH solutions can be reused without losing their effects for a long time. However, it is a good practice to replace the solutions once a year.
24. The surfaces of coverslips treated with NaOH are hydrophilic, which is favorable for surface adsorption. However, this treatment also etches the glass surface and renders the surface uneven [100], which is undesirable for MT binding. Thus, the NaOH incubation time was optimized to result in a sufficient surface absorption of PLL while preventing the distortion of MTs.
25. The incubation time of the PLL solution is important. Increasing the incubation time can result in too high a density of PLL on the coverslip. While the MTs will bind rigidly for a longer period of time with a higher PLL density, the increase in positive charge along the surface of the coverslip can be disruptive to the motility of microtubule-associated motor proteins, which have positively-charged MT-binding domains.
26. Various surface blocking agents have been utilized to block coverslip surfaces to prevent nonspecific binding. Besides Tween-20 and detergents such as Pluronic F-127 and Triton X-100, proteins such as BSA and casein, and polymers such as PEG have been used to block surfaces to various degrees of success. For single-molecule TIRF assays, other blocking agents can replace Tween-20. However, while BSA is a commonly used

blocking agent in optical trapping assays, in our experience, casein is significantly more effective in preventing nonspecific interactions between the beads and coverslip surface than BSA. It is therefore advised to rule out bead-surface interactions in the absence of motors when switching to a different blocking agent before an experiment is performed.

27. The increase in surface-bound PLL as a result of the second incubation with PLL is necessary to provide binding sites for the covalent attachment of NHS-biotin while leaving enough positively charged amine groups for electrostatic interactions with MTs.

Acknowledgments

The authors would like to thank Lisa Baker for her help in editing the manuscript. The authors are supported by NIH Grant R01GM098469.

References

1. Abe TK, Honda T, Takei K, Mikoshiba K, Hoffman-Kim D, Jay DG, Kuwano R (2008) Dynactin is essential for growth cone advance. Biochem Biophys Res Commun 372 (3):418–422
2. Grabham PW, Seale GE, Bennecib M, Goldberg DJ, Vallee RB (2007) Cytoplasmic dynein and LIS1 are required for microtubule advance during growth cone remodeling and fast axonal outgrowth. J Neurosci 27 (21):5823–5834
3. Kardon J, Vale R (2009) Regulators of the cytoplasmic dynein motor. Nat Rev Mol Cell Biol 10(12):854–865
4. Tai CY, Dujardin DL, Faulkner NE, Vallee RB (2002) Role of dynein, dynactin, and CLIP-170 interactions in LIS1 kinetochore function. J Cell Biol 156(6):959–968
5. Vallee RB, Williams JC, Varma D, Barnhart LE (2004) Dynein: An ancient motor protein involved in multiple modes of transport. J Neurobiol 58(2):189–200
6. Yamada M, Toba S, Yoshida Y, Haratani K, Mori D, Yano Y, Mimori-Kiyosue Y, Nakamura T, Itoh K, Fushiki S, Setou M, Wynshaw-Boris A, Torisawa T, Toyoshima Y, Hirotsune S (2008) LIS1 and NDEL1 coordinate the plus-end-directed transport of cytoplasmic dynein. EMBO J 27(19):2471–2483
7. Peeters K, Bervoets S, Chamova T, Litvinenko I, De Vriendt E, Bichev S, Kancheva D, Mitev V, Kennerson M, Timmerman V, De Jonghe P, Tournev I, MacMillan J, Jordanova A (2015) Novel mutations in the DYNC1H1 tail domain refine the genetic and clinical spectrum of dyneinopathies. Hum Mutat 36 (3):287–291
8. Chen XJ, Xu H, Cooper HM, Liu Y (2014) Cytoplasmic dynein: a key player in neurodegenerative and neurodevelopmental diseases. Sci China Life Sci 57(4):372–377
9. Gelineau-Morel R, Lukacs M, Weaver KN, Hufnagel RB, Gilbert DL, Stottmann RW (2016) Congenital cataracts and gut dysmotility in a DYNC1H1 dyneinopathy patient. Genes (Basel) 7(10):85–92
10. Harms MB, Ori-McKenney KM, Scoto M, Tuck EP, Bell S, Ma D, Masi S, Allred P, Al-Lozi M, Reilly MM, Miller LJ, Jani-Acsadi A, Pestronk A, Shy ME, Muntoni F, Vallee RB, Baloh RH (2012) Mutations in the tail domain of DYNC1H1 cause dominant spinal muscular atrophy. Neurology 78(22):1714–1720
11. Neveling K, Martinez-Carrera LA, Holker I, Heister A, Verrips A, Hosseini-Barkooie SM, Gilissen C, Vermeer S, Pennings M, Meijer R, te Riele M, Frijns CJ, Suchowersky O, MacLaren L, Rudnik-Schoneborn S, Sinke RJ, Zerres K, Lowry RB, Lemmink HH, Garbes L, Veltman JA, Schelhaas HJ, Scheffer H, Wirth B (2013) Mutations in BICD2, which encodes a golgin and important motor adaptor, cause congenital autosomal-dominant

spinal muscular atrophy. Am J Hum Genet 92 (6):946–954

12. Niu Q, Wang X, Shi M, Jin Q (2015) A novel DYNC1H1 mutation causing spinal muscular atrophy with lower extremity predominance. Neurol Genet 1(2):e20
13. Strickland AV, Schabhuttl M, Offenbacher H, Synofzik M, Hauser NS, Brunner-Krainz M, Gruber-Sedlmayr U, Moore SA, Windhager R, Bender B, Harms M, Klebe S, Young P, Kennerson M, Garcia AS, Gonzalez MA, Zuchner S, Schule R, Shy ME, Auer-Grumbach M (2015) Mutation screen reveals novel variants and expands the phenotypes associated with DYNC1H1. J Neurol 262 (9):2124–2134
14. Ding D, Chen Z, Li K, Long Z, Ye W, Tang Z, Xia K, Qiu R, Tang B, Jiang H (2016) Identification of a de novo DYNC1H1 mutation via WES according to published guidelines. Sci Rep 6:20423
15. Weedon MN, Hastings R, Caswell R, Xie W, Paszkiewicz K, Antoniadi T, Williams M, King C, Greenhalgh L, Newbury-Ecob R, Ellard S (2011) Exome sequencing identifies a DYNC1H1 mutation in a large pedigree with dominant axonal Charcot-Marie-Tooth disease. Am J Hum Genet 89(2):308–312
16. Reiner O, Carrozzo R, Shen Y, Wehnert M, Faustinella F, Dobyns WB, Caskey CT, Ledbetter DH (1993) Isolation of a Miller-Dieker lissencephaly gene containing G protein beta-subunit-like repeats. Nature 364 (6439):717–721
17. Vallee RB, Tai C, Faulkner NE (2001) LIS1: cellular function of a disease-causing gene. Trends Cell Biol 11(4):155–160
18. Poirier K, Lebrun N, Broix L, Tian G, Saillour Y, Boscheron C, Parrini E, Valence S, Pierre BS, Oger M, Lacombe D, Genevieve D, Fontana E, Darra F, Cances C, Barth M, Bonneau D, Bernadina BD, N'Guyen S, Gitiaux C, Parent P, des Portes V, Pedespan JM, Legrez V, Castelnau-Ptakine L, Nitschke P, Hieu T, Masson C, Zelenika D, Andrieux A, Francis F, Guerrini R, Cowan NJ, Bahi-Buisson N, Chelly J (2013) Mutations in TUBG1, DYNC1H1, KIF5C and KIF2A cause malformations of cortical development and microcephaly. Nat Genet 45(6):639–647
19. Willemsen MH, Vissers LEL, Willemsen MAAP, van Bon BWM, Kroes T, de Ligt J, de Vries BB, Schoots J, Lugtenberg D, Hamel BCJ, van Bokhoven H, Brunner HG, Veltman JA, Kleefstra T (2012) Mutations in DYNC1H1 cause severe intellectual disability with neuronal migration defects. J Med Genet 49(3):179–183
20. Fiorillo C, Moro F, Yi J, Weil S, Brisca G, Astrea G, Severino M, Romano A, Battini R, Rossi A, Minetti C, Bruno C, Santorelli FM, Vallee R (2014) Novel dynein DYNC1H1 neck and motor domain mutations link distal spinal muscular atrophy and abnormal cortical development. Hum Mutat 35(3):298–302
21. Munch C, Sedlmeier R, Meyer T, Homberg V, Sperfeld AD, Kurt A, Prudlo J, Peraus G, Hanemann CO, Stumm G, Ludolph AC (2004) Point mutations of the p150 subunit of dynactin (DCTN1) gene in ALS. Neurology 63(4):724–726
22. Puls I, Jonnakuty C, LaMonte BH, Holzbaur EL, Tokito M, Mann E, Floeter MK, Bidus K, Drayna D, SJ O, Brown RH, Ludlow CL, Fischbeck KH (2003) Mutant dynactin in motor neuron disease. Nat Genet 33 (4):455–456
23. Farrer MJ, Hulihan MM, Kachergus JM, Dächsel JC, Stoessl AJ, Grantier LL, Calne S, Calne DB, Lechevalier B, Chapon F, Tsuboi Y, Yamada T, Gutmann L, Elibol B, Bhatia KP, Wider C, Vilariño-Güell C, Ross OA, Brown LA, Castanedes-Casey M, Dickson DW, Wszolek ZK (2009) DCTN1 mutations in Perry syndrome. Nat Genet 41 (2):163–165
24. Vilariño-Güell C, Wider C, Soto-Ortolaza AI, Cobb SA, Kachergus JM, Keeling BH, Dachsel JC, Hulihan MM, Dickson DW, Wszolek ZK, Uitti RJ, Graff-Radford NR, Boeve BF, Josephs KA, Miller B, Boylan KB, Gwinn K, Adler CH, Aasly JO, Hentati F, Destée A, Krygowska-Wajs A, Chartier-Harlin M-C, Ross OA, Rademakers R, Farrer MJ (2009) Characterization of DCTN1 genetic variability in neurodegeneration. Neurology 72(23):2024–2028
25. Gennerich A, Vale RD (2009) Walking the walk: how kinesin and dynein coordinate their steps. Curr Opin Cell Biol 21(1):59–67
26. Schmidt H, Carter AP (2016) Structure and mechanism of the dynein motor ATPase. Biopolymers 105(8):557–567
27. Cianfrocco MA, DeSantis ME, Leschziner AE, Reck-Peterson SL (2015) Mechanism and regulation of cytoplasmic dynein. Annu Rev Cell Dev Biol 31:83–108
28. Roberts AJ, Kon T, Knight PJ, Sutoh K, Burgess SA (2013) Functions and mechanics of dynein motor proteins. Nat Rev Mol Cell Biol 14(11):713–726
29. Snider J, Houry WA (2008) AAA+ proteins: diversity in function, similarity in structure. Biochem Soc Trans 36(Pt 1):72–77

30. Tucker PA, Sallai L (2007) The AAA+ superfamily—a myriad of motions. Curr Opin Struct Biol 17:641–652
31. Erzberger JP, Berger JM (2006) Evolutionary relationships and structural mechanisms of AAA+ proteins. Annu Rev Biophys Biomol Struct 35:93–114
32. Bassler J, Kallas M, Pertschy B, Ulbrich C, Thoms M, Hurt E (2010) The AAA-ATPase Rea1 drives removal of biogenesis factors during multiple stages of 60S ribosome assembly. Mol Cell 38(5):712–721
33. Garbarino JE, Gibbons IR (2002) Expression and genomic analysis of midasin, a novel and highly conserved AAA protein distantly related to dynein. BMC Genomics 3(1):18
34. Barrio-Garcia C, Thoms M, Flemming D, Kater L, Berninghausen O, Bassler J, Beckmann R, Hurt E (2016) Architecture of the Rix1-Rea1 checkpoint machinery during pre-60S-ribosome remodeling. Nat Struct Mol Biol 23(1):37–44
35. Schmidt H, Gleave ES, Carter AP (2012) Insights into dynein motor domain function from a 3.3-Å crystal structure. Nat Struct Mol Biol 19(5):492–497
36. Carter AP, Cho C, Jin L, Vale RD (2011) Crystal structure of the dynein motor domain. Science 331(6021):1159–1165
37. Kon T, Sutoh K, Kurisu G (2011) X-Ray structure of a functional full-length dynein motor domain. Nat Struct Mol Biol 18 (6):638–642
38. Burgess SA, Walker ML, Sakakibara H, Knight PJ, Oiwa K (2003) Dynein structure and power stroke. Nature 421(6924):715–718
39. Roberts AJ, Numata N, Walker ML, Kato YS, Malkova B, Kon T, Ohkura R, Arisaka F, Knight PJ, Sutoh K, Burgess SA (2009) AAA + ring and linker swing mechanism in the dynein motor. Cell 136(3):485–495
40. Toropova K, Zou S, Roberts AJ, Redwine WB, Goodman BS, Reck-Peterson SL, Leschziner AE (2014) Lis1 regulates dynein by sterically blocking its mechanochemical cycle. elife 3:PMID:25380312
41. Kon T, Mogami T, Ohkura R, Nishiura M, Sutoh K (2005) ATP hydrolysis cycle-dependent tail motions in cytoplasmic dynein. Nat Struct Mol Biol 12(6):513–519
42. DeWitt MA, Cypranowska CA, Cleary FB, Belyy V, Yildiz A (2015) The AAA3 domain of cytoplasmic dynein acts as a switch to facilitate microtubule release. Nat Struct Mol Biol 22(1):73–80
43. DeWitt MA, Chang AY, Combs PA, Yildiz A (2012) Cytoplasmic dynein moves through uncoordinated stepping of the AAA+ ring domains. Science 335(6065):221–225
44. Qiu W, Derr ND, Goodman BS, Villa E, Wu D, Shih W, Reck-Peterson SL (2012) Dynein achieves processive motion using both stochastic and coordinated stepping. Nat Struct Mol Biol 19(2):193–200
45. Nicholas MP, Berger F, Rao L, Brenner S, Cho C, Gennerich A (2015) Cytoplasmic dynein regulates its attachment to microtubules via nucleotide state-switched mechanosensing at multiple AAA domains. Proc Natl Acad Sci U S A 112(20):6371–6376
46. Nicholas MP, Hook P, Brenner S, Wynne CL, Vallee RB, Gennerich A (2015) Control of cytoplasmic dynein force production and processivity by its C-terminal domain. Nat Commun 6:6206
47. Rao L, Romes EM, Nicholas MP, Brenner S, Tripathy A, Gennerich A, Slep KC (2013) The yeast dynein Dyn2-Pac11 complex is a dynein dimerization/processivity factor: structural and single-molecule characterization. Mol Biol Cell 24(15):2362–2377
48. Gennerich A, Carter AP, Reck-Peterson SL, Vale RD (2007) Force-induced bidirectional stepping of cytoplasmic dynein. Cell 131 (5):952–965
49. Kon T, Imamula K, Roberts AJ, Ohkura R, Knight PJ, Gibbons IR, Burgess SA, Sutoh K (2009) Helix sliding in the stalk coiled coil of dynein couples ATPase and microtubule binding. Nat Struct Mol Biol 16(3):325–333
50. Kon T, Nishiura M, Ohkura R, Toyoshima YY, Sutoh K (2004) Distinct functions of nucleotide-binding/hydrolysis sites in the four AAA modules of cytoplasmic dynein. Biochemistry 43(35):11266–11274
51. Cleary FB, Dewitt MA, Bilyard T, Htet ZM, Belyy V, Chan DD, Chang AY, Yildiz A (2014) Tension on the linker gates the ATP-dependent release of dynein from microtubules. Nat Commun 5:4587
52. Gennerich A (ed) (2017) Optical tweezers: methods and protocols, vol 1486. Methods in molecular biology. Springer, New York, NY
53. Nicholas MP, Rao L, Gennerich A (2014) Covalent immobilization of microtubules on glass surfaces for molecular motor force measurements and other single-molecule assays. Methods Mol Biol 1136:137–169
54. Nicholas MP, Rao L, Gennerich A (2014) An improved optical tweezers assay for measuring the force generation of single kinesin molecules. Methods Mol Biol 1136:171–246
55. Miné-Hattab J, Rothstein R (2012) Gene targeting and homologous recombination in

Saccharomyces cerevisiae. Top Curr Genet 23:71–89

56. Lundblad V, Hartzog G, Moqtaderi Z (2001) Manipulation of cloned yeast DNA. Curr Protoc Mol Biol Chapter 13:Unit13.10
57. Lorenz TC (2012) Polymerase chain reaction: basic protocol plus troubleshooting and optimization strategies. J Vis Exp 63:e3998
58. Roux KH (2009) Optimization and troubleshooting in PCR. Cold Spring Harb Protoc 2009(4):pdb ip66
59. Kawai S, Hashimoto W, Murata K (2010) Transformation of Saccharomyces cerevisiae and other fungi: methods and possible underlying mechanism. Bioeng Bugs 1(6):395–403
60. Gietz RD, Schiestl RH (2007) High-efficiency yeast transformation using the LiAc/SS carrier DNA/PEG method. Nat Protoc 2(1):31–34
61. Gietz RD, Schiestl RH (2007) Frozen competent yeast cells that can be transformed with high efficiency using the LiAc/SS carrier DNA/PEG method. Nat Protoc 2(1):1–4
62. Adames NR, Cooper JA (2000) Microtubule interactions with the cell cortex causing nuclear movements in Saccharomyces cerevisiae. J Cell Biol 149(4):863–874
63. Lee W-L, Kaiser MA, Cooper JA (2005) The offloading model for dynein function: differential function of motor subunits. J Cell Biol 168(2):201–207
64. Johnston M, Davis RW (1984) Sequences that regulate the divergent GAL1-GAL10 promoter in Saccharomyces cerevisiae. Mol Cell Biol 4(8):1440–1448
65. Reck-Peterson SL, Yildiz A, Carter AP, Gennerich A, Zhang N, Vale RD (2006) Single-molecule analysis of dynein processivity and stepping behavior. Cell 126(2):335–348
66. Trokter M, Mücke N, Surrey T (2012) Reconstitution of the human cytoplasmic dynein complex. Proc Natl Acad Sci U S A 109(51):20895–20900
67. Flick JS, Johnston M (1990) Two systems of glucose repression of the GAL1 promoter in Saccharomyces cerevisiae. Mol Cell Biol 10 (9):4757–4769
68. Weinhandl K, Winkler M, Glieder A, Camattari A (2014) Carbon source dependent promoters in yeasts. Microb Cell Factories 13:5
69. McKenney RJ, Huynh W, Vale RD, Sirajuddin M (2016) Tyrosination of alpha-tubulin controls the initiation of processive dynein-dynactin motility. EMBO J 35(11):1175–1185
70. Valentine MT, Fordyce PM, Krzysiak TC, Gilbert SP, Block SM (2006) Individual dimers of the mitotic kinesin motor Eg5 step processively and support substantial loads in vitro. Nat Cell Biol 8(5):470–476
71. Howard J, Hyman AA (1993) Preparation of marked microtubules for the assay of the polarity of microtubule-based motors by fluorescence microscopy. Methods Cell Biol 39:105–113
72. Williams RC Jr, Rone LA (1989) End-to-end joining of taxol-stabilized GDP-containing microtubules. J Biol Chem 264 (3):1663–1670
73. Ross JL, Shuman H, Holzbaur EL, Goldman YE (2008) Kinesin and dynein-dynactin at intersecting microtubules: motor density affects dynein function. Biophys J 94 (8):3115–3125
74. Fischer T, Agarwal A, Hess H (2009) A smart dust biosensor powered by kinesin motors. Nat Nanotechnol 4(3):162–166
75. Mazia D, Schatten G, Sale W (1975) Adhesion of cells to surfaces coated with polylysine. Applications to electron microscopy. J Cell Biol 66(1):198–200
76. Brown TB, Hancock WO (2002) A polarized microtubule array for kinesin-powered-nanoscale assembly and force generation. Nano Lett 2(10):1131–1135
77. Selvin PR, Ha T (eds) (2008) Single-molecule techniques: a laboratory manual. Cold Sping Harbor Laboratory Press, Cold Sping Harbor, NY
78. Yildiz A, Forkey JN, McKinney SA, Ha T, Goldman YE, Selvin PR (2003) Myosin V walks hand-over-hand: single fluorophore imaging with 1.5-nm localization. Science 300(5628):2061–2065
79. Yildiz A, Tomishige M, Vale RD, Selvin PR (2004) Kinesin walks hand-over-hand. Science 303(5658):676–678
80. Svoboda K, Block SM (1994) Force and velocity measured for single kinesin molecules. Cell 77(5):773–784
81. Svoboda K, Schmidt CF, Schnapp BJ, Block SM (1993) Direct observation of kinesin stepping by optical trapping interferometry. Nature 365(6448):721–727
82. Mallik R, Carter BC, Lex SA, King SJ, Gross SP (2004) Cytoplasmic dynein functions as a gear in response to load. Nature 427 (6975):649–652
83. Walter WJ, Koonce MP, Brenner B, Steffen W (2012) Two independent switches regulate cytoplasmic dynein's processivity and directionality. Proc Natl Acad Sci U S A 109 (14):5289–5293

84. Toba S, Watanabe TM, Yamaguchi-Okimoto L, Toyoshima YY, Higuchi H (2006) Overlapping hand-over-hand mechanism of single molecular motility of cytoplasmic dynein. Proc Natl Acad Sci U S A 103(15):5741–5745
85. Ishijima A, Kojima H, Funatsu T, Tokunaga M, Higuchi H, Tanaka H, Yanagida T (1998) Simultaneous observation of individual ATPase and mechanical events by a single myosin molecule during interaction with actin. Cell 92(2):161–171
86. Belyy V, Yildiz A (2014) Processive cytoskeletal motors studied with single-molecule fluorescence techniques. FEBS Lett 588 (19):3520–3525
87. Veigel C, Schmidt CF (2011) Moving into the cell: single-molecule studies of molecular motors in complex environments. Nat Rev Mol Cell Biol 12(3):163–176
88. Elting MW, Spudich JA (2012) Future challenges in single-molecule fluorescence and laser trap approaches to studies of molecular motors. Dev Cell 23(6):1084–1091
89. Yildiz A, Vale RD (2015) Tracking movements of the microtubule motors kinesin and dynein using total internal reflection fluorescence microscopy. Cold Spring Harb Protoc 2015 (9):pdb prot086355
90. Yildiz A, Vale RD (2015) Total internal reflection fluorescence microscopy. Cold Spring Harb Protoc 2015(9):pdb top086348
91. Ruhnow F, Zwicker D, Diez S (2011) Tracking single particles and elongated filaments with nanometer precision. Biophys J 100 (11):2820–2828
92. Gennerich A, Reck-Peterson SL (2011) Probing the force generation and stepping behavior of cytoplasmic dynein. Methods Mol Biol 783:63–80
93. Gutiérrez-Medina B, Fehr AN, Block SM (2009) Direct measurements of kinesin torsional properties reveal flexible domains and occasional stalk reversals during stepping. Proc Natl Acad Sci U S A 106(40):17007–17012
94. Parenteau J, Durand M, Veronneau S, Lacombe AA, Morin G, Guerin V, Cecez B, Gervais-Bird J, Koh CS, Brunelle D, Wellinger RJ, Chabot B, Abou Elela S (2008) Deletion of many yeast introns reveals a minority of genes that require splicing for function. Mol Biol Cell 19(5):1932–1941
95. Petracek ME, Longtine MS (2002) PCR-based engineering of yeast genome. Methods Enzymol 350:445–469
96. Janke C, Magiera MM, Rathfelder N, Taxis C, Reber S, Maekawa H, Moreno-Borchart A, Doenges G, Schwob E, Schiebel E, Knop M (2004) A versatile toolbox for PCR-based tagging of yeast genes: new fluorescent proteins, more markers and promoter substitution cassettes. Yeast 21(11):947–962
97. Hua SB, Qiu M, Chan E, Zhu L, Luo Y (1997) Minimum length of sequence homology required for in vivo cloning by homologous recombination in yeast. Plasmid 38 (2):91–96
98. Schlager MA, Hoang HT, Urnavicius L, Bullock SL, Carter AP (2014) In vitro reconstitution of a highly processive recombinant human dynein complex. EMBO J 33 (17):1855–1868
99. Ori-McKenney KM, Xu J, Gross SP, Vallee RB (2010) A cytoplasmic dynein tail mutation impairs motor processivity. Nat Cell Biol 12 (12):1228–1234
100. Eske LD, Galipeau DW (1999) Characterization of SiO2 surface treatments using AFM, contact angles and a novel dewpoint technique. Colloid Surface A 154(1–2):33–51

Part II

Single-Molecule Fluorescence Microscopy

Chapter 5

A Brief Introduction to Single-Molecule Fluorescence Methods

Siet M.J.L. van den Wildenberg, Bram Prevo, and Erwin J.G. Peterman

Abstract

One of the more popular single-molecule approaches in biological science is single-molecule fluorescence microscopy, which will be the subject of the following section of this volume. Fluorescence methods provide the sensitivity required to study biology on the single-molecule level, but they also allow access to useful measurable parameters on time and length scales relevant for the biomolecular world. Before several detailed experimental approaches will be addressed, we will first give a general overview of single-molecule fluorescence microscopy. We start with discussing the phenomenon of fluorescence in general and the history of single-molecule fluorescence microscopy. Next, we will review fluorescent probes in more detail and the equipment required to visualize them on the single-molecule level. We will end with a description of parameters measurable with such approaches, ranging from protein counting and tracking, single-molecule localization super-resolution microscopy, to distance measurements with Förster Resonance Energy Transfer and orientation measurements with fluorescence polarization.

Key words Microscopy, Confocal fluorescence, TIRF, Wide-field epi-fluorescence, Fluorophore

1 Introduction

1.1 A Brief Introduction to Fluorescence Spectroscopy

The name fluorescence was first used by Sir George Gabriel Stokes in his seminal 1852 paper "On the Change of Refrangibility of Light" [1], where he describes this phenomenon in many different materials, following the steps of Herschel's studies on quinine solutions [2, 3] and Brewster's on fluor-spar (fluorite) [4]. In a note Stokes states: "I am almost inclined to coin a word, and call the appearance fluorescence, from fluor-spar, as the analogous term opalescence is derived from the name of a mineral". By now, fluorescence spectroscopy has become an indispensable technique, in particular in biomolecular research [5]. Fluorescence is defined as light emitted by a molecule after absorption of light by the same molecule and involves a spin-allowed, singlet–singlet electronic transition. As an example, in Fig. 1a an imaginary absorption and fluorescence emission spectrum is shown. The energy levels

Erwin J.G. Peterman (ed.), *Single Molecule Analysis: Methods and Protocols*, Methods in Molecular Biology, vol. 1665, DOI 10.1007/978-1-4939-7271-5_5,

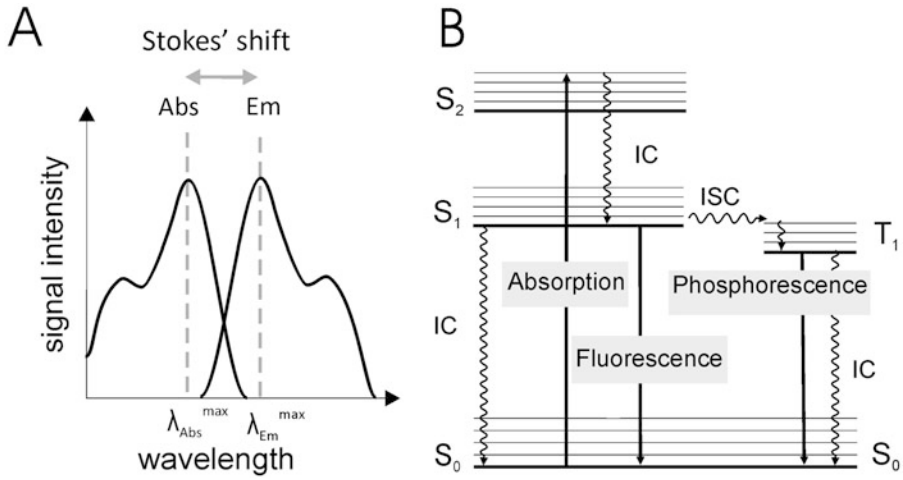

Fig. 1 (**a**) Absorption (Abs) and fluorescence emission (Em) spectrum of an imaginary molecule. The maximum of the emission spectrum is shifted towards the *red* (higher wavelength) with respect to the maximum of the absorption spectrum, a property called the Stokes' shift. (**b**) Jabłoński diagram. The electronic states (S_0, S_1, S_2) and their vibronic states are depicted by *horizontal lines*. The *straight arrows* indicate radiative transitions, the wavy ones non-radiative transitions

involved in absorption and fluorescence are usually depicted in a Jabłoński diagram (Fig. 1b). The electronic ground state and first and second excited singlet states are designated S_0, S_1, and S_2, respectively. The thin horizontal lines represent vibronic levels, involving in addition to electronic, vibrational excitation. Transitions between the levels are depicted as vertical arrows, straight ones involving radiative transitions, wavy ones radiation-less ones. From the ground state S_0 a molecule can absorb a photon, leading to an excited state, in Fig. 1a to S_2. Usually, excitation from a higher vibronic state is followed by fast (typical time scale: $\sim 10^{-12}$ s) radiation-less relaxation to the lowest vibrational level of S_1, a process called internal conversion, leading to the generation of heat. From S_1, the excited molecule can usually relax to the ground state in one of three ways. (1) The molecule can return to the ground state while emitting a photon, fluorescence ($\sim 10^{-8}$ s). (2) The molecule can get rid of the excitation energy without emitting a photon, via internal conversion (IC, $\sim 10^{-8}$ s). Finally, (3) the electrons in the molecule can undergo a spin conversion to a triplet state, a process called intersystem crossing (ISC, $\sim 10^{-8}$ s). The resulting triplet state (T_1) can decay to the ground state in a radiation-less way via internal conversion or while emitting a photon, phosphorescence, which usually takes place on a much longer time scale than fluorescence, since it involves a spin-forbidden transition. The time scales mentioned are typical values and vary substantially among different molecules and can also depend on the (solvent) environment. An important property of fluorescence of

molecules in condensed phases is the so-called Stokes' shift: the energy of the emitted photons is generally lower than that of the absorbed photons (Fig. 1a). The most important reason, as depicted in Fig. 1b, is fast relaxation of the excited state to the lowest vibrational level of S_1, from which transitions can occur to vibrationally excited states of S_0. In addition, in the liquid state, solvent effects can contribute to the energy shift [5].

1.2 A History of Single-Molecule Fluorescence Microscopy

A key cause for the popularity of fluorescence to study biomolecules is its sensitivity. The sensitivity is such that, using the appropriate instrumentation, the fluorescence emitted by a single fluorophore can be readily detected. An important reason for the sensitivity is the Stokes' shift, which allows, after proper filtering, detection of the fluorescence signal against a black background. Over the last decades, researchers have pushed the detection limit further and further. In the 1970s, Hirschfeld observed single antibodies, labeled with ~100 fluorescein molecules [6]. In the 1980s, single phycoerythrin proteins, also containing multiple fluorophores, were detected [7, 8]. In 1989, Moerner and coworkers succeeded in detecting, at liquid helium temperatures, the absorption of single dye molecules embedded in organic crystals [9]. At these low temperatures and in crystalline environment, the absorption line of a single molecule is extremely narrow but very strong, making the detection of a single molecule possible. Orrit and coworkers detected, for the first time, using the same molecular system, the fluorescence of a single fluorophore (at low temperature) [10]. For most biological applications, however, more ambient conditions are required: room temperature and solutions in water. Such conditions lead to different spectral properties (absorption and emission bands are often tens of nanometers wide) and quite different instrumentation is required. In 1990, Keller and coworkers were able to detect single Rhodamine-6G molecules flowing through a small detection volume [11]. This discovery paved the way for the new advancements in methodology described in this part of the book that have made single-molecule fluorescence microscopy to a successful tool to study the ways and means of biomolecules [5, 12–14]. In 2014, the Nobel Prize in Chemistry has been awarded to Stefan W. Hell, W. E. Moerner and Eric Betzig. Moerner and Betzig received the prize for their roles in the development of single-molecule localization super-resolution microscopy, one of the methods that allows breaking the diffraction limit, increasing the resolution of optical microscopes to better than half the wavelength of light used [12].

2 Fluorophores

2.1 Important Properties of Fluorescent Molecules Used for Single-Molecule Methods

Single-molecule fluorescence microscopy at ambient conditions relies on the accurate detection of photons emitted by one or more fluorophores attached to a single biomolecule while, at the same time, limiting the background signal using advanced microscopy techniques. The higher the signal-to-background ratio, the more detailed and clear the information is that can be obtained. Optimization of the signal-to-background ratio is therefore an essential element in single-molecule fluorescence microscopy [15]. Generally speaking, two approaches can be distinguished. (1) Increasing the signal, by creating the optimal conditions for the fluorophore to emit photons and by increasing the sensitivity and efficiency of photon collection and detection. (2) Decreasing the background, using advanced microscopy techniques that probe only small volumes around the molecule of interest. Under optimized conditions, the signal from a single fluorophore such as Rhodamine-6G (R6G) can be detected [11]. To provide an idea about the expected fluorescence intensity due to a single R6G, we will make a rough estimation of the number of photons that can be detected when a laser ($\lambda = 532$ nm), with an intensity of 100 W/cm^2, illuminates a single R6G molecule suspended in water. We first have to calculate how many photons are absorbed by the molecule, using its absorption cross section, σ, which can be determined from the molecular extinction coefficient, ε, of R6G (~100,000 L/mol/cm at 532 nm) using:

$$\sigma = \frac{2.303\varepsilon}{N_A}, \tag{1}$$

where N_A is Avogadro's constant. Use of this equation yields a cross section of 3.8×10^{-16} cm^2 for R6G [5]. Next, we calculate the energy of a single photon:

$$E = \frac{hc}{\lambda}, \tag{2}$$

with h Planck's constant, c the velocity of light and λ the excitation wavelength resulting in 3.7×10^{-19} J per photon. This means that with an illumination intensity of 100 W/cm^2 the sample is bombarded by 2.7×10^{20} photons/s/cm^2. Multiplying the photon flux per cm^2 (q_p) with the absorption cross section of R6G:

$$q_a = q_p \cdot \sigma_{R6G}, \tag{3}$$

we find that every second 1.0×10^5 photons are absorbed (q_a) by a single R6G molecule! From S_1, the molecule can relax to the ground state in one of three ways and thus not every photon that is absorbed by R6G leads to fluorescence. The fluorescence

quantum yield Φ_f is the ratio between photons absorbed and photons emitted. For R6G the fluorescence quantum yield is about 0.45 in water, resulting in an emission rate of 4.5×10^4 photons per second for a single R6G under the conditions defined above [16]. Even with fully optimized instrumentation only about 12% of the emitted photons can be counted by the detector [17]. Thus, one can expect a fluorescence photon flux of ~5×10^3 photons/s from a single R6G fluorophore illuminated with an intensity of 100 W/cm^2. R6G is a water-soluble, synthetic fluorophore with properties comparable to other fluorophores widely used in single-molecule microscopy. Below we will discuss the key fluorophore properties relevant for which fluorophore to use for what experiment.

2.2 Important Characteristics of Fluorescent Labels

Nowadays, a large array of different fluorophores exists that can be detected simultaneously to study different single molecules at the same time [18]. Four different classes of fluorescent labels can be distinguished: (1) synthetic dyes such as Cy3, Cy5, Rhodamine 6G, and fluorescein isothiocyanate (FITC), (2) semiconductor nanocrystals such as quantum dots (QDs), (3) genetically encoded fluorescent labels like eGFP and yellow fluorescent protein (YFP), and (4) natural occurring fluorophores such as flavin and chlorophyll. Every fluorophore has its own advantages and disadvantages. To determine which fluorophore to use for a certain experiment one has to look at the different fluorophore characteristics. Besides the fluorescence quantum yield and the molecular extinction coefficient, which were already described above, several other characteristics should be considered. Fluorophore excitation and emission wavelengths are the most important and determine the choice of the excitation source and filters. Not all colors are equally apt for single-molecule measurements. Wavelengths below ~450 nm are generally speaking problematic since detectors can be relatively insensitive, microscope optics are often not optimized in this range of the spectrum, and these colors often result in high background signals due to impurities in glass or sample. Another key fluorophore characteristic is the rate of photobleaching. In general, a fluorophore does not survive infinite absorption/emission cycles. In many cases, there is a certain probability that an absorption/emission cycle leads to an irreversible modification of the fluorophore, resulting in an abrupt loss of its ability to fluoresce called photobleaching. The propensity of a fluorophore to photobleach is expressed in the average number of photons a fluorophore can emit. Photostable synthetic dyes, such as Cy3 and Cy5 can emit 10^5–10^6 photons before photobleaching [19], QDs are orders of magnitude more photostable. Fluorescent proteins such as eGFP are usually slightly less stable than their optimized, synthetic equivalents [20]. Photobleaching is a probability process; in general the rate of bleaching decreases linearly with decreasing excitation

intensity. An important cause of photobleaching is molecular oxygen, which can react with the fluorophore's triplet to form singlet oxygen. Singlet oxygen in turn is very reactive and can readily react with the fluorophore or surrounding molecules [14]. Adding an oxygen scavenger system (a mixture of glucose, glucose oxydase and catalase is often used) to the sample decreases the concentration of molecular oxygen and can help to increase the lifetime of the fluorophores. Addition of antioxidants like Trolox® or ascorbic acid can have additional effect. Other problems with fluorophore photostability include triplet blinking, which can be a problem when the triplet lifetime is rather long (>ms). Certain fluorophores show different on-off blinking behavior, for example, fluorescent proteins are known to undergo cis-trans isomerization and intramolecular proton transfer, both resulting in long-lived dark states [20]. Another example is the photoblinking of QDs, which is caused by ejection of electrons from the semiconductor core [21]. Considering all the fluorophore characteristics mentioned above the ideal single-molecule fluorophore (1) has high fluorescence quantum yield and molecular extinction coefficient, (2) has well defined excitation and emission wavelengths, (3) shows steady emission intensity [22], (4) can be followed for a long time using high illumination intensity, (5) does not affect the natural behavior of the single molecule, (6) shows no blinking behavior, (7) can be easily attached to the molecule of interest, (8) is soluble in buffers used [23], (9) and its characteristics are well described.

2.3 Fluorophores Used for Single-Molecule Research

Next, we take a closer look at the different classes of fluorescent labels and compare and discuss some of their characteristics important for single-molecule research (Fig. 2). (1) Synthetic dyes have been around for decades, are commercially available and constructed to suit the means of use. They are constructed in a way that they contain different reactive groups such as maleimides or succynimidyl esters, which can be used for attachment of the label to a protein or biomolecule of interest. Succynimidyl esters react with free amino groups, which are available in large quantities on the surface of most proteins. Maleimides or other sulfhydryl reactive probes can be used for more specific labeling of cystein residues, which are generally less abundant. Because synthetic dyes have been around for a long time, their characteristics have been optimized and labeling protocols are widely available. Their small size (~0.5 nm) minimizes the chance of causing steric hindrance to the labeled molecule. Cyanine and rhodamine dyes (Fig. 2a) are most often used for in vitro single-molecule research, in particular Cy3, Cy5, Alexa555 of the cyanine family and Rhodamine 6G and Texas Red of the rhodamine family [22]. (2) QDs are very bright fluorophores with a very wide range of absorption wavelengths, narrow (about 10 nm) and symmetric emission bands and quantum yields close to 90% (Fig. 2c) [24, 25]. QDs in general consist of a

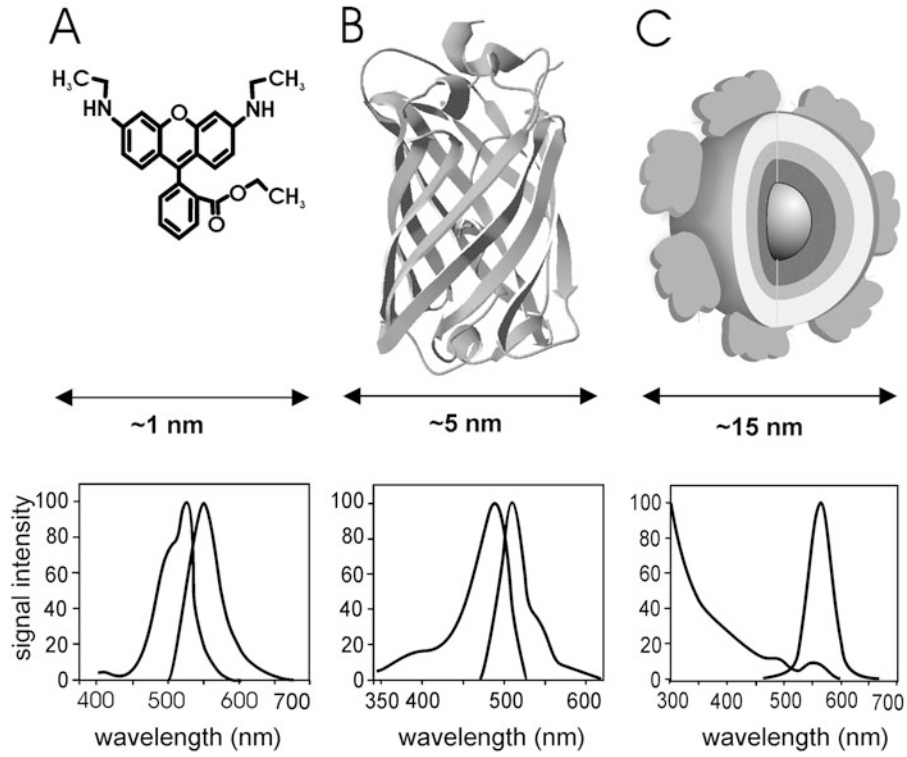

Fig. 2 Structure, size and spectra of different fluorescent probes used in single-molecule fluorescence microscopy. (**a**) Chemical structure and absorption/emission spectrum of the synthetic dye rhodamine 6G (R6G). (**b**) Structure (Protein Databank entry 1S6Z [71]) and absorption/emission spectrum of enhanced Green Fluorescent Protein (eGFP). (**c**) Schematic representation of a functionalized QD consisting of a core and different shells and corresponding absorption/emission spectrum

CdSe, CdTe, InP or InAs core, and a ZnS shell. Their size, shape, and structure can be controlled precisely, in order to tune the emission from visible to infrared wavelengths [26, 27]. For biological applications, QDs are normally coated to make them hydrophylic or prepare them for specific attachment to the biomolecule of interest [28]. Compared to organic dyes, QDs are brighter (molecular extinction coefficients between 10^5–10^6 L/mol/cm). They are also more photostable and therefore can be followed longer and their position can be determined with higher accuracy [23]. However, their size varies between 6–60 nm (with coating), which is relatively large in comparison to organic dyes (~0.5 nm). In addition, as mentioned above, they can suffer from on/off blinking on a wide range of time scales [21]. (3) Green fluorescent protein (GFP, Fig. 2b) is an autofluorescent protein from the jellyfish *Aequorea victoria*, which is very well suited for (but not restricted to) in vivo applications. A key advantage of GFP is that the protein is genetically encoded, does not require a cofactor and that every protein copy can be labeled by fusing its gene with that of

GFP [29]. Another advantage is that they are less sensitive to their surroundings than many synthetic dyes [30]. Disadvantages of GFP are that it is rather large (27 kDa, ~4 nm in diameter), its emission shows blinking behavior and its photostability is substantially less than good synthetic dyes [20]. By now, many different variants with different colors, optimized for different organisms have been developed on basis of the *Aequorea victoria* protein and related proteins in other organisms [31, 32]. Also photoactivatable and photoswitchable versions of fluorescent proteins exist, which are very well suited for single-molecule localization-based super-resolution methods [33]. (4) Biological materials also contain naturally occurring fluorescent molecules. Many of these (such as tryptophan and NADH), which are widely used in bulk fluorescence measurements, are not photostable enough and absorb and emit too far in the ultraviolet to allow single-molecule detection. Protein cofactors such as chlorophyll and flavin can be very fluorescent and have been used for in vitro applications [34, 35]. Their occurrence is however limited to a small subset of proteins, which hinders general application.

3 Methods

3.1 Microscopic Detection of Single Fluorophores

Single fluorescently labeled particles can be detected using a fluorescence microscope. The main components of such a microscope are an illumination source for excitation of the fluorophores, filters to extract light of wanted colors and suppress unwanted light, an objective to direct the excitation light and efficiently collect the emission light, and a detector. Since much of the emitted light is lost in the detection pathway and the total number of photons that a fluorophore can emit is restricted due to photobleaching, it is imperative in single-molecule fluorescence studies to use optimal components in each part of the instrument. In the next section we will discuss the different parts of a fluorescence microscope in more detail.

3.1.1 Light Sources

To maximize the signal obtained from a single fluorophore, it is essential to excite it with a wavelength close to its absorption maximum. In bulk fluorescence microscopy often broad-band sources such as metal halide or mercury arc lamps are used [36]. A key advantage of these sources is that they are broad-band and contain several intense spectral lines. This allows them to be used to excite spectrally distinct fluorophores, with the proper excitation filters to suppress unwanted lamp light. Relatively new on the market are LED sources, which are more monochromatic than lamps (spectra with a width of several tens of nanometers). LEDs are much more energy efficient and thus produce less heat. In single-molecule applications, in most cases, lasers are used for

fluorescence excitation since they emit monochromatic and collimated light, allowing better separation of excitation from fluorescence light and a more straightforward construction of complex optical paths using mirrors, lenses, filters, polarizers etc. In addition, collimated laser beams can be focused to diffraction limited spots (see below), which is indispensable for confocal fluorescence microscopy. Apart from cost, there are two key disadvantages of lasers. (1) Laser beams are Gaussian and this can result in uneven excitation intensity profiles. (2) Lasers are in many cases monochromatic meaning that for each spectrally distinct fluorophore an additional laser needs to be purchased and installed.

3.1.2 Filters and Dichroic Mirrors

Optical filters are used to separate fluorescence light from scattered excitation light and other background signals. On basis of their transmission spectra two classes of filters can be discerned: edge filters and band-pass filters. Edge filters transmit light above (long-pass) or below (short-pass) a specific wavelength, and block the other light. Band-pass filters transmit only a narrow range of wavelengths and block wavelengths on either side of this range. The performance of the filters depends on three aspects: the percentage of transmission of the desired light, the optical density in the blocked region of the spectrum and the steepness of the edges between the transmitted and blocked regions [15]. In the past, filters were based on stained glass, which often suffered from considerable autofluorescence. Later, thin film interference filters, consisting of repetitive, thin layers evaporated on a surface were developed with substantially better performance and flexibility. Recently, new technologies to make precise thin layers based on ion-beam sputtering have further improved filter performance. Nowadays, filters are available that are designed for simultaneous excitation and/or detection of several, spectrally distinct fluorophores.

A typical fluorescence microscope consists of three optical filters. (1) The excitation filter that selects one line or band from excitation source to illuminate the sample (in many cases use of an excitation filter is not required when using lasers). (2) A dichroic beam-splitting mirror that reflects excitation light in the direction of the objective, but transmits fluorescence light collected by the objective. (3) The emission filter that is used to select for an emission band and block any residual excitation light. In principle, for each light source and dye combination a separate combination of these filters needs to be used.

3.1.3 Detectors in Single-Molecule Fluorescence Microscopy

In single-molecule fluorescence methods the number of photons emitted is very limited, which makes it key to use a detector with a high quantum efficiency and low noise. Broadly speaking, two distinct classes of detectors can be used, depending on the imaging

modality (see below) [15, 37]. (1) Point detectors, such as avalanche photodiodes (APD) and photomultipliers, which do not provide position information but are capable of counting single photons with high time resolution. APDs have high quantum efficiency, but a small active area, which makes alignment tedious. Photomultipliers usually have a lower quantum efficiency and worse dark noise characteristics, but a larger active area. For single-molecule applications, photomultipliers are usually only used in the blue part of the spectrum, where APDs perform poorly. In general, point detectors are used in confocal instruments or when time resolution is important. Key applications are in burst analysis of diffusing molecules for example in fluorescence correlation spectroscopy (FCS) [38, 39] or in FCS-like experiments [40]. (2) Array detectors, such as Charged Coupled Devices (CCD) are the most widely used detectors in wide-field fluorescence microscopy. CCD detectors are two-dimensional array detectors that can be read out in one of three ways: full frame, frame transfer or interline transfer. The latter two are fast and allow for continuous detection. Limitations of CCD detectors are read-out noise due to analog-to-digital conversion (a problem solved in modern electron multiplying CCDs) and the relatively slow speed: an entire frame is integrated and read out. For single-molecule detection frame rates up to ~100 s^{-1} can be reached. Key advantages are the almost unity quantum efficiency (in the visible spectrum) and the very low dark currents. These detectors are, therefore, optimally suited in conditions when acquisition times of down to ~10 ms are sufficient [41]. In the last couple of years, a new kind of camera technology has been introduced, the scientific CMOS (complementary-metal-oxide semiconductor) [18]. In an sCMOS camera detector array, amplifiers and analogue-to-digital converters are integrated in one chip, which allows reading out of individual pixels. Current state-of-the-art sCMOS camera (Andor Zyla 4.2 or Hamamatsu ORCA-Flash4.0) contain 2048 × 2048 pixels, have a quantum efficiency exceeding 80% and can read out 100 full frames per second, with less than an electron read noise. Very recently, Photometrics has introduced 95% quantum efficiency sCMOS camera (Prime 95B). The key benefit of sCMOS cameras is that they allow acquisition with a larger field of view at higher acquisition rates than CCD cameras.

3.1.4 Microscope Objectives

The key optical element in a fluorescence microscope is the objective. The objective concentrates the excitation light in the sample and collects the emitted light. In principle, an objective is nothing more than a strong lens, but in order to fulfill its tasks it needs to be highly corrected for optical aberrations, which can only be achieved by complex designs involving multiple optical elements. Important properties with respect to single-molecule experiments are the

magnification, which determines the size of the field of view and the number of pixels over which a single fluorescent particle is imaged and the numerical aperture (NA), which is a measure of the angle over which photons can be detected, defined as [36]:

$$\mathrm{NA} = n \cdot \sin\theta_{\max}. \tag{4}$$

With n is the refractive index of the medium between the sample and the objective, and $\theta_{\max}$ is the maximum half-angle of the collection cone of the objective. A fluorophore emits light in all directions and to maximize the collected light the NA of the objective should be as high as possible. This may be achieved by using an objective designed to be immersed in a high-n medium [15, 42]. Furthermore, the NA is not only important for collection efficiency, but it also determines the resolution of the optical system, as will be discussed in the next section.

3.1.5 The Resolution of a Fluorescence Microscope

A fluorescent molecule is much smaller than the wavelength of visible light and after excitation the molecule emits photons in random direction. Using a single microscope objective it is impossible to collect light emitted in all directions and consequently only a fraction of the emitted photons can be collected. The circular apertures of the microscope optics (in particular the objective) will result in diffraction of the transmitted light, which causes the fluorescent particle not being imaged as an infinitely small point, but as an Airy disc, with a finite width and side lobes. A three-dimensional representation of this diffraction pattern is referred to as the point spread function (PSF). The diameter (d) of the PSF only depends on the NA of the objective and the wavelength of the light (λ) [36]:

$$d = \frac{1.22\lambda}{2\mathrm{NA}}. \tag{5}$$

The width of the PSF is also a measure of the resolution of the optical system: when the distance between two closely spaced point sources is less than d, the images of the sources overlap and their peaks cannot be resolved. This definition of the resolution is called the *Rayleigh criterion* [36]. For a typical fluorescence microscope (NA = 1.4, λ = 505 nm (eGFP)), the resolution is ~220 nm.

3.2 Key Imaging Modalities in Fluorescence Microscopy

3.2.1 Confocal Fluorescence Microscopy

In confocal fluorescence microscopy the sample is illuminated with a diffraction limited spot and an image is acquired by moving this spot over the sample (Fig. 3a). To this end, a collimated laser beam is coupled in the microscope objective, resulting in a tightly focused spot with a diameter of typically 200–300 nm, ruled by the same effects of diffraction as discussed above. The fluorescence resulting in the focus is collected by the objective, separated from the excitation beam by a dichroic mirror and further spectrally filtered by an

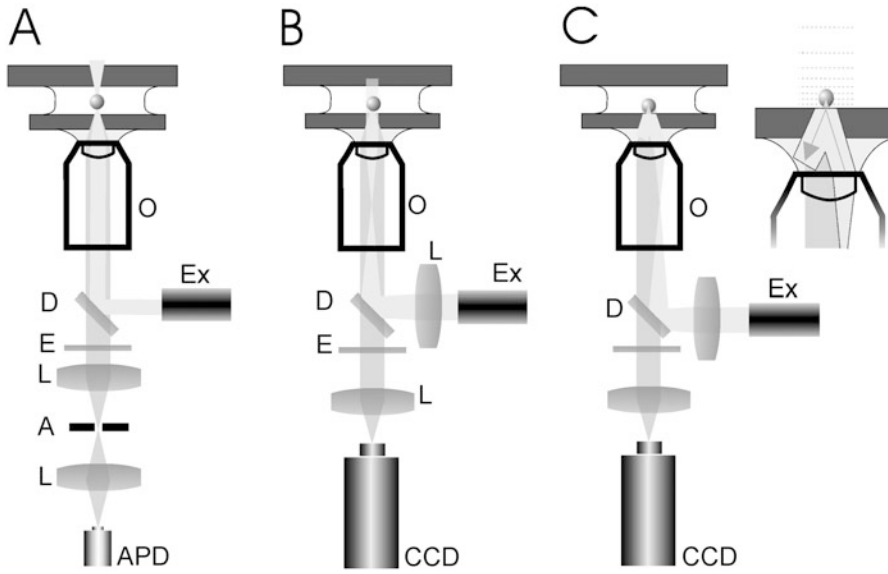

Fig. 3 Schematic representation of the three most common microscope-designs used in single-molecule fluorescence microscopy. (**a**) Confocal setup. (**b**) Epi-wide field setup. (**c**) TIRF-wide field setup. A zoom of the excitation path, the laser is coupled off-axis into the objective. The laser is reflected on the glass–water interface and creates an exponentially decaying evanescent wave in the sample. *Ex* excitation source, *L* lens, *O* objective, *E* emission filter, *D* dichroic mirror, *A* confocal aperture)

emission filter. In addition, the fluorescence light is spatially filtered with a pinhole before being detected with a point detector (APD or photomultiplier). The pinhole increases spatial resolution, but its key purpose is to suppress out-of-focus background signal, allowing optical sectioning. To create an image, scanning of the beam (using e.g. galvanic mirrors) or the sample (using a piezo stage) is required. In single-molecule experiments, excitation intensities need to be reduced to avoid saturation or limit photobleaching, resulting in rather long image acquisition times. Consequently, the most important single-molecule application of confocal microscopy is to study molecules freely diffusing in and out the confocal spot, for example using FCS.

3.2.2 Wide-Field Epi-fluorescence Microscopy

In wide-field epi-fluorescence microscopy, the excitation beam is not tightly focused to a diffraction-limited spot in the sample plane, but illuminates a substantially larger area (Fig. 3b). The fluorescence arising from this illuminated area can be detected with an array detector such as a CCD camera. Uniform illumination throughout the sample can be obtained by focusing the excitation beam in the back-focal plane of the objective. In case of a laser this results in a collimated, Gaussian-shaped beam illuminating the sample. Filters and dichroic mirrors are applied in exactly the same way as confocal fluorescence microscopy. Single-molecule wide-field fluorescence microscopy is particularly useful when

molecules are moving in the sample or when a time resolution of ~100 Hz is sufficient. As discussed above, modern CCD and sCMOS cameras are superior with respect to dark noise and quantum efficiency, compared to point detectors used in confocal microscopy. In addition, wide-field fluorescence microscopes are optically simpler and often require less frequent and precise alignment [15].

3.2.3 Total Internal Reflection Fluorescence Microscopy (TIRF)

As discussed above, wide-field approaches have, in certain cases, advantages over confocal approaches, at the cost of time resolution and worse suppression of out-of-focus background fluorescence than in confocal microscopy. This latter problem is addressed in TIRF microscopy, in which the evanescent wave resulting from a totally internally reflected laser beam is used for fluorescent excitation. The evanescent wave, generated by reflection on a glass–water interface, penetrates into the medium with lower refractive index (the water) and its intensity I drops exponentially with distance (z) into the low-index medium [43]:

$$I(z) = I_0 \cdot \exp(-z/d), \tag{6}$$

with I_0 the intensity at the surface and d the decay constant. The decay constant of the intensity of the evanescent wave is on the order of 100 nm, depending on the angle of incidence and the refractive indices of glass and medium. To obtain total reflection and generate an evanescent wave, the angle of incidence of the laser beam impinging on the glass–water interface needs to be larger than the critical angle (θ_c):

$$\theta_c = \arcsin(n_1/n_2), \tag{7}$$

where n_1 and n_2 are the refractive indexes of water and glass respectively. At the glass–water interface the internal reflection is achieved at an θ_c of 61°. These high angles of incidence are usually obtained in one of two ways: (1) by using a prism, coupled to the coverslip on the side of the sample opposite to the objective. (2) By using an ultra-high NA objective (>1.45) and coupling in the laser beam off axis, on the edge of the entrance pupil [44] (Fig. 3c). The key advantage of TIRF microscopy is that only fluorophores close to the interface will be excited and fluorophores deeper in the sample will not, resulting in a reduced background. Disadvantages of TIRF microscopy are that the excitation intensity strongly depends on the depth in the sample, making comparison of fluorescence intensities difficult and that the polarization of the evanescent wave is complex.

3.2.4 Selective-Plane Illumination Microscopy (SPIM)

A different imaging modality that has recently received a lot of attention is SPIM or light-sheet fluorescence microscopy [45]. In SPIM, the detection branch is essentially identical to that of a wide-

field fluorescence microscope. Excitation light, however, is provided by another objective, perpendicular to the detection objective. By using a weakly focusing excitation objective, a thin (on the order of one to several micrometers) sheet of excitation light is created, only illuminating the sample very close to the focal plane of the detection objective [46]. Because of limited space to arrange two perpendicular objectives, often water-dipping objectives are used with lower NA than would be desired for single-molecule applications. These instruments have found wide-spread application in studies of larger, living objects, such as developing embryos embedded in an agarose gel [47]. The key advantage of SPIM in these applications is that the light-dose is minimal, allowing long-term imaging without photo damage. Several implementations of SPIM employing higher-NA objectives have made single-molecule experiments possible, albeit using open sample chambers [48], or complex sample-cell designs implementing micro mirrors [49, 50]. It is very likely that SPIM techniques will find further application in the single-molecule fluorescence field, in particular inside living cells and organisms.

4 Measurables

4.1 Counting the Number of Fluorescent Molecules Within a Diffraction-Limited Spot

So when an instrument is built and a sample prepared, how does one know one is looking at a single molecule? Observation of a single diffraction-limited spot is not enough: the Rayleigh criterion tells us that when particles are too close they cannot be resolved and will be imaged as a single spot. The most straightforward signature of fluorescence arising from a single fluorophore is step-wise photobleaching: the intensity is for a while rather constant, until photobleaching occurs and the signal abruptly drops to the background level. Another signature is the intensity, which should be constant from molecule to molecule, however orientation or polarization effects can substantially modulate fluorescence intensity (see below). If the intensity of a fluorescent spot is due to more than one fluorophore, the number of fluorophores can be determined in two ways. (1) By comparing the fluorescence intensity of the spot to the average value of single fluorophores (Fig. 4a). To correct for possible bleaching within the first frame the intensity at $t = 0$ can be extrapolated by fitting an exponential decay to the fluorescence intensity profile over time [51]. (2) One can also determine the number of fluorophores by counting the number of bleaching steps. This approach has for example been used to determine the number of Ase1p dimers incorporated in multimers bound to microtubules [52]. On the other hand, at conditions when photobleaching is negligible the changes in numbers of molecules due to association or dissociation can be measured. This approach has been used to determine the number of Rad51 monomers disassembling from DNA in a single burst [53].

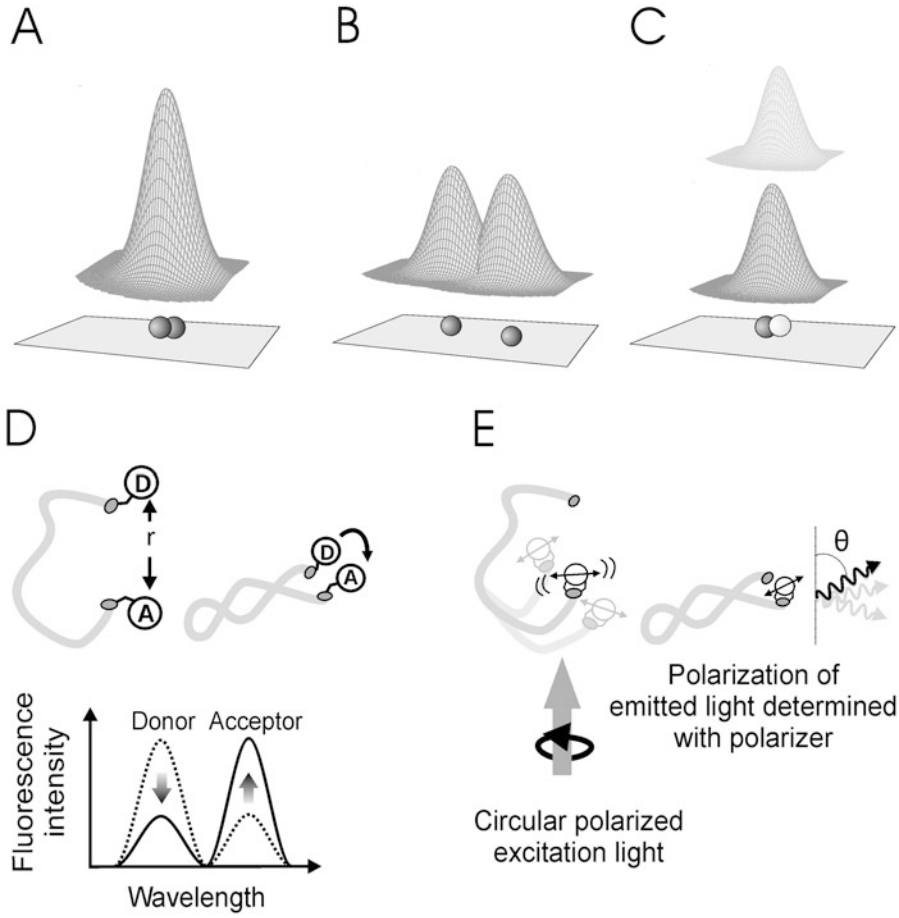

Fig. 4 Measurable parameters in single-molecule fluorescence microscopy. (**a**) The number of fluorophores within a fluorescent spot, even though they are not resolvable, can be deduced from the intensity of that spot. (**b**) Localization of single fluorophores. The fluorophores are imaged as Airy disks, which can be approximated with a 2D Gaussian. The limit in which two neighboring fluorophores can still be resolved is described by *Rayleigh criterion*. (**c**) Colocalization is achieved by using labels with different colors. By imaging both color channels simultaneously on a CCD camera the precise localization of both fluorophores can be determined. (**d**) FRET reports on the distance between two spectrally distinct dyes, and can be used to study for example intramolecular conformational changes. When the distance between the dyes is in the order of tens of Å (20 Å $< r <$ 90 Å), the energy can get transferred from the donor (D) to the acceptor (A) causing an increase in acceptor signal. When the distance between the dyes is large ($r >$ 90 Å) no energy transfer occurs and the acceptor signal will be low. (**e**) Fluorescence polarization reports on orientation or orientational dynamics. Circularly polarized light can be used to excite dyes in all orientations. Subsequently, the emitted light is filtered for a specific polarization

4.2 Localization of Single Molecule

We have seen above that the resolution of a fluorescence microscope is limited by diffraction, to about half the wavelength of the emitted light. The resolution is a measure for how close two point sources can be to be still resolvable (Fig. 4b), it does not restrict the accuracy with which the location of a single point source can be determined. By fitting the resulting image with the PSF (often an

approximation with a Gaussian is sufficient), the location of the maximum of the image can be determined with far greater accuracy than the width of the PSF. This method is frequently used in single particle tracking (SPT) [41, 54]. Given the noise encountered in most single-molecule experiments a PSF of the microscope with a full width at half maximum of ~1.5–2 pixel yields best results for the accuracy [55]. The uncertainty in the localization of a point source (Δx) depends on the size of the pixels (a), the number of photons (N), the background noise (b), the standard deviation of the point spread function (s) [55, 56]:

$$\left\langle (\Delta x)^2 \right\rangle = \frac{s^2}{N} + \frac{\left(a^2/12\right)}{N} + \frac{8\pi s^4 b^2}{a^2 N^2}. \tag{8}$$

The first term represents the photon counting noise (s^2/N), the second term represents pixelation noise arising from the uncertainty of where in the pixel the photon arrived ($a^2/12N$). The final term is due to background noise. Under typical single-molecule fluorescence conditions, position accuracies down to about 2 nm can be achieved [56].

4.3 Detection of Motion of Single Molecules

Given this high localization accuracy, the positions of an emitting fluorophore can be determined in each image from a time stack of images and subsequently a trajectory can be reconstructed by connecting the positions. Using this approach, the motion of single-molecules can be accurately determined. Care has to be taken that the motion of the molecules is not too large within the acquisition time of an image, since this can smear out the Gaussian intensity profile, complicating fitting. This problem can be avoided by using short acquisition times and increasing the excitation intensity, at the cost of enhanced photobleaching. It is important in single-molecule tracking to find the proper balance between movement of a particle within the acquisition time, and the total number of time points (frames) over which the particle is observed [57]. Motion of biomolecules can be directional (for example driven by motor proteins) or diffusive (like membrane proteins). To analyze the precise nature of mobility, often the mean square displacement (MSD) is calculated as a function of time. Motion with constant speed (and direction) leads to an MSD that increases with the square of time, while diffusive motion results in a linear increase of the MSD with time. The localization uncertainty leads to a constant offset in the MSD, due to its time-independence [41, 58]. The MSD analysis was for example used to show that, depending on the exact conditions, the motor protein kinesin-5 can switch between different modes of motility; diffusion and directed motion [59].

4.4 Single-Molecule Localization Super-Resolution Microscopy

As discussed in the previous paragraphs, the localization of a single fluorescent molecule can be determined with a substantially higher accuracy than the optical resolution of the microscope. This trait has been used to overcome the diffraction-limited resolution of an optical microscope (in the order of half the wavelength of the light used) in single-molecule localization super-resolution methods such as PALM [60] and STORM [61]. In these methods, many consecutive images of a sample are taken. The trick is that using photo activation of specific fluorophores [60, 61] or using chemical switching of the fluorescence [62], during a single image only a limited number of single fluorophores is active and recorded. The location of these single molecules can be determined as indicated above with a higher accuracy than the optical resolution. The localizations of many of such single molecules obtained after many cycles of photo activation, imaging and photo bleaching can be combined in a single reconstituted image with a substantially higher resolution (tens of nanometers) than the diffraction limit. The resolution depends both on the density of fluorophores and the localization accuracy achieved.

4.5 Colocalization of Fluorescent Molecules

One of the key interests in (cell) biology is to resolve which proteins interact and how. To this end, proteins of interest can be labeled with differently colored fluorophores [63–65] . Subsequently the different dyes can be excited by the appropriate lasers and the fluorescence signal can be separated in two or more wavelength channels and detected independently using different cameras or side-by-side on one. In this way, different biomolecules can be tracked simultaneously and their motion can be correlated to resolve whether they move independently or interact (part of the time) (Fig. 4c). High-resolution colocalization was applied to show myosin V's alternating heads while it walked hand-over-hand along an actin filament, for example [65].

4.6 Förster Resonance Energy Transfer (FRET)

Positions and distances of single fluorophores can be determined with an accuracy that is substantially smaller than the diffraction limit using PSF fitting (see above). This approach is very powerful, but has its limitations, in particular in its poor time resolution and its inability to resolve multiple molecules that are closer than the optical resolution, without photobleaching them. An excellent method to measure relative distances and changes on a length scale of ~2–9 nm is FRET (Fig. 4d). In FRET two spectrally distinct fluorophores are used. One, with the highest energy excited state, is excited and serves as donor, the other as acceptor. When the two fluorophores are close and their dipoles oriented favorably, dipole-dipole coupling can occur and excitations can be transferred from donor to acceptor. The distance dependency of the FRET efficiency (E) is:

$$E = \frac{1}{1 + (R/R_0)^6}. \tag{9}$$

With R the distance between donor and acceptor and R_0 the Förster distance. The Förster distance is defined as the distance at which half the fluorescence of the donor is transferred to the acceptor. The Förster distance depends on the overlap of the emission spectrum of the donor with the absorption spectrum of the acceptor, the relative orientation of donor and acceptor dipole moments and the fluorescence quantum yield of the donor. It has a typical value of about 5 nm [5]. FRET has proven to be a valuable tool to study conformational dynamics in nucleic acids and proteins. Examples are the folding of ribozymes [66] and the observation of conformational dynamics in kinesin-1 [67, 68].

4.7 Fluorescence Polarization

Another way to measure conformational dynamics of single biomolecules is to use the polarization of the fluorescence signal. Absorption and emission are governed by the interaction of the absorption and emission transition dipole moments of the chromophore, which are vectors, with the electric component of the electromagnetic light field, also a vector. Using polarized light for excitation and/or a polarizer in the emission path allows obtaining the orientation and dynamics of the transition dipole moment. Care needs to be taken that the fluorophore is not free to rotate with respect to the biomolecule of interest, but that its orientation is tightly linked to that of the biomolecule. This can be achieved by using bisfunctional fluorophores that are connected with two chemical links to the protein or nucleic acid of interest [69]. One way of determining dipole orientations on the single-molecule level is to excite with circularly polarized light and to split the resulting fluorescence in two perpendicular linearly polarized signals, detected with two APDs or side-by-side on a CCD chip (Fig. 4e). Another way is to detect without polarizers, but to use alternating (linear) polarization of the excitation light. If one combines polarized excitation with polarized detection, a separation can be obtained of the depolarization due to rapid fluorophore orientation (on the nanosecond scale) and much slower conformational changes. Polarization methods have for example been applied to study the conformational changes occurring during stepping of the kinesin-1 motor protein [70].

5 Concluding Remarks

Here we have provided a short and broad overview of the wealth of single-molecule fluorescence approaches and their backgrounds. These tools have become indispensable in the study of diverse processes such as the active and diffusive motion of biomolecules,

their conformational changes, and their assembly and disassembly. In the following Chapters 6 till 10, several approaches will be discussed in more depth, including detailed protocols.

References

1. Stokes GG (1852) On the change of refrangibility of light. Philos Trans R Soc Lond 142:463–562
2. Herschel JFW (1845) On a case of superficial colour presented by a homogeneous liquid internally colourless. Philos Trans R Soc Lond 135:143–145
3. Herschel JFW (1845) On the epipolic dispersion of light, being a supplement to a paper entitled, "on a case of superficial colour presented by a homogeneous liquid internally colourless". Philos Trans R Soc Lond 135:147–153
4. Brewster D (1846) On the decomposition and dispersion of light within solid and fluid bodies. Trans R Soc Edinb 16(3):11
5. Lakowicz JR (2006) Principles of fluorescence microscopy, 3rd edn. Springer, New York, NY
6. Hirschfeld T (1976) Optical microscopic observation of single small molecules. J Opt Soc Am 66(10):1124–1124
7. Nguyen DC, Keller RA, Jett JH, Martin JC (1987) Detection of single molecules of phycoerythrin in hydrodynamically focused flows by laser-induced fluorescence. Anal Chem 59 (17):2158–2161
8. Peck K, Stryer L, Glazer AN, Mathies RA (1989) Single-molecule fluorescence detection – auto-correlation criterion and experimental realization with phycoerythrin. Proc Natl Acad Sci U S A 86(11):4087–4091
9. Moerner WE, Kador L (1989) Finding a single molecule in a haystack - optical-detection and spectroscopy of single absorbers in solids. Anal Chem 61(21):A1217–A1223
10. Orrit M, Bernard J (1990) Single pentacene molecules detected by fluorescence excitation in a para-terphenyl crystal. Phys Rev Lett 65 (21):2716–2719
11. Shera EB, Seitzinger NK, Davis LM, Keller RA, Soper SA (1990) Detection of single fluorescent molecules. Chem Phys Lett 174 (6):553–557
12. Moerner WE, Shechtman Y, Wang Q (2015) Single-molecule spectroscopy and imaging over the decades. Faraday Discuss 184:9–36. doi:10.1039/c5fd00149h
13. Tinnefeld P, Sauer M (2005) Branching out of single-molecule fluorescence spectroscopy: challenges for chemistry and influence on biology. Angew Chem Int Ed 44(18):2642–2671
14. Weiss S (1999) Fluorescence spectroscopy of single biomolecules. Science 283 (5408):1676–1683
15. Moerner WE, Fromm DP (2003) Methods of single-molecule fluorescence spectroscopy and microscopy. Rev Sci Instrum 74 (8):3597–3619. doi:10.1063/1.1589587
16. Soper SA, Nutter HL, Keller RA, Davis LM, Shera EB (1993) The photophysical constants of several fluorescent dyes pertaining to ultrasensitive fluorescence spectroscopy. Photochem Photobiol 57(6):972–977
17. Wieser S, Schutz GJ (2008) Tracking single molecules in the live cell plasma membrane-do's and don't's. Methods 46(2):131–140
18. Kubitscheck U (2013) Fluorescence microscopy: from principles to biological applications. Weinheim, Wiley-Blackwell
19. Kapanidis AN, Weiss S (2002) Fluorescent probes and bioconjugation chemistries for single-molecule fluorescence analysis of biomolecules. J Chem Phys 117 (24):10953–10964. doi:10.1063/1.1521158
20. Peterman EJG, Brasselet S, Moerner WE (1999) The fluorescence dynamics of single molecules of green fluorescent protein. J Phys Chem A 103(49):10553–10560. doi:10.1021/jp991968o
21. Kuno M, Fromm DP, Hamann HF, Gallagher A, Nesbitt DJ (2000) Nonexponential "blinking" kinetics of single CdSe quantum dots: a universal power law behavior. J Chem Phys 112 (7):3117–3120. doi:10.1063/1.480896
22. Joo C, Balci H, Ishitsuka Y, Buranachai C, Ha T (2008) Advances in single-molecule fluorescence methods for molecular biology. Annu Rev Biochem 77:51–76
23. Resch-Genger U, Grabolle M, Cavaliere-Jaricot S, Nitschke R, Nann T (2008) Quantum dots versus organic dyes as fluorescent labels. Nat Methods 5(9):763–775
24. Alivisatos AP (1996) Semiconductor clusters, nanocrystals, and quantum dots. Science 271 (5251):933–937
25. Kaji N, Tokeshi M, Baba Y (2007) Single-molecule measurements with a single quantum dot. Chem Rec 7(5):295–304

26. Alivisatos P (2004) The use of nanocrystals in biological detection. Nat Biotechnol 22 (1):47–52
27. Gao XH, Yang LL, Petros JA, Marshal FF, Simons JW, Nie SM (2005) In vivo molecular and cellular imaging with quantum dots. Curr Opin Biotechnol 16(1):63–72
28. Michalet X, Pinaud FF, Bentolila LA, Tsay JM, Doose S, Li JJ, Sundaresan G, AM W, Gambhir SS, Weiss S (2005) Quantum dots for live cells, in vivo imaging, and diagnostics. Science 307 (5709):538–544
29. Chalfie M, Tu Y, Euskirchen G, Ward WW, Prasher DC (1994) Green fluorescent protein as a marker for gene-expression. Science 263 (5148):802–805
30. Giepmans BNG, Adams SR, Ellisman MH, Tsien RY (2006) Review – the fluorescent toolbox for assessing protein location and function. Science 312(5771):217–224
31. Shaner NC, Steinbach PA, Tsien RY (2005) A guide to choosing fluorescent proteins. Nat Methods 2(12):905–909. doi:10.1038/Nmeth819
32. Wu B, Piatkevich KD, Lionnet T, Singer RH, Verkhusha VV (2011) Modern fluorescent proteins and imaging technologies to study gene expression, nuclear localization, and dynamics. Curr Opin Cell Biol 23(3):310–317. doi:10.1016/j.ceb.2010.12.004
33. Patterson GH, Lippincott-Schwartz J (2002) A photoactivatable GFP for selective photolabeling of proteins and cells. Science 297 (5588):1873–1877. doi:10.1126/science.1074952
34. HP L, Xun LY, Xie XS (1998) Single-molecule enzymatic dynamics. Science 282 (5395):1877–1882. doi:10.1126/science.282.5395.1877
35. Rutkauskas D, Novoderezhkin V, Cogdell RJ, van Grondelle R (2005) Fluorescence spectroscopy of conformational changes of single LH2 complexes. Biophys J 88(1):422–435. doi:10.1529/biophysj.104.048629
36. Murphy DB (2001) Fundamentals of light microscopy and electronic imaging. Wiley-Liss, Inc., New York, NY
37. Michalet X, Siegmund OHW, Vallerga JV, Jelinsky P, Millaud JE, Weiss S (2007) Detectors for single-molecule fluorescence imaging and spectroscopy. J Mod Opt 54 (2–3):239–281. doi:10.1080/09500340600769067
38. Magde D, Elson EL, Webb WW (1974) Fluorescence correlation spectroscopy. 2. Experimental realization. Biopolymers 13(1):29–61
39. Eigen M, Rigler R (1994) Sorting single molecules – application to diagnostics and evolutionary biotechnology. Proc Natl Acad Sci U S A 91(13):5740–5747
40. Verbrugge S, Kapitein LC, Peterman EJG (2007) Kinesin moving through the spotlight: single-motor fluorescence microscopy with submillisecond time resolution. Biophys J 92 (7):2536–2545. doi:10.1529/biophysj.106.093575
41. Anderson CM, Georgiou GN, Morrison IEG, Stevenson GVW, Cherry RJ (1992) Tracking of cell-surface receptors by fluorescence digital imaging microscopy using a charge-coupled device camera – low-density-lipoprotein and influenza-virus receptor mobility at 4-degrees-C. J Cell Sci 101:415–425
42. Hecht E (1998) Optics, 3rd edn. Addison-Wesley, Boston, MA
43. Dickson RM, Norris DJ, Tzeng YL, Moerner WE (1996) Three-dimensional imaging of single molecules solvated in pores of poly(acrylamide) gels. Science 274(5289):966–969
44. Axelrod D (2001) Total internal reflection fluorescence microscopy in cell biology. Traffic 2(11):764–774. doi:10.1034/j.1600-0854.2001.21104.x
45. Verveer PJ, Swoger J, Pampaloni F, Greger K, Marcello M, Stelzer EH (2007) High-resolution three-dimensional imaging of large specimens with light sheet-based microscopy. Nat Methods 4(4):311–313. doi:10.1038/nmeth1017
46. Pitrone PG, Schindelin J, Stuyvenberg L, Preibisch S, Weber M, Eliceiri KW, Huisken J, Tomancak P (2013) OpenSPIM: an open-access light-sheet microscopy platform. Nat Methods 10(7):598–599. doi:10.1038/nmeth.2507
47. Huisken J, Swoger J, Del Bene F, Wittbrodt J, Stelzer EH (2004) Optical sectioning deep inside live embryos by selective plane illumination microscopy. Science 305(5686): 1007–1009. doi:10.1126/science.1100035
48. Ritter JG, Veith R, Veenendaal A, Siebrasse JP, Kubitscheck U (2010) Light sheet microscopy for single molecule tracking in living tissue. PLoS One 5(7):e11639. doi:10.1371/journal.pone.0011639
49. Galland R, Grenci G, Aravind A, Viasnoff V, Studer V, Sibarita JB (2015) 3D high- and super-resolution imaging using single-objective SPIM. Nat Methods 12 (7):641–644. doi:10.1038/nmeth.3402
50. Meddens MB, Liu S, Finnegan PS, Edwards TL, James CD, Lidke KA (2016) Single

objective light-sheet microscopy for high-speed whole-cell 3D super-resolution. Biomed Opt Express 7(6):2219–2236. doi:10.1364/BOE.7.002219

51. Leake MC, Greene NP, Godun RM, Granjon T, Buchanan G, Chen S, Berry RM, Palmer T, Berks BC (2008) Variable stoichiometry of the TatA component of the twin-arginine protein transport system observed by in vivo single-molecule imaging. Proc Natl Acad Sci U S A 105(40):15376–15381. doi:10.1073/pnas.0806338105
52. Kapitein LC, Janson ME, van den Wildenberg S, Hoogenraad CC, Schmidt CF, Peterman EJG (2008) Microtubule-driven multimerization recruits ase1p onto overlapping microtubules. Curr Biol 18(21):1713–1717. doi:10.1016/j.cub.2008.09.046
53. van Mameren J, Modesti M, Kanaar R, Wyman C, Peterman EJG, Wuite GJL (2009) Counting RAD51 proteins disassembling from nucleoprotein filaments under tension. Nature 457 (7230):745–748. doi:10.1038/nature07581
54. Schmidt T, Schutz GJ, Baumgartner W, Gruber HJ, Schindler H (1996) Imaging of single molecule diffusion. Proc Natl Acad Sci U S A 93(7):2926–2929
55. Thompson RE, Larson DR, Webb WW (2002) Precise nanometer localization analysis for individual fluorescent probes. Biophys J 82 (5):2775–2783
56. Yildiz A, Selvin PR (2005) Fluorescence imaging with one manometer accuracy: application to molecular motors. Acc Chem Res 38 (7):574–582. doi:10.1021/ar040136s
57. Saxton MJ (1997) Single-particle tracking: the distribution of diffusion coefficients. Biophys J 72(4):1744–1753
58. Gross D, Webb WW (1986) Molecular counting of low-density-lipoprotein particles as individuals and small clusters on cell-surfaces. Biophys J 49(4):901–911
59. Kwok BH, Kapitein LC, Kim JH, Peterman EJG, Schmidt CF, Kapoor TM (2006) Allosteric inhibition of kinesin-5 modulates its processive directional motility. Nat Chem Biol 2 (9):480–485. doi:10.1038/nchembio812
60. Betzig E, Patterson GH, Sougrat R, Lindwasser OW, Olenych S, Bonifacino JS, Davidson MW, Lippincott-Schwartz J, Hess HF (2006) Imaging intracellular fluorescent proteins at nanometer resolution. Science 313 (5793):1642–1645. doi:10.1126/science.1127344
61. Rust MJ, Bates M, Zhuang X (2006) Sub-diffraction-limit imaging by stochastic optical reconstruction microscopy (STORM). Nat Methods 3(10):793–795. doi:10.1038/nmeth929
62. Heilemann M, van de Linde S, Schuttpelz M, Kasper R, Seefeldt B, Mukherjee A, Tinnefeld P, Sauer M (2008) Subdiffraction-resolution fluorescence imaging with conventional fluorescent probes. Angew Chem Int Ed 47 (33):6172–6176. doi:10.1002/anie.200802376
63. Lacoste TD, Michalet X, Pinaud F, Chemla DS, Alivisatos AP, Weiss S (2000) Ultrahigh-resolution multicolor colocalization of single fluorescent probes. Proc Natl Acad Sci U S A 97(17):9461–9466
64. Agrawal A, Deo R, Wang GD, Wang MD, Nie SM (2008) Nanometer-scale mapping and single-molecule detection with color-coded nanoparticle probes. Proc Natl Acad Sci U S A 105(9):3298–3303. doi:10.1073/pnas.0712351105
65. Churchman LS, Okten Z, Rock RS, Dawson JF, Spudich JA (2005) Single molecule high-resolution colocalization of Cy3 and Cy5 attached to macromolecules measures intramolecular distances through time. Proc Natl Acad Sci U S A 102(5):1419–1423. doi:10.1073/pnas.0409487102
66. Zhuang XW, Bartley LE, Babcock HP, Russell R, Ha TJ, Herschlag D, Chu S (2000) A single-molecule study of RNA catalysis and folding. Science 288(5473):2048. doi:10.1126/science.288.5473.2048
67. Mori T, Vale RD, Tomishige M (2007) Conformation of kinesin dimer at ATP-waiting state probed by single molecule FRET. Biophys J 2007:498
68. Prevo B, Peterman EJ (2014) Forster resonance energy transfer and kinesin motor proteins. Chem Soc Rev 43(4):1144–1155. doi:10.1039/c3cs60292c
69. Corrie JET, Craik JS, Munasinghe VRN (1998) A homobifunctional rhodamine for labeling proteins with defined orientations of a fluorophore. Bioconjug Chem 9 (2):160–167. doi:10.1021/bc970174e
70. Asenjo AB, Sosa H (2009) A mobile kinesin-head intermediate during the ATP-waiting state. Proc Natl Acad Sci U S A 106 (14):5657–5662. doi:10.1073/pnas.0808355106
71. Rosenow MA, Huffman HA, Phail ME, Wachter RM (2004) The crystal structure of the Y66L variant of green fluorescent protein supports a cyclization-oxidation-dehydration mechanism for chromophore maturation. Biochemistry 43(15):4464–4472. doi:10.1021/bi0361315

Chapter 6

Fluorescent Labeling of Proteins

Mauro Modesti

Abstract

Many single-molecule experimental techniques exploit fluorescence as a tool to investigate conformational dynamics, molecular interactions, or track the movement of proteins in order to gain insight into their biological functions. A prerequisite to these experimental approaches is to graft one or more fluorophores on the protein of interest with the desired photophysical properties. Here, we describe procedures for efficient methods used to covalently attach fluorophores to proteins. Alternative direct and indirect labeling strategies are also described.

Key words Fluorescent protein labeling, Cys light, Lys light, Fluorescent tagging

1 Introduction

The design of fluorescence-based single-molecule experiments requires choosing an optimal fluorophore as marker to monitor a particular protein activity. Tryptophan intrinsic fluorescence emission can be very useful to study the folding, conformational dynamics, and interactions of a protein. However, since quartz optics are required, complicated photophysical properties and many proteins lack tryptophan residues, the choice of tryptophan as a fluorophore is often unpractical for single-molecule experimental techniques. Thus, attaching an "extrinsic" fluorophore moiety to the protein of interest is the most frequent route used to make the protein glow. One approach commonly used for in vivo experiments is to generate a chimer of the protein of interest by fusion to an intrinsically fluorescent protein that fluoresces in the visible/near infrared range of the electromagnetic spectrum. Collections of intrinsically fluorescent proteins exist, such as the jellyfish green fluorescent protein (GFP) and its variants that can be attached by genetic engineering to either the amino or the carboxyl terminus of a protein or even inserted in frame internally to the protein [1]. These protein-based fluorophores are very useful for in vitro experiments as well but they are relatively bulky and can perturb the original protein function. In

Erwin J.G. Peterman (ed.), *Single Molecule Analysis: Methods and Protocols*, Methods in Molecular Biology, vol. 1665, DOI 10.1007/978-1-4939-7271-5_6,

addition, their photophysical properties are complex and influenced by pH, ionic strength, or any factors affecting protein folding. Instead of fusing such an intrinsic fluorescent protein, small synthetic fluorescent organic compounds can covalently be attached to the protein of interest. A large number of small fluorophores including the ATTO dyes, the CF dyes, the cyanine dyes, the HiLyte Fluors, the Alexa Fluors, or the DyLight Fluors have been developed and are commercially available. These small, photostable and bright fluorophores are generally much less sensitive to buffer conditions as compared to intrinsically fluorescent proteins. Moreover, the chemical and photophysical properties of these small fluorophores are usually well defined, which allows selection of the dye with the most optimal properties for a given single-molecule application. In a fluorescence correlation spectroscopy experiment, for example, a dye with high quantum yield and weak nonspecific binding to the protein of interest, resistant to irreversible photobleaching and to triplet state excitation can be optimally selected. Or, if the application requires detection and visualization of a single fluorophore, one would want to select a dye with reduced blinking behavior.

Most of these chemical dyes can be purchased in a "functionalized" form with a reactive group for specific covalent attachment to proteins on, for instance, the -SH group of cysteine residues or the $-NH_2$ group of lysine residues. In this chapter, we describe procedures for labeling proteins with such functionalized fluorophores, as well as alternative procedures. The presentation of these protocols is intended to guide researchers in biophysics that do not have much experience with protein handling. Each method will be illustrated with an example from our laboratory, not only to show to the reader how results should look like but also to highlight commonly encountered problems and drawbacks when using these procedures.

2 Materials

2.1 Buffers and Solutions

1. 0.5 M MES-NaOH pH 6.2.
2. 0.5 M MOPS-NaOH pH 7.0.
3. 1 M Tris-HCl pH 7.5; 1 M Tris-HCl pH 8.0.
4. 1 M HEPES-NaOH pH 8.2.
5. 2 M Imidazole-HCl pH 7.5, stored at dark at +4 °C.
6. 0.5 M EDTA-NaOH pH 8.0.
7. IPTG dissolved in water at 1 M and stored at −20 °C.
8. 1 M DTT freshly prepared as a solution in water.
9. 5 M NaCl.

10. 3 M KCl.
11. Anhydrous DMSO, stored at +4 °C in a desiccator.
12. Glycerol.
13. SDS 20% (w/v).
14. β-mercaptoethanol.
15. Coomassie Brilliant Blue R-250.
16. Ampicillin sodium salt, solution at 100 mg/ml in water, store at −20 °C.
17. Chloramphenicol, solution made at 34 mg/ml in ethanol, store at −20 °C.
18. Storage buffer A: 0.3 M KCl, 20 mM Tris-HCl pH 8, 1 mM DTT, 0.5 mM EDTA and 10% glycerol.
19. Labeling buffer A: 0.5 M NaCl, 50 mM MOPS-NaOH pH 7, 0.5 mM EDTA and 10% glycerol.
20. Storage buffer B: 0.5 M KCl, 20 mM Tris-HCl pH 8, 1 mM DTT, 0.5 mM EDTA and 10% glycerol.
21. Labeling buffer B: 0.5 M NaCl, 50 mM HEPES-NaOH pH 8.2, 0.5 mM EDTA and 10% glycerol.
22. Labeling buffer C: 1 M NaCl, 50 mM MOPS-NaOH pH 7, 0.5 mM EDTA and 10% glycerol.
23. PBS: 137 mM NaCl; 2.7 mM KCl; 4.3 mM Na_2HPO_4; 1.47 mM KH_2PO_4. Adjust to pH 7.4 with NaOH.
24. 2× lysis buffer: 1 M NaCl, 40 mM Tris-HCl pH 7.5, 4 mM β-mercaptoethanol, 10 mM imidazole pH 8 and 20% glycerol.
25. Buffer R: 50 mM KCl, 20 mM Tris-HCl pH 7.5, 1 mM DTT, 0.5 mM EDTA and 10% glycerol.
26. Protein sample buffer: 2% w/v SDS, 62.5 mM Tris-HCl pH 6.8, 25% Glycerol, 0.01% w/v bromophenol blue, 0.72 M β-mercaptoethanol.
27. Staining solution: 10% ethanol, 7% acetic acid and 1 g/l Coomassie Brilliant Blue R-250.
28. Destaining solution: 10% ethanol, 7% acetic acid.

2.2 Dyes

Alexa Fluor dyes (Invitrogen), ATTO dyes (Sigma-Aldrich) are dissolved in anhydrous DMSO and used immediately.

2.3 SDS-PAGE

1. Precast NuPAGE Bis-Tris Gels with MOPS running buffer (Invitrogen).
2. Prestained Precision Plus Protein Standards (BIO-RAD).

2.4 Columns

1. Econo-Pac 10DG columns (BIO-RAD).
2. PD SpinTrap G-25, HisTrap FF, HiTrap Q HP, and HiTrap Heparin HP columns (GE Healthcare).

2.5 Media and Bacterial Expression

Rosetta/pLysS cells (Novagen) were used as host for inducible expression of hRPA-eGFP. Cells were grown in LB broth (bacto-tryptone 10 g/l, yeast extract 5 g/l, NaCl 10 g/l) supplemented with antibiotics as indicated.

3 Methods

The "Cys light" and "Lys light" methods for covalent attachment of small organic fluorophores to proteins will be described. Alternative labeling procedures will be presented that can be used in case the latter two methods fail to yield suitable reagents. Each method will be illustrated with an example from our laboratory, highlighting commonly encountered problems when using these methods. We will describe means to analyze the extent and the specificity of the labeling reaction. Importantly, whatever the labeling method used, it is essential to verify that the original activity of the protein has not been altered by the labeling procedure.

3.1 The Cys Light Method: Labeling of the hHOP2-MND1 Protein Complex

The maleimide chemical group reacts with the -SH group (thiol) of cysteine residues of proteins to form a covalent thioether bond (*see* **Note 1**). Because of the high specificity and efficiency of this reaction, the functionalization of organic fluorescent compounds with a maleimide group has developed as the method of choice over other -SH reactive groups such as iodoacetamide. A large selection of organic fluorophores functionalized with a maleimide group is available commercially. Below we present a modification of the labeling method recommended by Molecular Probes but adapted to the labeling of the hHOP2-hMND1 protein complex on cysteine residues. The hHOP2 and hMND1 proteins form a heterodimeric complex [2]. Each protein contains three cysteine residues. The lack of three-dimensional structural information does not allow prediction of the surface exposed cysteine residues of the complex. Since the focus of this chapter is on protein labeling procedures and not purification methods, we will assume that the researcher has access to a source of purified protein. For all procedures, work on ice or in the cold as much as possible and avoid exposure to light when handling fluorophores.

1. To ensure that surface exposed cysteines are in a reduced form and reactive toward the maleimide group, freshly prepared DTT (*see* **Note 2**) is added to a final concentration of 20 mM to 3 ml of the protein solution at a concentration of 2 mg/ml in storage buffer A, and incubated on ice for 30 min.
2. After reduction, the protein sample is buffer exchanged (*see* **Note 3**) into deoxygenated labeling buffer A (*see* **Notes 4** and **5**), and finally recovered into 4 ml.

3. Alexa Fluor 488 C5 maleimide (or Alexa Fluor 546 C5 maleimide) is dissolved in anhydrous DMSO (*see* **Note 6**) and immediately added to the protein solution at fivefold molar excess of dye over the protein (*see* **Note 7**). From this step on, protect the sample from exposure to light as much as possible using aluminum foil. The dye solution should be added rapidly drop by drop while stirring the solution with a small magnetic bar to avoid local concentration effects. The reaction mixture is left to incubate at +4 °C for 2 h with stirring.
4. At the end of the reaction, DTT is added to 10 mM final concentration and further incubated for 30 min to quench the excess reactive dye.
5. The volume is brought up to 6 ml with labeling buffer A and centrifuged at 20,000 × *g* in a Sorval SS34 rotor for 30 min to remove aggregates (*see* **Note 8**). The sample is divided into two aliquots of 3 ml and each aliquot is buffer exchanged into the desired buffer using Econo-Pac 10DG columns to remove excess dye (*see* **Note 3**). In this case we buffer exchange into storage buffer A. The two aliquots are pooled giving 8 ml of labeled protein solution that should be at around 0.7 mg/ml, if no loss by aggregation has occurred. At this stage the sample can be concentrated if desired (*see* **Note 9**), aliquoted and stored at −80 °C after flash freezing in liquid nitrogen. Even after passage on the Econo-Pac 10DG column, presence of free dye is often observed. To remove the residual free dye, we dialyze the protein samples (8 ml) prior to concentration for 4 h against 2 l of storage buffer A (*see* **Note 10**).
6. The extent of the labeling reaction was assessed by denaturing and reducing SDS-PAGE analysis, using 20 µl of the preparation (*see* **Note 11**). As shown in Fig. 1 the labeling is apparently complete since the mobility of both proteins after labeling is retarded compared to the unlabeled control (*see* **Note 12**). The dye has been covalently attached to both hHOP2 and hMND1 subunits. The degree of labeling (DOL or dye-to-monomer ratio) is estimated spectrophotometrically (*see* **Note 13**), giving in this case DOLs of 4.5 and 4.3 for the Alexa Fluor 488 C5 maleimide and the Alexa Fluor 546 C5 maleimide labeling reaction, respectively. This suggests that four of the possible six Cys residues in the heterodimeric complex are exposed to solvent. It can also be noticed that the fluorescent signal after labeling is more intense for hMND1 than for hHOP2 (*see* Fig. 1, bottom panel obtained by fluor imager scanning of the gel before Coomassie staining). This difference in intensity suggests that hMND1 has more cysteine residues exposed to solvent than hHOP2 but further analysis by mass spectrometry is required to prove this point.

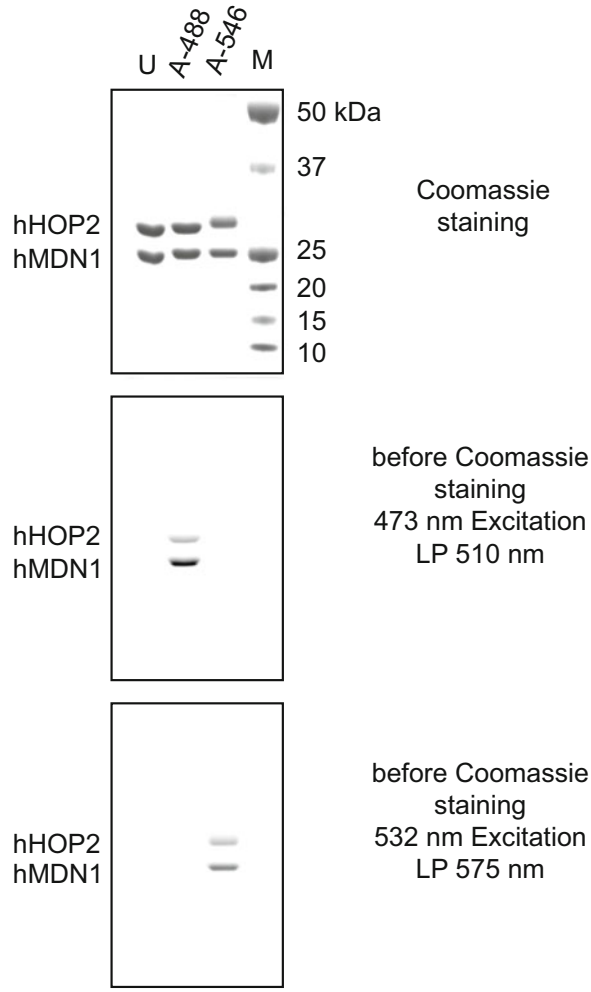

Fig. 1 Fluorescent labeling of the hHOP2-hMND1 complex by the Cys light method. The hHOP2-hMND1 complex was labeled with Alexa Fluor 488 maleimide (A-488) or Alexa Fluor 546 maleimide (A-546) and compared to the unlabeled preparation (U) by denaturing and reducing SDS-PAGE analysis. M = protein size standards. After electrophoresis, the gel was first scanned with a Fluor Imager FLA-5100 (Fujifilm) to detect emission of Alexa Fluor 488 (*middle panel*) or Alexa Fluor 546 (*bottom panel*). Next, the gel was stained with Coomassie Brilliant Blue R-250 to reveal all proteins and visualized by bright field illumination (*top panel*)

7. This protocol is relatively large scale but the reactions can be scaled down to 100 µl when optimizing reaction conditions keeping the protein concentration at around 1–2 mg/ml. First treat the protein sample with DTT as described in **step 1**. Then buffer exchange the protein into labeling buffer A using a PD SpinTrap G-25 column (*see* **Note 14**). Perform reaction series

to optimize labeling conditions (label-to-protein ratio, time of incubation, temperature of incubation, pH, buffer conditions and ionic strength, we typically use NaCl or KCl). The reaction is quenched by addition of DTT as in **step 4**. Ten microliter of each reaction mixture can directly be analyzed by SDS-PAGE analysis to verify covalent attachment of the dye. Excess free dye will be visible in the running front of the gel. The reaction that is most optimal can further be buffer exchanged into a desired storage buffer using a PD SpinTrap G-25 column as described above. In general, this small-scale preparation gives enough reagent to perform pilot experiments in single-molecule setups keeping in mind that free dye might still be present in the preparation.

8. When using recombinant protein that contains a polyhistidine tag the labeling reaction can be done on a 1 ml HisTrap FF. Load 1–5 mg of protein on the column in a labeling buffer free of DTT and EDTA and pH not lower than 7. As a general practice keep all fractions for analysis by SDS-PAGE analysis if required. Dilute the DMSO dye solution in 2 ml of labeling buffer at the desired dye-to-protein ratio. Gently flush the dye solution in the column and let incubate at the desired temperature for the desired time. After the reaction, flush 10 ml of labeling buffer to remove free dye. Elute the labeled protein with labeling buffer A containing 250 mM imidazole pH 8.0 (adding 1 mM EDTA to the elution buffer is fine but may strip the nickel). First flush 1 ml of elution buffer on the column and let sit for 15 min. Recover the protein by injecting 2 ml of elution buffer. Discard the column, as it is best to avoid reusing them to prevent contamination with different dyes. Dialyze into the desired storage buffer containing 10% glycerol. Aliquot, flash-freeze in liquid nitrogen and store at −80 °C.

3.2 Site-Specific Labeling by the Cys Light Method: Labeling of hRAD51

For many fluorescent single-molecule applications, it is advantageous to obtain a preparation of a fluorescent variant of the protein of interest in which every monomer is specifically labeled at a selected surface position. The development of such a reagent is of course more time consuming, but in the end, it will greatly help interpretation and analysis of results. As an example, we describe here how the Cys light method was used to specifically label a protein at a specific surface position [3]. The human RAD51 recombinase monomer contains five cysteine residues of which Cys31 and Cys319 are exposed to solvent according to structural predictions. To obtain a homogeneous population of monomers having a single and discrete label, each on the same position, namely residue Cys31, we mutated Cys319 to Ser by site-directed mutagenesis of the plasmid expression construct thereby removing the -SH group at position 319. Labeling of the C319S hRAD51

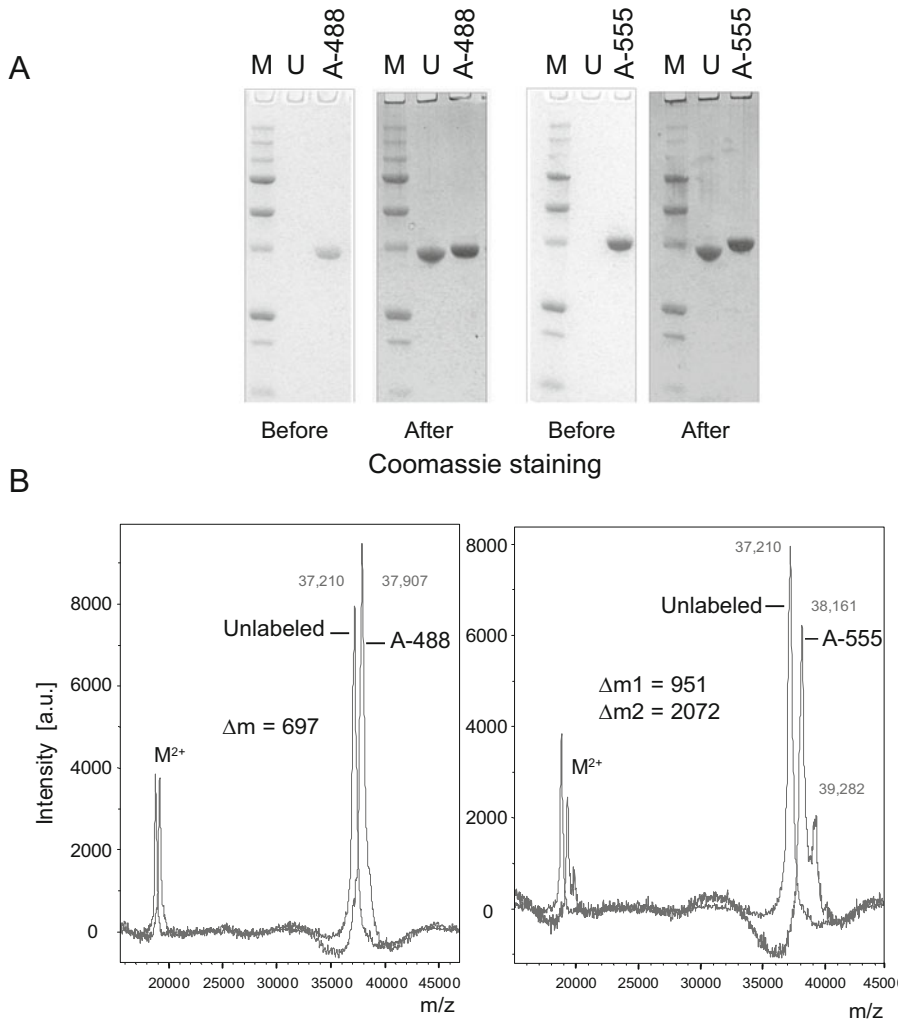

Fig. 2 Site-specific fluorescent labeling of hRAD51 by the Cys light method. (**a**) Preparations of the hRAD51 variant C319S were labeled with Alexa Fluor 488 maleimide (A-488) or Alexa Fluor 555 maleimide (A-555) and compared to the unlabeled preparation (U) by denaturing and reducing SDS-PAGE analysis. M = protein size standards. After electrophoresis, dye attachment was directly visualized by bright field illumination of the gels (*Before panels*) or after Coomassie Brilliant Blue R-250 staining (*After panels*). (**b**) The degree and homogeneity of labeling was analyzed by MALDI-TOF of the full-length protein preparations (*lower panels*)

variant with Alexa Fluor 488 C5 maleimide or Alexa Fluor 555 C2 maleimide was performed as described in Subheading 3.1 (**steps 1–6**). DOL of 0.8 and 1.1 were measured respectively and has shown in Fig. 2a, both labeling reactions went to completion as judged by the retarded mobility of the labeled samples in the gels. Mass spectrometry of the full-length labeled protein samples (*see* **Note 15**) shows that the Alexa Fluor 488 C5 maleimide labeled sample is homogeneous, containing mostly monomers with one single dye covalently attached (Fig. 2b, left panel). In contrast,

analysis of the Alexa Fluor 555 C2 maleimide labeled sample shows that a substantial fraction of monomers have incorporated two dye molecules (Fig. 2b, right panel). Thus different dyes with different carbon arm linkers may have different specificities. The identification of the residue(s) giving nonspecific labeling will require further detailed mass spectrometry analysis after protease digestion.

3.3 The Lys Light Method: Labeling of hSSB1 and hSSB2

The other popular chemistry used to covalently attach a fluorophore to a protein are succinimidyl-ester or *N*-hydroxysuccinimidyl (NHS)-ester conjugates, which are reactive towards amine groups such as ε-amino groups of lysines or the amine terminus of proteins, forming a chemically stable amide bond (*see* **Note 1**). Below we describe the labeling of hSSB1 and hSSB2 proteins with modifications of the procedure recommended by ATTO-TEC (*see* **Note 16**) [4]. Lysine residues are typically abundant in proteins and the procedure can give very high DOLs.

1. The protein sample (3 ml) is supplied in storage buffer B at a concentration of 2 mg/ml and buffered exchanged in labeling buffer B using an Econo-Pac 10DG column and recovered in 4 ml. Maintaining the pH just above 8 will ensure that the exposed ε-amino groups are sufficiently deprotonated and thus reactive towards the NHS ester and that the competing reaction with hydroxyl ions is minimized.
2. Atto 488-NHS ester is dissolved in anhydrous DMSO and added at twofold molar excess of dye over the protein (*see* **Notes 6** and **7**). The dye solution should be added rapidly drop by drop while stirring the solution with a small magnetic bar to avoid local concentration effects. The reaction mixture is left to incubate at +4 °C for 1 h or at room temperature for 30 min with stirring. We find that the reaction is quite fast and that with some samples 5 min incubation at room temperature is sufficient to label the protein to completion.
3. The reaction is quenched by addition of Tris-HCl pH 7.5 to 0.1 M and further incubated for 5 min.
4. The volume is brought up to 6 ml with labeling buffer and centrifuged at 20,000 × *g* in a Sorval SS34 rotor to remove aggregates. The sample is divided into two aliquots of 3 ml and each aliquot is buffer exchanged into the desired buffer using Econo-Pac 10DG columns to remove excess dye (*see* **Note 3**). In this case we buffer exchange into storage buffer B. The two aliquots are pooled giving 8 ml of labeled protein solution that should be at around 0.7 mg/ml if no loss by aggregation has occurred. At this stage the sample can be concentrated if desired (*see* **Note 9**), aliquoted and stored at −80 °C after flash freezing in liquid nitrogen. Even after passage on the Econo-Pac 10DG column, some low level of free dye is often

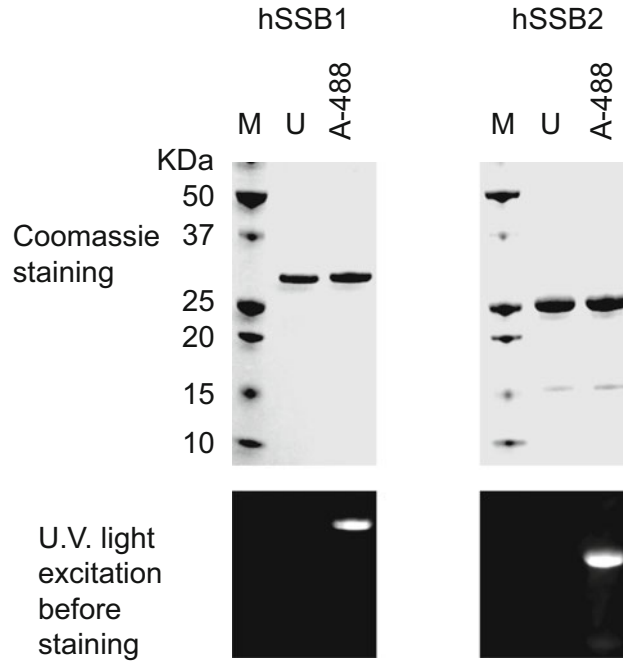

Fig. 3 Fluorescent labeling of hSSB1 and hSSB2 by the Lys light method. Preparations of hSSB1 or hSSB2 were labeled with ATTO 488 NHS (A-488) and compared to the unlabeled preparations (U) by denaturing and reducing SDS-PAGE analysis. M = protein size standards. After electrophoresis, dye attachment was visualized by U.V. light transillumination of the gel (*bottom panels*) or after Coomassie Brilliant Blue R-250 staining (*top panels*)

observed. To remove the residual free dye, we dialyze the protein samples (8 ml) for 4 h against 2 l of storage buffer B (*see* **Note 10**).

5. Figure 3 shows an assessment of the extent of the labeling procedure by SDS-PAGE analysis. DOLs of 6 and 5 dyes per monomer where measured for hSSB1 and hSSB2 respectively (13 and 11 possible lysine residues for hSSB1 and hSSB2, respectively). However, although we obtained very high DOLs with this method, the labeled proteins were not able to bind DNA as efficiently as the unlabeled protein. Further optimization (lower dye-to-protein ratio, shorter time and lower temperature of incubation) will be required to find labeling conditions that will preserve the original activity of the proteins. Alternatively, the Cys light method could be tried.

3.4 N-terminus Labeling by the Lys Light Method: RecA Labeling

Because the N-terminal amine group of proteins has a pKa value that is lower than 9, performing a labeling with a NHS-ester dye conjugate at pH 7 or lower can in principle target the attachment of the dye to the N-terminal amine group of proteins. At this pH,

ε-amino groups of solvent exposed lysines are expected to be fully protonated and nonreactive towards NHS esters. Thus, applying the Lys light method at low pH could in principle be a convenient method to generate a preparation of a fluorescent variant of the protein of interest in which every monomer is specifically labeled at a specific surface position. We tried to apply this principle to the labeling of the RecA protein. First, we produced a variant of RecA with a cleavable N-terminal polyhistidine tag that can be cut by incubation with the TEV protease (*see* Fig. 4a). After TEV protease cleavage we can therefore assess whether the incorporated label has been specifically attached to the N-terminus of the protein.

1. The protein sample (3 ml) is supplied in storage buffer A at a concentration of 2 mg/ml and buffer exchanged in labeling buffer C using Econo-Pac 10DG column and recovered in 4 ml.
2. ATTO 488-NHS ester or ATTO 633-NHS ester is dissolved in anhydrous DMSO and added rapidly drop by drop while stirring at twofold molar excess of dye over the protein (*see* **Notes 6** and **7**). The reaction mixture is incubated at room temperature for 30 min with stirring.
3. The reaction is quenched by addition of Tris-HCl (pH 7.5) to 0.1 M and further incubated for 5 min.
4. The reaction is processed as in Subheading 3.3, **step 4** using storage buffer A as recovery buffer.
5. Figure 4b shows the analysis of the extent of labeling and the label incorporation after TEV cleavage. Clearly, it can be seen that the label has been attached to the N-terminal fragment but also internally. DOLs of 2.2 and 2.3 for the ATTO 488 and ATTO 633 labeling were measured spectrophotometrically. Thus, under these conditions of pH 7, specificity of the reaction towards the N-terminus was not observed. Mass spectrometry analysis of the labeled full-length proteins shows that we obtained a very complex and heterogeneous mixture with species that have acquired even 4 dyes per monomer (*see* Fig. 4c). Perhaps, the ε-amino groups of solvent exposed lysine residues of RecA have a pKa value lower than expected due to their local environment. It can be noticed that the DOLs determined spectrophotometrically only give average and approximate values.
6. To further optimize the labeling reaction, we performed additional labeling reactions with ATTO 633 NHS as described in **steps 1–5** using labeling buffer C in which the MOPS-NaOH pH 7.0 is replaced with MES-NaOH pH 6.2 or HEPES-NaOH pH 8.2. Unfortunately, as judged by fluorescence quantification after TEV cleavage, the labeling in the three different pH conditions behaved similarly giving both N-terminal and

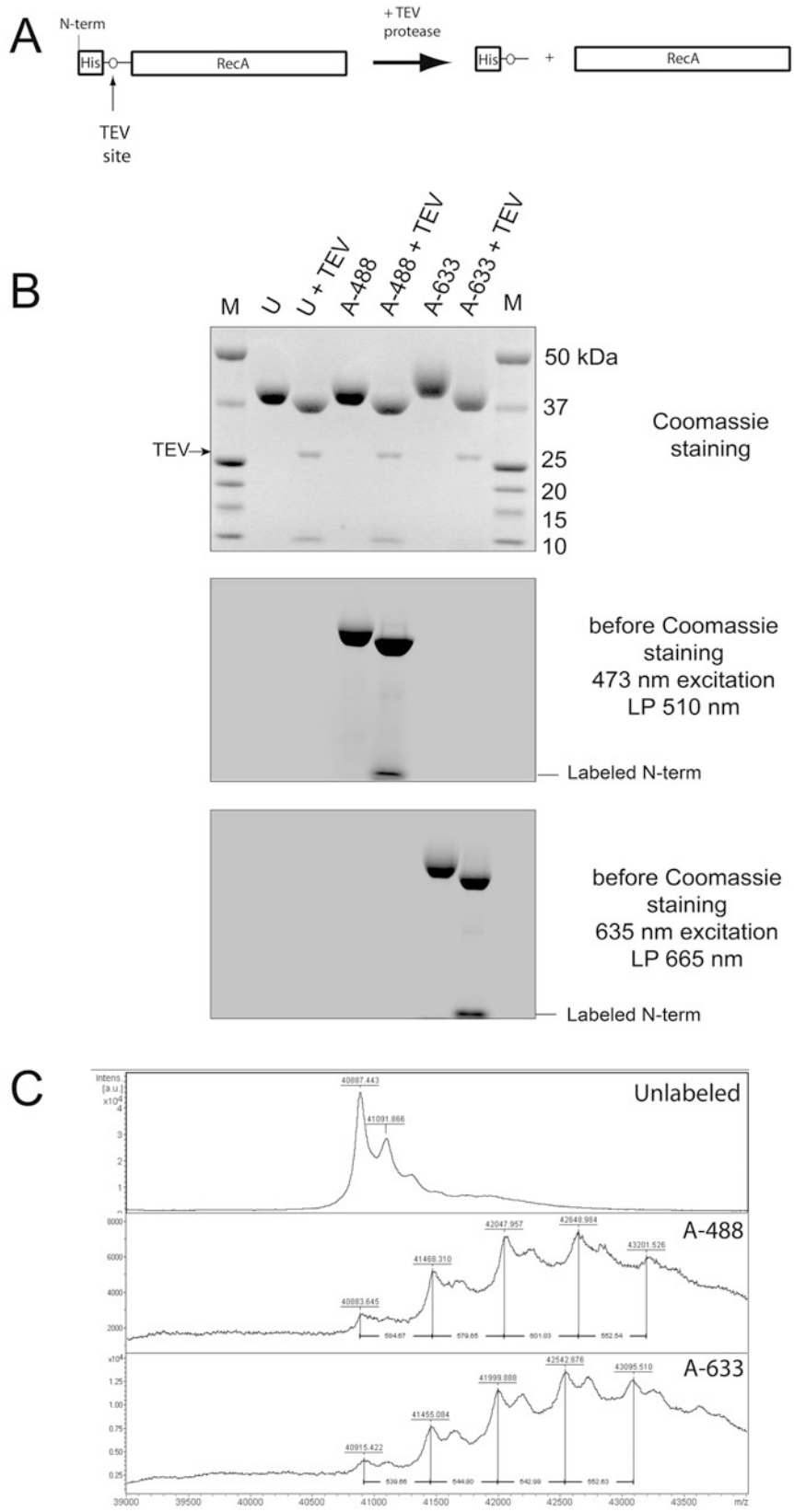

Fig. 4 Fluorescent labeling of RecA by the Lys light method at low pH. (**a**) The RecA protein was produced with an N-terminal His tag cleavable by the TEV protease. (**b**) The His-RecA preparation was labeled with either

internal attachment of the dye (data not shown). We conclude that at least one internal Lys residue is reactive towards the NHS ester group even when the pH is buffered at 6.2. Perhaps, the local environment is influencing the pKa of this putative surface-exposed lysine residue. However, another group has been successful in specifically labeling RecA at the N-terminus using a 5(6)-carboxyfluorescein, succinimidyl ester [5]. Thus, the chemical properties of the dye might also influence the specificity of the reaction. Alternatively, we will have to optimize the ratio of dye to protein and/or the reaction kinetics when working with ATTO NHS ester conjugates.

3.5 Fusion to an Intrinsically Fluorescent Protein: Production and Purification of hRPA-eGFP

Sometimes fluorescent labeling by chemical modification is not efficient or destroys the original activity of the protein. An alternative to make the protein glow is to generate a fusion of the protein to an intrinsically fluorescent protein such as eGFP. Below we describe this approach for the labeling of hRPA, a single-stranded DNA binding heterotrimeric protein complex [6, 7]. We generated a bacterial polycistronic expression construct phRPA-eGFP (or phRPA-mRFP1 expressing a red fluorescent construct) that produces the large subunit of hRPA tagged at its C-terminus with a polyhistidine tagged variant of eGFP to facilitate purification (details of plasmid constructs are available upon request). Below we describe the expression and purification procedures as well as the DNA binding activity analysis.

1. The expression plasmid is transformed in Rosetta/pLysS cells (Novagen) and cells containing the plasmid are selected on LB plates supplemented with ampicillin (100 μg/ml) and chloramphenicol (34 μg/ml). A single colony is used to inoculate 50 ml of LB + amp + cm and incubated overnight at 37 °C with agitation. The next morning, 3 l of medium in a 6 l flask are inoculated with 30 ml of overnight preculture and incubated at 37 °C with vigorous shaking until the OD at 600 nm reaches 0.5. At that stage, IPTG is added to a final concentration of 1 mM and the temperature of the incubator is turned down to +15 °C. Incubation at +15 °C is continued for at least 16 h. Cells are collected by centrifugation at 3500 × *g* and

Fig. 4 (continued) ATTO 488 NHS (A-488) or ATTO 633 NHS (A-633) and compared to the unlabeled preparations (U) before and after TEV protease cleavage (+TEV) by denaturing and reducing SDS-PAGE analysis. M = protein size standards. After electrophoresis, the gel was first scanned with a Fluor Imager FLA-5100 (Fujifilm) to detect emission of ATTO 488 (*middle panel*) or ATTO 633 (*bottom panel*). Next, the gel was stained with Coomassie Brilliant Blue R-250 to reveal all proteins and visualized by bright field illumination (*top panel*). (**c**) The degree and homogeneity of labeling was analyzed by MALDI-TOF of the full-length protein preparations

resuspended in 10 ml of PBS. The cell paste is flash-frozen in liquid nitrogen and stored at −80 °C.

2. To extract the protein, the frozen cell paste is quickly thawed in lukewarm water and immediately chilled on ice. Keep working in the cold from now on. The suspension should become very viscous due to cell lysis and release of genomic DNA. Add 1 volume of 2× lysis buffer and resuspend by mixing with a pipette (*see* **Note 17**). The viscosity of the sample is reduced by sonication (*see* **Note 18**). The mixture is clarified by centrifugation at 20,000 × *g* for 1 h at +4 °C (Sorval SS42 rotor). The supernatant containing RPA-eGFP is flushed through a filter device with 0.45 μm pores (Millipore). Cleaner preparations are usually obtained when using a chromatography system such as an ÄKTAFPLC (GE Healthcare). However, since most biophysics laboratories are not equipped with such equipment, we present a procedure that can be performed manually with a syringe and gives very pure preparations as shown in Fig. 5a. The supernatant is loaded (slowly, drop by drop) on a 1 ml HisTrap FF column pre-equilibrated with 1× lysis buffer. The column is washed with 10 volumes of 1× lysis buffer. The column is further washed in 5 ml steps by increasing the imidazole concentration starting from 5 to 10, 20, 50 and finally 250 mM imidazole in 1× lysis buffer. The bulk of hRPA-eGFP should elute in the last 250 mM imidazole step. The protein sample is dialyzed against 2 l of buffer R for at least 2 h at +4 °C but overnight is also fine (*see* **Note 10**). Slowly load the protein sample on a 1 ml HiTrap Heparin HP column equilibrated with buffer R, and wash with at least 10 ml of buffer R. Step wash the column (5 ml) by increasing the concentration of KCl in buffer R by 50 mM increments starting at 50–500 mM. The bulk of hRPA-eGFP elutes around 200–250 mM. Aliquot the fraction, flash freeze in liquid nitrogen and store at −80 °C. Presence of nucleases should be tested. If desired the protein can be further purified by chromatography through a 1 ml Hitrap Q HP column by performing exacting the same protocol as for the HiTrap Heparin HP. Elution of hRPA-eGFP occurs around 250–300 mM KCl. We advise to keep every fraction for analysis by SDS-PAGE.

3. Figure 5 shows the denaturing SDS-PAGE analysis of a hRPA-eGFP preparation obtained by the Histrap/Hitrap heparin protocol described above. Figure 5 presents the analysis of the single-stranded DNA binding activity by electrophoretic mobility shift assay. Reassuringly, the presence of the eGFP tag fused at the C-terminus of the large hRPA subunit does not affect its DNA binding activity in this assay.

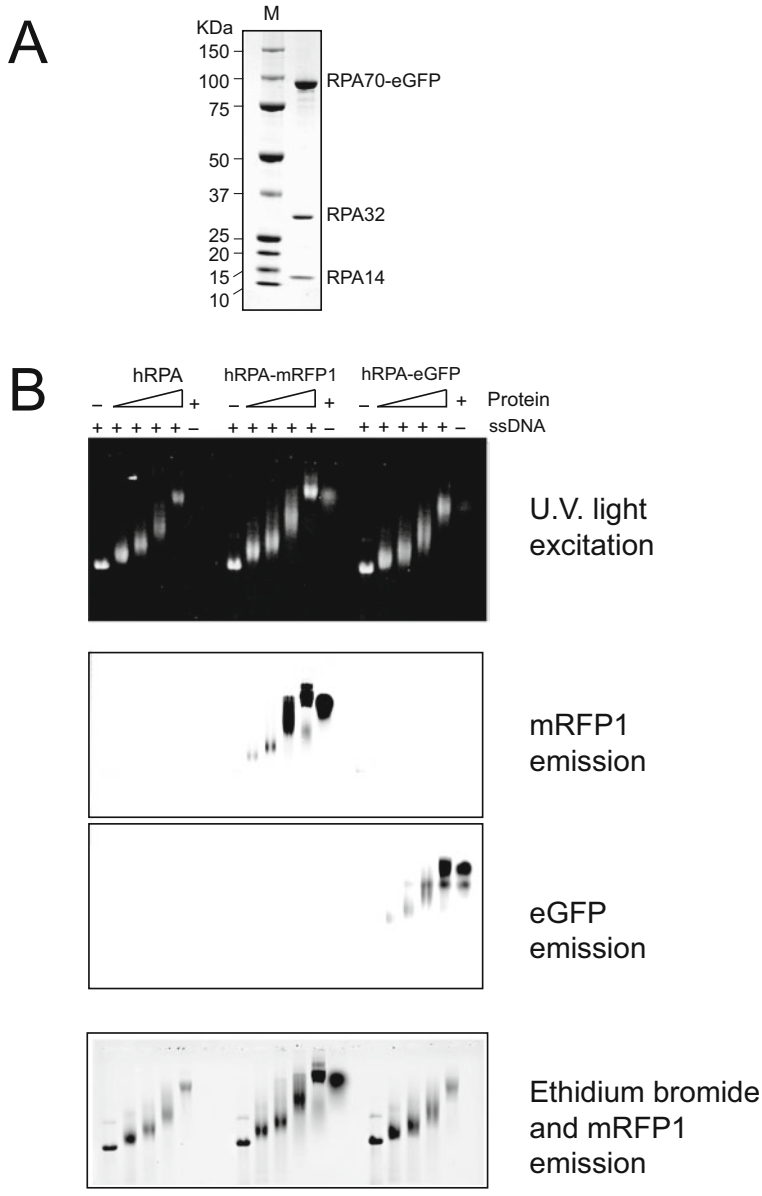

Fig. 5 Purification and single-stranded DNA binding of hRPA-eGFP. (**a**) SDS-PAGE/Coomassie staining of an aliquot of the hRPA-eGFP preparation (2 μg) purified on HisTrap and Heparin columns. M = molecular weight standard. (**b**) Electophoretic mobility shift assay showing that the fusion of eGFP or mRFP1 to C-terminus of the large subunit of hRPA does not interfere with its single-stranded DNA binding activity. For each preparation, the protein (1 μM for the highest final concentration, and diluted in twofold increments) was incubated with or without 200 ng of PhiX174 single-stranded DNA in a 10 μl reaction volume containing 50 mM KCl, 20 mM Tris-HCl pH 7.5, 5% glycerol, 1 mM EDTA, 1 mM DTT and 100 μg/ml BSA. After 20 min incubation, the binding reactions were directly analyzed by electrophoresis in a 0.6% agarose/Tris-Borate-EDTA. Before staining, the gel was scanned with a Fluor Imager for detection of mRFP1 or eGFP emission (*middle two panels*). Afterward, the gel was stained with ethidium bromide to detect DNA and visualized on a U.V. light transilluminator (*top panel*) or by scanning the gel with a Fluor Imager (*bottom panel*, notice that with these settings both mRPF1 and ethidium bromide emissions contribute to the signal)

3.6 Indirect Strategies for Protein Fluorescent Labeling

It is also possible to label a protein by adding an affinity tag by genetic engineering, allowing indirectly labeling with secondary fluorescent reagents specific for the tag. Here, we will enumerate and briefly describe a few of the possible tags that can be used and cite companies from which reagents can be obtained (*see* **Note 19**).

1. The AviTag (Avidity) consists in a 15 amino acid peptide tag (GLNDIFEAQKIEWHE) that can specifically be biotinylated in vivo or in vitro on the lysine residue using the biotin ligase (BirA) from *E. coli*. Commercially available fluorescent avidin or streptavidin can subsequently be attached "nearly covalently" to the AviTagged protein.
2. The strep tag (IBA-bioTAGnology) is a very small peptide that can be fused to a protein of interest by genetic engineering. The strep tag mimics biotin and can bind streptavidin or avidin with high affinity. Addition of fluorescently labeled streptavidin or avidin thus indirectly labels the biotinylated protein.
3. The FlAsH/ReAsH system (Invitrogen). The small 6-amino acid 1 kDa tetracysteine tag (CCPGCC), that can be fused to a protein of interest by genetic engineering, coordinates the FlAsH-EDT_2 or ReAsH-EDT_2 compounds with high affinity. These biarsenical compounds fluoresce upon coordination to the tetracysteine tag.
4. Fluorescently labeled antibodies specific to the protein of interest could also be used for indirect labeling as long as they do not interfere with its activities. Instead, a number of fluorescently labeled monoclonal antibodies specific for various epitopes that can be fused to the protein of interest by genetic engineering are commercially available. The FLAG, HA and myc epitopes are amongst the most popular ones. Finally, since many recombinant proteins are produced as fusions to the glutathione S-transferase or the maltose binding protein, these moieties can also be used as anchor point for a fluorescent antibody.
5. Fluorescent nanocrystals (quantum dots, Evident Technologies, Invitrogen) functionalized with NHS ester or maleimide groups, or coupled to streptavidin or antibodies, might be used for direct or indirect protein labeling.
6. Fluorescent protein labeling via the SNAP/CLIP tags (New England Biolabs), which are small proteins derived from human O^6-alkylguanine-DNA-alkyltransferase that can be fused by genetic engineering to the protein of interest. These tags efficiently and specifically react covalently with fluorescently label ligands.
7. Fluorescent protein labeling via the HaloTag (Promega) engineered from a bacterial haloalkane dehalogenase. Fluorescent

synthetic ligands of choice can be purchased that efficiently form stable covalent adducts with the HaloTag.

8. Fluorescent labeling of proteins at either the N- or the C-terminus can be achieved via bacterial Sortase A mediated ligation of fluorescently labeled peptides [8–10].

4 Notes

1. *See* Molecular Probes Handbook at http://www.invitrogen.com/site/us/en/home/References/Molecular-Probes-The-Handbook.html for a description of the chemistry.
2. The 1 M DTT stock solution should be prepared freshly.
3. The Econo-Pac 10DG column is first equilibrated by gravity flow with 20 ml of labeling buffer (or recovery buffer). The 3 ml sample is next loaded on the column and after it has fully entered the gel, add 4 ml of labeling buffer to elute the protein. When performing a buffer exchange after labeling, most of the dye should stay in the column bed.
4. Buffers are deoxygenated by gently bubbling argon gas for 30 min.
5. Most protocols do not recommend high salt concentrations during labeling. However, we find that many proteins that we work with require at least 250 mM salt (NaCl or KCl) to be maintained in solution. The high salt concentration does not affect the reactivity of the maleimide towards the -SH groups. Performing the labeling in the presence of 0.5 M NaCl (and sometimes even up to 1 M NaCl) helps in obtaining more homogeneous labeling by avoiding protein aggregate formation. It is important to keep the pH below 7.5 otherwise the maleimide group can also react with unprotonated primary amines.
6. We purchase dyes in small quantities, typically 1 mg, and use them promptly. Routinely, we dissolved the dye in anhydrous DMSO (stock kept in a desiccator) because many dyes have a poor solubility in water. Once dissolved in DMSO by vortexing, spin the solution in a microfuge to remove insoluble matters. It is best to immediately use the dye solution in a labeling reaction. However, we find that the dye solution in anhydrous DMSO can be kept for several weeks when stored at −20 °C in an O-ring screwcap tube. Reactivity will drop with time due to maleimide (or NHS-ester) hydrolysis. It is thus important to avoid contact with humid environment and test the labeling efficiency of the dye after prolonged storage in anhydrous DMSO.

7. To obtain complete labeling, the choice of the molar ratio of dye to protein during labeling can be critical as well as the incubation time and temperature. We typically use fivefold and one- to twofold molar excess of dye for maleimide and NHS ester reaction respectively. However, it is wise to first perform small-scale pilot reactions to optimize conditions (*see* Subheading 3.1, **step 7**).
8. It is common to find that some or all of the protein forms aggregates after labeling. This is not a surprise since the surface properties of the protein can be changed after labeling. Another dye can be tried or alternatively use a variant of the dye with a different charge for example.
9. Protein concentration can conveniently be achieved using Amicon Ultra centrifugal filter devices from Millipore. They come in different sizes and with different MWCOs. Follow the supplier recommendation for the choice of centrifugal speed. We first spin an aliquot of buffer through the filter before adding the protein sample. Be careful not to concentrate too much as the protein might aggregate at high concentration. Proceed first in 5 min time intervals and gentle resuspension with a Pasteur pipette without damaging the filter.
10. We use SnakeSkin Pleated Dialysis Tubing from Pierce (10,000 MWCO). Protein aggregation may occur after dialysis.
11. Before loading the protein sample on the gel, 1 volume of protein sample buffer is added to the protein aliquot and the mixture is heated at 95 °C for 5 min. After electrophoresis the gel is placed in destaining solution and can directly be scanned with a Fluor Imager to visualize and quantify fluorescent signals. Free dye runs with the electrophoresis front and will diffuse away after prolonged incubation. Note that this fluorescence imaging procedure is very useful to determine if the dye exhibits nonspecific binding to the protein of interest. For Coomassie staining, the gel is placed in staining solution and incubated for 1 h to overnight on a rotating table. The gel is next destained by several incubations in destaining solution (note that Coomassie will quench the fluorescence).
12. The mobility shift after labeling is often but not always detectable. The mobility shift depends on the mass-to-charge ratio, which can be affected by attachment of the dye to the protein, and the resolving power of the gel chosen.
13. Measurement and calculation of DOL by spectrophotometry is described in detailed at (http://www.atto-tec.com/index.php?id=62&L=1).

14. First equilibrate the PD SpinTrap G-25 spin column by five consecutive 400 µl washes in labeling buffer and then proceed as recommended by the supplier. Do not exceed 100 µl for the sample.
15. Mass spectrometry procedures will not be described here since most universities and research centers have nowadays access to a mass spectrometry service. For full-length protein mass measurements by MALDI-TOF, it is important to work at protein concentrations of at least 5 µM, to avoid salt, detergents and glycerol. Reversed-Phase ZipTips from Millipore can be very convenient. Sinapinic acid often works well as matrix for ionization of full-length proteins. Finer mass spectrometry analysis to identify modified residues after labeling can also easily be performed by in gel trypsin digestion (or using other proteases).
16. http://www.atto-tec.com/index.php?id=62&L=1.
17. Protease inhibitor cocktails can be added during resuspension. We typically use 1 mM PMSF in this protocol. Avoid EDTA in your sample because it will chelate the Ni^{2+}. Do not go higher than 20 mM β-mercaptoethanol or add DTT to avoid reducing Ni^{2+}.
18. Sonicate with a microtip in short intervals of max 1 min with interruption on ice to avoid heating of the sample. Alternatively, benzonase nuclease (Novagen) can be added to the sample but Mg^{2+} should then be added.
19. There is an important danger in using antibody, quantumdots, or fluorescent streptavidin to label proteins because these reagents may have multiple binding sites and can thus, under the wrong conditions, multimerize the protein of interest.

Acknowledgments

Work in our laboratory is supported by LASERLAB-EUROPE (grant agreement no 284464, EC's Seventh Framework Programme), the ARC Foundation for Cancer Research and the French National Cancer Institute. We thank Sabrina Lignon, Marielle Bauzan, and Yann Denis of the Institut de Microbiologie de la Méditerranée technical platforms for advice and help with instrumentation and services. We thank Marc Wold (University of Iowa) for the gift of the p11d-tRPA polycistronic expression construct.

References

1. Rodriguez EA, Campbell RE, Lin JY, Lin MZ, Miyawaki A, Palmer AE, Shu X, Zhang J, Tsien RY (2016) The growing and glowing toolbox of fluorescent and photoactive proteins. Trends Biochem Sci 42:111–129. doi:10.1016/j.tibs.2016.09.010
2. Bugreev DV, Huang F, Mazina OM, Pezza RJ, Voloshin ON, Daniel Camerini-Otero R, Mazin A V (2014) HOP2-MND1 modulates RAD51 binding to nucleotides and DNA. Nat Commun 5:4198. doi:10.1038/ncomms5198
3. Candelli A, Holthausen JT, Depken M, Brouwer I, Mariëlla M, Maman J, Pellegrini L, Bernard S, Garcin E, Wyman C, Wuite GJL, Peterman EJG (2014) Visualization and quantification of RAD51 filament formation at single-monomer resolution. Proc Natl Acad Sci U S A 111:15090–15095. doi:10.1073/pnas.1307824111
4. Huang J, Gong Z, Ghosal G, Chen J (2009) SOSS complexes participate in the maintenance of genomic stability. Mol Cell 35:384–393. doi:10.1016/j.molcel.2009.06.011
5. Galletto R, Amitani I, Baskin RJ, Kowalczykowski SC (2006) Direct observation of individual RecA filaments assembling on single DNA molecules. Nature 443:875–878. doi:10.1038/nature05197
6. Henricksen LA, Umbricht CB, Wold MS (1994) Recombinant replication protein A: expression, complex formation, and functional characterization. J Biol Chem 269:11121–11132
7. Ma CJ, Gibb B, Kwon Y, Sung P, Greene EC (2017) Protein dynamics of human RPA and RAD51 on ssDNA during assembly and disassembly of the RAD51 filament. Nucleic Acids Res 45:749–761. doi:10.1093/nar/gkw1125
8. Popp MW-L, Ploegh HL (2011) Making and breaking peptide bonds: protein engineering using sortase. Angew Chem Int Ed Engl 50:5024–5032. doi:10.1002/anie.201008267
9. Theile CS, Witte MD, Blom AE, Kundrat L, Ploegh HL, Guimaraes CP (2013) Site-specific N-terminal labeling of proteins using sortase-mediated reactions. Nat Protoc 8:1800–1807. doi:10.1038/nprot.2013.102
10. Guimaraes CP, Witte MD, Theile CS, Bozkurt G, Kundrat L, Blom AEM, Ploegh HL (2013) Site-specific C-terminal and internal loop labeling of proteins using sortase-mediated reactions. Nat Protoc 8:1787–1799. doi:10.1038/nprot.2013.101

Chapter 7

Single-Molecule Imaging of *Escherichia coli* Transmembrane Proteins

Aravindan Varadarajan, Felix Oswald, and Yves J.M. Bollen

Abstract

Single-molecule imaging in living cells can provide unique information about biological processes. Bacteria offer some particular challenges for single-molecule imaging due to their small size, only slightly larger than the diffraction limit of visible light. Here, we describe how reliable and reproducible single-molecule data can be obtained for a transmembrane protein in the Gram-negative bacterium *Escherichia coli* by using live-cell fluorescence microscopy. Fluorescent labeling of a protein by genetic fusion, cell culturing, sample preparation, imaging, and data analysis are discussed.

Key words Single-molecule tracking, Bacteria, *Escherichia coli*, Transmembrane protein, Diffusion, Fluorescence microscopy, Sample preparation

1 Introduction

Fluorescence microscopy is a powerful technique that enables scientists to probe macromolecular organization, localization, and dynamics in living cells. However, the maximum resolution achieved in standard fluorescence microscopy is intrinsically limited by the diffraction of light. This limitation is a serious problem for imaging bacteria, since the maximal resolution (~250 nm) is comparable to the size of the entire cell (typically ~1–2 μm). As a result, the structures and dynamics of key bacterial machineries, often smaller that the diffraction limit, are hard to be probed in vivo. In this chapter we describe a protocol for fluorescence labeling and imaging of transmembrane proteins that allows detection of single molecules within live *E. coli* cells and allows locating them with a better accuracy than the diffraction limit. To achieve this, we genetically fuse a fluorescent reporter to the amino-terminus or carboxy-terminus of the protein of interest. Then we clone the labeled protein into a low expression plasmid that produces ~10–100 fluorescently labeled protein molecules per cell. These cells are grown in a shaking flask and imaged on a temperature-controlled

Erwin J.G. Peterman (ed.), *Single Molecule Analysis: Methods and Protocols*, Methods in Molecular Biology, vol. 1665, DOI 10.1007/978-1-4939-7271-5_7,

microscope stage. Using wide-field fluorescence microscopy, individual fluorescent protein molecules within bacterial cells are visualized and their mobility is tracked using single-particle tracking software.

2 Materials

1. PCR Master Mix: mix 1–2 μl of template DNA (1–10 ng for plasmid DNA, up to 250 ng of genomic DNA), 2.5 μl (10 pmol) forward primer, 2.5 μl (10 pmol) reverse primer, 1.4 μl of a 5 mM dNTP solution, 5 μl of 10× concentrated polymerase buffer (provided with the enzyme), 1 μl (30 U/μl) high fidelity DNA polymerase, and add nuclease-free water up to a volume of 50 μl.
2. Gibson Master Mix: 50 μl Taq ligase (40 U/μl, New England Biolabs), 100 μl isothermal buffer (5× concentrated, NEB), 2 μl T5 exonuclease (1 U/μl, NEB), 6.25 μl Phusion polymerase (2 U/μl, NEB), 216.75 μl nuclease-free water. Store aliquots of 15 μl at −20 °C.
3. DNA Ligation Mix: 2 μl of 10× concentrated DNA ligase buffer (provided with the enzyme), 1 μl T4 ligase, 40 fmol of vector DNA (100 ng for a typical vector of 4 kb), and 60 fmol of insert DNA (37.5 ng of a typical insert of 1 kb) both restricted with the appropriate restriction enzymes; make the volume up to 20 μl with nuclease-free water.
4. YT Medium: add 16 g Tryptone, 10 g Yeast Extract, 5 g NaCl in ~900 ml of distilled water, Adjust the pH to 7.0 with NaOH, make the volume up to 1 l with distilled water, sterilize the solution by autoclaving.
5. M9 Medium: dissolve 6 g Na_2HPO_4, 3 g KH_2PO_4, 1 g NH_4Cl, 0.5 g NaCl in 900 ml deionized water and autoclave the solution. Subsequently add from filter-sterilized stock solutions: 2 ml of 1 M $MgSO_4$, 0.1 ml of 1 M $CaCl_2$, 20 ml of 20% glucose, 10 ml of 10% casamino acids, 10 ml of 1% (w/v) thiamine. Make the volume up to 1 l with sterile water.
6. Agarose: very pure low melting agarose.
7. VALAP wax: 10 g Paraffin, 10 g Lanolin, 10 g Vaseline, slowly heated to 60 °C while gently stirring.

3 Methods

3.1 Plasmid Construction and Cloning

1. Amplify the DNA sequence encoding the protein of interest from the chromosome of the *E. coli* strain of interest using Polymerase chain reaction (PCR). Protocols for genomic DNA

isolation, primer design, and PCR reactions are described elsewhere [1].

2. In order to fluorescently label the protein of interest, amplify the DNA sequence of a fluorescent protein (*see* **Note 1**) and fuse it to the N-terminal or C-terminal end of the protein of interest by cloning the two genes in one open reading frame, using for example Gibson isothermal assembly [2]. It is important to verify that folding, localization, and activity of the protein of interest are not affected by fusion to a fluorescent protein. Appropriate control experiments should be performed in order to check the activity of the fusion protein. Parameters that can be varied in order to reduce the influence of the fluorescent protein on the target protein's folding and function include the place where the fluorescent protein is fused (N-terminus, C-terminus, or sandwiched in a loop) and the introduction of short, polar, flexible linkers between the fluorescent protein and the target protein (*see* **Note 2**).
3. Clone the fused fragments into a low or medium copy number plasmid (*see* **Note 3**) that allows tight regulation of protein expression, for example by Gibson assembly [2] or by restriction and ligation [1]. If the correct functioning of the protein of interest strictly depends on the correct expression level, one could consider replacing the endogenous gene in the *E. coli* genome by a fluorescently tagged version of the same gene, for example by homologous recombination [3] or by CRISPR-Cas9-based technology [4].
4. Verify the genes on the plasmid by sequencing.
5. Transform the plasmid that contains the fusion fragments into *E. coli* cells of interest by electroporation or heat-shock. Then plate the transformants on YT agar plates supplemented with the appropriate antibiotics, for example ampicillin (100 μg/ml) for pBAD24 or chloramphenicol (34 μg/ml) for pBAD33.

3.2 Cell Culture and Sample Preparation

1. Pick one *E. coli* colony from the YT agar plate and inoculate the cells in 2–5 ml of fresh YT medium containing the appropriate antibiotics. Incubate in a shaker at 37 °C, long enough to reach an OD_{600} (optical density at 600 nm) that exceeds 1.0. We typically grow the pre-culture over-night.
2. Dilute the culture 100× in 5 ml fresh YT medium with appropriate antibiotics and incubate in a shaker at 37 °C.
3. Turn on the fluorescence microscope and set the objective lens heater to the desired imaging temperature. We use a stage-top incubator system (Tokai Hit, INU-ZILCS-F1) for equilibrating the apochromatic 100× 1.49 NA TIRF oil-immersion objective to 23 °C. Leave the microscope at this setting for

90–120 min in order for temperature equilibration to be complete (*see* **Note 4**).

4. The cells are ready for imaging when the OD_{600} equals 0.3–0.4 (at 37 °C, with an initial OD_{600} of 0.02, this will take about 90 min) (*see* **Note 5**). Centrifuge the culture at 1789 × *g* for 2 min in a benchtop microcentrifuge in order to obtain the cell pellet. In the meanwhile, start preparing the agarose gel pad (Subheading 3.3).
5. Discard the supernatant and add 5 ml fresh minimal medium M9 and resuspend the pellet gently (*see* **Note 6**).
6. Cells resuspended in 5 ml M9 medium can be directly used for short-term time-lapse imaging. For long-term time-lapse imaging, dilute the resuspended cells 10–100-fold in fresh M9 medium (*see* **Note 7**).

3.3 Preparation of Agarose Solution

1. Weigh approximately 75 mg agarose into a 5 ml tube.
2. Add appropriate volume (approximately 5 ml) of M9 minimal medium without antibiotics to make a 1.5% agarose solution.
3. Heat the agarose solution for 45–60 s in a microwave oven to dissolve the agarose. Shake the tube to ensure that the solution is completely clear and homogenous. The gel pad can be poured at this point (Subheading 3.4) or the agarose solution can be kept at 50 °C for several hours for later use.

3.4 Preparation of a Gel Pad on the Microscope Slide

1. About 60 min before imaging, clean the microscope slides and cover slip by blowing with compressed air. Then clean them with a plasma-cleaner (*see* **Note 8**). Each sample requires two slides and one cover slip.
2. Prepare two spacer slides by putting two layers of labeling tape on each of two microscope slides (Fig. 1). The microscope slides should have the same thickness as the ones used for imaging (*see* **Note 9**).
3. Clean the lab table with 70% alcohol and prepare the sample under a lit burner to avoid contamination of the slides. Alternatively, one could work in a laminar flow cabinet.
4. Place a clean microscope slide between the two spacer slides as shown in Fig. 1.
5. Apply 400 μl of the warm agarose solution (**step 3** in Subheading 3.3) to the center of the clean slide.
6. Rapidly top the agarose solution with a second clean slide as shown in Fig. 1.
7. Allow the agarose solution to solidify at room temperature for 1 min. Then cut excess agarose around the top slide with a clean razor blade.

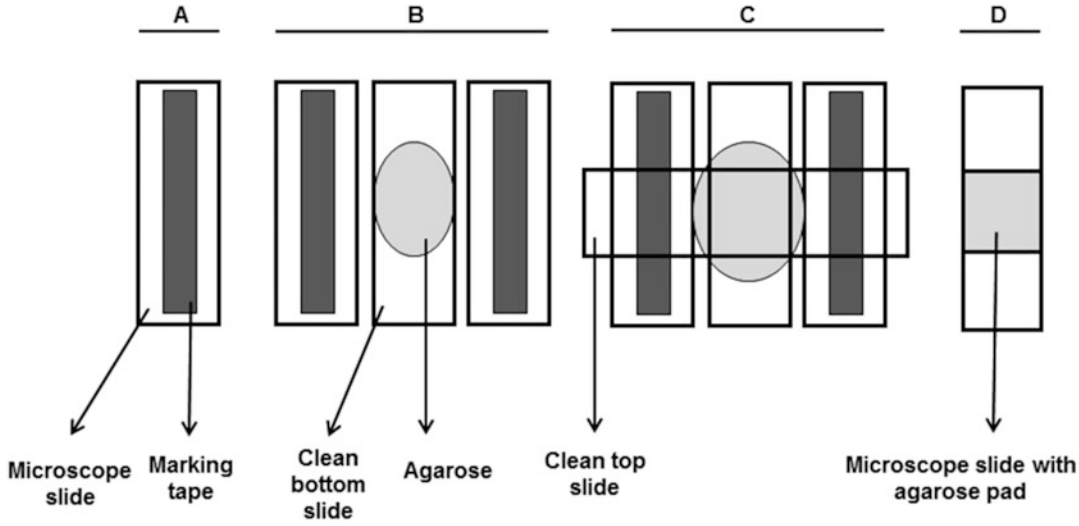

Fig. 1 Sample preparation for microscopy (**a**) Spacer slide with double-layered marking tape. (**b**) two spacer slides flanking a clean bottom slide with a 400 μl of agarose dissolved in M9 medium. (**c**) A clean top slide is added to level off agarose, (**d**) Finished slide with a thin square-shaped agarose pad

8. Carefully slide off the second glass slide from the top of the gel pad, and remove excess agarose gel at the sides of the bottom slide with a clean razor blade. Add 8 μl of cell culture suspended in M9 medium (from Subheading 3.2) to the top of the gel pad. Wait for ~20–30 s for the culture to be absorbed by the gel pad. It is important not to wait too long, such that the gel pad dries out, but long enough for cells to properly adhere to the gel pad. The ideal waiting time may vary with (room) temperature and humidity. Once the cell suspension is absorbed by the agarose gel, place a clean cover slip on top of the pad (*see* **Note 10**).
9. Seal the sample chamber with molten VALAP wax around the edges of the cover slip (*see* **Note 11**). The sample can now be used for imaging on the microscope (*see* **Note 12**).

3.5 Time-Lapse Imaging

1. Mount the sample on top of the microscope objective equilibrated at the desired measuring temperature for at least 90 min (*see* **Note 4**).
2. Let the sample be on top of the objective for ~15 min (this will equilibrate the cells to the exact measuring temperature, *see* **Note 13**). In practice, we use this time to find regions of interest and modify imaging scripts and file names as necessary for an experiment.
3. Find cells on the microscope using bright-field transillumination and position them in the center of the imaging region and bring them into focus (*see* **Note 14**). Best results are obtained when the bottom half of the cell is in focus (*see* **Note 15**). More

than one cell can be imaged in each image acquisition time window. For time-lapse imaging over several generations, ensure that imaged cells are initially separated from other cells by at least a few hundred micrometer so that other colonies will not enter the imaging region during growth.

4. Turn on the excitation laser with closed shutter, to avoid bleaching prior to acquisition. A laser intensity of ~200 W/cm^2 is required for imaging single molecules that diffuse in the membrane of a living bacterial cell (*see* **Note 16**).
5. Open the shutter and immediately record a continuous series of images until all fluorescent molecules have bleached. We typically record 200–300 images per region of interest. A sensitive camera is required to image single, diffusing fluorescent molecules (*see* **Note 17**).
6. Repeat **steps 3–5** until sufficient data have been recorded (*see* **Note 18**).
7. Images are analyzed to find the positions of individual molecules in each image and link the positions into trajectories, from which diffusion coefficients can be extracted. We use custom-written routines in MATLAB (MathWorks) described elsewhere [5, 6].

4 Notes

1. Our microscope has green and red detection channels. Out of the available green fluorescent proteins, we find that it is best to use eGFP for cytoplasmic labeling of *E. coli* membrane proteins due to its high photostability, high brightness, low blinking rate and fast maturation. We find that it is best to use sfGFP for periplasmic labeling of *E. coli* membrane proteins because of its robust folding and fluorescing property in the more oxidizing periplasmic environment [7]. Out of the red fluorescent proteins that we tried, mCherry gave the best results.
2. In our recent work, we chose to label the cytoplasmic N-terminal end of the following transmembrane proteins of *E. coli* strain MC4100 by fusion to green fluorescent protein (eGFP): YedZ, CybB, GlpT, CstA and WALP-KcsA [8]. For the transmembrane protein MscL we chose the cytoplasmic C-terminal end for eGFP fusion, because the N-terminus is located in the periplasm where eGFP does not mature. In the case of the transmembrane protein MscS, we chose the periplasmic N-terminal end for fusing to super folder green fluorescent protein (sfGFP) as the C-terminal end is involved heptamerization. The N-terminal sfGFP was translocated co-

translationally across the cytoplasmic membrane via a signal sequence derived from the protein DsbA [8].

3. We typically use an arabinose inducible plasmid, pBAD24 or pBAD33, because of their moderate copy number and tight regulation of protein expression in bacterial cells [9].
4. When measuring diffusion of membrane proteins, it is extremely important that the temperature of the microscope is stable when starting the experiment. Diffusion depends strongly on temperature, and also the composition of the bacterial membrane alters upon temperature changes. Even small changes in temperature during data acquisition can lead to very complex heterogeneous data.
5. We usually choose midlog phase cells for imaging because at this phase *E. coli* cells are generally healthy and metabolically homogeneous, and produce most of the intracellular proteins. However, the experiment can be performed at other growth phases if required for studying particular cellular processes.
6. We use M9 minimal medium for imaging due to its reduced auto-fluorescent property which reduces background fluorescence signal during image acquisition. An even stronger reduction of auto-fluorescence can be obtained by growing the cells in minimal medium (**step 2**) at the cost of slower growth.
7. Low cell densities are important for extended time-lapse imaging. Due to exponential growth of cells, high initial cell concentrations will result in micro-colonies rapidly growing on top of each other, and it can significantly deplete oxygen in the gel pad after prolonged growth, reducing fluorescent-protein maturation and affecting cell growth.
8. We clean the microscope slide and cover slip using plasma cleaner to reduce background noise emerging from the glass surface during image acquisition. Glass slides often contain small fluorescent organic compounds that, when not removed, can easily be mistaken for fluorescent proteins during data acquisition. We use a Harrick Plasma cleaner by setting the RF level high for 15 min. We use 76 × 26 mm microscope slides from Menzel-Gläser with the thickness of about 1 mm, and 22 × 22 mm cover slips from Menzel-Gläser with the thickness of 0.16–0.19 mm.
9. The strips of tape act as spacers, they provide an easy means to achieve agarose pads with homogeneous and reproducible thickness. More layers of tape will lead to thicker pads. The TimeMed tape that we use has a thickness of about 0.13 mm.
10. We use agarose-pads for immobilizing bacterial cells because they provide a suitable environment for the cells to adhere gently on their surface with less physical pressure. On agarose

pads, nearly all cells are lying horizontally, which is not the case in other immobilization methods that we tried.

11. We seal the microscope slides with VALAP to prevent the sample from drying.
12. We perform sample preparation at room temperature. The preparation, i.e., making the agarose pad, applying the cells and sealing the sample chamber with VALAP takes approximately 15 min.
13. We incubate the sample on the microscope for 15–30 min to allow the cells to adjust to the imaging temperature ($23 \pm 1\,^{\circ}C$). This is important because we initially grow cells at 37 °C in a shaking flask, then prepare the sample at room temperature, and later image them at 23 °C. Drastic temperature shift will cause significant changes in cellular functions and membrane lipid composition. Even small shifts in temperature during acquisition, in the order of 0.1 °C lead to significant drift of the diffusion coefficient. Therefore, allow sufficient time for the cells to adapt to required measuring temperature. We strictly follow the sample preparation and incubation timing (i.e. from the point where the cells are resuspended in M9 medium to imaging) to get reliable and reproducible data. The entire procedure is summarized in Fig. 2.
14. We typically use a motorized microscope stage controlled by a joystick (Applied Scientific Instrumentation, MS-2000). We then use the motorized focus system to bring the cells into right focus.
15. For the high-magnification objectives that are required for single-molecule tracking in bacteria, focal depth is approximately 500 nm, and *E. coli* cells are approximately 1 μm in diameter. Focusing to the middle of the cell thus has the disadvantage that the membranes on the top and bottom of the cell will not be in focus.
16. To image eGFP or sfGFP, we use a 491 nm diode-pumped solid-state laser (Cobolt Calypso 50™ 491 nm DPSS), in combination with a dichroic mirror (Semrock, 488/561 nm lasers Brightline® dual-edge laser-flat, Di01-R488/561-25×36) and an emission filter (Semrock, 525/50 Brightline® single-band band pass filter, FF03-525/50-25).
17. We use an EMCCD camera (Andor iXon3, type 897) for acquiring fluorescence images continuously with an integration time of 32 ms per image. We use a total magnification of 200×, corresponding to 80 nm by 80 nm in the image plane per pixel.
18. We acquire images for approximately 40–60 min. Longer imaging will lead to data collection from aging cells which are generally smaller in size and less fluorescent, which might be due to nutrient depletion or metabolic changes.

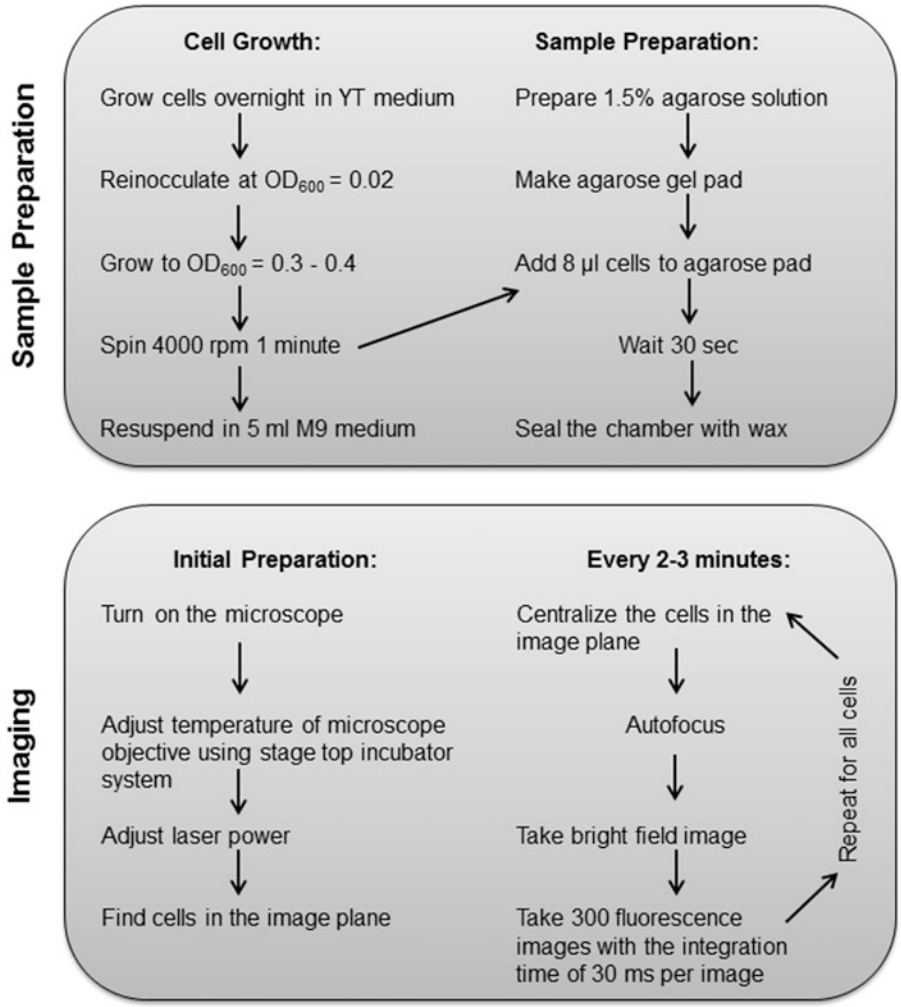

Fig. 2 Workflow of sample preparation and imaging of fluorescently labeled transmembrane proteins in *E. coli*

References

1. Green MR, Sambrook J (2012) Molecular cloning, 4th edn. Cold Spring Harbor Laboratory Press, Cold Spring Harbor, NY
2. Gibson DG, Young L, Chuang RY, Venter JC, Hutchison CA 3rd, Smith HO (2009) Enzymatic assembly of DNA molecules up to several hundred kilobases. Nat Methods 6(5):343–345. doi:10.1038/nmeth.1318
3. Sharan SK, Thomason LC, Kuznetsov SG, Court DL (2009) Recombineering: a homologous recombination-based method of genetic engineering. Nat Protoc 4(2):206–223. doi:10.1038/nprot.2008.227
4. Jiang Y, Chen B, Duan C, Sun B, Yang J, Yang S (2015) Multigene editing in the Escherichia coli genome via the CRISPR-Cas9 system. Appl Environ Microbiol 81(7):2506–2514. doi:10.1128/AEM.04023-14
5. Jaqaman K, Loerke D, Mettlen M, Kuwata H, Grinstein S, Schmid SL, Danuser G (2008) Robust single-particle tracking in live-cell time-lapse sequences. Nat Methods 5(8):695–702. doi:10.1038/nmeth.1237

6. Oswald F, ELM Bank, Bollen YJ, Peterman EJ (2014) Imaging and quantification of transmembrane protein diffusion in living bacteria. Phys Chem Chem Phys 16(25):12625–12634. doi:10.1039/c4cp00299g
7. Dinh T, Bernhardt TG (2011) Using superfolder green fluorescent protein for periplasmic protein localization studies. J Bacteriol 193 (18):4984–4987. doi:10.1128/JB.00315-11
8. Oswald F, Varadarajan A, Lill H, Peterman EJ, Bollen YJ (2016) MreB-dependent organization of the E. coli cytoplasmic membrane controls membrane protein diffusion. Biophys J 110 (5):1139–1149. doi:10.1016/j.bpj.2016.01.010
9. Guzman LM, Belin D, Carson MJ, Beckwith J (1995) Tight regulation, modulation, and high-level expression by vectors containing the arabinose PBAD promoter. J Bacteriol 177 (14):4121–4130

Chapter 8

Single-Molecule Fluorescence Microscopy in Living *Caenorhabditis elegans*

Jaap van Krugten and Erwin J.G. Peterman

Abstract

Transportation of organelles and biomolecules is vital for many cellular processes. Single-molecule (SM) fluorescence microscopy can expose molecular aspects of the dynamics that remain unresolved in ensemble experiments. For example, trajectories of individual, moving biomolecules can reveal velocity and changes therein, including pauses. We use SM imaging to study the dynamics of motor proteins and their cargo in the cilia of living *C. elegans*. To this end, we employ standard fluorescent proteins, an epi-illuminated, wide-field fluorescence microscope and mostly open-source software. This chapter describes the setup we use, the preparation of samples, a protocol for single-molecule imaging in *C. elegans* and data analysis.

Key words Single-molecule imaging, Live-cell imaging, Wide-field fluorescence microscopy, *Caenorhabditis elegans*

1 Introduction

In cells, it is of vital importance that biomolecules and organelles are transported from one side to the other. For transport of small particles over short distances, thermal-energy driven diffusion can be sufficient, but for larger particles and transport over large distances, active, motor-driven transport is required [1–3]. In many cases, single cargoes are transported by teams of motor proteins that use the cytoskeleton as tracks [4]. To unravel the molecular basis of intracellular transport, we use live-cell imaging of cargoes, motor proteins, and other factors involved. Key aspects of interest are how many motors of what type are involved in transport, how motors of the same or other (often opposite) directionality cooperate and how transport is regulated. We use a combination of ensemble imaging—visualizing single cargo trains with a multitude of components, including motors—and single-molecule (SM) imaging—where we focus for example on an individual motor protein. SM imaging can reveal interesting dynamics that are

Erwin J.G. Peterman (ed.), *Single Molecule Analysis: Methods and Protocols*, Methods in Molecular Biology, vol. 1665, DOI 10.1007/978-1-4939-7271-5_8,

hidden or averaged out in bulk experiments and can thus provide a better understanding of the transport mechanism.

As a model system for intracellular transport we use intraflagellar transport (IFT) in the chemosensory cilia of the nematode *Caenorhabditis elegans*. *C. elegans* is a widely used model organism, because it is relatively easy and cheap to keep, has a short reproduction cycle, the genome is known, as well as the lineage of all cells and the connectome of the nervous system. Furthermore, *C. elegans* is small (~1 mm long), thin (~100 μm) and transparent, which makes it ideal for fluorescence microscopy. A subset of the neurons in *C. elegans* is specialized in sensing the chemical composition of its surroundings, essential for the animal's survival [5]. From the ends of the dendrites of these neurons sensory cilia protrude. The tips of these cilia are in contact with the environment outside of the animal and can sense chemicals, resulting in signal transduction. The chemosensory cilia are ~8 μm long, ~100–300 nm diameter, membrane-enveloped structures protruding from the dendrite. Their core consists of a highly structured bundle of microtubules, an axoneme. For their development and maintenance, cilia depend upon a specific intracellular-transport pathway, IFT. IFT, driven by kinesin-2 and IFT-dynein motor proteins transports cargo, including receptors and ciliary components from base to tip and back again, in a continuous fashion.

In this chapter, we provide a comprehensive description of the methods we employ to image SM dynamics in a living, multicellular organism, with IFT in living *C. elegans* as an example. First, we explain the key features of our custom-built epi-illuminated wide-field fluorescence microscope. Next, we describe sample preparation, including anesthetizing the nematodes and placing them on agarose pads. Subsequently, we describe the actual imaging and, finally, the analysis of the obtained images. In this chapter we will not address the standard methods to maintain and transform *C. elegans*, since these have been described elsewhere in great detail [6].

2 Materials

2.1 Anaesthetizing and Mounting C. elegans

1. Multipurpose agarose.
2. M9 buffer: 5 g NaCl, 6 g Na_2HPO_4, 3 g KH_2PO_4, 1 mL 1 M $MgSO_4$, H_2O to 1 L. Sterilize by autoclaving.
3. Microscope slides: 76 × 26 mm.
4. Labeling tape.
5. Anesthetic: 5 mM Levamisole (tetramisole hydrochloride) in M9 (*see* **Note 1**).
6. Cover glass: 22 × 22 mm (we use Marienfeld, High Precision No. 1.5H, 0107052).

7. VaLaP: equal parts vaseline, lanolin, and paraffin wax.
8. *C. elegans*: transgenic young adults with no more than about eight eggs (*see* **Note 2**), expressing fluorescently labeled proteins of interest (*see* **Note 3**), maintained at 20 °C.

2.2 Microscope Setup

1. The system is built on the basis of a commercial, inverted microscope body (Nikon, Eclipse Ti), equipped with an eyepiece and bright-field imaging capabilities for searching nematodes.
2. As objective lens, a Nikon, CFI Apo TIRF 100×, N.A.: 1.49 oil-immersion objective is used.
3. Excitation light is provided by two diode-pumped solid-state lasers (Cobolt Jive 50 mW 561 nm and Cobolt Calypso 50 mW 491 nm).
4. Circularly polarized excitation light is obtained using an achromatic quarter-wave plate (Thorlabs, AQWP05M-600). Homogeneous and speckle-free illumination is obtained using a rotating diffuser (SUSS MicroOptics, rotating ground-glass diffuser (tilted version), $1° \pm 0.25°$ full width at half-maximum at 650 nm, AR-coating 400–750 nm $R < 0.5\%$, double sided).
5. Excitation and emission light are separated using a dichroic mirror (488/561 nm laser Brightline dual-edge laserflat, Semrock, Di01-R488/561-25×36). A dichroic longpass filter (Chroma, T565lpxr) is then used to filter and separate emission light inside a two-way image splitter (Cairn Research, Optosplit II). For single-color imaging, one of the light paths is blocked.
6. Fluorescence images are detected using an EMCCD camera (Andor, iXon 897, DU-897E-COO-#BV) at 152 ms per frame, at 5.3 pre amplifier gain and 300 EM gain with 10 MHz ADC readout.
7. The microscope is operated by Micro-Manager software (version 1.4, https://www.micro-manager.org).

3 Methods

3.1 Preparing Agarose Pads

1. Create microscope slides that each have two pieces of tape on top of each other of about 5 cm in length (*see* **Note 4**), in order to obtain a reproducible agarose-pad thickness.
2. Place a not-taped slide between two slides with tape. Repeat for as many slides as required.
3. Make sure you have at least ten clean microscope slides, with slides with tape on them next to it, available and place a pipet set to 600 μL next to the slides.

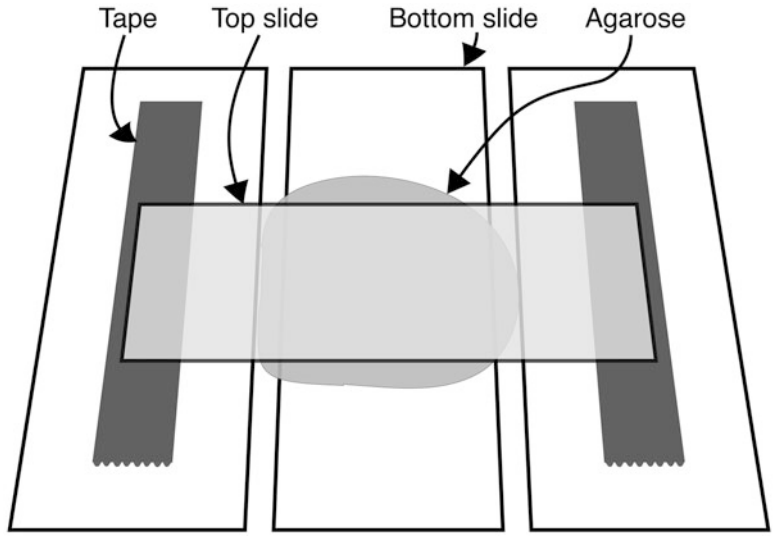

Fig. 1 Schematic of the preparation of a microscope slide with an agarose pad

4. Dissolve 0.4 g of multipurpose agarose (2%) in 20 mL M9 buffer and microwave until completely dissolved (*see* **Note 5**).
5. Pipet 600 μL of agarose in M9 on the middle of the first microscope slide that is positioned between two slides with tape (*see* **Note 6**).
6. Gently place a new (not-taped) microscope slide on top of the agarose, such that it spans from one slide with tape to the other (*see* **Note 7**) (Fig. 1). Repeat **steps 5** and **6** till all prepared slides are done, before moving to the next step.
7. Carefully remove the solidified agarose that spilled out between the two microscope slides with a scalpel (*see* **Note 8**). Repeat for all slides.
8. Pick up the two slides with agarose between them. Gently slide the top one from the bottom slide. The agarose should now be on the bottom slide.
9. Using the now detached top slide, remove the agarose that is hanging over the edges of the slide with the agarose pad. The flat part of the detached top slide can be pressed against the side with the agarose sticking out. This should result in a square agarose pad in the middle of the bottom slide.
10. Microscope slides with agarose pads can be stored in a vertical slide holder in an airtight container with a moisturized kim-wipe at the bottom for at least 2 weeks.

3.2 Mounting C. elegans

1. Place a coverslip on a clean microscope slide and pipet 5 μL 5 mM Levamisole (at room temperature) on the center of the coverslip.

2. Using a dissection stereo microscope, pick 6–8 young adult *C. elegans* and place them in the drop of Levamisole (*see* **Note 9**).
3. Once the worms have been in the Levamisole for 10 min, gently lower a prepared microscope slide with agarose pad, with the agarose pad down, on the coverslip (*see* **Note 10**).
4. Seal the agarose, now between microscope slide and coverslip, by connecting the two with VaLaP along the edges of the coverslip (*see* **Note 11**).
5. Label your microscope slide and wait for approximately half an hour for the worms to stop moving before imaging.

3.3 Imaging

1. Once the worms are mounted on the fluorescence microscope, check, using the ocular and bright-field imaging, whether the worms are not moving (*see* **Note 12**). Try to focus and position the region of interest of the worms into the approximate field of view of the camera.
2. Switch from bright-field to fluorescence imaging.
3. Bring the structure of interest carefully into focus and start recording (*see* **Note 13**).
4. Photobleach the sample up to a point when single fluorescence spots can be clearly distinguished (*see* **Note 14**).
5. Try to maintain focus once in the SM regime, and image until all fluorescent proteins (FPs) are bleached (*see* **Note 15**) (Fig. 2).

3.4 Data Analysis

Data analysis can be performed in many ways, depending on the behavior of the protein of interest and the question to be answered. Here, we will describe how we perform data analysis on SM data of IFT components in the phasmid cilia of *C. elegans*.

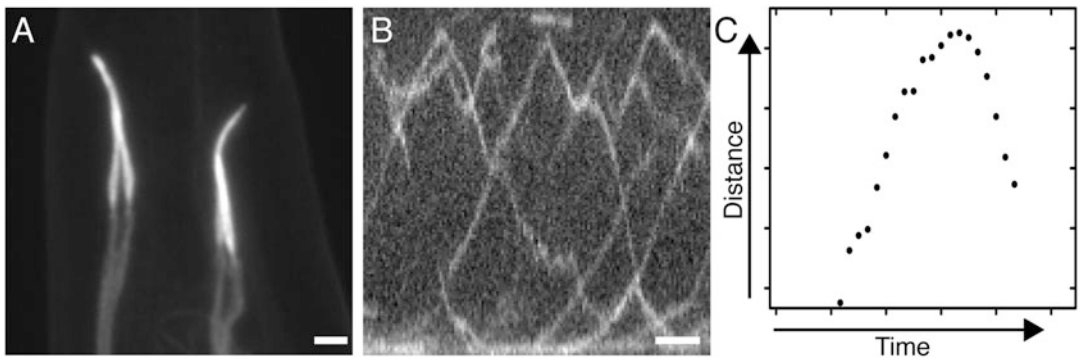

Fig. 2 Confocal picture of TBB-4::EGFP in *C. elegans* phasmid cilia (**a**). Scale bar 1 μm. SM kymograph of dynein motors transported towards the tip of the cilium (at the *top*) and driving IFT back towards the base (*bottom*) (**b**), recorded with our epi-illuminated wide-field microscope using XBX-1::EGFP. Scale bar 1 μm. SM trajectory output from our particle tracing software (**c**)

1. To prevent long software processing duration, it is advisable to visually check the image stacks and make separate folders with the frames (150–250) of high-quality parts of the stack (*see* **Note 16**).
2. If the signal-to-noise ratio is high enough, SM kymographs can be generated, which makes browsing the SM data substantially more efficient. Kymographs are generated using the ImageJ macro KymographClear [7]. The output comprises of a raw kymograph, a color-coded kymograph that is Fourier filtered for forward and backward direction, and static motion, and separate kymographs of forward and backward direction, and static motion (*see* **Note 17**).
3. For the analysis of (average) velocity and intensity over time and position of the tracks on the kymographs, we use the stand alone program KymographDirect. The program also allows one to export the data to Microsoft Excel or other software.
4. Finally, for the detailed analysis of the dynamics of IFT components, we employ tracking software custom-written in MATLAB, based on an existing linking-algorithm [8]. This software provides detailed data on the position as a function of time of single molecules on a local coordinate system that is established in the first steps of the script. Apart from the velocity, it can distinguish motion parallel to the cilium from perpendicular to the cilium, which can for example yield information about turn duration and location of molecules along the cilium. It can also determine whether a molecule appears to move freely or seems to be bound to a structure. The data is stored in output tables of MATLAB, it is straightforward to write small scripts to determine, in an automated way, for example whether pauses or directional turns occur in the trajectory and how long they take.

4 Notes

1. Choosing the right anesthetic is vital for the success of your experiment. Sodium azide is historically also used as an anesthetic, but inhibits the synthase of adenosine triphosphate (ATP) and cytochrome c oxidase, both essential for many cellular processes [9–11]. Levamisole immobilizes the worms by opening a subgroup of AChR channels that results in muscle contraction [12].
2. The endogenously labeled strains we use were generated by MoSCI insertions [13], however, the recently developed CRISPR/Cas9 system [14] provides a quicker and more straightforward way to label proteins endogenously. For

imaging single molecules, it is beneficial to select proteins with a location that is restricted to specific locations/structures in the worm, in order to limit out-of-focus background fluorescence and autofluorescence. For this reason, we mostly image the chemosensory cilia in the phasmid channels in the tail of the nematode. Back-ground and autofluorescence are substantially higher in for the amphid cilia around the head of the animal.

3. The specifications vary widely among the rich color palette of FPs. For the detection of single molecules, FPs with a high quantum yield and brightness are advisable. We mostly use EGFP or paGFP in our studies.
4. The brand one uses does not make a big difference, as long as the microscope slides with tape are ~0.27 mm thicker than the ones without tape. Molds can be reused.
5. In our experience, this works best with a 50 mL centrifuge tube that can stand upright. Place the tube in the microwave, place the lid on top, but do not fasten tightly. When the tube is fully closed, too much pressure will build up, when left open, too much M9 will evaporate. The agarose settles quickly, so frequent shaking is advised in order to prevent burning the agarose in the bottom of the tube. At our lowest (350 W) microwave setting, the M9 quickly boils over once it is warm. At this point, the agarose is not fully dissolved yet. Dissolving the agarose works best by heating in the microwave oven while watching the tube, quickly turning it off once it starts to boil over, shake the tube, and repeat till dissolved.
6. Once the agarose in M9 is dissolved and taken out of the microwave, it will solidify quickly. **Steps 5** and **6** are therefore best performed quickly. Prevent the formation of air bubbles in the agarose on the slide. After performing this step a couple of times, you will notice that the dissolved agarose will solidify in the tip of the pipet: just change the tip.
7. Place the top microscope slide on one of the taped microscope slides first, without it touching the agarose. Gently lower it over the agarose, wait till one can see condensation on the top microscope slide, and then press it down on both microscope slides with tape. This should not be done with too much force, since it will make the agarose pads too thin.
8. Try to prevent moving the bottom and top slide too much by pressing them down while one removes the excessive agarose.
9. Pick healthy looking young adults, and avoid transferring any bacteria to the drop of Levamisole. It is hence best to pick worms from outside the bacteria lawn. Bacteria and more than eight worms will cause too much background fluorescence and will therefore harm your ability to image single

molecules. As there are few worms on your coverslip, they will be hard to find. Aligning them in a circle in the drop of Levamisole will help one finding the rest on the fluorescence microscope once you spotted the first. Marking the circle of worms with a marker on the microscope slide under a dissection microscope can also help finding the worms once mounted on the fluorescence microscope.

10. In our hands, this works best while holding the microscope slide with the agarose pad at a 90° angle with respect to the one with the coverslip with worms on it. Make sure to center the coverslip in the agarose pad.
11. Melt the VaLaP by heating to approximately 75 °C before one starts sedating the worms. Use a cotton swab to apply the VaLaP on the corners of the coverslip to prevent it from moving, before connecting the corners with VaLaP to seal the agarose between the coverslip and microscope slide. Attempt to apply as little VaLaP as possible on the coverslip, as VaLaP can dissolve in immersion oil, harming image quality.
12. In practice, we mount the worms immediately after sealing the coverslip and search for the worms on our fluorescence microscope, and save their position using Micro-Manager. We then wait for the worms to completely stop moving, and start imaging.
13. The brighter the signal is, the easier it is to focus accurately. After bleaching many FPs, it will become harder to focus on the few that are still visible. Especially in the SM regime, there is a delicate trade-off between bringing the FPs better into focus and the risk of losing them while refocusing. Recording images and focusing, before the SM regime is reached, helps to obtain data good enough for data analysis.
14. Bleaching with high laser power will get one quickly in the SM regime. However, in our experience, it works best while bleaching with a low laser power. This results in a prolonged period in which single molecules are visible. We bleach the FPs with a low laser power until almost in SM regime, only then set the laser to maximum power and focus one last time. Do this quickly in order to avoid further photobleaching of the few molecules not bleached. We search and bring our FPs into focus with about 8% of the laser power (0.7 mW) and use maximum laser power to get the highest possible signal out of our FPs.
15. Analyzing your data will give insight in when it is time stop recording and to move on to the next sample. Spatially distinguishable individual FPs and invariant intensity between them is a good indicative for single molecules. Comparing the

intensity of single, purified FPs on glass with the intensity of the same type in vivo, and looking at the bleaching steps of the FPs in vivo can also help determining whether one is observing single molecules.

16. Enhancing the contrast using the likewise named feature from ImageJ will improve the visual recognition of the trajectory of your protein of interest. Although it will take time, to get an idea of how a kymograph will look like in relation to the movie, it can be insightful to make a kymograph of the entire recording.
17. A more detailed description of KymographClear and KymographDirect can be found in reference [15]. The software itself and a manual can be found in ref. 7.

Acknowledgements

We thank Bram Prevo, Jona Mijalkovic, Felix Oswald and Seyda Acar for their involvement in this project and discussions. This work is part of the research programme of the Foundation for Fundamental Research on Matter (FOM), which is part of the Netherlands Organisation for Scientific Research (NWO).

References

1. Brackley CA, Cates ME, Marenduzzo D (2013) Intracellular facilitated diffusion : searchers, crowders, and blockers. Phys Rev Lett 108101(September):1–5
2. Hirokawa N, Noda Y, Tanaka Y, Niwa S (2009) Kinesin superfamily motor proteins and intracellular transport. Nat Rev Mol Cell Biol 10 (10):682–696
3. Roberts AJ, Kon T, Knight PJ, Sutoh K, Burgess SA (2013) Functions and mechanics of dynein motor proteins. Nat Rev Mol Cell Biol 14(11):713–726
4. Prevo B, Mangeol P, Oswald F, Scholey JM, Peterman EJG (2015) Functional differentiation of cooperating kinesin-2 motors orchestrates cargo import and transport in C. elegans cilia. Nat Cell Biol 17(12):1536–1545
5. Bargmann, CI (2006) Chemosensation. *C. elegans*. In: The C. elegans Research Community (ed.), WormBook, WormBook, Pasadena, CA
6. Brenner S (1974) The genetics of Caenorhabditis elegans. Genetics 77:71–94
7. Mangeol, P, Prevo, B, Peterman, EJG (2016) Downloads of software and manuals of KymographClear and KymographDirect. http://www.nat.vu.nl/~erwinp/downloads.html. Accessed 20 Oct 2016
8. Jaqaman K, Loerke D, Mettlen M, Kuwata H, Grinstein S, Schmid SL, Danuser G (2008) Robust single-particle tracking in live-cell time-lapse sequences. Nat Methods 5 (8):695–702
9. van der Bend RL, Duetz W, Colen A-MAF, van Dam K, Berden JA (1985) Differential Effects of Triphenyltin and 8-Azido-ATP on the ATP Synthesis, ATP-Pi Exchange, and ATP Hydrolysis in Liposomes Containing ATP Synthase and Bacteriorhodopsin. Arch Biochem Biophys 241(2):461–471
10. Herweijer MA, Berden JA, Kemp A, Slater EC (1985) Inhibition of energy-transducing reactions by 8-nitreno-ATP covalently bound to bovine heart submituchondrial particles: direct interaction between ATPase and redox enzymes. Biochim Biophys Acta 809:81–89
11. Duncan HM, Mackler B (1966) Electron Transport Systems of Yeast. The Journal of Biologocal. Chemistry 241(8):1694–1697

12. Martin RJ, Robertson AP, Buxton SK, Beech RN, Claude L (2013) Levamisole receptors : a second awakening. Trends Parasitol 28 (7):289–296
13. Frøkjær-jensen C, Davis MW, Hopkins CE, Newman BJ, Thummel JM, Olesen S, Jorgensen EM (2008) Single-copy insertion of transgenes in Caenorhabditis elegans. Nat Genet 40 (11):1375–1383
14. Dickinson DJ, Ward JD, Reiner DJ, Goldstein B (2013) Engineering the Caenorhabditis elegans genome using Cas9-triggered homologous recombination. Nat Methods 10 (10):1028–1034
15. Mangeol P, Prevo B, Peterman EJG (2016) KymographClear and KymographDirect : two tools for the automated quantitative analysis of molecular and cellular dynamics using kymographs. Mol Biol Cell 27:1948–1957

Chapter 9

Purification and Application of a Small Actin Probe for Single-Molecule Localization Microscopy

Roderick P. Tas, Trusanne G.A.A. Bos, and Lukas C. Kapitein

Abstract

The cytoskeleton is involved in many cellular processes. Over the last decade, super-resolution microscopy has become widely available to image cytoskeletal structures, such as microtubules and actin, with great detail. For example, Single-Molecule Localization Microscopy (SMLM) achieves resolutions of 5–50 nm through repetitive sparse labeling of samples, followed by Point-Spread-Function analysis of individual fluorophores. Whereas initially this approach depended on the controlled photoswitching of fluorophores targeted to the structure of interest, alternative techniques now depend on the transient binding of fluorescently labeled probes, such as the small polypeptide lifeAct that can transiently interact with polymerized actin. These techniques allow for simple multicolor imaging and are no longer limited by a fluorophore's blinking properties. Here we describe a detailed step-by-step protocol to purify, label, and utilize the lifeAct fragment for SMLM. This purification and labeling strategy can potentially be extended to a variety of protein fragments compatible with SMLM.

Key words Actin, Sample fixation, Fluorophores, Super-resolution microscopy, Exchangeable probe

1 Introduction

Cellular morphology, migration, division, polarization, and differentiation are all processes that require very specific cytoskeleton organization and dynamics. The exact organization of microtubules and actin directly influences the available roads for active transport by kinesins/dyneins and myosins, respectively [1–3]. A specific actin organization is important during cell migration, neuronal growth cone extension, brush border formation, and many other processes [4, 5]. Different actin structures underlie different functions. For example, while dense structures of actin in the axon initial segment of neurons can mediate myosin-mediated anchoring of cargoes, cortical actin structures can drive directional motility in epithelial cells [6, 7]. Therefore, understanding the nanoscale organization of the actin and microtubule

Erwin J.G. Peterman (ed.), *Single Molecule Analysis: Methods and Protocols*, Methods in Molecular Biology, vol. 1665, DOI 10.1007/978-1-4939-7271-5_9,

cytoskeleton is important to understand the mechanisms and functions of these specialized structures.

Conventional fluorescence microscopy is widely available and continues to be a powerful tool to provide new insights in cytoskeleton organization and dynamics. Better objectives, faster cameras as well as genetic tools, and immunocytochemistry can be used to label and image individual proteins with high specificity and temporal resolution. However, conventional fluorescent microscopy is limited by the diffraction of light, which causes fluorophores to be imaged as a spatially extended structure of 200–300 nm. This detected pattern of a single fluorophore on the camera is called the Point Spread Function (PSF) which is shaped like an airy disk. When two fluorophores emit light at the same time while they are very close, the airy disks overlap and cannot be separated. This phenomenon limits the distance at which you can separate two fluorophores or structures to approximately half the wavelength of the detected light.

During the last decade several fluorescence-based microscopy techniques have been developed that are not limited by diffraction [8, 9]. Single-molecule localization microscopy (SMLM) is a super-resolution technique based on the sequential detection of individual fluorophores and subsequent midpoint determination with nanometer precision. All detected fluorophores that label the structure of interest can result in a single reconstructed image where all fluorophore locations are plotted with high precision [10]. Techniques that are based on SMLM are PALM (Photoactivated Localization Microscopy—[11]), STORM (Stochastic Optical Reconstruction Microscopy—[10]), dSTORM (direct STORM—[12]), GSDIM (Ground-State-Depletion and Single-Molecule return—[13]), and PAINT (Point Accumulation for Imaging in Nanoscale Topography—[14]). In fixed samples (d)STORM provides the highest resolution and is therefore commonly used to study the exact architecture of the cytoskeleton beyond the diffraction limit. One important breakthrough was the discovery of the periodic actin and spectrin rings in the axon [15]. A major limitation of dSTORM is the limited number of fluorophores compatible with robust multicolor imaging. Another limitation of dSTORM is the use of high laser intensities to bring the majority of the fluorophores in a dark-state so that individual molecules can be detected. This results in overall bleaching of fluorophores and reduces the amount of detections over time. Additionally, achieving such high laser intensities often requires illumination of only a small area of the sample.

PAINT-like methods overcome these limitations. They rely on the transient binding of fluorophores targeted to the structure of interest. Weakly interacting probes coupled to a fluorophore will bind stochastically, serve as point emitter for a limited time and diffuse back into solution (Fig. 1a) [16]. The imaging solution can

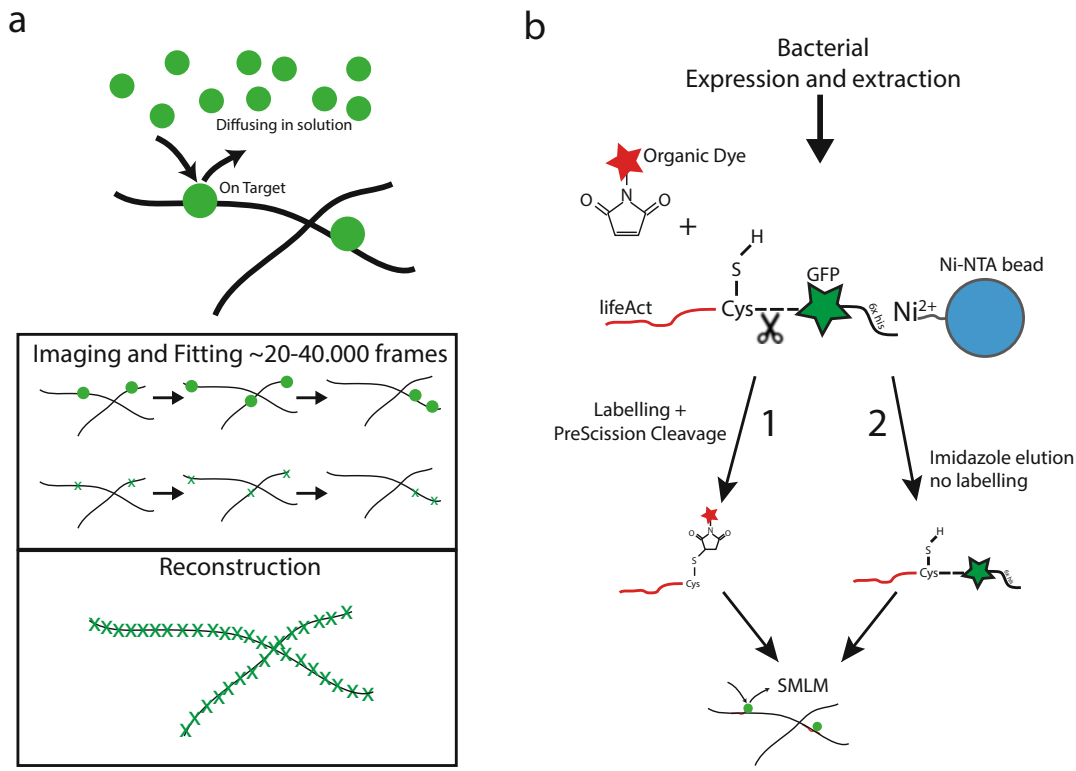

Fig. 1 Single-molecule localization microscopy (SMLM) by transient binding. (**a**) Principle of SMLM by transient binding. From solution, fluorophores targeted by a specific molecule transiently bind to the structure of interest so that single molecules can be observed. These single-molecule events are recorded through time. Subsequently midpoint determination and reconstruction lead to a super-resolved image. (**b**) Schematic representation of the purification and labeling lifeAct probe with GFP or organic dyes to label actin. *Arrow 1* represents purification through proteolytic cleavage. *Arrow 2* represents the purification with a GFP as fluorescent protein. Dashed line with scissors indicates PreScission cleavage site

then be washed and a second structure can be imaged using a similar or different fluorophore targeted to a different structure. The overall advantage of this technique lies within the transient binding. Unlike dSTORM, there is no need for high laser intensities to bring the majority of fluorophores to a dark state. In addition, the probes on the target are continuously replaced by fresh probes from solution resulting in a continuing imaging cycle not limited by bleaching. Furthermore, PAINT-like SMLM can be performed using a wide variety of fluorophores for multicolor imaging.

A limiting factor for PAINT-type approaches is the need for proper transiently interacting probes. Recently, a generic approach for PAINT, DNA-PAINT, was introduced in which structures labeled with an antibody conjugated to single-stranded DNA can be imaged very specifically with complementary DNA coupled to a

fluorophore [14]. Alternatively, protein–protein interactions can be used to target fluorophores to the desired structure. It has been shown that using small protein fragments/peptides coupled to a fluorophore, SMLM by transient binding could be performed on actin and other cytoskeleton structures. The major advantage of these interactions is that they are highly specific and can rely on very small probes. Recent work showed that using these transient protein–protein interactions, the actin cytoskeleton can be visualized in high detail by lifeAct coupled to an Atto-dye [17]. LifeAct is a small 17-amino acid fragment of the yeast Abp140 protein that was found to label actin [18]. Whereas this work used a commercially obtained synthesized lifeAct probe, we recently developed an approach to purify the lifeAct peptide, either fused to fluorescent proteins or conjugated with organic dyes after purification.

Here we describe a step-by-step protocol to purify the lifeAct domain for super-resolution microscopy. This method allows for SMLM using either a fused fluorescent protein or using any organic fluorophore coupled by thiol–maleimide chemistry. For this a construct that consists of "lifeAct-Cysteine-PreScission Cleavage Site-GFP-6× His" was created, as shown in Fig. 1. To perform SMLM using the fluorescent protein module (GFP) a rapid his-tag purification can be performed. To functionalize the small peptide with any organic dye, thiol–maleimide chemistry on the introduced cysteine and subsequent proteolytic cleavage by PreScission protease can be performed (Fig. 1b). The generation of this versatile probe can be extended to other protein fragments to label other structures of interest.

2 Materials

All imaging experiments are performed at room temperature unless indicated otherwise. Solutions are dissolved in ultrapure water (~18 MΩ cm at 25 °C). During purification, buffers and samples are kept on ice to avoid protein degradation.

2.1 Purification and Labeling

1. *E. coli* BL21DE3 transformed with an IPTG inducible expression vector for lifeAct-cys-PreScission Site-GFP-6×His (*see* **Note 1**).
2. Resuspension/lysis Buffer: 20 mM HNa_2PO_4, 300 mM NaCl, 0.5% glycerol, 7% glucose, EDTA-free protease inhibitor (Roche Diagnostics GmbH), 1 mM dithiothreitol (DTT), pH 7.4. To a beaker containing a magnetic stir bar, add 100 ml water, 0.71 g of HNa_2PO_4, 3.5 g of NaCl, 14 g of Glucose, and 1 ml 100% Glycerol. Adjust pH to 7.4 and add water to a final volume of 200 ml and readjust pH if necessary. Before purification add 1 tablet of EDTA-free protease inhibitor (Roche

Diagnostics GmbH) and 50 μl 1 M DTT per 50 ml of buffer and incubate on ice.

3. Wash Buffer: 10 mM HNa_2PO_4, 300 mM NaCl, 30 mM imidazole, 1 mM DTT, pH 7.4. Prepare as previous step.
4. Labeling Buffer: 10 mM TCEP in PBS.
5. Cleavage buffer: 50 mM Tris-HCl, 150 mM NaCl, 1 mM EDTA, 1 mM DTT, pH 7.0.
6. Elution Buffer: 10 mM HNa_2PO_4, 300 mM NaCl, 300 mM imidazole, 1 mM DTT, pH 7.4. Prepare as in the previous step.
7. Ni-NTA Agarose beads.
8. 10 mM (tris(2-carboxyethyl)phosphine (TCEP)) in PBS.
9. AlexaFluor®-Maleimide in anhydrous dimethyl sulfoxide (DMSO). Dissolve AlexaFluor®-Maleimide in fresh DMSO to ~100 μM or as indicated by the company.
10. Glutathione-sepharose 4B beads in 20% ethanol (GE Healthcare Life Sciences).
11. PreScission protease in cleavage buffer + 20% glycerol (GE Healthcare Life Sciences).
12. LB Broth.
13. 1 M Isopropyl β-D-1-thiogalactopyranoside (IPTG) in water.
14. Shaking incubator.
15. Probe-type Sonicator for cell disruption equipped with a tip suited for 50 ml tubes.
16. Cooled Centrifuge (18,000 × *g*).

2.2 Fixation

Cultured cells grown on any surface that is compatible with TIRF imaging: e.g. epithelial cells or neurons plated on glass coverslips (*see* **Note 2**).

1. Cytoskeleton Buffer: 10 mM MES, 150 mM NaCl, 5 mM $MgCl_2$, 5 mM EGTA, 5 mM Glucose, pH 6.1 [15].
2. 16% w/v Paraformaldehyde (PFA) dissolved in water.
3. 1× d-PBS.
4. Fixation Buffer: Cytoskeleton buffer supplemented with 0.5% Triton-X and 3.7% w/v PFA.
5. Blocking solution: 3% w/v BSA in d-PBS.
6. Optional: antibodies for detection of additional structures.

2.3 Sample Preparation

1. Tweezers.
2. Mounting chamber.
3. d-PBS.
4. Purified lifeAct coupled to a fluorophore.

2.4 Microscope Setup

1. Standard inverted fluorescence microscopy equipped with a high NA objective and a total internal reflection fluorescence (TIRF) module.
2. Fluorescent filters for imaging GFP or the conjugated fluorophore.
3. Excitation lasers with the appropriate wavelength.
4. EMCCD camera or CMOS camera, sensitive enough to image single molecules.
5. SMLM software for super-resolution reconstruction: e.g. DoM Utrecht (Detection of Molecules, https://github.com/ekatrukha/DoM_Utrecht [19]), QuickPalm, (http://imagej.net/QuickPALM [20]), Thunderstorm (http://zitmen.github.io/thunderstorm/, [21]), RapidSTORM (http://www.super-resolution.biozentrum.uni-wuerzburg.de/research_topics/rapidstorm/, [22]), NIS Elements (Nikon instruments).
6. Microscope control via PC and dedicated software, for example Micromanager (https://micro-manager.org/, [23]).

3 Methods

3.1 Expression and Passivation on Ni-NTA Beads

The correct expression and purification protocols vary between the two different options, i.e. with or without GFP. Because lifeAct coupled to GFP is highly soluble, standard purification protocols and buffers are used. For the lifeAct without GFP, the full recombinant protein is bound to the Ni-NTA beads and the cysteine containing lifeAct fragment is cleaved off by PreScission protease after on-bead labeling. Subsequently free PreScission is captured by glutathione beads. Full recombinant protein coupled to GFP or the short lifeAct fragment coupled to an Alexa dye by the maleimide–-cysteine reaction can be obtained at high yields. However, it should be noted that the free cysteine, which was introduced in the construct, is prone to form disulfide bonds with other free cysteines in the samples, resulting in precipitation. To overcome this problem, reducing reagents like DTT or TCEP are required at all steps. A detailed step-by-step description of purification follows below.

1. Grow 0.8 l *E. coli* BL21DE3 containing the lifeAct expression plasmid to $OD_{0.6}$ at 37 °C from an overnight 4 ml culture in LB. Induce protein expression by addition of 800 µL 1 M IPTG to achieve a final concentration of 1 mM. Incubate for 3.5 h at 37 °C or 16 h overnight at 17 °C.
2. After induction, transfer the bacteria into a centrifuge compatible bucket and spin at 4000 × *g* for 30 min at 4 °C. Decant supernatant carefully and incubate pellet on ice. Resuspend

bacterial pellet in resuspension buffer supplemented with protease inhibitors (5 ml/gram bacterial pellet) and transfer to a 50 ml tube.

3. To lyse the bacteria, sonicate the bacterial suspension 5 × 1 min with 5 min intervals on ice. Intermediate to high sonication powers can be used.
4. Following sonication, the soluble fraction of the bacterial suspension can be separated from the insoluble sample fraction through centrifugation at 18,000 × *g* at 4 °C for 40 min (*see* **Note 3**).
5. During centrifugation wash 1.0 ml of Ni-NTA resin (0.5 ml Beads) in resuspension buffer. Beads can be centrifuged at 1000 × *g* for 3 min with slow deceleration. Supernatant can then be removed by a vacuum pump or pipet and replaced by resuspension buffer. Repeat the bead wash three times in resuspension buffer with 10× the bead resin volume (10 ml).
6. To separate the soluble fraction from the insoluble fraction after centrifugation, transfer the supernatant into a 50 ml tube to separate it from pellet. Typically, the supernatant of bacteria is a yellowish solution. However, because lifeAct is tagged with a GFP, the supernatant can appear more greenish. The pellet should be brown/yellowish, but can also be greenish because it can contain some aggregated protein or non-lysed expressing cells.
7. Add the washed Ni-NTA beads to the soluble supernatant and incubate at 4 °C while gently rolling for 2 h. The His-Tag of the recombinant lifeAct will bind to the beads.
8. After incubation spin the beads at 1000 × *g* for 3 min with slow deceleration as described before. The lifeAct-Cys-PreScission-Site-GFP-6×His is now bound to the beads. Supernatant containing all other soluble proteins that do not contain a His-Tag can be discarded.
9. Wash the beads three times as described above in wash buffer to reduce nonspecific interactions of proteins with the beads. The lifeAct recombinant fragment has 6×His-Tag which binds tightly to Ni-NTA. This specific interaction will not be disrupted by the 30 mM imidazole in the wash buffer.

3.2 Purification with GFP

1. To obtain the full lifeAct-Cys-PreScissionSite-GFP-6×His for SMLM (*see* **Note 4**), the recombinant protein can be eluted by aspiration of the last wash step as described in Subheading 3.1. Addition of 3.5 ml Elution Buffer results in the elution of the recombinant His-tagged protein from the beads after 10 min incubation. Beads can be spun down and the supernatant containing lifeAct-GFP can be collected.

2. The eluted fraction can be used directly for SMLM as described in Subheading 3.5. For long-term storage, exchange the buffer to PBS + 1 mM DTT using a buffer exchange column, and add 10% glycerol. Snap-freezing followed by −80 °C storage is recommended. The purity of the final sample can be determined by SDS-page. Typically, this approach yields highly pure samples.

3.3 Labeling and Purification with Organic Dyes

The second mode in which this recombinant lifeAct fragment can be used is by labeling of the introduced cysteine through a maleimide–thiol interaction. The lifeAct-Cys, coupled to the thiol, can subsequently be cleaved off the GFP-6×His and further purified. The overall advantage is that almost all organic dyes and other chemical modifications are available conjugated to a maleimide. Therefore it can be used to label the lifeAct-Cys fragment with a variety of stable fluorophores, resulting in a high photon yield. Below we describe how the cysteine can be labeled with an Alexa647 through maleimide coupling on the beads, followed by cleavage at the PreScission site.

1. After the third wash in wash buffer (Subheading 3.1) wash the beads three additional times with labeling buffer. Because DTT contains two thiol groups, it is not compatible with maleimide coupling. Replacement with of DTT with TCEP is therefore essential for protein solubility and coupling efficiency.
2. For labeling, aspirate the final wash and transfer the beads into a 2 ml Eppendorf. Add 1000 μl labeling buffer supplemented with 80 μl of ~100 μM Alexa647-maleimide (~8 nmol Alexa647) in DMSO and incubate for 4 h at room temperature. After incubation add an additional 60 μL ~100 μM Alexa647-maleimide and incubate overnight at 4 °C. The maleimide-dye is added in excess and should, if incubation times are long enough, label almost all free cysteines in the sample.
3. Remove excess dye after labeling through three 1 ml washes in Cleavage Buffer. This buffer allows optimal cleavage at the PreScission cleavage site, releasing lifeAct-Cysteine labeled with Alexa647 while leaving GFP-6×His bound to the beads.
4. Cleave lifeAct-Cys-Alexa647 from the Ni-NTA beads by replacing the final wash step with 70 μL PreScission protease in 500 μL Cleavage Buffer for 5 h at 4 °C (or overnight) while gently rolling.
5. While cleaving, wash 250 μl glutathione beads with cleavage buffer as described above.
6. Capture PreScission protease on the glutathione beads by addition of the prewashed beads to the sample. Now, both PreScission and the GFP-6×His are bound to the glutathione and Ni-

NTA beads respectively while lifeAct-Cys-Alexa647 diffuses in the supernatant.

7. The supernatant containing soluble lifeAct-Cys-A647 can be collected. The final concentration of the lifeAct peptide can be determined using the Bicinchoninic Acid (BCA) protein assay [24]. The labeling efficiency can then be determined by measuring the dye concentration by spectroscopy and application of Beer-Lambert's law. Typical concentrations of labeled lifeAct range from 0.1 to 1 μM (*see* **Note 5**).
8. Finally, supplement the sample with a final concentration of 10% glycerol, snap-freeze in liquid nitrogen and store at −80 °C.

3.4 Sample Preparation

Because in super resolution all details and therefore also sample errors are visualized, optimized sample preparation and dense label coverage are essential for a successful final reconstruction. Fixations and staining protocols that would result in a smooth diffraction limited image might result in sparsely labeled structures in super resolution. Sample preparation should therefore be optimized for each individual structure or co-labeling of multiple structures. The buffer conditions during fixation also play an important role to preserve cytoskeletal structures. Whereas microtubule fixations are preferentially performed in PEM80 buffer [25], cytoskeleton buffer is the fixation buffer of choice for actin [15, 17]. Finally, fixatives should be chosen carefully and such that labeling is not perturbed and structures are maintained. Actin structures are preferentially fixed by PFA or Glutaraldehyde [26]. Below a simple and fast sample preparation is described with PFA in cytoskeletal buffer to preserve the actin network.

1. Pre-warm fixation buffer to 37 °C. Remove the medium from the cells coated on coverslips and gently add pre-warmed fixation buffer for 10 min. Triton-X ensures sufficient permeabilization of the cells, resulting in release of cytoplasm which allows the lifeAct probe to diffuse freely. Simultaneously, PFA fixes cellular structures like actin.
2. After fixation aspirate the fixation buffer and wash the sample with d-PBS for 5 min. Even though the samples are fixed, pipet with care not to perturb the samples. Repeat the wash three times.
3. After washing, block the sample with blocking solution for at least 30 min at room temperature. Blocking reduces the number of unspecific protein–protein interactions reducing the background signal in the final image.
4. To stain for structures additional to actin, the samples can be further incubated with antibodies after blocking. Antibodies compatible with PFA fixation can be diluted in blocking

solution and incubated on the sample for at least 1 h at room temperature. Subsequently, the primary antibody incubation can be stopped by three additional 5-min washes with d-PBS. Cells can then be incubated with a suitable secondary labeled antibody in blocking solution to finish the staining for the desired structure (*see* **Note 6**).

5. After blocking and optional staining, the samples are ready to be mounted in d-PBS + DTT (*see* **Note 7**). A suitable chamber that is compatible with the microscope stage can be used. Open chambers like Ludin chambers for 18 mm round coverslips provide easy access to the imaging medium and allows for the addition or dilution of the lifeAct probe during image acquisition.

3.5 Imaging

1. Secure a sample on the microscope and select a position of interest. Before image acquisition can be started, it is important to select the correct parameters for an optimal super-resolution image. Focusing before acquisition is important to image the correct plane of interest. Because the low concentration of lifeAct used for imaging does not provide a full overview of the cellular outline a co-transfection or staining of an additional marker is favorable. Alternatively, an excess of lifeAct conjugated to a fluorophore can be added to the sample which results in a faint outline of the cellular actin structures. If the latter is applied, the concentration should be strongly reduced through dilution and bleaching before SMLM acquisition to be able to visualize single molecules (*see* **Note 8**).
2. For an optimal super-resolution acquisition carefully take the following parameters into account. Optimizing each condition carefully every time can increase the signal-to-noise ratio per imaging session:
   (a) *Exposure time*. For super resolution based on probe exchange, the on- and off-rates should guide the exposure time. Low off rates allow for high exposure times and collection of more photons. However, a single molecule binding event should not be obscured by another molecule binding in the vicinity rendering the software unable to detect them both as separate localizations. The latter has a higher chance at higher on rates. Therefore, a balanced exposure time is necessary. For lifeAct the reported half-life on the actin filaments is 23 ms [17] and it is preferentially imaged with 50–100 ms exposure time.
   (b) *Laser Power*. Laser power and exposure time are co-dependent on each other and on fluorophore stability. Fluorescent proteins like GFP are easily bleached compared to organic dyes. It is important that a maximum

amount of photons is collected from one single molecule during the selected exposure time. Therefore, laser power can be varied between probes with higher laser powers for more stable probes (*see* **Note 7**). Because the sample is crowded with diffusing lifeAct-fluorophore molecules the laser power should also be kept at moderate levels to minimize background. Starting at low laser powers and gradually increasing them usually results in the rapid recognition of the optimum laser power.

(c) *Number of collected frames*. The more frames can be collected, the better. Reconstruction of a single-molecule image preferentially relies only on the most accurate localizations, which can be filtered based on localization precision. Collecting more frames at optimal settings allows more stringent filters on localization precision, but care should be taken to minimize and correct sample drift. Selecting only the most accurate detection already results in a full overview of the image with high resolution. Typically we record 30,000–40,000 frames.

(d) *Fluorophore density*. SMLM relies on the detection of individual fluorophores conjugated to lifeAct that are binding sequentially. Therefore, lifeAct should be diluted to a concentration such that in every frame single molecules can be observed. In 2D and 3D imaging the plane in focus will be the plane where the point spread function of the single molecules is symmetrical. For SMLM imaging, labeled lifeAct is typically diluted to 1–5 nM in d-PBS (*see* **Note 9**).

(e) *Laser angle*. Total Internal Reflection of the laser at the coverslip–sample interface results in an evanescent wave of typically a few hundred nanometers, which prevents excitation of out-of-focus fluorophores. Reducing the incident laser angle results in a more oblique illumination field which yields deeper sample penetration and fluorophore excitation. The latter can be favorable because of imaging depth, but also increases background fluorescence. The incident laser angle should thus be adjusted dependent on required imaging depth and the background intensity that is acceptable.

3.6 Analysis

The final super-resolution image is created by accumulation of all single-molecule positions that were acquired during imaging. Single-molecule positions can be accurately determined by fitting the PSF to a Gaussian and determine the midpoint. The midpoint can be localized with nanometer precision based on the width of the Gaussian. Detection/fitting and subsequent reconstruction of the super-resolved image is performed by dedicated software

packages. There are several freely available packages (e.g. DoM Utrecht [19], RapidSTORM [22], ThunderSTORM [21], QuickPALM [20]) or commercially available packages to reconstruct a super-resolved image.

1. Detection and fitting of the imaged fluorophores is dependent on the image parameters as well as on the recorded PSF. The software usually requires input of the pixel size and several threshold values like estimated PSF size to exclude abnormal detections that cannot result from single molecules. The midpoint of included localizations is then determined with nanometer precision by fitting or maximum likelihood estimation.
2. The detection and fitting process results in a table that contains information about all the individual detected fluorophores. Fluorophore parameters include: the *x*- and *y*-coordinate, the image number in which it was acquired, PSF symmetry (in *x* and *y*), PSF shape, PSF brightness etc.
3. Next, reconstruction of the super-resolution image can be done based on this particle table. All the stored *x*- and *y*-coordinate are used to plot the midpoint of these molecules. The midpoint can be plotted as a small Gaussian of a constant size or each midpoint can be plotted as a spot based on its individual localization error. This localization error can be calculated from the fitting parameters and used as a threshold. Fluorophores with more precise localizations can then be plotted as tight spots while less well localized fluorophores are represented as more spread localizations. Several parameters should be taken into account while reconstructing the final image. The pixel size of the reconstructed image should be selected in such a way that they are at least half the size of the smallest details according to the Nyquist criterion. Furthermore, the localizations used in the final reconstruction can be filtered on the localization precision. It should be noted that filtering too much or selecting a very low pixel size will eventually result in very sparse localizations. Both these parameters can be varied and optimized per image to obtain a successful and informative super-resolution reconstruction.
4. Drift correction is a final important step in the analysis. Because of the nanometer localization accuracy, any drift of the sample with respect to the objective will be clearly visible in the final reconstruction. Long imaging times combined with small thermal fluctuations will result in noticeable drift in the final reconstruction. The available software packages usually support drift correction based on frame-to-frame cross-correlation of fiducial markers or cross-correlation of intermediate super-resolution reconstructions [27, 28]. The fiducial markers can be small particles like beads that are fixed to the coverslip and do not

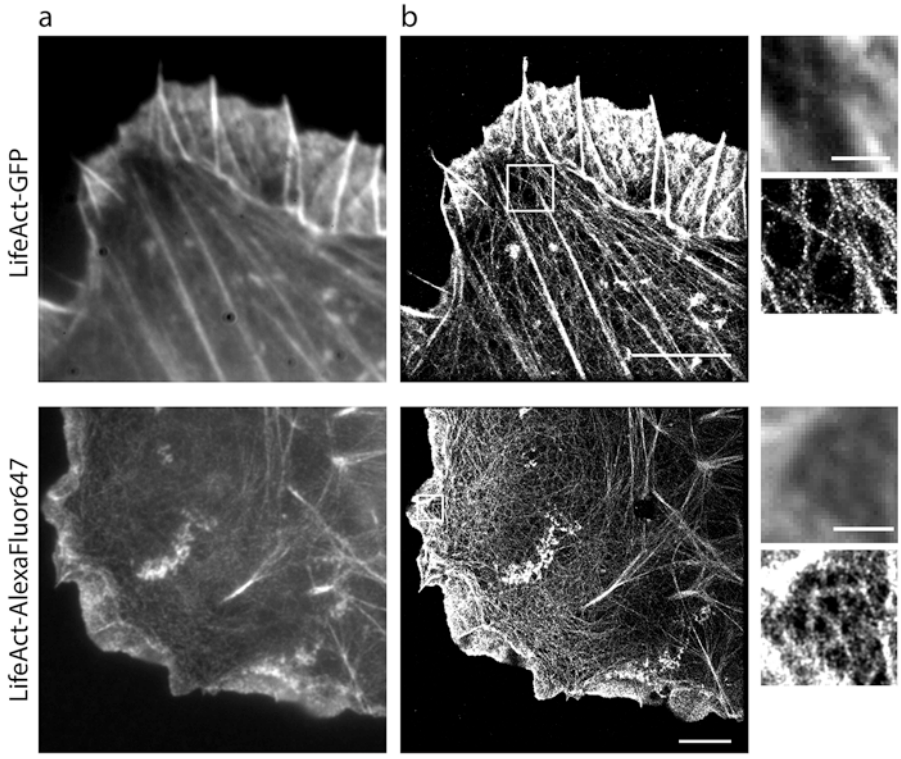

Fig. 2 Representative super-resolution images obtained using the lifeAct probes. Diffraction-limited overview **(a)**, super-resolved image **(b)**, and zooms of lifeAct-GFP used on a HeLa cell (*top*) or lifeAct-AlexaFluor647 used on a COS7 cell (*bottom*). Scale bars in super-resolved images are 5 μm in **a** and **b** and 1 μm in the zooms

move within the sample. When drift correction based on intermediate super-resolution reconstructions is applied, a frame interval should be chosen in such a way that the images can be correctly correlated and drift can be detected (*see* **Note 9**).

5. An example of a successful super-resolution reconstruction of actin, imaged with either GFP or Alexa647 coupled to lifeAct is shown in Fig. 2.

4 Notes

1. The amino acid sequence of the **lifeAct**-cysteine-***PreScission-Site***-GFP-6×His construct is
MGVADLIKKFESISKEEGSGS**C**EF***LEVLFQGP***VSKGEEL
FTGVVPILVELDGDVNGHKFSVSGEGEGDATYGKLTLK
FICTTGKLPVPWPTLVTTLTYGVQCFSRYPDHMKQHDF
FKSAMPEGYVQERTIFFKDDGNYKTRAEVKFEGDTLVRI
ELKGIDFKEDGNILGHKLEYNYNSHNVYIMADKQKNGI

KVNFKIRHNIEDGSVQLADHYQQNTPIGDGPVLLPDNH
YLSTQSKLSKDPNEKRDHMVLLEFVTAAGITLGMDELYK
LEHHHHHH

2. Identifying cells of interest. Because low concentrations of lifeAct do not provide a full overview of the cellular structures, a fill or other cellular marker can be expressed to identify cells of interest.
3. Optimizing protein yields.
   (a) A greenish bacterial pellet usually indicates sufficient expression.
   (b) During each step samples for SDS page can be taken to determine the presence of recombinant protein.
   (c) Release of soluble protein after lysis can be increased by the addition of small amounts of lysozyme to weaken the bacterial cell wall.
   (d) Overall low soluble protein levels can occur because the recombinant lifeAct can enter into inclusions bodies at too high concentrations. This can be prevented by reducing induction time to only a few hours at 20 °C. In addition, DTT concentration can be increased to prevent disulfide-bond formation after lysis.
4. Alternative construct for fluorescent protein imaging only. When lifeAct is only used conjugated to GFP or other fluorescent proteins, removal of the cysteine and PreScission site could result in higher solubility and protein yields.
5. In case of low labeling efficiency of lifeAct-Cysteine:
   (a) Measure the amount of labeled lifeAct by BCA assay and the concentration of labeled lifeAct as described in Subheading 3.4. When the protein concentration is much higher than the concentration of the fluorophore, the sample is most likely unsaturated due to an inefficient maleimide–thiol reaction or because too little dye was added during the reaction. In the latter case, repeat the purification with an increased dye concentration. The fluorophore to lifeAct-cysteine ratio should be 10–20.
   (b) In case of poor reaction efficiency, also check the pH of the buffers. Furthermore, make sure that DTT is washed from the solution and that TCEP exceeds the protein concentration approximately tenfold to reduce unwanted disulfide bond formation of the available cysteines.
6. Alternative protocol for multicolor super resolution:
   (a) Alternative to the protocol described in Subheading 3.4 an extraction and fixation protocol more optimal for co-staining with microtubules can be used. In Short: pre-

extract in 0.25% glutaraldehyde + 0.3% Triton-X in PEM80 for 1 min (37 °C). Replace pre-extraction with 4% PFA in PEM80 (37 °C) for 7 min. Proceed with washing as described in Subheading 3.4 and add an extra permeabilization step of 0.25% Triton-X in d-PBS for 8 min followed by three more washes and blocking. Use primary labeled antibodies or nanobodies against tubulin to speed up the staining process [19].

(b) Secondary antibodies can be labeled with a variety of functionalized probes. When super-resolution imaging of actin by lifeAct needs to be combined with dSTORM super-resolution imaging of the second structure, Alexa647 is the best label to be used on the secondary antibody. Alexa647 has rapid blinking properties in PBS supplemented with glucose oxygen scavenger [25]. LifeAct-based protein-PAINT is compatible with this buffer.

7. The rapid blinking properties make Alexa647 extremely suitable for dSTORM. However, when lifeAct-Cysteine is used for PAINT-like super resolution through transient binding a more stable fluorophore is required. Labeling lifeAct-Cysteine with other organic dyes might result in a higher photon yield. Alternatively, addition of methylviologen (MV) and ascorbic acid (AA) in the imaging buffer will stabilize Alexa647 significantly [29, 30]. Concentrations of MV and AA can be varied between 50 μM and 1 mM to optimize photon yield and binding properties.
8. Cell morphology and structures appear to be affected after fixation. Handle samples carefully. Samples are very fragile during extraction and fixation. Always pipet at the sides of the dish and not directly on the sample because sheer stress can perturb the cell integrity even when fixed. Take extra care while handling samples that are sensitive to fixation techniques like neurons and thick samples.
9. Super-resolution reconstruction is unclear:
   (a) SMLM relies on the localizations of truly individual fluorophores. Too little localizations will result in a dotty image that can be enhanced by an increase of the pixel size. This will increase the amount of localizations per pixels. However, labeling density can also be too high. When two fluorophores emit light too close together the PSFs will obscure each other and result in mislocalization and poor localization errors. False and poorly localized detections will result in a loss of details.
   (b) Adjust drift interval and other parameters of drift correction. Incorrect drift correction can be clearly visible as a jumped image but sometimes also more subtle as a blurry reconstruction.

References

1. Arnold DB, Gallo G (2014) Structure meets function: actin filaments and myosin motors in the axon. J Neurochem 129(2):213–220. doi:10.1111/jnc.12503
2. Kapitein LC, Schlager MA, Kuijpers M, Wulf PS, van Spronsen M, MacKintosh FC, Hoogenraad CC (2010) Mixed microtubules steer dynein-driven cargo transport into dendrites. Curr Biol 20(4):290–299. doi:10.1016/j.cub.2009.12.052
3. Vale RD (2003) The molecular motor toolbox for intracellular transport. Cell 112(4):467–480
4. Crawley SW, Mooseker MS, Tyska MJ (2014) Shaping the intestinal brush border. J Cell Biol 207(4):441–451. doi:10.1083/jcb.201407015
5. Kapitein LC, Hoogenraad CC (2015) Building the neuronal microtubule cytoskeleton. Neuron 87(3):492–506. doi:10.1016/j.neuron.2015.05.046
6. Kapitein LC, van Bergeijk P, Lipka J, Keijzer N, Wulf PS, Katrukha EA, Akhmanova A, Hoogenraad CC (2013) Myosin-V opposes microtubule-based cargo transport and drives directional motility on cortical actin. Curr Biol 23(9):828–834. doi:10.1016/j.cub.2013.03.068
7. Watanabe K, Al-Bassam S, Miyazaki Y, Wandless TJ, Webster P, Arnold DB (2012) Networks of polarized actin filaments in the axon initial segment provide a mechanism for sorting axonal and dendritic proteins. Cell Rep 2(6):1546–1553. doi:10.1016/j.celrep.2012.11.015
8. Hell SW (2007) Far-field optical nanoscopy. Science 316(5828):1153–1158. doi:10.1126/science.1137395
9. Huang B, Babcock H, Zhuang X (2010) Breaking the diffraction barrier: super-resolution imaging of cells. Cell 143(7):1047–1058. doi:10.1016/j.cell.2010.12.002
10. Rust MJ, Bates M, Zhuang X (2006) Sub-diffraction-limit imaging by stochastic optical reconstruction microscopy (STORM). Nat Methods 3(10):793–795. doi:10.1038/nmeth929
11. Betzig E, Patterson GH, Sougrat R, Lindwasser OW, Olenych S, Bonifacino JS, Davidson MW, Lippincott-Schwartz J, Hess HF (2006) Imaging intracellular fluorescent proteins at nanometer resolution. Science 313(5793):1642–1645. doi:10.1126/science.1127344
12. Heilemann M, van de Linde S, Schuttpelz M, Kasper R, Seefeldt B, Mukherjee A, Tinnefeld P, Sauer M (2008) Subdiffraction-resolution fluorescence imaging with conventional fluorescent probes. Angew Chem 47(33):6172–6176. doi:10.1002/anie.200802376
13. Folling J, Bossi M, Bock H, Medda R, Wurm CA, Hein B, Jakobs S, Eggeling C, Hell SW (2008) Fluorescence nanoscopy by ground-state depletion and single-molecule return. Nat Methods 5(11):943–945. doi:10.1038/nmeth.1257
14. Jungmann R, Avendano MS, Woehrstein JB, Dai M, Shih WM, Yin P (2014) Multiplexed 3D cellular super-resolution imaging with DNA-PAINT and Exchange-PAINT. Nat Methods 11(3):313–318. doi:10.1038/nmeth.2835
15. Xu K, Zhong G, Zhuang X (2013) Actin, spectrin, and associated proteins form a periodic cytoskeletal structure in axons. Science 339(6118):452–456. doi:10.1126/science.1232251
16. Molle J, Raab M, Holzmeister S, Schmitt-Monreal D, Grohmann D, He Z, Tinnefeld P (2016) Superresolution microscopy with transient binding. Curr Opin Biotechnol 39:8–16. doi:10.1016/j.copbio.2015.12.009
17. Kiuchi T, Higuchi M, Takamura A, Maruoka M, Watanabe N (2015) Multitarget super-resolution microscopy with high-density labeling by exchangeable probes. Nat Methods 12(8):743–746. doi:10.1038/nmeth.3466
18. Riedl J, Crevenna AH, Kessenbrock K, JH Y, Neukirchen D, Bista M, Bradke F, Jenne D, Holak TA, Werb Z, Sixt M, Wedlich-Soldner R (2008) Lifeact: a versatile marker to visualize F-actin. Nat Methods 5(7):605–607. doi:10.1038/nmeth.1220
19. Mikhaylova M, Cloin BM, Finan K, van den Berg R, Teeuw J, Kijanka MM, Sokolowski M, Katrukha EA, Maidorn M, Opazo F, Moutel S, Vantard M, Perez F, van Bergen en Henegouwen PM, Hoogenraad CC, Ewers H, Kapitein LC (2015) Resolving bundled microtubules using anti-tubulin nanobodies. Nat Commun 6:7933. doi:10.1038/ncomms8933
20. Henriques R, Lelek M, Fornasiero EF, Valtorta F, Zimmer C, Mhlanga MM (2010) QuickPALM: 3D real-time photoactivation nanoscopy image processing in ImageJ. Nat Methods 7(5):339–340. doi:10.1038/nmeth0510-339
21. Ovesny M, Krizek P, Borkovec J, Svindrych Z, Hagen GM (2014) ThunderSTORM: a comprehensive ImageJ plug-in for PALM and STORM data analysis and super-resolution

imaging. Bioinformatics 30(16):2389–2390. doi:10.1093/bioinformatics/btu202

22. Wolter S, Loschberger A, Holm T, Aufmkolk S, Dabauvalle MC, van de Linde S, Sauer M (2012) rapidSTORM: accurate, fast open-source software for localization microscopy. Nat Methods 9(11):1040–1041. doi:10.1038/nmeth.2224
23. Edelstein A, Amodaj N, Hoover K, Vale R, Stuurman N (2010) Computer control of microscopes using microManager. Curr Protoc Mol Biol Chapter 14:Unit14 20. doi:10.1002/0471142727.mb1420s92
24. Olson BJ, Markwell J (2007) Assays for determination of protein concentration. Curr Protoc Protein Sci Chapter 3:Unit 3 4. doi:10.1002/0471140864.ps0304s48
25. Yau KW, van Beuningen SF, Cunha-Ferreira I, Cloin BM, van Battum EY, Will L, Schatzle P, Tas RP, van Krugten J, Katrukha EA, Jiang K, Wulf PS, Mikhaylova M, Harterink M, Pasterkamp RJ, Akhmanova A, Kapitein LC, Hoogenraad CC (2014) Microtubule minus-end binding protein CAMSAP2 controls axon specification and dendrite development. Neuron 82(5):1058–1073. doi:10.1016/j.neuron.2014.04.019
26. Leyton-Puig D, Kedziora KM, Isogai T, van den Broek B, Jalink K, Innocenti M (2016) PFA fixation enables artifact-free super-resolution imaging of the actin cytoskeleton and associated proteins. Biol Open 5(7):1001–1009. doi:10.1242/bio.019570
27. Lee SH, Baday M, Tjioe M, Simonson PD, Zhang R, Cai E, Selvin PR (2012) Using fixed fiduciary markers for stage drift correction. Opt Express 20(11):12177–12183. doi:10.1364/OE.20.012177
28. Mlodzianoski MJ, Schreiner JM, Callahan SP, Smolkova K, Dlaskova A, Santorova J, Jezek P, Bewersdorf J (2011) Sample drift correction in 3D fluorescence photoactivation localization microscopy. Opt Express 19(16):15009–15019. doi:10.1364/OE.19.015009
29. Vaughan JC, Jia S, Zhuang X (2012) Ultrabright photoactivatable fluorophores created by reductive caging. Nat Methods 9(12):1181–1184. doi:10.1038/nmeth.2214
30. Vogelsang J, Kasper R, Steinhauer C, Person B, Heilemann M, Sauer M, Tinnefeld P (2008) A reducing and oxidizing system minimizes photobleaching and blinking of fluorescent dyes. Angew Chem 47(29):5465–5469. doi:10.1002/anie.200801518

Chapter 10

Fluorescence Microscopy of Nanochannel-Confined DNA

Fredrik Westerlund, Fredrik Persson, Joachim Fritzsche, Jason P. Beech, and Jonas O. Tegenfeldt

Abstract

Stretching of DNA in nanoscale confinement allows for several important studies. The genetic contents of the DNA can be visualized on the single DNA molecule level and both the polymer physics of confined DNA and also DNA/protein and other DNA/DNA-binding molecule interactions can be explored. This chapter describes the basic steps to fabricate the nanostructures, perform the experiments and analyze the data.

Key words DNA, Nanochannels, Single molecule, Fluorescence

1 Introduction

Single DNA molecules stretch spontaneously in nanochannels due to the confinement. The stretching is entirely passive and thus no active application of force is required apart from the driving force to move the DNA into the nanochannel. Therefore, in contrast to flow stretching or stretching using optical tweezers, no chemically attached anchor groups are needed. The first study of DNA in nanochannels was presented in 2004 [1] and since then the field has been growing vastly with applications in several different areas of research.

There are a few important parameters to consider when dealing with confined DNA:

1. Contour length—total length of the DNA backbone, here denoted L.
2. Persistence length—length-scale over which the DNA can be considered a rigid rod, here denoted P.
3. Effective width—a measure of the width of the DNA, composed of the physical width of the DNA (~2 nm) and an electrostatic contribution [2]. The effective width is here denoted w_{eff}.

Erwin J.G. Peterman (ed.), *Single Molecule Analysis: Methods and Protocols*, Methods in Molecular Biology, vol. 1665, DOI 10.1007/978-1-4939-7271-5_10,

When a long DNA molecule is free in aqueous solution it forms a coil, often characterized by its radius of gyration (R_G). When confined in a tube-like channel with an average cross-sectional diameter D_{av} smaller than R_G, the DNA stretches out along the length of the channel. As long as the diameter of the channel is larger than P, the DNA can backfold and adopt an elongated coiled up conformation. In this regime, commonly denoted the deGennes regime, the DNA can be modeled as a series of non-interacting blobs, where the DNA inside each blob behaves as it would in free solution. This leads to an extension, r, of the DNA along the channel of [3]:

$$\frac{r}{L} \propto \left(\frac{w_{\text{eff}} P}{D_{\text{av}}^2} \right)^{1/3}$$

Fabricated nanochannels are more commonly rectangular in cross section. Here, D_{av}^2, the parameter relating to the diameter of the tube, can be replaced by the geometric average of the height, D_1, and the width, D_2, of the rectangular channel, $D_{av}^2 = D_1 D_2$ for $D_1 \sim D_2$ [4]. For situations where $D < P$ the DNA molecule cannot fold back on itself and its extension can be described by a model developed by Odijk [5]. This is relevant for DNA in very small channels, but also in studies of protein–DNA interactions where the resulting protein–DNA complex has an increased persistence length [6]. The extension, r, of the DNA along the channel is here ($B \sim 0.091$ [7]):

$$\frac{r}{L} = 1 - B \left[\left(\frac{D_1}{P} \right)^{2/3} + \left(\frac{D_2}{P} \right)^{2/3} \right]$$

From an experimental point of view it is important to note that in both models r scales linearly with L. This means that a position along the stretched DNA can be directly related to a position along the contour of the DNA, i.e. the sequence, with a resolution primarily determined by the degree of stretching and the optics of the microscope. While the simple expressions above give adequate accuracy for designing a nanochannel device, recent improved understanding makes it possible to predict the behavior of the confined DNA with much better accuracy [8, 9]. Note however that not only the geometry of the confinement but also the buffer conditions have a strong influence on the behavior of the DNA. For further insight regarding the polymer physics of confined DNA the authors recommend refs. [10–12]. There is also a vast literature on general polymer theory, notably the books by deGennes [13], Doi and Edwards [14], and Rubinstein and Colby [15].

The first experimental studies of DNA in nanochannels were devoted to studies of DNA conformation and dynamics [1, 11, 16, 17], and to single-molecule studies of DNA–protein interactions [18, 19]. Since these first experiments the field has expanded in three main directions. Studies of the polymer physics of DNA have provided novel, more accurate theories about how DNA behaves in confinement [9, 20–22]. DNA–protein interactions have continued to receive significant attention with a main focus on proteins that change the physical properties of DNA [23]. Examples include RecA that forms a stiff filament on DNA [6], H-NS that compacts DNA [24] and T4 ligase that forms transient DNA links [25]. Optical DNA mapping is the third main direction of studies of DNA in nanochannels that has increased vastly during the last years [26, 27]. Optical DNA mapping has been commercialized by BioNanoGenomics, and the goal of this technique is to visualize the structure of the genetic sequence of large (several hundred kilobasepairs) single DNA molecules. To do this, the DNA has to be sequence-specifically labeled and this is done in two main different ways. One way is to use enzymes to attach fluorophores at specific sequences [28, 29], while the second relies solely on non-covalent interactions between DNA and fluorophores as described below [30, 31]. Finally, in analogy to standard gel electrophoresis, the nanochannels can be used to merely measure the length of DNA fragments. This may be used to size plasmids [32], and in combination with restriction enzymes for restriction mapping [19].

2 Materials

2.1 Fabrication of Chips

There are a multitude of ways to fabricate nanostructured chips depending on the facilities and equipment available (*see* **Note 1**) [33]. We present two fabrication schemes here, one based on fused silica and one on silicon.

For fabrication in fused silica the following is needed:

1. Fused silica wafers. (Available from Hoya Corporation).
2. 110 μm thick fused silica coverslips for sealing of the chips. The thickness is optimized for compatibility with oil immersion objectives. (Available from Valley Design.)
3. Access to cleanroom equipment for photo (UV) and electron-beam (e-beam) lithography and reactive ion etching (RIE) as well as standard resists (e.g. AZ (photo lithography) and ZEP (e-beam lithography) resists) and chemicals from any large supplier.

For fabrication in silicon the following is needed:

1. Silicon wafers. (Available from SiMat).

2. 170 μm-thick borosilicate coverslips for sealing of the chips. The thickness is optimized for compatibility with oil immersion objectives. (Available from Valley Design.)
3. Access to cleanroom equipment for photo (UV) and electron-beam (e-beam) lithography and reactive ion etching (RIE) as well as standard resists (e.g. AZ (photo lithography) and ZEP (e-beam lithography) resists) and chemicals from any large supplier.

2.2 Chemicals

Two important additives are β-mercaptoethanol (BME) (*see* **Note 2**) for suppression of photobleaching and polyvinylpyrrolidone (PVP) (*see* **Note 3**) for suppression of electroosmosis when using electrophoresis. Note that genomic length DNA should be handled with wide-orifice pipettes to avoid shear-induced breakage (provided by e.g. Molecular Bioproducts).

2.3 Buffers

2.3.1 Buffer for DNA Experiments

Tris-Borate-EDTA (TBE) is a standard buffer for DNA studies, especially for electrophoresis due to its low conductivity that ensures a low degree of Joule heating (as the borate is a suspected CMR (carcinogenic, mutagenic or toxic for reproduction), TAE is an alternative that is often used, *see* **Note 4**). TBE buffer consists of:

1. *Tris (tris(hydroxymethyl)aminomethane)*: Buffering agent for slightly basic conditions (pH = 7.9).
2. *Boric acid*: Weak acid that improves the buffering capabilities of Tris.
3. *EDTA (Ethylenediaminetetraacetic acid)*: Chelating agent that scavenges multivalent metal ions, in particular magnesium (Mg^{2+}). Since multivalent metal ions are common cofactors for many enzymes, like nucleases that digest DNA, the removal of these ions will prevent enzymatic degradation of DNA.

2.3.2 Protocol for Preparing 1 L 5× TBE Buffer

1. Prepare 0.5 L of 0.5 M EDTA solution by weighing out 93.06 g of disodium EDTA (372.24 g/mol) and adding it to 350 mL of water (*see* **Note 5**). EDTA will not go into solution until pH is adjusted to 8.0. Add NaOH pellets to the solution, one by one, while stirring vigorously on a magnetic stir plate. Monitor solution pH using a digital pH meter so as not to overshoot. Bring the final solution volume to 0.5 L with water.
2. Prepare a 5× TBE solution by adding 20 mL of 0.5 M EDTA solution from **item 1**, 54 g of Tris (121.1 g/mol) and 27.5 g of boric acid (61.8 g/mol) to 800 mL of water. Then adjust pH to 8.0–8.5 by adding HCl while monitoring pH. Bring final solution volume to 1 L with water.
3. Autoclave buffer.

The stock buffer can be diluted to any arbitrary ionic strength. For the following steps, 0.5× TBE buffer is used as an example. Note that the stretching of confined DNA varies significantly with ionic strength [34] and for particular applications, such as DNA mapping, the DNA should be stretched out as much as possible and hence a low ionic strength buffer is used.

4. Dilute the 5× TBE buffer ten times. Then use a syringe with a 0.2 μm filter to aliquot approximately 1.2 mL of buffer into a large number of 1.5 mL microcentrifuge tubes. Store these tubes in the refrigerator for future use. Degas the tubes at least 2 h prior use. The final 0.5× TBE solution contains 44.6 mM Tris, 44.5 mM boric acid, and 1 mM EDTA and has an ionic strength of approximately 15 mM at pH 8.5.

2.3.3 Protocol for Staining 1 mL of 10 μg/mL DNA at a Dye:bp Ratio of 1:10 in 0.5× TBE Buffer

Always use wide-orifice pipette tips to handle DNA solutions.

1. Create 250 μL of 50 μg/mL solution of DNA in 0.5× TBE (*see* **Note 6**).
2. Pipette 769 μL of 0.5× TBE buffer into a separate 1.5 mL microcentrifuge tube.
3. Pipette 47.5 μL of 0.5× TBE buffer into a 0.65 mL tube. Add 2.5 μL of YOYO-1 from the stock solution (1 mM). This creates a 50 μM dye solution. Work in low light from now on to avoid bleaching of the dye.
4. Pipette 31 μL of the 50 μM dye solution from **item 3** into the buffer-filled tube from **item 2**. This creates a solution with a dye concentration of 1.55 μM. Vortex and centrifuge the solution to evenly distribute the dye.
5. Pipette 200 μL of DNA from **item 1** into the buffer filled tube from **item 4**. Do *NOT* ever vortex or centrifuge solutions containing DNA—that will fragment the DNA. In order to mix the DNA, use a wide-orifice tip and gently pipette a part of the solution a minimum of three times while evenly distributing the ejected solution throughout the tube.
6. To evenly distribute the dye throughout the population of molecules, wrap the tube in aluminum foil and heat the solution to 50 °C for 3 h and then store at 4 °C. An alternative for efficient equilibration is to prepare the samples at high ionic strength (5× TBE), where equilibration is fast, and subsequently dilute the sample to the desired ionic strength [35].

To obtain an optical map of the DNA or to study DNA–protein interactions, more intricate sample preparations are needed (*see* **Notes 7** and **8**).

1. Mix 485 μL of degassed buffer with 15 μL of BME (*see* **Note 9**) in a 0.65 mL microcentrifuge tube. BME will collect at the

Table 1
Selection of commercially available DNA molecules

Name	Length (kbp)	Supplier
λ-DNA	48.5	New England Biolabs
λ-DNA concatamers (in gel)	$48.5 \times n$ ($n = 1 \sim 20$)	New England Biolabs
Yeast DNA (in gel plug)	~10–500	New England Biolabs
T4GT7-DNA	166	Nippon Gene
Charomid 9 (circular)	19.7–42.2	Nippon Gene
T7	39.9	Yorkshire Bioscience

2.3.4 Protocol for Preparing 400 μL Loading Buffer and 100 μL DNA in Loading Buffer

bottom of the tube, so mixing by pipetting and/or vortexing is essential at this stage. Note that vortexing should *not* be performed after the DNA has been added. Below we will refer to this as the *loading buffer*.

2. Pipette 95 μL of the loading buffer into a 0.65 mL microcentrifuge tube.
3. Add 5 μL of the 10 μg/mL solution of stained DNA using wide-orifice pipettes. Mix the solution very gently with the pipette. Work in low light to protect the DNA, and wrap the tube in aluminum foil once the DNA-solution is made. Below we will refer to this as the *DNA loading sample*.

2.4 DNA Samples

In order to characterize the experimental techniques, it is necessary to use monodisperse DNA. There are a few different purified monodisperse DNA solutions commercially available, and using restriction enzymes different size distributions can be obtained. Table 1 lists a few common examples of commercially available, purified and monodisperse DNA.

2.5 Fluorescence Microscopy

For a thorough introduction to microscopy the authors recommend the MicroscopyU website from Nikon (www.microscopyu.com), especially the tutorial section on fluorescence microscopy (www.microscopyu.com/articles/fluorescence/index.html), as well as ref. [36].

Due to the low light levels and the risk of photodamaging the DNA, the optical system must be designed to maximize photon detection probability and signal-to-noise ratio. Key considerations are:

1. High-quality filters with high transmission (~90%) in the wavelength region relevant for the dye used and low transmission in the rest of the spectrum, corresponding to a high optical density (OD > 5).

2. Objectives (40–100×) with high numerical apertures (NA). Oil immersion objectives readily achieve NA of 1.4 and are perfectly suited for devices sealed with standard coverslips with a thickness of 170 μm. To combine a good NA and a large WD, a 60× water immersion objective with an NA of 1.0 and a WD of 2 mm, originally designed for electrophysiology by Nikon, can be used. This provides sufficient clearance in situations when normal cover glass cannot be used.
3. A detector with high quantum yield (QY) and low noise. Electron-multiplying CCDs (EMCCD) have an integrated noise-less amplification on the CCD chip. As opposed to intensification technologies based on multichannel plates, the EMCCD is not easily damaged by excessive light levels. The EMCCD can be back-thinned to allow for a QY approaching 90–95% over the visible spectrum. Less expensive EMCCDs are not back-thinned and thus suffer from QY that are roughly a factor of 2 lower. To minimize thermal noise the EMCCD is normally cooled to −50 to −100 °C in modern cameras. EMCCD cameras are available from e.g. Andor, Photometrics, and Hamamatsu.

See **Notes 10** and **11** for examples of additional optical tools and technologies.

2.6 Addressing the Chip

The two most common ways of manipulating DNA in fluidic systems are by electrophoresis or pressure-driven fluid flow. In order to have both these capabilities, a chip holder with both electrical and air pressure connections to internal reservoirs can be used [30]. The holder can be fabricated in Lucite® (PMMA), allowing the sample to be illuminated from the top and making it easy to detect bubbles trapped in the reservoirs in the chip holder. However, Lucite® has poor resistance to solvents, as it swells and dissolves easily. For experiments involving more aggressive solvents, a holder made in PEEK (PolyEtherEtherKetone) is more suitable, but then the holder is opaque.

An updated holder design is shown in Fig. 1. It has a modular design where the chip is glued to a plastic frame that is readily mounted in the stage adapater. This way the integrity of the chip is better protected as compared to previous designs.

Pumps are needed for controlling DNA using pressure-driven flow. Standard diaphragm pumps capable of producing pressures of up to 5 Bar are sufficient in most cases (available from VWR). When using pressure-driven flow the pressure is routed through a network of valves giving the possibility of applying pressures to selected reservoirs while others are kept at ambient pressure. To control the pressure, a needle valve can be used as a leak valve, which enables the pressure to be controlled with an accuracy of down to ±2 mBar. Accessories such as for example manifolds, needle valves,

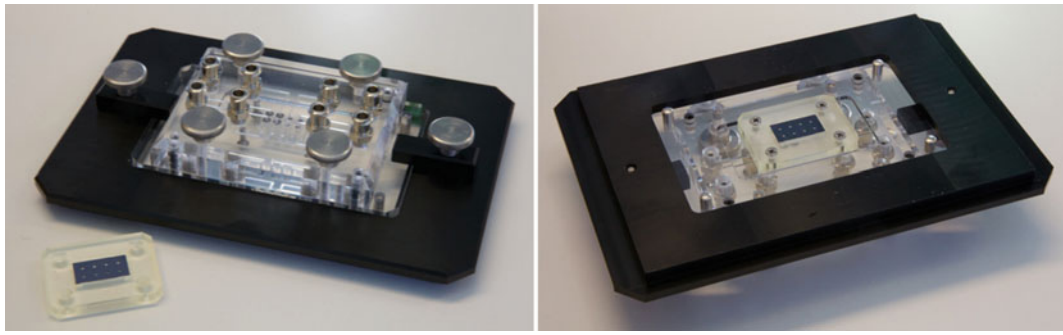

Fig. 1 Example of chuck for mounting samples. Modular design with separate parts for frame and fluidics. The device chips are mounted in plastic holders for easy handling. Eight reservoirs linked by o-rings to the fluidic access holes on the chip. Reservoirs are individually addressable by pressure and electrical connections. (*LEFT*) Top view. Device chip is not mounted. (*RIGHT*) Bottom view with mounted device chip

and tubing to direct and control the pressure are available from Cole Parmer. Note that by using nitrogen as a driving gas, the oxygen in the sample buffer is depleted and photobleaching and photodamage is minimized.

When using electrophoresis to control the DNA, a power supply and electrodes are needed. Platinum wires dipped into the DNA solution in the reservoir are often sufficient as electrodes. The electrophoretic mobility of DNA is on the order of 1 μm/s per V/cm.

2.7 Data Analysis

Commonly used software packages for data analysis are:

1. ImageJ—A Java™-based freeware image processing and analysis software developed at the National Institutes of Health, USA (http://rsbweb.nih.gov/ij/). The software benefits from the extensive use of open-source plugins developed by users. Plugins from the ImageJ Cookbook are recommended (https://imagej.net/Cookbook).
2. MatLab—A common high-level technical computing language from The Mathworks™.
3. FreeMat—Open-source freeware available at http://freemat.sourceforge.net/
4. GNU Octave—Freeware available at http://www.gnu.org/software/octave/

Data analysis in optical DNA mapping is more intricate than simply determining the sizes of DNA molecules (*see* **Note 12**).

3 Methods

A careful design of the DNA-visualization device is crucial for its user-friendliness. Typically, two or four U-shaped inlet channels

3.1 Design and Fabrication of Chips

3.1.1 Design

(50 μm × 1 μm, each connected to two reservoirs) for efficient fluid transport are combined with nanoscale channels for stretching of the DNA. In this way the sample can be transported quickly through the large channels to the entrance of the nanochannels by applying a driving force across the microchannel, enabling rapid exchange of buffer. Using nanochannels of dimensions 100 nm × 100 nm ensures both a relatively high degree of DNA stretching (typically~60%) without encountering many of the problems that appear when the channel size approaches the persistence length of DNA (~50 nm). The degree of stretching can be tuned by altering the buffer conditions [34], such as the ionic strength.

See **Notes 13–15** for examples on how to include extra functionalities on the chip.

3.1.2 Fabrication

When fabricating nanofluidic channels for optical observation of stretched DNA, there are some requirements to consider:

1. The channels should be sealed.
2. At least one side (substrate or lid) must be optically transparent.
3. The surface of the channels should be negatively charged with a minimal roughness to prevent sticking and entanglement of the DNA.
4. The material used should be hydrophilic to allow for easy wetting of the channels.

In the following section, two commonly used fabrication processes based on fused silica and on composites of silicon and borosilicate glass are outlined. Note that to be compatible with electrophoresis the devices should be made in glass or silica, or, if silicon is used, that the surface oxide is of high enough quality such that no pinholes are formed.

A full-scale cleanroom, with spinners for resist deposition, mask aligners for exposure of micron scale patterns and an electron-beam writer for definition of nanoscale structures, is required for both fabrication schemes (*see* **Note 16**). Reactive-ion etchers are used for etching channels with straight walls.

In order to align the nanostructures and the microchannels it is useful to first define alignment marks in the wafer periphery. This can be done by either etching or depositing metals on the wafer (*see* **Note 17**), the latter described below. It is assumed that the cleanroom used has its own standard processes for the following steps.

3.1.3 Definition of Alignment Marks

Fused silica:

1. Treat the fused silica wafers with HMDS (hexamethyldisilazane) to increase resist adhesion.

2. Spincoat and bake a combination of resists used for liftoff, e.g. LOR/AZ or other similar sandwich constructs, to enable a pattern with an undercut.
3. Expose and develop the resist to create the undercut structure.
4. Run a low-power oxygen descum plasma to remove remaining resist residues.
5. Evaporate a 5 nm Cr (or Ti) adhesion layer and subsequently a 50–80 nm thick Au layer.
6. Strip the resist using a chemical stripper, e.g. Microposit Remover 1165 or acetone (*see* **Note 18**).

Silicon–borosilicate glass:

1. Thermally oxidize the surfaces of the Si-wafers to a thickness greater than the intended depth of the microchannels in order to accommodate both nanochannels and microchannels in the oxide layer.
2. See the processing steps (**steps 1–6**) above for the case of fused silica.

3.1.4 Definition of Nanochannels

Fused silica:

1. Treat the fused silica wafers with HMDS to increase resist adhesion.
2. Spincoat and bake a 150–250 nm thick layer of ZEP520A e-beam resist. ZEP is chosen because of its good dry-etch resistance. Other resists can be used but they often require deposition of an additional metallic etch mask.
3. Thermally evaporate 15 nm Al on top as a discharge layer. (This is only needed when working with isolating substrates such as fused silica.)
4. Expose the resist (exposure dose approximately 280 $\mu C/cm^2$ at 100 kV).
5. Remove the Al layer using e.g. MF322 developer.
6. Develop the resist using e.g. ZED N50 developer.
7. Run a low-power oxygen descum plasma in order to remove remaining resist residues.
8. Etch the nanochannels into the fused silica using RIE with CHF_3/CF_4 chemistry.
9. Strip the resist using a chemical stripper, e.g. Microposit Remover 1165.

Silicon–borosilicate glass: See the processing steps (**steps 1**, **2**, **4**, **6–9**) above for the case of fused silica. Note that application and removal of a discharge layer (**steps 3** and **5**, respectively) are not needed when processing conductive substrates.

3.1.5 Definition of Microchannels (Fused Silica and Silicon–Borosilicate Glass)

1. Treat the wafers with HMDS to increase resist adhesion.
2. Spincoat and bake a 2–5 μm thick layer of photoresist, e.g. an AZ resist, that has relatively high etch resistance.
3. Expose and develop the resist.
4. Run a low-power oxygen descum plasma in order to remove remaining resist residues.
5. Etch the microchannels (approximately 1 μm deep) using RIE with CHF_3/CF_4 chemistry.
6. Strip the resist using a chemical stripper, e.g. Microposit Remover 1165 or acetone.

3.1.6 Processing of Access Holes

Fused silica: There is a multitude of ways of producing access holes through a wafer (*see* **Note 19**). Here we describe a setup based on powder blasting.

1. Spincoat at least 5 μm photoresist on both sides of the wafer.
2. Cover the backside (i.e. the non-structured side) with an adhesive plastic film, e.g. 70 μm thick Nitto SWT 20 film (*see* **Note 20**).
3. Make holes through the film over the reservoir structures using a scalpel or e.g. laser ablation.
4. Powder blast using 50–110 μm-sized Al_2O_3 particles from the backside of the wafer (i.e. the non-structured side). A small powder-blasting tool and the powder can be obtained from Danville Materials.
5. Remove the film, strip the resist in a chemical stripper and/or acetone and carefully clean the wafers in an ultrasonic bath.

Silicon–borosilicate glass:

1. Deposit 150 nm Al on the processing side of the silicon wafer by either sputtering or evaporation.
2. Spincoat and bake a 2–5 μm thick layer of photoresist, e.g. an AZ resist.
3. Expose and develop the resist.
4. Run a low-power oxygen descum plasma in order to remove remaining resist residues.
5. Remove the Al-layer in the openings of the resist with Al-wet etch, ensuring that the used resist is compatible with, e.g. 80% H_3PO_4 + 5% HNO_3 + 5% HAc + 10% H_2O.
6. Etch through the Si-wafer with a deep reactive-ion etch (Bosch) process. Note that this processing step will typically consume the applied photoresist and thus relies on the Al-layer as a hard mask.
7. Remove the Al-mask with standard Al wet etch.

Table 2
Two fusion-bonding protocols for fused silica (*see* Note 22)

RCA-based		Piranha-based	
Chemical	**Time**	**Chemical**	**Time**
RCA2 at 80 °C (1:1:5 HCl:H_2O_2:H_2O)	10 min	Piranha (1:3 H_2O_2:H_2SO_4)	20 min
Rinse carefully with DI water for 5 min			
RCA1 at 80 °C (1:1:5 NH_4OH:H_2O_2:H_2O)	10 min	Ammonium hydroxide (NH_4OH)	40 min
Rinse carefully with DI water for 5 min			
Blow dry in N_2			
Press together by hand to form a prebond			
Anneal at 1050 °C for at least 3 h (ramp temperature at approximately 300 °C/h for both heating and cooling)			

3.1.7 Sealing of the Chips

The last step in the production of the chips is sealing. This can be done in several different ways depending on the material of the chips (*see* **Note 21**). Fused silica can be bonded covalently via condensation of hydroxyl groups when two surfaces are brought together. Table 2 summarizes two standard ways of creating a high density of the necessary hydroxyl groups, involving thorough cleaning to remove organic residues and subsequent surface activation.

For the RCA-based method the hydrogen peroxide should be added after the mixture has reached the correct temperature to avoid disintegration of the hydrogen peroxide.

3.2 Chemicals

When studying single DNA molecules it is very important that the molecules are kept in a controlled environment and not subjected to reactive contaminants such as radicals or enzymes that damage or digest DNA. Some of these enzymes, such as endonucleases, are present on our skin in order to break down foreign DNA that we come in contact with. It is therefore crucial that gloves are worn at all times when handling DNA and that all tools and pipette tips that come in contact with either the buffer or the DNA samples have been autoclaved or sterilized in another way, e.g. by wiping them with ethanol.

3.2.1 Fluorescent Labeling of DNA

Dimeric cyanine dyes like YOYO®-1 (YOYO) (Invitrogen, Carlsbad, California, USA) are extensively used for imaging single DNA molecules due to their high binding affinity to DNA ($K_A = 10^{10}$–10^{12} M^{-1}) and a fluorescence enhancement upon binding to DNA of over 1000, which ensures a low fluorescence background from unbound dye molecules [37]. Figure 2 shows the

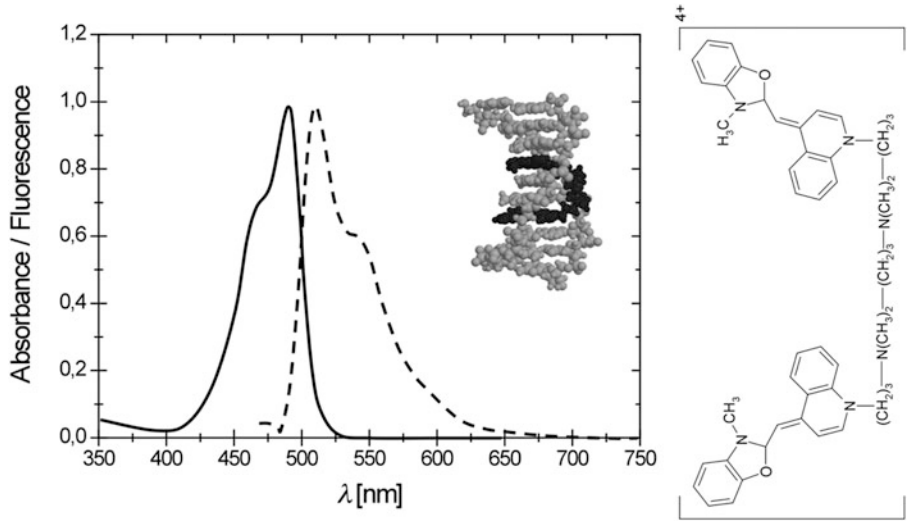

Fig. 2 (*LEFT*) Excitation (*solid*)/emission (*dashed*) spectra of YOYO®-1 bound to DNA. Adapted from data from Invitrogen. *Inset*: TOTO®-1 intercalating in DNA, visualized using the open-source viewer JMol. The structure (PDB ID: 108D) was determined by nuclear magnetic resonance [35]. (*RIGHT*) Chemical structure of YOYO®-1

absorption and emission spectra as well as the chemical structure of YOYO [38]. Staining of the DNA with intercalators affects the physical properties of the DNA. The effect on the persistence length of the DNA due to intercalation has been an area of controversy with a wide range of reported effects. Recently it has been concluded that the persistence length is unaffected [39]. The contour length of DNA is however increased by approximately 0.68 nm per intercalating YOYO molecule (one basepair (0.34 nm) per intercalation event) [40, 41] at moderate binding densities.

When staining the DNA it is important to know the resulting dye:bp ratio ([dye molecule]:[basepair]). The easiest way of calculating this is to use the molar concentrations of the dye and DNA, respectively. If the concentration of DNA is known in μg/mL it is easily converted using the average molar mass of one DNA basepair (bp), $M_{bp} = 618$ g/mol. The DNA concentration can also be determined by absorbance measurements, using the molar absorption coefficient for DNA at $\lambda = 260$ nm, $\epsilon_{260} = 13{,}200\ \text{cm}^{-1}\ \text{M}^{-1}$ (basepair) or 50 μg/mL for OD 1 (1 cm optical path length). Knowing the molar concentrations of the DNA and the dye, the dye:bp ratio is readily obtained. In the case of dimeric cyanine dyes, like YOYO, the dye concentration should not exceed a value corresponding to a dye:bp ratio of 1:5 in order to avoid crowding of dye on the DNA. It is important to note that the binding constant of YOYO decreases significantly at high ionic strength. This means that at higher ionic strengths, the amount of dye bound will not correspond to the amount of dye added [35].

3.3 Running Experiments (Loading of DNA)

Prior to mixing the loading buffer, the TBE buffer can be degassed in a vacuum chamber for 2 h in order to reduce the amount of dissolved air in the system and to avoid bubble formation in the channels. The degassing process can be shortened to about 10–20 min by ultrasonic agitation. If nitrogen is used to pressurize the system instead of air, the degassing can be shortened or even completely skipped. Fresh loading buffer should be prepared in conjunction with every experiment, since the BME degrades with time (*see* **Note 23**).

Use the loading buffer to wet the chip, either before mounting in the chuck or after. Placing droplets over the fluidic access holes is normally sufficient to wet the chip by capillary forces (*see* **Note 24**). Remaining air bubbles can be removed by applying a pressure across the channels. Using degassed buffer solution during experiments ensures that bubbles formed during the capillary wetting [42] are absorbed into the liquid and also prevents the DNA from degrading.

When the chip is properly wetted, the DNA loading sample is added to the desired reservoirs and loading buffer to the remaining reservoirs. For experiments on DNA–protein interactions it is important to passivate the nanochannels before running the experiments to avoid non-specific binding of the proteins to the channel walls (*see* **Note 25**).

The DNA can be moved through the chip by electrokinetic transport or pressure-driven flow. A pressure difference of approximately 100 mBar results in reasonable sample velocities when transporting the DNA in the micron-sized channels, from the inlet reservoirs to the nanostructures. Once the DNA molecules are in close proximity to the inlets of the nanochannels, the driving force is shifted so that it is applied across the nanochannel array instead. At this point a low driving pressure makes it possible to collect a desired amount of DNA at the entrance of the nanochannels due to the entropic barrier. The most convenient way to subsequently introduce DNA into the nanochannels is to pulse the pressure, switching rapidly between a low pressure and 1–3 Bar. When the DNA molecule of interest is in the nanochannel and in the field of view of the CCD, stacks of images of at least 200 frames are recorded (*see* **Note 26**). During the measurements the coordinates of at least two alignment marks on the chip as well as the stage coordinates for all the recorded stacks can be recorded. This allows for both rotational correction as well as accurate localization of the molecule within the fluidic network in the case of a more intricate design of the chip.

There are a few things to be aware of during image/data acquisition:

1. If one of the ends of the DNA molecule appears much brighter, it might have been folded while entering the nanochannel.

Given time (usually minutes) the end will unfold [43], else the molecule can be pushed out into the microchannels and re-injected into the nanochannels.

2. A small pressure offset when using pressure-driven flow can cause the molecule to not be in its equilibrium state while imaging.
3. Photonicking may cause the DNA to be cut into smaller pieces while imaging. However, the ordering of the fragments will not change since two pieces cannot diffuse past each other while confined in a nanochannel (although very short fragments can pass).
4. During long imaging periods, the molecules will most likely fade significantly in fluorescence intensity due to photobleaching, especially in the absence of BME.
5. The DNA present close to the nanochannels can suffer from some degree of photobleaching and photonicking during imaging of the DNA in nanochannels. Therefore, an important consideration is to make sure that the illuminated area does not extend beyond the region of interest, if necessary using the field aperture.
6. DNA molecules may become pinned at one or several points along their length due to interactions with the surface of the channel. Pinned molecules are straight forward to identify and exclude from analysis.

The techniques used to fabricate nanochannel chips are time-consuming and expensive. It is therefore of interest to clean and reuse devices if possible. This can be done without removing the chip from the holder. The basic idea is to thoroughly remove all of the running buffer and the sample from the entire chip and chip holder, replacing it with DI water. DI water should be flowed through the device at maximum pressure in various directions, while repeatedly replacing the solution in the reservoirs with clean DI water, until no sample can be seen. Illuminating the important areas of the chip with maximum power can help to break up/photo-bleach any stuck DNA or background fluorescence due to surface-adsorbed dye. Close attention to cleaning can make it possible to use chips for many experiments over several months.

3.4 Data Analysis

To extract essential parameters from the movies (or rather stacks of images) of DNA molecules confined in a nanofluidic structure, a simple pattern recognition and fitting script can be used [1] The key steps of the analysis are listed and explained below.

1. The position of the DNA molecule is detected. A region of interest (ROI) is created around the molecule and the rest of

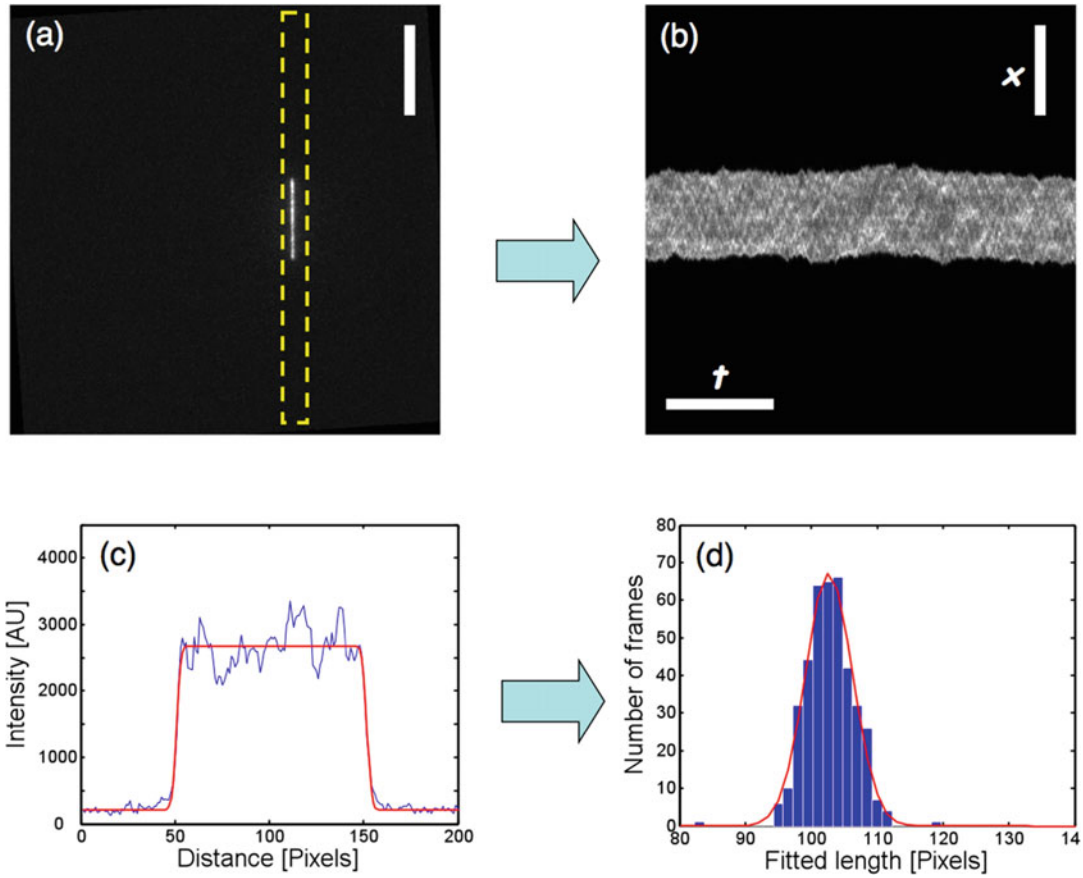

Fig. 3 (**a**) The first fluorescence image in an image stack. A box is drawn enclosing the extended DNA molecule. The scale bar corresponds to 20 μm. (**b**) Time trace obtained by averaging over the molecule shown in (**a**) in the direction transverse to the DNA extension for every frame. Each column of pixels corresponds to the averaged intensity profile of one frame. The scale bars correspond to 20 μm and 10 s, respectively. (**c**) The intensity profile $I(x)$ and the corresponding fit for one column of the time trace. (**d**) A histogram over all the fitted lengths from one movie containing 400 frames. The data is well described by a Gaussian distribution (*solid line*). Reproduced with permission from ref. 41

the image is discarded in order to reduce the amount of data to store (Fig. 3a) [44].

2. The pixels are summed over the width of the extended DNA yielding a one-dimensional intensity profile of the molecule.
3. **Step 2** is repeated for each frame in the movie, except that the molecule is identified based on its position in the previous frame. Stacking these intensity profiles next to each other yields a timetrace (also known as a kymograph) (Fig. 3b). In this way a whole movie can be reduced to one single composite image.
4. The intensity profiles are fitted to a model profile, described below, by a least-square algorithm (Fig. 3c). This fitting provides the center position, intensity (with subtracted

background) and length of the DNA for each frame in the original movie.

The model intensity profile, $I(x)$, consists of a convolution of a modified box function (height I_0, length L_X) with a Gaussian point-spread function (PSF), with a full width at half maximum (FWHM) of $2.35\sigma_0 = 0.61\lambda/\mathrm{NA}$ (λ is the wavelength of the light and NA is the numerical aperture of the objective) [1]. The model is represented by:

$$I(x) = I_{\mathrm{bg}} + \frac{I_0}{2}\left[(1-B)\mathrm{Erf}\left(\frac{x-x_0}{\sigma_0\sqrt{2}}\right) - (1+B)\mathrm{Erf}\left(\frac{x-(x_0+L_0)}{\sigma_0\sqrt{2}}\right)\right],$$

where I_{bg} is the background intensity value, B is a numerical factor introduced to allow for a non-constant background, Erf is the error function and x_0 is the center position of the box function (*see* **Note 27**).

It is important to realize that the biologically relevant gauge of resolution in these experiments is basepairs and not nanometers or pixels. Standard fluorescence microscopy has a resolution limited by diffraction to roughly half the wavelength of the detected light. The resolution in basepairs is determined by the degree of DNA stretching, the DNA fluctuations and the total photon budget. Thus, maximum resolution is obtained in channels with the smallest possible cross section yielding fully stretched DNA with a minimum of thermal fluctuations. In practice there is an optimum resolution for each experiment and it is important to design the experiments accordingly. For example, studies of a selected region of interest along the genome may require the highest possible resolving power, requiring extensive efforts in terms of data acquisition, storage and handling. In some applications the resolving power per se is not relevant, instead the positioning of one or more specific labels contains the important information. In this case the measurement uncertainty scales roughly as $1/\sqrt{N}$ where N is the number of detected photons, giving accuracies approaching a single nanometer [45].

The exact degree of stretching for a particular experimental condition can be determined using a DNA of known length, such as λ-DNA (from NEB), as reference.

For experiments regarding optical DNA mapping, the data analysis is more intricate, *see* **Note 12** for an example regarding competitive binding-based optical DNA mapping.

4 Notes

1. One common fabrication method uses nanoimprint lithography (NIL). This has the benefit that it is possible to order

finished master stamps commercially (available from NIL Technology, Denmark), thus eliminating the need for an electron-beam lithography system. A common mass production technique, capable of defining nanostructures, is injection molding. With suitable choice of low-fluorescence polymer matrix it may prove useful for large series of devices. Although focused ion beam (FIB) milling is a slow linear technique, it may find use for creating complicated three-dimensional structures with resolution comparable to that of electron-beam lithography. Direct laser writing systems (available from Nanoscribe GmbH, Germany) are now also capable of creating complex three-dimensional structures with feature sizes below 100 nm.

A multitude of more exotic alternative fabrication techniques are described in the literature.

2. 0.1 M dithiothreitol (DTT) can replace BME as reducing agent.
3. POP6 (Performance Optimized Polymer 6) from Applied Biosystems can be used as an alternative to PVP.
4. TAE buffer is a useful alternative to TBE that replaces the borate with acetate. While borate has been identified as a substance that may pose risks with respect to CMR, acetate is considered a safe alternative. Compared to TBE it has less buffering capacity and for running gels it must be exchanged more often. Standard concentration is 1× TAE: 40 mM TRIS acetate and 1 mM EDTA. TAE is readily available in 50× solution or it can be made by mixing 242 g of TRIS base, 57.1 mL glacial acetic acid, 100 mL of 0.5 M EDTA in water, finally adjusting the volume to 1 L.
5. Whenever water is mentioned in the context of buffer composition, we refer to ultrapure water with resistivity 18.2 MΩ cm (at 25 °C) (referred to as Milli-Q water when using water purification equipment from the Millipore Corporation).
6. DNA in stock solutions at concentrations of 100–500 μg/mL is very viscous and hard to pipette accurately. Tip the tube sideways and suck in the solution very slowly to ensure that the correct amount of DNA is withdrawn. (For λ-DNA from New England Biolabs the stock solution is 500 μg/mL, so 25 μL of the solution is added to 225 μL of 0.5× TBE in a 1.5 mL microcentrifuge tube to obtain a DNA concentration of 50 μg/mL.).

   When working with lambda phage DNA, it may be advisable to heat it to 50 °C for 10 min in a microcentrifuge tube heater and quench in icy water to avoid concatamers due to the hybridization of the single-strand overhangs.
7. One way of obtaining sequence information from DNA stretched in nanochannels is to tag specific sequences with a bright fluorophore. The most common way to do this is to use

an enzyme that nicks the DNA at a specific sequence and subsequently repair that nick with a ligase and polymerase that incorporate fluorescent nucleotides [28, 29]. The recognition sites for commercially available nicking enzymes range from 4 to 7 bases in length but a recent report used a mutated CRISPR/Cas9 system to obtain a recognition size of 23 bases [46]. In recent studies, methyltransferases have been used for the same type of experiments, where the main advantage is that the DNA is not damaged as part of the labeling process [47]. The result is a DNA stretched in nanochannels with a series of dots at specific distances that represents the underlying sequence. This principle has gained increasing attention and also been commercialized via BioNanoGenomics.

8. An alternative way to obtain sequence information is affinity-based labeling. In these assays the principle is that the affinity of the YOYO-dye used to stain the DNA is altered in some way to make its binding sequence selective. Two main strategies have been presented in the literature. The first is to locally melt the DNA by increasing the temperature and/or adding formamide that weakens the hydrogen bonds between the bases. Since AT-bases are connected via two hydrogen bonds and GC-bases by three, AT-bases melt at a lower temperature. Since YOYO-1 only binds to base-paired DNA, it will bind preferably to GC-rich regions in a partly melted DNA and an intensity variation along the DNA, where GC-regions are bright and AT-regions are dark, will be formed.

   A different way of forming the affinity-based barcode is to add netropsin as the same time as YOYO is added. Netropsin is a molecule that has a strong preference for AT-rich DNA and hence blocks those regions from YOYO binding. As a consequence YOYO will mostly bind to GC-rich regions and the result is again an intensity variation along the DNA where AT-rich regions are dark and GC-rich regions are bright. Competitive binding-based barcodes have recently been extensively used for identification and characterization of bacterial plasmids coding for antibiotic resistance [48–50].
9. BME, a highly toxic chemical that serves as a biological antioxidant by scavenging oxygen and hydroxyl radicals in the buffer, thereby preventing photobleaching and photoinduced damage (photonicking) of the DNA.

   An enzymatic oxygen scavenger system may constitute a useful alternative when reducing agents cannot be used. It consists of 0.2 mg/mL glucose oxidase, 0.04 mg/mL catalase and 4 mg/mL β-D-glucose (available from Sigma-Aldrich). The oxygen scavenger system can be combined with BME but typically does not provide any additional benefit for the experiments listed.

10. One useful option in a fluorescence microscope is a unit that sends a selected field of view through two different optical paths and projects the resulting images on two separate areas of the CCD. This allows the user to acquire two (or more) colors or two polarization directions simultaneously. Existing systems include DV2™ from Photometrics and OptoSplit™ from Cairn Research.
11. To improve imaging resolution, a wide range of novel techniques have been developed, each one capable of reaching a resolution of below 100 nm [5]. They essentially fall in three categories: local suppression of the fluorescence emission (STED), repeated photoactivation and subsequent imaging of a subset of the fluorophores in the sample (STORM, FPALM) and structured illumination (SIM).

    Most imaging is carried out with B/W cameras giving information on the intensity in each pixel. For additional contrast information, multicolor (spectroscopic) or fluorescence lifetime imaging (FLIM) may be utilized.
12. For affinity-based optical DNA mapping, described in **Note 8**, the theoretical framework for creating theoretical barcodes, comparing experimental and theoretical barcodes, forming consensus barcodes from several individual barcodes etc. can be found in the literature [48, 49, 52].
13. In order to expose the DNA to a gradual change in confinement in one single chip, it is possible to use funnel-like channels [11]. This is an analogue to force spectroscopy techniques using optical tweezers that allows for probing of low DNA extensions, corresponding to forces in the femtonewton regime, without anchoring the molecules. Another feature that can be added to the chip is demonstrated in Fig. 4 (right). In this chip design a nanoslit is etched orthogonal to the nanochannels. This allows for enrichment of DNA in the nanogrooves by applying moderate positive pressures at both ends of the nanochannels. If the slit is sufficiently shallow, entropy keeps the DNA in the grooves while buffer flows through the slit. This design also allows for changing the chemical environment of the DNA, by flushing the desired solution in the slit, while monitoring the DNA in real time.
14. When analyzing long, genomic DNA extra care has to be taken due to the relatively large size of the molecules. For intermediate size DNA such as from bacteria, a meandering nanochannel can be used [53], so that the entire DNA can be visualized in one single frame. Considering human DNA, it can be noted that the largest single DNA molecule has a fully extended length of over 8 cm (chromosome 1). If the DNA molecule is too long for the whole molecule to be easily extended in a

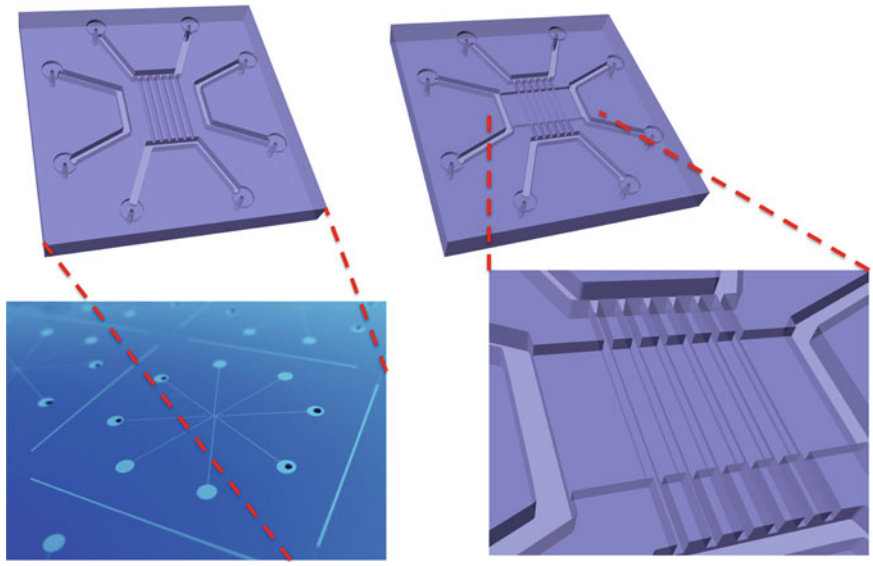

Fig. 4 (*LEFT*) Chip design with nanochannels spanning two U-shaped microchannels. This design enables fast buffer exchange since all of the liquid does not have to pass through the nanochannels. The size of each chip as seen in the lower image is 1 × 1 in. In order to visualize the nanochannel region, the central region is exaggerated. (*RIGHT*) Schematics of a similar design as the *left* one with an added nanoslit oriented perpendicular to the nanochannel array. In the nanoslit the nanochannels become nanogrooves in the bottom, working as entropic traps for the DNA. This design also allows for enrichment of DNA in the nanogrooves by applying positive pressures at both ends of the nanochannels. In order to visualize the nanochannel region, the central region is exaggerated. The nanoslit and nanochannels are 50 μm and 100 nm wide respectively. Reproduced from ref. 12 with permission from The Royal Society of Chemistry

single nanochannel, one possibility is to stretch it by shear flow [54, 55] in a device made by conventional photolithography. With this approach there is no need for nanofabrication. However, it is a dynamic system in which the DNA conformation will not be at equilibrium as compared to DNA confined in nanochannels.

15. The layout of a DNA analysis chip may also contain features for sample preparation such as cell-sorting, cell lysis, DNA extraction and purification, and DNA staining in addition to the actual analysis of the DNA molecules. This kind of integration would enable the analysis of DNA from a single cell, which would be especially useful in the study of e.g. rare circulating tumor cells. A potentially very useful development with this regard is the use of deterministic lateral displacement to continuously guide cells and chromosomes through different chemical environments for cell lysis and DNA staining [56].
16. Even without an e-beam writer, slit-like channels (depth in the nanometer range and widths larger than 0.5 μm) can readily be defined with UV lithography and carefully tuned RIE etching.

17. Alignment marks can alternatively be formed by anisotropic RIE etching, and in the case of silicon also through anisotropic wet etching using e.g. KOH. If etching is used to define the alignment marks it is important that they provide a sufficient contrast for the alignment in the mask aligner. An etch depth of at least 200 nm is recommended. For metal alignment marks it is also possible to first deposit a layer of metal and subsequently spin on and pattern a photoresist and in a last step etch away the exposed metal. Al is commonly etched using either a wet etch using phosphoric acid or a dry etch containing chlorine chemistry. Au is commonly etched by using wet etches of either potassium iodine or aqua regia (1:3 HNO_3:HCl).
18. Instead of using chemicals, the resist can be stripped by an oxygen plasma treatment. However, this is not recommended since it can burn the resist, making it very hard to remove, and also induces roughness on the sample surface.
19. Examples include micromilling, deep reactive ion etching (DRIE) or ultrasonic drilling. However, these techniques often demand some specialized equipment, which is very expensive compared to that needed for powder blasting.
20. Instead of using a soft film in order to mask the wafers/chips during powder blasting, a metal mask defined in a thick brass plate can be used. The chip is then attached to the metal mask using reversible thermal glue. It should be noted that since the metal mask is hard, it will also be degraded by the powder blasting, which attacks hard surfaces.
21. Polymer-based devices are generally sealed using polymer fusion bonding. The device is bonded to a lid with a polymer film by heating until the polymer layers on the chip and lid intermix. The combination of polymer compositions and temperatures must be carefully chosen to create a sufficiently strong bond while maintaining the structural integrity of the micro- and nanochannels. Anodic bonding is the standard technique to bond borosilicate glass to silicon, also for silicon with a hydrophilic oxide layer, but it might cause wide nanochannels (nanoslits) to collapse.
22. The Piranha-based protocol can be used to bond silicon with a thin layer of oxide (<150 nm) and borosilicate glass. However, the final annealing should in this case be done at 400–450 °C to avoid excessive strain due to the difference in thermal expansion coefficient between silicon and glass [57].
23. BME degrades in the presence of oxygen and therefore a small amount should be transferred to a microcentrifuge tube and used for the experiments in order to avoid opening the main bottle too many times. The main bottle should be filled with nitrogen after each time it is opened. A sealed bottle should be

stable for at least 3 years. The BME in a mixed loading buffer will last approximately 1 day.

24. For chips that are difficult to wet, e.g. in the case of hydrophobic materials or dead-end channels, critical point wetting [58] can be used. However, critical point wetting requires that the material used is capable of withstanding at least the temperature at the critical point of water, $T = 374\ ^{\circ}C$.
25. Using lipid bilayers is an efficient way of passivating nanofluidic structures [59]. Lipid bilayers are superior to common passivating strategies in microfluidics, such as non-specific binding of BSA, since a lipid bilayer is a 2D liquid and hence very smooth and defect free due to its inherent self-repair capability. Lipid bilayers have been used in several studies of DNA–protein interactions in nanochannels [60, 61].
26. The frame rate should be selected based on the timescales of interest. Long exposure times might blur the image due to drift and diffusion of the DNA. Signal-to-noise might become insufficient for very short exposure times. For typical imaging applications, 10 fps is a suitable choice. Very short exposure times enable detailed studies of dynamics and fluctuations, typically occurring at higher rates than 10 Hz. Long exposure times can on the other hand be used to discern bound molecules from freely diffusing molecules. It has also been shown that altering the exposure times makes it possible to obtain binding kinetics for transcription factors on DNA [62].
27. It should be noted that to be mathematically rigorous, an Airy function should be used for an ideal optical system rather than the more convenient-to-use Gaussian approximation. Furthermore, to fully optimize the analysis, it has been shown that a careful choice of fitting function that closely mimics the real PSF will give a slight but significant improvement.

Acknowledgements

This work was supported by the European Community's Horizon2020 under grant agreement number 634890 entitled BeyondSeq (J.O.T., J.P.B. and F.W.), the Swedish Research Council under grant number 2015-05062 (F.W.), ERA-NET EuroNanoMed II under grant number E0748601 entitled NanoDiaBac (J.O.T., J.P.B. and F.W.). J.O.T. and J.P.B. acknowledges support from NanoLund at Lund University.

References

1. Tegenfeldt JO, Prinz C, Cao H, Chou S, Reisner WW, Riehn R, Wang YM, Cox EC, Sturm JC, Silberzan P, Austin RH (2004) The dynamics of genomic-length DNA molecules in 100-

nm channels. Proc Natl Acad Sci U S A 101 (30):10979–10983
2. Vologodskii A, Cozzarelli N (1995) Modeling of long-range electrostatic interactions in DNA. Biopolymers 35(3):289–296
3. Daoud M, de Gennes PG (1977) Statistics of macromolecular solutions trapped in small pores. J Phys 38:85–93
4. Turban L (1984) Conformation of confined macromolecular chains - crossover between slit and capillary. J Phys 45(2):347–353
5. Odijk T (1983) On the statistics and dynamics of confined or entangled stiff polymers. Macromolecules 16(8):1340–1344
6. Frykholm K, Alizadehheidari M, Fritzsche J, Wigenius J, Modesti M, Persson F, Westerlund F (2014) Probing physical properties of a DNA-protein complex using nanofluidic channels. Small 10(5):884–887. doi:10.1002/smll.201302028
7. Yang YZ, Burkhardt TW, Gompper G (2007) Free energy and extension of a semiflexible polymer in cylindrical confining geometries. Phys Rev E 76(1):011804. doi:10.1103/PhysRevE.76.011804
8. Smithe TSC, Iarko V, Muralidhar A, Werner E, Dorfman KD, Mehlig B (2015) Finite-size corrections for confined polymers in the extended de Gennes regime. Phys Rev E 92(6):5. doi:10.1103/PhysRevE.92.062601
9. Werner E, Mehlig B (2015) Scaling regimes of a semiflexible polymer in a rectangular channel. Phys Rev E 91(5):5. doi:10.1103/PhysRevE.91.050601
10. Reisner W, Pedersen JN, Austin RH (2012) DNA confinement in nanochannels: physics and biological applications. Rep Prog Phys 75 (10). doi:10.1088/0034-4885/75/10/106601
11. Persson F, Utko P, Reisner W, Larsen NB, Kristensen A (2009) Confinement spectroscopy: probing single DNA molecules with tapered nanochannels. Nano Lett 9 (4):1382–1385. doi:10.1021/nl803030e
12. Persson F, Tegenfeldt JO (2010) DNA in nanochannels - directly visualizing genomic information. Chem Soc Rev 39(3):985–999. doi:10.1039/B912918A
13. de Gennes PG (1979) Scaling concepts in polymer physics. Cornell University Press, Ithaca, NY
14. Doi M, Edwards SF (1986) The theory of polymer dynamics, The International Series of Monographs on Physics, vol 73. Oxford University Press, Inc., New York
15. Rubinstein M, Colby RH (2003) Polymer physics. Oxford University Press, New York
16. Reisner W, Morton KJ, Riehn R, Wang YM, Yu ZN, Rosen M, Sturm JC, Chou SY, Frey E, Austin RH (2005) Statics and dynamics of single DNA molecules confined in nanochannels. Phys Rev Lett 94(19):196101
17. Persson F, Westerlund F, Tegenfeldt JO, Kristensen A (2009) Local conformation of confined DNA studied using emission polarization anisotropy. Small 5(2):190–193
18. Wang YM, Tegenfeldt JO, Reisner W, Riehn R, Guan XJ, Guo L, Golding I, Cox EC, Sturm J, Austin RH (2005) Single-molecule studies of repressor-DNA interactions show long-range interactions. Proc Natl Acad Sci U S A 102 (28):9796–9801
19. Riehn R, Lu MC, Wang YM, Lim SF, Cox EC, Austin RH (2005) Restriction mapping in nanofluidic devices. Proc Natl Acad Sci U S A 102(29):10012–10016
20. Iarko V, Werner E, Nyberg LK, Müller V, Fritzsche J, Ambjörnsson T, Beech JP, Tegenfeldt JO, Mehlig K, Westerlund F, Mehlig B (2015) Extension of nanoconfined DNA: quantitative comparison between experiment and theory. Phys Rev E 92(6):062701
21. Werner E, Mehlig B (2014) Confined polymers in the extended de Gennes regime. Phys Rev E 90(6):5. doi:10.1103/PhysRevE.90.062602
22. Gupta D, Miller JJ, Muralidhar A, Mahshid S, Reisner W, Dorfman KD (2015) Experimental evidence of weak excluded volume effects for nanochannel confined DNA. ACS Macro Lett 4(7):759–763. doi:10.1021/acsmacrolett.5b00340
23. Frykholm K, Nyberg LK, Westerlund F (2017) Exploring DNA–protein interactions on the single DNA molecule level using nanofluidic tools. Integr Biol. doi:10.1039/C7IB00085E
24. Zhang C, Guttula D, Liu F, Malar PP, Ng SY, Dai L, Doyle PS, van Kan JA, van der Maarel JRC (2013) Effect of H-NS on the elongation and compaction of single DNA molecules in a nanospace. Soft Matter 9(40):9593–9601. doi:10.1039/c3sm51214b
25. Roushan M, Kaur P, Karpusenko A, Countryman PJ, Ortiz CP, Fang Lim S, Wang H, Riehn R (2014) Probing transient protein-mediated DNA linkages using nanoconfinement. Biomicrofluidics 8(3):034113. doi:10.1063/1.4882775
26. Müller V, Westerlund F (2017) Optical DNA mapping in nanofluidic devices: principles and applications. Lab Chip 17:579–590
27. Bogas D, Nyberg L, Pacheco R, Azevedo NF, Beech JP, Gomila M, Lalucat J, Manaia CM, Nunes OC, Tegenfeldt JO, Westerlund F (2017) Applications of optical DNA mapping

in microbiology. BioTechniques 62 (6):255–267

28. Jo K, Dhingra DM, Odijk T, de Pablo JJ, Graham MD, Runnheim R, Forrest D, Schwartz DC (2007) A single-molecule barcoding system using nanoslits for DNA analysis. Proc Natl Acad Sci U S A 104(8):2673–2678
29. Das SK, Austin MD, Akana MC, Deshpande P, Cao H, Xiao M (2010) Single molecule linear analysis of DNA in nano-channel labeled with sequence specific fluorescent probes. Nucleic Acids Res 38(18):e177. doi:10.1093/nar/gkq673
30. Reisner W, Larsen NB, Silahtaroglu A, Kristensen A, Tommerup N, Tegenfeldt JO, Flyvbjerg H (2010) Single-molecule denaturation mapping of DNA in nanofluidic channels. Proc Natl Acad Sci U S A 107(30):13294–13299
31. Nyberg LK, Persson F, Berg J, Bergstrom J, Fransson E, Olsson L, Persson M, Stalnacke A, Wigenius J, Tegenfeldt JO, Westerlund F (2012) A single-step competitive binding assay for mapping of single DNA molecules. Biochem Biophys Res Commun 417(1):404–408. doi:10.1016/j.bbrc.2011.11.128
32. Frykholm K, Nyberg LK, Lagerstedt E, Noble C, Fritzsche J, Karami N, Ambjornsson T, Sandegren L, Westerlund F (2015) Fast size-determination of intact bacterial plasmids using nanofluidic channels. Lab Chip 15 (13):2739–2743. doi:10.1039/c5lc00378d
33. Madou MJ (2011) Fundamentals of microfabrication and nanotechnology, 3rd edn. CRC Press, Boca Raton, FL
34. Reisner W, Beech JP, Larsen NB, Flyvbjerg H, Kristensen A, Tegenfeldt JO (2007) Nanoconfinement-enhanced conformational response of single DNA molecules to changes in ionic environment. Phys Rev Lett 99 (5):058302. Artn 058302
35. Nyberg L, Persson F, Åkerman B, Westerlund F (2013) Heterogeneous staining: a tool for studies of how fluorescent dyes affect the physical properties of DNA. Nucleic Acids Res. doi:10.1093/nar/gkt755
36. Mertz J (2010) Introduction to optical microscopy. Roberts and Company, Greenwood Village
37. Glazer AN, Rye HS (1992) Stable dye-DNA intercalation complexes as reagents for high-sensitivity fluorescence detection. Nature 359 (6398):859–861
38. Spielmann HP, Wemmer DE, Jacobsen JP (1995) Solution structure of a DNA complex with the fluorescent Bis-intercalator TOTO determined by NMR-spectroscopy. Biochemistry 34(27):8542–8553
39. Kundukad B, Yan J, Doyle PS (2014) Effect of YOYO-1 on the mechanical properties of DNA. Soft Matter 10(48):9721–9728. doi:10.1039/c4sm02025a
40. Lerman LS (1961) Structural considerations in interaction of DNA and acridines. J Mol Biol 3 (1):18–30
41. Reinert KE (1973) DNA stiffening and elongation caused by binding of ethidium bromide. Biochim Biophys Acta 319(2):135–139
42. Thamdrup LH, Persson F, Bruus H, Kristensen A, Flyvbjerg H (2007) Experimental investigation of bubble formation during capillary filling of SiO_2 nanoslits. Appl Phys Lett 91(16). doi:10.1063/1.2801397
43. Levy SL, Mannion JT, Cheng J, Reccius CH, Craighead HG (2008) Entropic unfolding of DNA molecules in nanofluidic channels. Nano Lett 8(11):3839–3844. doi:10.1021/nl802256s
44. Persson F (2009) Nanofluidics for single molecule. Technical University of Denmark, Kongens, Lyngby
45. Thompson RE, Larson DR, Webb WW (2002) Precise nanometer localization analysis for individual fluorescent probes. Biophys J 82 (5):2775–2783
46. McCaffrey J, Sibert J, Zhang B, Zhang YG, Hu WH, Riethman H, Xiao M (2016) CRISPR-CAS9 D10A nickase target-specific fluorescent labeling of double strand DNA for whole genome mapping and structural variation analysis. Nucleic Acids Res 44(2):8. doi:10.1093/nar/gkv878
47. Grunwald A, Dahan M, Giesbertz A, Nilsson A, Nyberg LK, Weinhold E, Ambjornsson T, Westerlund F, Ebenstein Y (2015) Bacteriophage strain typing by rapid single molecule analysis. Nucleic Acids Res 43(18): e117–e117. doi:10.1093/nar/gkv563
48. Muller V, Karami N, Nyberg LK, Pichler C, Pedreschi PCT, Quaderi S, Fritzsche J, Ambjornsson T, Ahren C, Westerlund F (2016) Rapid tracing of resistance plasmids in a nosocomial outbreak using optical DNA mapping. Acs Infect Dis 2(5):322–328. doi:10.1021/acsinfecdis.6b00017
49. Nyberg LK, Quaderi S, Emilsson G, Karami N, Lagerstedt E, Muller V, Noble C, Hammarberg S, Nilsson AN, Sjoberg F, Fritzsche J, Kristiansson E, Sandegren L, Ambjornsson T, Westerlund F (2016) Rapid identification of intact bacterial resistance plasmids via optical mapping of single DNA molecules. Sci Rep 6:10. doi:10.1038/srep30410
50. Müller V, Rajer F, Frykholm K, Nyberg LK, Quaderi S, Fritzsche J, Kristiansson E,

Ambjörnsson T, Sandegren L, Westerlund F (2016) Direct identification of antibiotic resistance genes on single plasmid molecules using CRISPR/Cas9 in combination with optical DNA mapping. Sci Rep 6:37938. doi:10.1038/srep37938. http://www.nature.com/articles/srep37938 - supplementary-information

51. Sydor AM, Czymmek KJ, Puchner EM, Mennella V (2015) Super-resolution microscopy: from single molecules to supramolecular assemblies. Trends Cell Biol 25(12):730–748. doi:10.1016/j.tcb.2015.10.004
52. Nilsson AN, Emilsson G, Nyberg LK, Noble C, Stadler LS, Fritzsche J, Moore ERB, Tegenfeldt JO, Ambjornsson T, Westerlund F (2014) Competitive binding-based optical DNA mapping for fast identification of bacteria - multi-ligand transfer matrix theory and experimental applications on Escherichia coli. Nucleic Acids Res 42(15). doi:10.1093/nar/gku556
53. Freitag C, Noble C, Fritzsche J, Persson F, Reiter-Schad M, Nilsson AN, Graneli A, Ambjornsson T, Mir KU, Tegenfeldt JO (2015) Visualizing the entire DNA from a chromosome in a single frame. Biomicrofluidics 9(4). doi:10.1063/1.4923262
54. Perkins TT, Smith DE, Chu S (1997) Single polymer dynamics in an elongational flow. Science 276(5321):2016–2021
55. Marie R, Pedersen JN, Bauer DLV, Rasmussen KH, Yusuf M, Volpi E, Flyvbjerg H, Kristensen A, Mir KU (2013) Integrated view of genome structure and sequence of a single DNA molecule in a nanofluidic device. Proc Natl Acad Sci U S A 100(13):4893–4898. doi:10.1073/pnas.1214570110
56. Morton KJ, Loutherback K, Inglis DW, Tsui OK, Sturm JC, Chou SY, Austin RH (2008) Crossing microfluidic streamlines to lyse, label and wash cells. Lab Chip 8(9):1448–1453. doi:10.1039/b805614e
57. Persson F, Thamdrup LH, Mikkelsen MBL, Jaarlgard SE, Skafte-Pedersen P, Bruus H, Kristensen A (2007) Double thermal oxidation scheme for the fabrication of SiO_2 nanochannels. Nanotechnology 18(24):245301. doi:10.1088/0957-4484/18/24/245301
58. Riehn R, Austin RH (2006) Wetting micro- and nanofluidic devices using supercritical water. Anal Chem 78(16):5933–5934
59. Persson F, Fritzsche J, Mir KU, Modesti M, Westerlund F, Tegenfeldt JO (2012) Lipid-based passivation in nanofluidics. Nano Lett 12:2260–2265. doi:10.1021/nl204535h
60. Fornander LH, Frykholm K, Fritzsche J, Araya J, Nevin P, Werner E, Cakir A, Persson F, Garcin EB, Beuning PJ, Mehlig B, Modesti M, Westerlund F (2016) Visualizing the nonhomogeneous structure of RAD51 filaments using nanofluidic channels. Langmuir 32 (33):8403–8412. doi:10.1021/acs.langmuir.6b01877
61. Frykholm K, Berntsson RPA, Claesson M, de Battice L, Odegrip R, Stenmark P, Westerlund F (2016) DNA compaction by the bacteriophage protein Cox studied on the single DNA molecule level using nanofluidic channels. Nucleic Acids Res 44(15):7219–7227. doi:10.1093/nar/gkw352
62. Elf J, Li GW, Xie XS (2007) Probing transcription factor dynamics at the single-molecule level in a living cell. Science 316 (5828):1191–1194

Chapter 11

Use of Single Molecule Fluorescence Polarization Microscopy to Study Protein Conformation and Dynamics of Kinesin–Microtubule Complexes

Matthieu P.M.H. Benoit and Hernando Sosa

Abstract

Single molecule fluorescence polarization microscopy (smFPM) is a technique that enables to monitor changes in the orientation of a single labeled protein domain. Here we describe a smFPM microscope set-up and protocols to investigate conformational changes associated with the movement of motor proteins along cytoskeletal tracks.

Key words Kinesin, Microtubule, Molecular motor, Fluorescence polarization, Dichroism, Single molecule, BSR

1 Introduction

A variety of single molecules techniques have been used to elucidate the mechanism of action of biological motors at the molecular level with a high level of detail [1–3]. Fluorescence polarization microscopy methods in general (ensemble and single molecule) allow to investigate the orientation and reorientation (angular mobility) of macromolecules in space and time. They have been used to monitor conformational changes in a variety of biological systems (e.g. [4–8]) and are particularly well suited to the study of cytoskeletal motors where key conformational changes usually involve reorientation of protein domains relative to the associated cytoskeletal filament track [1]. We describe a microscope set-up and experimental protocols to measure the orientation and angular mobility of single kinesin molecules interacting and moving along microtubules, as well as complementary ensemble FPM measurements. In the experimental set-up used, the projected angle on the microscope stage plane and angular mobility of the transition dipole moment of a fluorophore (hereinafter referred simply as the dipole) labeled protein domain is determined from the relative absorption

Erwin J.G. Peterman (ed.), *Single Molecule Analysis: Methods and Protocols*, Methods in Molecular Biology, vol. 1665, DOI 10.1007/978-1-4939-7271-5_11,

of light polarized in various directions. With this system we have detected and characterized conformational changes associated with movement along microtubules of motile [9–12] and microtubule depolymerizing kinesins [13].

2 Material

2.1 Solutions

All solutions should be prepared using ultra pure water (resistance of 18 MΩ cm at 25 °C) and analytical grade reagents.

2.1.1 Buffers

1. BRB80: 80 mM K-PIPES, 2 mM $MgCl_2$, 1 mM EGTA, pH 6.8 adjusted at 25 °C by titration with a 10 M KOH solution (*see* **Note 1**).
2. BRB12: 12 mM K-PIPES, 2 mM $MgCl_2$, 1 mM EGTA, pH 6.8 adjusted at 25 °C by titration with a 10 M KOH solution (*see* **Note 2**).
3. Purification buffer: BRB80 supplemented with 250 mM KCl, 5 mM β-mercaptoethanol, 50 μM ATP.
4. Labeling buffer: BRB80 (pH adjusted to 7.4), 250 mM KCl, 50 μM ATP (*see* **Note 3**).

2.1.2 Stock Solutions

1. 75 mg/ml Bovine Serum Albumin (BSA) in BRB12 (*see* **Note 4**).
2. 2 mM Paclitaxel (Taxol) solution in DMSO.
3. Nucleotide stock solutions: 100 mM nucleotide (e.g. AMPPNP, ADP, ATP), 100 mM $MgCl_2$, in BRB80 (*see* **Note 5**).
4. 80% w/v Sucrose in purification buffer.
5. 1 μM Protocatechuate-3,4-dioxygenase (PCD) solution in 100 mM Tris–HCl pH 8, 50% (v/v) glycerol, 50 mM KCl.
6. 100 mM Protocatechuic acid (PCA, the PCD substrate) in BRB80.
7. 100 mM Trolox in BRB80.

All stock solutions are aliquoted, flash frozen in liquid nitrogen and stored at −80 °C.

2.1.3 Others

1. Imaging solution: BRB12 supplemented with 7.5 mg/ml BSA, 20 μM paclitaxel, 2.5 mM protocatechuic acid (PCA), 10 nM protocatechuate-3,4-dioxygenase (PCD), 1 mM Trolox, nucleotides and kinesin at the desired experimental concentrations. The imaging solution is prepared fresh for each experimental session by mixing the appropriate stock solution to the indicated final concentrations. PCA, PCD, and Trolox are used to reduce fluorophore bleaching [14].

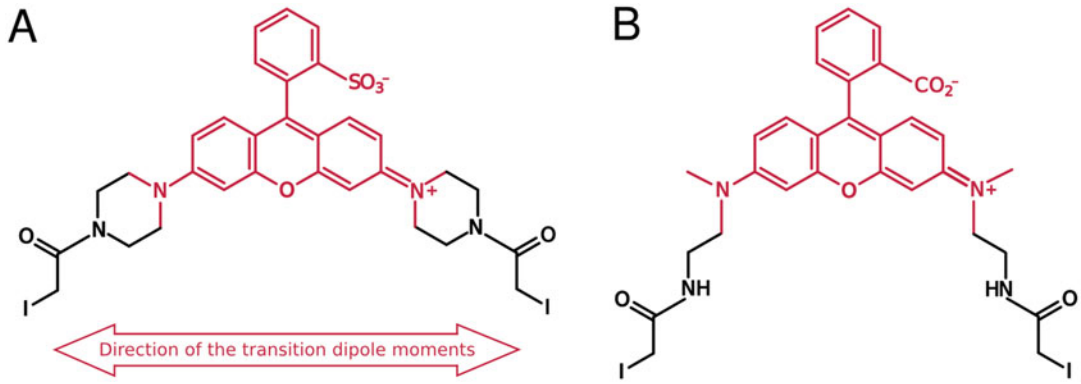

Fig. 1 Structure of two rhodamine-derived bifunctional probes used for single molecules fluorescence polarization studies. The rhodamine part is indicated with *lighter lines* (*red* in color figure). The direction of the dipole is indicated by the *double arrow*. (**a**) BSR (bis-((*N*-iodoacetyl)piperazinyl)sulfonerhodamine). (**b**) BR (*N*,*N*′-Bis[2-(iodoacetamido)ethyl]-*N*,*N*′-dimethylrhodamine)

2. DETA solution: 0.1% (v/v) of DETA (*N*1-(3-Trimethoxysilylpropyl) diethylenetriamine) in water with 1 mM acetic acid.

2.2 Fluorescent Probe

1. A bifunctional fluorescence probe is used to cross-link two cysteines so that it restrains the direction of the dipole relative to the targeted protein domain's 3D structure. We have used a sulfhydril reactive fluorescent probe to specifically label cysteine residues on the target protein, bis-((*N* iodoacetyl)piperazinyl) sulfonerhodamine (BSR also called BSR-I_2). This probe has the direction of the dipole collinear to the main axis of the xanthene (Fig. 1, [15]). BSR was commercially available until recently from ThermoFisher/Molecular Probes, but this is no longer the case at the time of writing. A probe similar to BSR, but with more flexible linkers, *N*,*N*′-Bis[2-(iodoacetamido) ethyl]-*N*,*N*′-dimethylrhodamine (BR-I_2), available from Santa Cruz Biotechnology, has also been effectively used in several fluorescence polarization studies [16, 17]. In our experience, and consistent with other reports [16, 17], BR-I_2 is less reactive than BSR resulting in a lower yield of labeled protein for similar labeling conditions. For the protocols and results described here the use of the BSR probe is assumed.
2. Prepare BSR aliquots of known concentration. The rhodamines and especially the iodoacetamide groups in solution are light sensitive, so all the manipulations with the BSR are performed under subdued light. Resuspend the BSR in DMSO. Estimate its concentration assuming an extinction coefficient of 88,000 l/mol/cm at 549 nm. Adjust the concentration to no less than 5 mM to avoid adding significant amount of DMSO during the incubation with the kinesin. Aliquot the BSR solution and store at −20 °C protected from light.

2.3 Proteins

1. Kinesin: *Homo sapiens* (KF5B) and *Drosophila melanogaster* (KLP10A) recombinant kinesins proteins are expressed in *Escherichia coli* (BL21) cells and purified according to standard protocols.
2. The strategy to site-specific label kinesin proteins with a bifunctional fluorophore (Subheading 3.1) involves: (a) The mutation of all of the exposed cysteines to either alanines or another residue based on substitutions found in homologous sequences (cysteine to serine is a common one) to create a cys-lite version. (b) The mutation of the two residues to cysteines in the target region. We have effectively cross-linked with BSR cysteines with a predicted separation between Cβ carbons of 14–17 Å. For BR-I_2 a distance range of 10–16 Å has been reported [16].
3. Tubulin: We either purified tubulin from bovine brain following the protocol of [18] or obtained it from a commercial supplier (Cytoskeleton, porcine brain tubulin). In both cases, the purified tubulin is eventually aliquoted at 5 mg/ml (45 μM) in BRB80 $pH_{25°C}$ 6.8, flash frozen in liquid nitrogen and stored at −80 °C.

2.4 Microscope

For FPM we used a custom modified wide field inverted epifluorescence microscope [19, 20]. All the instrumentation necessary to control the direction of polarization of the light is kept outside the microscope so the system can be adapted to most microscopes with minimal or no modifications (Fig. 2).

1. The source of excitation light is a laser with a wavelength of 532 nm close to the excitation maximum of the BSR probe (549 nm).

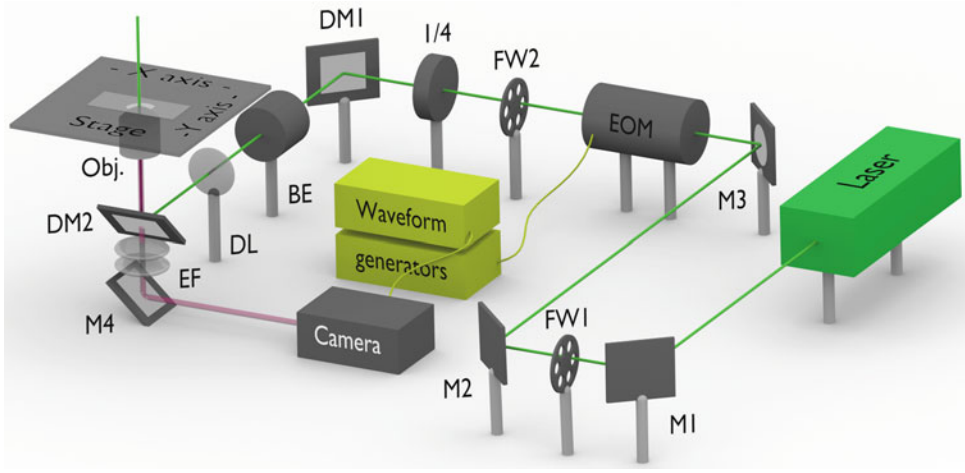

Fig. 2 Main components of the fluorescence polarization setup used. M1, M2, M3, and M4: mirrors. DM1 and DM2 dichroic mirrors. FW1 and FW2: filter wheels. EOM: electro optic modulator. 1/4: quarter wave plate. BE: beam expander. DL: defocusing lens. Obj: Objective lens

2. Adjustable mirrors M1, M2, and M3 are used to reorient and align the beam path.
3. A filter wheel with a variety of neutral density filter enables the regulation of the light intensity.
4. An electro-optic modulator (EOM) followed by a quarter wave plate ($\lambda/4$) modulate the laser linear polarization in four distinct directions ($0°, 45°, 90°$ and $135°$) in the microscope stage plane.
5. A filter wheel is used to alternatively block the laser path (beam shutter), pass the beam through a linear polarizer (to test the polarization direction of the beam), or open the beam. The linear polarizer is inserted temporarily at the beginning of each movie to determine the correspondence between frame number and beam polarization direction.
6. To compensate for phase distortions introduced by a single dichroic mirror, two identical dichroic mirrors (DM1 and DM2) with reflection planes perpendicular to each other are used. The first dichroic (DM1) is outside the microscope and the second one (DM2) is located in one of the microscope filter cubes.
7. The beam is expanded by a beam expander (BE).
8. A defocusing lens (DL) provides wide field illumination of the sample which is directed to the epifluorescence port of an inverted microscope.
9. The beam is directed towards the objective ($100\times$, oil immersion, 1.45 NA) and the sample by reflection in a dichroic mirror (DM2).
10. The fluorescence light emitted by the sample passes through the dichroic mirror and is filtered by additional emission filters (EF) to further eliminate unwanted background fluorescent and scattered light.
11. Images of the emitted light are recorded on a high sensitivity digital camera (Andor iXon +897 back-illuminated EMCCD). The resulting image pixel size in this set up is 48 nm.
12. Movie data acquisition is synchronized by the waveform generators with the electro-optic modulator so that every four frames images corresponding to each of the four excitation polarization directions are recorded.

2.5 Protein Preparation

1. Desalting column: Biorad, Econo-Pac 10DG.
2. AKTA Basic Fast Performance Liquid Chromatography (FPLC), GE Healthcare Life Sciences.
3. Size exclusion column: GE Healthcare Life Sciences, Superdex 200 Increase 10/300 GL.
4. Ultracentrifuge: Beckman Optima TLX with TLA 100 and TLA 100.3 rotors.

3 Methods

3.1 Kinesin Labeling

1. Using a desalting column or size exclusion column, exchange the buffer in which the protein was purified or stored to the labeling buffer.
2. Incubate the protein solution with the BSR probe overnight at 4 °C with a 1:1 BSR:kinesin ratio. Alternatively, a shorter incubation time (40 min) with a higher BSR:kinesin ratio (up to 3.5:1) also produces a good yield of labeled protein. We usually achieve 80–100% labeling efficiency with these protocols. For BR-I_2 or with other proteins different incubation times or different probe:protein ratios may be required (*see* **Note 6**).
3. Stop the labeling reaction by adding 1 mM DTT for 10 min.
4. To separate the labeled protein from un-reacted BSR pass the reaction through a desalting column equilibrated with purification buffer. The pink color of the labeled kinesin makes it easily traceable while it migrates through the column.
5. Concentrate the kinesin to the required volume for the loading loop of the FPLC apparatus for the next step.
6. To purify the protein from potentially present aggregates or higher molecular weight cross-linked species pass the labeled-kinesin solution through a size exclusion column equilibrated with purification buffer.
7. Check the purity of the preparation with a SDS-PAGE with UV exposition followed by Coomassie staining. Protein labeled with the BSR will emit fluorescence under UV illumination.
8. Check the labeling efficiency. Measure the absorption at 549 nm of the purified labeled sample to estimate the BSR concentration and any suitable method to estimate the protein concentration (Bradford assay or measuring the band density in a calibrated Coomassie stained SDS-PAGE gel).
9. To the purified protein add sucrose from the concentrated stock to a final 20% w/v.
10. Aliquot the labeled kinesin (4–10 μl per aliquot), flash freeze and store the aliquots at −80 °C protected from light. For every experiment, new kinesin aliquots are thawed on ice.
11. To check for cross-linking of the target cysteines perform tryptic digestion followed by liquid chromatography mass spectrometry and ensemble FPM measurements (*see* **Note 7**).
12. Biochemical or motility functional assays should be performed to characterize potential alterations introduced by labeling and the cysteines substitutions introduced. Depending on the type of kinesin used, properties like microtubule activated ATPase activity, microtubule binding, mobility along microtubule, or microtubule depolymerization activity should be tested.

3.2 Flow Chamber Preparation

Samples are imaged in flow-chambers made with two glass coverslips. One of the coverslips is treated with DETA (Subheading 3.2.1) to increase microtubule attachment [21].

3.2.1 Preparation of DETA Treated Coverslips

1. Put 22 × 50 mm coverslips in a metallic slide rack.
2. Rinse them with ultrapure water.
3. Sonicate the coverslips for 15 min in a solution of 0.5 M KOH.
4. Wash three times for 15 min (3 × 15) by sonication in ultrapure water.
5. In a glass container, incubate the coverslips with DETA solution. Take into consideration that the DETA solution is corrosive; use gloves.
6. Incubate overnight at room temperature (~20–25 °C).
7. Wash three times for 15 min (3 × 15) by sonication in ultrapure water.
8. Place coverslips in an oven at 130 °C until dry.
9. Store the coverslips interleaved with filter paper in a Petri dish in a desiccator. We have stored the slides for over a month without detecting problems with microtubule attachment.

3.2.2 Flow Chambers Assembly

On the DETA treated coverslip apply two double-sided sticky tape bands ~5 mm wide along the coverslip leaving a ~5 mm space in between. Attach a smaller 18 × 18 mm untreated coverslip to the tape to form the chamber.

3.3 Microtubules

1. Thaw an aliquot of tubulin on ice.
2. To remove aggregated tubulin, spin the tubulin at 313,000 × *g* for 10 min at 4 °C in ultracentrifuge and recover the supernatant.
3. Add 1 mM GTP to the supernatant and incubate at 35 °C during 40 min.
4. Add paclitaxel to the GTP microtubules to a final concentration of 20 μM and further incubate 40 min at 35 °C.
5. Eliminate unpolymerized tubulin by spinning the microtubule solution at 15,000 × *g* at 25 °C and resuspend the pellet in BRB80 with 20 μM paclitaxel.
6. Store the polymerized microtubules at 25 °C.
7. Estimate the tubulin concentration of the resuspended microtubules by an appropriate method [22].

3.4 Sample Preparation for an Imaging Session

For each imaging session, a fresh imaging solution is prepared using new aliquots for every component. When starting with a new system, it is advisable to prepare in parallel several slides having different concentrations of kinesin and microtubules to find the

best concentrations for the collection of ensemble or single molecule data.

1. Thaw on ice one aliquot of each of the stock solutions of BSA, PCD, PCA, Trolox, Taxol and the particular nucleotide to be used.
2. Prepare the imaging solution by mixing the appropriate stock solutions. To 165 µl of BRB12, add at room temperature 20 µl of BSA, 2 µl of paclitaxel, 5 µl of PCA, 2 µl of PCD, 2 µl of Trolox, and 4 µl of the appropriate nucleotide to get 200 µl total volume. Place 100 µl of the imaging solution on ice to use for kinesin dilutions.
3. Dilute the microtubules to 40 nM in BRB80 supplemented with 20 µM paclitaxel (room temperature).
4. Add 5 µl of microtubule into the flow chamber and incubate for 5 min to let them bind to the coverslip surface.
5. Block the glass surface by adding 15 µl of imaging buffer at 25 °C. Flow the solution into the chamber by placing the pipette tip at one of the openings ends and the tip of a cut filter paper at the other end. Be careful not to dry the chamber by drawing to much liquid with the filter paper. Incubate for 5 min.
6. Dilute the kinesin in the imaging solution to the desired concentration and flow it into the chamber as done in the previous step (*see* **Note 8**).
7. To prevent the sample from drying during imaging, seal the two openings of the chamber with rubber cement.

3.5 Laser Illumination Alignment and Beam Polarization Adjustment

Before recording a data set it is important to check and adjust if needed the polarization direction and purity for each of the four polarizations directions used, as well as the general alignment of the microscope laser illumination.

1. If necessary align the laser path moving slightly mirrors M1, M2, and M3 to make sure that the beam comes straight up after reflecting from the dichroic mirror (DM2, Fig. 2) and going through the objective. Then check that the sample illumination center gets imaged near the center of the camera CCD.
2. Check that each of the four voltage setting of the waveform generator used to modulate the EOM produces the correct polarization directions; if not, adjust the EOM amplifier bias and/or waveform amplitude of the waveform generator. To check the polarization directions, place a calibrated polarizer in the beam path on the microscope stage with the beam coming straight up from the dichroic without the objective (wear protective glasses). Set the DC output voltage of the waveform generator to each of the four voltages predetermined to

produce each of the four polarization directions to be used. For each voltage rotate the dichroic until minimum intensity is detected. In this situation, the orientation of the polarizer should then be 90° from the desired orientation. If not, adjust the waveform output voltage until this condition is met. After finding the right voltages for the four polarization directions, create a staircase waveform with these values to be sent to the EOM during movie collection.

3. Check the polarization purity for each of the four polarizations directions. With a calibrated linear polarizer in the path, set the polarization beam in a particular direction η (by adjusting the waveform generator DC output to one of four predetermined voltages), measure the beam intensity with the linear polarizer oriented at η and $\eta + 90°$, and calculate the ratio between the intensities $p_\eta = (I_\eta - I_{\eta+90})/(I_\eta + I_{\eta+90})$. The ratio p measures the polarization purity ranging from zero (non polarized light) to 1 (pure linearly polarized light). Typical p values in our set-up for each of the four laser polarization directions used are $p_0 = 0.98$, $p_{45} = 0.97$, $p_{90} = 0.99$, and $p_{135} = 0.96$.

3.6 Imaging

1. Digital movies are recorded using Andor Solis software to control the camera. Set the desired acquisition parameters in the Solis program (kinetic mode, frame rate externally controlled by the waveform generator, gain, number of frames to be collected etc.).
2. Prepare a sample as described previously in Subheading 3.4. The flow chamber is placed in the microscope with the DETA treated cover slide facing the objective. Adjust the focus and find a region of interest using the minimum possible laser excitation light to avoid bleaching. For single molecule recording we use a kinesin concentration between 0.1 and 4 nM (*see* **Note 9**).
3. Once that a region of interest is found and in focus, block the beam using the shutter in FW2 and set the beam to the desired illumination intensity using the appropriate ND filter in FW1. Beam intensity and frame rate are set to optimize signal to noise and time resolution. Higher beam intensity is at the expense of a higher bleaching rate and a higher frame rate for better time resolution is at the expense of lower signal to noise ratio. We typically collect data at 10 or 40 Hz (100 or 25 ms/frame) with an illumination intensity between 0.5 and 5 kW/cm^2.
4. Start movie recording with the Solis software and start the illumination-sequence-protocol. We use a protocol in which a few frames are collected first with the beam blocked, then a few frames collected with the beam open and a tester linear polarizer (0° direction) in the excitation path (FW2 Fig. 2), and then

with the beam open and no tester polarizer for the rest of the movie data collection period. Illumination intensity control and the opening beam protocol are performed by rotating the filter wheels (FW1 and FW2, Fig. 2) to the appropriate positions using a custom control program (Wheel_control.exe, *see* **Note 10**). The frames with the beam blocked are used to determine the background light intensity level of each movie. The frames with the tester polarizer are used to determine the phase of the excitation beam polarization direction (i.e. the correspondence between frame number and excitation polarization direction). After a movie is recorded move to another area and repeat from **step 3** above to collect data from multiple microtubules from each prepared flow chamber. Individual movies are usually recorded for 3–6 min. We record data for no longer than 1 h per chamber.

3.7 Data Analysis

The raw data collected are digital movies of the fluorescent samples where the excitation light polarization direction changes between four possible values (0°, 45°, 90°, 135°). From these movies, we extract background corrected fluorescent intensity values (I_0, I_{45}, I_{90}, I_{135}) in space and time for each of the four polarization excitation directions using a custom Windows GUI program (FRVIEW, *see* **Note 10**). From the intensity values of single and ensemble of molecules we estimate the orientation of the fluorescent dipoles and their mobility (*see* Fig. 3 for angle definitions). The program FRVIEW reads the digital movie files (Andor .sif file format) and displays image frames or position vs. time kymographs. The kymographs are used to select single molecule trajectories for analysis (Fig. 4a). Assigning the corresponding excitation polarization direction to each movie frame is done automatically in FRVIEW based on the illumination-sequence-protocol (*see* Subheading 3.4). The program generates tab separated text files with all the pertinent data such as excitation light polarization direction, fluorescent intensity, calculated linear dichroism values (LD), coordinates in the (X,Y) plane, time, etc. These files can be conveniently read by other software programs for further analysis.

3.7.1 Analysis of Single Molecule Data

1. Manually mark single molecule trajectories from a position vs. time kymograph display (Fig. 4a, b). Coordinate points between manually selected ones are estimated by linear or polynomial interpolation. The center position of the fluorescent spot at each time frame is then estimated as the center of mass within a region of interest centered at the initially marked coordinates.
2. The fluorescence intensity for each spot frame is determined as the average number counts in an appropriate region of interest (7×7 pixel with our setup) centered at the estimated center of

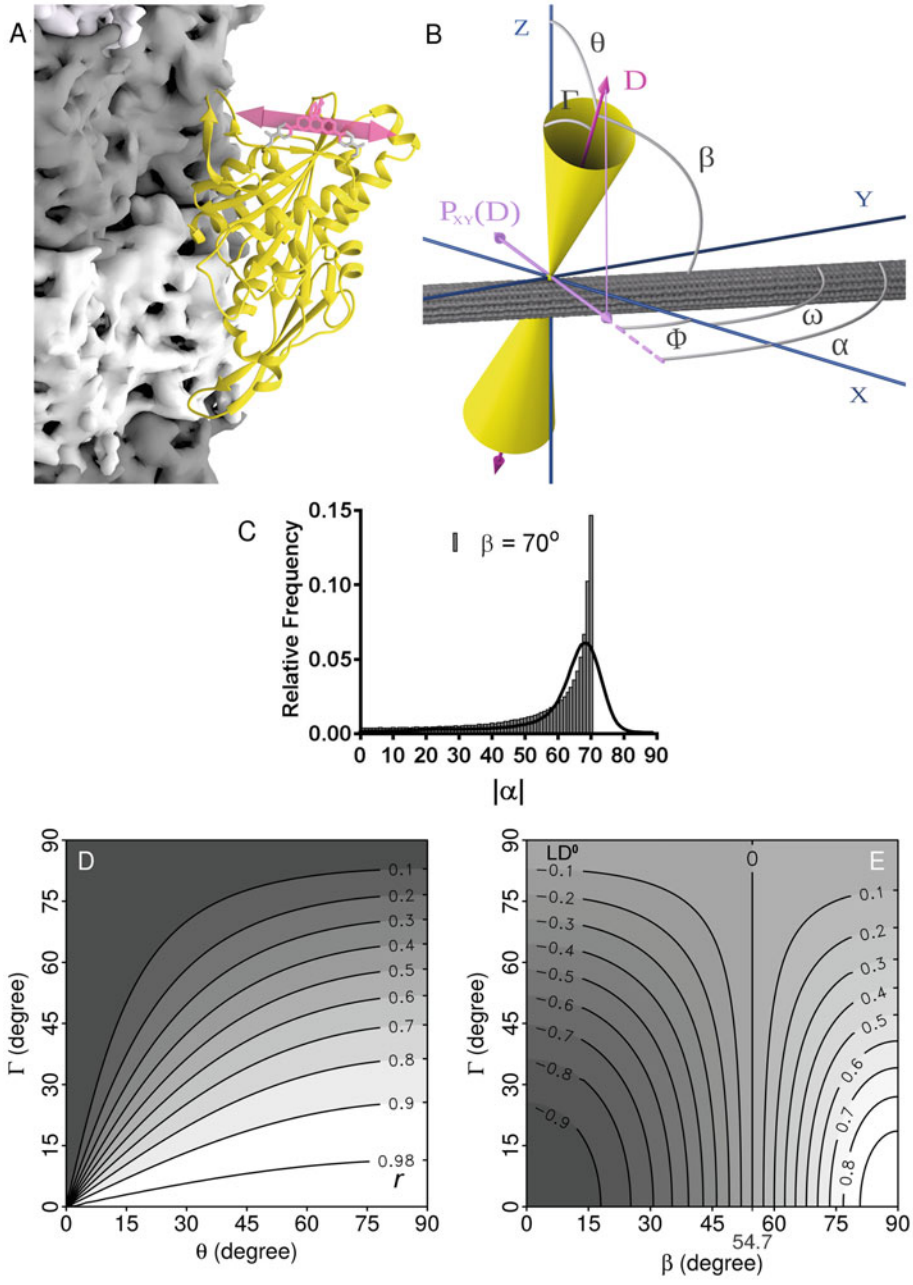

Fig. 3 Probe orientation and angles definitions. (**a**) Model of a kinesin microtubule complex in the typical tight bound configuration with the BSR probe attached in one of the target regions used in smFPM studies. The Kinesin motor domain is represented with ribbons (*yellow* in color figure), the microtubule as a *gray surface*, and the BSR probe as atom and sticks (*magenta* in color figure). The *double arrow* indicates the direction of the BSR fluorescence transition dipole moment. (**b**) Definition of the angles used in the eqs. (*X*,*Y*) is the plane of the microscope stage with the *X* axis oriented as the left-right translation direction of the microscope stage (*see* also Fig. 2). The direction of the fluorescence transition dipole moment is represented as a *double arrow* and noted *D*. It's projection on the (*X*,*Y*) plane is noted P_{XY} (*D*). β is the mean axial angle (referred simply as the axial angle) with the filament axis of a probe that pivots rapidly within a cone of semi-angle Γ (mobility cone

the fluorescence spot minus the background intensity. Estimate the background as the average counts in an area close by without fluorescence trajectories or after the molecule bleaching event. Coordinate and intensity data for each selected trajectory in a movie are saved to tab delimited text files for further analysis.

3. Select trajectories corresponding to single molecules. We restrict the analysis to single molecule trajectories that end by an abrupt drop to near zero intensity due to a photobleaching or unbinding event. Multiple stair case drops in intensity are evidence of more than one molecule present. We exclude molecules that have multiple time and position overlaps with other molecules (evidenced as kymograph trajectories with multiple crossings).
4. Refine the coordinates. A custom python script (evnrawreproc.py, *see* **Note 10**) reads the files created by FRVIEW and the original movie files to further refine the *xy* coordinates of the fluorescent spot center positions. The script fit 2D Gaussian functions to the intensity profile of each selected single molecule trajectory frame.
5. The fluorescence intensity for each of the four polarization directions (I_0, I_{45}, I_{90}, I_{135}) in a given time period is calculated as the average of all the values corresponding to each polarization direction during such a period (with the shortest possible period corresponding to four frames, one for each polarization excitation direction).
6. From the four intensity values (I_0, I_{45}, I_{90}, I_{135}) calculate the two linear dichroism ratios LD_1 and LD_2 ($\mathrm{LD}_1 = \mathrm{LD}_{0,90}$ and $\mathrm{LD}_2 = \mathrm{LD}_{45,135}$) as:

$$\mathrm{LD}_{\eta,\eta+90^\circ} = \frac{I_{\eta+90} - I_\eta}{I_{\eta+90} + I_\eta} \tag{1}$$

Fig. 3 (continued) angle). α is the probe dipole angle projected in the *XY* plane minus the filament axis angle in the plane (ω). **c** and **e** shows the relationship between β and Γ for a cylindrically symmetric distribution of probes (such as the one expected for a kinesin decorated microtubule) with the values α, *r*, and LD^0 obtained from single molecule and ensemble FPM measurements. (**c**) Simulated frequency distribution of single molecule α values for a distribution of probes uniformly bound around a cylindrical axis with axial angle β without adding noise (*bars*) or adding Gaussian noise (*lines*) to the simulated intensity values. The $|\alpha|$ distribution has a peak near the β angle and a tail towards 0°. (**d**) Contour plot showing the relationship between the order *r* factor (contour values and *grey level*), the mobility cone angle Γ (*Y*-axis), and the angle θ (*X*-axis) of the probe from the *Z* axis (from Eq. 3). (**e**) Contour plot showing the relationship between the ensemble LD^0 (contour values and *grey level*), the mobility cone angle Γ (*Y*-axis), and the axial angle β (*X*-axis) according to Eq. 6

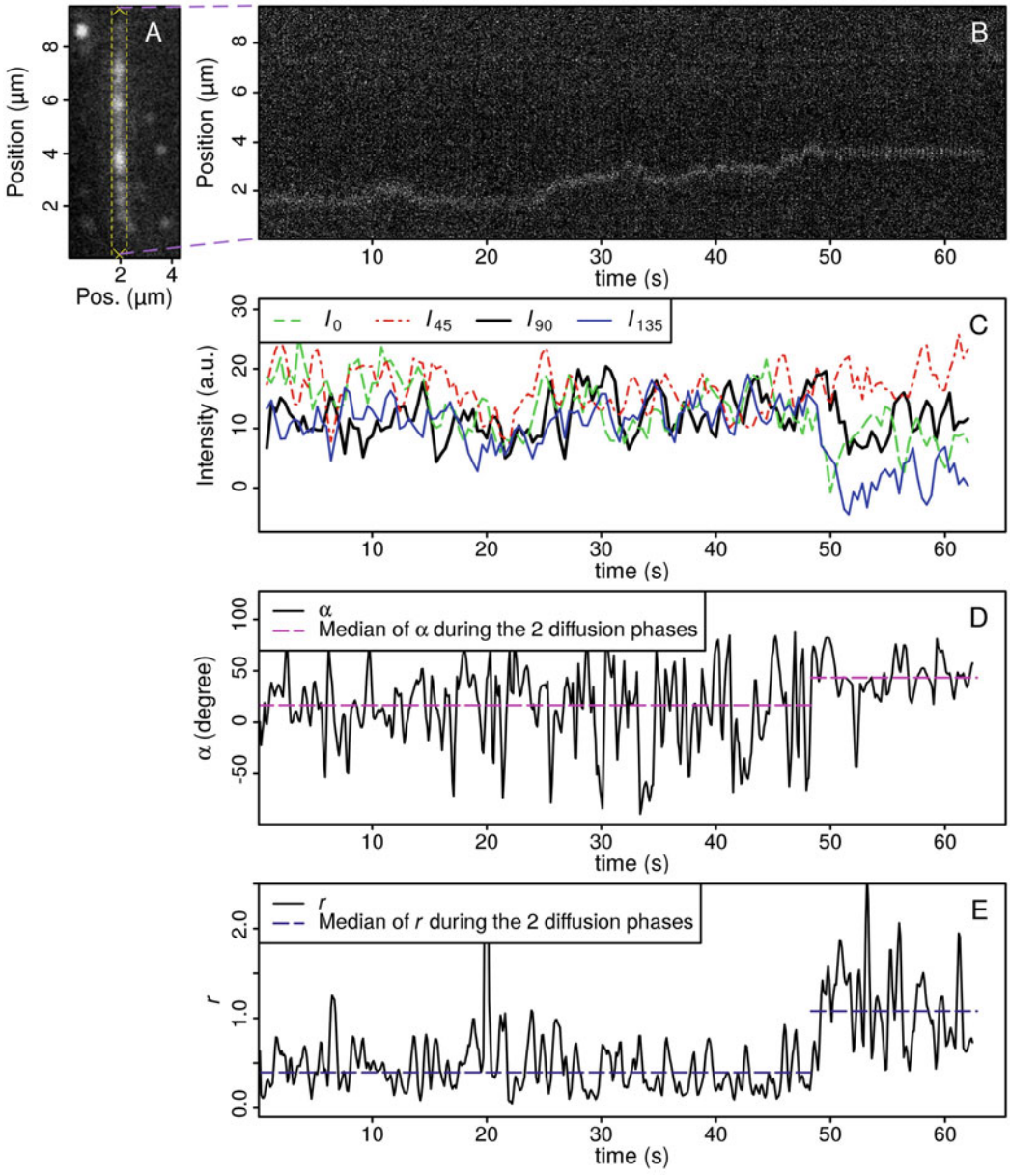

Fig. 4 Example of time resolved single molecule data with estimation of the dipole direction projected angle (α) and order factor (r) along the trajectory. The kinesin used is a construct of the *Drosophila melanogaster* kinesin-13 KLP10A labeled with BSR in the location indicated in Fig. 2a. In this example a kinesin molecule is bound to the microtubule with high rotational mobility (low order r factor) while undergoing one-dimensional diffusion along the microtubule and then become stationary (at time 50 s in **b**) with reduced angular mobility (higher order r value). (**a**) Image of the microtubule analyzed. To produce this image several frames involving several kinesin binding events were averaged. (**b**) Position vs. time kymograph taken from the microtubule shown in **a**. The kymograph shows a single kinesin labeled molecule undergoing one-dimensional-diffusion. (**c**) Fluorescence intensities corresponding to each of the four excitation polarization directions for the trajectory molecule shown in (**b**). (**d**) Calculated projected angle α of the molecule (three frames-set running

7. The mean projected angle Φ of the fluorophore in the XY plane and the order r factor is calculated form LD_1 and LD_2 as (Eqs. 5, 6, 7 from [20]):

$$\begin{cases} r = \sqrt{{LD_1}^2 + {LD_2}^2} \\ \cos^2(\Phi) = \frac{1}{2}\left(1 - \frac{LD_1}{r}\right) \\ \cos^2(\Phi - 45) = \frac{1}{2}\left(1 - \frac{LD_2}{r}\right) \end{cases} \tag{2}$$

The order r factor depends on Γ and θ according to the following expression derived from [19]:

$$r(\Gamma, \theta) = \frac{3\sin^2(\theta)}{1 + \frac{4}{\cos(\Gamma) + \cos^2(\Gamma)} - 3\cos^2(\theta)} \tag{3}$$

The r factor strongly depends on Γ, the mobility cone semi-angle (Fig. 3d) and therefore gives an indication of the probe mobility going from zero for fully mobile probes to 1 for perfectly localized ones.

The projected angle relative to the microtubule axis α is calculated as:

$$\alpha = \Phi - \omega \tag{4}$$

From the distribution of α values of many kinesin molecules the axial angle β of the probes with the microtubule axis can be inferred (Fig. 3c).

8. The resulting simultaneous recording of fluorophore orientation, mobility and position obtained by smFPM can then be used to obtain structural and functional insights into the molecule of interest. For example using this method we were able to determine that the two motor domains of kinesin-1 alternate between a disordered and a well oriented configuration as the molecule walks processively along microtubules at limiting ATP concentrations [12]. We also observed a correlation between the angular orientation of the kinesin-13 motor domain and its ability to diffuse along the microtubule lattice [13].

Fig. 4 (continued) average). The median α value during each of the two movement phases is indicated by the *magenta dashed lines*. (**e**) Calculated order *r* factor (three frames-set running average). The median *r* value during each of the two movement phases is indicated by the *dashed lines*. The traces show changes in angular mobility (rapid changes in orientation of the kinesin motor domain to which the BSR probe is attached) that correlate to whether the molecule is undergoing one-dimensional-diffusion or being stationary

3.7.2 Analysis of Fluorescence Polarization of Microtubule Covered by an Ensemble of Kinesins

1. We usually collect ensemble FPM data before smFPM experiments as they: (a) can serve to check if the labeling strategy worked (*see* **Note 7**) and (b) provide data complimentary to the smFPM data (*see* **Note 11**). Ensemble FPM data is collected in a similar way that the smFPM data but the kinesin concentration used in the experiments is higher (typically around 100–200 nM) and the larger fluorescence intensity produced by the ensemble allows the use of lower laser excitation (typically 0.02–0.2 kW/cm^2).
2. Collect digital movies of microtubules decorated with fluorescently labeled proteins randomly oriented in the (X,Y) plane.
3. From the digital movies measure the average intensity of the microtubule area (MTa) and an adjacent area (BKGa) to estimate the fluorescence intensity (I) of the microtubule over the background ($I = I_{\mathrm{MTa}} - I_{\mathrm{BKGa}}$) for each of the four excitation polarization excitations used. From the four fluorescent intensities calculate the LDs values as done with the smFPM data (This is all done automatically in FRVIEW by selecting a region of interest on the microtubule, another in an adjacent area and given the time period to average intensities).
4. Estimate the LD^0 value. LD^0 is equal to the LD_1 of microtubules oriented with their axes oriented parallel to the X axis ($\omega = 0^\circ$) and is estimated from the LD_1 values of many randomly oriented microtubules by non-linear fitting the data to the equation [19]:

$$\mathrm{LD}_1 = \mathrm{LD}^0 \cos(2\omega) \tag{5}$$

For a distribution of fluorophores with cylindrical symmetry (such as the one produced by microtubules decorated with many labeled kinesin molecules) the LD^0 is related to axial angle of the fluorophores with the microtubule axis β and their mobility semi cone angle Γ by the following equation [19]:

$$\mathrm{LD}^0 = \frac{-3}{1 + 8/[(3\cos^2(\beta) - 1)(\cos(\Gamma) + \cos^2(\Gamma))]} \tag{6}$$

For a distribution of probes close to perpendicular or parallel to the microtubule axis (β close to 90° or 0° respectively) LD^0 is strongly dependent on the mobility cone semi-angle Γ, going from zero for fully mobile probes ($\Gamma = 90^\circ$) to 1 or −1 respectively for fully localized ones ($\Gamma = 0^\circ$) (Fig. 3e).

4 Notes

1. We use PIPES from Sigma (PIPES dipotassium salt, P7643), which produces less autofluorescence than other PIPES we have used.
2. To increase kinesin-microtubule binding we usually use a lower ionic strength buffer (BRB12 vs. BRB80). Experiments performed with BRB12 also have less background fluorescence (autofluorescence).
3. A higher pH than the regular BRB80 (7.4 vs. 6.8) buffer improves the labeling yield.
4. To avoid autofluorescence we use high purity BSA (Sigma #A0281, fatty acid and globulin free). In addition we spin the BSA stock solution (220,000 × *g*, 15 min) to precipitate and eliminate impurities. After centrifugation, the supernatant is taken and the small black precipitate that usually forms is discarded.
5. The nucleotide to be included in the imaging solution depends on the experiment to be performed. Other nucleotide analogues conditions we have used are presence of ADP + AlF_4^- (made from 100 mM ADP, 198 mM AlCl and 1 M KF) and absence of nucleotides (by including the enzyme apyrase to hydrolyze any ATP and ADP present in the solution).
6. For experiments with the BR-I_2 probe a step-wise addition of the fluorophore at room temperature (addition of four equal amounts of probe every 30 min to a final 2:1 probe:protein ratio) has been used [17].
7. If possible, the location of the target cysteines should be chosen such that the direction of the probe dipole will be near parallel or perpendicular to the microtubule axis in some standard condition (e.g. when a labeled motor domain is strongly bound to the microtubule). In these conditions, successful labeling and cross-linking with the probe can be verified by the expected signed anisotropy values obtained in ensemble FPM measurements (*see* Subheading 3.7.2). If the labeling location on the kinesin protein is such that the probe would be near perpendicular ($\beta = 90°$) or parallel ($\beta = 0°$) to the microtubule axis then verification that they produce the expected LD^0 in the given conditions is strong confirmation that the probe is cross linked to the protein as expected (i.e. LD^0 values near 1 or −1 respectively for perpendicular or parallel oriented probes). Lack of anisotropy ($LD^0 \sim 0$) in these conditions suggests highly mobile probes, either because the protein does not bind to the microtubules as expected or

the bifunctional probe is not properly attached to the protein (single rather than double attachment).

8. An alternative way to prepare the sample (**steps 2–6**) is to pre-incubate microtubules and kinesin together in the imaging solution and flow the mix into the flow chamber.
9. Focusing and finding microtubules to image can be difficult at low kinesin concentrations given that we usually use unlabeled microtubules. To avoid this problem, it is recommended to have the focus position of the microscope pre-determined before placing the experimental chamber in the microscope stage. This can be done by focusing a cover slip with the surface marked by lines made with a red sharpie magic marker (they conveniently fluoresce when illuminated with the laser light). If kinesin decorated microtubules are still not found, this may indicate a problem with the microtubules (e.g. low concentration of polymer) or the kinesin preparation. This can be quickly ruled out by doing an experiment with a labeled prep known to bind well to microtubules and using a higher kinesin concentration. It is also advisable to start any imaging session with a high kinesin concentration (appropriate to ensemble imaging) and then lower the concentration as needed to resolve single molecules.
10. All custom software programs referenced in the manuscript are available for academic use upon request to the authors.
11. The ensemble polarization data provides anisotropy LD^0 values that depend on the axial angle (β) of the probes with the microtubule axis and the probe mobility (expressed as the mobility cone angle Γ). The ensemble LD^0 values must be consistent with the angles and mobility values derived from the distribution of many smFPM measurements obtained in similar conditions.

Acknowledgements

We thank members of the Sosa's lab A.B.. Asenjo and M. Airo for discussions and proofreading the manuscript. This work was supported by NIH grant R01GM113164.

References

1. Peterman EJ, Sosa H, Moerner WE (2004) Single-molecule fluorescence spectroscopy and microscopy of biomolecular motors. Annu Rev Phys Chem 55:79–96
2. Belyy V, Yildiz A (2014) Processive cytoskeletal motors studied with single-molecule fluorescence techniques. FEBS Lett 588 (19):3520–3525. doi:10.1016/j.febslet.2014.05.040
3. Elting Mary W, Spudich James A (2012) Future challenges in single-molecule fluorescence and laser trap approaches to studies of

molecular motors. Dev Cell 23(6):1084–1091. doi:10.1016/j.devcel.2012.10.002

4. Warshaw DM, Hayes E, Gaffney D, Lauzon AM, Wu J, Kennedy G, Trybus K, Lowey S, Berger C (1998) Myosin conformational states determined by single fluorophore polarization. Proc Natl Acad Sci U S A 95(14):8034–8039
5. Adachi K, Yasuda R, Noji H, Itoh H, Harada Y, Yoshida M, Kinosita K Jr (2000) Stepping rotation of F1-ATPase visualized through angle-resolved single-fluorophore imaging. Proc Natl Acad Sci U S A 97(13):7243–7247
6. Ha T, Laurence TA, Chemla DS, Weiss S (1999) Polarization spectroscopy of single fluorescent molecules. J Phys Chem B 103 (33):6839–6850
7. Axelrod D (1989) Fluorescence polarization microscopy. Methods Cell Biol 30:333–352
8. Forkey JN, Quinlan ME, Shaw MA, Corrie JET, Goldman YE (2003) Three-dimensional structural dynamics of myosin V by single-molecule fluorescence polarization. Nature 422:399–404
9. Sosa H, Peterman EJ, Moerner WE, Goldstein LS (2001) ADP-induced rocking of the kinesin motor domain revealed by single-molecule fluorescence polarization microscopy. Nat Struct Biol 8(6):540–544
10. Asenjo AB, Krohn N, Sosa H (2003) Configuration of the two kinesin motor domains during ATP hydrolysis. Nat Struct Biol 10 (10):836–842
11. Asenjo AB, Weinberg Y, Sosa H (2006) Nucleotide binding and hydrolysis induces a disorder-order transition in the kinesin neck-linker region. Nat Struct Mol Biol 13 (7):648–654
12. Asenjo AB, Sosa H (2009) A mobile kinesin-head intermediate during the ATP-waiting state. Proc Natl Acad Sci U S A 106 (14):5657–5662. doi:10.1073/pnas.0808355106. 0808355106 [pii]
13. Chatterjee C, Benoit Matthieu PMH, DePaoli V, Diaz-Valencia Juan D, Asenjo Ana B, Gerfen Gary J, Sharp David J, Sosa H (2016) Distinct interaction modes of the kinesin-13 motor domain with the microtubule. Biophys J 110(7):1593–1604. doi:10.1016/j.bpj.2016.02.029
14. Aitken CE, Marshall RA, Puglisi JD (2008) An oxygen scavenging system for improvement of dye stability in single-molecule fluorescence experiments. Biophys J 94(5):1826–1835
15. Penzkofer A, Wiedmann J (1980) Orientation of transition dipole moments of rhodamine 6G determined by excited state absorption. Opt Commun 35(1):81–86
16. Corrie JET, Brandmeier BD, Ferguson RE, Trentham DR, Kendrick-Jones I, Hopkins SC, van der Heide UA, Goldman YE, Sabido-David C, Dale RE, Criddle S, Irving M (1999) Dynamic measurement of myosin light-chain-domain tilt and twist in muscle contraction. Nature 400(6743):425–430
17. Chen C, Cui X, Beausang JF, Zhang H, Farrell I, Cooperman BS, Goldman YE (2016) Elongation factor G initiates translocation through a power stroke. Proc Natl Acad Sci 113 (27):7515–7520
18. Miller HP, Wilson L (2010) Preparation of microtubule protein and purified tubulin from bovine brain by cycles of assembly and disassembly and phosphocellulose chromatography. Methods Cell Biol 95:3–15. doi:10.1016/S0091-679X(10)95001-2. S0091-679X(10)95001-2 [pii]
19. Peterman EJ, Sosa H, Goldstein LS, Moerner WE (2001) Polarized fluorescence microscopy of individual and many kinesin motors bound to axonemal microtubules. Biophys J 81 (5):2851–2863
20. Sosa H, Asenjo AB, Peterman EJ (2010) Structure and dynamics of the kinesin-microtubule interaction revealed by fluorescence polarization microscopy. Methods Cell Biol 95:505–519. S0091-679X(10)95025-5 [pii]. doi:10.1016/S0091-679X(10)95025-5
21. Verbrugge S, Kapitein LC, Peterman EJ (2007) Kinesin moving through the spotlight: single-motor fluorescence microscopy with submillisecond time resolution. Biophys J 92 (7):2536–2545
22. Hackney DD, Jiang W (2001) Assays for kinesin microtubule-stimulated ATPase activity. Methods Mol Biol 164:65–71

Chapter 12

Single Molecule FRET Analysis of DNA Binding Proteins

Kathy R. Chaurasiya and Remus T. Dame

Abstract

The complex binding dynamics between DNA and proteins are often obscured by ensemble averaging effects in conventional biochemical experiments. Single-molecule fluorescence methods are powerful tools to investigate DNA–protein interaction dynamics in real time. In this chapter, we focus on using single-molecule Förster Resonance Energy Transfer (smFRET) to probe the binding dynamics of individual proteins on single DNA molecules. We provide a detailed discussion of total internal reflection fluorescence (TIRF) instrument design, nucleic acid labeling with fluorophores, flow cell surface passivation, and data analysis methods.

Key words Single molecule, FRET, TIRF, Nucleic acid–protein interaction, DNA binding protein, PEG surface passivation

1 Introduction

Single-molecule spectroscopy has contributed significant insights into the complex dynamics of a wide range of biological systems, including DNA [1–3] and RNA polymerases [4–7], helicases [8–11], DNA binding proteins [12–16], and molecular motors [17–19]. These methods readily allow quantitative characterization of kinetic intermediates and heterogeneous populations that may be obscured by ensemble averaging effects in conventional biochemical experiments.

Single-molecule fluorescence imaging is a particularly useful tool to observe important biological processes in real time. Common fluorescence illumination methods include confocal scanning, epifluorescence, and total internal reflection (TIR). In TIR microscopy, the laser beam penetrates a surface–solution interface at a greater angle of incidence than the critical angle θ_c:

$$\theta_c = \sin^{-1}\left(\frac{n_1}{n_2}\right)$$

Erwin J.G. Peterman (ed.), *Single Molecule Analysis: Methods and Protocols*, Methods in Molecular Biology, vol. 1665, DOI 10.1007/978-1-4939-7271-5_12,

where n_1 and n_2 are the refractive index of the solution and surface, respectively [20]. This generates an evanescent wave with intensity I that penetrates the solution as a function of distance z:

$$I(z) = I_0 e^{\frac{-z}{d}}$$

where I_0 is initial intensity and d is the decay constant [21]. The penetration depth is approximately 100 nm from the surface. TIRF is therefore used to excite fluorophores near the surface–solution interface, which is an illumination method well-suited for single-molecule Förster Resonance Energy Transfer (smFRET).

FRET occurs when energy is transferred from a donor fluorophore to an acceptor fluorophore through dipole–dipole interactions [22]. The FRET pair shares spectral overlap such that donor emission overlaps with acceptor excitation. The energy transfer efficiency E is:

$$E = \frac{1}{1 + \left(\frac{R}{R_0}\right)^6}$$

where R is the distance between the two fluorophores and R_0 is the characteristic distance at which half of the energy is transferred [23]. This strong distance dependence allows sensitive measurements on the molecular scale, in the range of 2–10 nm [24], which makes FRET a powerful tool for characterizing the structure and dynamics of individual molecules in solution.

In smFRET experiments involving nucleic acids and nucleic-acid-binding proteins, fluorophore-labeled nucleic acids and proteins can be immobilized on a surface, extending imaging lifetimes. The fluorophores are excited by an evanescent wave generated by TIRF at the surface–sample interface. This combined approach has the key advantage of constraining fluorescence excitation to molecules within 100 nm of the surface, sharply reducing background from untethered molecules further in solution. Here, we discuss smFRET with TIRF excitation as a method to study DNA–protein interactions in real time. We present protocols for TIRF instrument design, nucleic acid labeling, surface passivation, sample immobilization, data acquisition, and data analysis.

2 Materials

2.1 TIRF Instrument

TIRF instruments are commonly designed using either a prism or a microscope objective, and each method has its advantages (*see* **Note 1**). Here, we describe an objective-based TIRF instrument with fiber-coupled lasers.

1. Green laser (532 nm, diode-pumped solid state, 80 mW, fiber-coupled, Coherent; *see* **Note 2**).
2. Red laser (640 nm, diode, 75 mW, fiber-coupled, Coherent; *see* **Note 3**).
3. Beam combiner (single mode fiber output, Coherent; *see* **Note 4**).
4. Two lenses for beam expansion (plano-convex, Thorlabs; *see* Subheading 3.1, **step 2**).
5. Lens to converge beam (plano-convex, 5 cm diameter, 350–400 mm focal length, Thorlabs).
6. Mirror (broadband dielectric, 5 cm diameter, Thorlabs).
7. Translation stage (4 cm range, Thorlabs).
8. Microscope frame (inverted, Nikon).
9. Dichroic mirror (longpass, 550 nm, Chroma).
10. Dichroic mirror (longpass, 655 nm, Chroma).
11. Objective lens (air, 40×, Nikon; optional, *see* Subheading 3.1, **step 7**).
12. Objective lens (for TIRF, 1.4 NA, oil immersion, 100×, Nikon).
13. Immersion oil (refractive index 1.5).
14. Dichroic mirror (longpass, 610 nm, Chroma).
15. Emission image splitter (Optosplit II, Cairn; *see* **Note 5**).
16. Electron-multiplying charge-coupled device (EMCCD) camera (iXon Ultra, Andor; *see* **Note 6**).
17. Bandpass filter (680/20 nm, Semrock).

2.2 DNA Construct Labeling

Nucleic acid oligonucleotides are biotin-modified at either terminus for surface immobilization, with amino-modified C6-dT nucleotides incorporated for fluorophore labeling. Here, we describe labeling and purification methods for synthetic, commercially available nucleic acid oligonucleotides.

2.2.1 Reverse-Phase High-Performance Liquid Chromatography (HPLC)

1. Nucleic acid oligonucleotides (biotin-modified, with amino-modified C6-dT at desired label position, desalted, 1 nmol, dry, Invitrogen).
2. Triethylammonium acetate (TEAA) buffer: 15 mM trimethylamine, 5% acetonitrile, pH 7.0. Adjust pH with glacial acetic acid (HPLC grade).
3. Acetonitrile (HPLC grade).
4. DNA storage buffer: 10 mM Tris–HCl, pH 8.0.
5. Vacuum concentrator (DNA SpeedVac, Thermo Scientific).

2.2.2 Fluorophore Labeling

1. Cy3, Cy5 (*N*-hydroxysuccinimide (NHS) ester form, 20 nmol, Amersham CyDye Mono-Reactive NHS Ester, GE Healthcare Life Sciences).
2. Dimethyl sulfoxide (DMSO).
3. Labeling buffer: 0.1 M sodium tetraborate, pH 8.5, −20 °C (*see* **Note 8**).
4. Thermomixer (Thermomixer Comfort, Eppendorf).

2.2.3 Ethanol Precipitation

1. 3 M sodium acetate.
2. 100 mM dNTPs.
3. Ethanol.

2.3 Sample Chamber Preparation

There are a number of slide cleaning and surface modification methods to minimize background fluorescence [25–27]. Here, we describe surface passivation with polyethylene glycol (PEG; *see* **Note 7**).

2.3.1 Slide Assembly

1. Drill with diamond bit (Dremel 3000, Dremel).
2. Glass microscope slides (76 × 26 mm, Thermo Scientific).
3. Glass coverslips (24 × 24 mm, Thermo Scientific).
4. Double-sided tape (Scotch).
5. Epoxy (Devcon).

2.3.2 Slide Cleaning

1. Double distilled water (ddH_2O).
2. Razor blades.
3. Powder detergent (Alconox, VWR).
4. Ethanol (200 proof).
5. Basic piranha solution: 150 mL ddH_2O, 30 mL 30% H_2O_2, 30 mL NH_4OH (ACS grade).
6. Beaker (250 mL).
7. Magnetic stir plate and stir bar (1.6 cm; *see* **Note 8**).
8. Tweezers (*see* **Note 9**).
9. Bunsen burner.
10. Slide rack (Micro Slide Staining Rack, VWR).
11. Coplin staining jars (Wheaton Scientific).
12. Sonicator.
13. 1 M KOH.
14. Methanol (ACS grade).

2.3.3 Aminosilanization

1. Aminosilanization solution: 100 mL methanol, 5 mL glacial acetic acid (ACS grade), 1 mL 3-aminopropyltriethoxysilane (Vectabond, Vector Laboratories; *see* **Note 10**).
2. Nitrogen gas.
3. PEGylation chambers (*see* **Note 11**).

2.3.4 PEGylation

1. PEGylation buffer: 84 mg $NaHCO_3$ dissolved in 10 mL ddH_2O, syringe-filtered (0.2 μm membrane; *see* **Note 12**).
2. PEGylation reaction solution: 7 mg biotinylated PEG succinimidyl carboxymethyl (Bio-PEG-SCM, MW 3400, Laysan Bio), 80 mg methoxy PEG SCM (mPEG-SCM, MW 5000, Laysan Bio), 380 μL bicarbonate PEGylation buffer (*see* **Notes 13** and **14**).

2.4 Sample Immobilization

Nucleic acids and proteins can be tethered to the surface in a variety of ways, which lends flexibility to the design of in vitro FRET experiments. Here, we describe DNA construct immobilization through a biotin–streptavidin linkage (*see* **Note 15**).

1. DNA (biotin- and fluorophore-labeled, *see* Subheadings 2.2 and 3.2).
2. Annealing buffer: 50 mM MOPS, pH 7.4, 5 mM $MgCl_2$, 60 mM NaCl, 2 mM Trolox. (This buffer is for dsDNA constructs; *see* **Note 16**.)
3. Dry block heater (Grant Instruments).
4. T50 buffer: 50 mM Tris–HCl, pH 7.0, 50 mM NaCl.
5. Bovine serum albumin (BSA) solution: 0.2 mg/mL BSA in T50 buffer. (To use BSA for surface passivation in experiments without PEG, *see* **Note 17**).
6. Streptavidin solution: 1 mg/mL streptavidin in T50 buffer.
7. Experimental buffer: 40 mM Tris–HCl, pH 7.9, 5 mM $MgCl_2$, 60 mM NaCl, 0.2 mg/mL BSA, 2 mM 6-hydroxy-2,5,7,8-tetramethylchroman-2-carboxylic acid (Trolox; *see* **Note 18**), 2.5 mM 3,4-dihydroxybenzoic acid (PCA), 250 nM protocatechuate dioxygenase (PCD; *see* **Note 19**), up to 20 nM protein (*see* **Note 20**).

2.5 Data Acquisition and Analysis

Data is acquired with LabView, using a custom data acquisition (DAQ) card for the EMCCD. Fluorescent beads are used to match donor and acceptor signals using IDL, and single-molecule traces are analyzed using Matlab.

1. Fluorescent beads (FluoSpheres Carboxylate-Modified Microspheres, 0.2 μm, Red (580/605)).
2. 1 M $MgCl_2$.

3. LabView (National Instruments).
4. IDL (Harris).
5. Matlab (MathWorks).

3 Methods

3.1 TIRF Instrument

1. Mount the fiber-coupled lasers (*see* **Note 21**) and plug them into the beam combiner (Fig. 1).
2. Expand the beam output from the single mode fiber so that it is approximately 20 mm in diameter (*see* **Note 22**). Ensure that the beam is well-collimated.
3. Mount the mirror on a translation stage, and place it behind the microscope frame so that beam path enters the back port.
4. Insert the 550 nm and 655 nm longpass dichroic mirrors (for the green and red lasers, respectively) in separate, labeled cubes inside the filter turret. Begin with the 550 nm dichroic mirror first, so that the green laser beam enters perpendicular to the plane of the objective.
5. Converge the beam by placing the lens one focal length (350–400 mm) away from the objective.
6. Insert the beam target in one of the empty spaces in the objective turret. The beam should be clearly visible on the ceiling. If the beam is clipped, correct the beam path with the mirror on the translation stage (*see* **Note 23**).
7. Establish epifluorescence with the 40× objective to check the beam's alignment (optional, *see* **Note 24**). The beam will form a concentric ring pattern on the ceiling. If this pattern is angled or elongated, use the mirror to adjust the beam position laterally and horizontally so that the beam enters the objective at the correct angle of incidence.
8. Move the lens longitudinally along the beam path, minimizing the diameter of this concentric pattern. This precisely focuses the beam on the back focal plane of the objective so that the beam emerges collimated.
9. Insert the 100× TIRF objective and re-establish epifluorescence. This involves a small adjustment of the lens in order to focus the beam on the back focal plane of this particular objective (*see* **step 8**).
10. Establish TIRF by adjusting the lateral position of the beam with the mirror. As the beam moves towards the edge of entrance pupil of the objective, the illuminated pattern on the ceiling slides down the wall and disappears. Adjust the beam to

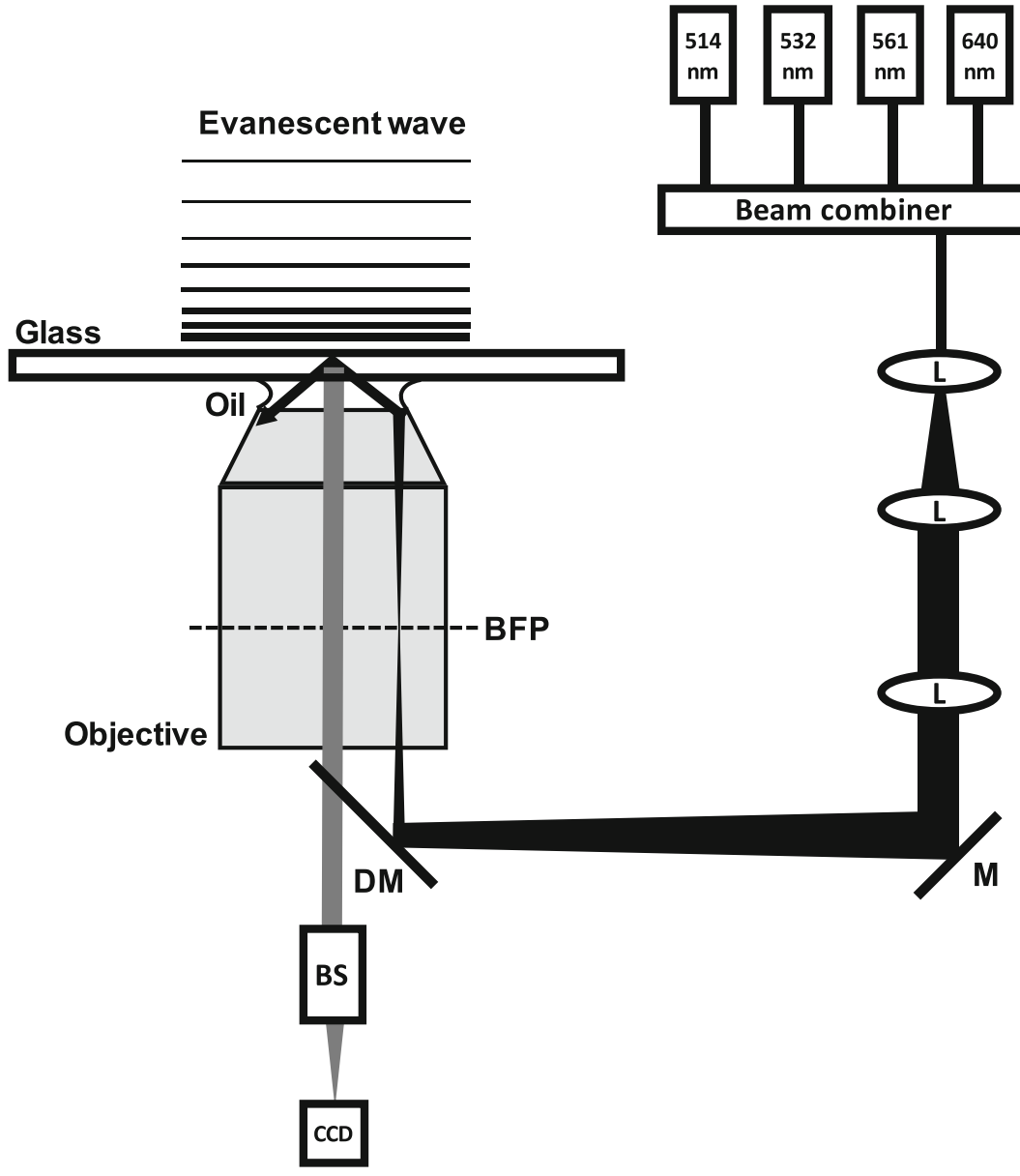

Fig. 1 Schematic representation of an objective-based TIRF instrument. Individual fiber-coupled lasers are combined and coupled into a single excitation beam, which is expanded with a set of lenses (L). The collimated beam is focused on the back focal plane of the objective with a lens, and steered with a mirror (M). A dichroic mirror (DM) directs the excitation beam into the objective. The beam enters at the edge of the objective, and TIR occurs at the glass–water interface, generating an evanescent wave to excite the molecules immobilized on the surface. The emission beam travels through objective, and the dichroic mirror (DM) directs it into the beam splitter (BS), where the donor and acceptor signals are separated and detected by a back-illuminated EMCCD camera

a position just before the vanishing point, so that it propagates along the outer edge of the objective.

11. Mount a fluorescent bead slide (*see* Subheading 3.5, **step 1**) above the objective, careful to ensure that the coverslip surface is in contact with the immersion oil. The beam will no longer be visible on the wall, due to total internal reflection at the interface between the coverslip and the sample chamber.
12. Direct the fluorescence signal through the eyepiece, adjusting the objective height to bring the beads into focus.
13. Insert the 610 nm longpass dichroic mirror in the image splitter. Install the image splitter on a side port of the microscope frame.
14. Install the EMCCD on the image splitter, careful to ensure that the unit is at the same height as the side port in order to avoid geometric aberration.
15. Direct the fluorescence signal through a side port. Adjust the mirror to achieve a uniform field of illumination. Align the short (donor) and long (acceptor) wavelength images on the left and right, respectively.
16. Adjust the lateral position of the beam with the mirror to visually optimize the signal-to-background ratio of the beads using the image on the EMCCD.
17. Remove the beads slide and mount a slide with Cy3-labeled DNA molecules (*see* Subheadings 3.3 and 3.4). Adjust the lateral position of the beam until Cy3 molecules suddenly become brighter as the background simultaneously sharply decreases (*see* **Note 25**).
18. Remove the Cy3-only slide and mount a slide with both Cy3- and Cy5-labeled DNA molecules. The donor and acceptor signals should be well-separated, with minimal cross-talk (*see* **Note 26**). If significant leakage of the donor signal into the acceptor channel is observed, insert the 680/20 nm bandpass filter into the long wavelength slot of the image splitter.
19. To confirm the presence of the acceptor, switch to the 655 nm dichroic mirror in the filter turret and use the red laser to excite Cy5 directly.

3.2 DNA Construct Labeling

The distance sensitivity of FRET requires relatively short nucleic acid oligonucleotides, typically up to 100 bp in length. Such short constructs are commercially available with a number of convenient modifications, such as biotinylation at the terminus for surface immobilization and amino-modification of C6-dT nucleotides incorporated for fluorophore labeling. Here, we describe HPLC analysis to check the purity of synthetic DNA (*see* **Note 27**), followed by a detailed discussion of DNA labeling and purification.

3.2.1 HPLC Analysis

1. Dissolve DNA pellet in 50–100 µL DNA ddH_2O, varying the volume depending upon reported concentration of the synthetically prepared DNA.
2. Add to an Eppendorf tube, for 100 µL total: (a) 2 µL DNA oligonucleotides, and (b) 98 µL TEAA HPLC buffer.
3. Confirm DNA purity with reverse-phase HPLC on an analytical C18 column. If synthesis products are detected, purify the whole DNA sample before proceeding with the labeling reaction (*see* **Note 28**).

3.2.2 Fluorophore Labeling

1. Add 14 µL DMSO directly to Cy5 tube. Vortex and centrifuge to mix the solution well. Use 7 µL for each labeling reaction (*see* **Note 29**).
2. Add to a 1.5 mL Eppendorf tube, for a total of 100 µL: (a) 25 µL purified DNA, (b) 10 µL 0.1 M Na_2CO_3, pH 8.5, −20 °C, (c) 7 µL Cy5 with DMSO, and (d) 58 µL ddH_2O.
3. Vortex, and then centrifuge quickly to collect any droplets into the solution. Cover with aluminum foil to protect the dye from photobleaching. Shake gently overnight on the Thermomixer Comfort at 27 °C, 500 rpm.

3.2.3 Ethanol Precipitation

1. Add to each Eppendorf tube, for a total of 360 µL: (a) 10 µL (1/10th volume) 3 M NaOAc, (b) 0.5 µL 100 mM dNTPs (for a final concentration of 140 µM, *see* **Note 30**), and (c) 250 µL (2–2.5× volume) 100% ethanol.
2. Shake well and store at −20 °C overnight or −80 °C for 4 h.
3. Centrifuge the sample for 30 min at 4 °C, 19,000 × *g*.
4. Pour off the brightly colored supernatant. This is excess dye, which does not precipitate with the DNA.
5. Add 500 µL 70% ethanol and centrifuge for 15 min at 4 °C, 19,000 × *g*.
6. Repeat **steps 4** and **5** (*see* **Note 31**).
7. Pour off supernatant and vacuum-dry the DNA. A colored pellet will be clearly visible at the bottom of the tube.
8. Dissolve the DNA in 100 µL TEAA HPLC buffer for separation of labeled and unlabeled fractions (*see* **Note 32**).

3.2.4 HPLC Purification

1. Add to an Eppendorf tube, for 100 µL total: 5 µL DNA oligonucleotides (*see* **Note 33**) and 98 µL TEAA HPLC buffer.
2. Run analytical HPLC to determine approximate positions of unlabeled and labeled DNA peaks.
3. Modify the preparation method as necessary to separate peaks and collect fractions.
4. Vacuum-dry the appropriate fractions (*see* **Note 34**).
5. Resuspend labeled and unlabeled DNA in 25 µL DNA storage buffer. Store at 4 °C.

3.3 Sample Chamber Preparation

Sample chambers are prepared using microscope slides with predrilled holes for the purpose of creating a flow channel. Here, we describe how to clean the slides and coverslips in order to remove impurities that contribute to background fluorescence. Then, we describe amino functionalization of the slide surface in order to coat it with NHS ester-labeled linear PEG, which minimizes nonspecific protein interactions (Fig. 2) [25]. Finally, we provide a detailed protocol for sample chamber assembly and storage.

3.3.1 Slide Cleaning

1. Prism-based TIRF methods require the use of expensive quartz slides that can be reused. In this case, boil previously used slides in ddH_2O for 30–40 min. Remove the coverslip and any debris from previous applications using a razor blade. In the case of new slides, omit this step.
2. For new slides, drill holes with a diamond drill bit while the microscope slides are submerged in water.
3. Clean slides using a 1:1 mixture of Alconox and ddH_2O. The slide surface should be scrubbed vigorously with this paste (*see* **Note 35**). Rinse slides thoroughly with distilled water to remove any remaining soap (*see* **Note 36**).

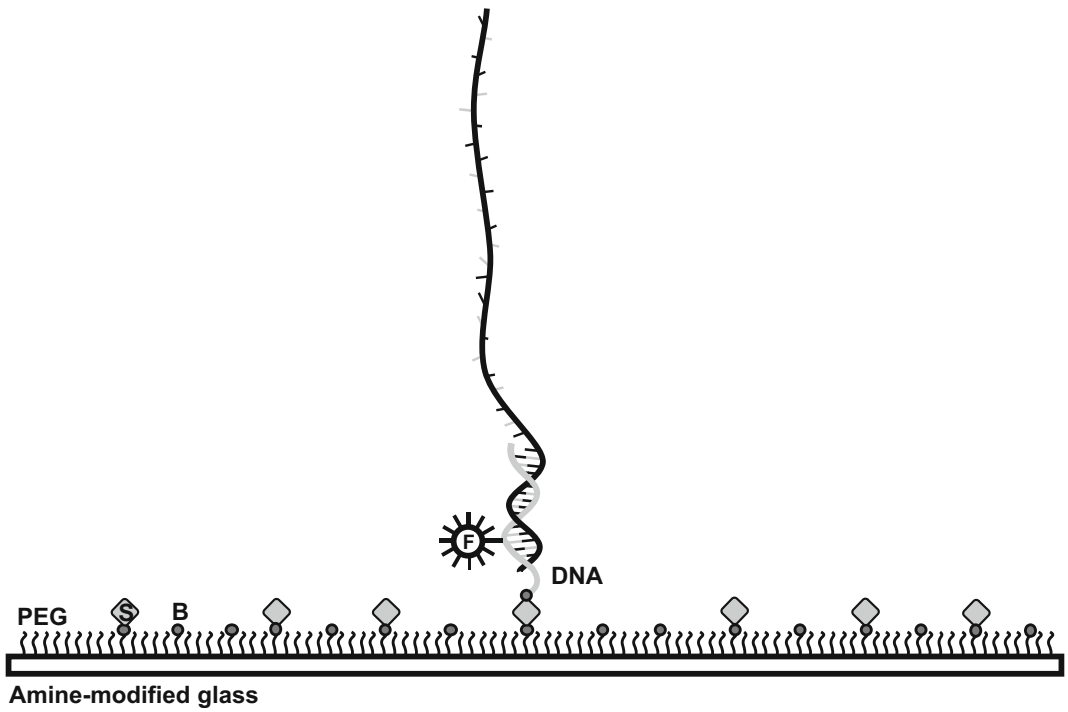

Fig. 2 Schematic representation of sample immobilization. The glass coverslip is amine-modified, and the NHS-ester form of mPEG and biotin-PEG are covalently conjugated to the surface. Streptavidin (S, *squares*) specifically binds to a fraction of the biotin (B, *circles*). DNA molecules labeled with a fluorophore (F) are then tethered to the surface via a biotin–streptavidin linkage

4. Scrub and rinse slides twice with ethanol and ddH_2O on both sides for 1–2 min each.
5. Boil slides for 40 min in freshly prepared basic piranha solution in order to regenerate the slide surface. Use a 250 mL beaker for five slides, which allows sufficient room so that the slides do not touch each other (*see* **Note 37**). Ensure the PEGylation surface faces the solution and both drilled holes are submerged.
6. Carefully remove the slide with tweezers, and rinse thoroughly with ddH_2O. Flame slide on both sides with a Bunsen burner to pyrolyse organic residues on the surface. Ensure that the PEGylation surface is well-sterilized. Place hot slide on the slide rack, with the PEGylation surface facing up. Repeat for remaining slides.
7. Place five slides and five coverslips into two clean, dry Coplin jars, ensuring that the PEGylation surface faces towards the solution at both ends.
8. Fill the jars with 1 M KOH and sonicate for 30 min to remove any remaining debris.
9. Rinse slides with ddH_2O (*see* **Note 38**).
10. Rinse with methanol.
11. Fill the jars with methanol and sonicate for 30 min.

3.3.2 Aminosilanization

1. Rinse a clean 200 mL beaker with methanol. Prepare the aminosilanization solution with Vectabond equilibrated to room temperature (*see* **Note 10**).
2. Mix the solution with the pipette tip, and fill the Coplin jars with it, ensuring that all slide surfaces are submerged. (a) Incubate for 10 min, (b) sonicate for 2 min, and (c) incubate for 10 min.
3. Decant aminopropylsilane solution into the waste container, then rinse the slides with (a) methanol, (b) ddH_2O, and (c) methanol.
4. Dry slides and coverslips with nitrogen (*see* **Note 39**). Place dried slides in PEGylation chambers, prepared with a 1 cm layer of distilled water in the bottom to create a humid environment. (This prevents the coverslips from sticking to the slides as they incubate overnight, as described in **step 5** of Subheading 3.3.3). Place coverslips in a box lined with a clean paper towel. Ensure that the PEGylation surface is always facing upwards.

3.3.3 PEGylation

1. Prepare the PEGylation buffer and use it to prepare the PEGylation reaction solution. Vortex the solution to dissolve the PEG, then centrifuge briefly to remove any bubbles.

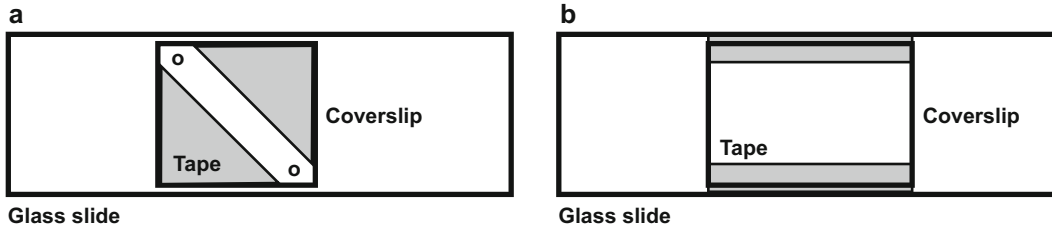

Fig. 3 Schematic diagram of sample chambers for (**a**) single-molecule experiments and (**b**) fluorescent bead calibration. Flow channels are formed with two layers of double-sided tape (*gray*), and the chamber is sealed with epoxy applied between the slide and coverslip

2. Place 80 μL of the PEGylation reaction solution onto the surface of each slide (*see* **Note 40**).
3. Gently place coverslips onto the slides with tweezers, ensuring there are no bubbles trapped underneath coverslip (*see* **Note 41**).
4. Use a marker to mark the PEGylated surface of the slide and the non-PEGylated surface of the coverslip in the lower right corner.
5. Close the PEGylation chambers and incubate them overnight at room temperature in the dark.

3.3.4 Slide Assembly

1. Rinse slides and coverslips gently with ddH_2O and dry with nitrogen (*see* **Note 42**). Place slides on the slide tray and coverslips in a box lined with a clean paper towel.
2. Apply double-sided sticky tape to create a straight, 4 mm wide channel on either side of the holes. Apply a second layer of tape on top of the first one to make the channel depth approximately 100 μm (Fig. 3a).
3. Deposit a coverslip on the top of the sticky layer with caution so that both holes are covered on either side. Gently press the coverslip on the sticky tape to ensure proper adhesion.
4. Remove any excess tape around the coverslip using a razor blade (*see* Note about technique).
5. Dispense epoxy into a small weigh boat, mix with a 200 μL pipette tip and wait 1–2 min for glue to thicken. Use the pipette tip to apply the epoxy, sealing the gap between the coverslip and the tape. The glue will spread upon application, so be careful not to use so much glue that it seals the holes.
6. Cover and allow glue to dry for 10 min.
7. Place sample chambers in 50 mL tubes filled with nitrogen gas. Store in the dark for 1–2 weeks.

3.4 Sample Immobilization

Approximately 8% of PEG molecules used for surface passivation are labeled with biotin in order to enable immobilization of DNA

molecules through a biotin–streptavidin linkage. Here, we describe sample preparation procedures for imaging single DNA molecules on the coverslip surface.

1. Add to an Eppendorf tube, for 10 μL total: (a) 1 μL of 10 μM biotinylated DNA, (b) 2 μL of 10 μM non-biotinylated DNA, and (c) 7 μL annealing buffer (*see* **Note 43**).

   Gently flick to mix, and briefly centrifuge to collect the liquid. Wrap the tube in aluminum foil to protect the fluorophores and heat on a dry block heater at 90 °C for 45 s. Remove the block and allow it to slowly cool the sample to room temperature.
2. In two serial dilutions, prepare a 200 μL solution of the DNA in annealing buffer, for a final concentration of 25–50 pM. Store both solutions on ice and protect them from ambient light to minimize photobleaching.
3. Cut a 200 μL pipette tip to fit exactly inside one of the holes that form the channel in the slide. Inject 85 μL BSA solution (*see* **Note 44**) and incubate for 10 min at room temperature (*see* **Note 45**).
4. Inject 200 μL T50 buffer to wash out excess BSA.
5. Inject 200 μL streptavidin solution and incubate for 10 min (*see* **Note 46**).
6. Inject 200 μL annealing buffer to wash out excess streptavidin.
7. Inject 200 μL of the final DNA dilution (25–50 pM DNA, *see* **step 2**) and incubate for 10 min (*see* **Note 47**).
8. Inject 200 μL experimental buffer to wash out excess DNA.
9. Inject 200 μL of the final imaging solution in experimental buffer (*see* **Note 48**).

3.5 Data Acquisition and Analysis

To accommodate minor optical alignment issues, the position of the donor and acceptor signal on the image splitter is matched using a fluorescent bead reference. Here, we describe this calibration procedure, and briefly discuss data analysis methods.

1. Prepare a calibration sample chamber using a clean glass slide, without pre-drilled holes, by applying double-sided sticky tape across the top and bottom of the slide. Apply a second layer of tape on top of the first one to make the channel depth approximately 100 μm (Fig. 3b).
2. Deposit a coverslip on the top of the sticky layer. Gently press the coverslip on the sticky tape to ensure proper adhesion.
3. Remove any excess tape around the coverslip using a razor blade.
4. Make a 500-fold dilution of the fluorescent beads in ddH_2O. Use a 200 μL pipette tip to inject the bead solution into the square sample chamber. Incubate for 10 min.

5. Wash out excess beads with 1 M $MgCl_2$. Incubate for 10 min.
6. Dispense epoxy into a small weigh boat, mix with a 200 μL pipette tip and wait 1–2 min for glue to thicken. Use the pipette tip to apply the epoxy around the coverslip, sealing the sample chamber closed.
7. Cover and allow glue to dry for 10 min. The sealed slide will last 1–2 months.
8. Mount the calibration slide on the microscope. The fluorescent beads will be clearly visible through the eyepiece. Adjust the objective position to bring them into sharp focus (*see* **Note 49**).
9. Direct the beam through the side port. Two mirror images will be visible on the camera. Adjust the mirror to achieve roughly uniform illumination across the field of view. Record a short calibration movie (approximately 1000 frames is sufficient).
10. Remove the beads slide and mount the DNA sample on the microscope, careful to ensure that the coverslip faces the immersion oil. Single molecules will be visible on the camera. Bring them into focus with minor adjustments to the objective position.
11. Movies are typically recorded from different areas of the sample chamber on the scale of minutes to hours, depending upon experimental design (*see* **Note 50**). Record the laser power after each movie (*see* **Note 51**).
12. Glass slides may be discarded after use. Expensive quartz slides required for prism-based TIRF may be cleaned and reused (*see* Subheading 3.3.1, **step 1** and **Note 52**).
13. Using a custom script written in IDL (available upon request), select three beads from the calibration movie to obtain a polynomial map of the overlay between donor and acceptor image (*see* **Note 53**).
14. For each single-molecule movie, use the IDL script to extract the intensity over time for each spot. The IDL script uses an optimized threshold to identify molecules, which are individually confirmed with manual analysis.
15. Analyze individual traces using a script written in MatLab (available upon request). A single molecule is identified by single-step photobleaching of the dye. The script calculates the apparent FRET efficiency:

$$\text{FRET} = \frac{I_A}{(I_D + I_A)}$$

where and I_D is the donor intensity and I_A is the cross-talk corrected acceptor intensity (*see* **Notes 54–56**).

16. FRET traces can be used to build FRET histograms for a range of solution conditions (*see* **Note 57**). The kinetics of a two-state system can be extracted with dwell-time analysis (*see* **Note 58**). It is often useful to synchronize molecules to an initial binding event to quantify the distribution of FRET states over time (*see* **Note 59**). In the case of a multiple-state system, more advanced analysis tools, such as hidden Markov modelling (HaMMy) may be helpful (*see* **Note 60**).

4 Notes

1. Although we describe an objective-based TIRF instrument, the methods discussed here are also applicable for prism-based TIRF. A prism-based instrument is simpler to build, align, and maintain, and it easily accommodates flow-based experiments. However, matching the index of refraction of the prism to the imaging surface requires expensive quartz slides that need to be thoroughly cleaned before reuse. Furthermore, the sample chamber surface is covered with a prism in this instrument design, making it difficult to accommodate sample chambers commonly used for live cell imaging.
2. A number of lasers are typically used to achieve TIR, including Nd:YAG solid state lasers (Coherent, Newport) or diode lasers (Vortran).
3. A red laser is useful for direct excitation of the acceptor dye. Diode lasers (Coherent, Vortran), diode-pumped solid state lasers (Cobolt), and HeNe lasers (Melles Griot) are commonly used for this purpose.
4. A beam combiner provides alignment stability, which is often a priority in biological laboratories. We couple multiple lasers into our single mode fiber, and recommend a long (2 m), reinforced steel fiber for this purpose (Coherent, Cobolt). However, it is common, and relatively straightforward, to use dichroic mirrors to combine the excitation beams.
5. We use an emission image splitter (Cairn, Hamamatsu, Photometrics) for alignment stability, since the dichroic mirror may simply be exchanged between experiments with different dyes. However, it is relatively straightforward to use dichroic mirrors to split the emission beam.
6. Single-molecule experiments commonly use EMCCD cameras for detection (Andor, Hamamatsu, Photometrics). Their advantages include uniform amplification, low noise, and high quantum yields achieved by back-thinning. Thermal noise is reduced by cooling the chip, typically to −80 °C.

7. Surface passivation is commonly performed with PEG, particularly for experiments involving fluorophore-labeled proteins that contribute to high background signal when they collapse on the imaging surface. However, it may be sufficient to use BSA to passivate the surface for experiments without such stringent requirements.
8. Magnetic stir bars should be sufficiently large for stability while spinning in a 250 mL beaker, but sufficiently small not to disturb glass slides standing along the edges.
9. Tweezers with wide, flat ends to grip the slide by one end are preferred.
10. Store Vectabond sealed with nitrogen gas at 4 °C to avoid oxidation. (It should be a colorless solution, and signs of yellowing indicate oxidation.) Allow Vectabond to equilibrate to room temperature for 30 min before use. Make aminosilanization solution immediately prior to use. Exchange air in the Vectabond bottle with nitrogen gas, seal with parafilm, and store at 4 °C.
11. PEGylation chambers can be made from old pipette tip boxes by machining out a rectangular section in the plastic inserts to hold five vertically arranged slides. Clean boxes thoroughly with ddH_2O before each use.
12. Make PEGylation buffer immediately prior to use.
13. Aliquot biotin-PEG and mPEG in 1.5 mL Eppendorf tubes, and store at −20 °C. Allow aliquots to equilibrate to room temperature for 30 min prior to use. Store unopened PEG bottles wrapped in foil at −20 °C. For partially used bottles, exchange air with nitrogen gas and seal with parafilm prior to wrapping in foil and storing at −20 °C.
14. Make PEGylation reaction solution immediately prior to use.
15. Surface attachment may also be achieved using a biotin–neutravidin linkage, with little to no discernible differences in immobilization efficiency.
16. If using an ssDNA construct with no dsDNA region, omit annealing buffer and dilute DNA directly in experimental buffer.
17. Molecules can also be immobilized in the absence of PEG, using BSA for surface passivation (*see* **Note 7**) and molecule immobilization. In this case, use a biotinylated BSA solution: 0.2 mg/mL BSA in T50 buffer. Aliquot biotin-BSA in 1.5 mL Eppendorf tubes and store at 4 °C.
18. Trolox enhances fluorophore photostability, reducing blinking and photobleaching. Store Trolox at 4 °C. Instead of ddH_2O, a saturated solution of Trolox may be used to prepare reagents

for single-molecule experiments. To prepare the Trolox solution, dissolve 5 mg Trolox in 10 mL ddH_2O. Shake at room temperature for 30 min. Syringe filter the solution, and store at 4 °C for up to 2 weeks.

19. PCA/PCD is an oxygen scavenging system that decreases dissolved oxygen levels in the experimental buffer. This increases fluorophore photostability, reducing blinking and photobleaching. Aliquot PCA and PCD and store at −20 °C.
20. Single-molecule experiments are performed at low protein concentrations, particularly in the case of labeled proteins, in order to minimize background signal.
21. We use a power supply box (Coherent) to facilitate mounting multiple fiber-coupled lasers.
22. A 2 mm output from a single mode fiber can be expanded to a 20 mm beam using lenses of 10 and 100 mm focal length.
23. If the beam is not visible on the ceiling, ensure the correct dichroic mirror is in place in the filter turret. If so, reduce the laser power, ensure appropriate safety goggles are in place, and look directly down at the target to locate the beam. If a bright spot is not visible, or partially visible, use the mirror to steer the beam so that it enters the objective and a spot is clearly visible in the middle of the target.
24. It may be tricky to go directly to working with the 100× TIRF objective, where the concentric ring pattern is larger and more difficult to visualize on the ceiling when the beam is not focused on the back focal plane of the objective. We therefore recommend beginning with the 40× objective to adjust the lens position, but this step is optional.
25. Single molecules will be visible in epifluorescence mode, albeit with a high background signal. Upon visual estimation, the background may appear higher relative to the background in the prism-based TIRF method. However, quantitative signal-to-noise comparisons do not exhibit any appreciable differences.
26. Cross-talk decreases FRET resolution, as donor signal is observed in the acceptor channel and vice versa. The donor signal is more likely to leak into the acceptor channel due to the long wavelength tail of fluorescence emission spectra. Crosstalk is therefore usually measured using the donor-only sample to quantify the signal in the acceptor channel. This leakage will typically be 5–10%, and should be no more than 15%. Inserting bandpass emission filters reduces cross-talk, albeit at a small cost to the overall signal. Cross-talk will vary for different sets of dyes, and is therefore measured and corrected based on each

experimental design (*see* Subheading 3.5, **step 15** and **Note 55**).

27. Although we discuss DNA labeling, the methods described here are applicable for nucleic acids in general, and therefore include RNA.
28. To purify the commercially prepared DNA, vacuum-dry the sample to obtain a pellet again, and dissolve it in 100 μL TEAA HPLC buffer. Modify the HPLC collection method based on the peaks in the initial analysis spectrum, and isolate the peak representing the full synthesis product. Vacuum-dry the DNA and dissolve the pellet in ddH_2O.
29. Seal tube with remaining dye, cover with foil, and store at 4 °C.
30. The nucleotides increase the yield of labeled DNA in the ethanol precipitation, and provide a clear reference peak for HPLC analysis and purification.
31. Handle the tube carefully to avoid shaking the pellet loose. If the solution is accidentally mixed in the process, repeat the centrifugation step to reform the pellet.
32. For constructs with amino-modification of internal C6-dT nucleotides, it may be helpful to repeat the fluorophore labeling reaction in order to achieve at least 80% labeling efficiency. In this case, dissolve the DNA in 25 μL ddH_2O and repeat Subheadings 3.2.1–3.2.3.
33. The increase in DNA sample for HPLC analysis after labeling accommodates for DNA loss during the purification steps in ethanol precipitation.
34. Labeling efficiency is approximately 80%, which yields sufficient DNA for single-molecule experiments. However, store the purified, unlabeled fraction at −20 °C in case it becomes useful for a future labeling reaction.
35. Quartz slides used in prism-based TIRF are brittle, and will easily break with too much force. Clean them thoroughly, but maintain a gentle grip.
36. To save time, use distilled water directly from the tap instead of ddH_2O from a squeeze bottle, for all but the final rinse.
37. First set up the stir bar to mix the solution at a stable rate. Then add the slides one at a time, carefully leaning them against the sides of the beaker. Ensure that their bottom edge is not in the path of the stir bar, which can cause the slides to tip over into one another and crack (*see* **Note 8**).
38. Cover the Coplin jar and use the lid to carefully decant the solution into the waste beaker.
39. Affix a 1 mL pipette tip to the end of the nitrogen gas tube coming from the regulator valve. Hold the slide by the bottom

edge, angled towards you. Use your dominant hand to hold the pipette near the top edge of the slide and use the force of the gas to systematically slide the droplets towards the bottom edge.

40. Hold the pipette tip just above the middle of the slide, careful not to touch the surface. Dispense the solution onto the middle of the sample chamber, and watch it spread evenly over the surface, forming a pool covering both holes. If the solution begins to spread unevenly, due to small imperfections on the surface or the slide sitting unevenly in the PEGylation chamber, adjust your position over the slide to compensate. Pipette slowly and steadily to avoid the formation of bubbles.
41. Grip the coverslip by the bottom edge, and gently place the top edge onto the slide. Release the coverslip gradually in order to minimize bubble formation. Any small bubbles that do form will move towards the edge of the coverslip and escape. If large bubbles form and do not move on their own, gently move the coverslip around to encourage them towards the edges. An even, bubble-free layer is necessary to coat both surfaces. Wait 10 min to ensure that the coverslips do not move out of position. If they do, use the tweezers to gently guide them back into place.
42. Rinse slides and coverslips at the bench over a waste beaker. It typically takes 2 L of ddH_2O to rinse five slides and coverslips.
43. Use a twofold excess of the non-biotinylated strands to ensure complex formation with the labeled strand. This yields an annealed DNA complex concentration of approximately 1 μM in the 10 μL sample volume.
44. If using BSA for surface passivation and sample immobliliza-tion (*see* **Notes 7** and **17**), inject biotin-labeled BSA instead.
45. Ensure that the pipette tip fits tightly inside the chosen hole, or the solution will leak out instead of flowing through the sample chamber. During injection, hold the slide vertically, solely with the pipette tip, such that the injection hole is at the bottom of the slide, and the solution flows upwards into the chamber. Pipette slowly and carefully, so that injection takes at least 30 s. It is crucial to avoid introducing bubbles into the sample chamber.
46. It is important not to vortex the streptavidin to avoid damage to the protein.
47. These incubation times are a guideline, but may be further optimized for each construct. The surface density of the molecules should be sufficiently high to conduct an efficient experiment, but still allow image processing algorithms to establish a separate ROI around each molecule. This limit is

approximately 500 molecules per field of view, which is 512 × 512 pixels for the EMCCD chip discussed here (actual area in μm^2 depends upon magnification).

48. The buffer can be adjusted depending on the biological system under investigation. For example, dNTPs may be added for DNA polymerization experiments, or rNTPs added for transcription experiments.
49. If the fluorescent beads are not easily visible through the eyepiece by moving the vertical position of the 100× TIRF objective to bring them into focus, switch to the 40× objective to roughly identify the correct objective position. The beads will then be slightly out of focus with 100× objective, requiring only minor adjustments to the objective position.
50. At 1 byte (8 bits) per pixel on a 512 × 512 EMCCD chip, a 2 min movie at 17 ms/frame occupies 1.72 Gigabytes (GB). Longer integration times, such as those useful for observing slower biological processes, yield smaller file sizes in addition to decreasing the laser power required to achieve a good signal-to-noise ratio (S/N). Image processing of movies significantly reduces data volumes.
51. Use the lowest laser power necessary to achieve a good S/N in order to minimize dye photobleaching.
52. Quartz slides last for approximately 50 uses, or 6 months. After that, scratches, chips, or other surface imperfections appear. Keep a dated record of the slide used for each experiment, and discard slides that give a consistently high background.
53. Due to minor fluctuations in optical alignment, perform this calibration on the day of the experiment. Do not reuse polynomial maps generated on previous days, since even minor shifts in image overlap will skew intensity profiles.
54. The apparent FRET efficiency reports upon relative fluorescence intensities for each molecule, which mitigates the effects of non-uniform illumination across molecules. Molecules can therefore be compared, both within and across samples, despite minor variations in excitation intensity during data acquisition.
55. The measured intensities are generally corrected for cross-talk by a factor α, which is the percent of the donor signal detected in the acceptor channel. This is empirically measured from a donor-only sample by determining the value of α where the acceptor intensity is zero. The corrected acceptor intensity I_A is therefore:

$$I_A = I_{A0} - \alpha I_{D0}$$

where I_{A0} is the raw acceptor intensity and I_{D0} is the raw donor intensity. It is possible, if not particularly widely practiced, to correct the donor intensity I_D by adding the subtracted signal back:

$$I_D = I_{D0} + \alpha I_{D0}.$$

Additional correction factors may also apply, such as a correction for acceptor signal observed in donor channel, or corrections to compensate for small differences in the detection efficiencies and quantum yields of the two fluorophores. In the case of the Cy3-Cy5 FRET pair discussed here, these additional corrections are negligible, such that the apparent FRET efficiency is effectively the absolute FRET efficiency.

56. In principle, FRET values range between 0 and 1. However, when the signal intensities are very small or large (at zero and maximum FRET, respectively), the background noise becomes relatively high, leading to correction effects (*see* **Note 55**) that yield values slightly below 0 and slightly above 1.
57. A FRET histogram is a collection of the average FRET efficiency for $N > 100$ molecules. This analysis method can identify the FRET value of a single state with a statistical uncertainty of ± 0.1 FRET. To avoid sampling bias due to the length of FRET traces, use the first 100 frames for each molecule.
58. A dwell time histogram is a collection of the dwell times dt in each state for $N > 100$ molecules, where the trace may be categorized into each state manually or automatically using thresholding. A fit to this histogram yields a characteristic lifetime τ, which can be used to obtain the kinetic transition rates k_{on} and k_{off}.
59. A post-synchronization histogram (PSH) is a collection of time-binned FRET traces synchronized at the initial binding event. This analysis method reveals changes in the distribution of FRET states upon initial binding as a function of time.
60. Hidden Markov modelling is a method to distinguish multiple FRET states within a single FRET trajectory that is more stable and reproducible than standard thresholding algorithms. The model generates a predicted FRET trajectory that is typically overlaid on top of the original trace to confirm visually identified FRET states that are not easily quantifiable. These fits can be used to calculate interconversions between multiple discrete FRET states. FRET trajectories that visit all the proposed FRET states multiple times within a single trajectory are good candidates for HaMMy analysis.

Acknowledgements

The authors thank all the members of the David Rueda laboratory for training in single-molecule FRET methods. This work was supported in part by the Human Frontiers Science Program [RGP0014/2014] and the Netherlands Organization for Scientific Research [VICI 016.160.613].

References

1. Wuite GJ, Smith SB, Young M, Keller D, Bustamante C (2000) Single-molecule studies of the effect of template tension on T7 DNA polymerase activity. Nature 404 (6773):103–106. doi:10.1038/35003614
2. Abbondanzieri EA, Bokinsky G, Rausch JW, Zhang JX, Le Grice SF, Zhuang X (2008) Dynamic binding orientations direct activity of HIV reverse transcriptase. Nature 453 (7192):184–189. doi:10.1038/nature06941
3. Kim S, Schroeder CM, Xie XS (2010) Single-molecule study of DNA polymerization activity of HIV-1 reverse transcriptase on DNA templates. J Mol Biol 395(5):995–1006. doi:10.1016/j.jmb.2009.11.072
4. Abbondanzieri EA, Greenleaf WJ, Shaevitz JW, Landick R, Block SM (2005) Direct observation of base-pair stepping by RNA polymerase. Nature 438(7067):460–465. doi:10.1038/nature04268
5. Kapanidis AN, Margeat E, Ho SO, Kortkhonjia E, Weiss S, Ebright RH (2006) Initial transcription by RNA polymerase proceeds through a DNA-scrunching mechanism. Science 314(5802):1144–1147. doi:10.1126/science.1131399
6. Herbert KM, Greenleaf WJ, Block SM (2008) Single-molecule studies of RNA polymerase: motoring along. Annu Rev Biochem 77:149–176. doi:10.1146/annurev.biochem.77.073106.100741
7. Sorokina M, Koh HR, Patel SS, Ha T (2009) Fluorescent lifetime trajectories of a single fluorophore reveal reaction intermediates during transcription initiation. J Am Chem Soc 131(28):9630–9631. doi:10.1021/ja902861f
8. Lee KS, Balci H, Jia H, Lohman TM, Ha T (2013) Direct imaging of single UvrD helicase dynamics on long single-stranded DNA. Nat Commun 4:1878. doi:10.1038/ncomms2882
9. Byrd AK, Matlock DL, Bagchi D, Aarattuthodiyil S, Harrison D, Croquette V, Raney KD (2012) Dda helicase tightly couples translocation on single-stranded DNA to unwinding of duplex DNA: Dda is an optimally active helicase. J Mol Biol 420(3):141–154. doi:10.1016/j.jmb.2012.04.007
10. Cheng W, Arunajadai SG, Moffitt JR, Tinoco I Jr, Bustamante C (2011) Single-base pair unwinding and asynchronous RNA release by the hepatitis C virus NS3 helicase. Science 333 (6050):1746–1749. doi:10.1126/science.1206023
11. Ha T, Rasnik I, Cheng W, Babcock HP, Gauss GH, Lohman TM, Chu S (2002) Initiation and re-initiation of DNA unwinding by the Escherichia coli Rep helicase. Nature 419 (6907):638–641. doi:10.1038/nature01083
12. Chaurasiya KR, Ruslie C, Silva MC, Voortman L, Nevin P, Lone S, Beuning PJ, Williams MC (2013) Polymerase manager protein UmuD directly regulates Escherichia coli DNA polymerase III alpha binding to ssDNA. Nucleic Acids Res 41(19):8959–8968. doi:10.1093/nar/gkt648
13. Chaurasiya KR, McCauley MJ, Wang W, Qualley DF, Wu T, Kitamura S, Geertsema H, Chan DS, Hertz A, Iwatani Y, Levin JG, Musier-Forsyth K, Rouzina I, Williams MC (2014) Oligomerization transforms human APOBEC3G from an efficient enzyme to a slowly dissociating nucleic acid-binding protein. Nat Chem 6(1):28–33. doi:10.1038/nchem.1795
14. Driessen RP, Sitters G, Laurens N, Moolenaar GF, Wuite GJ, Goosen N, Dame RT (2014) Effect of temperature on the intrinsic flexibility of DNA and its interaction with architectural proteins. Biochemistry 53(41):6430–6438. doi:10.1021/bi500344j
15. Senavirathne G, Bertram JG, Jaszczur M, Chaurasiya KR, Pham P, Mak CH, Goodman MF, Rueda D (2015) Activation-induced deoxycytidine deaminase (AID) co-transcriptional scanning at single-molecule resolution. Nat Commun 6:10209. doi:10.1038/ncomms10209
16. Brouwer I, Sitters G, Candelli A, Heerema SJ, Heller I, de Melo AJ, Zhang H, Normanno D, Modesti M, Peterman EJ, Wuite GJ (2016) Sliding sleeves of XRCC4-XLF bridge DNA

and connect fragments of broken DNA. Nature 535(7613):566–569. doi:10.1038/nature18643

17. Funatsu T, Harada Y, Tokunaga M, Saito K, Yanagida T (1995) Imaging of single fluorescent molecules and individual ATP turnovers by single myosin molecules in aqueous solution. Nature 374(6522):555–559. doi:10.1038/374555a0
18. Yildiz A, Forkey JN, McKinney SA, Ha T, Goldman YE, Selvin PR (2003) Myosin V walks hand-over-hand: single fluorophore imaging with 1.5-nm localization. Science 300(5628):2061–2065. doi:10.1126/science.1084398
19. Verbrugge S, Lansky Z, Peterman EJ (2009) Kinesin's step dissected with single-motor FRET. Proc Natl Acad Sci U S A 106 (42):17741–17746. doi:10.1073/pnas.0905177106
20. Nguyen DC, Keller RA, Jett JH, Martin JC (1987) Detection of single molecules of phycoerythrin in hydrodynamically focused flows by laser-induced fluorescence. Anal Chem 59 (17):2158–2161. doi:10.1021/ac00144a032
21. Hirschfeld T (1976) Optical microscopic observation of single small molecules. Appl Opt 15(12):2965–2966. doi:10.1364/ao.15.002965
22. Förster T (1948) Intermolecular energy migration and fluorescence. Ann Phys 2:55–75
23. Clegg RM (1992) Fluorescence resonance energy transfer and nucleic acids. Methods Enzymol 211:353–388
24. Selvin PR (2000) The renaissance of fluorescence resonance energy transfer. Nat Struct Biol 7(9):730–734. doi:10.1038/78948
25. Sofia SJ, Premnath VV, Merrill EW (1998) Poly(ethylene oxide) grafted to silicon surfaces: grafting density and protein adsorption. Macromolecules 31(15):5059–5070. doi:10.1021/ma971016l
26. Jeyachandran YL, Mielczarski JA, Mielczarski E, Rai B (2010) Efficiency of blocking of nonspecific interaction of different proteins by BSA adsorbed on hydrophobic and hydrophilic surfaces. J Colloid Interface Sci 341(1):136–142. doi:10.1016/j.jcis.2009.09.007
27. Hua B, Han KY, Zhou R, Kim H, Shi X, Abeysirigunawardena SC, Jain A, Singh D, Aggarwal V, Woodson SA, Ha T (2014) An improved surface passivation method for single-molecule studies. Nat Methods 11(12):1233–1236. doi:10.1038/nmeth.3143

Part III

Atomic Force Microscopy and Other Force Methods

Chapter 13

Atomic Force Microscopy: An Introduction

Melissa C. Piontek and Wouter H. Roos

Abstract

Imaging of nano-sized particles and sample features is crucial in a variety of research fields. For instance in biological sciences, where it is paramount to investigate structures at the single particle level. Often two-dimensional images are not sufficient and further information such as topography and mechanical properties are required. Furthermore, to increase the biological relevance, it is desired to perform the imaging in close to physiological environments. Atomic force microscopy (AFM) meets these demands in an all-in-one instrument. It provides high-resolution images including surface height information leading to three-dimensional information on sample morphology. AFM can be operated both in air and in buffer solutions. Moreover, it has the capacity to determine protein and membrane material properties via the force spectroscopy mode. Here we discuss the principles of AFM operation and provide examples of how biomolecules can be studied. By including new approaches such as high-speed AFM (HS-AFM) we show how AFM can be used to study a variety of static and dynamic single biomolecules and biomolecular assemblies.

Key words Atomic force microscope (AFM), High-speed AFM, Topography, Force spectroscopy, Cantilever, Contact mode, Intermittent contact mode, Biological applications, Nano-indentation

1 Introduction

While performing research at the cellular and subcellular level, suitable imaging tools are essential to come to an in-depth description of the processes that occur at these length scales. A variety of instruments has been developed to study biology at the micro- to nanoscale. A landmark invention was the light microscope, which uses photons interacting with the sample surface and lenses to create a magnified image of the specimen. At the end of the seventeenth century, Antonie van Leeuwenhoek made this technique popular under biologists. Significant development of this technique occurs up to date. In the early 1930s E. Ruska and M. Knoll invented another instrument making a specimen and its surface visible: the Electron Microscope (EM). Here, electrons instead of photons function as probes to create an image of the sample surface. Images acquired with EM have a significantly higher

Erwin J.G. Peterman (ed.), *Single Molecule Analysis: Methods and Protocols*, Methods in Molecular Biology, vol. 1665, DOI 10.1007/978-1-4939-7271-5_13,

resolution than the ones obtained with the optical microscope. For both approaches the resolution is basically being limited by the used wavelength, which is much smaller in the case of EM [1]. Still, the corresponding data does not provide quantitative height information and, consequently, is two-dimensional.

Successful experiments providing three-dimensional information at the nanoscale were conducted using Scanning Tunneling Microscopy (STM). They were first presented by Binnig and Rohrer in 1982 [2]. The technique uses a metal tip mounted at the end of a cantilever. The tip is approached to the surface and scans the surface while the tunnel current is kept constant with a feedback control. The voltage applied to the piezo-drivers is used to move the tip in the *z*-direction, keeping the tunnel current constant, and to move the tip in the *x*- and *y*-direction to scan the surface. Hereby the topography of the sample's surface is being reconstructed. Since the tunnel current is extremely sensitive to alteration of the distance (exponential dependence), atomic resolution is achievable [1, 2]. Drawback of this technique is the need for conductive samples and probes. For instance, biological samples are insulators and thus it is impossible to image them with this approach. Coating of the sample with a conducting layer can solve this problem, however, thereby making the substrate less relevant for biological experiments.

With the advent of the Atomic Force Microscope (AFM) by Binnig *et al.* in 1986 [3], not only the limitations of the resolution of optical microscopes were overcome, but also the requirements of the sample being conductive. Instead of using the tunneling current, an AFM takes advantage of the interacting force between the tip and the surface, which deflects the cantilever. In combination with a feedback control, the topography of the sample surface can be reconstructed [4, 5]. The big advantage of this approach is that any sample can be investigated, because there is no need for conductivity. This invention facilitates great possibilities especially in biological sciences as proteins, viruses, cells, and membranes can be imaged at nanometer resolution [1, 6–10].

The principle of AFM is also applicable for magnetic samples. The corresponding measurement instrument is called Magnetic Force Microscopy (MFM). The main difference between an AFM and a MFM is the tip itself. In an AFM it is nonmagnetic, while the tip of a cantilever inserted in a MFM is made of ferromagnetic material. In MFM the magnetic field gradient causes a force acting on the tip which bends the cantilever and imaging is performed by measuring the interaction between the tip and this magnetic field. The range in which a high spatial resolution can be obtained is 10 nm–100 nm [11].

With all of the aforementioned devices, that provide more than two-dimensional information, a new level of data acquisition has become possible. STM, AFM and MFM all belong to the group

called "Scanning probe microscopes," which in a way can be regarded as a combination of the techniques of profilers and SEM [5]. The invention of the electron microscope and the STM was awarded with the 1986 Nobel Prize in Physics. E. Ruska, G. Binnig, and H. Rohrer received the prize, the former for his work on EM and the latter two for their work on the STM.

Besides nanometer spatial resolution, many researchers were also looking for instruments reporting information on the fourth dimension, i.e. high temporal resolution. While for traditional AFM it typically takes several minutes to record one image, the endeavor was to reach sub-second temporal resolution. Several approaches to develop so-called high-speed AFM (HS-AFM) have been undertaken [12]. The approach of T. Ando has turned out to be the most practical for observing biomolecular processes and imaging rates of >10 frames per second are now routinely possible [13, 14]. Using HS-AFM the observation of real-time dynamic processes in liquid is possible and therefore, has a great potential in biological sciences [15].

2 Basics of AFM

This section discusses the basics of the AFM technique, the set-up as well as various operation modes.

2.1 Set-Up and Principle

AFM image acquisition is based on attractive and repulsive interactions with the sample. The set-ups typically consist of, among others, the following components [5, 16]:

- A cantilever, which has a sharp tip at its end.
- A detection system of the cantilever's bending.
- A feedback control of the applied force and the distance.
- A movement system (e.g. piezo tubes) to enable the scanning of the sample surface in all three dimensions with respect to the cantilever.
- A graphical visualization system of the acquired data.

A simplified schematic illustration of an AFM is shown in Fig. 1a and an example image of a virus acquired with an AFM is presented in Fig. 1b.

The so-called optical beam deflection (OBD) method is a common method to detect topography changes by AFM [18]. For the measurement of the bending of the cantilever, a laser beam is focused on the rear side of the cantilever. The rear side itself can be coated to enhance the amount of the reflected laser light, but this coating is not always necessary and it should be kept in mind that this coating could affect the thermal stability [19]. In either case, with or without coating, the reflected light will be

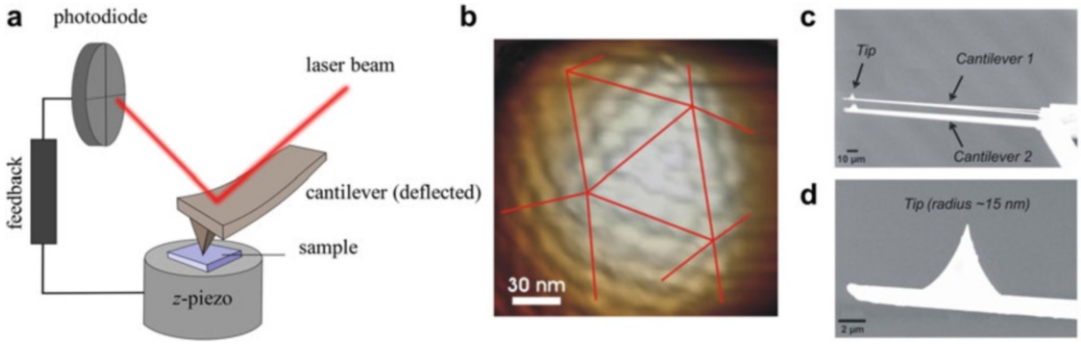

Fig. 1 AFM set-up. (**a**) This schematic represents a so-called sample-scanning configuration. An alternative is a system where the cantilever is scanned, i.e. a tip-scanning configuration. Combinations using linear piezos are also possible. (**b**) Example image of AFM. This picture of a virus, imaged in buffer solution, shows how AFM imaging can reveal structural features of biological substrates such as in this case protein clusters and icosahedral facets. Reproduced from ref. 17 with permission from PNAS. (**c**) Cantilever electron microscopy image. Two cantilevers with different spring constants are attached to the chip. Cantilever 1 is in focus, cantilever 2 is out of focus. (**d**) Zooming in onto the tip reveals that it is not infinitely sharp, but actually has a radius of curvature of approximately 15 nm.

directed to a quadrant photodiode, which detects positional alterations in the reflected light. Whenever the interaction force between the tip and the sample surface changes, the cantilever will bend, and thus the position of the laser spot on the photodiode changes. The measured signals are transmitted to the feedback electronics, processed and converted into a voltage which is used to retract or extend the piezo. Dependent on the actual AFM configuration, the movement of the piezo is used either to change the position of the sample or the cantilever. These are the two different ways to scan the sample surface. One possibility is that the position of the cantilever is fixed while the sample is moved by the piezoelectric element. Alternatively, the sample is fixed and the cantilever including the OBD-system is translated. The maximum scan range for x and y is on the order of ~100 μm times ~100 μm, while in z-direction this is ~30 μm. However, systems with larger scan ranges are also being used and many systems have (much) smaller scan ranges.

The cantilevers are typically fabricated from silicon or silicon nitride. To ensure operation in a variety of different AFM instruments, the dimensions of the cantilever base are industrially standardized. The base (chip) of cantilevers is usually about 3.5 mm long, 1.6 mm wide and it has a thickness of 0.5 mm. The typical length for rectangular cantilevers is ~200 μm–400 μm with a width of ~20 μm–40 μm [5]. Next to rectangular cantilevers also triangularly shaped ones are common, which are also called "V-shaped". The tip radius is typically ~15 nm–20 nm, but oxide sharpened tips with smaller radii are also available. Figure 1c, d show electron micrographs of example cantilever and tip. Besides the tip radius,

the cantilever spring constant k is also a characteristic quantity. It is dependent on the dimensions of the cantilever and the Young's modulus of the used material. Next to the often used vertical spring constant, also the lateral and torsional spring constant can be of importance. Typical values for the vertical spring constant range from a bit below 0.1 N/m to higher than 10 N/m [5]. While the manufacturer provides the specifications of their product, it is recommended to calibrate the cantilever spring constant before each measurement [20].

2.1.1 Tip Sample Interactions

The dimension of the tip strongly affects the resolution of the acquired topography. Because the tip dimension is finite, the resulting image is always a convolution of the tip and the sample. Figure 2 shows three possible imaging scenarios. In case the tip is small compared to the sample, an image which represents mostly the sample is acquired (Fig. 2a). Figure 2b shows a situation where the tip radius and sample size are roughly equal to each other, resulting in an image representing features from both tip and sample. In contrast, images acquired with a tip which is much larger than the sample, predominantly reflect the tip geometry itself (Fig. 2c).

The tip size can be reconstructed using an array of spikes. One of such spikes is shown in Fig. 2c. Furthermore, the tip size and geometry can be altered. For instance, it is possible to use controlled wear of the tip to create a defined spherical tip shape with increased radius. Corresponding experiments and results were recently reported by Vorselen *et al.* [21]. Here, high roughness polycrystalline titanium and ultrananocrystalline diamond surfaces were used to map the tip dimension. This mapping was performed at low imaging forces. Furthermore, by increasing the imaging force, the authors were able to dynamically increase the tip radius and to monitor this increase in real-time. While typical wear experiments result in blunted tips, in this approach spherical tips with the

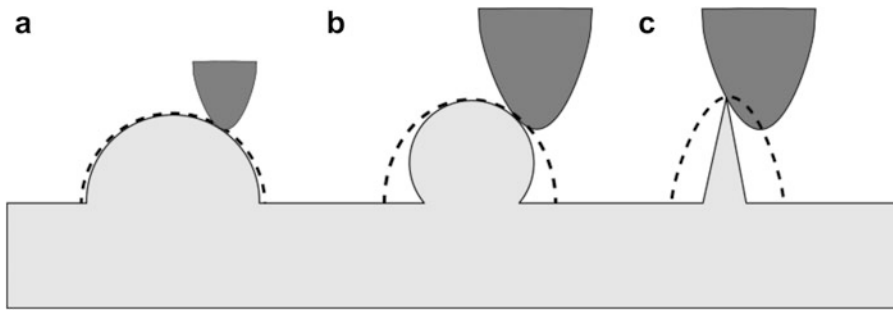

Fig. 2 Tip geometry affects the data in AFM imaging. The *dashed lines* represent the measured height profile. (**a**) The tip size is much smaller than the sample; (**b**) sample and tip dimensions are comparable; and (**c**) the tip is much larger than the sample.

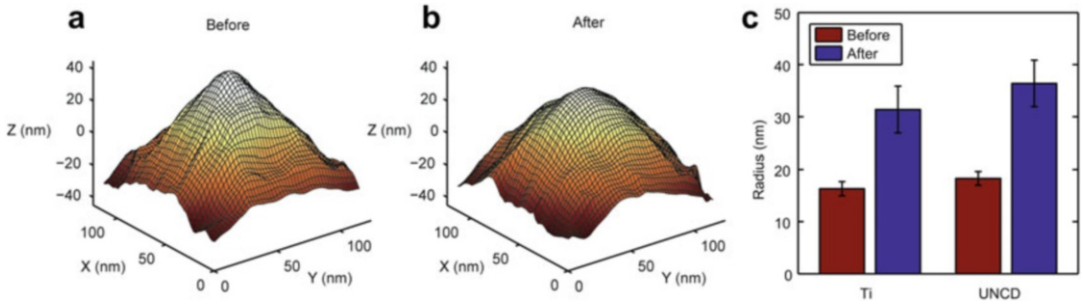

Fig. 3 Results of controlled wear experiments of an AFM tip. Reconstruction of an AFM tip before (**a**) and after (**b**) wear on an ultrananocrystalline diamond. (**c**) Increase in curvature radii of silicon nitride tips by wear experiments on titanium (Ti) and ultrananocrystalline diamond (UNCD) surfaces. Figure reproduced from ref. 21 with permission from Nature Publishing Group.

same chemical properties, but different radii were created. Furthermore, a new method for estimation of tip diameter was presented and compared to the conventionally used blind tip estimation method. In this new approach individual peaks were fit, by using parabolic functions, to the extracted line profiles of the fast scanning axis of AFM images. Figure 3 shows example images of the increase in tip size and a quantification of the increase in tip radii.

We will now take a closer look at the force which acts between the cantilever tip and the sample surface. For this reason, one needs a description of the occurring force while approaching the tip to the surface. A Lennard-Jones potential is suitable to describe the interaction of a surface atom and the tip. In total, the potential is the sum of the interaction of the tip with each surface atom [22]. The expression $U(r) = -\frac{A}{r^6} + \frac{B}{r^{12}}$, where r is the distance between the tip and the sample and $A \approx 10^{-77}$ Jm^6 and $B \approx 10^{-134}$ Jm^{12}, represents the interaction of atoms in a solid [4]. Using the relationship $F(r) = -(\mathrm{d}U/\mathrm{d}r)$, one can calculate the interaction force between the tip and the surface atom. Figure 4 illustrates such a schematic force–distance curve.

Since the force can be attractive ($F < 0$) and repulsive ($F > 0$), there are different regimes that have to be considered. Transferring such a curve on a real AFM system, such a force–distance curve can be acquired by displaying the deflection of the cantilever. Imagine the situation that the cantilever is far away from the sample surface. Here it is unaffected by interactions with the surface and therefore not bent. Approaching the surface, the tip experiences an attractive force. Once the gradient of the attractive force equals the cantilever spring constant the tip jumps into contact with the surface. With further "approach," a force is applied to the surface. According to Newton's third law the sample also exerts the same force on the tip. Thus, the tip is now getting into the repulsive force regime. The force will increase until a certain deflection value, as set by the

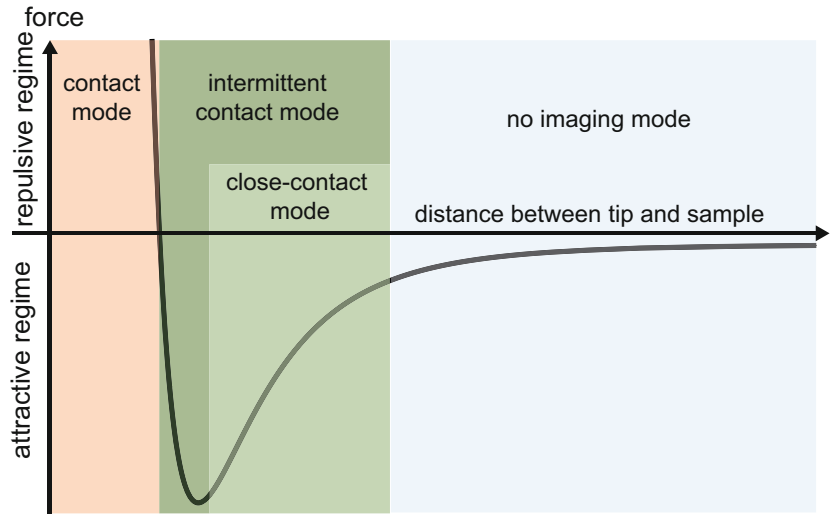

Fig. 4 Schematic illustration of a force–distance curve to illustrate the interaction between the cantilever tip (probe) and the sample surface labeling the different operation modes.

operator, is reached. Reversing the direction of movement, the force is decreased, passing the attractive force regime again, until a jump off occurs. The connection between the tip and the surface is interrupted [4, 5].

2.2 Operation Modes

Having considered the process of approach of the tip towards the sample surface, the various operation modes of AFM can be discussed. By means of Fig. 4, the different force regimes enable a classification of some of these modes. In the following, we will introduce the main modes and their function. In addition, some of their advantages and drawbacks will be discussed.

2.2.1 Contact Mode

The most intuitive operation mode of an AFM is the contact mode. As the name suggests, in this operation mode the tip is continuously in contact with the sample surface. Contact mode operates in the repulsive force regime (Fig. 4) and a force is continuously applied to the surface. In constant force mode, the tip is approached to the surface until a set deflection/force occurs. In this configuration, the surface is scanned while keeping the set force constant with feedback control. The latter implies an "error," meaning the correction voltage that is used to adjust the position of the cantilever. Next to the piezo extension, this "error signal" can also be used to display surface features of the sample. Besides constant force mode, it is also possible to operate in the so-called constant height mode, in which the height of the scanner is fixed. Here, the change in cantilever deflection, and thus the interaction force, is used to directly map the topography of the surface. Consequently, this mode is typically only used for relatively flat surfaces.

An advantage of this operation mode is the high resolution of the obtained images, since there exists a constant contact between the probe and the sample. Another advantage is that it is a fast and straightforward imaging mode. For biological and other soft samples, however, contact mode operation also has some clear disadvantages. Since a force is constantly applied to the surface, chances of sample damage increase. In particular, a constant lateral force arises while scanning, which can drag and slide features over the surface. The result is a distorted image of the sample. It can also happen that the feature of interest is damaged or removed from the surface. In contrast, not only the tip can damage the surface, but also the tip can be damaged by the sample or the scanning process itself, which typically can occur while imaging relatively hard surfaces.

2.2.2 Oscillating Modes

Contact mode imaging is based on the contact between the tip and the surface throughout the whole scan period, which causes large interaction forces with possible destruction of the sample. In order to minimize these forces, there are other operation modes developed based on the oscillation of the cantilever. Such modes are also referred to as dynamic operation modes. In these modes, the cantilever is driven near or at its resonance frequency. The tip touches the surface periodically and during most of the cycle no vertical force is applied to the sample. Furthermore, the lateral forces are markedly reduced during scanning as the major part of the lateral movement occurs when the tip is not in contact with the surface. These two features result in an overall gentler treatment of the sample. Due to the acting force between the surface and the oscillating cantilever when it is approached, the amplitude, the phase as well as the frequency of the oscillation are affected. An integrated feedback control records this change and adapts the piezo element settings if corrections are needed. The choice of the amplitude value can lead to a further distinction of this operation mode class. A variety of different descriptions has been reported and they are partially still under debate. We give a few examples here. If the amplitude that is set is small ($\leq$20 nm [23]), the operation mode is sometimes called “close-contact mode”. This mode has also been referred to as “non-contact mode”, whereby this term can be misleading, because at least temporarily there exists contact between the probe and the sample. Working in the attractive force regime has the big advantage, that only small interaction forces occur while a high resolution is maintained. To prevent the cantilever from jumping into the repulsive force regime, stiff cantilevers (~40 N/m) are used [24]. When a large amplitude (up to ~100 nm) is set, the corresponding operation mode is called “intermittent contact mode” [24]. Oscillated with a large amplitude, the cantilever passes through the different force regimes, where the interaction force between the probe and the sample can be

repulsive, attractive or even negligible. Consequently, a higher force is applied, which can lead to damage of the sample. On the other hand, the implementation is much easier [5].

2.2.3 Jumping Mode Imaging

Another imaging mode, which has recently gained a lot of attention, measures force vs. distance curves at each pixel and moves the cantilever laterally when the tip is not in contact with the surface. The corresponding operation mode is known under a variety of names, for instance "jumping mode" [25, 26], "Quantitative Imaging (QI^{TM}) mode" [27] or "peak force mode" [28] depending on the manufacturer of the appropriate AFM. As the applied force to the surface is precisely controlled and shear forces are practically absent, this imaging mode allows for controlled measurements on soft, biological samples with possible imaging forces below 100 pN. On each position of the surface a force–distance curve is performed and thereby it does not only give topography information on the sample, but also quantitative mechanical information. Therefore, this imaging mode can be regarded as an extension of traditional "force spectroscopy" AFM. Force spectroscopy is not an AFM imaging mode, but a mode that probes mechanical properties at a certain location at the surface. In particular, the cantilever is pulling or pushing at a set position to exert a force onto the surface. Jumping mode imaging and the related imaging techniques are extending the one-dimensional force spectroscopy to three dimensions to include topography information on the surface. This imaging technique is especially suited to image fragile samples as for instance large protein shells or vesicles.

2.2.4 Operation Environments

AFM imaging can be carried out in liquid, gas or in vacuum. Especially for biological samples the *in-liquid* imaging capability of the technique is of great advantage, because in such a way a near-physiological environment can be obtained. Furthermore, the interfering influences caused by a meniscus of water covering the tip or the sample when imaging in air are eliminated. Fluorescence imaging of biomolecules can relatively easily be combined with AFM in liquid. Working in a liquid environment requires a liquid cell and care must be taken to prevent any harm to the sensitive electronics, in particular the piezo elements. Heating and cooling of the sample is possible under in-liquid conditions, but a decrease in imaging stability is likely the result.

While many biological samples are imaged in liquid [8, 29], in the protein-nucleic acid interaction research field imaging under ambient conditions (i.e. in air) is common practice [30, 31]. For these in air studies it is even possible to combine the imaging with fluorescence microscopy [32]. The fact that the fluorophores still work well under ambient conditions is probably related to the presence of a hydrating water layer on the surface. It is also possible

to operate the AFM in air under controlled temperature conditions. However, it should be considered that heating up the sample can destroy the scanner, while by cooling it down condensation on the sample surface and the optics can occur. An investment in thermal isolation and working in a dry environment is recommended to conduct this kind of experiments.

3 The New Perspective: High-Speed AFM

As the capture of an AFM image takes several minutes, only a snapshot of each line in the sample is obtained and typically only static surfaces are imaged. Still it is possible to study dynamics on surfaces such as AFM-induced changes in biomaterials. Viruses can for instance be moved around by the tip on a surface [33] and AFM tip-induced dissociation of RecA-DNA filaments was performed at a frame rate of 80 s/frame [34]. However, in order to study dynamic biological processes this imaging rate is not sufficient and "real-time" observation is required which is impossible using traditional AFM. This lack of temporal resolution has been a great draw-back of AFM imaging ever since its invention and has effectively prohibited the study of dynamic biological processes. Efforts to achieve a faster scanning rate have been conducted at least since the early 1990s [13]. A high-speed AFM (HS-AFM) approach was reported in 2001, where myosin V conformational changes were studied in real time in liquid. 100×100 pixels^2 images (scan size: 240 nm $\times$ 240 nm) were recorded with a frame rate of 80 ms/frame [35]. Further progress occurred and in 2008 imaging rates of ~40 ms/frame over an area of ~250 nm $\times$ ~250 nm with 100 scan lines were reported [13, 14]. Still at that time this was far from a common approach and only recently HS-AFM is becoming available to a larger group of researchers. How was the increase in imaging rate achieved for HS-AFM? Next to an improvement of the electronics and feedback system, this was done by increasing the resonance frequency of the cantilevers to allow for faster scanning. The resonance frequency could be increased by drastically decreasing the dimensions of the cantilever. Furthermore, the interaction force between the tip and the surface is decreased as well. The latter allows for the investigation of sensitive biological samples. The ratio of the cantilever's resonance frequency and its spring constant affects the sensitivity of the force gradient between the tip and the sample surface. In addition, for the acquisition of high resolution AFM images in dynamic mode in liquid, a balance between the amplitude of the oscillation and the cantilever's stiffness needs to be found. This balance should accommodate a high stability and, simultaneously, an interaction force that facilitates sensitive measurements [13]. To increase the scope of applications in biological sciences, a larger

scan size is desirable. In 2016 Uchihashi *et al.* presented a HS-AFM wide-area scanner which facilitates scanning of an area of ~46 μm × 46 μm. By means of this wide-area scanner a topographic image of *Bacillus subtilis* at 15 s/frame was acquired and bacteriolysis of *B. subtilis* after exposure to lysozyme was observed at 20 s/frame [36]. To position the tip in the right place with this scanner a light microscope was used. The addition of a light microscope has created the possibility of combining HS-AFM with confocal and (super-resolution) fluorescence microscopy. All in all the development of HS-AFM has led to a major increase in temporal resolution thereby opening the door to a wide range of applications including the study of biological processes that occur at time scales of 10s of milliseconds to seconds [15, 37, 38].

4 AFM Applications in Biological Sciences

The field of application of AFM measurements in biological sciences is wide. Not only the imaging of proteins is possible, but also lipid membranes, prokaryotic and eukaryotic cells and nucleic acids can be visualized [1, 5, 29, 39–41] . In addition, AFM can be used to determine the roughness of potential implants including determining the effect of surface treatments of such implants [42–44]. Next to imaging, another broad field of AFM application is force spectroscopy. It does not only give information about adhesion factors [45], but can also be used to study inter- and intramolecular forces including unbinding and unfolding of proteins [7, 46–50]. Such experiments include, as examples, unbinding events in virus-cell interactions and the unfolding of an autotransporter passenger protein [51, 52]. In the former a virus was bound to a cantilever tip and approached to the cell surface to initiate binding, upon which the cantilever was retracted to measure the unbinding events, as shown in Fig. 5a. In the latter, it was revealed how protein secretion through the outer membrane is driven by the folding of the protein into a helical structure which is stabilised by aromatic residues. Figure 5b shows an example unfolding curve, which was used in an inverse approach to reveal the folding and secretion mechanism of this autotransporter protein. In another approach conformational changes related to gating of membrane channels were probed by force spectroscopy [53] (Fig. 5c). Here it was shown that the channel open state exhibits essential differences in mechanical coupling between the transmembrane domains with respect to the closed state.

The above described experiments are “pulling”-type of experiments, but it is also possible to perform “pushing”-type of experiments. This is typically called nano-indentation. During these experiments, the tip is approached to the sample at a fixed position until a set force is reached. This force is typically much larger than

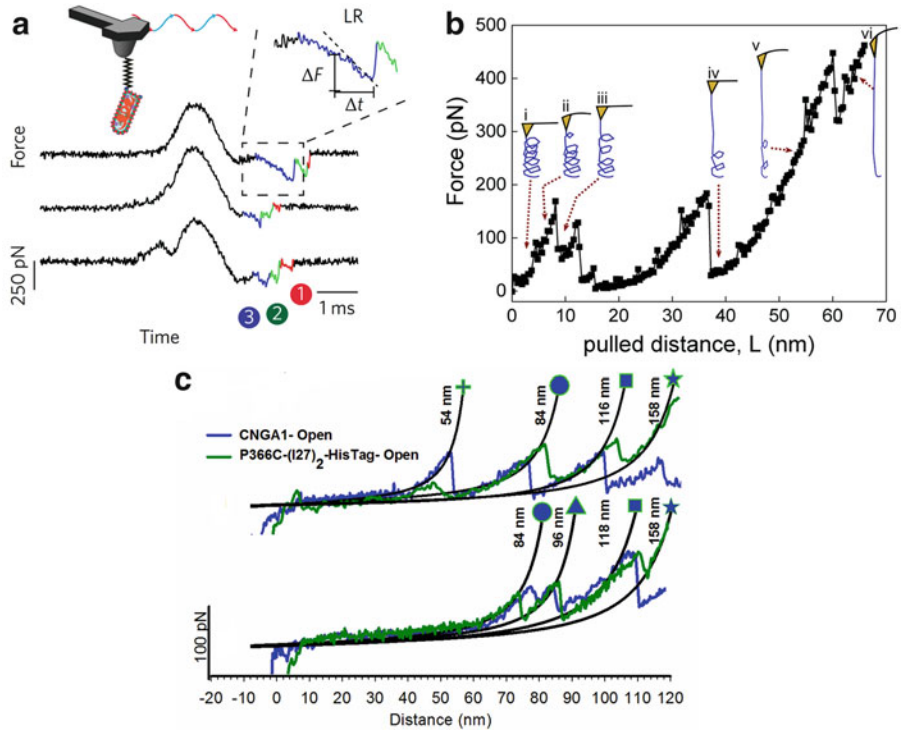

Fig. 5 (**a**) Three virus-cell unbinding event curves in which each curve shows, in color coding, three unbinding events, labeled *1*, *2,* and *3*. Reproduced from ref. 52 with permission from Nature Publishing Group. (**b**) Complete unfolding of an autotransporter protein construct with schematically added figures of the protein at different unfolding stages and the associated cantilever bending (bending is exaggerated for clarity). Reproduced from ref. 51 with permission from American Chemical Society (Copyright 2016). (**c**) Example force curves of unfolding channels in the open state. Worm like chain fits are performed to deduce the increase in contour length during unfolding. Reproduced from ref. 53 with permission from Nature Publishing Group.

the force used for imaging, i.e. it is in the 100s of pN to nN range. Nano-indentation experiments were performed on a variety of particles such as for instance viral protein shells [54–56]. These studies have revealed how viruses possess intriguing mechanical structures [57–59]. We will briefly discuss AFM experiments on the bacteriophage HK97 [57]. This phage self-assembles into an icosahedral procapsid structure, without the dsDNA genome in place. As a next step a maturation step takes place, in which the DNA is packaged with the help of a molecular motor. Concomitantly with this packaging, an increase of the capsid diameter of ~50 nm to ~60 nm occurs. During this expansion, no material is added, so it logically follows that the shell turns thinner. The intriguing question is whether this decrease in thickness is changing the mechanical properties of the protein shell. Nano-indentation experiments were set out to address this question. Figure 6 shows

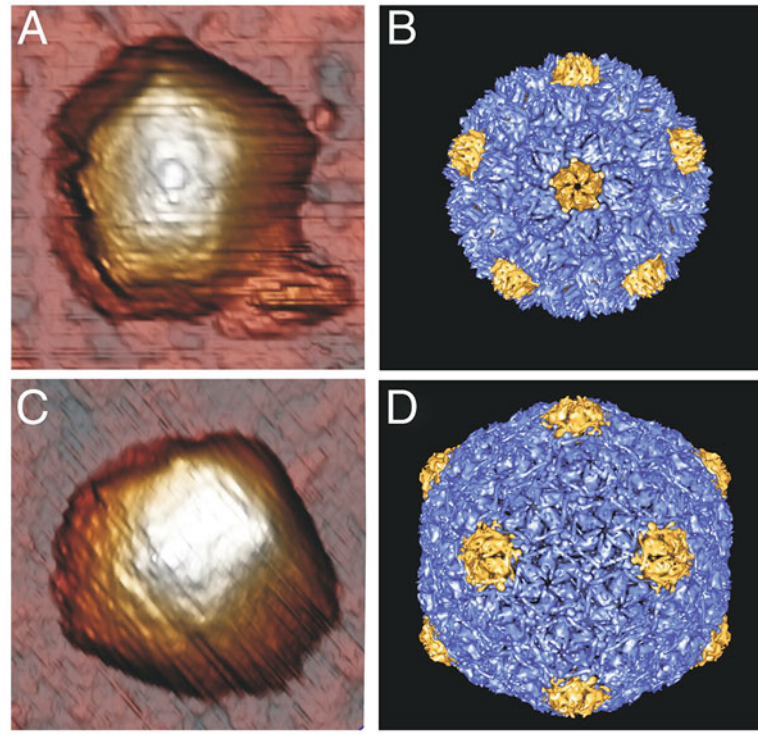

Fig. 6 HK97 procapsid and mature capsid. (**a**, **b**) Respectively AFM image and reconstruction of procapsid lying on its fivefold icosahedral axis. (**c**, **d**) Respectively AFM image and reconstruction of mature capsid lying on its twofold icosahedral axis. Reproduced from ref. 57 with permission from the US National Academy of Sciences.

images of the procapsid and the mature capsid before indentation and for reference the reconstructions of the particles are shown as well. In these images, one can readily differentiate between the icosahedral orientations along which the particles are adsorbed onto the surface. Indentation studies showed a marked difference in material properties between the two types of particles. It turns out that despite its thinner shell, the mature capsid is much stronger than the procapsid. This can only be explained by a detailed scrutinizing of the particle's structure. While the procapsid proteins are loosely attached, during maturation covalent crosslinking occurs between the capsid proteins. This leads to a chainmail like configuration strengthening the particles in an effective manner. These effects are directly related to the bacteriophage infection cycle. During self-assembly the proteins need to be loosely attached, to correct for possible mistakes during assembly. However, after the complete shell has closed, DNA packaging occurs with the help of a molecular packaging motor and considerable forces are exerted

onto the capsid. To be able to withstand these forces a strengthening of the shell is needed and HK97 solved this challenge by adding covalent crosslinks to link the capsid proteins to each other in a solid manner.

5 Conclusion

In this chapter the fundamentals of AFM as well as some of its applications for studying biological samples were presented. This technique can be used for high-resolution three-dimensional imaging at the nanometer scale. Various imaging modes and their suitability to investigate biological samples were discussed. Furthermore, it was shown how force spectroscopy approaches can be used to obtain mechanical information on biological samples, e.g. of protein nanocages and single proteins. Next to traditional AFM, the prospects of high-speed AFM with a focus on biological research fields were indicated. Due to the largely increased imaging speed of this instrument, it is possible to investigate dynamic biological processes on the ms time scale. For instance the movement of myosin V could be observed in real-time [37]. Consequently, AFM is shown to be a versatile technique in biological sciences to obtain morphological and mechanical information on proteins, proteinaceous assemblies, membranes, and nucleic acids. Furthermore, by using high-speed AFM also dynamic processes can be studied. With the advent of new, gentle imaging techniques and fast scanning approaches it is expected that the use and applicability of AFM in life sciences will become even more relevant in the time to come.

Acknowledgement

This work is supported by the STW Perspectief grant CANCER-ID and a Nederlandse Organisatie der Wetenschappen Vidi vernieuwingsimpuls grant (both to WHR).

References

1. Demtröder W (ed) (2010) Experimentalphysik 3, Kern-, Teilchen- und Astrophysik, 4th edn. Springer, Berlin
2. Binnig G, Rohrer H, Gerber C, Weibel E (1982) Surface studies by scanning tunneling microscopy. Phys Rev Lett 49:57–61
3. Binnig G, Quate CF (1986) Atomic force microscope. Phys Rev Lett 56:930–933
4. de Pablo PJ (2011) Introduction to atomic force microscopy. Meth Mol Biol 783:197–212
5. Eaton P, West P (eds) (2010) Atomic force microscopy. Oxford Univesity Press, Oxford
6. Kodera N, Ando T (2014) The path to visualization of walking myosin V by high-speed atomic force microscopy. Biophys Rev 6:237–260
7. Santos NC, Castanho MARB (2004) An overview of the biophysical applications of atomic force microscopy. Biophys Chem 107:133–149

8. Baclayon M, Wuite GJL, Roos WH (2010) Imaging and manipulation of single viruses by atomic force microscopy. Soft Matter 6:5273–5285
9. Marchetti M, Wuite GJL, Roos WH (2016) Atomic force microscopy observation and characterization of single virions and virus-like particles by nano-indentation. Curr Opin Virol 18:82–88
10. Morris VJ, Kirby AR, Gunning AP (eds) (2009) Atomic force microscopy for biologists, 2nd edn. London, Imperial College Press
11. Gross R, Marx A (eds) (2012) Festkörperphysik, 1st edn. München, Oldenbourg Verlag
12. Ando T (2012) High-speed atomic force microscopy coming of age. Nanotechnology 23:062001
13. Ando T, Uchihashi T, Fukuma T (2008) High-speed atomic force microscopy for nano-visualization of dynamic biomolecular processes. Prog Surf Sci 83:337–437
14. Ando T, Uchihashi T, Kodera N *et al.* (2008) High-speed AFM and nano-visualization of biomolecular processes. Pflügers Arch Eur J Physiol 456:211–225
15. Eghiaian F, Rico F, Colom A *et al.* (2014) High-speed atomic force microscopy: Imaging and force spectroscopy. FEBS Lett 588:3631–3638
16. Rugar D, Hansma P (1990) Atomic force microscopy. Phys Today 43:23–30
17. Roos WH, Radtke K, Kniesmeijer E *et al.* (2009) Scaffold expulsion and genome packaging trigger stabilization of herpes simplex virus capsids. Proc Natl Acad Sci USA 106:9673–9678
18. Meyer G, Amer NM (1988) Novel optical approach to atomic force microscopy. Appl Phys Lett 53:1045
19. Churnside AB, Sullan RMA, Nguyen DM *et al.* (2012) Routine and timely sub-picoNewton force stability and precision for biological applications of atomic force microscopy. Nano Lett 12:3557–3561
20. Sader JE, Chon JWM, Mulvaney P (1999) Calibration of rectangular atomic force microscope cantilevers. Rev Sci Instrum 70:3967–3969
21. Vorselen D, Kooreman ES, Wuite GJL, Roos WH (2016) Controlled tip wear on high roughness surfaces yields gradual broadening and rounding of cantilever tips. Sci Rep 6:36972
22. Hölscher H, Allers W, Schwarz UD *et al.* (2000) Interpretation of "true atomic resolution" images of graphite (0001) in noncontact atomic force microscopy. Phys Rev B 62:6967
23. Ho H, West P (1996) Optimizing AC-mode atomic force microscope imaging. J. Scan Microsc 18:339–343
24. García R, Pérez R (2002) Dynamic atomic force microscopy methods. Surf Sci Rep 47:197–301
25. de Pablo PJ, Colchero J, Gómez-Herrero J, Baró AM (1998) Jumping mode scanning force microscopy. Appl Phys Lett 73:3300
26. Moreno-Herrero F, Colchero J, Gómez-Herrero J, Baro AM (2004) Atomic force microscopy contact, tapping, and jumping modes for imaging biological samples in liquids. Phys Rev E 69:1–9
27. JPK Instruments (2011) Nanowizard 4 – the next benchmark for BioAFM. JPK Instruments, Berlin
28. Bruker Nano Surfaces Division (2015) PeakForce tapping – how AFM should be. Bruker Nano Surfaces Division, Goleta, CA
29. Engel A, Müller DJ (2000) Observing single biomolecules at work with the atomic force microscope. Nat Struct Biol 7:715–718
30. Bustamante C, Rivetti C (1996) Visualizing protein-nucleic acid interactions on a large scale with the scanning force microscope. Annu Rev Biophys Biomol Struct 25:395–429
31. Farge G, Mehmedovic M, Baclayon M *et al.* (2014) In vitro-reconstituted nucleoids can block mitochondrial DNA replication and transcription. Cell Rep 8:66–74
32. Sanchez H, Kanaar R, Wyman C (2010) Molecular recognition of DNA–protein complexes: a straightforward method combining scanning force and fluorescence microscopy. Ultramicroscopy 110:844–851
33. Falvo MR, Washburn S, Superfine R *et al.* (1997) Manipulation of individual viruses: friction and mechanical properties. Biophys J 72:1396–1403
34. van der Heijden T, Moreno-Herrero F, Kanaar R *et al.* (2007) Comment on "Direct and Real-Time Visualization of the Disassembly of Single RecA-DNA-ATP(gamma)S Complex" using AFM imaging in fluid. Nano Lett 6:3000–3002
35. Ando T, Kodera N, Takai E *et al.* (2001) A high-speed atomic force microscope for studying biological macromolecules. Proc Natl Acad Sci U S A 98:12468–12472
36. Uchihashi T, Watanabe H, Fukuda S *et al.* (2016) Functional extension of high-speed AFM for wider biological applications. Ultramicroscopy 160:182–196
37. Kodera N, Yamamoto D, Ishikawa R, Ando T (2010) Video imaging of walking myosin V by

high-speed atomic force microscopy. Nature 468:72–76

38. Nievergelt AP, Erickson BW, Hosseini N *et al.* (2015) Studying biological membranes with extended range high-speed atomic force microscopy. Sci Rep 5:11987
39. Henderson E (1992) Imaging and nano dissection of individual supercoiledplasmids by atomic force microscopy. Nucleic Acids Res 20:445–447
40. Baclayon M, Roos WH, Wuite GJL (2010) Sampling protein form and function with the atomic force microscope. Mol Cell Proteomics 9:1678–1688
41. Lekka M (2016) Discrimination between normal and cancerous cells using AFM. Bionanoscience 6:65–80
42. Lamolle SF, Monjo M, Lyngstadaas SP *et al.* (2009) Titanium implant surface modification by cathodic reduction in hydrofluoric acid: Surface characterization and in vivo performance. J Biomed Mater Res A 88:581–588
43. Larsson Wexell C, Thomsen P, AronssonB-O*et al.* (2013) Bone response tosurface-modifiedtitanium implants: studies on the early tissue response to implants with different surface characteristics. Int J Biomater 2013:1–10
44. Kroeze RJ, Helder MN, Roos WH *et al.* (2010) The effect of ethylene oxide, glow discharge and electron beam on the surface characteristics of poly(L-lactide-co-caprolactone) and the corresponding cellular response of adipose stem cells. Acta Biomater 6:2060–2065
45. de Pablo PJ, Colchero J,Gomez-HerreroJ *et al.* (1999) Adhesion maps using scanning force microscopy techniques. J Adhes 71:339–356
46. Mitsui K, Hara M, Ikai A (1996) Mechanical unfolding of α_2-macroglobulinatomic force microscope. FEBS Lett 385:29–33
47. Rief M, Gautel M, Oesterhelt F *et al.* (1997) Reversible unfolging of individual titin immunoglobulin domains by AFM. Science 276:1109–1112
48. Hinterdorfer P, Dufrêne YF (2006) Detection and localization of single molecular recognition events using atomic force microscopy. Nat Methods 3:347–355
49. Kasas S, Thomson NH, Smith BL *et al.* (1997) Escherichia coli RNA polymerase activity observed using atomic force microscopy. Biochemistry 36:461–468
50. Kasas S, Dietler G (2008) Probing nanomechanical properties from biomolecules to living cells. Pflügers Arch Eur J Physiol 456:13–27
51. Baclayon M, van Ulsen P, Mouhib H *et al.* (2016) Mechanical unfolding of an autotransporter passenger protein reveals the secretion starting point and processive transport intermediates. ACS Nano 10:5710–5719
52. Alsteens D, Newton R, Schubert R *et al.* (2016) Nanomechanical mapping of first binding steps of a virus to animal cells. Nat Nanotechnol 12(2):177–183. doi: 10.1038/nnano.2016.228
53. Maity S, Mazzolini M, Arcangeletti M *et al.* (2015) Conformational rearrangements in the transmembrane domain of CNGA1 channels revealed bysingle-moleculeforce spectroscopy. Nat Commun 6:7093
54. van Rosmalen MGM, Roos WH, Wuite GJL (2015) Material properties of viral nanocages explored by atomic force microscopy. Meth Mol Biol 1252:115–137
55. Roos WH, Wuite GJL (2009) Nanoindentation studies reveal material properties of viruses. Adv Mater 21:1187–1192
56. Mateu MG (2012) Mechanical properties of viruses analyzed by atomic force microscopy: a virological perspective. Virus Res 168:1–22
57. Roos WH, Gertsman I, May ER *et al.* (2012) Mechanics of bacteriophage maturation. Proc Natl Acad Sci U S A 109:2342–2347
58. Carrasco C, Luque A, Hernando-Pérez M *et al.* (2011)Built-inmechanical stress in viral shells. Biophys J 100:1100–1108
59. Baclayon M, Shoemaker GK, Uetrecht C *et al.* (2011) Prestress strengthens the shell of Norwalk virus nanoparticles. Nano Lett 11:4865–4869

Chapter 14

Imaging of DNA and Protein by SFM and Combined SFM-TIRF Microscopy

Małgorzata Grosbart, Dejan Ristić, Humberto Sánchez, and Claire Wyman

Abstract

Direct imaging is invaluable for understanding the mechanism of complex genome transactions where proteins work together to organize, transcribe, replicate and repair DNA. Scanning (or atomic) force microscopy is an ideal tool for this, providing 3D information on molecular structure at nm resolution from defined components. This is a convenient and practical addition to in vitro studies as readily obtainable amounts of purified proteins and DNA are required. The images reveal structural details on the size and location of DNA bound proteins as well as protein-induced arrangement of the DNA, which are directly correlated in the same complexes. In addition, even from static images, the different forms observed and their relative distributions can be used to deduce the variety and stability of different complexes that are necessarily involved in dynamic processes. Recently available instruments that combine fluorescence with topographic imaging allow the identification of specific molecular components in complex assemblies, which broadens the applications and increases the information obtained from direct imaging of molecular complexes. We describe here basic methods for preparing samples of proteins, DNA and complexes of the two for topographic imaging and quantitative analysis. We also describe special considerations for combined fluorescence and topographic imaging of molecular complexes.

Key words Scanning force microscopy, Atomic force microscopy, DNA-protein complexes, Single-molecule imaging, Combining fluorescence and topography

1 Introduction

Proper expression and maintenance of genomic DNA is executed with precision and control by the coordinated action of proteins arranged in specific assemblies on DNA. Understanding how these proteins work together to package, transcribe, replicate and repair DNA, requires knowing how they are arranged into functional assemblies. Direct images of protein–DNA complexes are an essential tool to achieve this understanding. They reveal a wealth of inherently correlated information on structures, their variation and distributions. Scanning force microscopy (SFM), also

Erwin J.G. Peterman (ed.), *Single Molecule Analysis: Methods and Protocols*, Methods in Molecular Biology, vol. 1665, DOI 10.1007/978-1-4939-7271-5_14,

commonly known as atomic force microscopy (AFM), is an excellent and practical method for direct imaging of proteins, DNA and complexes of the two at the single molecule/complex level. Molecules and complexes are individually analyzed providing information on the variety of arrangements possible and their frequency in a mixture. Importantly, this type of single molecule structural analysis allows coherent description of features that would otherwise be lost in the averaging of bulk analysis. In addition, direct observation allows correlation of multiple structural features of individual molecular complexes. Sample preparation is relatively simple and requires components biomolecules in easily obtainable amounts and purity. SFM imaging has literally provided a new view of the molecular machinery responsible for DNA processing and by this new insight into molecular mechanisms of vital processes such as DNA packaging, repair, replication and transcription [1, 2]

Mechanistic information is obtained by quantitative analysis of image data. Typically, it is necessary to devise an appropriate scheme to divide complexes or structures observed into relevant categories and determine the distribution of these categories in different conditions. For instance, the percentage of DNA bound by a protein at a specific binding site versus at nonspecific sites would be determined as a function of conditions such as the addition of a nucleotide cofactor or another protein. SFM images are also ideal for revealing mechanistically important protein-induced distortions in DNA such as changes in DNA bending, contour length and flexibility. Protein-induced distortions of DNA can be determined at specific binding sites and at nonspecific sites for comparison, usually from the same sample [3]. DNA substrates are constructed with specific sequence or structural features at defined locations, such as a recognition sequence, a single modified or damaged base, nicks, gaps, various lengths of single- and double-stranded DNA and complex DNA junctions such as those recognized by replication or recombination proteins. In all cases the DNA strands not including the specific feature are by definition nonspecific binding sites and serve as unavoidable internal control DNA. Proteins and their functional assemblies often involve multiple DNA sites and strands. These functional assemblies, for example DNA looped between protein bound at two sites or proteins associating to join or connect multiple DNA molecules, are sometimes hard to define by indirect means but obvious by simply looking at images.

Biomolecules are typically deposited onto an atomically flat mica surface and imaged in air. The samples are dried of bulk water but not desiccated and likely retain their native structure [4]. The volume of the particles observed can be used to estimate size and multimeric state. DNA can be deposited on mica by equilibration on the surface so that it is not kinetically trapped. In this way, the arrangement of the DNA on the surface accurately

reflects its properties in solution, such as contour length, flexibility, and presence of bent segments. Protein–DNA complexes prepared in appropriate biochemical conditions are deposited onto mica in a similar fashion. Changes in the DNA induced by bound proteins can be accurately measured. Some proteins have features that are distinct in SFM images, such as long coiled regions or multiple globular lobes, but most proteins appear as similar globular objects. Here we describe basic methods for obtaining topographic images of DNA, proteins, and their complexes that can be used for a variety of quantitative structural analyses.

Many functionally important protein–DNA complexes include multiple component proteins. The identity of components in multiprotein complexes can be estimated based on their volume and known molecular weights. However, it is not always possible to determine molecular composition and stoichiometry unambiguously by volume alone. It is therefore necessary to label or tag specific proteins to identify different, possibly similarly sized, components in complex assemblies. Combining fluorescence and topographic imaging allows specific identification of fluorescently labeled proteins and greatly expands the application of SFM to analysis of increasingly complex molecular assemblies. Several instruments that combine SFM topographic imaging with fluorescent imaging are currently commercially available. There are specific challenges for using these instruments for analysis of protein–DNA complexes that we address here. It is necessary to deposit the molecules of interest onto an atomically flat surface such as mica for topography but this substrate must also be sufficiently optically transparent to allow fluorescence. In addition, appropriate marker objects are essential to achieve nm accuracy in aligning optical and topographic images when the objects of interest are smaller than optical resolution. We briefly describe methods for sample preparation and image alignment that allow properly correlated SFM and fluorescence imaging.

2 Materials

2.1 Instrumentation

1. Scanning probe microscope: These instructions are guided toward eventual imaging by intermittent contact mode in air. We have a Digital Instruments MultiMode Scanning Probe Microscopes. The methods for sample preparation and guidelines for data acquisition are applicable to any similar instrument and imaging mode (*see* **Note 1**).
2. Computers (PC, Mac) that meet requirements of image analysis software. Software like SFMetrics [5], ImageJ (http://rsbweb.nih.gov/ij/), Image SXM (extended version of NIH image by Steve Barrett, Surface Science Research Centre, Univ.

of Liverpool, Liverpool, U.K.), WSxM (Nanotec Electronica S. L.), or similar image analysis software is required for quantifications of various features of visualized molecules.

2.2 General Supplies

1. Glass pasture pipettes.
2. Standard facial tissues.
3. Lens cleaning tissues (Whatman 105).
4. Forceps (DZM, Italy).
5. A source of filtrated air or N_2.
6. For preparation of all solutions, MiliQ filtered de-ionized water (Resistivity $\leq$16 MΩ cm, TOC 1–5ppb).
7. Standard protein deposition buffer consisting of: 20 mM HEPES-KOH pH 7–8, 50–100 mM KCl (or NaCl), 1 mM DTT (chemical supplied by Sigma-Aldrich).
8. Standard DNA deposition buffer consisting of: 5–10 mM HEPES-KOH pH 7.5, 5–10 mM $MgCl_2$ (chemical supplied by Sigma-Aldrich).

2.3 Sample Substrates

1. Metal discs such as those usually supplied with scanning probe microscope.
2. Mica sheets (Muscovite Mica V-5 Quality, Thickness = 0.15–0.21 mm, Electron Microscopy Sciences).
3. Punch and die set (Precision brand) for cutting mica into discs. The diameter of mica discs is 1–2 mm smaller than diameter of metal discs.
4. Superglue to attach mica discs to metal discs.
5. Invisible tape (19 mm width, Magic from 3 M) to cleave mica.

2.4 DNA Preparation

General molecular biology reagents and instruments for preparation of DNA (purification from bacteria or PCR amplification) are needed. General knowledge on methods for DNA preparation, such as those found in various editions of *Molecular Cloning: A Laboratory Manual* from CSHL Press, is assumed.

2.5 Combining Fluorescence and SFM

2.5.1 Instrumentation

For identifying specific molecules and nano-objects in SFM topography images we use a combined SFM-fluorescent microscope set up which consists of: An inverted fluorescence microscope equipped with high numerical aperture (1.45) objectives with a minimum magnification of 60× (Nikon TE2000); signal detections with a Cascade II:512B EMCCD camera (Princeton Instruments); running MetaMorph software (Molecular Devices) or custom-made Labview (National Instruments) software for microscope operation and image acquisition; and a coupled NanoWizard®II scanner (JPK instruments). Similar instruments and equivalent components would perform as well.

2.5.2 Sample Substrates for Combined Fluorescence and SFM

1. Mica sheets (Muscovite V-1 quality, from Electron Microscopy Science).
2. Glass cover slips, round, 24 mm diameter, thickness 00 (from Menzel-Gläser).
3. Optical adhesive NOA88 (Norland products).
4. Hand held UV lamp.
5. Sodium tetrahydridoborate 0.25% w/v solution in water (*see* **Note 2**).
6. Invisible tape (19 mm width, Magic from 3M).

2.5.3 Fluorescent Markers and Labels

1. FluoSpheres® carboxylate-modified microspheres (0.04 μm diameter, yellow-green fluorescent (505/515), orange fluorescent (540/560) and red fluorescent (580/605) from Invitrogen).
2. TransFluoroSpheres® (0.04 μm diameter, dual green and red fluorescent (488/645) from Invitrogen).

3 Methods

3.1 Considerations for Preparing Proteins Used in SFM Imaging

Purified proteins should be stored and used without addition of stabilizing proteins such as BSA. The protein purity requirements differ with application and the nature of possible contaminants. For example, if the protein of interest binds to DNA, contaminating proteins not bound to DNA can be ignored. Also, DNA binding proteins should be without any trace of DNA. In general, $\geq$80% protein purity, estimated by coomassie blue staining of the purified protein displayed by gel electrophoresis, is sufficient for SFM analysis.

3.2 Considerations for Preparing DNA Used in SFM Imaging

The length of DNA to be used depends on the eventual data desired and the specific experimental question. In general, DNA should be at least 500 bp or longer so that it is obviously DNA by appearance based on relative width, height and length. We commonly use DNA in the range of 500–3000 bp. Linear DNA is generally more useful. Circular DNA tends to fold over itself on the surface making it harder to analyze. In addition, linear DNA allows determining the location of a specific sequence or feature of interest by its relative position from an end. DNA should be clean, free of proteins or other material that will deposit onto mica and complicate the imaging. Kits/columns for DNA purification (Quiagen, GE Healthcare, Sigma-Aldrich) usually produce DNA of sufficient purity for SFM, though some problems with residual column material or buffer components occasionally occur. The cleanest DNA is obtained by the following methods depending on the source: from solutions such as PCR reactions or Enzyme

digestion purify DNA by phenol:chloroform extraction followed by chloroform extraction; from gel slices purify DNA by electroelution; DNA from plasmid or phage preparations by cesium gradient purification. These DNA purification and isolation methods often reduce final yield. Therefore, the trade-off between purity and yield has to be considered when choosing purification methods for individual applications. Ethanol precipitation tends to result in contaminating material when imaging, often assumed to be excess salt. For that reason, ethanol precipitation is avoided or preformed with care to wash excess salt from pellets before resuspension.

3.3 Preparation of Mica Substrates

1. Attach mica to metal by applying a very small drop of superglue onto the metal discs placing the mica disc over the glue and gently pressing. Avoid glue spreading beyond the mica as this will interfere with cleaving the mica.
2. Freshly cleaved mica is prepared by applying Invisible Tape to the mica glued to metal and peeling off the top mica layers. The peeled off layer stuck to the tape is inspected to see if it is a complete circle. If a complete layer was not cleaved off the procedure is repeated until a complete layer, smooth unbroken circle, is removed. The mica is usually cleaved only a few minutes to a half hour before use to assure a clean surface.

3.4 Immobilizing Molecules on Mica: General Considerations

In order to visualize molecules in scanning force microscopy they have to be immobilized on a surface. However, molecules have to be free from the surface to enable their dynamic interactions and to prevent steric hindrance that might affect molecular interactions. Thus, the immobilization of molecules on the surface has to be carefully controlled to enable imaging while minimizing disturbing the relevant molecular interactions. Molecules can be deposited on a surface through specific or nonspecific interaction. We most often take advantage of relatively nonspecific electrostatic adsorption, which depends on charge of the surface and molecules, and is sufficient to provide controlled attachment of DNA, proteins and their complexes. Specific interactions, such as streptavidin and biotin or digoxigenin and anti-digoxigenin, provide much stronger attachment of molecules to the surface with defined molecule orientation. However, surface modification also increases roughness and interferes with imaging.

The most commonly used surface for deposition of biomolecules is muscovite mica. Mica can be cleaved at crystal planes that produce large atomically flat surfaces. This uniform flat surface allows detection of biomolecules that are only a few nanometers high. The mica surface is negatively charged and the heterogeneous charged domains on most proteins result in sufficient deposition without additional treatment of either surface or protein. HEPES buffers, in biologically relevant pH range (pH 7–8), are preferred for protein deposition. Tris–HCl buffers tend to deposit on mica

and interfere with SFM imaging. Other common protein storage or reactions buffer components, such as KCl, $MgCl_2$, DTT, ATP, low concentration of detergents like NP40, and glycerol, do not interfere with protein deposition or eventual imaging in our experience. The composition of buffers used for deposition of proteins is less strict than for deposition of DNA because proteins deposit effectively onto mica in a wider range of salt and pH conditions. Thus, it is a good first step to deposit proteins in buffers that are optimal for maintaining protein structure and/or activity. If the protein of interest is already biochemically characterized, the optimal buffer for deposition for SFM would be the same (or very similar) as the optimal buffer for protein activity. In case of an uncharacterized protein, SFM deposition can be done in a standard deposition buffer consisting of: 20 mM HEPES pH 7–8, 50–100 mM KCl (or NaCl), 1 mM DTT. If the protein appears aggregated upon deposition increasing salt concentration and/or including some NP40 (0.05%) often helps to prevent undesired protein-protein interaction.

Adsorption of negatively charged DNA on negatively charged mica surface requires the presence of divalent cations. Those interested in the effects of different divalent cations on DNA deposition on mica are referred to published studies on this topic [5–8]

The mica surface can be modified for more efficient adsorption of DNA. This has advantages and disadvantages. The treatment of mica with either 3-aminopropyltriethoxysilane (APTES) or poly-L-lysine results in a positively charged surface. DNA binding to such surfaces does not require the addition of divalent cations. The resulting DNA is strongly attached to the modified surface and can be imaged by SFM both in air and in buffer. However, on these modified surfaces DNA does not equilibrate but become kinetically trapped [9].

Spermidine can be added to the sample to increases the affinity of nucleic acids to mica. The presence of spermidine allows DNA binding to mica without divalent cations and/or in the presence of higher concentrations of monovalent salt. By altering the concentration of spermidine DNA deposition can be controlled to be either by equilibration or by kinetic trapping (Fig. 1). A final concentration of 0.05 mM spermidine is sufficient to provide DNA deposition by equilibration in a sample with 150 mM KCl even without Mg^{2+}.

Deposition by kinetic trapping results in DNA conformations on mica that are strongly influenced by interaction with the surface. This complicates and, in some cases, precludes determining experimentally important changes in DNA conformation, such as measuring DNA bends or distortions induced by protein binding or changes in DNA conformation induced by binding small molecules prior to deposition. In order to measure and analyze protein-induced changes in DNA we do not use treated mica [9]. In

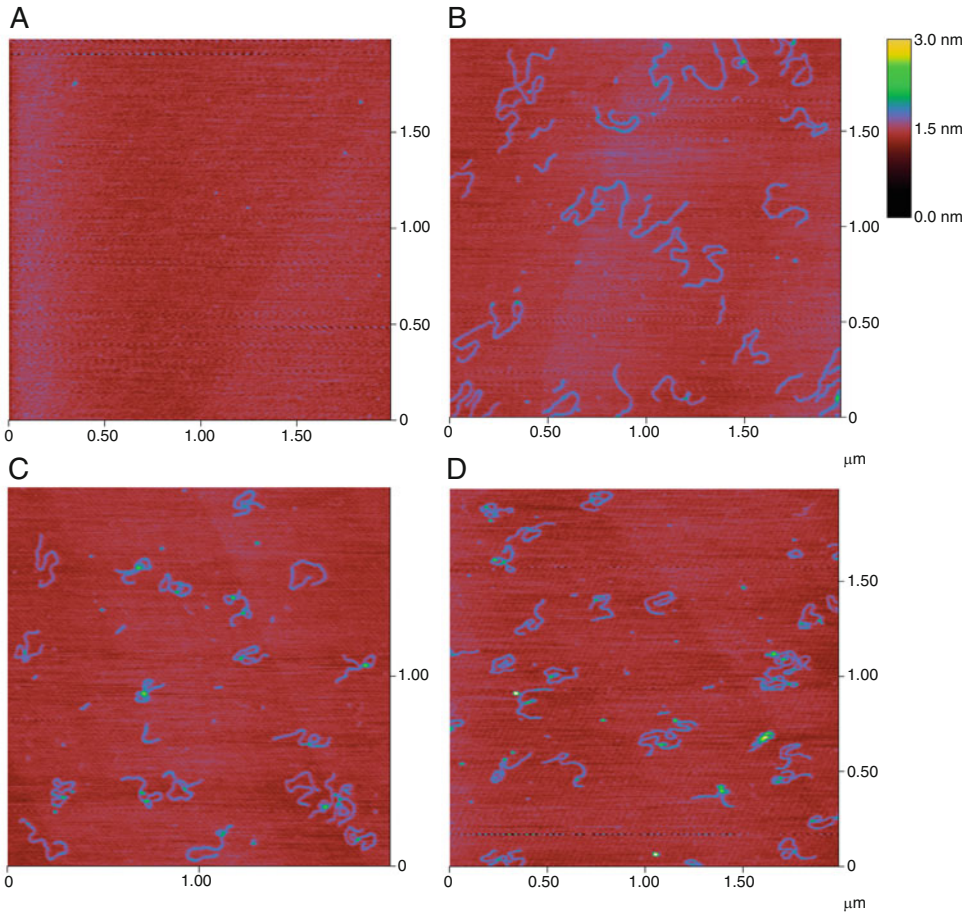

Fig. 1 Example of different concentrations of spermidine on DNA deposition (linear double-stranded 1.8 kb) at 0.5 ng/μl in 10 mM Hepes and 150 mM KCl was used for deposition. (**a**) Addition of 0.01 mM spermidine was not enough to provide binding of DNA for mica. (**b**) Addition of 0.05 mM spermidine-enabled deposition of DNA by equilibration. Increasing concentration of spermidine to 0.1 mM (**c**) or 1 mM (**d**) caused kinetic trapping of DNA on the surface. The image dimensions are labeled; height is indicated by the gray scale shown to the *right*

addition, any mica treatment results in a rougher surface that can complicate imaging.

The persistence length of DNA can be determined from SFM images and is used as a test of deposition by equilibration on the surface. Persistence length reflects intrinsic flexibility of a polymer and is a well-characterized feature of DNA. Persistence length is obtained by measurements of the contour length and the end-to-end distance of deposited DNA as described in [9]. A persistence length of ~50 nm is characteristic of DNA and thus indicates deposition by equilibration.

We have descried that proteins adhere to mica in a wider variety of buffer conditions than DNA. Because of this, also protein bound DNA can adhere to mica due to the behavior of the proteins. Thus, a protein-bound DNA will often adhere to mica in deposition

conditions that are effective for the protein alone without the need to add Mg^{2+} or reduce monovalent cation concentration. It should be noted however that free DNA, not bound by proteins, will behave differently and may not adhere to mica in conditions where protein–DNA complexes. Thus, deposition conditions should be chosen carefully depending on the goal of the experiment. For instance, if it is necessary to quantify the amount of protein bound and protein free DNA, controls that show equal deposition of these need to be included.

The best conditions for protein–DNA complex formation should be determined by standard quantitative biochemical assays prior to initiating SFM imaging experiments. This will form the starting point for conditions to use in SFM imagining. Binding reactions for SFM typically require more concentrated DNA than many biochemical assays and there are limitations to the excess of protein that can be used. As a rule, the solution deposited onto mica should have DNA at 1–10 ng/μl and proteins should not be more than 50-fold molar excess to their binding sites. The upper limit to excess protein is due to problems observing DNA if the surface becomes covered by protein or even more dramatically if protein saturates the surface and prevents DNA binding. Thus, protein to DNA ratios and protein concentrations optimal for biochemical assays may not be optimal for SFM imaging.

3.5 Deposition of Protein for SFM Imaging

1. Prepare a solution of protein to be deposited, concentration of about 0.5 μM in an appropriate buffer is a good starting point. Optimal protein concentration for deposition will differ for each protein depending, for instance, on purity, size and oligomeric state. Usually, protein concentrations of less than 0.5 μM (final in deposition buffer) provide reasonable coverage of the mica surface for further analysis.
2. Place a drop, 5–30 μl depending on the size of the mica surface, of protein solution onto the freshly cleaved mica surface and let it sit to deposit for ~30 s.
3. Rinse the mica surface with Milli-Q filtered de-ionized water, about one pasture pipette full as shown in Fig. 2.
4. Excess of water is blotted by touching a piece of facial tissue to the edge of the mica.
5. The mica surface is then dried in a stream of filtrated air (or N_2).
6. Observe the sample with the SFM, typically scanning fields of 1 μm × 1 μm with a *Z* scale of 5 nm or less will give a good impression of the protein coverage.
7. Assess the protein coverage and modify deposition if needed. If deposition is too crowded (Fig. 3a), additional dilution of five- to tenfold usually results in surface coverage where proteins are nicely separated on the surface and can be analyzed (Fig. 3b).

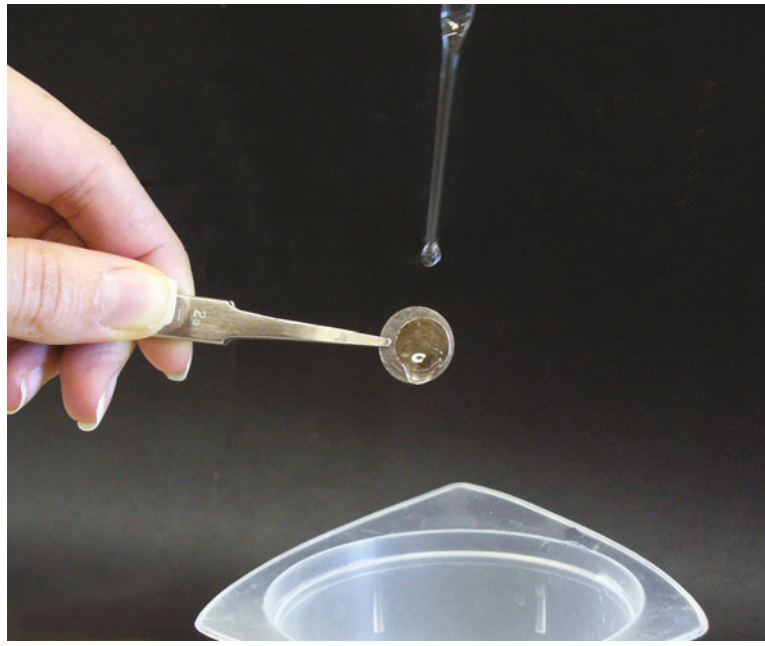

Fig. 2 Washing mica surfaces with water. The sample substrate is held by forceps on the edge of the metal disc, not over the mica. Water or buffer is washed over the surface using a pasture pipette

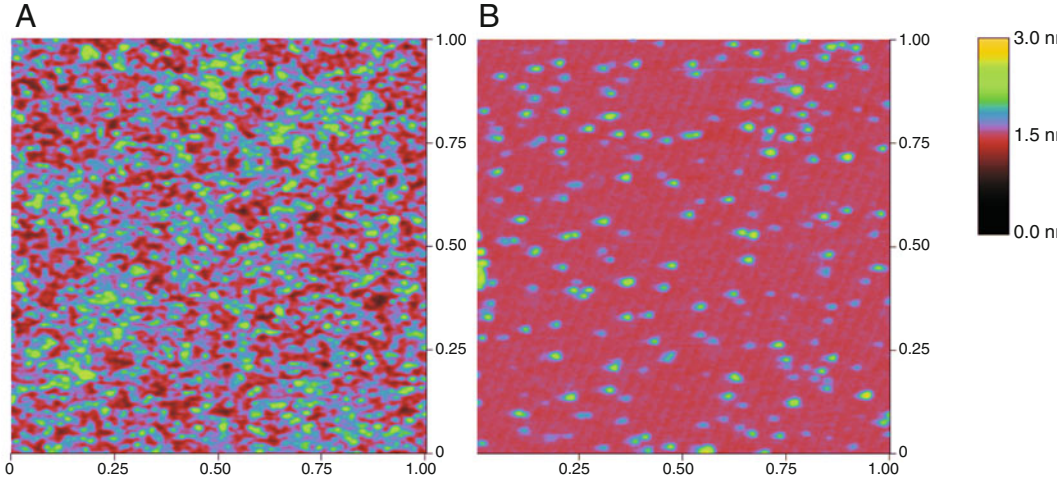

Fig. 3 Examples of excess or appropriate protein coverage. The 37 kDa human RAD51 protein was deposited as described from a buffer containing 25 mM HEPES-KOH pH 8.0 and 100 mM KCl and imaged in tapping mode in air with a Digital Instruments multimode NanoScope. (**a**) Too much protein covering the mica surface prevents identification and analysis of individual molecules. Here a 2 μM solution was used for deposition onto mica. (**b**) Adequate protein deposition showing many single molecules well separated and few overlapping unresolved molecule pairs. Here a 0.2 μM solution was used for deposition onto mica. The image dimensions are shown; height is indicated by *color* according the scale shown on the *right*

3.6 Deposition of DNA for SFM Imaging

1. Prepare a solution of DNA to deposit, DNA 0.5–10 ng/μl in deposition buffer of 5–10 mM HEPES pH7.5, 5–10 mM $MgCl_2$. Since the presence of monovalent cations dramatically reduces Mg^{2+} promoted adsorption of DNA to mica, the concentration of monovalent salt in the solution being deposited should be less than or equal to the concentration of Mg^{2+}.
2. Place a drop, 5–30 μl depending on the size of the mica surface, of the solution containing DNA onto the freshly cleaved mica surface and let it sit to deposit for 30 s to 1 min.
3. Wash the mica surface with Milli-Q filtered de-ionized water, about one pasture pipette full, as shown in Fig. 2.
4. Excess of water is blotted by touching a piece of facial tissue to the edge of the mica.
5. The mica surface is then dried in a stream of filtrated air (or N_2).
6. Observe the sample with the SFM, typically scanning fields of 2 μm × 2 μm with a *Z* scale of 2 nm will give a good impression of the DNA coverage.
7. Assess the DNA coverage and modify deposition if needed. Excess DNA coverage is shown in Fig. 4a and appropriate coverage of DNA on mica is shown in Fig. 4b. If the DNA

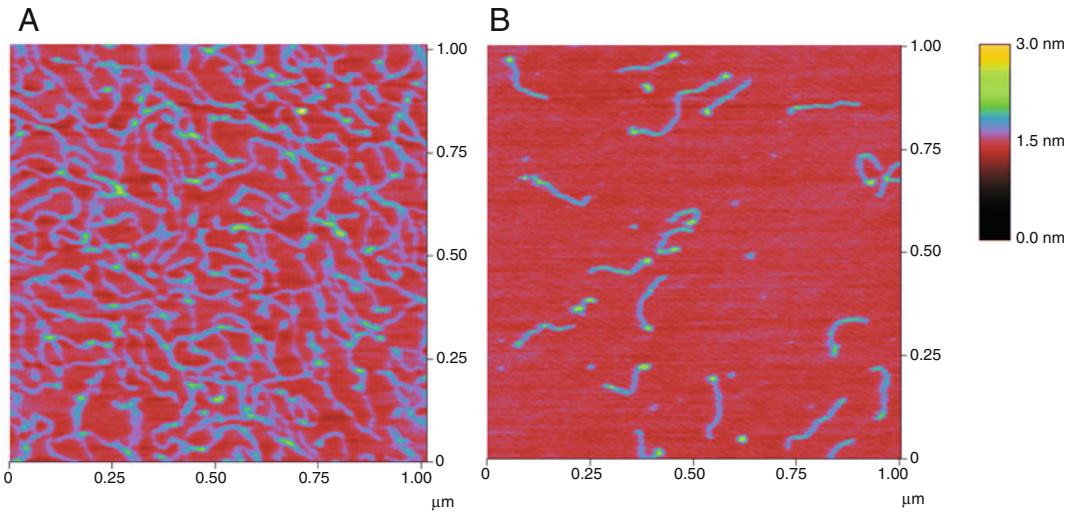

Fig. 4 Examples of excess and appropriate DNA coverage DNA was deposited onto mica as described and imaged in tapping mode in air with a Digital Instruments multimode NanoScope. (**a**) Too much DNA covering mica prevents identification of individual molecules and precludes any meaningful analysis. Here a solution of 800 bp linear double-stranded DNA at 10 ng/μl in 10 mM HEPES, 10 mM MgCl was used for deposition onto mica. (**b**) Appropriate DNA density with clearly separated and non-overlapping DNA molecules. Depending on the length of the DNA there should be 5–20 molecules in a field. Here a solution of 0.5 ng/μl DNA in 10 mM MgCl was used for deposition onto mica. This resulted in about 15 isolated, identifiable and analyzable DNA linear DNA molecules. This linear DNA consists of a 500 bp double-stranded and 300 nt single-stranded segment. The single-stranded DNA appears as a small knob at one end of the linear molecule. The image dimensions are shown; height is indicated by *color* according the scale shown on the *right*

on the surface is too crowded, try two- to tenfold dilution of the solution for deposition. If there is not enough DNA on the surface (only one, a few or no molecules in a 2 μm × 2 μm scan) one of several variations in the deposition will usually help: increase the time for the DNA solution sitting on mica to 1–2 min, increase the DNA concentration, increase the Mg^{2+} concentration, or decrease the monovalent cation concentration.

3.7 Deposition of Protein–DNA Complexes for SFM Imaging

1. Prepare a protein–DNA binding reaction for deposition. This typically should include DNA at 1–10 ng/μl (*see* **Note 3**).
2. Place a drop of the protein–DNA complex sample onto mica, as described above for protein or DNA alone, and allow to sit for 30 s to 1 min.
3. Unbound material is washed off with a small volume of binding buffer as shown in Fig. 2.
4. Excess buffer is removed by touching a tissue the edge of the mica surface, but the surface is *not dried*.
5. The surface is then covered with 30–40 μl of buffer containing 10 mM HEPES-KOH (pH 7.5), 10 mM $MgCl_2$ for DNA to attach to mica.
6. Almost immediately or after about 5 s the mica is washed with water, about 1 Pasteur pipette full, as shown in Fig. 2.
7. Excess liquid is then blotted by touching a tissue to the edge of the mica, and the surface is dried in a stream of filtered air as described above.

3.8 Deposition of Protein–DNA Complexes and Free DNA in Binding Reactions for SFM Imaging

1. Prepare a binding reaction and dilute with deposition buffer (10 mM HEPES, 10 mM $MgCl_2$) so that the concentration of DNA is 1–10 ng/μl. Since the presence of monovalent cations dramatically reduces Mg^{2+} promoted adsorption of DNA to mica, the concentration of monovalent salt in the solution being deposited should be less than or equal to the concentration of Mg^{2+} (*see* **Note 4**). This will allow free DNA as well as protein-bound DNA to adhere to mica. The initial binding reaction may need to be adjusted so that after dilution the solution that will be deposited still contains DNA at 1–10 ng/μl (*see* **Note 5**). If the concentration of monovalent salt in the solution being deposited has to stay high, addition of 0.05 mM spermidine (final concentration) will allow both free DNA and protein-bound DNA to bind to mica.
2. Place a drop of the protein–DNA complex sample onto mica, as described above for protein or DNA alone, and allow to sit for 30 s to 1 min.

3. Unbound material is washed off with water, about 1 pasture pipette full, as shown in Fig. 2.
4. Excess water is blotted by touching a piece of facial tissue to the edge of the mica.
5. The mica surface is then dried in a stream of filtrated air (or N_2).
6. Observe the sample with the SFM, typically scanning fields of 2 μm × 2 μm or 4 μm x 4 μm with a *Z* scale of 2–5 nm will give a good impression of the sample. Density of DNA on the surface, either with or without bound protein, similar to that shown in Fig. 4b is sufficient for most analysis (*see* **Note 6**).

3.9 Guidelines for Collecting Images Sets for Analysis

Once the stoichiometry of DNA and protein is optimized for imaging and good coverage of mica is achieved, for proteins alone, DNA alone or protein–DNA complexes, a collection of images needs to be obtained for eventual analysis.

1. Issues of actual microscope operation and image acquisition are not discussed or described here (refer to specific instrument operating manual). The operation of a SFM and data acquisition differ depending on the instrument and are beyond the scope of this article. The samples we have described are usually imaged in our lab using intermittent contact or "tapping" mode in air. We use standard silicon tapping tips for a variety of suppliers with equivalent success. It is important that the tips have a confirmed end radius of curvature of about 10 nm or less (*see* **Note 7**).
2. For most applications scan sizes ranging from 1 μm × 1 μm up to 4 μm × 4 μm are most useful. For instance, when analyzing proteins, scans of 1 μm × 1 μm usually provide sufficient resolution and sufficient data per image. For DNA-protein complexes that individually cover more surface scans of 2 μm × 2 μm or 4 μm × 4 μm are better (*see* **Note 8**). In any case, all images to be used in the same analysis need to be the same size and resolution.
3. Images should be collected from non-overlapping fields without selection for areas of interest. If scanning is stable and interference free, images can be collected without changing scanning parameters, the autoscan function of the microscope software can be used to collect an unbiased series.
4. Most analysis requires a significant number of molecules or complexes to measure. For example, if 100 or more DNA-protein complexes have to be analyzed and the reaction results in one fifth of the DNA molecules being bound by protein and deposition results in ten DNA molecules of about 1 kpb long in a 2 μm × 2 μm field, then a minimum of 50 such images need

to be collected. It will take considerable time to collect these 50 images. In the optimistic case that everything works well this is a half-day of collecting images. Considering that images are needed for control samples, planning is a very important to perform efficient imaging experiments.

3.10 Guidelines for Standard Image Analysis

A number of features of protein, DNA and protein–DNA complexes can be measured from SFM images [1]. The size of proteins alone or bound to DNA can be accurately determined from SFM images. Also, protein-induced changes in DNA, such as wrapping, elongating, and bending of can be quantitatively described.

DNA length can be measured from SFM images imported into specialized software such as IMAGE SXM, a customized version of Image J modified to automatically import image data from a variety of commercial scanning probe microscopes, or SFMetrics a recently develop tool based on MATLAB that can be run in different platforms and adds several features like skeleton length to analyze irregular objects applying user-adjusted thresholds [5].

1. We determine DNA contours by manually tracing in an appropriate image analysis program. In the case of DNA–protein complexes, contour length is traced as the shortest possible DNA path through the bound protein. Custom software that can automate DNA length measurements has been developed in several labs but is not currently commercially available. The length of DNA ± protein will indicate whether bound protein alters DNA by wrapping or stretching (*see* for example [10]).
2. The volume of proteins (not bound to DNA) can be determined using a semi-automated method developed by Glenn C. Ratcliff and Dorothy A. Erie [11]. Using this approach, large protein populations can be analyzed in a rapid and accurate manner.
3. The volume of DNA-bound protein complexes has to be determined by manual tracing. Area and average height of complex are measured, and a background volume of the same traced area at an adjacent position including DNA is subtracted [12, 13].
4. DNA bending is a feature of many DNA binding proteins, *see* for example [3, 14]. Using SFM, DNA bending can be directly evaluated. A comparison of different methods to determine DNA bend angles is presented in [15, 16].

3.11 Preparation of Mica Substrates for Combined SFM-Fluorescence

1. Cut the mica disc slightly smaller than the size of the cover slips.
2. Using a scalpel, split the individual mica discs into two or three thinner layers.

3. Cleave the layered mica disc with tape until almost transparent. The color at this stage should still be slightly brownish. Be sure that one side of the mica surface is clearly flat (by eye) with no irregularities (as described in Subheading 3.3). The flat side of the mica is to be glued to the cover slip.
4. Place the cover slip to be used onto a lens cleaning tissue.
5. Put a small drop of the optical glue in the end of a yellow tip pipette.
6. Place the mica disc over the glue with the flat side facing the glue.
7. Tape the mica and the cover slip and attach to the lens cleaning tissue as shown in Fig. 4. Press down on the middle of the mica with your thumb for a homogeneous distribution of the glue under the surface.
8. Cure the UV glue by placing the UV light around 4 cm over the cover slips and switch on the 350 nm light for 3 min (*see* **Note 9**). It is most convenient to keep the glass-glued mica taped to the lens tissue (Fig. 5). A piece of lens tissue including the taped down cover slip is cut to about the size of a microscope slide. Accidentally breaking the cover slip is avoided by handling the tissue. The mica-cover slips can be stored for future use for as long as necessary.

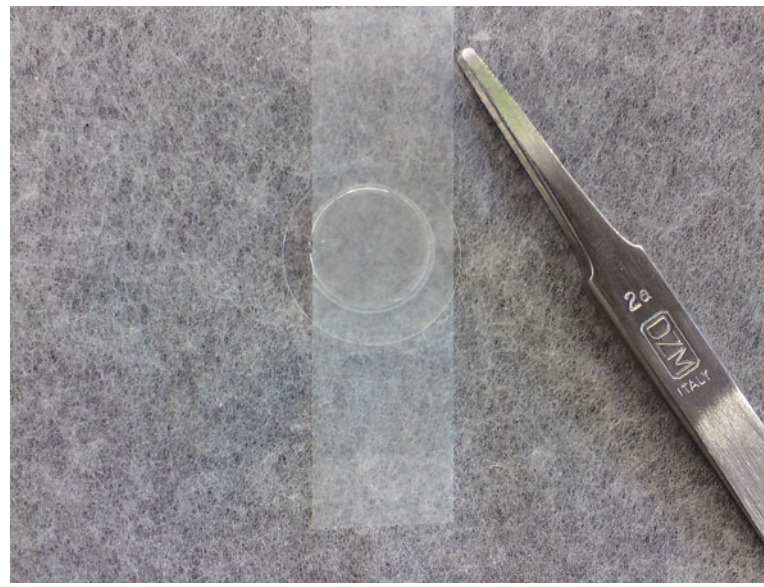

Fig. 5 Illustration of preparing mica glued to glass cover slips. The mica is glued to a glass cover slip as described and then attached with tape to a lens cleaning tissue as shown. The tissue is used to pick up the fragile glass cover slip and the sample surfaces are also stored in this way

9. Before using the mica-cover slip, the mica surface should be made as thin as possible, by cleaving as many layers as possible using the Scotch tape. The transparency of the mica now should be close to 100%, without cracks or other visible imperfections, otherwise the focusing step with the short distance working objectives would be simply impossible (*see* **Note 10**).
10. Once the thickness of the mica-coverslip has been assessed (*see* **Note 10**), it can be treated by placing a 200 µl drop of 0.25% w/v sodium tetrahidroborate on the mica for 20 min to reduce autofluorescence. Wash with water 4–5 times as shown in Fig. 2. The surface is now ready for depositing the solution containing the DNA and protein complex to be analyzed.

3.12 Fluorescent DNA and Proteins for Combined SFM-Fluorescence: General Considerations

General considerations for DNA and proteins: Fluorescence labels can be attached to DNA and/or protein. DNA is typically labeled by: (1) PCR using fluorescence nucleotides analogs for uniform labeling if the fluorophore does not interfere with protein interactions; (2) with PCR primers including a 5′ fluorophore; (3) Conjugating biotin to DNA, also introduced by PCR with 5' biotin modified primers, bound to any of a variety of streptavidin coupled fluorophores. Protein can be labeled with fluorophores by a variety of methods such as those described in Chapter 6 by Modesti.

3.13 Sample Preparation for Combined SFM-Fluorescence

1. Prepare a DNA, Protein, or DNA-protein complex binding reactions in appropriate functional conditions.
2. Dilute the binding reaction into 20 µl of deposition buffer (10 mM HEPES, 10 mM $MgCl_2$, including 3 pM (Trans) FluoSpheres® (*see* **Note 11**) markers) according to guidelines given above in Subheadings 3.4–3.8. Note, that the distribution of molecules should be 5–10 times sparser than in conventional SFM imaging in order to achieve a clear image of single fluorophores (Fig. 6).
3. Place a 20–40 µl drop of the diluted sample onto the freshly cleaved mica surface and let sit for 1 min.
4. Unbound material is washed off with water, about 1 pasture pipette full, as shown in Fig. 2.
5. Blot off excess liquid by touching a tissue to the edge of the mica.
6. Dry the sample in a stream of filtered air.
7. If the use of deposition buffer needs to be omitted (for instance if dealing with cation-sensitive reactions), the sample can be diluted in reaction buffer and spermidine added just prior to deposition to a final concentration of 5 µg/ml. If any charged molecules need to be avoided in the reaction mixture, 3 pM fiducial markers should be deposited separately in total of 20 µl of deposition buffer, as described in **steps 3–6**. After washing and drying the mica, reaction mixture diluted in adequate buffer can be re-deposited in the same fashion.

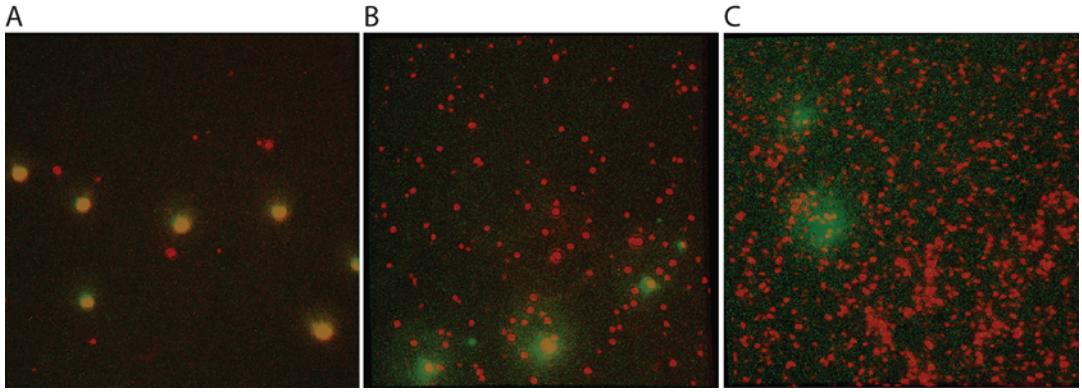

Fig. 6 Examples of sparse, appropriate, and excessive fluorescent signal. TransFluoroSpheres® (488/645) and single-stranded DNA oligo coupled to Cy5 were deposited for combined SFM and TIRF imaging as described. The samples were imaged in tapping mode in air with a JPK NanoWizard scanner mounted on a Nikon TE2000 microscope. All three panels represent overlays of 35 × 35 μm optical images created by excitation at 488 and 633. (**a**) Example of deposition in which the Cy5 fluorescent signal is too sparse considering the size of area imaged. (**b**) An appropriate coverage of the area with Cy5 signal is plentiful, but clearly separated into individual spots. (**c**) Example of excessive coverage of the surface with signal coming from Cy5. Individual spots merge and cannot be distinguished in most cases. In gray-scale image FluoSpheres® signal (*green* in color) appears as larger diffuse spots, Cy5 signal (*red* in color) appears as smaller defined spots

3.14 General Considerations for Imaging with Combined SFM-Fluorescence

Familiarity with the available fluorescence microscope setup is assumed. Specific operating instructions will vary depending on the setup and are in any case beyond the scope of this article. With respect to excitation light source we note that a mercury lamp is often sufficient for visualization of quantum dots, (Trans) FluoSpheres®, and to a limited extent single fluorophores like Alexa 633. Laser excitation specific to the dyes used is preferable for most single fluorophore visualization applications. In our setup, the optical microscope is coupled to a NanoWizard®II scanner (JPK instruments). In this instrument correlation of fluorescence and topographic images is accomplished first by DirectOverlay™ software. Further registration accuracy can be achieved using numerical computing software like MATLAB [17]. Optical images are obtained at the highest magnification possible, usually as 60 μm fields. We typically use total internal reflection for optimal imaging of surface attached molecules. Topographic images are obtained as fields of 2–35 μm depending on the size of the objects deposited and the eventual analysis needed.

3.15 Using (Trans) FluoSpheress® to Align Topographic and Optical Images

1. Find an area of interest and optimize focus for optical signals. After mounting the sample in the holder on the microscope, find the fluorescent signal coming from the FluoroSpheres® and biological sample. Focus on the fluorescent signal coming from the sample (smaller, less intense spots). Due to bleaching

fluorescence from the sample, it is recommended to move into a new field to obtain an image that will be later used for overlay.

When using TransFluoroSpheres® to bring the sample into focus, use an excitation wavelength of the fiducial marker that does not match the fluorophore coupled to the sample to optimize focus. Once that is done switch to the excitation wavelength that will reveal both the sample and fiducial, adjust focus and proceed. When using TransFluoroSpheres® obtain an image or image stack at both excitation wavelengths

2. Obtain an optical image with at least three (Trans)FluoSpheres® (*see* **Note 12**). For single molecule nanometer localization and eventual quantification of fluorophore number based on intensity, obtain a stack of images (time lapse). The exposure time, intervals and frame number should be chosen such that complete bleaching of the sample is achieved (for example 300 ms exposure, 350 ms interval, 300 frames). Maximum intensity image created from the stack will be used for registration by overlaying with the SFM scan.
3. Monitor the progress of image acquisition; should the sample go out of focus or when noticeable drift occurs, the entire process needs to be repeated. In our experience drift occurs when the mica is not optimally thin and the objective exerts pressure on the cover slip to focus. Alternatively, an unstable sample holder can result in drift.
4. Before obtaining the SFM image, minimize sources of vibration in the vicinity of the measurement. When using an immersion lens and a sample holder, make sure that both are not touching the sample during SFM imaging in order to minimize background vibrations. Retract the lens and, if necessary, detach the sample holder (depending on microscope set up this may or may not convey vibrations).
5. Obtain a topographic scan of the same area captured in the optical image at a resolution that will allow clear identification of the 20–40 nm diameter (Trans)FluoSpheres®. For example, optimal parameters for 35 × 35 μm field are 512 × 512 lines at scan rate 2–2.5 Hz.
6. Use the microscope software to overlay the two images so that the topographic image of the spheres (always smaller than the diffraction limited fluorescent spot) coincides with the center of the optical spots (Fig. 7). This overlay now defines the register of the fluorescent and topographic images with accuracy in the tens of nm range (depending on the microscope software routine applied) and can be used to identify fluorescent signals as belonging to specific topographic features (such as specific proteins or fluorescently labeled sites on DNA). If using TransFluoroSpheres®, use the (maximum intensity)

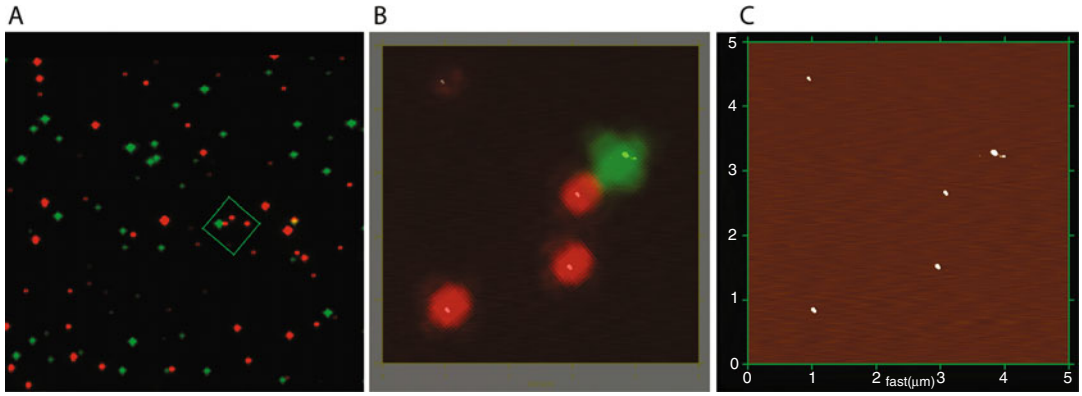

Fig. 7 Aligning optical and topographic images using FluoSpheres®. A mixture of polystyrene spheres with three different colors: *red*, *green,* and *orange*, were deposited for combined SFM and fluorescence imaging as described. The samples were imaged in tapping mode in air with a JPK NanoWizard scanner mounted on a Nikon TE2000 microscope. The density of FluoSpheres® shown is appropriate for both optical and topographic imaging. (**a**) Optical image, 60 µm × 60 µm, of a mixture of polystyrene spheres with three different colors: *green* and *red* channel were overlaid. *Orange* polystyrene beads are recognized by the colocalization of both signals. The indicated area (5 µM × 5 µM, *green square*) was chosen for scanning force microscopy. (**b**) Overlay of the fluorescence signal with the height image. (**c**) Topography image of the selected area, *Z* scale 0–30 nm. The overlay in **b** shows that the optical and topographic images can be aligned by centering the height image of the FluoSpheres® in the optical signals from the same objects. Panels **b** and **c** present the area scanned rotated about 135° clockwise relative to its position in panel **a**

image showing only the fiducial spheres to identify their position in the SFM scan.

7. Once the images are correctly registered in the microscope software, select a region of interest to obtain a SFM image of the desired resolution. Multiple small scan images, for example 2 × 2 µm fields at 512 × 512 lines, can be collected. The best overlay/resolution combination is obtained by imaging large areas; we typically collect images as 35 × 35 µm fields at 4096 × 4096 lines at a scan rate of 0.2 Hz (overnight). For nanometer localization, this area should contain at least three fiducial spheres.
8. Overlay the (maximum intensity) optical image of the fluorescent signal corresponding to the biological sample with the high resolution SFM scan.

4 Notes

1. Here we describe the use of SFM imaging of air-dried samples with the following standard settings: scanned in intermittent contact mode (air), using Silicon Tapping/Non-Contact Mode tips 125 mm in length with a spring constant of 25–75 N/m from Applied Nanostructures, drive frequency of the

cantilevers on average 300 kHz, and a line rate of 2 Hz to acquire images.

2. Tetrahydridoborate is a flammable solid and should be handled following all precautions indicated by the supplier. The solution should be made in a fume hood.
3. Because deposition is not always perfect but is easy to repeat, it is a good idea to make several depositions of the same sample. When working with protein–DNA binding reactions depositions should be done at the same time to keep the binding conditions, such as incubation time, constant. It is also a good idea to deposit different dilutions, differing by a factor of 2–5, at once to assure that one will be appropriate for analysis without requiring repetitive binding reactions and additional material.
4. After dilution, the sample should be transferred to mica as fast as possible to avoid changes in binding behavior due to changed salt conditions. Typically adding a small volume of binding reaction to a premeasured volume of deposition buffer for dilution and immediately pipetting onto mica takes less than 20 s.
5. The optimal buffer conditions, stoichiometry of DNA and protein as well as expected number of complexes are best extracted from previous biochemical characterizations. As mentioned above, these will indicate starting conditions as the amounts and concentration of DNA and proteins that are optimal for SFM imaging may be different. Based on the initial SFM results, it may be necessary to vary the stoichiometry of DNA and protein to obtain sufficient protein–DNA complexes for analysis or to minimize background of unbound proteins. This is best done in small steps, such as twofold changes in concentration of proteins or DNA, in order to improve the image data that can be obtained.
6. If not enough material is deposited on mica, small variations in the dilution step that may affect cation concentrations by twofold or less can also make a big difference.
7. The sharpness of the tips determines the resolution and detail of the images obtained. Although specialized tips with end radius of curvature considerably less than the usual 10 nm (some as small as 2 nm) are available they are still rather expensive. In our experience, for most applications, the added resolution and detail are minimal and do not justify the extra cost. We use uncoated tips. Even though coatings that increase reflectivity of the back of the cantilevers should not influence the size of the end of the tips, in our experience coated tips produced poorer resolution.

8. Many commercial SFMs produce images with maximally 512 × 512 pixels, independent of the scan size. Thus, larger scan sizes produce data with lower resolution. Higher resolution is achieved with smaller scan size (scan of 1 μm × 1 μm, 1 pixel ~2 nm vs. scan of 4 μm × 4 μm, 1 pixel ~8 nm). Due to the size of the scanning tips, we typically use standard silicon noncontact tips with a radius of curvature of about 10 nm, resolution does not improve much by decreasing scan size below 1 μm x 1 μm.
9. When using UV light, wear UV safety goggles and avoid skin exposure.
10. To check if the mica glued to glass thickness is appropriate, deposit the fluorescent test object like the FluoSpheres® (3 pM solution in deposition buffer), and check if it is possible to focus on the surface in the fluorescent microscope. When this is not possible, more mica layers need to be cleaved off.
11. We have also tested quantum dots as markers for aligning fluorescence and topographic images. However, due to the relatively large percentage of dark quantum dots in the preparations we have used it is not easy to unambiguously align the patterns from the topographic and fluorescence image. Thus, in our experience quantum dots are not a robust marker for alignment.
12. Dual color fluorescence imaging is most beneficial when dealing with samples described in this chapter. Therefore, we recommend using TransFluoroSpheres®, which are characterized by broad excitation spectrum. This allows collecting images at a wavelength visualizing both fiducials and sample as well as a wavelength for fiducials only, minimizing sample bleaching. in combination with biological sample coupled with fluorophore which excitation spectrum partly overlays with that of the fiducial sphere (for example TransFluoroSpheres® (488/675) and Cy5 (650)).

References

1. Janicijevic A, Ristic D, Wyman C (2003) The molecular machines of DNA repair: scanning force microscopy analysis of their architecture. J Microsc 212:264–272
2. Dame RT, Wyman C, Goosen N (2003) Insights into the regulation of transcription by scanning force microscopy. J Microsc 212:244–253
3. Erie DA, Yang G, Schultz HC, Bustamante C (1994) DNA bending by Cro protein in specific and nonspecific complexes: implications for protein site recognition and specificity. Science 266:1562–1566
4. Ristic D, Modesti M, van der Heijden T, van Noort J, Dekker C, Kanaar R, Wyman C (2005) Human Rad51 filaments on double- and single-stranded DNA: correlating regular and irregular forms with recombination function. Nucleic Acids Res 33:3292–3302
5. Sánchez H, Wyman C (2015) SFMetrics: an analysis tool for scanning force microscopy images of biomolecules. BMC Bioinformatics 16:1–9
6. Bustamante C, Vesenka J, Tang CL, Rees W, Guthold M, Keller R (1992) Circular DNA molecules imaged in air by scanning force microscopy. Biochemistry 31:22–26

7. Vesenka J, Guthold M, Tang CL, Keller D, Delaine E, Bustamante C (1992) Substrate preparation for reliable imaging of DNA molecules with the scanning force microscope. Ultramicroscopy 42-44:1243–1249
8. Hansma HG, Laney DE (1996) DNA binding to mica correlates with cationic radius: assay by atomic force microscopy. Biophys J 70:1933–1939
9. Han W, Lindsay SM, Dlakic M, Harrington RE (1997) Kinked DNA. Nature 386:563
10. Rivetti C, Guthold M, Bustamante C (1996) Scanning force microscopy of DNA deposited onto mica: equilibration versus kinetic trapping studied by statistical polymer chain analysis. J Mol Biol 264:919–932
11. Beerens N, Hoeijmakers JH, Kanaar R, Vermeulen W, Wyman C (2005) The CSB protein actively wraps DNA. J Biol Chem 280:4722–4729
12. Ratcliff GC, Erie DA (2001) A novel single-molecule study to determine protein—protein association constants. J Am Chem Soc 123:5632–5635
13. Wyman C, Rombel I, North AK, Bustamante C, Kustu S (1997) Unusual oligomerization required for activity of NtrC, a bacterial enhancer-binding protein. Science 275:1658–1661
14. van der Linden E, Sanchez H, Kinoshita E, Kanaar R, Wyman C (2009) RAD50 and NBS1 form a stable complex functional in DNA binding and tethering. Nucleic Acids Res 37:1580–1588
15. Janicijevic A, Sugasawa K, Shimizu Y, Hanaoka F, Wijgers N, Djurica M, Hoeijmakers JH, Wyman C (2003) DNA bending by the human damage recognition complex XPC-HR23B. DNA Repair (Amst) 2:325–336
16. Dame RT, van Mameren J, Luijsterburg MS, Mysiak ME, Janicijevic A, Pazdzior G, van der Vliet PC, Wyman C, Wuite GJ (2005) Analysis of scanning force microscopy images of protein-induced DNA bending using simulations. Nucleic Acids Res 33:e68
17. Sánchez H, Kertokalio A, van Rossum-Fikkert S, Kanaar R, Wyman C (2013) Combined optical and topographic imaging reveals different arrangements of human RAD54 with presynaptic and postsynaptic RAD51-DNA filaments. PNAS 110:11385–11390

Chapter 15

Atomic Force Microscopy of Protein Shells: Virus Capsids and Beyond

Natalia Martín-González, Alvaro Ortega-Esteban, F. Moreno-Madrid, Aida Llauró, Mercedes Hernando-Pérez, and Pedro J. de Pablo

Abstract

In Atomic Force Microscopy (AFM) the probe is a nanometric tip located at the end of a microcantilever which palpates the specimen under study as a blind person uses a white cane. In this way AFM allows obtaining nanometric resolution images of individual protein shells, such as viruses, in liquid milieu. Beyond imaging, AFM also enables the manipulation of single protein cages, and the characterization a variety physicochemical properties able of inducing any measurable mechanical perturbation to the microcantilever that holds the tip. In this chapter we start revising some recipes for adsorbing protein shells on surfaces. Then we describe several AFM approaches to study individual protein cages, ranging from imaging to spectroscopic methodologies devoted to extracting physical information, such as mechanical and electrostatic properties.

Key words Atomic force microscopy, Force vs. distance curve, Nanoindentation, Beam deflection, AFM tip, AFM cantilever, Topography, Disruption, Breaking, Fatigue, Electrostatics

1 Introduction

A protein cage can be roughly stated as any closed structure built out of protein subunits that defines an internal cavity at the nanometer scale. Although viruses illustrate at most the definition of protein cages, nonviral structures, such as Bacterial Microcompartments (BMCs) [1], vault particles [2], and artificial virus-like structures [3–5] can also be included in this description. The basic architecture of a virus consists of the capsid, a shell made up of repeating protein subunits (capsomers), which encapsulate the viral genome [6]. Far from being static structures, viruses are highly dynamic nucleoprotein complexes that transport and deliver their genome from host to host in a fully automatic process. Viral particles are endorsed with specific physicochemical properties that

Erwin J.G. Peterman (ed.), *Single Molecule Analysis: Methods and Protocols*, Methods in Molecular Biology, vol. 1665, DOI 10.1007/978-1-4939-7271-5_15,

confer to their structures certain meta-stability whose modulation permits fulfilling each task of the viral cycle at the right time. These natural designed capabilities have impelled using viral capsids as protein containers of artificial cargoes (drugs, polymers, enzymes, minerals) [7] with applications in biomedical and materials sciences. Both natural and artificial protein cages have to protect their cargo against a variety of physicochemical aggressive environments, including molecular impacts in highly crowded media [8], thermal and chemical stresses [9], and osmotic shocks [10]. Thus, it is important to use methodologies that supply information about protein cages stability evolution upon structural changes during the viral cycle but also under different environments. In this vein, structural biology techniques such as electron microscopy (EM) and X-ray crystallography are used to unveil the structure–function interplay, revealing high-resolution impressive structures of protein cages [11]. However, these methodologies require a heavy average of millions of particles present in the crystal (X-ray) or thousands of structures for the model reconstruction (cryo-EM). Thus, they provide limited information on structural differences between individual particles in population. In addition, these approaches require conditions (i.e. vacuum) far away of those where protein shells are functional (liquid). These techniques preclude the characterization of protein shells dynamics and properties in real time. Indeed, the advent of single molecule technologies has demonstrated that mechanical properties of biological molecular aggregates are essential to their function [12]. It is evident that the exploration of these properties would complete the structural biology methodologies (EM and X-ray) to find the structure–function–property interplay of protein cages. Atomic Force Microscopy (AFM) may not only characterize the structure of individual protein-made particles in liquid milieu, but also to obtain physicochemical properties of each particle. In addition, the nano-disectional abilities of AFM allows the local manipulation of protein shells to learn about their assembly/disassembly processes. In this chapter, we give a general overview of how to apply AFM methods to protein shells. Our tour starts with a basic review of the recipes for attaching protein cages to solid surfaces. Afterwards we describe the most successful modes for imaging protein shells with AFM so far and comment on inherent artifacts, such as dilation. Subsequently we describe the nanoindentation methodology, which probes the stiffness, breaking force, brittleness, and electrostatics of individual protein shells. Afterwards we focus on the effects of cyclic loading on individual particles and the access to the inner cavity to probe the cargo.

2 Materials

2.1 Particles adsorption on the surface of solid substrates.

Protein shells are typically attached to substrates by using the physical forces with the substrate, including polar, nonpolar, and van der Waals interactions [13]. Physisorption traps protein cages on the surface without creating chemical bonds that might alter their structure. Each type of protein shell has individualized features such as hydrophobic patches or local charge densities [14] that can be used for adsorption, via hydrophobic and/or electrostatic interactions, on different substrates, such as glass, mica, and HOPG (Highly Oriented Pyrolytic Graphite) (Fig. 1a). Mica and HOPG surfaces are layered materials whose preparation consist on removing the last layer with adhesive tape, exposing a fresh surface ready for experiments (*see* **Note 1**). HOPG presents a nonpolar surface and protein cages adsorb via hydrophobic interactions [15]. Each protein shell has a different methodology. Let us focus in the specific case of human adenovirus particles (HAdV). About 20 μl of virus solution presenting $1.5–2.0 \times 10^{12}$ particles/ml was incubated on the surface and washed out with the corresponding buffer after 20 min (*see* **Note 2**). Afterwards the liquid cell forms between the cantilever holder and the sample (Fig. 1b). Figure 1c shows that HOPG collapses some HAdV particles, indicating a strong nonpolar (hydrophobic) interaction. However, hexamethyldisilazane (HMDS) silanized glass [16] reduces the adsorption force and allows imaging intact icosahedral particles exhibiting five-, two- and threefold symmetry orientations on the surface (*see* Fig. 1c, d). Interestingly, using $NiCl_2$ 150 mM on mica [13] induces the adsorption of HAdV particles at the threefold symmetry orientation only, thus protein particles exhibit a triangular facet (right, Fig. 1c). Adsorption of protein cages on surfaces also may induce a reduction of the particle height [17]. This variety of adsorption phenomena may change for each type of protein shells, since different structures expose different residues in the external layer, thus requiring different adsorption methodology (*see* **Note 3**).

2.2 AFM Cantilevers

Olympus OMCL-RC includes a variety of four spring constants: 0.39, 0.76, 0.05, and 0.10 N/m. The chip holding the cantilever attaches to the quartz window of the liquid cell by using vacuum grass, although any removable glue can be used, as long as it does not dissolve in the buffer (*see* **Note 4**).

3 Methods

3.1 Imaging

In AFM the tip scans the sample in *x*, *y*, and *z* directions by using piezo actuators. While *x* and *y* scanners move in a pre-established way over a square region, the cantilever bends following the surface

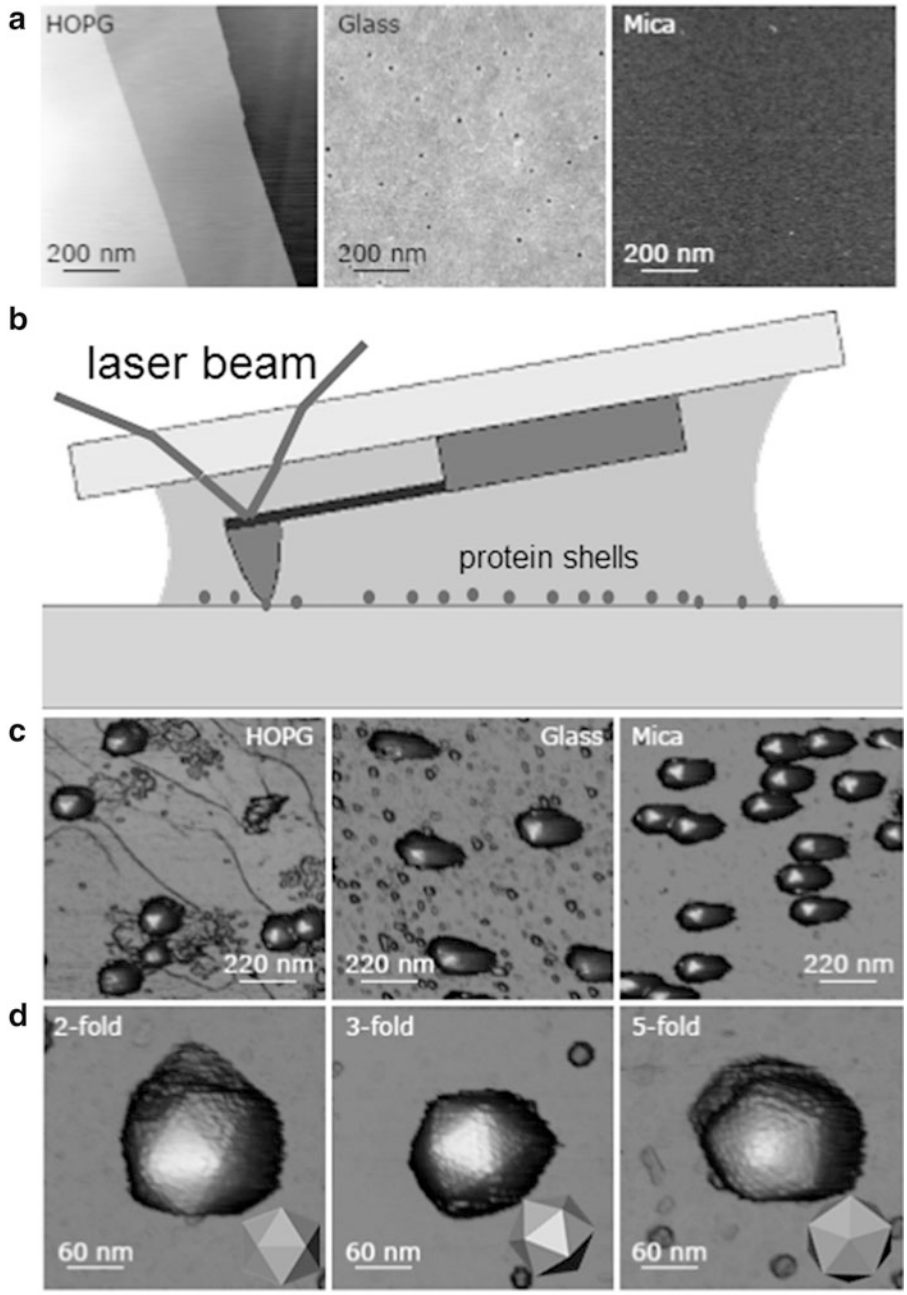

Fig. 1 Attaching protein shells on surfaces. (**a**) HOPG, glass, and mica bare substrates before attaching the samples. (**b**) Cartoon of the experimental system. Protein cages and cantilever are not in scale. (**c**) HAdV on HOPG, glass, and mica. (**d**) Individual HAdV particles showing two-, three- and fivefold symmetry orientations after adsorption on the surface

topography. The cantilever deflects in twofold. It bends perpendicularly to the surface applying a normal force (F_n) (Fig. 2a), and laterally by torsion exerting a dragging force parallel to the surface (F_l) (Fig. 2b). Both F_n and F_l are monitored by focusing a laser

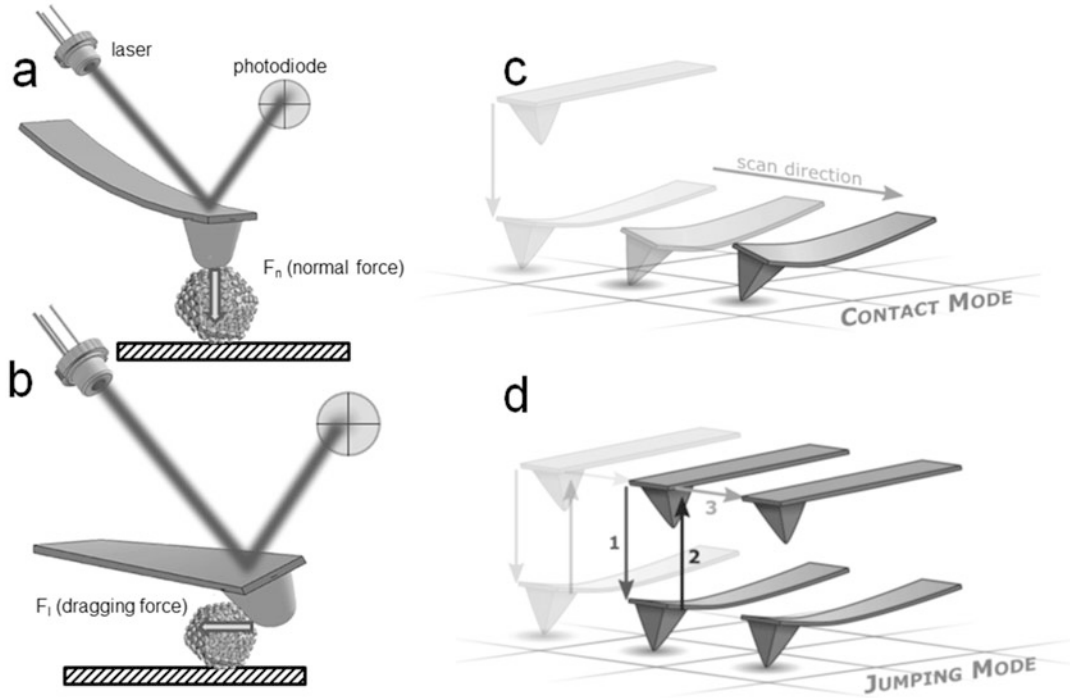

Fig. 2 AFM working modes. (**a**) and (**b**) show the normal and lateral forces concepts, respectively. (**c**) and (**d**) indicate contact and jumping modes, respectively

beam at the end of the cantilever, whose reflection is registered in a four quadrant photodiode. Thus, each pixel of the image located at a particular position of the planar coordinates (x,y), will be associated with certain bending values of the cantilever F_n and F_l. If the particle is not strongly enough attached or if it is too soft, it can be swept or modified under large bending forces. To avoid this effect as much as possible, a feedback loop is engaged to F_n to move the z piezo position in such way that F_n is kept constant. In this operational approach, termed as contact mode (Fig. 2c), the AFM topography map will have x, y and z coordinates. The torsional bending force F_l of the cantilever exerts about 40 times the flexural bending force F_n [18]. Individual protein shells are thus susceptible to undesired modifications by lateral forces. Their size of tens of nanometers offer a large topographical aspect ratio that is difficult to track by the feedback loop. A typical approach for surpassing this limitation is using fixation agents, such as glutaraldehyde. In such conditions AFM provide images whose resolution is comparable to that of some EM images [19]. Nevertheless, glutaraldehyde cross-links the proteins structure [20, 21], and precludes dynamic processes or properties of intact native viruses, such as assembly/disassembly or physical properties [22]. Other approach includes developing imaging modes that avoid dragging forces as much as

possible. In jumping mode (JM), also termed pulse force mode [23, 24], the lateral tip displacement occurs when the tip and sample are not in mechanical contact, thereby avoiding shear forces to a large extent (Fig. 2d). JM performs consecutive approach–release cycles at every pixel of the sample. In each cycle, known as force vs. distance z curve (FZ, Fig. 3a), z-piezo approaches tip and sample from noncontact (label 1 at Fig. 3a) until establishing mechanical contact (label 2 at Fig. 3a) and reaching certain feedback force (label 3 at Fig. 3a). After a few milliseconds, the z-piezo retracts about 100 nm until releasing the tip from the surface (label 4 at Fig. 3a) [24]. Subsequently the scanner moves laterally to the next pixel, and the process starts again. In air condition (Fig. 3a, left) forward and backward curves are similar after releasing the surface and the feedback force (Fig. 3a, right) is always above cantilever deflection. An AFM cantilever experiences a viscous drag while moving up and down in liquid, giving rise to a hysteresis loop (Fig. 3b, left). As the cantilever approaches the surface, the dragging force produces a deflection that hides the tip-sample contact point (Fig. 3b, right). If the dragging deflection equals the

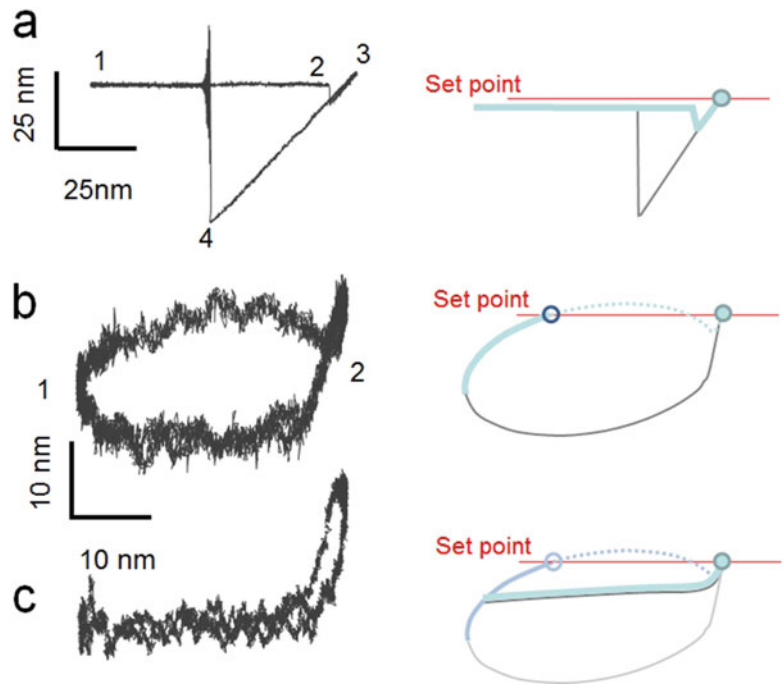

Fig. 3 Force curves used for imaging in JM. (**a**) Illustrates the normal force signal during an FZ in air condition (*left*) and the corresponding *cartoon* (*right*) remarking the set point of the maximum F_n. (**b**) Same that of "a" in water. (**c**) Corrected FZ after subtracting the viscous force (Reprinted with permission from [25]. Copyright 2012 Elsevier)

feedback set-point force the z piezo retracts before tip-sample contact. This imposes to the feedback set-point force to be higher than the viscous drag (Fig. 3b, left). This viscous hysteresis can be removed in jumping mode *plus* [25] from the curve (Fig. 3c, left), allowing to use set point feedback forces of about the cantilever thermal noise, i.e. ~50 pN (Fig. 3c, right). Although AFM dynamic modes have also able of imaging protein shells in liquid conditions, it is difficult to control the applied force [26].

3.2 Dilation

The typical radius of the tip apex for usual cantilevers (OMCL-RC800PSA) is ~20 nm, and it is comparable to the protein shells diameter. In this case, tip size plays an important role on the image resolution by inducing a lateral expansion, namely dilation, of the specimen [27]. Since dilation very often impairs high resolution in proteins, it is convenient to estimate how tip-size is going to affect to AFM images. WSxM software implements a geometrical dilation algorithm that allows simulating the dilation of protein shells structure. By using Chimera software [28] it is possible to access to a particular protein shell structure, such as the electron microscopy model. The "Surface Color By Height" option generates a gray-scale image that captures the topography variation in a given orientation. The TIFF format of this image can be imported by WSxM software and calibrated (www.WSxMsolutions.com) (*see* **Note 5**). The dilation algorithm asks for the tip radius, and the dilated structure is calculated (*see* **Note 6**). Figure 4 exemplifies the dilation of P22 bacteriophage prohead EM structure [29]. Figure 4a shows the twofold symmetry oriented EM model used for dilation with a 10 nm in diameter tip (Fig. 4b). AFM image of a twofold oriented P22 shell (Fig. 4c) present similar conspicuous features to those of Fig. 4b. Dilation strongly depends on the tip size, as shown in Fig. 4d.

3.3 Mechanical Properties of Protein Shells: Nanoindentation

Single FZ experiments consist on pushing on the top of a selected protein shell (Fig. 5a) (*see* **Note 7**). The FZ is executed on the particle at a constant speed that can vary from tens of nm/s to a couple of hundreds of nm/s, in order to allow the water leaving the virus when it is squeezed [30]. After the contact between tip and particle is stablished, FZ typically shows an approximate linear behaviour, which corresponds to the elastic regime of the shell and ascribes to the mixed bending of the cantilever and sample deformation (Fig. 5b, label 2). By controlling the z-piezo elongation, it is possible to go back and forth several times, and the particle elastically deforms in a reversible way. When the z-piezo elongation surpasses the critical indentation, particle breaks (Fig. 5c) inducing a variety of peaks in the FZ, that resemble the penetration of the tip apex trough the cage (Fig. 5b, 3). Afterwards FZ is linear again and represents the cantilever bending. By performing an FZ on the substrate, and assuming that it is much more rigid that the cantilever, we can obtain the cantilever

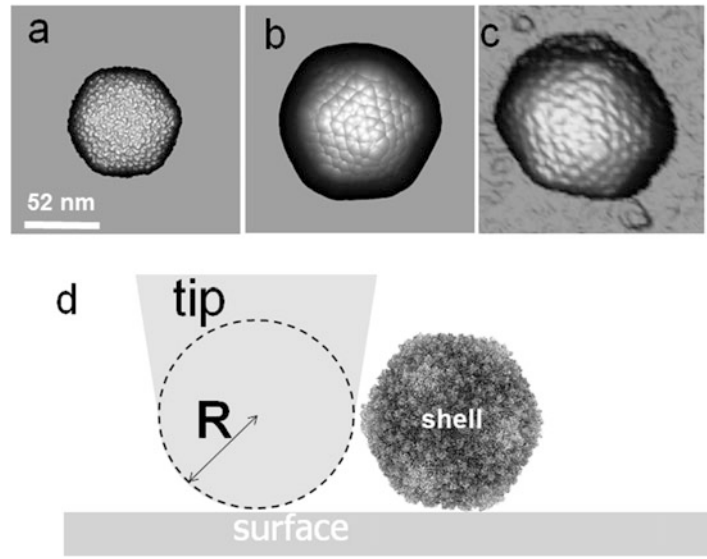

Fig. 4 Dilation effects in the protein shell of bacteriophage P22. (**a**) Represents the EM-1826 model of P22 bacteriophage oriented at the twofold symmetry axis. (**b**) Dilated data of (**a**) obtained with a tip of 10 nm in diameter by using the dilation algorithm of WSxM software. (**c**) AFM image of a single P22 bacteriophage oriented at twofold symmetry axis. The *cartoon* of (**d**) indicates the dilation as a function of the tip size: *dark*, *dark-gray* and *light-gray* curves are the topographical profiles obtained with tips of 0.5, 10.0, and 15.0 nm in diameter, respectively

deformation (Fig. 5b, solid line) (*see* **Note 8**). The subtraction of sample from substrate curves allows isolating the deformation of the cage (Fig. 5d). From these data we can obtain a few mechanical parameters: Fitting of the elastic part from 0 to 8 nm results in the stiffness or spring constant of virus shell ($k = 0.18$ N/m). The breaking or yield force is the force value when the elastic regime finish at 8 nm ($F_b = 1.4$ nN). The critical indentation δ_c, is the deformation of the virus when it breaks (8 nm). Thin shell theory relates the protein shell stiffness with the Young's modulus as $k \approx E\frac{t^2}{R}$, where t is the thickness of the shell and R its radius [31]. The area enclosed between forward and backward curves from indentation 0 up to 8 nm is the energy used to break the cage. In this case, it is about 8.8 nm × nN, i. e. 8.8×10^{-18} J or 2140 $k_B T$, which approaches the order of magnitude of the total energy used for assembling all the proteins [32]. In addition, the critical strain $\varepsilon_c = \delta_c/h$, where h is the initial height of the protein cage as measured with AFM, informs about the brittleness or the mechanical stability of protein cages [17]. In this case, $\varepsilon_c = 8/60 = 0.13$ (*see* **Note 9**).The analysis of the chaotic part of the data after the breaking point provides further information. For instance, in vaults particles it was associated with the individual proteins unzipping

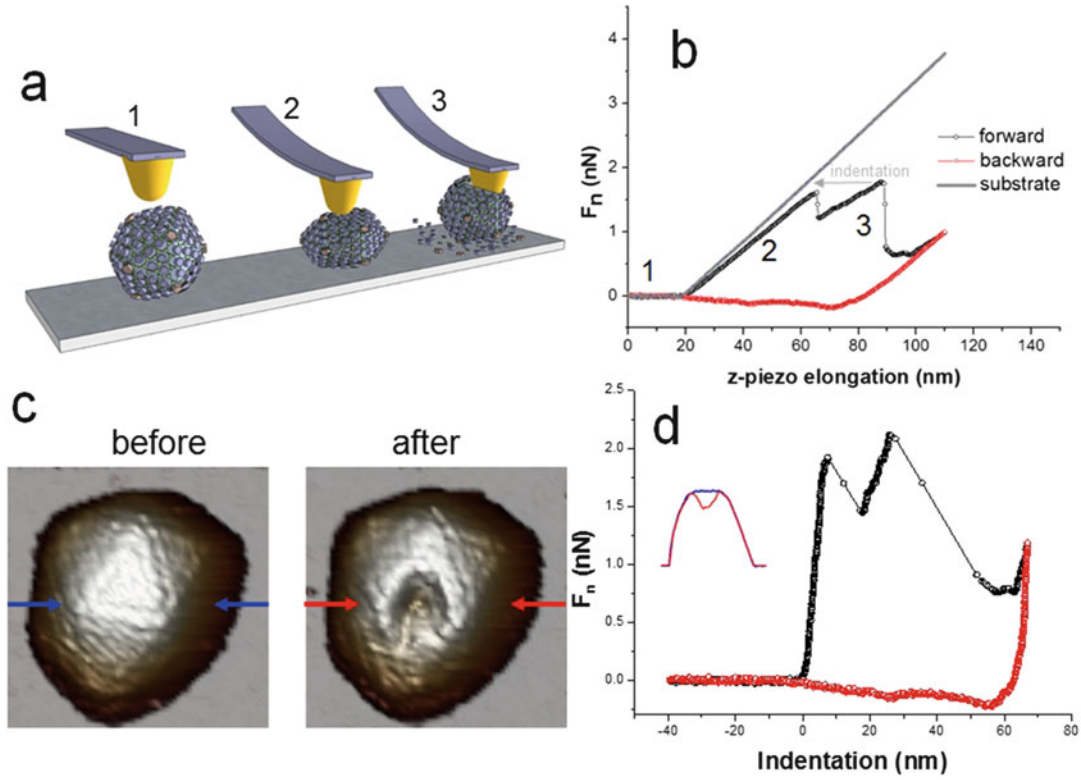

Fig. 5 Single indentation assay on a HAdV particle. (**a**) *Cartoon* showing the three main stages during nanoindentation experiment on a protein cage: before contact (*1*), during deformation, (*2*) and after breaking (*3*). (**b**) AFM topographies before and after nanoindentation showing a crack with the typical inverted pyramid shape due to the tip. (**c**) Evolution of F_n along the z-piezo elongation. Forward curve exhibits the three stages commented in **a**. (**d**) Nanoindentation data extracted from **c**, showing the shell deformation. *Inset* compares topographical profiles of **b**

while the particle was being broken [15]. The precise control of nanoindentation permits the access to the inner cargo of protein cages. Specifically, the consecutive application of nanoindentaion cycles in human adenovirus crack-open the shell in a controlled fashion to probe the mechanical properties of the core [33]. These mechanical properties relate with the condensation state of dsDNA.

3.4 Molecular Fatigue and Disassembly

The breaking force describes the maximal force survivable by the shell and collapses the particle by inducing large and uncontrollable changes in its structure. It is thus difficult to derive consequences about disassembly, since in the cycle of many virus shells, for instance, disassembly takes place by losing individual capsomers in an ordered manner [6]. A protein cage must also resist a constant barrage of sublethal collisions in crowded environments [34]. Equipartition theorem provides an estimation of the energy transferred in a molecular collision to be $\sim\frac{3}{2}k_{\mathrm{B}}T$, which is far below that the energy supplied by single indentation assay experiments.

Imaging of individual protein shells with AFM in jumping mode requires thousands of load cycles (FZs) at low force (~100 pN per pixel, Fig. 3c) [25]. A rough estimation indicates that ~$10k_BT$ is transferred to the particle at every cycle [35], very close to the molecular collisions value. The continuous imaging of a particle enables the evaluation of any structural alteration while subjected to cycle load at low forces (*see* **Note 10**). In this vein, molecular fatigue experiments have demonstrated to be a disassembly agent able of recapitulating the natural pathway of adenovirus uncoating [25]. Therefore molecular fatigue provide additional mechanical information by reporting on shell stability against such multiple deformation cycles at low force (~100 pN) [36], well below the breaking force (Fig. 5d). Let us exemplify the molecular fatigue methodology in the case study of lambda bacteriophage [35] which infects *E. coli*. Upon maturation, cementing protein gpD adds to hydrophobic patches of the external surface of the expanded shell [37]. Molecular fatigue offers an excellent workbench for probing the resistance of undecorated and decorated particles by mimicking molecular impacts. The experiment consists on continuously imaging individuals of each structure and monitor the creation of the first damage (Fig. 6). The label of each topography (Fig. 6a) indicates the times that the particle has been scanned from being intact to collapse. The average loading cycles needed for first damage on seven and eight undecorated and decorated particles, respectively, are depicted in Fig. 6b. It is worth to notice that a force of 120 pN was used on decorated particles, because 100 pN was not enough to induce any damage [35].

3.5 AFM/ Fluorescence Combination

Here we discuss the methodology for studying the mechanical unpacking of protein shells by combining AFM and Total Internal Reflection Fluorescence Microscopy (TIRFM). When a virus is broken, its genome releases outside the cage, but it does not necessary attach to the surface and it is difficult to monitor this process with AFM solely. However, fluorescence microscopy allows exploring non-immobilized biomolecules. The genome exposure can be tracked with a DNA-specific intercalating fluorescent dye (YOYO-1) that can only access the DNA after the capsid has been opened (Fig. 7a). The integration of a single molecule fluorescence microscope with AFM requires to monitor the fluorescence signal at the surface to avoid not only the background signal of the AFM probe itself, but also the light coming from the bulk solution [38]. By using TIRFM, the tip apex and cantilever remain largely out of the evanescent excitation field (~100 nm) [39]. Figure 7b shows simultaneous FZ and fluorescence signals while the particle is being cracked with FZ: fluorescence emission starts right after the particle is broken. Figure 7c presents simultaneous AFM and fluorescence images of a single HAdV particle before and after nanoindentation. Fluorescence image shows emission only after the particle is broken.

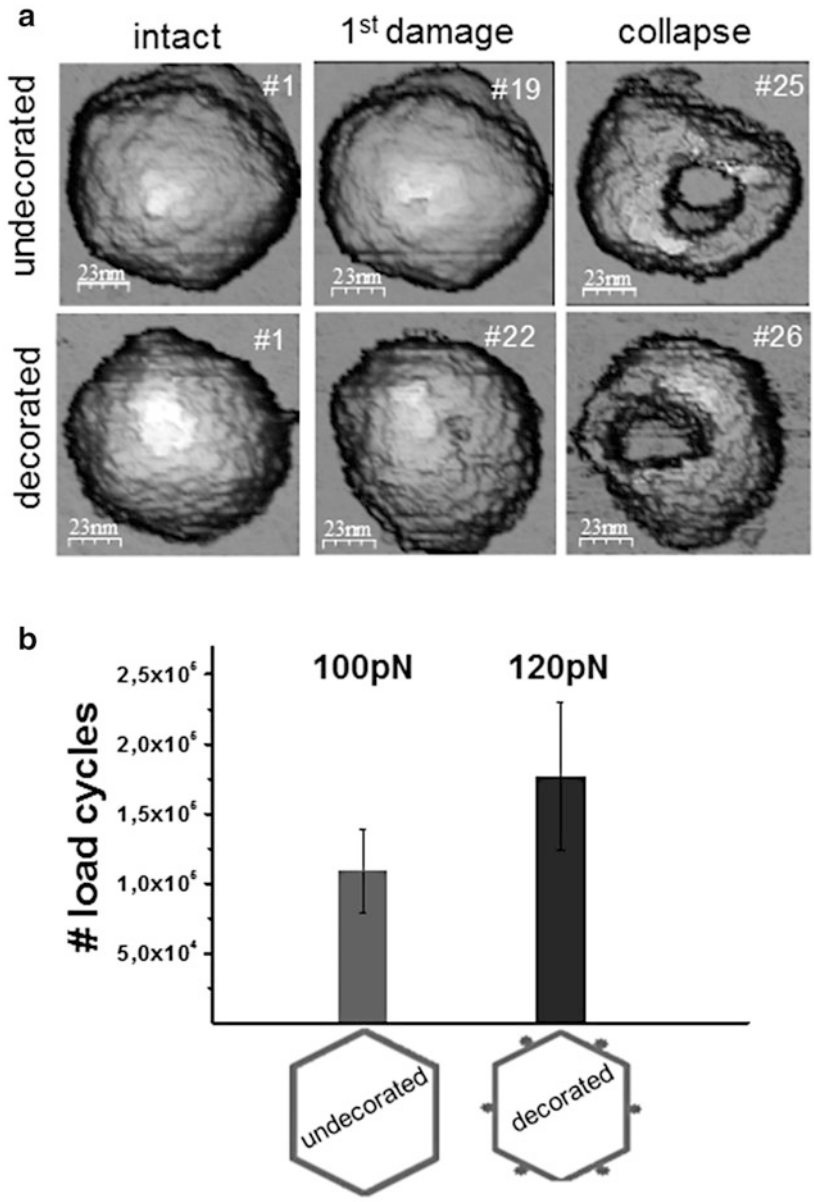

Fig. 6 Mechanical fatigue of lambda bacteriophage shells. (**a**) AFM topographies undecorated and decorated particles, showing intact, damaged, and collapsed states. *Labels* indicate the number of images obtained on the same particle. (**b**) Average number of cycles applied to induce the first damage on decorated and undecorated particles (Adapted from [35])

3.6 Electrostatic Characterization

Although there is a variety of AFM dynamic methods to measure electrostatic charge [40, 41] we will focus in the simplest methodology based in nanoindentations assay. It is convenient to take a careful look at the contact between tip and sample of Fig. 5d. We see that this contact does not show a sharp kink but it is a little

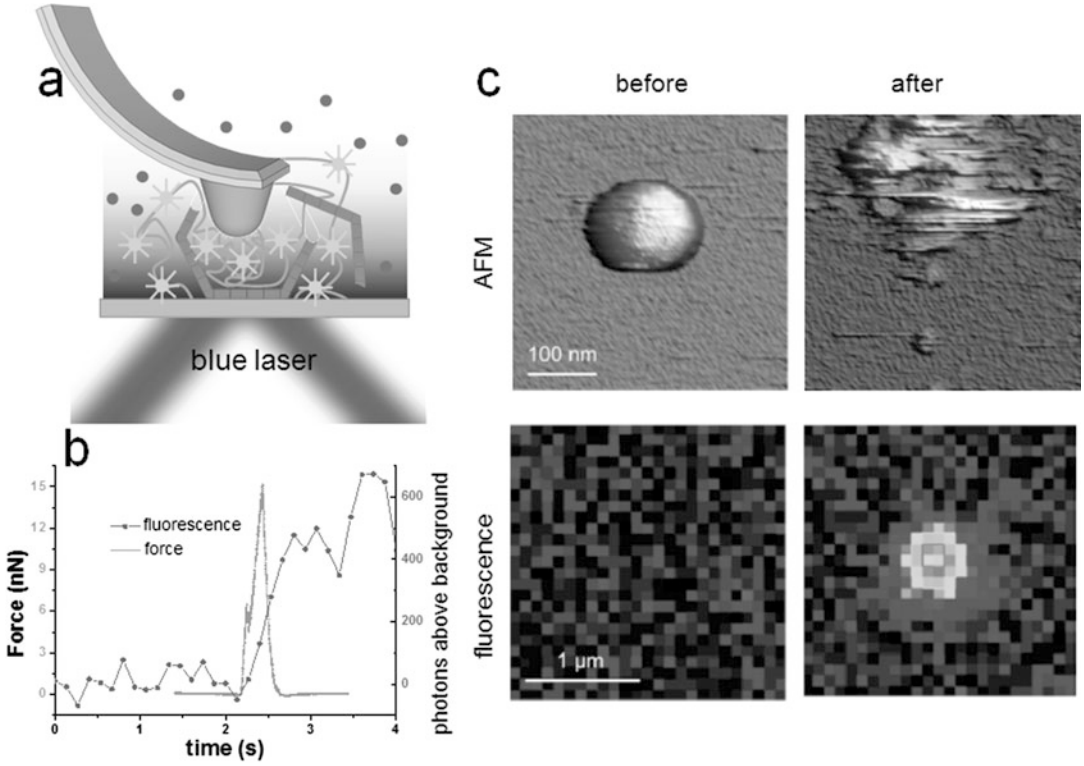

Fig. 7 AFM/fluorescence combination. (**a**) Sketch of AFM/fluorescence combination for monitoring the access of YOYO-1 to released DNA. (**b**) Simultaneous force and fluorescence data during a nanoindentation experiment that disrupts the particle. (**c**) AFM and fluorescence images of a HAdV particle before and after releasing DNA (Reprinted with permission from [38]. Copyright 2015 American Chemical Society)

curved. The origin of this curvature is the repulsive electrostatic force between the protein cage and the Si_3N_4 tip, both negatively charged. In particular, when the tip approaches the protein shell, the interaction force before contact can be described in the frame of Derjaguin-Landau-Verwey-Overbeek model (DLVO) [42], which accounts for repulsive electrostatic double layer (EDL) force F_{ELD} an van der Waals F_{vdW} forces. The Debye length (*see* **Note 11**) determines the range of the electrostatic forces (double Debye layer). The Debye length depends of the concentration of the electrolyte c in the solution as $\lambda_D \tilde{} \frac{1}{\sqrt{c}}$ (*see* **Note 12**). Thus, salt concentration is as a knob to either maximize or remove the electrostatic interaction (*see* **Note 11**), even in the case of large charge densities. While high salt concentration decreases λ_D to low values and suppress electrostatics until very short z (sharp kink in FZ), low salt concentration increases λ_D and facilitates the detection of electrostatics (soft kink in FZ, *see* **Note 12**). If we use HOPG for as supporting surface for protein cages (Fig. 8a), the neutral character of this substrate would suppress F_{EDL}. However, electrostatics will

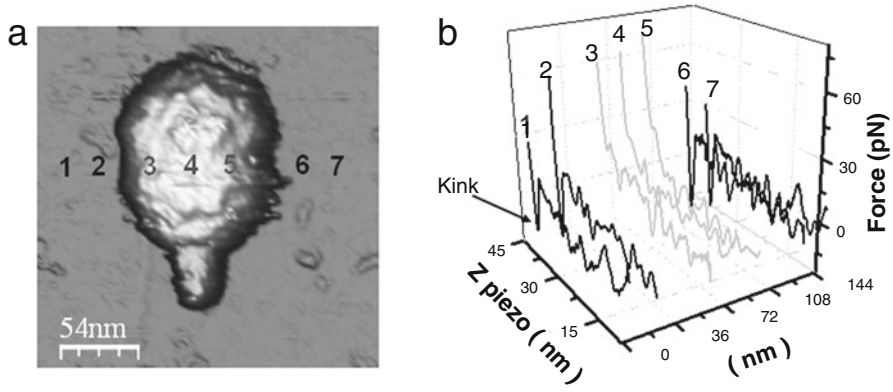

Fig. 8 Electrostatics. (**a**) AFM topography of a phi29 bacteriophage on HOPG. (**b**) FZs performed along the labels of (**a**): HOPG (*dark*) and particle (*gray*) (Reprinted with permission from [43]. Copyright 2015 Royal Society of Chemistry)

be detectable if there exists any density of charge on it. Figure 8b shows nanoindentations performed on the HOPG substrate (dark) and the virus (gray) of Fig. 8a. While FZs on HOPG show a sharp kink just before contact due to F_{vdW}, indentation data on virus show a soft landing of the cantilever due to electrostatic repulsion F_{EDL}. The charge of a particle can be estimated by fitting nanoindentation curves to two-sphere DLVO models [43].

4 Notes

1. When peeling from the HOPG or mica surface with adhesive tape, be careful on leaving a flat surface as much as possible. Watch out on micrometer whiskers formed on dangling pieces on the area where the meniscus will be. These whiskers would crash with the cantilever while scanning.
2. Pipet right at the center of the substrate. The solution meniscus covers a circle with a 5–10 mm in diameter.
3. From a practical point of view predictions on proteins shells adsorption are difficult to make, and one uses the try-and-error methodology to find the best conditions.
4. In order to avoid a drastic bending that can break the cantilever when it is soaked in the liquid meniscus, it is convenient to wet the cantilever with ~20 μl of buffer before immersion.
5. Produce tiff images where the shell structure is centered and occupies about 1/4 of the image size. If shell structure is too big, dilation will expand the structure outside the image. Do not use more than ~1000 × 1000 pixels, since images will be too heavy to be processed.

6. Start using low tip radius for testing purposes, such as 1 nm, since large values increase the computation time. Then increase gradually this value until ~50 nm.
7. Zoom the particle in a progressive way by reducing the *x*–*y* scanning size until the bump of the very top is under the whole scan (~50 × 50 nm^2) and switch-off *y* scan. Progressive means to reduce the scanning size sequentially: 1 μm^2, 0.36 μm^2, 0.09 μm^2, 0.01 μm^2, and 0.025 μm^2; always centering the scanning on the particle. This procedure helps to reduce the effects of thermal drift and piezo-drift.
8. It is convenient to perform FZ before and after each experiment on the particle to account for any change of the laser position on the cantilever due to thermal drift.
9. This value implies that the particle deforms about 13% before breakage.
10. Although keeping the AFM head inside a thermal isolation box to avoid thermal drift is always a good idea, it is specially recommended for this kind of experiments where a particle has to be imaged many times.
11. The interaction between two planes is expressed by: $F_{\mathrm{DLVO}} = F_{\mathrm{EDL}} + F_{\mathrm{vdW}} = \frac{2\sigma_s\sigma_p}{\varepsilon_0\varepsilon} e^{\frac{-z}{\lambda_D}} - \frac{H_a}{6\pi z^3}$ where σ_s and σ_t are the charge density of sample and tip, respectively; $\varepsilon\varepsilon_0$ is the dielectric constant times the permittivity of vacuum; z is the tip-sample distance, H_a is the Hammaker constant of the-sample system, and λ_D is the Debye length.
12. For the monovalent NaCl salt concentration of 2 mM, $\lambda_D = \frac{0.304}{\sqrt{0.002}} = 6.8$ nm [42].

Acknowledgements

We acknowledge to our collaborators and projects FIS2014-59562-R, FIS2015-71108-REDT, Fundación BBVA and "María de Maeztu" Program for Units of Excellence in R&D (MDM-2014-0377).

References

1. Cheng S, Liu Y, Crowley CS, Yeates TO, Bobik TA (2008) Bacterial microcompartments: their properties and paradoxes. BioEssays 30 (11–12):1084–1095. doi:10.1002/bies.20830
2. Querol-Audí J, Casañas A, Usón I, Luque D, Castón JR, Fita I, Verdaguer N (2009) The mechanism of vault opening from the high resolution structure of the N-terminal repeats of MVP. EMBO J 28(21):3450
3. Wimmer E, Mueller S, Tumpey TM, Taubenberger JK (2009) Synthetic viruses: a new opportunity to understand and prevent viral disease. Nat Biotechnol 27(12):1163. doi:10.1038/nbt.1593

4. Wörsdörfer B, Woycechowsky KJ, Hilvert D (2011) Directed evolution of a protein container. Science 331(6017):589
5. Lai Y-T, Reading E, Hura GL, Tsai K-L, Laganowsky A, Asturias FJ, Tainer JA, Robinson CV, Yeates TO (2014) Structure of a designed protein cage that self-assembles into a highly porous cube. Nat Chem 6(12):1065–1071. doi:10.1038/nchem.2107. http://www.nature.com/nchem/journal/v6/n12/abs/nchem.2107.html#supplementary-information
6. Flint SJ, Enquist LW, Racaniello VR, Skalka AM (2004) Principles of virology. ASM Press, Washington, DC
7. Douglas T, Young M (1998) Host-guest encapsulation of materials by assembled virus protein cages. Nature 393(6681):152–155
8. Minton AP (2001) The influence of macromolecular crowding and macromolecular confinement on biochemical reactions in physiological media. J Biol Chem 276(14):10577–10580. doi:10.1074/jbc.R100005200
9. Agirre J, Aloria K, Arizmendi JM, Iloro I, Elortza F, Sánchez-Eugenia R, Marti GA, Neumann E, Rey FA, Guérin DMA (2011) Capsid protein identification and analysis of mature Triatoma virus (TrV) virions and naturally occurring empty particles. Virology 409 (1):91–101. doi:10.1016/j.virol.2010.09.034
10. Cordova A, Deserno M, Gelbart WM, Ben-Shaul A (2003) Osmotic shock and the strength of viral capsids. Biophys J 85 (1):70–74
11. Baker TS, Olson NH, Fuller SD (1999) Adding the third dimension to virus life cycles: three-dimensional reconstruction of icosahedral viruses from cryo-electron micrographs. Microbiol Mol Biol Rev 63(4):862–922
12. Hinterdorfer P, Van Oijen A (2009) Handbook of single-molecule biophysics. Springer, Dordrecht
13. Muller DJ, Amrein M, Engel A (1997) Adsorption of biological molecules to a solid support for scanning probe microscopy. J Struct Biol 119(2):172–188
14. Armanious A, Aeppli M, Jacak R, Refardt D, Sigstam T, Kohn T, Sander M (2016) Viruses at solid-water interfaces: a systematic assessment of interactions driving adsorption. Environ Sci Technol 50(2):732–743. doi:10.1021/acs.est.5b04644
15. Llauró A, Guerra P, Irigoyen N, Rodríguez José F, Verdaguer N, de Pablo Pedro J (2014) Mechanical stability and reversible fracture of vault particles. Biophys J 106(3):687–695
16. Ivanovska IL, Pablo PJC, Ibarra B, Sgalari G, MacKintosh FC, Carrascosa JL, Schmidt CF, Wuite GJL (2004) Bacteriophage capsids: tough nanoshells with complex elastic properties. Proc Natl Acad Sci U S A 101 (20):7600–7605
17. Llauro A, Luque D, Edwards E, Trus BL, Avera J, Reguera D, Douglas T, Pablo PJ, Caston JR (2016) Cargo-shell and cargo-cargo couplings govern the mechanics of artificially loaded virus-derived cages. Nanoscale 8 (17):9328–9336. doi:10.1039/c6nr01007e
18. Carpick RW, Ogletree DF, Salmeron M (1997) Lateral stiffness: a new nanomechanical measurement for the determination of shear strengths with friction force microscopy. Appl Phys Lett 70(12):1548–1550
19. Xiao C, Kuznetsov YG, Sun SY, Hafenstein SL, Kostyuchenko VA, Chipman PR, Suzan-Monti M, Raoult D, McPherson A, Rossmann MG (2009) Structural studies of the giant mimivirus. PLoS Biol 7(4):958–966. doi:10.1371/journal.pbio.1000092. ARTN e1000092
20. Vinckier A, Heyvaert I, Dhoore A, Mckittrick T, Vanhaesendonck C, Engelborghs Y, Hellemans L (1995) Immobilizing and imaging microtubules by atomic-force microscopy. Ultramicroscopy 57(4):337–343
21. Carrasco C, Luque A, Hernando-Perez M, Miranda R, Carrascosa JL, Serena PA, de Ridder M, Raman A, Gomez-Herrero J, Schaap IAT, Reguera D, de Pablo PJ (2011) Built-in mechanical stress in viral shells. Biophys J 100 (4):1100–1108. doi:10.1016/j.bpj.2011.01.008
22. Roos WH, Bruinsma R, Wuite GJL (2010) Physical virology. Nat Phys 6(10):733–743. doi:10.1038/Nphys1797
23. Miyatani T, Horii M, Rosa A, Fujihira M, Marti O (1997) Mapping of electrical double-layer force between tip and sample surfaces in water with pulsed-force-mode atomic force microscopy. Appl Phys Lett 71(18):2632–2634
24. de Pablo PJ, Colchero J, Gomez-Herrero J, Baro AM (1998) Jumping mode scanning force microscopy. Appl Phys Lett 73 (22):3300–3302
25. Ortega-Esteban A, Horcas I, Hernando-Perez M, Ares P, Perez-Berna AJ, San Martin C, Carrascosa JL, de Pablo PJ, Gomez-Herrero J (2012) Minimizing tip-sample forces in jumping mode atomic force microscopy in liquid. Ultramicroscopy 114(0):56–61
26. Legleiter J, Park M, Cusick B, Kowalewski T (2006) Scanning probe acceleration microscopy (SPAM) in fluids: mapping mechanical properties of surfaces at the nanoscale. Proc Natl Acad Sci U S A 103(13):4813–4818

27. Villarrubia JS (1997) Algorithms for scanned probe microscope image simulation, surface reconstruction, and tip estimation. J Res Natl Inst Stand Technol 102(4):425–454
28. Pettersen EF, Goddard TD, Huang CC, Couch GS, Greenblatt DM, Meng EC, Ferrin TE (2004) UCSF Chimera—a visualization system for exploratory research and analysis. J Comput Chem 25(13):1605–1612. doi:10.1002/jcc.20084
29. Chen DH, Baker ML, Hryc CF, DiMaio F, Jakana J, Wu W, Dougherty M, Haase-Pettingell C, Schmid MF, Jiang W, Baker D, King JA, Chiu W (2011) Structural basis for scaffolding-mediated assembly and maturation of a dsDNA virus. Proc Natl Acad Sci U S A 108(4):1355–1360. doi:10.1073/pnas.1015739108
30. Zink M, Grubmuller H (2009) Mechanical properties of the icosahedral shell of southern bean mosaic virus: a molecular dynamics study. Biophys J 96(4):1350–1363. doi:10.1016/j.bpj.2008.11.028
31. Landau LD, Lifshizt E (1986) Theory of elasticity, 3rd edn. Pergamon, London
32. Zlotnick A (2003) Are weak protein-protein interactions the general rule in capsid assembly? Virology 315(2):269–274. doi:10.1016/S0042-6822(03)00586-5
33. Ortega-Esteban A, Condezo GN, Perez-Berna AJ, Chillon M, Flint SJ, Reguera D, San Martin C, de Pablo PJ (2015) Mechanics of viral chromatin reveals the pressurization of human adenovirus. ACS Nano 9(11):10826–10833. doi:10.1021/acsnano.5b03417
34. Zhou HX, Rivas G, Minton AP (2008) Macromolecular crowding and confinement: biochemical, biophysical, and potential physiological consequences. Annu Rev Biophys 37:375–397. doi:10.1146/annurev.biophys.37.032807.125817
35. Hernando-Pérez M, Lambert S, Nakatani-Webster E, Catalano CE, de Pablo PJ (2014) Cementing proteins provide extra mechanical stabilization to viral cages. Nat Commun 5:4520. doi:10.1038/ncomms5520
36. Ortega-Esteban A, Pérez-Berná AJ, Menéndez-Conejero R, Flint SJ, San Martín C, de Pablo PJ (2013) Monitoring dynamics of human adenovirus disassembly induced by mechanical fatigue. Sci Rep 3:1434
37. Medina E, Nakatani E, Kruse S, Catalano CE (2012) Thermodynamic characterization of viral procapsid expansion into a functional capsid shell. J Mol Biol 418(3–4):167–180. doi:10.1016/j.jmb.2012.02.020
38. Ortega-Esteban A, Bodensiek K, San Martin C, Suomalainen M, Greber UF, de Pablo PJ, Schaap IA (2015) Fluorescence tracking of genome release during mechanical unpacking of single viruses. ACS Nano 9(11):10571–10579. doi:10.1021/acsnano.5b03020
39. Gaiduk A, Kuhnemuth R, Antonik M, Seidel CA (2005) Optical characteristics of atomic force microscopy tips for single-molecule fluorescence applications. ChemPhysChem 6(5):976–983. doi:10.1002/cphc.200400485
40. Zhang S, Aslan H, Besenbacher F, Dong MD (2014) Quantitative biomolecular imaging by dynamic nanomechanical mapping. Chem Soc Rev 43(21):7412–7429
41. Cartagena A, Hernando-Perez M, Carrascosa JL, de Pablo PJ, Raman A (2013) Mapping in vitro local material properties of intact and disrupted virions at high resolution using multi-harmonic atomic force microscopy. Nanoscale 5(11):4729–4736. doi:10.1039/c3nr34088k
42. Israelachvili J (2002) Intermolecular and surface forces. Academic, London
43. Hernando-Perez M, Cartagena-Rivera AX, Losdorfer Bozic A, Carrillo PJ, San Martin C, Mateu MG, Raman A, Podgornik R, de Pablo PJ (2015) Quantitative nanoscale electrostatics of viruses. Nanoscale 7(41):17289–17298. doi:10.1039/c5nr04274g

Chapter 16

Combined Magnetic Tweezers and Micro-mirror Total Internal Reflection Fluorescence Microscope for Single-Molecule Manipulation and Visualization

Yeonee Seol and Keir C. Neuman

Abstract

Magnetic tweezers is a versatile yet simple single-molecule manipulation technique that has been used to study a broad range of nucleic acids and nucleic acid-based molecular motors. In this chapter, we combine micro-mirror-based total internal reflection microscopy with a magnetic tweezers instrument, permitting simultaneous single-molecule visualization and mechanical manipulation. We provide a simple method to calibrate the evanescent wave penetration depth via supercoiling of DNA with a fluorescent nanodiamond-labeled magnetic bead and a complementary method employing a surface-immobilized fluorescent nanodiamond.

Key words Magnetic tweezers, TIRF, Image tracking, Single-molecule enzymology

1 Introduction

Magnetic tweezers (MT) is a highly versatile and technically simple to implement single-molecule manipulation technique that provides control over force and torque on micron-sized magnetic particles [1–4]. Magnetic tweezers have been used to study the mechanical properties of nucleic acids and nucleic acid-protein interactions [5–10]. Moreover, the technique is well-suited for the study of enzymes that affect DNA topology such as topoisomerases since the topology of rotationally constrained DNA molecules can be precisely manipulated and measured [11, 12].

In a typical MT assay, a biomolecule such as DNA is attached to a micron-scale magnetic bead at one end and the surface of a microscope flow cell at the other end via a biotin-streptavidin linkage, an antigen antibody linkage, or a covalent chemical linkage [13]. An external magnetic field, typically, but not exclusively, imposed by a pair of permanent magnets, applies force and torque on the magnetic particle. The position of the magnetic particle is

Erwin J.G. Peterman (ed.), *Single Molecule Analysis: Methods and Protocols*, Methods in Molecular Biology, vol. 1665, DOI 10.1007/978-1-4939-7271-5_16,

tracked in real-time by camera-based particle-tracking analysis with typical acquisition rates of 30–500 Hz for CCD cameras and up to 10 kHz for CMOS cameras [1, 3, 14–16]. A conventional magnetic tweezers instrument is capable of applying forces from a few femtonewtons (10^{-15} N) to hundreds of piconewtons (10^{-12} N) dependent on the size of the magnetic particle and the magnet configuration [17]. Force is calibrated as function of the height of the magnet relative to the surface of the flow cell by tacking the Brownian motion of a magnetic particle tethered by a long DNA (>10 kb) and applying either equipartition theorem or power spectrum analysis [18–20]. Camera-based magnetic tweezers tracking routines generally obtain the three-dimensional position of a magnetic particle with an accuracy of ~1 nm (10^{-9} m) or better at a sample rate of ~100 Hz [14] and up to 10^{-10} m at lower effective sampling rates [14, 15]. As is the case for all single-molecule manipulation techniques, MT can only probe biological activities that lead to a change in the position of a magnetic particle associated with a change in DNA extension caused, for example, by a change in tension or torsion applied to the DNA or by protein enzymatic or binding activity that alters the extension or mechanical properties of the DNA. However, for enzymes that bind or move along DNA without altering the mechanical properties of the DNA, these activities cannot be detected. This limitation can result in an incomplete or ambiguous understanding of DNA-enzyme interactions. Questions concerning the number of enzymes associated with activity, their binding affinity, their direction of movement on the DNA, and the relationship between binding and mechanical activity, among many others are challenging, if not impossible, to resolve solely with manipulation-based measurements. Recently, a hybrid technique [21–24] that combines MT with total internal reflection fluorescent microscopy (TIRF) was developed, which overcomes these limitations on understanding DNA-enzyme interactions by providing orthogonal information to the mechanical signal obtained with conventional magnetic tweezers.

TIRF is a frequently employed wide-field single-molecule fluorescent technique that generates a sub-wavelength localized excitation above the surface of the flow cell (evanescent wave) reducing the background noise and subsequently enabling single-molecule fluorescent detection with a sensitive fluorescent detection camera. The physical principle of total internal reflection and the generation of an evanescent wave is well explained elsewhere [25, 26]. Briefly, the evanescent wave is generated when the incident light is totally reflected at the interface between two media of different refractive indices, i.e., the interface between glass and water. The condition for total reflection is easily explained in terms of Snell's law at which the incident angle of light at the interface is larger than a critical angle, $\theta_c = \arcsin\left(\frac{n_2}{n_1}\right)$ where n_1 and n_2 are the refractive indices of

the first and second medium, respectively. The amplitude of the sine function cannot exceed 1, setting a condition for the total internal reflection to only occur when n_1 is larger than n_2. The intensity of the evanescent wave decreases as ~exp($-z/d$) where z is the distance from the surface of the interface and d is a characteristic penetration depth expressed as:

$$d = \frac{\lambda}{4\pi}\left(n_1^2 \sin^2\theta_1 - n_2^2\right)^{-\frac{1}{2}} \quad (1)$$

Here λ is the wavelength of the excitation light and θ_1 is the incident angle that should equal or exceed θ_c, in order to achieve a total internal reflection. As shown in Eq. 1, the penetration depth, d, can be tuned to the optimal value for different applications. For Förster resonance energy transfer (FRET) measurements, the FRET signal provides a measure of the absolute distance between two dyes, thus the calibration of the evanescent wave is not strictly required as the short penetration depth serves primarily to reduce background noise. On the other hand, a longer d may be useful for tracking out of plane (along the optical propagation, or z-, axis) motion, for example, to measure the motion of a fluorescently labeled DNA helicase moving along an extended DNA molecule, or to capture the full three-dimensional motion of a DNA-tethered particle [27]. The motion of the fluorescently labeled helicase can be deduced from the intensity change. However, in order to estimate the distance, it is necessary to calibrate the TIRF field intensity profile along the z-axis. In principle, the field profile can be estimated based on d calculated using eq. 1 by precisely measuring the incident angle [28]. Recently, the development of a hybrid MT-TIRF instrument [29, 30] makes it feasible to directly obtain the TIRF field profile along the z-axis by measuring the autofluorescence intensity change of a magnetic bead as its height above the surface is decreased by supercoiling the DNA tether [31].

In this chapter, we provide a detailed description of how to incorporate micro-mirror-based total internal reflection fluorescence microscopy (TIRF) into magnetic tweezers (Fig. 1). Instead of using a dichroic mirror, we utilize two micro-mirrors to introduce the excitation laser into, and collect the reflected excitation light from, the objective lens (Fig. 1). This configuration simplifies multi-wavelength excitation and also reduces the effort and cost to separate the excitation light from the emission path [32, 33]. Using the combined instrument, we employ DNA supercoiling as a way to calibrate the penetration depth of an evanescent wave similar to the method discussed in [31]. Previously, the autofluorescence of a magnetic bead was utilized to calibrate the penetration depth. In our method, we use biotinylated fluorescent nanodiamond (bio-FND) labeled magnetic beads that are tethered to DNA molecules since the autofluorescence of the magnetic beads is significantly reduced in our set-up (Excitation at 560 nm and emission

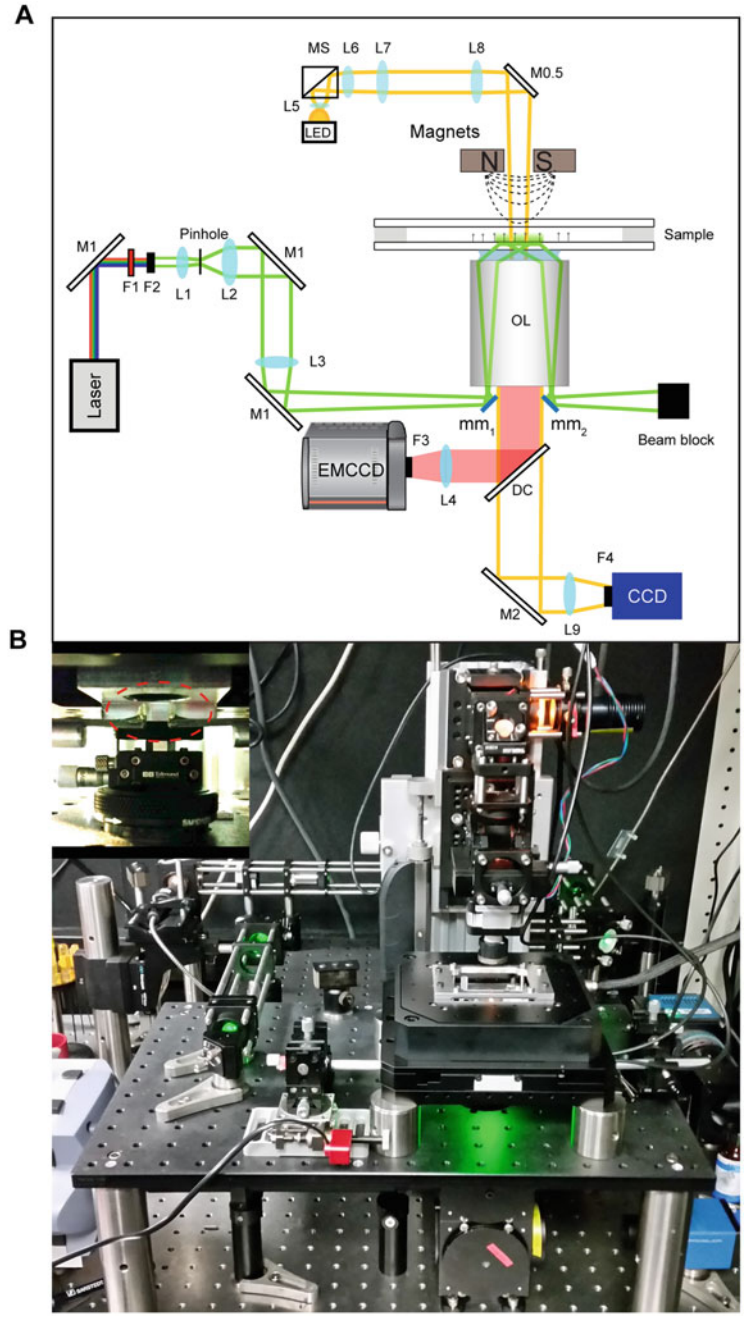

Fig. 1 (**a**) Schematic of magnetic tweezers combined with micro-mirror total internal reflection fluorescence microscopy. The bright-field imaging path is indicated by a *solid yellow line*. The 590 nm light emitting diode (LED) is collimated and weakly focused by multiple lenses (*L5*, *L6*, *L7*, and *L8*) onto the sample via a turning mirror (*M0.5*). The sample is imaged on to a CCD with a 60× oil immersion objective lens (OL) and a 150 mm achromatic lens (*L9*). The illumination light passes through a 590 nm bandpass filter (*F4*). The excitation light path is indicated by a *solid green line*. 560 nm excitation is obtained by passing a supercontinuum laser source through a heat absorbing colored glass filter (*F1*) to remove the IR region and a 560 nm bandpass filter (*F2*). The laser beam is expanded tenfold via two lenses (*L1* and *L2*) with a pinhole placed at the focus of *L1* to

>640 nm) (Fig. 2a). FNDs are fluorescent particles that are excited under broad range of excitation wavelengths (~500–600 nm) and, importantly, are indefinitely optically stable [27, 34]. The emission intensity of FNDs decrease in a magnetic field, but this effect saturates at ~50% for a applied field of ~500 Gauss or greater [34]. Thus, the FNDs are saturated for the majority of our force range (>0.2 pN) and their fluorescent intensity remains constant. In order to set a desired d, we establish the relationship between d and the distance of the micro-mirror (mm_1) to the center of the optical axis, r as in the micro mirror TIRF set-up, the incident angle, θ_1 is adjusted by changing r (Fig. 3a). We measure d for a range of r from subcritical to supercritical conditions by supercoiling the DNA to which the FND bound magnetic particle is attached as shown in Figs. 2 and 3. We also provide a complementary method to estimate d based on the intensity of surface-immobilized fluorescent particles. The emission intensity from an immobilized fluorescent particle is expected to vary as $\exp(-z_{\text{fixed}}/d(r))$ for a particle at a fixed z position z_{fixed}. We show that the intensity of a fixed, non-bleaching, particle provides a complementary measurement of d as a function of r (Fig. 3b). To set d in situ, we characterize r vs d using a simple exponential function rather than using Eq. 1 (Fig. 3c). In addition, we characterize I_{fixed} vs d by fitting with $I_c \exp(-\text{FND}_r/d)$ using I_c and FND_r as free fitting parameters (Fig. 3c). Together these calibration routines provide a means to precisely define the intensity versus z-position relationship that affords quantitative fluorescent-based measurements of protein binding and translocation on DNA extended in the magnetic tweezers instrument.

2 Materials

2.1 PCR Reaction for DNA Substrate Preparation

1. pET28b plasmid (EMD4Biosciences).
2. pBluescript II KS plasmid (Stratagene).

2.1.1 PCR Templates

2.1.2 PCR Primers

1. 5 kb forward: 5′ GCTGGGTCTCGCAAC-GAAACCCGACA GGACTATAAAG 3′.

Fig. 1 (continued) spatially filter the excitation light. The excitation beam is refocused and directed into the objective lens via a lens (*L3*) and multiple mirrors (two M1 and mm_1). The totally internally reflected light emerging from the objective is directed by mm_2 to a beam block. The emission light is reflected by a dichroic mirror (DC) and imaged onto an EMCCD via OL and a 400 mm focal length lens (*L4*). The emission light is filtered with a 640 nm long-pass filter (*F3*). (**b**) Picture of magnetic tweezers combined with micro-mirror TIRF. The micro mirrors (highlighted with *red dashed circle*) located under the objective back aperture are shown in the *inset*

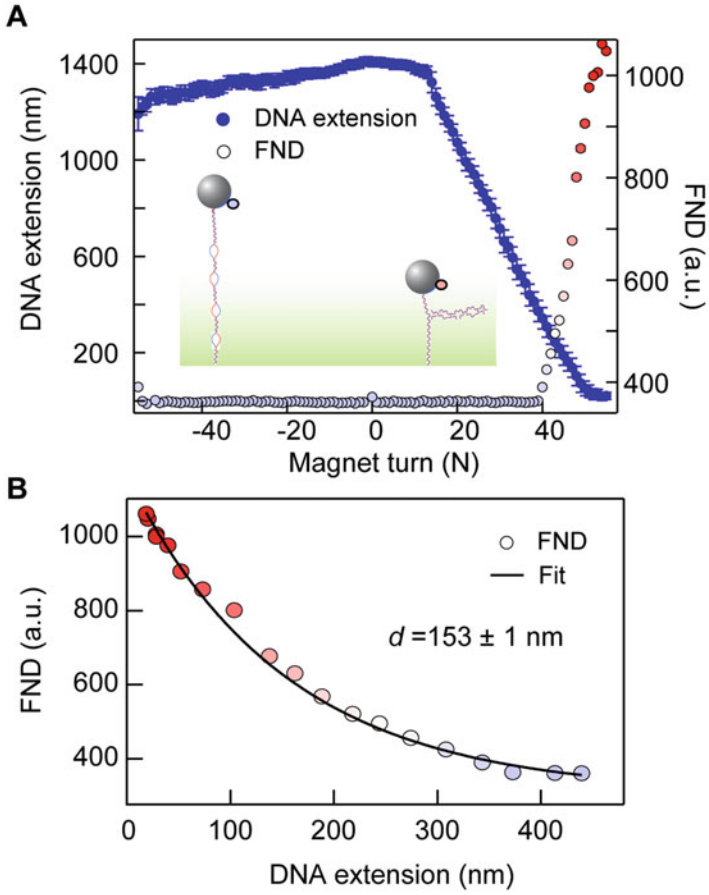

Fig. 2 Calibrating the evanescent wave penetration depth by simultaneously measuring FND emission intensity and the *z*-position of DNA tethered magnetic particle as a function of DNA supercoiling. (**a**) Rotation of magnetic bead by turning the magnet assembly results in overwinding (positive turn) or underwinding of DNA (negative turn). At 1 pN, underwinding of DNA results in no significant change in DNA extension due to melting of DNA duplex (*inset left*) whereas overwinding of DNA leads to reduction of DNA extension because of plectoneme formation after the buckling transition (*inset right*). As DNA extension (*left axis*) decreases, the magnetic bead labeled with a FND approaches the surface and the fluorescence emission intensity increases (*right axis*, FND). (**b**) FND emission intensity is plotted as a function of DNA extension and fitted with an exponential to estimate the evanescent field penetration depth, *d*

2. 5 kb reverse: 5′ GCTGGGTCTCGACCA-CTCTGATGCCG CATAGTTAAG 3′.
3. Bio handle forward: 5′ GCTGGGTCTCGGTTG- TTCCC TTTAGTGAGGGTTAATTG 3′.
4. Dig handle forward: 5′ GCTGGGTCTCGTGGT-TTCCC TTTAGTGAGGGTTAATTG 3′.
5. Dig/Bio Handle Reverse primer: 5′ TATAGTCCTG TCGGGTTTCG 3′.

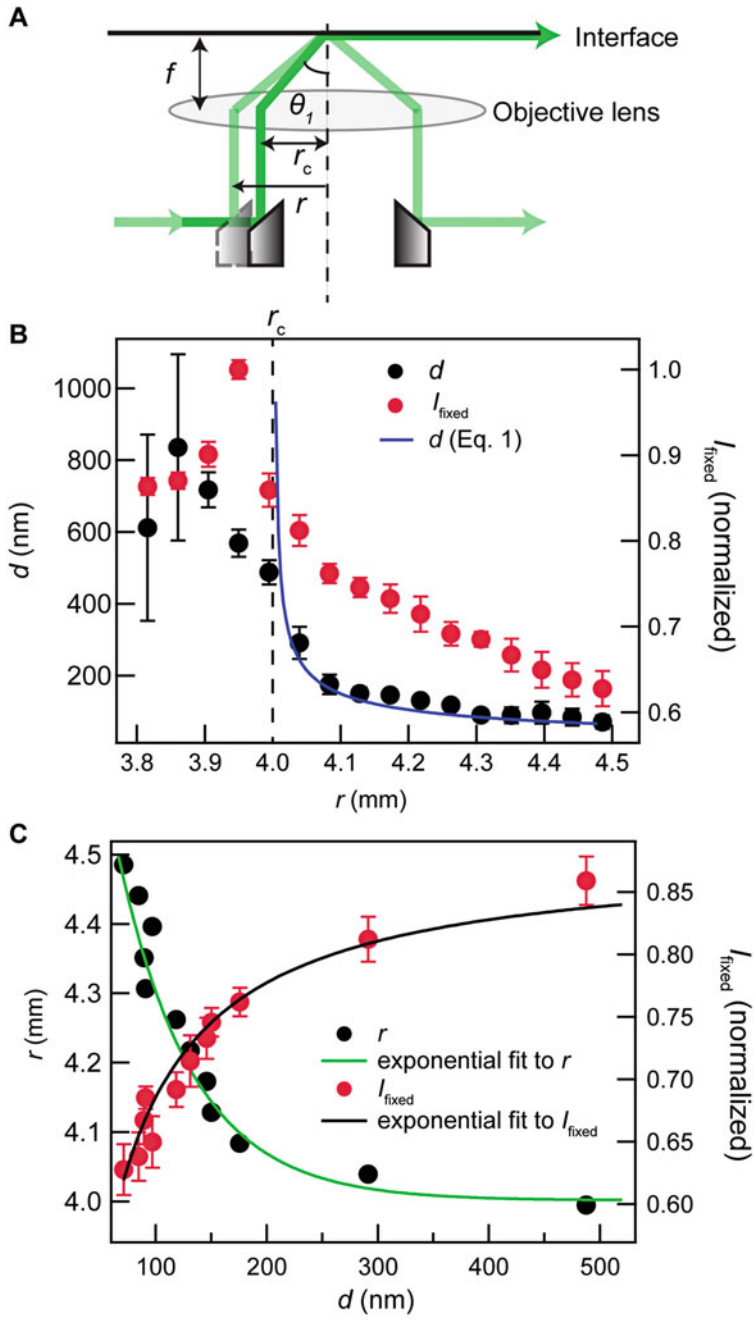

Fig. 3 (**a**) A simple description of the relationship between the incident angle, θ_1 and the micro-mirror lateral displacement *r*. The lateral movement of the micro-mirror under the objective lens (*r*) results in a change of the incidence angle, $\theta_1 = \text{asin}(r/n_1 f)$ at the interface between glass and the medium (buffer). Here *f* is the effective focal length of the objective lens and n_1 is the refractive index of glass. r_c indicates the critical displacement at which total internal reflection occurs. (**b**) *d* and the intensity of FND immobilized on surface, I_{fixed}, are plotted as a function of *r*. The characteristic penetration depth, *d*, and I_{fixed} decrease as *r* increases beyond r_c (*dashed vertical line*). I_{fixed} is normalized by its maximum intensity. The calculated *d* from Eq. 1 (*blue solid line*) is overlaid with the experimentally measured *d*. (**c**) *r* and I_{fixed} are plotted as a function of *d* and individually fitted with exponential functions

2.1.3 PCR Enzymes, Nucleotides and Kits

1. Phusion High-Fidelity DNA polymerase (M0530, NEB) and supplied buffer.
2. *Taq* DNA polymerase (M0273, NEB) and supplied buffer.
3. 100 μM Deoxynucleotide (dNTP) Solution.
4. Biotin-16-dUTP (11093070910, Roche).
5. Digoxigenin-11-dUTP (11093088910, Roche).
6. DNA purification kit (QIAquick PCR purification kit, Qiagen).

2.1.4 Restriction Enzyme Digestion

1. BsaI-HF (R3535, NEB) and supplied buffer.
2. Products from PCR reactions.
3. DNA clean-up kit (11732668001, Roche).

2.1.5 DNA Ligation

1. T4 DNA ligase (M1804, Promega) and supplied buffer.
2. Products from restriction digestion reactions.

2.1.6 DNA Tethering

1. Anti-digoxigenin, polyclonal (11333089001, Roche).
2. 1× Phosphate buffered saline (PBS).
3. Trizma base.
4. NaCl.
5. Products from DNA ligation reaction.
6. Bovine serum albumin (BSA).
7. Tween-20.
8. Magnetic beads (Dynabeads MyOne Streptavidin T1; 35,601, Invitrogen).
9. Wash buffer (WB): 1× PBS, 0.1% w/v BSA, 0.01% v/v Tween-20.
10. Bead wash buffer (BWB): 10 mM Tris (pH 7.5), 1 M NaCl.

2.1.7 TIRF Calibration

Biotinylated fluorescent nanodiamonds (e.g. Adamas Nanodiamonds).

2.1.8 General Supplies

1. 200 μl thin-wall PCR tubes.
2. 1.5 ml Eppendorf tubes.

2.2 Coverglass Cleaning

1. #1½ cover glass (24 mm × 60 mm).
2. #1 cover glass (24 mm × 60 mm).
3. KOH pellets (3141, JT Baker).
4. 95% ethanol (3791, Macron).
5. Glass beaker, 1 l.
6. Cover glass holder (custom made).
7. Sonicator.

2.3 Sample Cell Assembly

1. Cleaned coverglasses.
2. Nylon standoff (10SC008062; 10SC002037, McMaster Carr).
3. 58 μm thickness adhesive transfer tape (9671LE, 3M).
4. CO_2 Laser engraver/cutter.
5. Bead blaster cabinet.
6. Epoxy.
7. Vacuum grease.
8. Acetone, HPLC grade.
9. Ethanol, HPLC grade.
10. 2 μm Polystyrene beads (PS05N, Bangs Laboratories).

2.4 Magnetic Tweezers and Micro-mirror TIRF Components

Listed in Table 1.

3 Methods

3.1 Construction of Magnetic tweezers and Micro-mirror TIRF

The physical principle of magnetic tweezers and the details of the instrumentation have been extensively described in previously published chapters [1, 3, 17]. Here, we focus on updated information on the magnetic tweezers instrumentation and protocols. Briefly, the custom-built magnetic tweezers are comprised of two permanent magnets that are controlled by a linear translation motor and a rotary stepper motor. The hollow shaft of the stepper motor allows us to directly mount the magnet holder to the motor, which replaces the belt-driven systems used to control magnet rotation. This assembly is located above the sample cell centered along the *z*-axis of the illumination and imaging path. The sample cell is mounted on a custom-built cell holder that sits on a pair of stacked piezo-driven stages; one that provides nanometer scale position control in three dimensions, the other that provides large displacements in the *x*–*y* plane, which replaces a manual stage (Fig. 1b). The stages were mounted via four 1.5″ posts to an optical bread board that was modified with additional mounting threads, a cut-out for the 95 mm structural rail and a 30 mm through-hole for the optical path. The magnetic tweezers instrument is assembled on a vibration isolation table and housed in a temperature-controlled and vibration-isolated clean room. The 95 mm structural rail supports the magnet and illumination assemblies (Fig. 1b). The illumination source is a 590 nm LED light that is weakly focused using four lenses (Fig. 1).

Our micro mirror TIRF (mmTIRF) system was assembled following the protocol of Larson et al. [32] with a few

Table 1
List of components for magnetic tweezers and micro-mirror TIRF instrument

Item	Description	Company	Catalogue number
Excitation components			
Laser	Supercontinuum laser	NKT Photonics	ETW-12
F1	Infra-red filter	Newport	FSR-KG2
F2	560 nm bandpass filter	Semrock	FF01-560/14-25
L1	Objective lens, $f = 16.5$ mm	Newport	M-10x
L2	Collimating lens, $f = 150$ mm, AR = 14	Newport	PAC058AR.14
L3	Focusing lens, $f = 250$ mm, AR = 14	Newport	PAC067AR.14
mm	45° Rod mirror	Edmunds Optics	54-092
M1	Silver mirror, Ø = 1″	Thorlabs	PF10-03-P01
OL	Objective lens, 60×, N.A. = 1.45, Oil	Olympus	PLAPON60XOTIRFM
Emission components			
DC	Dichroic filter, Ø = 2″	Semrock	FF611-SDi01-50.8D
F3[a]	642 nm long-pass filter	Semrock	FF01-642/LP
L4	Imaging lens, $f = 400$ mm, AR = 14	Newport	PAC090AR.14
EMCCD	Electron multiplying charge coupled device camera	Andor	iXon + DU-879E
Magnetic tweezers illumination and imaging components			
F4	590 nm long-pass filter	Newport	FSR-OG590LP
LED	Mounted light emitting diode (LED), Amber, 1000 mA, 160 mW	Thorlabs	M590L3
L5	Aspheric lens, $f = 3.1$ mm	Thorlabs	C330TMD-A
L6	Aspheric condenser lens, $f = 20.1$ mm	Thorlabs	ACL2520U-A
L7	Collimating lens, $f = 80$ mm	Thorlabs	
L8	Focusing lens, $f = 250$ mm	Thorlabs	
L9	Imaging lens, $f = 150$ mm	Newport	PAC086AR.14
MS	Mounted silver mirror	Thorlabs	CM1-P01
M0.5	Silver mirror, Ø = 0.5″	Thorlabs	PF05-03-P01
M2	Silver mirror, Ø = 2″	Thorlabs	PF20-03-P01
CCD	Charge coupled device camera	Prosilica	GE-680
Magnetic tweezers and microscope components			
Structural rail	Mount illumination and linear/rotary motors	Thorlabs	XT95-50
Sample cell platform	Aluminum breadboard, 12″ × 18″ × 1/2″, ¼-20 Threaded		MB1218
Mounting posts and post bases	6″ height mounting posts and bases for supporting a sample cell platform 1.5″ height posts for mounting PILine stage		P6; PB2; P1.5

Cage cube system	Build 3-D optical path		LC6W LB1C, LB5C1, CPVM
Rail carrier for illumination assembly	Illumination assembly height control		XT95P12
Rail carrier for magnet assembly	Mount for Linear and rotary stages to the structural rail	Newport	CXL95-120
Objective lens coarse focus stage	Micrometer Z-Stage	Edmunds Optics	66-495
Optical table	Vibration isolation table (29″ × 35″ × 4″)	Technical Manufacturing Corporation	Micro-g Laboratory table 63-533
Micro-mirror control			
Micro-mirror mount and extension	3/32″ square machine key stock	Grainger	5UU68
	Key shaft	McMaster	1570K21
Shaft holder	Plate Holder	Thorlabs	FP01
3-D position control of mms	Three axis stage	Thorlabs	DT12XYZ
1-D position control of mm_1	Linear stage	New Focus	9062-X
	A nanopositioning actuator and controller		8301NF 8751-CL
Custom parts			
Objective lens holder Flow cell holder Magnet holder		Custom machined	NA
Magnets	Rectangular magnets N52; NdFeBr; Ni-plated; 5 × 8 × 3 mm	Pacific PAC	NA
Stages, computer, and software			
Computer	Computer for hardware control and data analysis	HP	HP workstation Z820
Stages	PILine® Piezo Motor XY open frame stage system	Physik Instumente	M-686.XYPM C-867
	PIMars™ XYZ piezo nanopositioning/scanning stage and controller		P-561.3CD/E-710
	Linear motor for the magnet assembly and controller	Newport	LTA-HS/ESP300
	Stepper motor for the magnet assembly	Lin Engineering	ZH-417
Software	NI developer suite	National Instruments	Labview and NI vision

[a]Discontinued. Alternative choice: BLP01-635R-25 (Semrock)

modifications (Fig. 1). In order to incorporate the mmTIRF system, a custom objective lens mount was machined and attached to a vertical stage that provided manual coarse focus control. Directly underneath the back aperture of the objective lens, two micro mirrors are glued to two individual 3/32″ square machine key stocks that are each fitted to a key shaft on a 3-D axis stage (Fig. 1b). Two stacked cage cubes below the objective are centered on the optical axis. The top cube holds a dichroic that reflects the fluorescent emission from the objective onto a EMCCD camera with an imaging lens after passing through an emission filter. The bottom cube holds a turning mirror to steer the illumination light from the objective to an imaging lens, which projects an image onto a CCD camera.

3.2 Making DNA Substrate

3.2.1 PCR Reaction for a 5 kb DNA

1. Prepare 1× 1.5 ml Eppendorf tube and 6× 200 µl PCR tubes on ice.
2. Add the following components to the 1.5 ml tube and mix well by gently rocking the tube ten times.

Component	50 µl volume	300 µl volume	Final concentration
Nuclease-free water	To 50 µl	To 300 µl	
5× Phusion HF Buffer	10 µl	60 µl	1X
100 µM Forward Primer	0.25 µl	1.5 µl	0.5 µM
100 µM Reverse Primer	0.25 µl	1.5 µl	0.5 µM
pET28-b	5 ng	30 ng	<5 ng/µl
10 mM dNTPs	1 µl	6 µl	200 µM
Phusion DNA Polymerase	0.5 µl	3 µl	1.0 units/ 50 µl PCR

3. Transfer 50 µl of the reaction mixture to each PCR tube and run PCR reaction using the following condition.

Step	Temp. °C	Time
Initial denaturation	98	30 s
30 cycles	98 66 72	10 s 15 s 2 min 30 s
Final extension	72	30 min
Hold	4	

4. Check the size of PCR products on a 1% DNA agarose gel.
5. After PCR reaction, purify DNA using PCR purification kit. Follow the provided protocol but at the final step before

adding the elution buffer, do an additional 5 min spin down to remove any residual wash buffer. Additionally, increase the incubation time to 15–30 min before collecting the DNA sample after adding the elution buffer.

6. Quantify DNA product and its purity.

3.2.2 PCR Reaction for Bio- or Dig-Labeled DNA Handles

1. Prepare 2× 1.5 ml Eppendorf tubes and 12 × 200 µl PCR tubes on ice.
2. Add the components to 1.5 ml tube, depending on the reaction volume and labeling type (one for biotin and the other for digoxigenin) and mix well by gently rocking the tubes ten times:

Component	50 µl reaction	300 µl reaction	Final concentration
Nuclease-free water	To 50 µl	To 300 µl	
10× standard Taq Buffer	5 µl	30 µl	1×
100 µM Forward Primer (either bio or dig)	0.25 µl	1.5 µl	0.5 µM
100 µM Reverse Primer	0.25 µl	1.5 µl	0.5 µM
pBluescript II KS	1 ng	6 ng	
low dTTP-dNTP mixture (10 mM of dATP, dCTP, dGTT and 7.0 mM of dTTP)	1 µl	6 µl	200 µM except for dTTP (140 µM)
Either Biotin-16-dUTP or Digoxigenin-11-dUTP[a]	3 µl	18 µl	60 µM
Taq DNA pol	0.5 µl	3 µl	1.0 units/50 µl PCR

[a]Lower this amount if PCR is not working, particularly for digoxigenin

3. Transfer 50 µl of the reaction mixture to 6 individual PCR tubes and run the following PCR reaction.

Step	Temp., °C	Time
Initial denaturation	95	30 s
30 cycles	95 60 68	30 s 30 s 2 min
Final extension	68	30 min
Hold	4	

4. Check the size of PCR products on a 1% DNA agarose gel.
5. After PCR reaction, purify DNA using PCR purification kit. Follow the provided protocol but at the final step before

adding the elution buffer, do an additional 5 min spin down to remove any residual wash buffer. Additionally, increase the incubation time to 15–30 min before collecting the DNA sample after adding the elution buffer.

6. Quantify DNA product and calculate the molar concentration.

3.2.3 Restriction Digestion

1. Add the following components in a 200 μl PCR tube:

Component	50 μl reaction
Nuclease-free water	To 50 μl
10× Buffer 4	5 μl
PCR product	<1 μg
BsaI-HF	2 μl

2. Restriction digestion reaction.

Step	Temp. °C	Time
Incubation	37	6 h
Add additional 2 μl BsaI-HF to the reaction sample	37	
Incubation	37	6 h
Stop reaction	65	20 min
Hold	4	

3. Purify the digestion product using purification kit (Roche). Follow the provided protocol but at the final step before adding the elution buffer, spin down the tube for 5 min to remove any residual wash buffer. Additionally, incubate the sample tube after adding the elution buffer at 65 °C for 5 min before elution.
4. Quantify the purified DNA and calculate the molar concentration.

3.2.4 T4 DNA Ligation

1. Add the following components in a 200 μl PCR tube:

Component	50 μl reaction	Final concentration
Nuclease-free water	To 50 μl	
10× T4 DNA ligase Buffer	5 μl	1×
5 kb	~0.50 pmol	10 nM
Biotinylated DNA handle[a]	~0.50 pmol	10 nM
Digoxigenin DNA handle[a]	~0.50 pmol	10 nM
T4 DNA ligase	1 μl	1 unit

[a]Typical concentration.

2. T4 DNA ligation reaction.

Step	Temp., °C	Time, h
Incubation	25	3
Incubation	16	15
Hold	4	

3. Run the ligated product on 1% DNA agarose gel to check the ligation efficiency. If the ligation efficiency is less than 80%, redo the restriction digestion and repeat ligation.

3.3 Preparing and Assembling Sample Cells

3.3.1 Cover Glass Cleaning (Notes 1–2)

1. Place cover glasses in a Teflon cover glass holder that holds the cover glass vertically.
2. Prepare enough KOH-ethanol solution (6% w/v) in a 1 l glass beaker to submerge cover glass holder (~500 ml).
3. Sonicate the cover glass in the KOH solution for 30 min.
4. Remove the holder and place it in a 1 l glass beaker containing deionized water.
5. Sonicate for 30 min.
6. Repeat **steps 4** and **5** twice.
7. Take out the holder and rinse each cover glass 2–3 times with deionized water to remove remaining KOH.
8. Squirt 100% ethanol over each cover glass.
9. Dry the cover glass either by microwaving for 3 min or baking for 15 min at 150 °C.
10. Store the cover glasses in an air-tight container.

3.3.2 Sample Cell Assembly

1. Assemble a sample cell by attaching a cleaned top glass (#1 coverglass with two inlet holes) to a bottom glass (#1–1/2 coverglass) with double-sided tape with a central 40 mm × 4 mm channel (Fig. 4). The channel is cut in the double-sided adhesive using a CO_2 laser engraver/cutter. Two 2 mm diameter through-holes are drilled on the top coverslip using a bead blaster and a soft plastic template.
2. Two different sizes of nylon screw inserts are attached at the centers of the individual holes for the buffer reservoir (larger one) and the outlet (small one) channels by spreading vacuum grease on the bottom surface and applying epoxy around the edge of the inserts.
3. Cure the epoxy for an hour.

3.3.3 Stuck Bead Generation (8–10 Sample Chambers)

1. Add 200 µl of deionized water in a 1.5 ml Eppendorf tube.
2. Add 2 µl of 2 µm polystyrene beads (4% w/v) to the tube and mix by quickly vortexing.

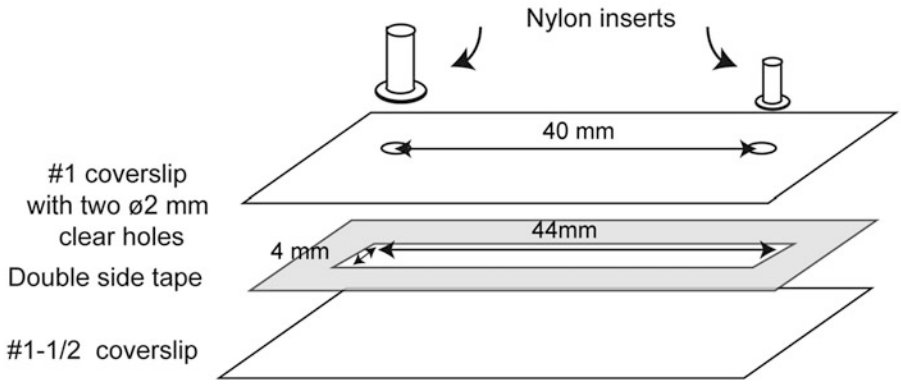

Fig. 4 Sample cell assembly. A typical sample cell is composed of a #1–1/2 coverslip as a bottom surface and a #1 coverslip with two holes separated by 40 mm as a top surface. The two coverslips are attached by double-sided adhesive film with a rectangular slot that results in a sample channel in the assembled flow cell. Two different sized nylon standoffs are attached to the centers of the two holes. The larger one is used as a buffer reservoir and the smaller one is used as an outlet to remove buffer from the sample channel

3. Sonicate the bead solution for 5 min.
4. Add 200 μl of Acetone to the bead solution and mix by quickly vortexing.
5. Introduce ~40 μl (slightly larger than a sample chamber volume) of the bead solution to each sample chamber immediately after **step 4**.
6. Incubate for 10–20 min. The distribution of stuck beads on the surface can be checked on a microscope.
7. Wash the sample cell with 200 μl of deionized water followed by 300 μl of 100% ethanol (HPLC grade).
8. Completely remove ethanol from chamber using a vacuum line.
9. Bake sample cells on a hot plate at 125 °C for 15 s.

3.4 Preparing a Sample for TIRF Calibration

1. Mix 3 μl of anti-digoxigenin solution (0.2 mg/ml in 1× PBS), 1 μl of 0.2 nM coilable DNA (Subheading 3.1 above), 10 μl of 5× PBS containing 0.5 mM EDTA, 1 μl of bioFND for surface immobilization (0.5 mg/ml), and water up to 50 μl.
2. Incubate for 15–20 min at room temperature (RT).
3. Pipette 40 μl into a sample chamber.
4. Incubate the sample chamber overnight at 4 °C or 1 h at RT.
5. Wash the sample chamber twice with 200 μl of wash buffer and incubate for 10 min.
6. While waiting, pipette 2 μl of a 1% w/v 1 μm streptavidin magnetic particle suspension and put it in an Eppendorf tube.

7. Pull beads to the bottom of the tube by placing it on top of a permanent magnet.
8. Gently pipette out the supernatant.
9. Add 200 μl of bead wash buffer (BWB) and vortex the tube quickly to mix.
10. Repeat **steps 7–9** three times.
11. After the final wash, instead of adding BWB, add 50 μl of WB.
12. Introduce the bead solution into the flow-cell and wait for 30 min.
13. Remove unbound beads by washing 1 ml of WB through the sample chamber.
14. Add 5 μl of 0.5 mg/ml bioFND in WB and incubate overnight.
15. Before use, remove unbound FND by washing 1 ml of WB through the sample chamber.

3.5 TIRF Field Calibration (Note 3)

1. Add one drop of oil immersion oil on top of the objective lens and place a prepared sample cell on the sample cell holder.
2. Adjust the objective lens focus on a surface-immobilized FND based on the fluorescent image of FND.
3. Find a coilable DNA molecule and a surface immobilized FND in the same field of view.
4. Adjust the micro-mirror position, r (Fig. 3a) to maximize the fluorescent intensity of the FND, which corresponds to an incident angle close to the critical angle for total internal reflection (Fig. 3b).
5. Set the force to 1 pN and perform supercoiling of DNA by rotating the magnet from 0 to 52 turns. Do the following measurements each turn:
   - Measure the fluorescent intensity of FND that is immobilized on the surface, I_{fixed}.
   - Measure the magnetic bead position by video tracking [1, 3] and the intensity of FND attached to the bead simultaneously (Fig. 2).
6. Repeat the measurements (**step 4** and **5**) for increasing r.
7. Estimate d by fitting the fluorescent intensity as a function of z-position (Fig. 2b) for all r positions.
8. Obtain the relationships between I_{fixed} and d as well as r and d by fitting an exponential function that will be used as a calibration to adjust r to obtain a desired d (Fig. 3c).

4 Notes

1. Use the ethanol and KOH from the listed vendors as we have found that KOH pellets do not dissolve well and/or the solution becomes cloudy if KOH and ethanol from different sources are used, which results in poor cleaning efficiency. Alternatively, if KOH or ethanol from other sources are used, the cleaning efficiency should be carefully evaluated.
2. KOH-ethanol solution can be reused at least 3–4 times.
3. The profile of $I_{\text{fixed}}(r)$ and subsequently the relationship between I_{fixed} and d depends on the size of the surface-immobilized FND. When using this calibration to set d, make sure that the maximum intensity of the surface immobilized FND and the profile of $I_{\text{fixed}}(r)$ are similar to those of the FND used in the initial measurement of the relationship between I_{fixed} and d.

Acknowledgements

We thank Ganesh Shenoy, Haksung Jung, and Rolf Swenson for providing biotinylated fluorescent nanodiamonds. We thank Gary Melvin for machining. This research was supported by the Intramural Research Program of the National Heart Lung and Blood Institute, National Institutes of Health.

References

1. Lionnet T, Allemand J-F, Revyakin A, Strick TR, Saleh OA, Bensimon D, Croquette V (2012) Single-molecule studies using magnetic traps. Cold Spring Harb Protoc 2012(1):pdb.top067488. doi:10.1101/pdb.top067488
2. Neuman KC, Nagy A (2008) Single-molecule force spectroscopy: optical tweezers, magnetic tweezers and atomic force microscopy. Nat Methods 5(6):491–505
3. Seol Y, Neuman KC (2011) Magnetic tweezers for single-molecule manipulation. In: Peterman EJ, Wuite G (eds) Single molecule enzymology, vol. 783. Methods in molecular biology. Humana, New York, NY, pp 265–293
4. Vlaminck ID, Dekker C (2012) Recent advances in magnetic tweezers. Annu Rev Biophys 41(1):453–472. doi:10.1146/annurev-biophys-122311-100544
5. Fulconis R, Bancaud A, Allemand J-F, Croquette V, Dutreix M, Viovy J-L (2004) Twisting and untwisting a single DNA molecule covered by RecA protein. Biophys J 87 (4):2552–2563. doi:10.1529/biophysj.104.043059
6. Kemmerich FE, Kasaciunaite K, Seidel R (2016) Modular magnetic tweezers for single-molecule characterizations of helicases. Methods 108:4–13. doi:10.1016/j.ymeth.2016.07.004
7. Koster DA, Crut A, Shuman S, Bjornsti M-A, Dekker NH (2010) Cellular strategies for regulating DNA supercoiling: a single-molecule perspective. Cell 142(4):519–530. doi:10.1016/j.cell.2010.08.001
8. Lionnet T, Dawid A, Bigot S, Barre F-X, Saleh OA, Heslot F, Allemand J-F, Bensimon D, Croquette V (2006) DNA mechanics as a tool to probe helicase and translocase activity. Nucleic Acids Res 34(15):4232–4244. doi:10.1093/nar/gkl451
9. Manosas M, Xi XG, Bensimon D, Croquette V (2010) Active and passive mechanisms of helicases. Nucleic Acids Res 38(16):5518–5526. doi:10.1093/nar/gkq273

10. Seol Y, Strub M-P, Neuman KC (2016) Single molecule measurements of DNA helicase activity with magnetic tweezers and t-test based step-finding analysis. Methods 105:119–127. doi:10.1016/j.ymeth.2016.04.030
11. Charvin G, Strick TR, Bensimon D, Croquette V (2005) Tracking topoisomerase activity at the single-molecule level. Annu Rev Biophys Biomol Struct 34(1):201–219. doi:10.1146/annurev.biophys.34.040204.144433
12. Neuman KC (2010) Single-molecule measurements of DNA topology and topoisomerases. J Biol Chem 285(25):18967–18971. doi:10.1074/jbc.R109.092437
13. Seol Y, Neuman K (2011) Single-molecule measurements of topoisomerase activity with magnetic tweezers. In: Mashanov GI, Batters C (eds) Single molecule enzymology, vol 778. Methods in molecular biology. Humana, New York, NY, pp 229–241. doi:10.1007/978-1-61779-261-8_15
14. Dulin D, Cui TJ, Cnossen J, Docter Margreet W, Lipfert J, Dekker Nynke H (2015) High spatiotemporal-resolution magnetic tweezers: calibration and applications for DNA dynamics. Biophys J 109(10):2113–2125. doi:10.1016/j.bpj.2015.10.018
15. Huhle A, Klaue D, Brutzer H, Daldrop P, Joo S, Otto O, Keyser UF, Seidel R (2015) Camera-based three-dimensional real-time particle tracking at kHz rates and Ångström accuracy. Nat Commun 6:5885. doi:10.1038/ncomms6885. http://www.nature.com/articles/ncomms6885#supplementary-information
16. Lansdorp BM, Tabrizi SJ, Dittmore A, Saleh OA (2013) A high-speed magnetic tweezer beyond 10,000 frames per second. Rev Sci Instrum 84(4):044301. doi:10.1063/1.4802678
17. Lipfert J, Hao X, Dekker NH (2009) Quantitative modeling and optimization of magnetic tweezers. Biophys J 96(12):5040–5049. doi:10.1016/j.bpj.2009.03.055
18. te Velthuis AJW, Kerssemakers JWJ, Lipfert J, Dekker NH (2010) Quantitative guidelines for force calibration through spectral analysis of magnetic tweezers data. Biophys J 99(4):1292–1302. doi:10.1016/j.bpj.2010.06.008
19. Yu Z, Dulin D, Cnossen J, Köber M, van Oene MM, Ordu O, Berghuis BA, Hensgens T, Lipfert J, Dekker NH (2014) A force calibration standard for magnetic tweezers. Rev Sci Instrum 85(12):123114. doi:10.1063/1.4904148
20. Lansdorp BM, Saleh OA (2012) Power spectrum and Allan variance methods for calibrating single-molecule video-tracking instruments. Rev Sci Instrum 83(2):025115. doi:10.1063/1.3687431
21. Guo Q, He Y, Lu HP (2014) Manipulating and probing enzymatic conformational fluctuations and enzyme-substrate interactions by single-molecule FRET-magnetic tweezers microscopy. Phys Chem Chem Phys 16(26):13052–13058. doi:10.1039/C4CP01454E
22. Kemmerich FE, Swoboda M, Kauert DJ, Grieb MS, Hahn S, Schwarz FW, Seidel R, Schlierf M (2015) Simultaneous single-molecule force and fluorescence sampling of dna nanostructure conformations using magnetic tweezers. Nano Lett. doi:10.1021/acs.nanolett.5b03956
23. Lebel P, Basu A, Oberstrass FC, Tretter EM, Bryant Z (2014) Gold rotor bead tracking for high-speed measurements of DNA twist, torque and extension. Nat Methods 11(4):456–462. doi:10.1038/nmeth.2854. http://www.nature.com/nmeth/journal/v11/n4/abs/nmeth.2854.html#supplementary-information
24. Swoboda M, Grieb M, Hahn S, Schlierf M (2014) Measuring two at the same time: combining magnetic tweezers with single-molecule FRET. In: Toseland CP, Fili N (eds) Fluorescent methods for molecular motors, vol. 105. Experientia supplementum. Springer, Basel, pp 253–276. doi:10.1007/978-3-0348-0856-9_12
25. Axelrod D (2013) Evanescent excitation and emission in fluorescence microscopy. Biophys J 104(7):1401–1409. doi:10.1016/j.bpj.2013.02.044
26. Martin-Fernandez ML, Tynan CJ, Webb SED (2013) A 'pocket guide' to total internal reflection fluorescence. J Microsc 252(1):16–22. doi:10.1111/jmi.12070
27. Bumb A, Sarkar SK, Billington N, Brechbiel MW, Neuman KC (2013) Silica encapsulation of fluorescent nanodiamonds for colloidal stability and facile surface functionalization. J Am Chem Soc 135(21):7815–7818. doi:10.1021/ja4016815
28. Burghardt TP (2012) Measuring incidence angle for through-the-objective total internal reflection fluorescence microscopy. J Biomed Opt 17(12):126007–126007. doi:10.1117/1.JBO.17.12.126007
29. Long X, Parks JW, Stone MD (2016) Integrated magnetic tweezers and single-molecule FRET for investigating the mechanical properties of nucleic acid. Methods 105:16–25. doi:10.1016/j.ymeth.2016.06.009

30. Swoboda M, Grieb MS, Hahn S, Schlierf M (2014) Measuring two at the same time: combining magnetic tweezers with single-molecule FRET. In: Toseland CP, Fili N (eds) Fluorescent methods for molecular motors. Springer, Basel, pp 253–276. doi:10.1007/978-3-0348-0856-9_12
31. Duboc C, Graves ET, Strick TR (2016) Simple calibration of TIR field depth using the supercoiling response of DNA. Methods 105: 56–61. doi:10.1016/j.ymeth.2016.03.028
32. Larson J, Kirk M, Drier EA, O'Brien W, MacKay JF, Friedman LJ, Hoskins AA (2014) Design and construction of a multiwavelength, micromirror total internal reflectance fluorescence microscope. Nat Protoc 9 (10):2317–2328. doi:10.1038/nprot.2014.155
33. Friedman LJ, Gelles J (2015) Multi-wavelength single-molecule fluorescence analysis of transcription mechanisms. Methods 86:27–36. doi:10.1016/j.ymeth.2015.05.026
34. Sarkar SK, Bumb A, Wu X, Sochacki KA, Kellman P, Brechbiel MW, Neuman KC (2014) Wide-field in vivo background free imaging by selective magnetic modulation of nanodiamond fluorescence. Biomed Opt Express 5 (4):1190–1202. doi:10.1364/BOE.5.001190

Chapter 17

Tethered Particle Motion: An Easy Technique for Probing DNA Topology and Interactions with Transcription Factors

Daniel T. Kovari, Yan Yan, Laura Finzi, and David Dunlap

Abstract

Tethered Particle Motion (TPM) is a versatile in vitro technique for monitoring the conformations a linear macromolecule, such as DNA, can exhibit. The technique involves monitoring the diffusive motion of a particle anchored to a fixed point via the macromolecule of interest, which acts as a tether. In this chapter, we provide an overview of TPM, review the fundamental principles that determine the accuracy with which effective tether lengths can be used to distinguish different tether conformations, present software tools that assist in capturing and analyzing TPM data, and provide a protocol which uses TPM to characterize *lac* repressor-induced DNA looping. Critical to any TPM assay is the understanding of the timescale over which the diffusive motion of the particle must be observed to accurately distinguish tether conformations. Approximating the tether as a Hookean spring, we show how to estimate the diffusion timescale and discuss how it relates to the confidence with which tether conformations can be distinguished. Applying those estimates to a *lac* repressor titration assay, we describe how to perform a TPM experiment. We also provide graphically driven software which can be used to speed up data collection and analysis. Lastly, we detail how TPM data from the titration assay can be used to calculate relevant molecular descriptors such as the *J* factor for DNA looping and *lac* repressor–operator dissociation constants. While the included protocol is geared toward studying DNA looping, the technique, fundamental principles, and analytical methods are more general and can be adapted to a wide variety of molecular systems.

Key words Tethered particle microscopy, DNA looping, *lac* repressor, Brownian motion

1 Introduction

Tethered Particle Motion (TPM) assays are simple but powerful tools for characterizing the effective length and behavior of various biomolecules. The basic idea behind TPM is to use a macromolecule of interest (such as DNA) to tether a sub-micron-sized, mobile reporter particle to an immobile point on a surface. The tethered particle exhibits Brownian motion influenced by rapidly changing configurations of the tethering molecule. By tracking the particle, the end-to-end distance of the molecule can be monitored and used to create length vs. time recordings that can be interpreted in terms of molecular conformations. TPM has been used to measure

Erwin J.G. Peterman (ed.), *Single Molecule Analysis: Methods and Protocols*, Methods in Molecular Biology, vol. 1665, DOI 10.1007/978-1-4939-7271-5_17,

kinesin-driven motion, transcription by RNA polymerases, protein synthesis, transcription factor–DNA binding, and to characterize transcription factor-mediated DNA loop topology [1–14]. In this chapter, we review the principles of TPM and detail how to employ it to study *lac* repressor-mediated DNA looping.

In *E. coli* the *lac* repressor (LacI) regulates the genes responsible for lactose metabolism. It represses transcription by binding the O_1 sequence (operator) adjacent to the lacZ promoter of the *lac* operon. Two additional binding sites, O_2 and O_3, allow tetrameric LacI to form one of three possible looped structures. To simplify the looping topology, DNA sequences used in TPM experiments typically include only two operators. In addition to the wild-type operators, there is a palindromic operator, O_S, for which LacI has an affinity roughly five times that of O_1 [15, 16]. LacI concentration modulates the probability of LacI-induced looping; however, loop formation events depend on fluctuations of the DNA molecule, which themselves are affected by physical factors including protein–DNA binding, distortions in the DNA molecule, and length of the DNA loop.

The mechanics of double-stranded DNA have been well studied, and at lengths longer than 150 bp it readily forms loops due to thermally induced fluctuations [17, 18]. The propensity of a DNA molecule to loop can be characterized using a quantity called the "J" factor [19]. The *J* factor is essentially a measurement of the effective, local concentration of one end of the looping segment relative to the other, and has units of molarity. The length of the loop segment greatly influences *J* factor values [20]. Over short lengths, the flexural stiffness of DNA prevents bending, which lowers the *J* factor. Intermediate lengths bend more easily and the ends meet often enough to spontaneously form loops. Long lengths also bend easily, but as the randomly coiled polymer extends through larger volumes, it becomes statistically unlikely that the two ends of a DNA molecule will meet, yielding a low *J* factor. The *J* factor versus length dependence has been measured in several experiments. For 400 bp-length loops, such as those measured here, *J* is in the range 1–20 nM [19, 21].

In the protocol that follows, we use a DNA construct containing the O_S and O_1 operators. Since looping depends on one LacI tetramer binding simultaneously to two operators, the likelihood of forming such a loop has a modal dependence on LacI concentration. Below 1 pM, a LacI tetramer is unlikely to occupy either operator, and although random thermal fluctuations may bring the operators together, no repressor stabilizes this conformation. In the range up to 1 nM, the O_S operator is very likely to be occupied, given that the dissociation constant, K_D, of O_S is about 8–10 pM [13, 16]. This O_S-bound tetramer can stabilize a loop if the corresponding O_1 operator is unoccupied. As a result, looping probability depends primarily on the *J* factor of the DNA sequence

and the degree of O_1 occupancy. At higher LacI concentrations ($>K_D$ of O_1 = 0.82 nM; see below), separate tetramers occupy both operators, and reciprocally inhibit stabilization of a loop.

TPM experiments offer insight into the thermodynamics and kinetics of looping reactions. These reactions manifest as switching between distinct looped states, each with distinct effective tether lengths. Longer tether states correspond to unlooped DNA, while looped tethers are shorter. The ratio of the time spent in looped conformations divided by the duration of the experiment is proportional to the free energy of the reaction and indicates the looping probability

$$p_{\text{loop}} \approx \frac{T_{\text{loop}}}{T_{\text{unloop}} + T_{\text{loop}}}. \tag{1}$$

For LacI concentrations between the K_D values of O_S and O_1, O_S will remain occupied while O_1 occupancy changes. In that range, one can expect an approximately linear relationship between the ratio of time spent in the unlooped and looped states and the LacI concentration [19, 20].

$$\frac{T_{\text{unloop}}}{T_{\text{loop}}} \approx \frac{2K_{D,O_1}}{J_{\text{loop}}} + \frac{2[LacI]}{J_{\text{loop}}}. \tag{2}$$

1.1 Parameters Affecting TPM Accuracy

Efforts to characterize the caveats and limitations of TPM include experimentation, numerical simulation, and analysis rooted in first-principles [8, 20, 22–26]. In this section, we summarize those caveats and highlight critical features of TPM experiments.

The customary readout of TPM experiments is the root mean square of excursions by the particle about the anchor point of the tether.

$$\rho_{\text{RMS}} = \sqrt{\langle \rho^2 \rangle} = \sqrt{\left\langle (x - \bar{x})^2 + (y - \bar{y})^2 \right\rangle}. \tag{3}$$

For linear macromolecules, such as DNA, the value of ρ_{RMS} scales with tether length; however, the precise functional relationship between the two depends on the physical characteristics of the molecule. At lengths greater than ~100 bp, DNA is well described by a worm-like chain polymer model [27]. In the absence of boundary constraints (i.e. chamber wall and reporter particle), statistical-dynamics leads one to expect

$$\rho_{\text{RMS}} \approx \sqrt{2 l_p L_0}, \tag{4}$$

where l_p is the chain's persistence length (about 50 nm for DNA in physiological salt conditions) and L_0 is the contour length (about 0.34 nm/bp) [28]. In practice, however, steric effects of the

chamber wall and reporter particle alter this scaling behavior [23]. While there is no analytical solution for the exact relationship between ρ_{RMS} and length, numerical simulations and corresponding experiments have been used to estimate the scaling law when a bead and wall are included [23, 24, 29].

When relating ρ_{RMS} to tether length, the time interval over which the excursion is averaged should be chosen carefully. The diffusive motion of the reporter particle is correlated over short time intervals such that the position of a particle at time $t_0 + \delta t$ is related to the position at time t_0. Consequently, averaging over excessively short time intervals will underestimate the excursion ($\langle \rho^2 \rangle_{\Delta t} < \langle \rho^2 \rangle_{\infty}$). Approximating the tether as an entropic spring that pulls the reporter particle with a characteristic Hookean spring constant, K, illustrates this problem. In this case, the Smoluchowski equation describes the time evolution of the probability distribution of the location of the reporter particle. For Hookean-spring type systems the solution to that differential equation is

$$P(x, t|x_0, t_0) \propto \exp\left(-K\frac{\left(x - x_0 \mathrm{e}^{-2(t-t_0)/\tau}\right)^2}{2k_{\mathrm{B}}T \cdot S(t, t_0)}\right), \tag{5}$$

where

$$S(t, t_0) = 1 - \exp\left(-\frac{4(t - t_0)}{\tau}\right), \tag{6}$$

with time constant

$$\tau = \frac{2k_{\mathrm{B}}T}{KD}, \tag{7}$$

and D is the diffusion constant given by the Stokes-Einstein equation [30]

$$D = \frac{k_B T}{6\pi\eta R}. \tag{8}$$

In the limit $t \to \infty$, the distribution decays to the steady-state

$$P(x) \propto \mathrm{e}^{-\frac{Kx^2}{2k_{\mathrm{B}}T}}, \tag{9}$$

which yields a mean square excursion of $\langle \rho^2 \rangle_{\infty} = \frac{2k_{\mathrm{B}}T}{K}$. Equation 5 shows that the probability distribution for a particle localized at position x_0, $P(x, t_0) = \delta(x - x_0)$, will decay to the steady-state distribution with time constant τ, the approximate temporal resolution for TPM. For short time scales $\Delta t \ll \tau$, the tether has a negligible effect on the particle trajectory which exhibits apparently unrestricted diffusion. Consequently, to detect changes in the properties of the tether (such as length or effective spring constant)

those changes must endure/be observed for longer than τ, the time required for the particle to diffuse such a distance that the work done on the tether approaches the scale of the available thermal energy (Eq. 7).

In the low-force regime, DNA has an effective spring constant of $K \approx \frac{3k_B T}{2L_0 L_P}$ [30]. For a 900 bp tether and a particle with radius $R = 160$ nm Eq. 7 yields a time constant of $\tau \approx 18$ ms. In practice, this is only a lower estimate. Experimental measurements of τ produce values nearly twice as large as predicted [31]. One reason for the disparity is that the effective diffusion coefficient of a particle increases near a wall, increasing the time constant [22, 32].

For a series of independent measurements of a normally distributed quantity, we can establish with what confidence the variance of the distribution lies within the limits

$$\frac{(N-1)s^2}{\chi^2_{1-\frac{\alpha}{2},N-1}} < \sigma^2 < \frac{(N-1)s^2}{\chi^2_{\frac{\alpha}{2},N-1}}, \tag{10}$$

where N is the number of samples, s^2 is the sample variance and χ^2 is the chi-square distribution for critical value α and $N - 1$ degrees of freedom. For TPM, because particle positions are correlated over timescales shorter than τ, the relevant sample number N is the number of measurements made with frequency $1/\tau$ [20], yielding

$$N \approx \frac{\Delta t}{\tau}. \tag{11}$$

In summary, two main factors establish the limits for studying a given macromolecular system using TPM: the expected scale of changes in tether length, and the time scale of those changes. As a rough approximation, the length and stiffness of a molecule can be used to estimate the expected RMS-excursion (Eq. 4). Similarly, the tether length and stiffness, along with the size of the reporter particle can be used to estimate the relevant time scale (Eq. 7) and confidence limits for a given measurement (Eqs. 10 and 11).

The TPM protocol included in this chapter reveals the looping of a DNA segment due to the binding of *lac* repressor protein to flanking operator sites. Previous experiments have demonstrated that such loops persist for many seconds. The approximate lengths of the tether were 909 bp (~300 nm) before and 509 bp (~170 nm) after looping. Those lengths translate to expected RMS-excursions of approximately 180 and 130 nm respectively, with a time-constant $\tau \approx 20$–40 ms. When comparing the variance of two populations the ratio of variances follows the *F*-distribution with confidence limits given by (*see* **Note 1**)

$$\frac{s_1^2}{s_2^2}\left(\frac{1}{F_{\alpha(2),N_1-1,N_2-1}}\right) < \frac{\sigma_1^2}{\sigma_2^2} < \frac{s_1^2}{s_2^2}\left(F_{\alpha(2),N_1-1,N_2-1}\right). \tag{12}$$

Additionally, the number of samples needed to resolve the two populations with a significance level α and power $1-\beta$ is given by

$$N \approx \left[\frac{Z_{\alpha(2)} + Z_{\beta(1)}}{\ln\frac{\sigma_1^2}{\sigma_2^2}}\right]^2 + 2, \tag{13}$$

where Z is the inverse of the cumulative normal distribution. Using Eq. 13 with significance $\alpha = 0.05$ and power $1-\beta = 0.9$, and given our estimates for ρ_{RMS}, $N = 28$ observations are required. Assuming a time constant of $\tau = 40$ ms, that translates to an averaging interval of $\Delta t = 1.12$ s.

2 Materials

2.1 Microscope and Camera

The technical requirements for TPM are relatively simple. *See* **Note 2** for tips on microscope and camera selection. One implementation includes:

1. An upright DM LB2 Microscope (Leica Microsystems GmbH, Wetzlar, Germany).
2. A 100× 1.2–1.4 numerical aperture, oil-immersion objective (Leica).
3. A Dark-field condenser unit (Leica).
4. A JAI GigE CM-140GE Camera (JAI Inc., San Jose, CA).
5. A custom-built PC running Windows 7 ×64, with an Intel i7 Quad-core 3.4 Ghz processor and 8 GB RAM.
6. MATLAB version R2014b or newer acquisition and analysis software.

2.2 Particle Tracking Software

The protocol presented here featured custom software based on MATLAB and MicroManager (www.micro-manager.org). It includes a routine for real-time tracking of particles in dark field images based on a radial symmetry detection algorithm [33]. The algorithm used for tracking particles in DIC images calculates an intensity weighed center-point in a specified region of interest. Both routines are included with the control software (http://www.physics.emory.edu/faculty/finzi/research/code.shtml). For alternative particle-tracking routines *see* **Note 3**.

2.3 Stock Solutions

Unless otherwise noted, all reagents were stored at 4 °C. To minimize risk of contamination with nucleases, all stock solutions and reaction buffers should be prepared using nuclease free, Milli-Q water.

1. Nuclease-Free Milli-Q Water.
2. 10× Phosphate Buffered Saline (PBS).
3. 3 M Potassium Chloride Solution.
4. DMSO.
5. 0.5 M EDTA Solution.
6. 1 M Tris–HCl pH 7.4.
7. 10 mM Tris–HCl pH 8.0.
8. Ethanol 100%.
9. 100 mM DTT (store at −20 °C).

2.4 Buffers

1. Pre-wash buffer: 10 mM Tris–HCl pH 7.4, 0.1 mM EDTA, 0.5 mg/mL α-casein, 200 mM KCl.
2. Experiment ("λ") buffer: 10 mM Tris–HCl pH 7.4, 0.1 mM EDTA, 0.1 mg/mL α-casein, 200 mM KCl, 5% v/v DMSO, 0.2 mM DTT (*see* **Note 4**).
3. DNA binding buffer: 10 mM Tris–HCl pH 7.4, 200 mM KCl.

2.5 Preparation of DNA Tethers

1. 1 μg/mL pYY-I1_400 plasmid DNA (*see* **Note 5**).
2. Forward Primer: 10 μM 5′-Biotin-(C6)-tgggaaggagaagataa-gatgg-3′ stored in 10 mM Tris–HCl pH 8.0. Purchased from Eurofins MWG Operon LLC, Louisville, KY. *See* **Note 6**.
3. Reverse Primer: 10 μM 5′-Digoxigenin-cgttagggtcaatgcgggtc-3′ stored in 10 mM Tris–HCl pH 8.0. Purchased from Eurofins MWG Operon LLC. *See* **Note 6**.
4. Taq polymerase with 10× Standard Taq Buffer (New England Biolabs, Ipswich, MA).
5. 10 mM dNTP mix (New England Biolabs).
6. QIAquick PCR Purification Kit (QIAGEN Inc., Valencia, CA).
7. Nuclease-free 200 μL PCR Tubes.
8. Thermocycler (MJ Mini Thermal Cycler, Biorad, Hercules, CA).
9. UV spectrophotometer (NanoDrop, Thermo Fisher Scientific).

2.6 Tethered Particles

1. 200 μg/mL polyclonal sheep anti-digoxigenin antibody in 1× PBS (Sigma-Aldrich, St. Louis, MO).
2. 1% w/v Streptavidin-coated polystyrene microspheres 320 nm (Spherotech Inc., Lake Forest, IL).
3. Microcentrifuge.

2.7 Flow Chambers

Note: Glass slides used to construct chambers were washed with 18 MΩ deionized water.

1. Laboratory tissue.
2. Alconox detergent.

3. Parafilm spacer cut to form chamber to hold 45–50 μL of fluid (*See* **Note 7**).
4. 75 × 25 mm standard microscope slide.
5. 22 × 22 mm microscope coverslip.
6. Microscope slide staining rack (Electron Microscopy Sciences).
7. Coverslip staining rack (Electron Microscopy Sciences).
8. Hot plate.
9. Humid storage box: petri dish or empty pipette tip box with wet sponge placed at the bottom.
10. Bath sonicator or, alternatively, an orbital shaker.

2.8 LacI Titration

1. *lac* repressor was provided by Kathleen Matthews at Rice University.

3 Methods

3.1 Producing DNA Tethers Using PCR

1. Mix the following in a thin-walled PCR tube.

Reagent	Concentration	Volume (μL)
Milli-Q Water		23.8
Taq polymerase buffer	10×	3.0
pYY-I1-400	100 ng/μL	0.1
Taq Polymerase	5 U/μL	0.5
dNTP Mix	10 mM	0.6
forward primer	10 μM	1.0
reverse primer	10 μM	1.0
	Total (μL)	30.0

2. Set thermocycler to execute the following sequence. *See* **Note 8**.

Step	Name	Time (min)	Temp. (°C)
1	Initial denaturation	2:00	95
2	Denaturation	0:15	95
3	Annealing	0:30	51
4	Elongation Go To 2 (repeat 30–40×)	0:45 –	68 –
5	Final Elongation	1:00	72
6	Final Annealing Hold	5:00 –	37 4

3. Purify the amplicon using a QIAquick PCR cleanup kit following the manufacturer's protocol. Elute DNA in 50 μL of 10 mM Tris–HCl pH 8.0. Verify the 909 bp linear DNA amplicon by electrophoresis through a 1% agarose gel in TAE buffer.
4. Measure the concentration of DNA by UV absorption. *See* **Note 9**.
5. Dilute the DNA to a final concentration of 20 ng/μL (about 30 nM) in 10 mM Tris–HCl pH 8.0.

3.2 Flow Chamber Assembly

1. Rinse microscope slides and coverslips with deionized water to remove dust or other debris.

3.2.1 Prewashing

2. Place slides and coverslips into staining racks and submerge in a jar filled with 0.5% w/v Alconox detergent in deionized water.
3. Sonicate slides for 15–30 min or agitate slides on an orbital shaker for 1–2 h.
4. Remove the slides from the Alconox solution and rinse thoroughly with tap water for 15 min.
5. Rinse the slides with deionized water by placing staining racks in a jar of fresh deionized water. Repeat 3–4 times.
6. Place the slide rack in ethanol and store sealed, at room temperature until you are ready to use the slides.

3.2.2 Assembly

1. With forceps remove a slide and coverslip from ethanol and carefully dry with N_2 or filtered compressed air. Be sure to inspect slides for streaks or water spots. Place in a closed container to shield from dust.
2. If using laser-cut Parafilm spacers, place a spacer in a beaker of ethanol to soften the paper backing. Once backing has softened, use a scalpel or razor to tease the edge until the backing can easily be removed.
3. Place the Parafilm spacer between two tissues to remove ethanol droplets and allow it to dry for about a minute.
4. Next place Parafilm spacer on glass slide and then cover with coverslip, leaving wells on either side exposed. *See* an assembled chamber in Fig. 1.
5. Set a hot-plate to a low setting, 50 °C. Place the glass chamber on the hot-plate surface to gently melt the Parafilm without sputtering or boiling. The Parafilm spacer becomes clear and tacky as it melts. Using a metal spatula or tweezer press the coverslip to seal the Parafilm to the glass surfaces and force any bubbles out of the melting Parafilm. Note that bubbles can cause leaks in the chamber.
6. Once the spacer has sealed to the glass surfaces, remove the chamber from the hot plate. The Parafilm should turn cloudy as it cools. *See* Fig. 1.

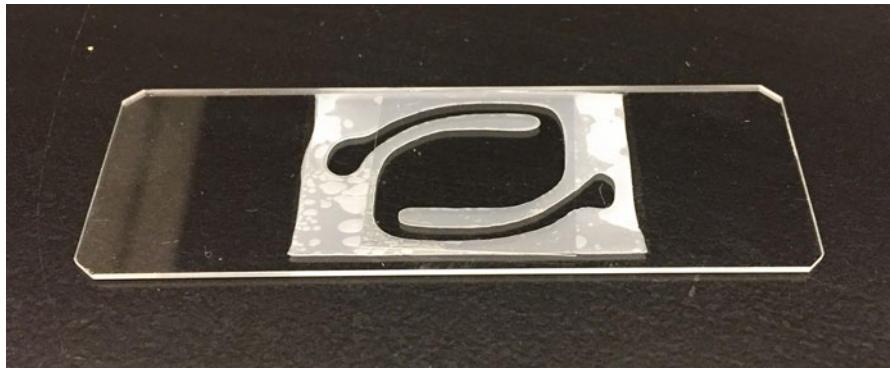

Fig. 1 A TPM chamber. The parafilm spacer was cut using a laser cutter and melted between the microscope slide and coverslip. The exposed ends of the channel serve as reservoirs for depositing/removing fluid

3.2.3 Anti-digoxigenin Functionalization

1. Flush the chamber with PBS by pipetting 100–200 μL of solution into a well at one end (inlet) of the serpentine channel under the coverslip. Capillary force should draw the fluid into and fill the chamber.
2. Further rinse the chamber by adding more buffer to the inlet well and then touching a tissue to the solution emerging from the opposite end of the channel (outlet). As the solution wicks into the tissue at the outlet, additional fluid is drawn through the channel inlet. Gently draw the solution through the chamber without exhausting the supply of solution at the inlet to prevent bubbles from entering the chamber.
3. Dilute the anti-digoxigenin stock to produce 200 μL of a 4 μg/mL solution in PBS. Repeat the previous step, to exchange the buffer within the chamber with the antibody solution.
4. Place the chamber in a sealed, humid box and store at 4 °C overnight or room temperature for approximately 1 h.

3.3 Preparing Tethered Particles

1. Dilute 2.5 μL of 1%w/v 320 nm dia. Streptavidin-coated particles into 200 μL of 1× PBS. Be sure to vigorously mix the stock particle suspension before use as particles will settle during storage.
2. Centrifuge the diluted suspension at 17,000 × *g* for 2 min. to form a pellet. Discard the supernatant and resuspend in PBS. Repeat once.
3. Centrifuge the diluted suspension again at 17,000 × *g* for 2 min. to form a pellet and remove the supernatant. Resuspend the particles in DNA binding buffer and mix vigorously to break up bead aggregates.

4. Wash excess anti-digoxigenin out of the chamber by gently flushing ~200 μL of PBS through the chamber.
5. Gently flush the chamber with 150 μL of pre-wash buffer and incubate for 5–10 min at room temperature.
6. Mix 1 μL of 20 ng/μL DNA stock with 100 μL of DNA binding buffer.
7. Gently draw 50 μL of the diluted DNA solution into the chamber and incubate at room temperature for 15 min.
8. Gently flush the chamber with 150 μL of pre-wash buffer. Then incubate for 5–10 min at room temperature.
9. Draw 50 μL of the bead suspension to the chamber and incubate at room temperature 10 min.
10. Gently flush the chamber with 100 μL of pre-wash buffer to remove un-bound beads. Store the chamber in the humidity box at 4 °C for at most 1–3 days before starting an experiment.
11. To begin an experiment, gently flush the chamber with 100 μL of λ-Buffer, followed by 100 μL of λ-Buffer supplemented with the desired LacI concentration. To prevent evaporation during experiments, cover the wells at the inlet and outlet of the chamber with small pieces of tape. For the data presented here, LacI was titrated over a range of 150 pM to 20 nM.

3.4 Microscope Operation

1. Turn on the microscope and dark-field/bright-field lamp at least 1 h before observing tethers to avoid drift during thermal equilibration. The chamber should also be at room temperature to avoid re-equilibration after placing it on the microscope.
2. Place the chamber on the microscope stage and observe using the oculars or the live video stream from the TPM capture program to bring the beads into focus.

3.5 Installing TPM capture Software

1. After downloading the TPM capture software and MicroManager, install MicroManager, and copy the TPM capture software to an accessible path.
2. Using MicroManager, setup and verify your camera is working (*see* instructions on micro-manager.org). Note the camera device module and device name.
3. Open MATLAB. Navigate to the TPM capture software folder. Open the "MM-Core" subfolder and run MMsetup_javaclass.m. It should prompt you to navigate to the folder in which you installed MicroManager. This will import the interface for MicroManager into the MATLAB environment.
4. Restart MATLAB.

5. To run the TPM capture program simply navigate to the folder containing the script "CaptureTPM.m". On the first run, it will ask you to specify the camera module and device names as well as the pixel scale. This can be measured using a calibration slide and the ImageJ "caliper.txt" macro included in the "Calibration Tools" directory with the TPM capture software.

3.6 Data Collection

1. Launch MATLAB, navigate to the folder containing the TPM capture software, and "run" "CaptureTPM.m".
2. If using DIC microscopy, select "DIC" in the algorithm selection drop-down on the "Tracking Controls" window, otherwise select "Radial Symmetry."
3. Focus the microscope on the particles at the chamber surface. Adjust the camera gain and lamp intensity to minimize "speckle" noise, so that the particles are clearly visible.
4. If chamber is prepared correctly, many of the particles will jiggle and a few will be immobile. The jigglers are tethered by DNA molecules. The fixed particles are stuck to the coverglass.
5. From the menu bar in the "Tracking Controls" window select "Add Track". A crosshair cursor will appear with which to draw a region of interest around a particle to begin tracking it.
6. Select 3–6 stuck particles to use as references for drift correction. Only one suffices but choosing several provides redundancy in case a bead detaches. Select as many moving beads as desired (Fig. 2). With a modern, multi-core CPU, it is possible to track more than 30 particles without a loss in performance.
7. Next, select "Experiment → Record Live Data" from the program menu. This launches a dialog for the selection of a directory in which to save the tracking data. After choosing a directory, click "Run." Data will be collected and automatically saved in the specified directory using a binary-file format. Saved data can be loaded into MatLab for analysis using the included TPManalysis Toolbox (next section).

3.7 Analysis of Tethered Particle Motion

As introduced in section 1.1, the time-averaged, root-mean-square of particle excursions reflects the effective tether length. However, the excursion data recorded for tracked particles must first be corrected to eliminate drift (Fig. 3), an artifact due to mechanical instability of the microscope. In addition, data corresponding to particles with multiple tethers must be culled from the ensemble. A package of MATLAB scripts for refining and manipulating TPM data can be found at http://www.physics.emory.edu/faculty/finzi/research/code.shtml

1. To use the scripts, navigate to directory containing LoadTPMdata.m, TPManalysis.m and the +TPManalysis package, or include this directory in the MATLAB path.

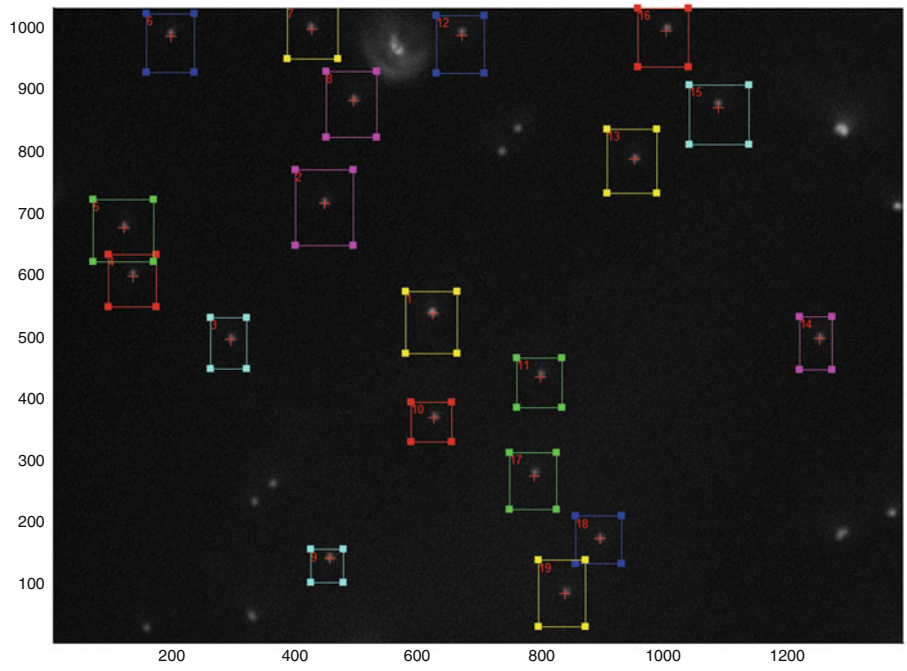

Fig. 2 A screen shot from the microscope control program with regions of interest (*boxes*) superimposed on a dark field image of 320 nm, tethered particles. The cursors update continuously within the stationary boxes in the live image

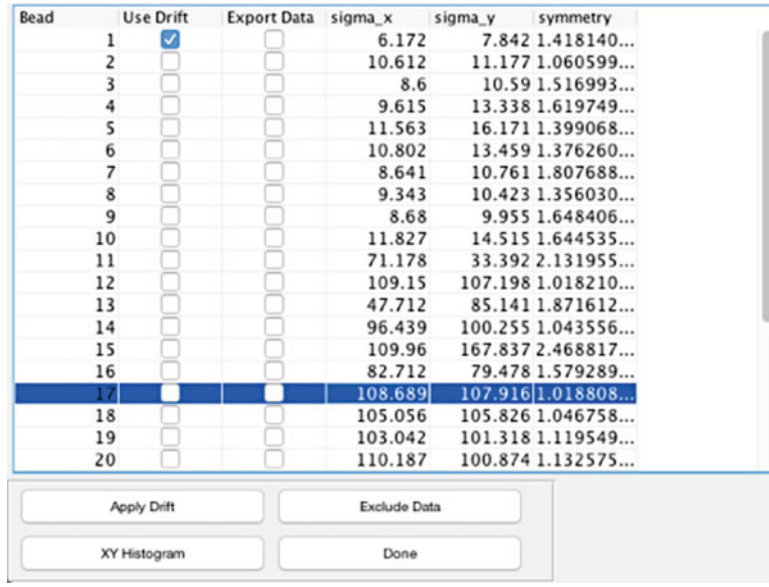

Fig. 3 TPManalysis–Main Window. Particles are listed in the order of ROI origination along with the standard deviations along the *X* and *Y* directions and symmetry values. Particle 1 is selected as a reference for drift correction. "Export Data" check-boxes can be toggled to mark data for analysis. The "symmetry" column lists values for $\sqrt{\lambda_1/\lambda_2}$

2. Run LoadTPMdata.m to load saved TPM data into the MatLab workspace. If the pixel scale was not specified during data acquisition, then change this value to reflect the correct scaling when given the option.
3. By default, LoadTPMdata.m will create a variable called "TPMdata", but a different output variable name may be specified when executing LoadTPMdata.m (e.g. YourVarName = LoadTPMdata();).

3.7.1 *Drift Correction*

The "TPMdata" variable data can be refined with TPManalysis.m, a toolbox for data selection and drift-correction.

1. In the list of trajectories presented within TPManalysis.m (Fig. 3), use the check-boxes under "Use Drift" to select the reference (stuck) particles and click "Apply Drift". Drift is calculated by first applying a 1-s moving average to the trajectories for each selected reference particle, and then averaging the trajectories of all the reference particles, yielding a single drift-trajectory. The drift-trajectory is then subtracted from each of the particle trajectories, producing "drift free" traces. Figure 4 illustrates the trajectories of a tethered particle and an associated reference particle before drift correction. The two-dimensional histogram is elongated and plots of the X or Y positions show clear drift over time. After drift correction, the two-dimensional histogram for the same particle becomes symmetrical and the average X and Y positions remain constant over time (Fig. 5). The standard deviations along X and Y (σ_x, σ_y) are almost identical for this particle attached to a single tether, and can be used as rough estimates of tether length.

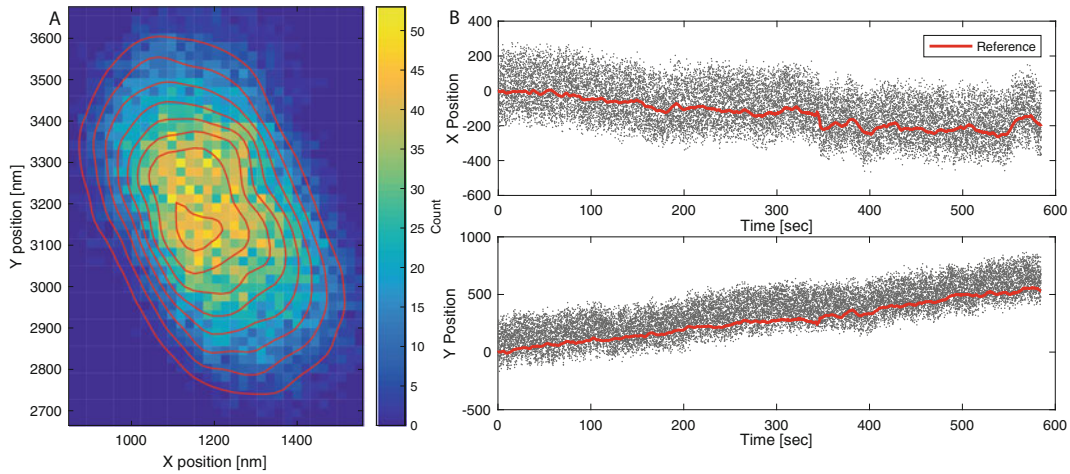

Fig. 4 The *XY* trajectory of a tethered particle before drift correction. (**a**) A two-dimensional histogram of particle positions. *Shades* indicate bin counts (colored online); contours delineate constant height profiles of the distribution. (**b**) *X* and *Y* positions vs. time trajectories for the tethered bead (*dots*); the *thick lines* (*red* online) correspond to the 1-s moving average of the trajectory of a single reference particle

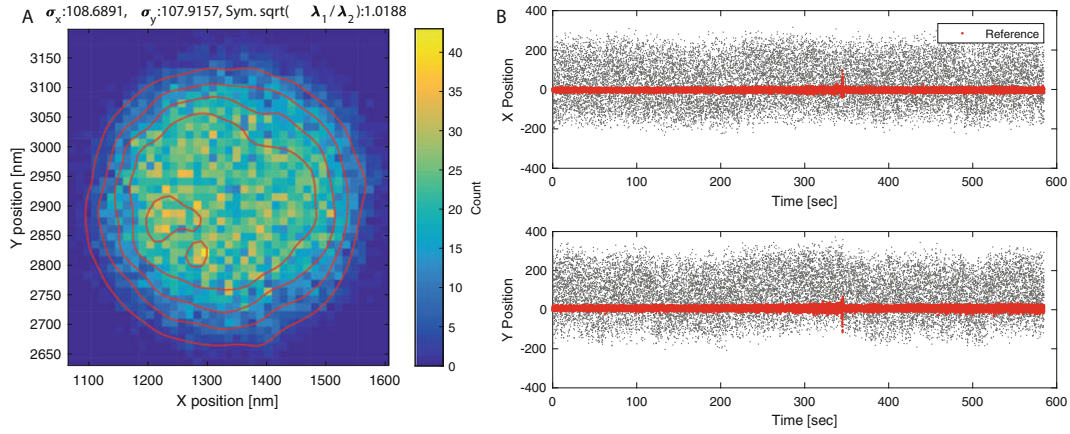

Fig. 5 The *XY* trajectory of the tethered particle shown in Fig. 3 after drift correction. (**a**) Two-dimensional histogram of particle positions. *Shades* indicate bin counts (colored online); contours delineate constant height profiles of the distribution. The standard deviations along *x* and *y* (σ_x, σ_y) are almost identical for this particle attached to a single tether. The value of a symmetry indicator, $\sqrt{\lambda_1/\lambda_2}$, near unity indicates highly symmetric excursions. (**b**) *X* and *Y* positions vs. time trajectories for the tethered bead after drift subtraction (*black dots*); the *thick dots* (*red* online) indicate the (unaveraged) trajectory of a reference particle after subtracting drift

3.7.2 Symmetry Test

1. Particles tethered by multiple molecules often exhibit asymmetric $X\Upsilon$ motion. A simple symmetry metric identifies those that should be discarded from the analysis. For two-dimensional scatter plots, the distribution of excursions is oriented along the eigenvectors of the covariance matrix for X and Υ positions. The eigenvalues (λ_1, λ_2 in Fig. 5) indicate the relative sizes of the distributions along their associated eigenvectors [34]. In TPManalysis.m the square root of the ratio of the eigenvalues , $\sqrt{\lambda_1/\lambda_2}$, is used to gauge the symmetry of the excursions ("Symmetry" column in Fig. 3). Particles with a root-ratio >1.08 should be discarded as they likely correspond to a particle anchored by multiple DNA tethers [22].
2. Select the "Export Data" checkboxes for each particle that will be analyzed further. The checkbox sets a flag in each corresponding element of the TPMdata structure. After exiting TPManalysis, type "[TPMdata.Bead.UseForMeasurement]" on the command line to list the flags. Similarly, the command: TPMdata.Bead(###).
will list all the data associated with the particle specified by ###.

3.7.3 Restricting Data

During an experiment, a particle may transiently stick to the chamber surface, anomalously drift, or be obscured by a freely diffusing particle passing through the region of interest (ROI). For analyses in which contiguous recording is not required, data corresponding to such interruptions may be excluded using the TPManalysis.m script.

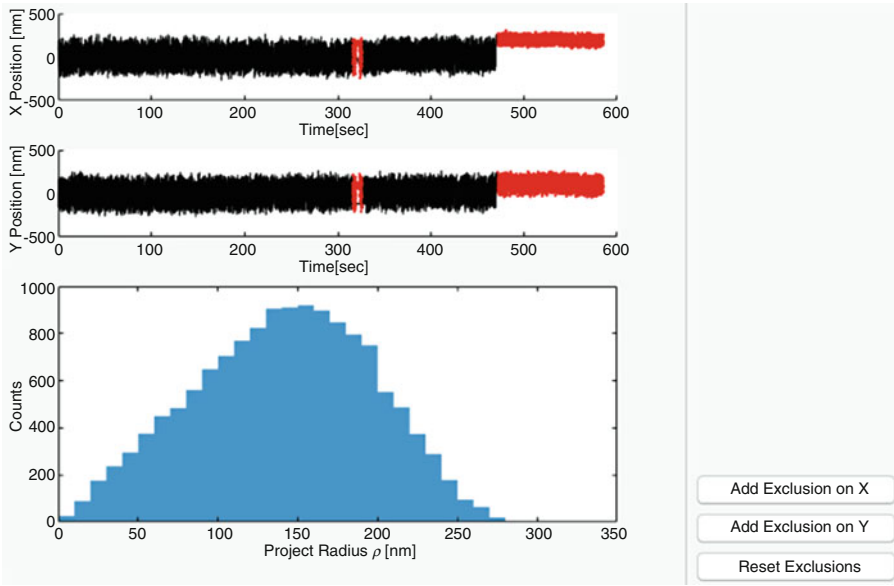

Fig. 6 TPManalysis—data exclusion. The *upper panels* show *X* and *Y* trajectories for a tethered particle. The *lower panel* shows a *histogram* of the magnitude of radial excursions about the average *X* and *Y* values for the entire segment. Adding exclusions by clicking "Add Exclusion on X" or "Add Exclusion on X" and extending rectangular selections across segments of the *X* or *Y* trajectories renders those segments in *gray* (*red* online)

1. To inspect and exclude data, highlight a particle and click "Exclude Data" to display a new window with buttons to exclude *X* or *Y* data (Fig. 6).
2. Select either "Add Exclusion on X" or "Add Exclusion on Y" and draw rectangular selections on regions of the *X* or *Y* vs. time plots (respectively) to discard those segments of the data.
3. When finished with drift correction and data exclusion, click "Done" to export the edited data back to the MATLAB main workspace. If TPManalysis.m was called without an output argument, the data will be saved to (or overwrite) a variable named "TPMdata" in the workspace.
4. Save the modified data using the standard "save" command (e.g. save('YourFileName.mat','TPMdata'); if using default variable names).

3.8 Looping Probability Measurement

Looping and unlooping due to the binding and unbinding of *lac* repressor to operators manifests as switching between long and short RMS-excursions (Fig. 7a). The square of the excursion was averaged using a moving window 4 seconds wide (*see* **Note 10**). 95% confidence limits determined using Eq. 10 were based on a 50 Hz frame rate with exposures of 1 ms such that the window included 200 points. Due to parallel or anti-parallel DNA alignments and switching of the *lac* repressor between open and closed

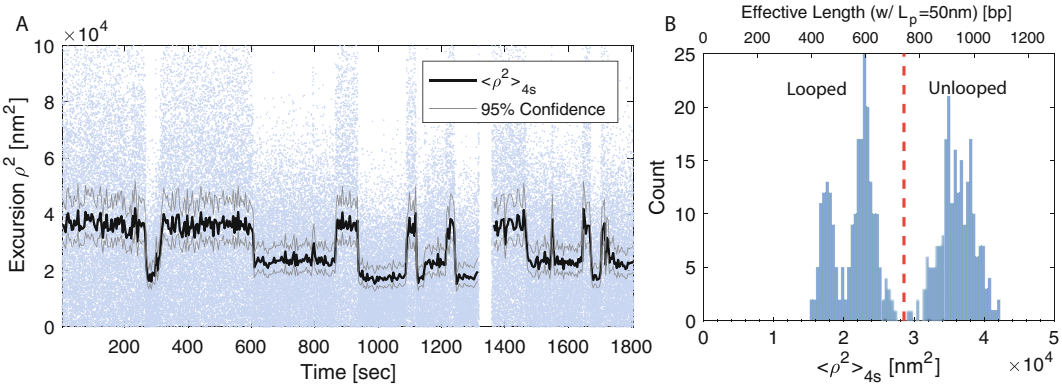

Fig. 7 Tethered particle excursions in presence of 1 nM Lac-Repressor. (**a**) Squared-excursion vs. time. *Dots* indicate instantaneous excursions of the particle (*blue dots* online). The *black* trace shows a 4 s moving average of excursions. It switches between values of approximately 4×10^4 nm^2, 2.3×10^4 nm^2, and 1.7×10^4 nm^2. The largest excursion corresponds to when the tether is unlooped. Lower values correspond to looped DNA with different topologies. 95% confidence intervals were calculated using Eq. 10. (**b**) A *histogram* of a 4 s moving average of excursions exhibits three peaks. Squared-excursion can be roughly converted to effective DNA length (*upper axis*) using Eq. 4 with Lp = 50 nm

conformations, LacI-looped states exhibit a variety of topologies (*see* Fig. 7b). For more details about loop topology *see* **Note 11**. Looping probability as defined in Eq. 1, can be measured by calculating the fraction of time that a tether exhibits short RMS-excursions.

1. For each TPM particle trace, inspect the histogram of $<\rho^2>_{4s}$ values to identify ranges corresponding to unlooped and looped states. Choose a mean-squared excursion value as a threshold. Below the threshold, the tether is considered looped, while above the threshold it is unlooped. Note that due to differences in bead size, histograms of mean-squared-excursions are likely to shift slightly from particle to particle. Consequently, slightly different thresholds may be established for individual particles. In the case of the tether shown in Fig. 7b, the threshold was 2.8×10^4 nm^2.
2. The total time spent in each state is simply a sum of the number of samples above (unlooped) or below (looped) the threshold. Looping probability was calculated on a per-particle basis using Eq. 1.
3. The looping probability for an ensemble of particles in identical conditions can be averaged together using a total-duration weighted average:

$$\overline{p_{\text{loop}}} = \frac{\sum_i p_i^{\text{loop}} \cdot T_i^{\text{total}}}{\sum_i T_i^{\text{total}}}. \tag{14}$$

The normal-approximation of the weighted sample variance can be calculated as

$$s_{\mathrm{W}}^2 = \frac{\sum_i T_i^{\mathrm{loop}} \cdot \left(p_i^{\mathrm{loop}} - \overline{p_{\mathrm{loop}}}\right)^2}{\sum_i T_i^{\mathrm{total}}}. \tag{15}$$

The weighted standard error of the mean can be estimated as

$$\mathrm{SEM_w} \approx \sqrt{\frac{s_{\mathrm{W}}^2 \cdot \sum_i T_i^{\mathrm{total}} 2}{\left(\sum_i T_i^{\mathrm{total}}\right)^2}}. \tag{16}$$

4. After analyzing the data for each LacI concentration, a titration curve can be assembled and fit to Eq. 2 assuming uninterrupted occupancy of O_{S} (Fig. 8). The fit yields a K_{D} of 0.82 ± 1.76 nM

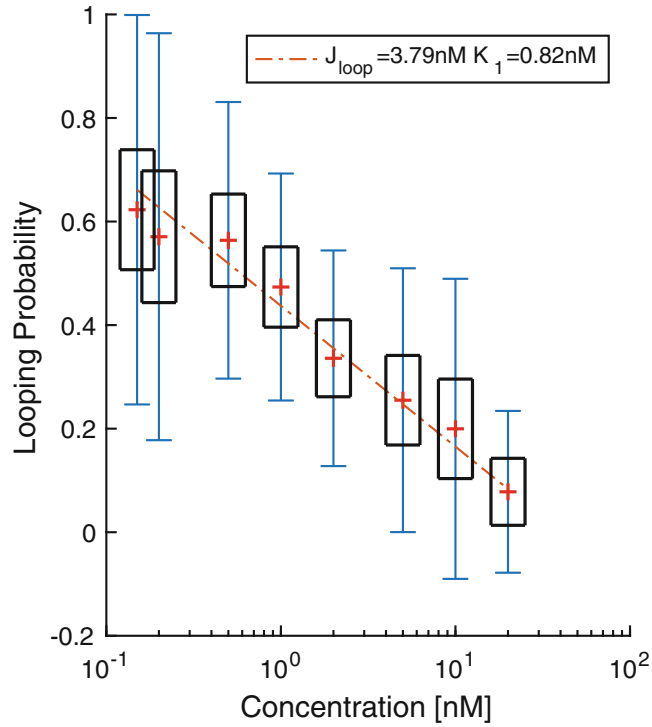

Fig. 8 LacI titration for a 400 bp O_{S}–O_1 loop. Markers (+, *red* online) indicate the average looping probability at each concentration. *Black boxes* indicate $\pm 1.96 \times \mathrm{SEM_W}$ confidence limits as determined using Eq. 17. Error bars (*blue* online) indicated weighted standard deviation defined by Eq. 16. The *dashed line* corresponds to linear fit of data (Eq. 2) to estimate J_{loop} and K_1. A minimum of 27 tethers were measured at each concentration, with each particle being tracked for an average of 1400 s

for LacI binding to O_1 and a J factor of 3.79 ± 0.77 nM. These indicate that tethering LacI 400 bp away at the O_S site increases the effective concentration of LacI at the O_1 site fourfold with respect to the 1 nM free LacI concentration of the solution.

3.9 Conclusion

This chapter is a description of the materials necessary to perform a typical TPM experiment and includes references to software for capturing and analyzing TPM data (Subheadings 2.1 and 3.6). While TPM is relatively simple to implement, care must be taken to ensure that the time-scales of a process of interest match the temporal resolution of the technique. To that end, approximating the tether as a Hookean spring yields a useful first-order approximation of the time-scales necessary to resolve different molecular conformations (Eqs. 7–13).

As an example, this TPM protocol was used to quantitatively assess how *lac* repressor concentration regulates the stability of loops in a DNA sequence flanked by *lac* operators. For these experiments, the effective tether lengths of the various DNA conformations intermittently switched between approximately 400 and 900 bp. Distinguishing the TPM excursions associated with those looped and unlooped states required observations lasting 1–2 s (Eq. 13). LacI-induced loop states typically persist for several seconds to minutes, so TPM is an ideal approach for this system. However, TPM experiments are somewhat tunable in that measuring even faster dynamics using shorter observation times would be possible for shorter tethers or molecules that have stiffer effective spring constants, both of which yield correspondingly lower TPM time constants (Eq. 7).

In this example, a *lac* titration was used to assess the effect of both looping energetics (characterized by the J factor) and operator occupancy via the approximation in Eq. 2. An effective J factor of 3.79 ± 0.77 nM and a dissociation constant $K_D \approx 0.82 \pm 1.76$ nM for O_1 are commensurate with what has been reported previously [19]. Beyond simply distinguishing looped and unlooped states, TPM also reveals variation in DNA loop conformations, which manifest as distinct peaks in the histogram of particle excursions shown in Fig. 7b. In fact, other authors have used TPM, combined with analysis methods based on Bayesian statistics and hidden Markov-models, to characterize looped conformations, revealing differences that would be otherwise unobservable [31, 35].

In summary, TPM is a versatile technique, useful for assessing protein–DNA interactions and capable of revealing protein-induced DNA loop conformations that would be difficult to detect with other techniques. Moreover, the discussion of the technical underpinnings of TPM presented here is not exclusive to DNA, but rather applies to any linear macromolecule. Consequently, both the technique and analytical methods presented in this chapter can be adapted to a wide variety of molecular systems.

4 Notes

1. For a Hookean spring potential, particle positions along X and Y are independent and are drawn from the distribution in Eq. 5. In the steady-state limit, Eq. 5 simplifies to a Gaussian with variance $\sigma^2 = \frac{k_B T}{K}$. Assuming the spring constant is the same along both X and Y, a change of variable from the joint probability distribution $P(x, y) = P(x)P(y)$ to $P\left(\rho = \sqrt{(x-\bar{x})^2 + (y-\bar{y})^2}\right)$ yields a Rayleigh distribution

$$P(\rho) = \frac{\rho}{\sigma^2} e^{-\frac{\rho^2}{2\sigma^2}}. \tag{17}$$

It is important to note that $\langle \rho^2 \rangle_\tau$ is not simply the variance $\left(\mathrm{Var}(\rho) = \left\langle (\rho - \overline{\rho})^2 \right\rangle\right)$. Rather, in the limit of $\tau \to \infty$, $\langle \rho^2 \rangle = 2\sigma^2$. Consequently, although the ρ-distribution (Eq. 18) is non-normal, the Fisher test used in Eq. 12 still applies to $\langle \rho^2 \rangle$ since σ comes from the normal distributions of X and Y positions.

2. In most cases a standard research-grade microscope equipped with an objective with NA > 1 is sufficient for observing tethered motion. Particles can be imaged with either dark-field or bright-field contrast. For bright-field, it is helpful to image using a contrast enhancement scheme such as DIC or phase-contrast microscopy. In this chapter we present methods for both dark-field and DIC imaging; in principle the particle tracking algorithms could also be adapted for phase-contrast microscopy.

   The choice of camera is slightly more specific. In selecting a camera one needs to consider the camera speed (frame rate), minimum exposure time, and effective pixel size when combined with the objective. Equation 7 provides an estimate of the minimum time interval required to assess Brownian (uncorrelated) motion of a particle. To maximize data-capture rates, roughly estimate the necessary frame rate with $1/\tau$. (Slower rates can be used in conjunction with longer measurement periods.) Care must also be taken to minimize exposure time. Excessive exposure time effectively blurs the image of the particle and shrinks the measured RMS-excursion [34]. For an exposure of δt, the measured RMS-excursion decreases by a factor of approximately.

$$\rho_{\mathrm{measured}} \approx \rho \frac{\tau}{\delta t}\left(1 - e^{-\frac{\delta t}{\tau}}\right). \tag{18}$$

   The experiments presented here were conducted with an exposure time of 1 ms. Using the estimate of τ given in Eq. 7

this corresponds to a scale factor of 0.98; although, as noted in the introduction, near-wall drag effects tend to increase τ, meaning that the actual scaling effect is smaller.

The effective resolution of the camera needs to be chosen to accurately localize the particle by at least an order of magnitude less than the expected RMS-excursion. In the presence of moderate noise, the tracking algorithms used here localize a particle centroid to within about 5–10% of a pixel, and improve with less noise. For our system, the combination of camera and 100× objective has a pixel size of about 65 nm, yielding an accuracy of 3–6 nm, which is sufficient for discriminating between $\rho_{\mathrm{RMS}_{\mathrm{unlooped}}} = 180$ nm and $\rho_{\mathrm{RMS}_{\mathrm{looped}}} = 130$ nm.

3. The widespread use of particle tracking techniques in various fields has led to the development of numerous packages implemented in various computer languages; *see* http://www.physics.emory.edu/faculty/weeks//idl/ for more software.
4. α-casein can be difficult to weigh and dissolve. Therefore, it is helpful to prepare a stock solution of 0.2% w/v in 1× Phosphate Buffered Saline and store at 4 °C. Dried α-casein should be stored at −20 °C per the manufacturer's instructions.
5. Plasmid pYY_I1_400 (available upon request) was constructed using Gibson assembly (New England Biolabs, Ipswitch, MA) to simultaneously insert five synthetic fragments into the BsaI site of pBR322. The first fragment included the T7A1 promoter with CTP-dependent stall site at +37. Coupling to the other fragments positioned a proximal O_S operator site at +261, a distal O_1 operator site at +660, and a terminator at +1272. *See* supplementary info for the sequence.
6. Primers should have strong hybridization (GC-rich) at the 3′-end from which extension must proceed. Many researchers select primers with G and/or C as the final two bases. Primers should also be selected to minimize intramolecular hairpins and intermolecular pairing that would interfere with hybridization to the template strands. Oligo suppliers offer web pages with programs for predicting hybridization that might interfere, and they are useful for discarding undesirable base pairing. In practice, these predictions are not always accurate and several primer pairs for a given template sequence may need to be screened to optimize the yield.
7. Parafilm chamber spacers should be cut to form two 1 mm-wide channels that lead into a larger 5 mm × 10 mm channel that forms the central chamber. Parafilm spacers can be cut by hand using a straight-razor or scalpel using the template in Fig. 9. Alternatively, a vector template is available for automated Laser cutting. *See* Supplementary Information. A 50 W CO_2 laser cutter with the power set to 90% and pulse frequency of 500 PPI cuts Parafilm without excess melting or charring.

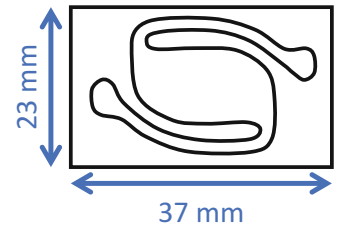

Fig. 9 Parafilm spacer template

8. Thermocycling parameters may require adjustment to optimize PCR yield and specificity. *See* New England Biolabs website for tips on maximizing PCR product [36].
9. Most standard UV-Visible spectrophotometers can be used to measure absorption at 260 and 280 nm. A NanoDropLite Spectrophotometer from Thermo Fisher is convenient for determining DNA concentrations.
10. Based on the estimates in Subheading 1.1, 1.12 s should provide enough data to resolve the two populations with 95% significance; however, we chose 4-s-long windows which have often been used for TPM experiments [20].
11. Due to the torsional flexibility of DNA over length scales larger than 100 bp, LacI binding between two operators can generate a number of different loop topologies [13, 19, 20]. Each results in a slightly different effective tether length. For the 909 bp sequence containing the O_S and O_1 operators separated by 400 bp, $<\rho^2>_{4s}$ is expected to switch between $\approx 3 \times 10^4$ nm^2, corresponding to the unlooped state, and a looped states around $<\rho^2>_{4s} \approx 2 \times 10^4$ nm^2. Variation in effective loop lengths are due to the switching between alternate loop conformations. Figure 7b depicts a tether transitioning between what appear to be three distinct states. The largest corresponds to the unlooped state and the lower two correspond to looped topologies. Based on Monte-Carlo simulations and fitting TPM data to hidden Markov models, the larger of the two looped state likely corresponds to the DNA forming a crossed-loop, while the shortest state corresponds to the DNA in one of a few different uncrossed topologies [13, 19, 20].

Acknowledgements

We would like to thank Kathleen Matthews for graciously providing us with the *lac* repressor used in this work. We also acknowledge former Finzi Lab members Chiara Zurla, Carlo Manzo, Suleyman Ucuncuoglu, and Sandip Kumar who forged earlier versions of our TPM protocols. This work was supported by the NIH, Grant: R01 GM084070.

References

1. Gelles J, Schnapp BJ, Sheetz MP (1988) Tracking kinesin-driven movements with nanometre-scale precision. Nature 331:450–453. doi:10.1038/331450a0
2. Schafer DA, Gelles J, Sheetz MP, Landick R (1991) Transcription by single molecules of RNA polymerase observed by light microscopy. Nature 352:444–448. doi:10.1038/352444a0
3. Ucuncuoglu S, Engel KL, Purohit PK et al (2016) Direct characterization of transcription elongation by RNA polymerase I. PLoS One 11:e0159527. doi:10.1371/journal.pone.0159527
4. Vanzi F, Vladimirov S, Knudsen CR et al (2003) Protein synthesis by single ribosomes. RNA 9:1174–1179. doi:10.1261/rna.5800303.these
5. Gao N, Shearwin K, Mack J et al (2013) Purification of bacteriophage lambda repressor. Protein Expr Purif 91:30–36. doi:10.1016/j.pep.2013.06.013
6. Wang H, Dodd IB, Dunlap DD et al (2013) Single molecule analysis of DNA wrapping and looping by a circular 14mer wheel of the bacteriophage 186 CI repressor. Nucleic Acids Res 41:5746–5756. doi:10.1093/nar/gkt298
7. Priest DG, Kumar S, Yan Y et al (2014) Quantitation of interactions between two DNA loops demonstrates loop domain insulation in E. coli cells. Proc Natl Acad Sci U S A 111:E4449–E4457. doi:10.1073/pnas.1410764111
8. Laurens N, Bellamy SRW, Harms AF et al (2009) Dissecting protein-induced DNA looping dynamics in real time. Nucleic Acids Res 37:5454–5464. doi:10.1093/nar/gkp570
9. Laurens N, Rusling DA, Pernstich C et al (2012) DNA looping by FokI: the impact of twisting and bending rigidity on protein-induced looping dynamics. Nucleic Acids Res 40:4988–4997. doi:10.1093/nar/gks184
10. Nir G, Lindner M, Dietrich HRC et al (2011) HU protein induces incoherent DNA persistence length. Biophys J 100:784–790. doi:10.1016/j.bpj.2010.12.3687
11. Pouget N, Turlan C, Destainville N et al (2006) IS911 transpososome assembly as analysed by tethered particle motion. Nucleic Acids Res 34:4313–4323. doi:10.1093/nar/gkl420
12. Zurla C, Manzo C, Dunlap D et al (2009) Direct demonstration and quantification of long-range DNA looping by the λ bacteriophage repressor. Nucleic Acids Res 37:2789–2795. doi:10.1093/nar/gkp134
13. Johnson S, Lindén M, Phillips R (2012) Sequence dependence of transcription factor-mediated DNA looping. Nucleic Acids Res 40:7728–7738. doi:10.1093/nar/gks473
14. Fan HF (2012) Real-time single-molecule tethered particle motion experiments reveal the kinetics and mechanisms of Cre-mediated site-specific recombination. Nucleic Acids Res 40:6208–6222. doi:10.1093/nar/gks274
15. Simons A, Tils D, von Wilcken-Bergmann B et al (1984) Possible ideal lac operator: Escherichia coli lac operator-like sequences from eukaryotic genomes lack the central G X C pair. Proc Natl Acad Sci U S A 81:1624–1628. doi:10.1073/pnas.81.6.1624
16. Frank DE, Saecker RM, Bond JP et al (1997) Thermodynamics of the interactions of lac repressor with variants of the symmetric lac operator: effects of converting a consensus site to a non-specific site. J Mol Biol 267:1186–1206. doi:10.1006/jmbi.1997.0920
17. Jeong J, Le TT, Kim HD (2016) Single-molecule fluorescence studies on DNA looping. Methods 105:34–43. doi:10.1016/j.ymeth.2016.04.005
18. Phillips R, Kondev J, Theriot J (2009) Beam theory: architecture for cells and skeletons. In: Morales M (ed) Physical biology of science. Garland Science, Taylor and Francis Group, LLC, New York, NY, pp 371–373
19. Han L, Garcia HG, Blumberg S et al (2009) Concentration and length dependence of DNA looping in transcriptional regulation. PLoS One 4(5):e5621. doi:10.1371/journal.pone.0005621
20. Towles KB, Beausang JF, Garcia HG et al (2009) First-principles calculation of DNA looping in tethered particle experiments. Phys Biol 6:25001. doi:10.1016/j.bpj.2008.12.3653
21. Priest DG, Cui L, Kumar S et al (2014) Quantitation of the DNA tethering effect in long-range DNA looping in vivo and in vitro using the Lac and λ repressors. Proc Natl Acad Sci U S A 111:349–354. doi:10.1073/pnas.1317817111
22. Kumar S, Manzo C, Zurla C et al (2014) Enhanced tethered-particle motion analysis reveals viscous effects. Biophys J 106:399–409. doi:10.1016/j.bpj.2013.11.4501

23. Segall DE, Nelson PC, Phillips R (2006) Volume-exclusion effects in tethered-particle experiments: Bead size matters. Phys Rev Lett 96:1–4. doi:10.1103/PhysRevLett.96.088306
24. Nelson PC, Zurla C, Brogioli D et al (2006) Tethered particle motion as a diagnostic of DNA tether length. J Phys Chem B 110:17260–17267. doi:10.1021/jp0630673
25. Pouget N, Dennis C, Turlan C et al (2004) Single-particle tracking for DNA tether length monitoring. Nucleic Acids Res 32:e73. doi:10.1093/nar/gnh073
26. Dietrich HRC, Rieger B, Wiertz FGM et al (2009) Tethered particle motion mediated by scattering from gold nanoparticles and dark-field microscopy. J Nanophoton 3:31795. doi:10.1117/1.3174445
27. Marko JF, Siggia ED (1995) Stretching DNA. Macromolecules 28:8759–8770. doi:10.1021/ma00130a008
28. Rubinstein M, Colby R (2003) Polymer physics. Oxford University Press, New York, NY
29. Brinkers S, Dietrich HRC, De Groote FH et al (2009) The persistence length of double stranded DNA determined using dark field tethered particle motion. J Chem Phys 130 (21):215105. doi:10.1063/1.3142699
30. Lindner M, Nir G, Vivante A et al (2013) Dynamic analysis of a diffusing particle in a trapping potential. Phys Rev E 87:1–5. doi:10.1103/PhysRevE.87.022716
31. Beausang JF, Nelson PC (2007) Diffusive hidden Markov model characterization of DNA looping dynamics in tethered particle experiments. Phys Biol 4:205–219. doi:10.1088/1478-3975/4/3/007
32. Bevan MA, Prieve DC (2000) Hindered diffusion of colloidal particles very near to a wall: revisited. J Chem Phys 113:1228–1236. doi:10.1063/1.481900
33. Parthasarathy R (2012) Rapid, accurate particle tracking by calculation of radial symmetry centers. Nat Methods 9:724–726. doi:10.1038/nmeth.2071
34. Han L, Lui BH, Blumberg S et al (2009) Calibration of tethered particle motion experiments. In: Benham CJ, Harvey S, Olson WK et al (eds) Mathematics of DNA structure, function and interactions. Springer, New York, NY, pp 123–138
35. Johnson S, van de Meent J-W, Phillips R et al (2014) Multiple LacI-mediated loops revealed by Bayesian statistics and tethered particle motion. Nucleic Acids Res 42:10265–10277. doi:10.1093/nar/gku563
36. NEB (2015) PCR reagents. https://www.neb.com/~/media/NebUs/Files/Brochures/PCR_Brochure.pdf. Accessed 14 Nov 2016

Chapter 18

Single-Molecule Measurements Using Acoustic Force Spectroscopy (AFS)

Douwe Kamsma and Gijs J.L. Wuite

Abstract

Single-molecule force spectroscopy is a powerful tool to investigate the forces and motions related to interactions of biological molecules. Acoustic Force Spectroscopy (AFS) is a recently developed measurement tool to study single molecules making use of acoustic standing waves. AFS permits high experimental throughput, because many individual molecules can be manipulated and tracked in parallel. Moreover, a wide range of forces can be applied, as well as a force loading rate with range of six orders of magnitude. At the same time, AFS stands out because of its simplicity and the compactness of the experimental setup. Even though the AFS setup is simple, it can still be challenging to perform high-quality measurements. Here we describe, in detail, how to setup, perform, and analyze an AFS measurement.

Key words Acoustic Force Spectroscopy (AFS), DNA tethering, Multiplexed single-molecule method, Molecular biophysics

1 Introduction

Using single-molecule experiments, properties of individual biomolecules are investigated in order to distinguish inhomogeneity and stochasticity, which are difficult to measure in ensemble measurements. Force spectroscopy explores biomechanical properties and can thus provide insights in the structure, binding properties, and interactions of biomolecules [1, 2]. Techniques that can be used for this purpose are, for example, atomic force microscopy, optical tweezers, and magnetic tweezers [3, 4]. Here we discuss AFS, a recently developed technique that uses acoustic standing waves to apply forces on a field of single tethered biomolecules. The main advantage of AFS is that it is relatively simple and compact, and that it works in a highly multiplexed fashion. Forces in AFS can be applied in the range of sub-pN to hundreds of pNs, with force loading rates ranging between 10^{-4} pN/s and 10^{2} pN/s, on thousands of constructs in parallel. It has been shown that AFS can be used to study the mechanical properties of DNA molecules,

Erwin J.G. Peterman (ed.), *Single Molecule Analysis: Methods and Protocols*, Methods in Molecular Biology, vol. 1665, DOI 10.1007/978-1-4939-7271-5_18,

the strength of DNA–protein interactions and to probe the energy landscape of antigen–antibody bonds [5].

The original implementation AFS [5] had several drawbacks and the technique was greatly improved as described in Kamsma et al., 2016 [6]. A newly developed transparent piezo element [7] was combined with AFS to allow for trans illumination, improving the tracking accuracy and the measurable field of view. It was also shown that AFS can be used with high NA water- and oil-immersion objectives. The acoustic properties of AFS were improved by optimizing the layer thickness of the chips in order to generate a more efficient force at the coverslip side. These improvements resulted in better optical and acoustic performances making the AFS more compatible for integration in existing microscopes, giving rise to many new measurement possibilities.

Even though the AFS employs a relatively simple experimental setup and is even commercially available (LUMICKS B.V.), it can still be challenging to perform a good single-molecule measurement. Therefore we describe here in detail how to perform an AFS experiment on DNA molecules. We will list all hardware, software, and biomaterials necessary to perform an AFS measurement. Furthermore, we will describe in detail the biological protocols used to make a DNA tethered surface. Lastly, we will describe step-by-step an AFS measurement, where we select single DNA tethers, calibrat the force per construct and make an overstretching curve of DNA.

2 Material

2.1 AFS Experimental Setup

Most AFS experiments are done with the AFS module or the AFS stand-alone from LUMICKS B.V. The AFS stand-alone is a complete system including microscope, while the AFS module only includes the chip, the holder and the function generator. Here, measurements are performed with the LUMICKS AFS module together with the following additional equipment is used.

1. Inverted microscope: Nikon eclipse TI equipped with CFI Plan Fluor DLL 40×, 0.75 NA objective (Nikon) and a tube 0.45× c-mount adaptor (Nikon, MQD42040).
2. Illumination light: a collimated LED (Thorlabs, M660L4).
3. Digital camera: 1 Megapixel CMOS (Thorlabs, DCC3240M), recording 60 frames per second at full resolution.
4. Translation stage: multi-axis piezo translation stage (PI, P-517.2CL), driven by a digital piezo controller (PI, E-710.4CL).
5. Computer: desktop computer, with two Xeon E5 2643v2 processors to run the live tracking software.
6. Oscilloscope: Two channels signal input and data readout by the computer.

2.2 DNA Labeling

1. pKYBI plasmid (8393 bp; *see* **Note 1**).
2. Cutting enzymes: EcoRI-HF (R3101S) and KpnI-HF (R3142S), used in CutSmart Buffer (New England Biolabs).
3. Nucleotides: 2 mM dTTP and 0.4 mM Biotin-14-dATP.
4. Klenow Fragment exo-.
5. Custom KpnI_Dig primer: 5′-C(T-Dig)CTC(T-Dig)CT CTC (T-Dig)TC TC(T-Dig) CTT CTC TT GTAC-3′.
6. T4 DNA Ligase and T4 DNA Ligase buffer (Thermo Scientific).
7. Nuclease-free sterile water.
8. PCR Purification kit: we use QIAquick (QIAGEN).
9. Centrifugal filters: Amicon Ultra 0.5 mL (Sigma-Aldrich).
10. Microcentrifuge tubes: DNA LoBind Tubes (Eppendorf).
11. dH_2O: ultrapure water.

2.3 Surface Chemistry Buffers

1. Bleach: <5% (w/v) sodium hypochlorite.
2. 1 M $Na_2S_2O_3$ in ultrapure water.
3. PBS buffer: 138 mM NaCl, 2.7 mM KCl and 10 mM phosphate pH 7.4; supplemented with 5 mM sodium azide and 0.5 mM EDTA.
4. 20 μg/mL anti-digoxigenin antibody from sheep (Sigma-Aldrich) in PBS. Store aliquoted at −20 °C.
5. Streptavidin coated polystyrene microspheres: 4.5 μm diameter, 0.5% (w/v). Stored at 4 °C.
6. Casein buffer: stock solution 1% (w/v) in PBS.
7. BSA buffer: stock solution 1% (w/v) in PBS.
8. Pluronic (F-127) buffer: stock solution 5% (w/v) in PBS.
9. DNA measuring buffer: PBS buffer supplemented with 0.02% (w/v) Casein and 0.02% (w/v) Pluronic.
10. 0.5 M Borate, pH 8.3; supplemented with 5 mM sodium azide and 0.5 mM EDTA.
11. 0.5 M HEPES, pH 7.5.
12. Digoxigenin-NHS: ε-(Digoxigenin-3-0-acetamido)caproic acid N-hydroxysuccinimide ester.

3 Methods

3.1 Calibrating the Impedance of the AFS Chip

The acoustic and electric properties of the AFS chip can be modeled [6]; however, we have noticed that significant deviations from the ideal behavior exist from chip to chip. To account for that, we calibrate each AFS chip. The resonance frequencies and the

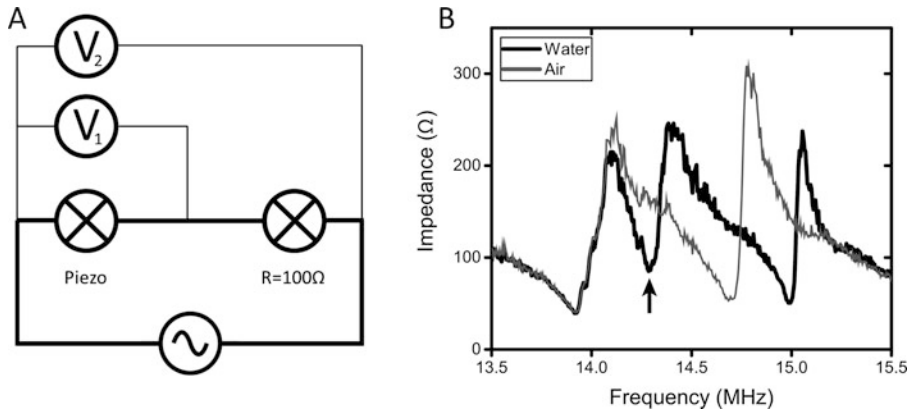

Fig. 1 Measuring the impedance of the AFS chip. (**a**) Electric diagram used to measure the impedance of the AFS chip. (**b**) A graph showing the impedance of the AFS chip measured between 13.5 and 15.5 MHz filled with air and water channel. The arrow shows the used resonance for this chip configuration (14.3 MHz)

impedance (Z) of the chip can be determined electronically in the following way.

1. Connect the AFS chip to the function generator and add a resistance (R) in series to the chip. Measure with the oscilloscope the electrical potential (V) over the piezo and electrical potential over the piezo plus the resistance (*see* Fig. 1a).
2. The impedance of the AFS chip can be calculated using Ohm's law:

$$\boldsymbol{V}_R = \boldsymbol{V}_{\text{all}} - \boldsymbol{V}_{\text{piezo}}$$
$$I = \frac{V_R}{R} = \frac{V_{\text{all}} - V_{\text{piezo}}}{R}$$
$$Z = \frac{V_{\text{piezo}}}{I} = \frac{V_{\text{piezo}} \times R}{V_{\text{all}} - V_{\text{piezo}}}$$

   Here I is the electric current.
3. Connect the oscilloscope to the computer and sweep the frequency while keeping the voltage constant. Using the equations above, the impedance can be calculated. An example is shown in Fig. 1b, here a resonance frequency is found at 14.3 and 15.0 MHz. The impedance is around 80 Ω for both these resonance frequencies.

3.2 DNA Labeling Protocol for Surface Tethering

DNA labeling is performed in three steps (Fig. 2). First a DNA plasmid is linearized by cutting it with two digesting enzymes and directly labeled at the 5′ side with Biotin using polymerase and biotin-labeled nucleotides. In the second step, the 3′ is labeled with digoxigenin using a primer. Finally, the DNA is ligated to

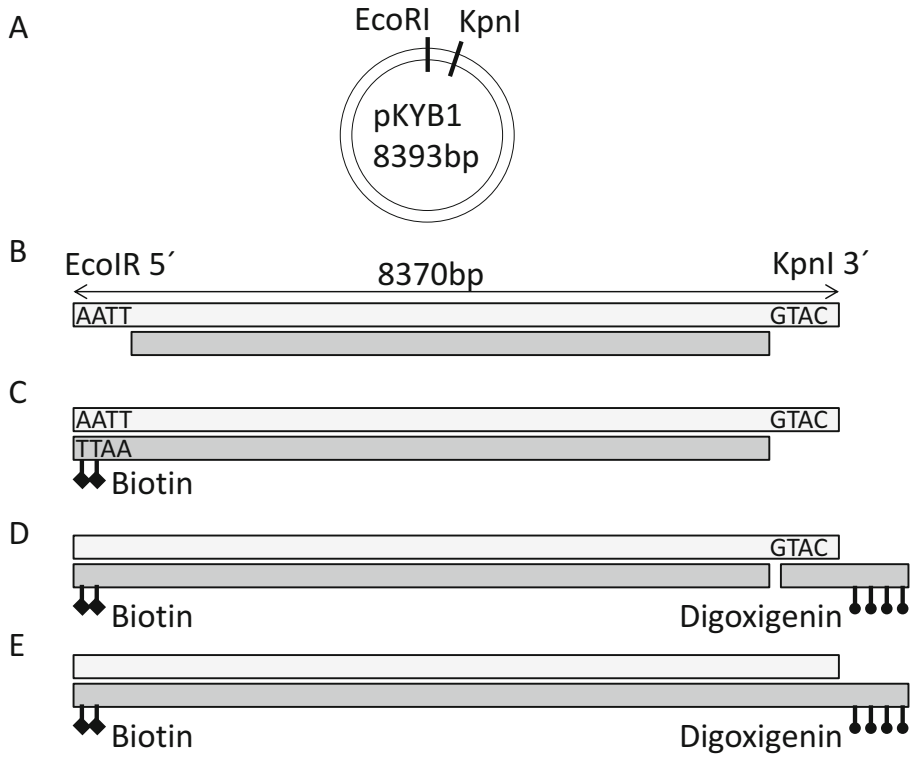

Fig. 2 A schematic drawing of the DNA labeling protocol. In the first step (**a**) the pKYBI DNA plasmid is cut with EcoRI and KpnI. This results in a DNA strand with an overhang at the 5′ end at one side and an overhang on the 3′ end at the other side (**b**). First the 5′ side is labeled via polymerase with Biotin-14-dATP (**c**). After the primer can be attached to the 3′ end side (**d**). In the last step the DNA is ligated (**e**)

repair the backbone of the DNA. *See* **Note 2** for other constructs. The detailed procedure is as follows.

1. Mix 27 μL dH_2O, 5 μL 10× Cut Smart buffer, 15 μL pKYB1 (216 ng/μL), 1.5 μL EcoRI-HF and 1.5 μL KpnI-HF. Volume of pKYB1 and dH_2O can be adjusted according to the pKYB1 concentration.
2. Incubate for 45 min at 37 °C (a to b in Fig. 2).
3. Use PCR Purification Kit to remove the remaining nucleotides and elute in 60 μL (*see* **Note 3**).
4. Mix 23.5 μL dH_2O, 5 μL 10× Klenow buffer, 60 μL pKYBI cut and purified (**step 3**), 8 μL of 0.4 mM Biotin-14-dATP, 1.5 μL of 2 mM dTTP and 2 μL Klenow polymerase exo-.
5. Incubate at 37 °C for 1 h (b to c in Fig. 2).
6. Use PCR Purification Kit to remove the remaining nucleotides and elute in 30 μL (*see* **Note 3**).
7. Mix 5 μL 10× T4 DNA Ligase buffer, 5 μL dH_2O, 30 μL pKYBI cut and purified vector (**step 6**), 8 μL KpnI-DIG primer, 2 μL T4 DNA Ligase.

8. Incubate at 23 °C for 2 h (c to e in Fig. 2).
9. Use Amicon Ultra 0.5 mL centrifugal filters to purify the DNA construct.

3.3 Labelling Microspheres with Digoxigenin

Microspheres labelled with digoxigenin are used to stick beads on the surface in order to correct for drift during the measurement.

1. Mix 8 μL streptavidin-coated polystyrene, microspheres with 30 μM digoxigenin-NHS, 100 mM borate and 0.05% (w/v) Pluronic in a total volume of 400 μL.
2. Incubate for 3 h at room temperature, while tumbling the sample constantly.
3. Wash the microspheres by spinning down with 2000 × *g*, removing the residue and add 1 mL of 10 mM HEPES plus 0.1% Pluronic. Repeat the washing step two times.
4. Finally, store these beads in 1 mL of 10 mM HEPES plus 0.1% Pluronic at 4 °C.

3.4 Preparation of DNA Tethered to the Surface and Microspheres

DNA tethered surfaces are prepared fresh each day to prevent interference between measurements and degradation of the surface. All steps are performed at room temperature and liquids are flushed in at room temperature.

1. To clean the surface, incubated bleach for at least 10 min. After, flush the channel dry and flush bleach through again, repeat this step multiple times. End by flushing it dry and incubated Sodium Thiosulfate for 10 min, this will inactivate the residual bleach. Flush with MQ and flush dry. The chamber is now cleaned and ready for surface preparation.
2. Flush in with PBS and make sure that there are no bubbles in the chamber. Flush 30 μL of 20 μg/mL Anti-Digoxigenin and let it incubate for 20 min.
3. For passivation, use a combination of BSA and pluronic is used. First flush with 400 μL of PBS with 0.2% (w/v) BSA and let this incubate for 30 min. Then flush with 400 μL of PBS with 0.5% (w/v) pluronic, Incubate for 30 min.
4. To attach the DNA to the surface, flush first 400 μL of the DNA buffer. Then Flush in the 30 μL of 11.4 pg/μL DNA and let it incubate for 20 min.
5. Clean the microspheres before measuring. Take 10 μL of microsphere solution, add 1 mL DNA measuring buffer and spin down for 2 min at 2000 × *g* and remove the residue. Add 1 mL DNA measuring buffer again, spin down for 2 min at 2000 × *g* and remove residue. Now fill up to 30 μL with DNA

measuring buffer and add 1 μL of digoxigenin beads (*see* Subheading 3.3).

6. Flush with DNA measuring buffer. Now flush in the microsphere and let them incubate for 20 min. After, flush out all the microspheres that have not attached to the surface. Be careful not to flush too fast, otherwise your tethers will detach from the surface (*see* **Note 4**). The tethers are now ready for measuring.

3.5 Measurements on Tethered Particles

The tracking software we used is provided with the stand-alone LUMICKS system, a previous academic generation of this software is available online https://figshare.com/articles/AFS_software/1195874 [5]. The tracking software analyzes the images from the camera in real time and also controls the function generator and the piezo stage or step motor. A detailed manual is also provided with the software.

1. The microspheres can be selected by double-clicking on the screen. Their X and Y position are directly tracked and displayed in the preview tap. Algorithms of determining the position of the bead are based on cross correlation (XCOR) [8] or Quadrant interpolation (QI). Where QI is more precise; however, XCOR costs less computation power.
2. Before measuring the z dimension, a look up table (LUT) has to be made, where the range of the LUT has to be bigger than the maximal extension of the molecule. Here (Fig. 3) a 2.8 μm DNA molecule is used, when overstretching the DNA molecule it reaches a length of ~4.8 μm. There the range of the LUT should be bigger than 5 μm.
3. Turn on the Perfect Focus System (PFS), this keeps the objective at a constant distance from the bottom of the flow cell.
4. The measurement can now be started. A typical measurement is shown in Fig. 3.

3.6 Data Analysis

We use a LabVIEW-based program to analyze our data. This program is available online at https://figshare.com/articles/AFS_software/1195874 [5]. Here we explain how single tethered constructs can be selected, forces can be calibrated and force–distance curves can be extracted. The steps required to make a force–distance curve of DNA are shown in Fig. 3.

1. To select single tethers we use a histogram of the XY location of the tethered particle. A typical XY histogram of a particle attached with a single tether is round and has specific RMS value (Fig. 3a). To remove double tethers or other none specific interaction we quantify the XY motion with the RMS and

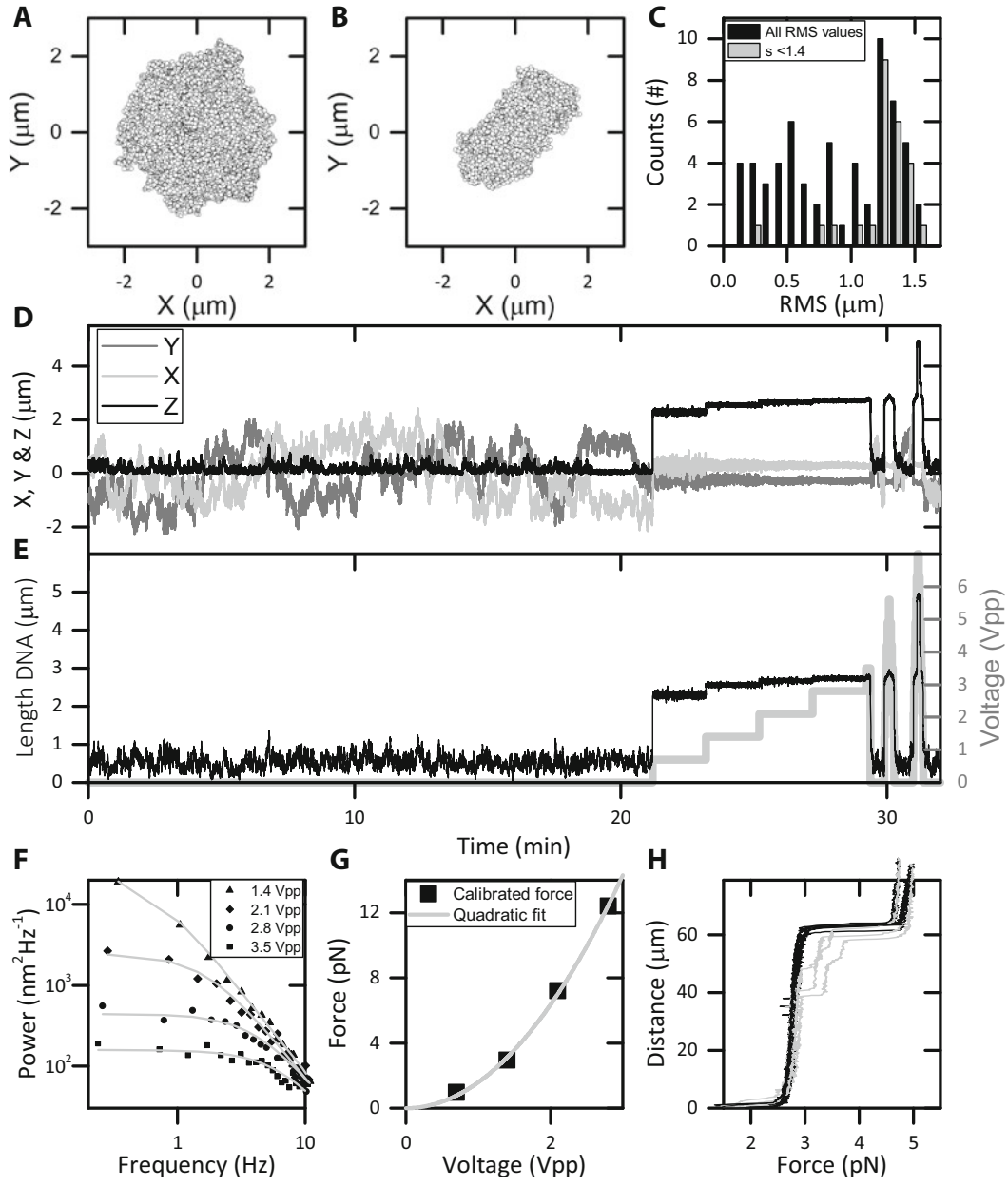

Fig. 3 AFS data analyses tethered particles. **a** and **b** showing XY plot of tethered particle with an RMS of respectively 1.3 and 0.8 μm a symmetry values of 1.1 and 2.5. (**c**) A histogram of the RMS values of one measurement, in black all RMS values are plotted and in gray the RMS values with a symmetry value below 1.4. (**d)** A plot of the X, Y, and Z values measured. (**e**) A plot of the end-to-end length of the DNA molecule and the applied voltage on the piezo. (**f**) Measured and fitted power-spectra values of the microsphere's X and Y positions using a Lorentzian function (piezo driven at 14.3 MHz). (**g**) Forces acting on the tethered microsphere as determined from power-spectrum analysis (panel **f**), in gray a quadratic fit yielded a quadratic constants of 1.6 pN/V^2. (**h**) Overstretching curve of 8.4-kbp torsionally unconstrained pKYBI DNA, using the force voltage relation calculated in panel **g**

symmetry number [9]. A higher symmetry value can suggest a double tether (Fig. 3b). However, some XY pattern cannot be explained with single or double tethers only (*see* **Note 5**). Here, we excluded all tether with a symmetry values lower than 1.4 (Fig. 3c).

2. Remove system drift by subtracting the displacements of at least two surface-attached microsphere.
3. To determine the end-to-end length of the DNA molecule, the anchoring point to the surface should be found. This is done in a region where no force is applied to the tether (0–20 min Fig. 3d, e). The X and Y movement is subtracted with their average location and the minimum of the Z location is used as the zero position where the bead touches the surface. Using Pythagoras' theorem, the end-to-end of the DNA molecule can be calculated.
4. To calibrate the force-voltage relation, a constant force is applied on the molecule (22–20 min Fig. 3d, e). Taking the power spectrum of the X and Y position, the force acting on the tethered microsphere can be derived from the corner frequency [10, 11] (*see* Fig. 3f). To verify power spectrum fit *see* **Note 6**.
5. From theoretical considerations it is known that the force scales quadratically with the voltage [12]. By making a quadratic fit through the measured forces the set-force can be calibrated for different voltages (*see* Fig. 3g).
6. In the final part of the measurement, the voltage is ramped with a square-root function, resulting in a linear force ramp. Using the force–voltage relationship a force–distance curve can be extracted (*see* **Note 7**, for fitting the force–distance curve).

4 Notes

1. The pKYBI plasmid is not commercially available anymore; however, it can be extracted from an *E. coli* strain that contains the plasmid. This can be obtained using miniprep kit (27104, Qiagen). The concentration of a stock can be measured with a Nanodrop.
2. In this chapter it is explained how to make a DNA-tethered construct. After making the construct it is relatively straightforward to flush in other buffers or proteins and measure the mechanical effect on the DNA molecules. We use a Dig::anti-Dig bond to attach the DNA to the surface and Biotin::streptavidin to attach the DNA to the beads. The DNA molecule could also be replaced with any other biomolecule to measure the mechanical properties, as long as it has the digoxigenin and

biotin handles. At last, rupture forces could be measured as seen in Sitters et al. [5] or even more elegantly by using DNA nanoswitches [13].

3. For PCR Purification, the protocol of QIAGEN can be used. We modified the elution volume for optimal reaction concentration of the DNA in the next step. Also, we decreased the centrifugation force to 12,000 $\times$ *g* to reduce nicking of the DNA.
4. Flushing liquid through the flow cell can be tricky: flow drag acting on a bead attached to the surface can result in breaking the construct. To prevent this, flow speeds can be controlled with a syringe pump. Another way to control drag forces is to keep an air column in the syringe, since air is compressible this will slow down the flow in the chamber.
5. XY location histograms of tethered particles can vary substantially in shape due to multiple tethers, nonspecific interactions, inhomogeneous microspheres or irregularities in the surface [14]. By analyzing the XY motion the DNA-tethering protocol can be optimized.
6. The way we fit our power spectrum is described by Norrelykke and Flyvbjerg [11]. It fits the corner frequency and the diffusion coefficient. The corner frequency depends on the force applied; however, the diffusion coefficient dependence could be theoretically predicted from the bead size and the distance from the surface [15]. It is always a good check to see if the theoretically predicted diffusion coefficient overlaps with the fitted one.
7. The force–distance curve of DNA can be fitted with the Worm Like Chain (WLC) model. Since this model uses three non-independent variables it can be quite tricky to get reliable fit values. In Broekmans, O. D. [16] a method is described to do this fitting in a reproducible way.

Acknowledgements

We thank A.S. Biebricher, S.E.D. Haene, and S. Acar for biochemical help; F. Oswald and G. Sitters for collaborating and discussing results. We acknowledge support by NWO VICI as well as a European Research Council (ERC) starting grant (G.J.L.W.).

Competing financial interests
D.K. and G.J.L.W. are inventors on the patent application (PCT/NL2014/050377) covering the acoustic force spectroscopy method. G.J.L.W. is co-owner of LUMICKS B.V.

References

1. Bustamante C, Cheng W, Mejia YX (2011) Revisiting the central dogma one molecule at a time. Cell 144:480–497
2. Brouwer I, Sitters G, Candelli A et al (2016) Sliding sleeves of XRCC4–XLF bridge DNA and connect fragments of broken DNA. Nat Publ Group 535:566–569
3. Ritort F (2006) Single-molecule experiments in biological physics: methods and applications. J Phys Condens Matter 18:R531–R583
4. Neuman KC, Nagy A (2008) Single-molecule force spectroscopy: optical tweezers, magnetic tweezers and atomic force microscopy. Nat Methods 5:491–505
5. Sitters G, Kamsma D, Thalhammer G et al (2014) Acoustic force spectroscopy. Nat Methods 12:47–50
6. Kamsma D, Creyghton R, Sitters G et al (2016) Tuning the music: acoustic force spectroscopy (AFS) 2.0. Methods 105:26–33
7. Brodie GWJ, Qiu Y, Cochran S et al (2014) Optically transparent piezoelectric transducer for ultrasonic particle manipulation. IEEE Trans Ultrason Ferroelectr Freq Control 61:389–391
8. Gosse C, Croquette V (2002) Magnetic tweezers: micromanipulation and force measurement at the molecular level. Biophys J 82:3314–3329
9. Han LIN, Lui B, Blumberg S et al (2009) Calibration of tethered particle motion experiments. In: Mathematics of DNA structure, function and. Springer, New York, pp 123–138
10. te Velthuis AJW, Kerssemakers JWJ, Lipfert J et al (2010) Quantitative guidelines for force calibration through spectral analysis of magnetic tweezers data. Biophys J 99:1292–1302
11. Norrelykke SF, Flyvbjerg H (2009) Power spectrum analysis with least-squares fitting: amplitude bias and its elimination, with application to optical tweezers and atomic force microscope cantilevers. Rev Sci Instrum 81:75103
12. Settnes M, Bruus H (2012) Forces acting on a small particle in an acoustical field in a viscous fluid. Phys Rev E 85:16327
13. Yang D, Ward A, Halvorsen K et al (2016) Multiplexed single-molecule force spectroscopy using a centrifuge. Nat Commun 7:11026
14. Visser EWA, van IJzendoorn LJ, Prins MWJ (2016) Particle motion analysis reveals nanoscale bond characteristics and enhances dynamic range for biosensing. ACS Nano 10:3093–3101
15. Schäffet E, Nørrelykke SF, Howard J (2007) Surface forces and drag coefficients of microspheres near a plane surface measured with optical tweezers. Langmuir 23:3654–3665
16. Broekmans OD, King GA, Stephens GJ et al (2014) DNA twist stability changes with magnesium(2+) concentration. Phys rev Lett 116:258102

Chapter 19

Repurposing a Benchtop Centrifuge for High-Throughput Single-Molecule Force Spectroscopy

Darren Yang and Wesley P. Wong

Abstract

We present high-throughput single-molecule manipulation using a benchtop centrifuge, overcoming limitations common in other single-molecule approaches such as high cost, low throughput, technical difficulty, and strict infrastructure requirements. An inexpensive and compact Centrifuge Force Microscope (CFM) adapted to a commercial centrifuge enables use by nonspecialists, and integration with DNA nanoswitches facilitates both reliable measurements and repeated molecular interrogation. Here, we provide detailed protocols for constructing the CFM, creating DNA nanoswitch samples, and carrying out single-molecule force measurements.

Key words Centrifuge Force Microscope, Single-Molecule Force Spectroscopy, DNA Nanoswitches

1 Introduction

Single-molecule force studies have led to significant insights in biology, including the regulatory role of mechanical force in systems ranging from bleeding to development [1–6]. While instruments such as optical tweezers, magnetic tweezers, and atomic force microscopes (AFM) have matured and gained acceptance as important scientific tools [2, 4], in general, force spectroscopy has found limited adoption among nonspecialists. The high cost of equipment and the required infrastructure (e.g. temperature-regulated, vibration-isolated rooms) is a significant barrier, as is the expertise required to build and operate most single-molecule instruments. Limited throughput poses another important challenge, which is starting to be addressed with multiplexed approaches [7–14]. Furthermore, instrumentation is only part of the equation limiting widespread adoption—the challenge of preparing and analyzing reliable single-molecule assays is an equal challenge, one which is exacerbated by the large volumes of data that result from parallel approaches. To enable the widespread use

Erwin J.G. Peterman (ed.), *Single Molecule Analysis: Methods and Protocols*, Methods in Molecular Biology, vol. 1665, DOI 10.1007/978-1-4939-7271-5_19,

of single-molecule manipulation throughout biomedical and chemical research, all of these challenges must be met.

In 2010, we presented a proof-of-concept Centrifuge Force Microscope (CFM), and demonstrated the ability to carry out thousands of independent single-molecule force spectroscopy experiments in parallel by video-tracking tethered particles subject to centrifugal forces [15]. More recently, we introduced a benchtop CFM that builds upon an instrument that almost all biomedical researchers already have and use: the benchtop centrifuge [16]. This miniature microscope that fits into a standard centrifuge bucket was created to bring high-throughput single-molecule manipulation to nonspecialists. Furthermore, to solve significant issues of sample preparation and data analysis, we integrated modular nanoscale mechanical switches into this next-generation CFM. These nanoswitches serve as tethers that provide a distinct molecular signature, facilitating reliable and automated analysis of the resulting large data sets [16, 17]. In addition, these tethers enable the repeated interrogation of single receptor-ligand pairs, to both increase the throughput of measurements and to reveal heterogeneity at the single-molecule level.

In order to facilitate the adoption of these two techniques, we present detailed protocols here for both the construction of the benchtop CFM and the preparation, integration, and use of DNA nanoswitch samples for performing high-throughput force spectroscopy. We note that while these two technologies work well in tandem, readers interested solely in incorporating DNA nanoswitches into other assays, or in building a CFM for other purposes, will also find the protocols presented here invaluable.

2 Materials

The main component of the Centrifuge Force Microscope (CFM) is a compact optical microscope with a video acquisition system that can be integrated within a benchtop centrifuge. We are using a Thermo Fisher Scientific Heraeus X1R upgraded with computer control module provided by Thermo Fisher Scientific R&D, but any sufficiently-sized commercial centrifuge should be suitable. The microscope design is based on the Thorlabs lens tube system with a few custom parts. This first part of the protocol describes the construction of the optical microscope and the centrifuge modification required for real-time control and image acquisition through a fiber rotary joint. We note that if high-bandwidth, real-time data collection is not needed, video data could be stored locally or streamed via wireless networking [18]. This section concludes with a list of the materials and reagents needed to create the sample chamber and DNA nanoswitch assay.

Table 1
Centrifuge Force Microscope instrumentation part list

Item no.	Vendor	Part number	Description	QTY.
1	Thorlabs	S1LEDM	SM1-Threaded Mount for LED	1
2	Thorlabs	SM1T1	SM1 (1.035″-40) Coupler	1
3	Thorlabs	SM05RR	Retaining Ring for diffuser	1
4	Thorlabs	DG05-220	Light Source Diffuser, Ø1/2″ N-BK7 Ground Glass	1
5	Thorlabs	SM1A6T	Diffuser and sample cell mount	1
6	SI Howard Glass Co	B-270	Ø 25 mm, 0.9 mm Thick	1
7	Kapton Tape	PPTDE-3	Sample Cell Assembly	1
8	VWR	63782-01	Gold Seal, #1 19 mm coverglass	1
9	Thorlabs	SM1L03	Sample Holder, SM1 Lens Tube, 0.3″ Thread Depth	1
10	Thorlabs	SM1V05	Focusing Ø1” SM1 Lens Tube	1
11	Edmund Optics	#86-815	40× Olympus Plan Achromat Objective, 0.65 NA, 0.6 mm WD	1
12	Thorlabs	SM1A3	Objective Adaptor with External SM1 Threads and Internal RMS Threads	1
13	Thorlabs	AC254-100	Tube Len, f = 100.0 mm, Ø1″ Achromatic Doublet, ARC: 400-700 nm	1
14	Thorlabs	SM1RR	Tube Lense SM1 Retaining Ring	1
15	Thorlabs	SM1M20	Objective SM1 Lens Tube Without External Threads, 2″ Long	1
16	Thorlabs	SM1A6T	Adaptor with External SM1 Threads and Internal SM05 Threads, 0.40″ Thick	2
17	–	–	Custom made turning block, aluminum	1
18	Thorlabs	PFE10-P01	Turning Mirror, 1″ Silver Elliptical Mirror, 450 nm to 20 μm	2
19	Thorlabs	SM1NT	Camera SM1 (1.035″-40) Locking Ring, Ø1.25″ Outer Diameter	1
20	Thorlabs	SM1A9	Camera Adaptor with External C-Mount Threads and Internal SM1 Threads	1
21	Allied Vision Technologies	Prosilica GC2450	Sony ICX625 CCD sensor, 2448 × 2050 resolution, 15 fps, 12 bit	1
22	IMC Network	855-10734	MiniMc-Gigabit Twisted Pair to Fiber Media Converter	1
23	PrinceTel	MJX	Fiber Optic Rotary Joint	1

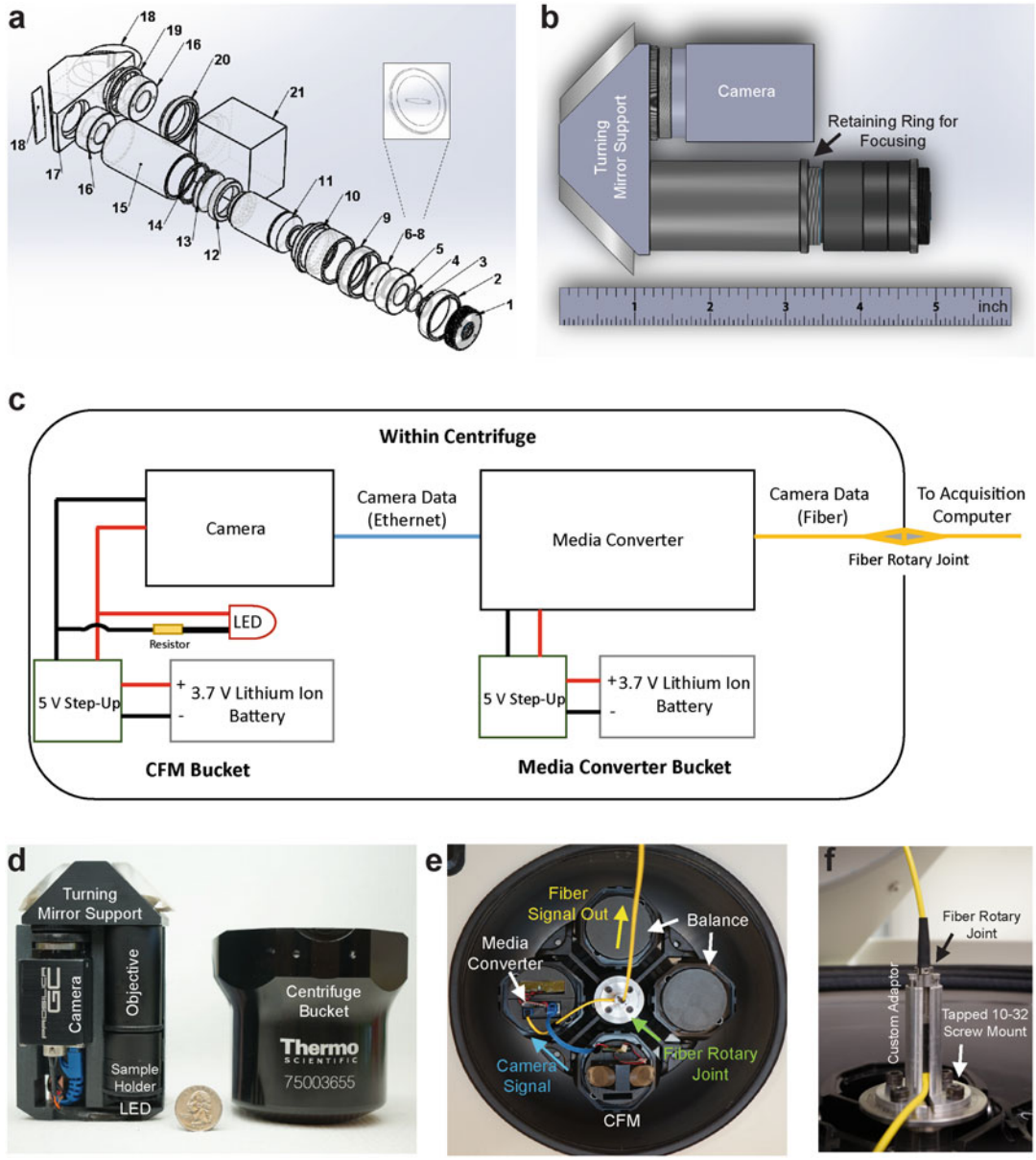

Fig. 1 Design and assembly of the benchtop CFM. (**a**) Exploded view of the CFM. The numbers correspond to the Item No. in Table 1. (**b**) Assembled model of the CFM. (**c**) Electrical and data wiring diagram. (**d**) The CFM module in part of the 3D printed adaptor next to the TX-400 400 mL centrifuge bucket. The LED, sample holder, and objective are housed within the lens tubes that are mounted to the turning mirror support. (**e**) Photograph of the benchtop CFM module inside of a centrifuge with batteries and wires connected. (**f**) Details of the fiber rotary joint mounted to a custom adaptor then onto the benchtop centrifuge. Panels (**a**), (**b**), (**d**), (**e**), and (**f**) adapted from [16]

2.1 Centrifuge Force Microscope

1. Obtain microscope components listed in Table 1. The custom-fabricated turning mirror support (Item No. 17) can be obtained from a machine shop. Use epoxy glue to secure the

mirrors (Item No. 18) to the turning mirror support. A technical drawing of the turning mirror support can be downloaded from https://goo.gl/bClf9J.

2. Assemble the centrifuge force microscope following the mechanical assembly diagram (Fig. 1a, b). This compact microscope is based on the Thorlabs SM1 threaded lens tube system. Turning the lens tubes clockwise or counter-clockwise for tightening and loosening, respectively. Mount a red LED (Thorlabs, LED630E) to the LED mount (Item No. 1 in Table 1).
3. Solder pin #1 and #2 of a 12-pin Hirose connector (HIROSE, HR10A-10J-12S) to the ground and power of a DC-to-DC step-up circuit board (SparkFun, PRT-08290), respectively. In parallel to this circuit, solder a LED socket (Thorlabs, 8060-2) with a 68 Ω resistor on the power wire. The Hirose connector and the LED socket are used to power the camera and illuminating LED, respectively, once a lithium ion battery (SparkFun, PRT-0034) is connected to the input of the step-up circuit (Fig. 1c).
4. Solder the power input of an Ethernet-to-Fiber gigabit media converter (IMC Networks, 855-10734) to another DC-to-DC step-up circuit (SparkFun, PRT-08290) (Fig. 1c).
5. Use a 3D-printer to fabricate the enclosure made of acrylonitrile butadiene styrene (ABS) to secure and integrate the imaging and acquisition system inside the centrifuge bucket (Thermo Fisher Scientific, 75003655) (Fig. 1d). Print the enclosure to secure the Ethernet-to-Fiber gigabit media converter in another bucket (Fig. 1e). Include data and power cables passages and battery housing in the enclosure design. Place the media converter containing bucket adjacent to the CFM containing bucket. A technical drawing of the enclosure can be downloaded from https://goo.gl/bClf9J.
6. Use a 6-in. Ethernet cable to connect the camera to the media converter across the buckets (Fig. 1c, e).

2.2 Centrifuge Modification

1. Tap the four existing holes surrounding the center quick release button of the centrifuge rotor (Thermo Fisher Scientific, TX-400 4 × 400 mL Swinging Bucket Rotor, 75003181) to accept 10–32 screws (Fig. 1f). Custom fabricate fiber rotary joint adaptor mount and attach to the center of the centrifuge rotor utilizing the four threaded holes (Fig. 1f).
2. Remove the center viewing window on the centrifuge cover to allow optical data fiber pass through the centrifuge lid.
3. Attach the fiber optic rotary joint (PrinceTel, MJX-131-28-SC) to the custom adaptor mount (Fig. 1f). Connect the fiber cable

connector inside the centrifuge to the media converter (Fig. 1c, e). Connect the other end of the fiber optic cable connector to the computer through another media converter that converts the data signal into Ethernet connector.

4. Use counterweight to balance the mass and the center-of-mass of the counter centrifuge buckets. One option is to use metal coins stacked in a fitted 3D–printed enclosure (Fig. 1e).

2.3 DNA Nanoswitches

1. M13mp18 Single-stranded DNA, M13 ssDNA (New England Biolabs, N4040S).
2. Nuclease-free water: UltraPure™ DNase/RNase-Free Distilled Water (Thermo Fisher Scientific, 10977015).
3. 10× NEBuffer 2 (New England Biolabs, B7002S).
4. Synthetics oligonucleotide:
   (Sequence: 5′-CTACTAATAGTAGTAGCATTAACATCCAA-TAAATCATACA-3′).

   BtsCI restriction enzyme (New England Biolabs, R0647S).

2.4 Sample Chamber Assembly

1. Coverslips: Gold Seal 19 mm circle #1 (VWR, 100502-528).
2. Cleaning solution: Hellmanex III (Sigma-Aldrich, Z805939-1EA) in Milli-Q water to a final concentration of 1% (v/v).
3. Nitrocellulose coating solution: nitrocellulose membranes paper (Bio-Rad Laboratories, 1620150) in amyl acetate to a final concentration of 0.2% (w/v).
4. Support cover glass: custom 25 mm diameter, 1 mm thick circular (S.I. Howard Glass, B-270).
5. Double-sided Tape: double-sided polyimide Kapton tape (Kapton Tape, PPTDE-3).

2.5 Sample Chamber Surface Functionalization and Beads Tethering

1. Anti-digoxigenin (Roche Diagnostics, 11333089001).
2. Phosphate buffered saline, PBS, pH 7.4 (Thermo Fisher Scientific, 10010023).
3. Blocking reagent (Roche Diagnostics, 11096176001).
4. Centrifuge tube top filter (Millipore, SCGP00525).
5. Streptavidin Dynabeads, M-270 (Thermo Fisher Scientific, 65305).
6. Silicone grease (Sigma-Aldrich, Z273554-1EA).
7. Blunt needle tip (Instech, LS22).

3 Methods

The first part of this section describes the construction of DNA Nanoswitches, self-assembled mechanical switches that provide a well-defined molecular signature to identify the force-induced molecular rupture of a ligand-receptor pair [16]. Specifically, ligand and receptor molecules of interest are attached to specific locations of a linear DNA scaffold, with binding between the ligand and receptor resulting in an internally looped structure with a shorter overall tethering length than the linear scaffold. The well-defined change in tethering length from the looped to the linear structure (or vice versa) provides the quantitative signature of a molecular rupture (or binding) event. Moreover, the DNA Nanoswitch scaffold allows repeated measurement of the same molecular pair, which enables characterization of population heterogeneity. Subsequent subsections describe chamber assembly, surface preparation and bead tethering, and data collection and analysis.

3.1 Construction of DNA Nanoswitch

1. Linearize circular M13 ssDNA to make the DNA Nanoswitch scaffold. Mix 10 μL of 100 nM circular M13 ssDNA with a 38 μL mixture consisting of 32 μL of nuclease-free water, 5 μL of 10× NEBuffer 2, and 1 μL of 100 μM synthetic oligonucleotide complementary to the BtsCI restriction site.
2. Use a thermal cycler to bring the above mixture to 95 °C, hold for 30 s and then cool to 50 °C. Add 1 μL of the BtsCI enzyme and mix thoroughly. Incubate the mixture further at 50 °C for 1 h and then bring the temperature up to 95 °C for 1 min to heat deactivate the enzyme. This will result in 50 μL of 20 nM linearized DNA Nanoswitch scaffold in NEB Buffer 2. Make 5 μL aliquots of the linearized M13 and store at −20 °C till needed.
3. Based on the sequence map of M13mp18, obtain a set of 120 60-nt oligonucleotides and one 49-nt oligonucleotide that are complementary to the linearized M13 DNA scaffold. Among those, select the first and last 60-nt regions at the ends of the scaffold to be the tethering handle attachments and two additional specific regions that are at least 3000 nt apart to attach the ligand and receptor molecules (*see* **Note 1**). A more detailed protocol is described previously in the supplemental protocol of ref. 19.
4. Leave out the handle attachments, ligand, and receptor oligonucleotides. Create a complementary tiling oligonucleotide mixture consisting of the remaining 117 oligonucleotides, at equal molar concentration and total oligonucleotide concentration of 100 μM. Store the mixture at −20 °C till needed. A more detailed protocol is described previously in the supplemental protocol of ref. 19.

5. Create a handle attachment oligonucleotide mixture by mixing 1 μL of 100 μM of digoxigenin- and biotin-functionalized tethering oligonucleotides and diluting to 100 μL with nuclease-free water. Store the mixture at −20 °C till needed.
6. Mix 5 μL of 20 nM linearized DNA Nanoswitch scaffold (from **step 2**) with 1.17 μL of the complementary tiling oligonucleotide mixture (from **step 4**) and 0.5 μL of the handle attachment oligonucleotide mixture (from **step 5**). Use a thermal cycler to heat the mixture to 90 °C for 1 min then cool the sample 1 °C/min until it reaches 20 °C. This will result in 6.67 μL of ~15 nM biotin and digoxigenin-functionalized M13 scaffold with two single-stranded regions for ligand and receptor attachment. The mixture can be stored at 4 °C for up to 2 weeks or −20 °C for long term storage.
7. Covalently attach the molecules of interest to the ligand and receptor oligonucleotides using chemical attachment strategies such as SMCC, click chemistry, EDC, sortase-based conjugation [20] etc., or utilizing commercially available oligonucleotide conjugation kits (*see* **Note 1**).
8. Hybridize ligand- and receptor-coupled oligonucleotides at a 1.25 M excess to the M13 scaffold at a final M13 concentration of 250 pM in the experimental buffer at room temperature for 1–2 h (*see* **Note 2**).

3.2 Sample Chamber Assembly

1. Submerge coverslips loaded in a coverslip rack in cleaning solution. Use the microwave oven to heat up the solution to a gentle boil, then use a bath sonicator to sonicate for 30 min. Rinse the coverslips thoroughly with Milli-Q water then dry with nitrogen gas flow.
2. Coat one side of the cleaned and dried coverslips with 1 μL of nitrocellulose coating solution using the side of a pipette tip. Bake the nitrocellulose-coated coverslips in an 80 °C oven for 5 min.
3. Drill two 0.75 mm diameter holes, 10 mm apart, on support cover glass for flow chamber inlet and outlet ports (*see* **Note 3**).
4. Cut a rectangle (1×10 mm^2) of flow cell pattern with rounded edges centered in a 25 mm diameter circle on a double-sided tape using cutting plotter (*see* **Note 4**).
5. Sandwich the tape between the nitrocellulose-coated coverslip and support cover glass with the fluid ports aligned to the edges of the flow channel. Use a soft plastic pipette tip or cotton swap to seal the tape. Be gentle pressing over the flow channel region which can be easily cracked. The assembled flow chamber can be stored under vacuum at room temperature for up to a month.

3.3 Sample Chamber Surface Functionalization and Beads Tethering

1. Dissolve 200 μg of anti-digoxigenin antibody with 1 mL of PBS to the final concentration (0.2 mg/mL). Centrifuge the reconstituted anti-digoxigenin at 13,000 × *g* for 5 min. Make 100 μL aliquots of the supernatant and store at 4 °C for up to 6 months.
2. Add 500 mg of blocking reagent to 50 mL of PBS to make the blocking solution. Autoclave (121 °C, 20 min) the mixture to dissolve the blocking reagent. Use a centrifuge tube top filter to remove the undissolved particles. Add sodium azide (0.02%, w/v) to prevent bacterial growth. Make 1.5 mL aliquot and store at −20 °C for up to 1 year. Use a fresh aliquot for each experiment.
3. Incubate the flow channel with anti-digoxigenin by adding in 20 μL of anti-digoxigenin solutions (0.1 mg/mL in PBS) for 30 min. Wash the channel with 20 μL of PBS two times. All incubation steps are done at room temperature under humidified conditions, i.e. in a glass petri dish with wet Kimwipes. Avoid pipetting air-bubble into the flow channel. Throughout the protocol, use Kimwipes to soak up the fluid from the outlet.
4. Incubate the flow channel with blocking solution for 1 h by flowing in 20 μL of blocking solution every 20 min.
5. Wash the flow channel with 20 μL of the experimental buffer two times after the blocking step. If the channel contains air bubbles flush the channel with 30–60 μL of experimental buffer (*see* **Note 5**).
6. Incubate the flow channel with 100 pM of functionalized DNA Nanoswitch construct for 30 min. Wash the channel with 20 μL of experimental buffer two times after the DNA Nanoswitch attachment (*see* **Note 6**).
7. Prepare 5 μL of Streptavidin Dynabeads per sample. First wash the beads with 50 μL of blocking solution, vortex for 10 s, and use a magnetic sample rack to exchange solution. Carry out this step twice. Then wash the beads with 50 μL experimental buffer five times. Resuspend the beads with 5 μL of experimental buffer per sample (*see* **Note 7**).
8. Pipette ~1–2 μL of the washed beads into the flow channel. Stop the pipetting flow immediately when the channel is filled with beads. Seal the flow inlet and outlet by injecting silicone grease using a syringe with a blunt needle tip (*see* **Note 8**).
9. Let the beads contacting the DNA-functionalized glass surface for 1 min. If the sample is to be measured in more than 5 min, flip and orient the flow chamber such that the beads are being pulled from the DNA-functionalized glass surface by gravity force. The nontethered beads will be pulled away from the surface as well (*see* **Note 9**).

3.4 Data Collection and Analysis

Here we describe how to carry out experiments using the CFM instrumentation and DNA Nanoswitch samples, and how to analyze the resulting microscopy videos to identify and validate force-induced molecular rupture events by using the molecular signature afforded by the Nanoswitch constructs.

3.4.1 Sample Mounting and CFM Operation

1. Mount the sealed sample chamber (shown as Item No. 6–8 in Table 1 and *see* Fig. 1a) in the sample holder (Item No. 5 and 9 in Table 1 and *see* Fig. 1a). Attach the LED illumination assembly (Item No. 1–3 in Table 1 and *see* Fig. 1a) to the sample holder.
2. Mount the sample holder with the LED illumination assembly to the focusing tube (Item No. 10 in Table 1 and *see* Fig. 1a).
3. Attach the LED socket to the LED. Connect the battery to the step-up circuit that powers the camera and LED. Connect another battery to the media converter in the adjacent bucket.
4. With the LED and camera powered and the signal connected to the computer through the fiber-optic rotary joint, use the focusing tube (Item No. 10 in Table 1 and *see* Fig. 1a) to bring the tethered beads to focus. Live images can be acquired using the VIMBA software (Allied Vision) or customized LabVIEW software (National Instrument). Use the retaining ring (Fig. 1b) to secure the focus.
5. Place the CFM within the 3D printed adaptor and carefully place it in the centrifuge bucket.
6. Spin the rotor by hand to make sure centrifuge spinning is not obstructed by electrical wiring and no sign of imbalance. Close the centrifuge lid.
7. If your centrifuge includes the option for computer control, use the software provided by the centrifuge manufacturer to set the desired acceleration and rotational speed profile. Our Heraeus X1R centrifuge can be controlled using WinMass (Thermo Fisher Scientific), which also records the measured speed of rotation. If computer control is not available, simply control the operation of the centrifuge manually using the standard front-panel interface. Record the camera-acquired images during centrifugation using software provided by the camera manufacturer or customized LabVIEW (National Instrument) software.

3.4.2 Data Analysis of DNA Nanoswitch Rupture

With this particular CFM design based on the TX-400 rotor, the angle of the centrifuge swing bucket does not swing up to the full 90° with respect to the axis of rotation, resulting in a component of the centrifugal force directed in the x–y image plane (Fig. 2a). Furthermore, the off-radial orientation of the CFM will also result in a force component in the x–y plane (Fig. 2d). As the rotational

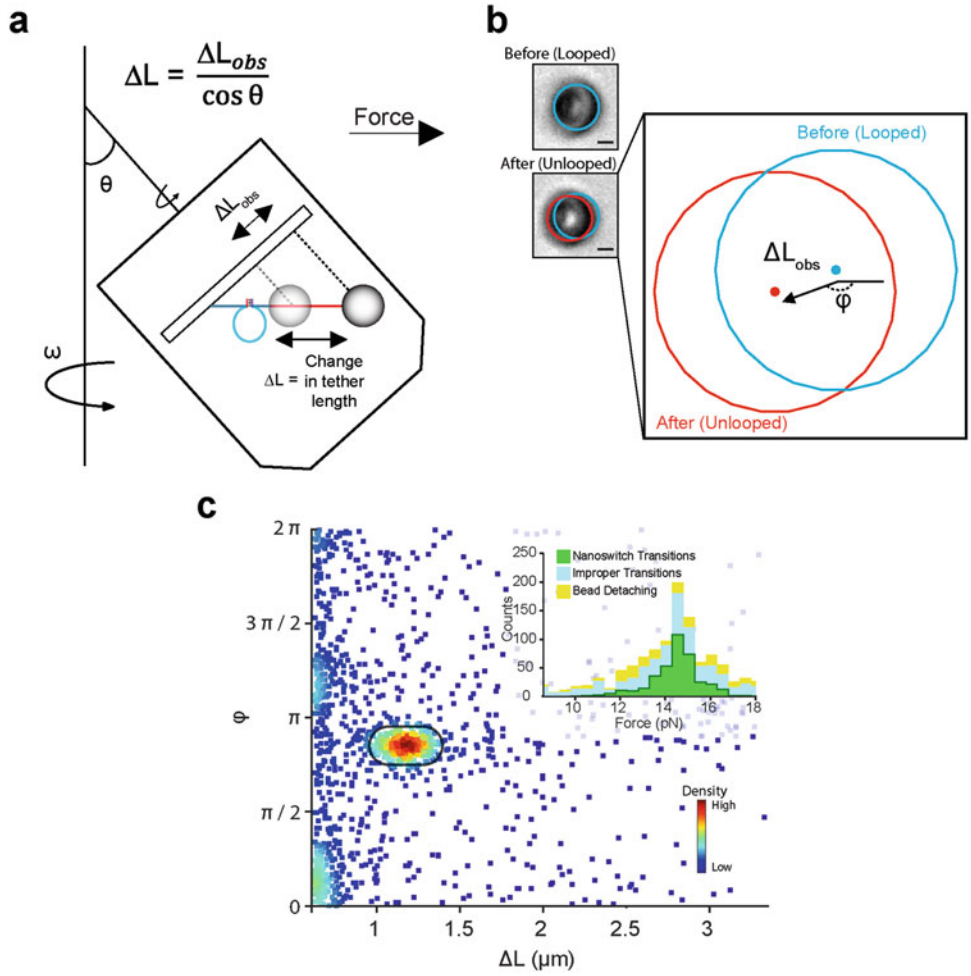

Fig. 2 Analysis of DNA Nanoswitch unlooping. (**a**, **b**) When the centrifuge bucket is at angle θ, the centrifugal force has components in both perpendicular and parallel directions to the sample surface (*x*–*y* plane). When the bond is ruptured, the DNA Nanoswitch goes from looped (*blue*) to unlooped (*red*) that leads to a change in length ΔL. This is identified by measuring the projected change in length in the *x*–*y* plane $\Delta L_{obs} = \Delta L/\cos\theta$. The orientation of the miniCFM in the bucket also sets the direction of ΔL_{obs}. (**c**) A scatter plot of all contour length changes detected for all directions. The transitions within the boxed region are accepted as nanoswitch transitions. A histogram of transition forces for three different types of transitions: beads which leave the surface (*yellow*), beads which display discontinuous transition with (*green*) and without (*light-blue*) correct direction and magnitude is shown as insert. Figure adapted from [16]

speed of the CFM increases, the looped DNA tethers will be continuously extended. The opening of the loop is identified as a discontinuous change in the extension (Fig. 2b).

1. Use the function "imfindcircles" in Matlab (Mathworks) to identify the beads.
2. Store a template image for each bead. To identify the bead position in the subsequent frame, use the template image to

scan in the *x*–*y* plane to find the position of maximum correlation.

3. Take the median position change in *x* and *y* for all beads being tracked from frame to frame as the reference to correct drift in the *x*–*y* plane during the course of the experiment. This drift correction is sufficient for identifying the DNA Nanoswitch looped-to-unlooped transition.
4. Identify the DNA Nanoswitch transition by filtering out all bead trajectories except those that contain a discontinuous change in extension with both the correct magnitude and direction (Fig. 2c).
5. Convert the frame at which the DNA Nanoswitch transition occurs into time or force for subsequent data analysis.

4 Notes

1. Ligand and receptor molecules localized on the DNA scaffold should be at least 3000 nt apart so that an internal loop around 1 μm in length is made when the ligand binds to the receptor. This will provide a very clear signature for identifying bond rupture events.
2. The efficiency of the hybridization process of the ligand- and receptor-coupled oligonucleotides to the M13 scaffold can be improved by incubation at a higher temperature that melts the internal secondary structure of the oligonucleotides. If the ligand or receptor molecule is sensitive to the elevated temperature, the oligonucleotide and its complementary target region should be free of internal secondary structure so that the hybridization can be carried out at room temperature or below.
3. Mechanical drilling of the inlet and outlet ports using a drill press and diamond-coated bit can often crack the glass or produce uneven cylindrical port. One solution is to bind the circular support glass to a 1 mm thick microscope slide (VWR, 16005-106) with a thin layer of melted natural rosin (D'Addario, VR200) using a heat plate. The drilling should also be carried out slowly with a layer of water between the drill bit and glass. After the holes are drilled, the support glass can be removed from the microscope slide by soaking in acetone solution.
4. We use a Graphtech cutting plotter, model CE5000, to cut out a flow channel on the double-sided Kapton tape. The cutting can also be done using smaller desktop size cutting plotter or by hand. Secure the double-sided Kapton tape using other tapes on

a cutting mat (VWR, 14222-832) with one adhesive side facing up during cutting.

5. To avoid pipetting air-bubbles into the flow channel, use the reverse pipetting technique. Load an excess amount of solution into the pipette tip by press the knob to the second stop to load. Dispense the solution into the flow channel by pressing the pipette knob only to the first stop. Discard the tip containing the excess solution.
6. Control experiments should be carried out to verify the surface passivation and tethering efficiency. Negative controls such as sample preparation without anti-digoxigenin surface activation, DNA Nanoswitch incubation, biotin- and digoxigenin-DNA functionalization, etc., should be performed to ensure that the beads are tethered through specific interaction and not nonspecifically sticking. To limit multiple tethers on each bead, either utilize the DNA as the limited component to ensure that the spacing of each immobilized DNA is larger than the bead size, or perform a DNA concentration series to measure the concentration range in which the number of tethered beads is linearly dependent.
7. Adjust the resuspension volume if necessary to achieve 60–70% bead surface coverage during the bead tethering step.
8. Avoid creating air-bubbles at the fluid–grease interface. Make sure the fluid ports are filled with solution and create a small dab of vacuum grease at the needle tip prior to injecting the grease into the channel.
9. The sample can also be stored at 4 °C overnight with the tethered beads hanging down under gravitational force to avoid beads from nonspecifically sticking to the surface. Avoid any strong magnetic fields and mechanical impacts on the sample.

Acknowledgement

W.P.W. acknowledges support from the Arnold and Mabel Beckman Foundation through the Beckman Young Investigator Award, US National Institutes of Health NIGMS R21 RGM107907A and R35 GM119537, the Wyss Institute at Harvard University and Boston Children's Hospital startup funds.

References

1. Bustamante C, Cheng W, Meija YX (2011) Revisiting the central dogma one molecule at a time. Cell 144(4):480–497. doi:10.1016/j.cell.2011.01.033
2. Neuman KC, Nagy A (2008) Single-molecule force spectroscopy: optical tweezers, magnetic tweezers and atomic force microscopy. Nat

Methods 5(6):491–505. doi:10.1038/Nmeth.1218

3. Ritort F (2006) Single-molecule experiments in biological physics: methods and applications. J Phys Condens Matter 18(32):R531–R583. doi:10.1088/0953-8984/18/32/R01
4. Neuman KC, Block SM (2004) Optical trapping. Rev Sci Instrum 75(9):2787–2809. doi:10.1063/1.1785844
5. Svoboda K, Block SM (1994) Biological applications of optical forces. Annu Rev Biophys Biomol Struct 23:247–285. doi:10.1146/annurev.bb.23.060194.001335
6. Bustamante CJ, Kaiser CM, Maillard RA, Goldman DH, Wilson CAM (2014) Mechanisms of cellular proteostasis: insights from single-molecule approaches. Annu Rev Biophys 43:119–140. doi:10.1146/annurev-biophys-051013-022811
7. Sitters G, Kamsma D, Thalhammer G, Ritsch-Marte M, Peterman EJG, Wuite GJL (2015) Acoustic force spectroscopy. Nat Methods 12(1):47–50
8. Soltani M, Lin J, Forties RA, Inman JT, Saraf SN, Fulbright RM, Lipson M, Wang MD (2014) Nanophotonic trapping for precise manipulation of biomolecular arrays. Nat Nanotechnol 9(6):448–452. doi:10.1038/Nnano.2014.79
9. Limmer K, Pippig DA, Aschenbrenner D, Gaub HE (2014) A force-based, parallel assay for the quantification of protein-DNA interactions. PLoS One 9(2):e89626. doi:10.1371/journal.pone.0089626
10. De Vlaminck I, Henighan T, van Loenhout MTJ, Pfeiffer I, Huijts J, Kerssemakers JWJ, Katan AJ, van Langen-Suurling A, van der Drift E, Wyman C, Dekker C (2011) Highly parallel magnetic tweezers by targeted DNA tethering. Nano Lett 11(12):5489–5493. doi:10.1021/Nl203299e
11. Fazio T, Visnapuu ML, Wind S, Greene EC (2008) DNA curtains and nanoscale curtain rods: high-throughput tools for single molecule imaging. Langmuir 24(18):10524–10531. doi:10.1021/La801762h
12. Ribeck N, Saleh OA (2008) Multiplexed single-molecule measurements with magnetic tweezers. Rev Sci Instrum 79(9):094301. doi:10.1063/1.2981687
13. Kim SJ, Blainey PC, Schroeder CM, Xie XS (2007) Multiplexed single-molecule assay for enzymatic activity on flow-stretched DNA. Nat Methods 4(5):397–399. doi:10.1038/Nmeth1037
14. Assi F, Jenks R, Yang J, Love C, Prentiss M (2002) Massively parallel adhesion and reactivity measurements using simple and inexpensive magnetic tweezers. J Appl Phys 92(9):5584–5586. doi:10.1063/1.1509086
15. Halvorsen K, Wong WP (2010) Massively parallel single-molecule manipulation using centrifugal force. Biophys J 98(11):L53–L55. doi:10.1016/j.bpj.2010.03.012
16. Yang D, Ward A, Halvorsen K, Wong WP (2016) Multiplexed single-molecule force spectroscopy using a centrifuge. Nat Commun 7:11026
17. Halvorsen K, Schaak D, Wong WP (2011) Nanoengineering a single-molecule mechanical switch using DNA self-assembly. Nanotechnology 22(49):494005. doi:10.1088/0957-4484/22/49/494005
18. Hoang T, Patel DS, Halvorsen K (2016) A wireless centrifuge force microscope (CFM) enables multiplexed single-molecule experiments in a commercial centrifuge. Rev Sci Instrum 87(8):083705
19. Koussa MA, Halvorsen K, Ward A, Wong WP (2015) DNA nanoswitches: a quantitative platform for gel-based biomolecular interaction analysis. Nat Methods 12(2):123–126
20. Koussa MA, Sotomayor M, Wong WP (2014) Protocol for sortase-mediated construction of DNA–protein hybrids and functional nanostructures. Methods 67(2):134–141

INDEX

Erwin J.G. Peterman (ed.), *Single Molecule Analysis: Methods and Protocols*, Methods in Molecular Biology, vol. 1665, DOI 10.1007/978-1-4939-7271-5, © Springer Science+Business Media LLC 2018

G

H

I

J

K

L

M

N

O

P

Q

R

S

T

U

W

Y